Biochemical and Biophysical Research Communications 420 (2012) 1–5

Contents lists available at SciVerse ScienceDirect

Biochemical and Biophysical Research Communications

journal homepage: www.elsevier.com/locate/ybbrc

Floating assembly of diatom *Coscinodiscus* sp. microshells

Yu Wang, Junfeng Pan, Jun Cai, Deyuan Zhang *

Bionic and Micro/Nano/Bio Manufacturing Technology Research Center, School of Mechanical Engineering and Automation, Beihang University, XueYuan Road No. 37, Beijing 100191, PR China

ARTICLE INFO

Article history:
Received 9 February 2012
Available online 24 February 2012

Keywords:
Nanopores
Buoyancy test
AFM
Micro-range attractive forces
Self-assembly monolayer
Nanotechnology

ABSTRACT

Diatoms have silica frustules with transparent and delicate micro/nano scale structures, two dimensional pore arrays, and large surface areas. Although, the diatom cells of *Coscinodiscus* sp. live underwater, we found that their valves can float on water and assemble together. Experiments show that the convex shape and the 40 nm sieve pores of the valves allow them to float on water, and that the buoyancy and the micro-range attractive forces cause the valves to assemble together at the highest point of water. As measured by AFM calibrated glass needles fixed in manipulator, the buoyancy force on a single floating valve may reach up to 10 μN in water. Turning the valves over, enlarging the sieve pores, reducing the surface tension of water, or vacuum pumping may cause the floating valves to sink. After the water has evaporated, the floating valves remained in their assembled state and formed a monolayer film. The bonded diatom monolayer may be valuable in studies on diatom based optical devices, biosensors, solar cells, and batteries, to better use the optical and adsorption properties of frustules. The floating assembly phenomenon can also be used as a self-assembly method for fabricating monolayer of circular plates.

1. Introduction

Diatoms are unicellular and photosynthetic microalgae found everywhere in fresh and seawater [1]. They range in size from 2 to 2000 μm and form thousands of different morphologies [2]. Frustules, which are the rigid cell walls of diatoms [3,4], have transparent structures composed of amorphous silica. They have arrays of large pores (foramen) on their outer or inner surfaces and myriad sieve pores of about 40 nm for exchanging nutrients and gases [5]. The porous structure also increases the surface area of the frustules (>200 m^2/g). In addition, the biosilica structure has special optical effects, such as photoluminescence (PL) and light gather ability [6,7].

Over the last two decades, an increasing number of studies began examining the unique structures and properties of frustules to produce diatom-based materials and micro devices that are superior to current products. The reported studies on diatom frustules include characterization and tests of architecture [3–5,8,9], exploitation of physical and chemical properties [6,7,10], methods of structure separation and modification [11–15], processes of material modification [16–22], and so on. Excellent reviews focusing on the potential of diatoms in microfluidic applications (filtration and drug delivery), biosensors (bio carrier and gas sensor), solar cells, and batteries are available [23–25]. In these studies, the valves (also called microshells) of the diatom *Coscinodiscus* sp. are frequently used for their multilevel pores that are well arranged in a two-dimensional plane, unique optical properties, large size, and flat surface, which make them easy to arrange and fix [26,27].

Although the diatom cells of *Coscinodiscus* sp. live underwater, we found that their valves can float on water and assemble together. In the present paper, the reasons behind and the essential conditions for the floating assembly are explored, the buoyancy forces of the valves in water and ethanol solution are tested; and a monolayer film of valves fixed on glass or polydimethylsiloxane (PDMS) surface is obtained.

2. Materials and methods

2.1. Acid clean of diatom frustules

The cultivated *Coscinodiscus* sp. diatoms were obtained from Xiamen University. Prior to the experiments, residual organic materials and metal oxides were removed by heating the diatoms, which were mixed with adequate amounts of H_2SO_4 at 80 °C for 20 min. The mixture was filtered through a polytetrafluoroethylene filter cloth to remove micro-impurities and frustule debris. The residual mixture on the filter cloth (clean frustules) was fully washed with deionized water until pH = 7 and then dried at 80 °C.

2.2. Observation of particles distribution on water droplet

Deionized water (20 μL) was added to a flat glass/PDMS surface to form a droplet. A few clean frustules of diatom *Coscinodiscus* sp.

* Corresponding author. Fax: +86 1082316603.
E-mail address: zhangdy@buaa.edu.cn (D. Zhang).

0006-291X/$ - see front matter © 2012 Elsevier Inc. All rights reserved.
doi:10.1016/j.bbrc.2012.02.080

were added to the water droplet. A light microscope was used to observe the frustules floating on water and the frustules settled at the bottom of the water. A glass needle or a pipettor was used to stir the water droplet for observing the change of the floating frustules.

2.3. Buoyancy test of the floating valves

The buoyancy of the floating diatom valves in water and ethanol solution was tested with glass needles and manipulator. A thick glass needle with a terminal diameter of 60 μm was fixed vertically in a manipulator to press on a single floating valve until the valve began to sink. The vertical displacement of manipulator d equals the maximum depth of the floating valve D (see Fig. 1A). The displacement of manipulator d can be read by software, so the maximum depth D can be measured. Then, a thin and flexible glass needle with a terminal diameter of 15 μm was horizontally fixed in a manipulator to press a single floating valve until it sank. The vertical displacement of manipulator d equals the maximum depth D plus the needle deformation (see Fig. 1B). The thin glass needle have a deformation coefficient of $k = 80.15$ nN μm^{-1}, as calibrated by atomic force microscopy. The buoyancy force F of a single valve can be calculated through the equation: $F = k\cdot(d-D)$.

2.4. Floating phenomenon of valves on vacuum condition

A total of 10 centrifuge tubes with a capacity of 2 mL were each filled with 1.5 mL of deionized water and each had 10–100 floating valves. The centrifuge tubes were slowly pumped using a vacuum pump, and then kept under vacuum state for 15–45 min. Deflation was also conducted slowly. Compare the quantity of floating valves before and after vacuum pumping.

2.5. Floating phenomenon of valves on pores enlarging condition

Hydrofluoric acid (HF) can be used to etch frustules and their pores [13]. HF droplets with different concentrations (0.5/1/10%) were used to redo the floating experiment. Observe the quantity change of the floating valves.

2.6. Control experiment using agarose coated diatomite

Another type of *Coscinodiscus* valves obtained from diatomite (C292, Celite) was used for the control experiment. The diatomite valves have diameters of ~40 μm and flatter shapes (not fully convex or concave, see Fig. S1 in Supplemental figures). Prior to the experiment, the valves were modified with 1.2% agarose to cover their sieve pores and large pores (see Fig. S2 in Supplemental figures), because the sieve pores were damaged after thousands of years of being buried under the earth and calcination in a factory.

3. Results and discussion

3.1. SEM observation of clean Coscinodiscus frustules

Fig. 2 shows the clean diatom frustules of *Coscinodiscus* sp. This type of centric diatom has round valves and girdles that are ~80 μm in diameter (Fig. 2A and D). As shown in Fig. 2A, the exterior of the valve has a convex shape, where sieve pores that are ~40 nm in diameter can be seen [5] (Fig. 2C). Fig. 2D shows the concave internal surface of the valve, where a regular pattern of large pores (called foramen) can be seen.

3.2. Floating assembly of diatom valves

When a few clean frustules of diatom *Coscinodiscus* sp. were added to a water droplet, some white powders quickly assembled at the highest point of the droplet and formed a compact film, which can be seen by the naked eye. Fig. 3A shows the floating film comprising frustules under a microscope. We observed that the floating frustules are mostly valves, and that their convex surface (external surface with sieve pores) contact with water like floating boats. Fig. 3B shows that the particles distributed at the bottom of

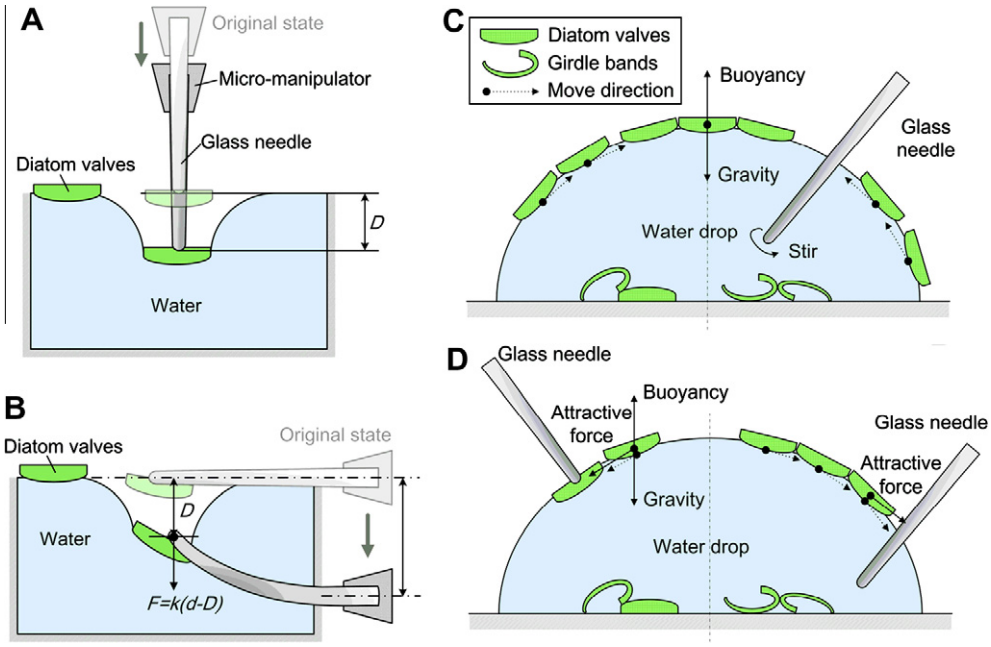

Fig. 1. Schematic illustrations of the buoyancy test and particles operation using glass needles. (A) Maximum depth test using a thick and rigid glass needle; (B) maximum buoyancy test using a thin and flexible glass needles; (C) movement trends of the floating valves after the water droplet is stirred; and (D) attractive force between valves and glass needles.

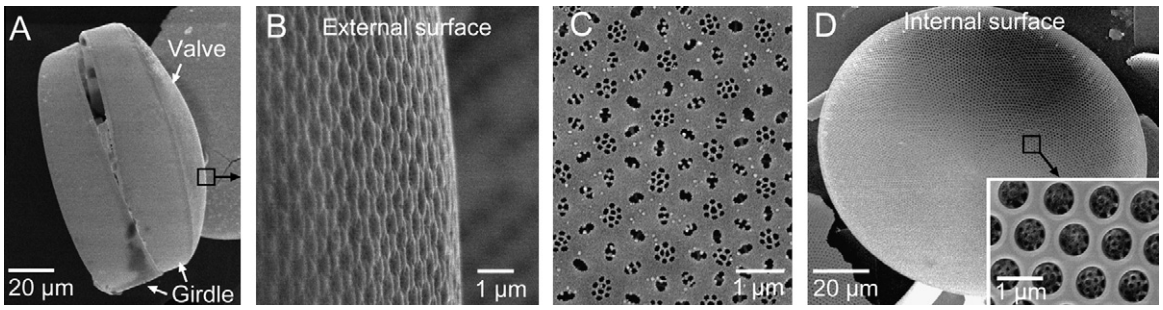

Fig. 2. Diatom frustules of *Coscinodiscus* sp. after acid clean: (A) complete frustule, (B) external surface, (C) sieve pores on external surface, and (D) internal surface and pattern of large pores.

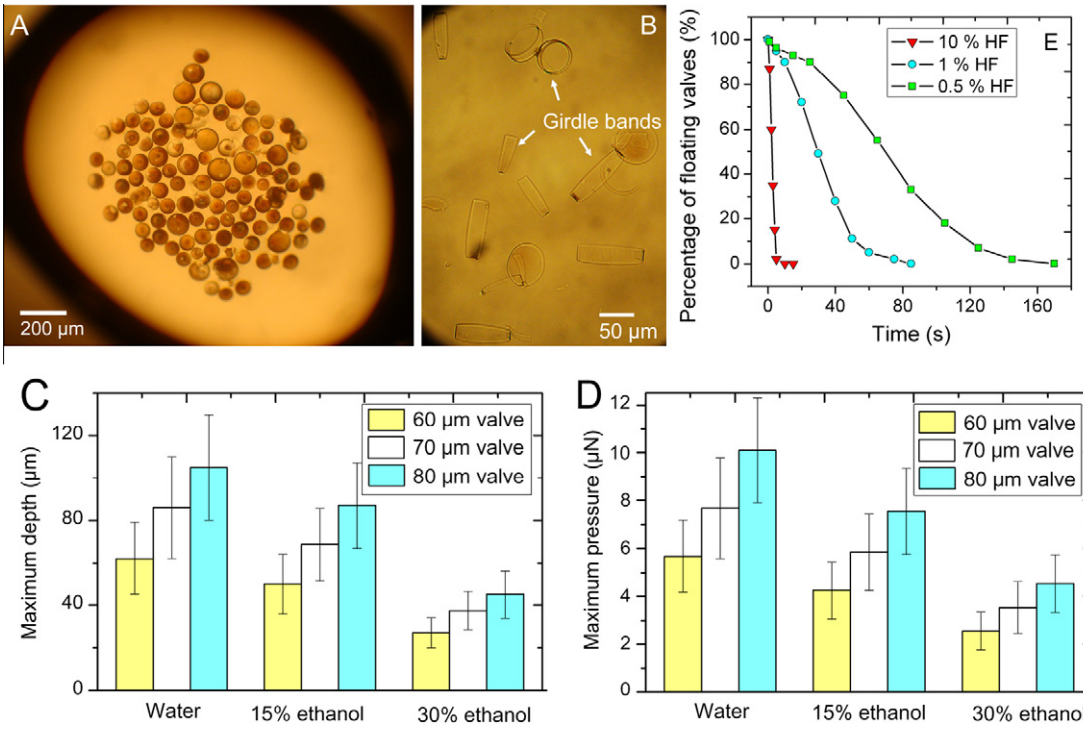

Fig. 3. Floating phenomenon of diatom valves on surface of water, ethanol solution and HF solution. Microscopic images of *Coscinodiscus* frustules distributed (A) on the surface of the water droplet and (B) at the bottom of the water droplet. (C and D) shows the results of buoyancy test of floating valves in water and in ethanol solution: (C) shows the maximum depth that a single floating valve can reach, and (D) shows the buoyancy force of a single valve. (E) Percent change of the floating valves versus time in HF droplet.

the water droplet are primarily girdle bands (>80%) and a few valves.

By stirring the water droplet using a glass needle or a pipettor, the floating valves drifted apart and then assembled again shortly at the highest point (see Video 1 in Supplementary information). As shown in Fig. 1C, a type of buoyancy force causes the valves to move toward the highest point. Video 2 shows that an attractive force exists between the diatom valves and the valve-glass needle, attracting each other within a very short range of ~100 μm and even causing the valves to drift apart at the highest point (Fig. 1D). Hence, "buoyancy" and this attractive force may work together to cause the valves to float on water and assemble into a compact film.

3.3. Reason and condition for the floating of valves

We attempt to discuss the reason and the condition for the "buoyancy force". The valves were added to a beaker fully filled with water, and then stored for 72 h. During this period the quantity of the floating valves did not change, indicating that floating is a stable state. The valve is composed of hydrated silica ($SiO_2{\cdot}xH_2O$), the density ($\sim 2.1 \times 10^3$ kg m^{-3}) of which is greater than that of water. Moreover, the myriad sieve pores across the valve increase the surface area of the valve and make the valve hydrophilic. However, the floating phenomenon indicates that water must not enter or pass through the sieve pores and fill the inner space of valve, which may cause the valve to sink. Hence, the tension coefficient of the liquid and the size of sieve pores seem to be the key factors.

The tension coefficient of the liquid affects the floating of the valves. When added to anhydrous ethanol, all the valves immediately sank. The tension coefficient of water is 72.75 mN m^{-1}, whereas that of anhydrous ethanol is 22.32 mN m^{-1}, which does not have sufficient surface energy to keep the sieve pores vacant.

Videos 3 and 4 show the buoyancy test of the valves in water and in 30% ethanol, respectively. Figs. 3C and D show the maximum depth and buoyancy of different valves in water and in ethanol solution, respectively. The results show that a floating valve with a diameter of 80 μm can reach a floating depth of 105 μm

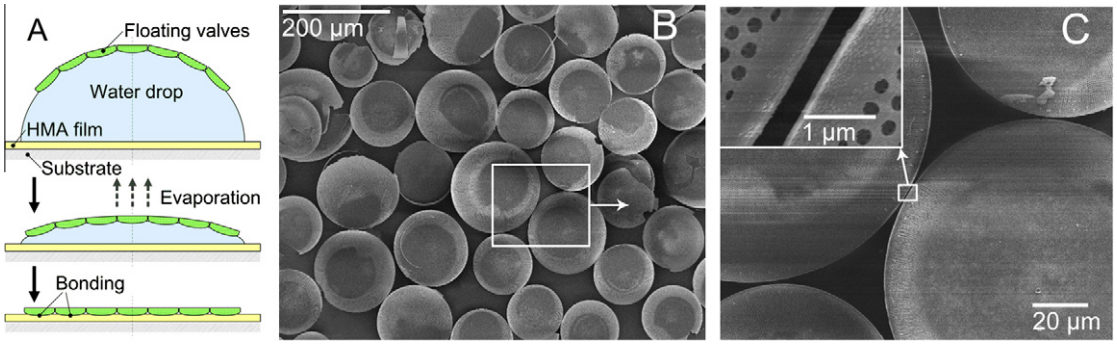

Fig. 4. Self-assembly monolayer film of valves fixed on glass surface: (A) schematic diagram of the forming of the valve monolayer film. Due to the micro-range attractive force between valves, the floating valves maintained their assembly state during evaporation. (B) SEM images of the valve monolayer fixed on glass surface and (C) contact points of adjacent valves.

and bear a pressure of 10 μN in water, whereas these values decrease to 45 μm and 4.54 μN, respectively, in 30% ethanol.

The degree of vacuum also affects the floating of the valves. Comparing the quantity of floating valves before and after vacuum pumping, we found that the floating valves were reduced by 12–18% after 15 min in vacuum and that no valves floated on water after 45 min in vacuum. This result shows that water enters sieve pores more easily at a very low air pressure.

Finally, the size of the sieve pores affects the floating of the valves. The sieve pores of diatom valves fast enlarged in HF solution and the cribellum layer was destroyed, which may result in the sinking of valves. Video 5 shows the sinking of valves in 1% HF solution, and Fig. 3E shows the results. At 0.5% and 1% HF concentration, most of the valves sank in 145 s and 69 s, respectively, whereas at 10% HF concentration, they all sank in 5 s. These results indicate that sustained enlargement of sieve pores will finally result in the injection of water and sinking of the valves, and the valves with no complete cribellum and only large pores of ~1 μm diameter will not float on water.

Moreover, the convex shape is necessary for the floating of the valves. Turning the floating valve over with a glass needle will cause the valve to sink, indicating that a concave surface will not keep the valve afloat. The control experiment shows that the valves of diatomite *Coscinodiscus* (not fully convex or concave, see Fig. S1 in Supplemental figures) would not float on water even when their pores were covered. Acid cleaned valves of *Nitzschia* sp. have a flat valve (see Fig. S3 in Supplemental figures), and can hardly float on water as well (only 3–7% of the valves floated on water). These results indicate that a convex surface is important for the floating of valves.

3.4. Self-assembly monolayer film of Coscinodiscus valves

Self-assembly, primarily studies the methods for arranging nano-/micro-/mesoscale objects with uniform sizes and structures, such as spheres, rods, and polyhedrons [28–30]. The valves of *Coscinodiscus* sp. have irregular round plates and non-uniform sizes, which are difficult to arrange using existing self-assembly methods. We observed that the floating valves maintained their assembly state after the water has evaporated, regardless of the glass or PDMS surface, mainly due to the micro-range attractive force between valves (see Fig. 4A). The compact monolayer film of the valves can be fixed onto any surface with hot melt adhesive (HMA) or chemically bonded onto a PDMS surface [26].

Fig. 4B shows the SEM images of a monolayer film fixed on a glass surface with HMA. Adjacent valves assemble near each other and stacking of valves seldom occurs (Fig. 4C). Hence, the floating assembly can be used as a simple self-assembly method to form a monolayer film. For frustules which hardly float on water, octadecyltrichlorosilane can be used to improve their hydrophobicity and make them float and assemble. The details will be discussed in another publication.

3.5. Summary and potential use

As discussed above, the valves of diatom *Coscinodiscus* sp. can float on water because of their convex shape and 40 nm sieve pores. The buoyancy and the micro-range attractive force cause the valves to assemble together at the highest point of water. Turning the valves over, enlarging the sieve pores, reducing the surface tension of the liquid, or vacuum pumping all cause the floating valves to sink. The buoyancy of a single floating valve can reach up to 10 μN in water. Hence, the floating valves, which are easily attracted by other objects, such as valves and glass needles, may have potential use in some microfluidic chips, for the transport of substances or for analysis. After the evaporation of water, the floating valves maintained their assembled state and formed a monolayer film. The valve monolayer can be fixed onto a glass or a PDMS surface. This fixed compact monolayer of diatom micro shells is valuable in recent studies on diatom devices, such as optical devices, diatom-based biosensors, solar cells, and batteries, to better use the optical and adsorption properties of diatom frustules. The floating assembly also can be used as a self-assembly method to fabricate monolayer films of irregular micro scale plates with non-uniform sizes, because certain modification methods are available to make the plates float.

Acknowledgments

This work was supported by the National Science Foundation of China (No. 50805005, 51075020), the 863 Project of China (No. 2009AA043804), the National Special Fund of Outstanding Doctoral Dissertation of China (No. 2007B32) and the Doctoral Candidate Academic Newcomer Award of Beihang University.

Appendix A. Supplementary data

Supplementary data associated with this article can be found, in the online version, at doi:10.1016/j.bbrc.2012.02.080.

References

[1] F.E. Round, R.M. Crawford, D.G. Mann, The Diatoms: Biology and Morphology of the Genera, Cambridge University Press, Cambridge, 1990.

[2] A. Bozarth, U.-G. Maier, S. Zauner, Diatoms in biotechnology: modern tools and applications, Applied Microbiology and Biotechnology 82 (2009) 195–201.

[3] D. Losic, K. Short, J.G. Mitchell, R. Lal, N.H. Voelcker, AFM nanoindentations of diatom biosilica surfaces, Langmuir 23 (2007) 5014–5021.
[4] C.E. Hamm, R. Merkel, O. Springer, P. Jurkojc, C. Maier, K. Prechtel, V. Smetacek, Architecture and material properties of diatom shells provide effective mechanical protection, Nature 421 (2003) 841–843.
[5] D. Losic, G. Rosengarten, J.G. Mitchell, N.H. Voelcker, Pore architecture of diatom frustules: potential nanostructured membranes for molecular and particle separations, Journal of Nanoscience and Nanotechnology 6 (2006) 982–989.
[6] L. De Stefano, I. Rendina, M. De Stefano, A. Bismuto, P. Maddalena, Marine diatoms as optical chemical sensors, Applied Physics Letters 87 (2005) 233902–233903.
[7] L. De Stefano, I. Rea, I. Rendina, M. De Stefano, L. Moretti, Lensless light focusing with the centric marine diatom *Coscinodiscus walesii*, Optics Express 15 (2007) 18082–18088.
[8] M. De Stefano, L. De Stefano, R. Congestri, Functional morphology of micro- and nanostructures in two distinct diatom frustules, Superlattices and Microstructures 46 (2009) 64–68.
[9] T. Qin, T. Gutu, J. Jiao, C.-H. Chang, G.L. Rorrer, Photoluminescence of silica nanostructures from bioreactor culture of marine diatom *Nitzschia frustulum*, Journal of Nanoscience and Nanotechnology 8 2392–2398.
[10] K. Umemura, Y. Noguchi, T. Ichinose, Y. Hirose, S. Mayama, Morphology and physical–chemical properties of baked nanoporous frustules, Journal of Nanoscience and Nanotechnology 10 (2010) 5220–5224.
[11] H.E. Townley, K.L. Woon, F.P. Payne, H. White-Cooper, A.R. Parker, Modification of the physical and optical properties of the frustule of the diatom *Coscinodiscus wailesii* by nickel sulfate, Nanotechnology 18 (2007) 295101.
[12] D.Y. Zhang, Y. Wang, J.F. Pan, J. Cai, Separation of diatom valves and girdle bands from *Coscinodiscus* diatomite by settling method, Journal of Materials Science 45 (2010) 5736–5741.
[13] D.Y. Zhang, Y. Wang, W.Q. Zhang, J.F. Pan, J. Cai, Enlargement of diatom frustules pores by hydrofluoric acid etching at room temperature, Journal of Materials Science 46 (2011) 5665–5671.
[14] K. Umemura, Y. Noguchi, T. Ichinose, Y. Hirose, R. Kuroda, S. Mayama, Diatom cells grown and baked on a functionalized mica surface, Journal of Biological Physics 34 (2008) 189–196.
[15] D. Losic, G. Triani, P.J. Evans, A. Atanacio, J.G. Mitchell, N.H. Voelcker, Controlled pore structure modification of diatoms by atomic layer deposition of TiO_2, Journal of Materials Chemistry 16 (2006) 4029–4034.
[16] T. Qin, T. Gutu, J. Jiao, C.-h. Chang, G.L. Rorrer, Biological fabrication of photoluminescent nanocomb structures by metabolic incorporation of germanium into the biosilica of the diatom Nitzschia frustulum, Acs Nano 2 (2008) 1296–1304.
[17] Z.H. Bao, E.M. Ernst, S. Yoo, K.H. Sandhage, Syntheses of porous self-supporting metal-nanoparticle assemblies with 3D morphologies inherited from biosilica templates (diatom frustules), Advanced Materials 21 (2009) 474–478.
[18] Y. Cai, S.M. Allan, K.H. Sandhage, Three-dimensional magnesia-based nanocrystal assemblies via low-temperature magnesiothermic reaction of diatom microshells, Journal of the American Ceramic Society 88 (2005) 2005–2010.
[19] K.H. Sandhage, M.B. Dickerson, P.M. Huseman, M.A. Caranna, J.D. Clifton, T.A. Bull, T.J. Heibel, W.R. Overton, M.E.A. Schoenwaelder, Novel, bioclastic route to self-assembled, 3D, chemically tailored meso/nanostructures: Shape-preserving reactive conversion of biosilica (diatom) microshells, Advanced Materials 14 (2002) 429–433.
[20] M.R. Weatherspoon, S.M. Allan, E. Hunt, Y. Cai, K.H. Sandhage, Sol-gel synthesis on self-replicating single-cell scaffolds: applying complex chemistries to nature's 3-D nanostructured templates, Chemical Communications (2005) 651–653.
[21] Z. Bao, M.-K. Song, S.C. Davis, Y. Cai, M. Liu, K.H. Sandhage, High surface area, micro/mesoporous carbon particles with selectable 3-D biogenic morphologies for tailored catalysis, filtration, or adsorption, Energy & Environmental Science 4 (2011) 3980–3984.
[22] Z. Bao, M.R. Weatherspoon, S. Shian, Y. Cai, P.D. Graham, S.M. Allan, G. Ahmad, M.B. Dickerson, B.C. Church, Z. Kang, H.W. Abernathy Iii, C.J. Summers, M. Liu, K.H. Sandhage, Chemical reduction of three-dimensional silica micro-assemblies into microporous silicon replicas, Nature 446 (2007) 172–175.
[23] W. Yang, P.J. Lopez, G. Rosengarten, Diatoms: self assembled silica nanostructures, and templates for bio/chemical sensors and biomimetic membranes, Analyst 136 (2011) 42–53.
[24] R. Gordon, D. Losic, M.A. Tiffany, S.S. Nagy, F.A.S. Sterrenburg, The glass menagerie: diatoms for novel applications in nanotechnology, Trends in Biotechnology 27 (2009) 116–127.
[25] C. Jeffryes, J. Campbell, H. Li, J. Jiao, G. Rorrer, The potential of diatom nanobiotechnology for applications in solar cells, batteries, and electroluminescent devices, Energy & Environmental Science 4 (2011) 3930–3941.
[26] Y. Wang, J. Pan, J. Cai, A. Li, M. Chen, D. Zhang, Assembling and patterning of diatom frustules onto PDMS substrates using photo-assisted chemical bonding, Chemistry Letters 40 (2011) 1354–1356.
[27] W. Wang, T. Gutu, D.K. Gale, J. Jiao, G.L. Rorrer, C.-h. Chang, Self-assembly of nanostructured diatom microshells into patterned arrays assisted by polyelectrolyte multilayer deposition and inkjet printing, Journal of the American Chemical Society 131 (2009) 4178–4179.
[28] Z. Quan, J. Fang, Superlattices with non-spherical building blocks, Nano Today 5 (2010) 390–411.
[29] G.M. Whitesides, M. Boncheva, Beyond molecules: self-assembly of mesoscopic and macroscopic components, Proceedings of the National Academy of Sciences 99 (2002) 4769–4774.
[30] H. Cölfen, S. Mann, Higher-order organization by mesoscale self-assembly and transformation of hybrid nanostructures, Angewandte Chemie International Edition 42 (2003) 2350–2365.

Biochemical and Biophysical Research Communications 420 (2012) 6–10

Contents lists available at SciVerse ScienceDirect

Biochemical and Biophysical Research Communications

journal homepage: www.elsevier.com/locate/ybbrc

Rsf-1 is overexpressed in non-small cell lung cancers and regulates cyclinD1 expression and ERK activity

Qingchang Li, Qianze Dong, Enhua Wang *

Department of Pathology, First Affiliated Hospital and College of Basic Medical Sciences, China Medical University, Shenyang, Liaoning, China

ARTICLE INFO

Article history:
Received 13 February 2012
Available online 24 February 2012

Keywords:
Rsf-1
Non-small cell lung cancer
Proliferation

ABSTRACT

Rsf-1 (HBXAP) was recently reported to be overexpressed in various cancers and associated with the malignant behavior of cancer cells. However, the expression of Rsf-1 in primary lung cancer and its biological roles in non-small cell lung cancer (NSCLC) have not been reported. The molecular mechanism of Rsf-1 in cancer aggressiveness remains ambiguous. In the present study, we analyzed the expression pattern of Rsf-1 in NSCLC tissues and found that Rsf-1 was overexpressed at both the mRNA and protein levels. There was a significant association between Rsf-1 overexpression and TNM stage ($p = 0.0220$) and poor differentiation ($p = 0.0013$). Furthermore, knockdown of Rsf-1 expression in H1299 and H460 cells with high endogenous Rsf-1 expression resulted in a decrease of colony formation ability and inhibition of cell cycle progression. Rsf-1 knockdown also induced apoptosis in these cell lines. Further analysis showed that Rsf-1 knockdown decreased cyclin D1 expression and phospho-ERK levels. In conclusion, Rsf-1 is overexpressed in NSCLC and contributes to malignant cell growth by cyclin D1 and ERK modulation, which makes Rsf-1 a candidate therapeutic target in lung cancer.

1. Introduction

Gene amplification represents one of the molecular genetic hallmarks of human cancer. Among the genes within the 11q13.5 amplicon, Rsf-1 (also known as HBXAP) was proposed as a candidate cancer-associated gene because it showed the highest correlation between DNA copy number and RNA copy number in ovarian cancer tissues [1]. Previous studies have shown that higher Rsf-1 RNA or protein levels are associated with the most aggressive type of ovarian cancer and shorter overall survival in cancer patients [1–3]. Furthermore, Rsf-1 gene knockdown inhibited cell growth in ovarian cancer cells that harbor Rsf-1 amplification, suggesting an important role of Rsf-1 amplification in maintaining survival and growth in ovarian cancer. The 11q13 region is also amplified in other types of neoplastic diseases including lung cancers [1,4–8]. However, the expression of Rsf-1 in primary lung cancer and its relationship with clinicopathological factors have not yet been examined. In addition, the biological roles of Rsf-1 in lung cancer cells are still unclear. In order to address the above questions, we examined Rsf-1 expression in non-small-cell lung cancer (NSCLC) tissues by immunohistochemistry. In addition, we also explored the association of Rsf-1 with proliferation ability in lung cancer cell lines.

2. Materials and methods

2.1. Patients and specimens

The study protocol was approved by the Institutional Reviewer Board of China Medical University. Primary tumor specimens were obtained from 90 patients diagnosed with lung cancer who underwent resection in the First Affiliated Hospital of China Medical University between 2005 and 2007. None of the patients received radiotherapy or chemotherapy before surgical resection. There were 66 male and 24 female patients. The histological diagnosis and differentiation grade were evaluated for sections stained with hematoxylin and eosin according to the World Health Organization (WHO) classification guidelines. Squamous cell carcinoma (SCC) was identified in 44 cases, and adenocarcinoma was identified in 46 samples. Well-differentiation was identified in 15 cases, moderate differentiation was identified in 53 cases, and poor differentiation was identified in 12 cases. Lymph node metastases were identified in 48 of the 90 patients. The p-TNM staging system of the International Union Against Cancer (7th Edition) was used to classify specimens as stage I ($n = 37$), II ($n = 21$), III ($n = 32$). A set of tumor samples with paired normal lung tissues from 25 patients was collected for real time PCR analysis.

2.2. Quantitative real-time PCR (SYBR Green method)

Quantitative real-time PCR was performed using the SYBR Green PCR master mix (Applied Biosystems) in a total volume of

* Corresponding author. Fax: +86 24 23261638.
E-mail address: wangenhuacmu@hotmail.com (E. Wang).

0006-291X/$ - see front matter © 2012 Elsevier Inc. All rights reserved.
doi:10.1016/j.bbrc.2012.02.095

20 μl on a 7900HT Fast Real-Time PCR System (Applied Biosystems) as follows: 95 °C for 30 s, 40 cycles at 95 °C for 5 s, 60 °C for 30 s. A dissociation step was performed to generate a melting curve to confirm the specificity of the amplification. β-Actin was used as the reference gene. The relative levels of gene expression were represented as ΔCt = Ct gene −Ct reference, and the fold change of gene expression was calculated by the 2-ΔΔCt method. The primer sequences are provided in Table 1. Experiments were repeated in triplicate. The primer sequences are as followers: Rsf-1 forward, 5′ GATACTATGCGTCTCCAGCCAA 3′, Rsf-1 reverse, 5′ CAACTCGTTTCGATTTCTGACAA 3′; β-actin forward, 5′ ATAGCACAGCCTGGATAGCAACGTAC 3′, β-actin reverse, 5′ CACCTTCTACAATGAGCTGCGTGTG 3′.

2.3. Immunohistochemistry

Surgically excised tumor specimens were fixed in 10% neutral formalin and embedded in paraffin, and 4-μm-thick sections were prepared. Immunostaining was performed using the avidin–biotin–peroxidase complex method (Ultrasensitive™, MaiXin, Fuzhou, China). The sections were deparaffinized in xylene, rehydrated with graded alcohol, and then boiled in 0.01 M citrate buffer (pH 6.0) for 2 min in an autoclave. Hydrogen peroxide (0.3%) was applied to block endogenous peroxide activity, and the sections were incubated with normal goat serum to reduce nonspecific binding. Tissue sections were incubated with Rsf-1 mouse monoclonal antibody (1:1500, Upstate, USA). Mouse immunoglobulin (at the same concentration as the antigen-specific antibody) was used as a negative control. Staining for both antibodies was performed at room temperature for 2 h. Biotinylated goat anti-mouse serum IgG was used as a secondary antibody. After washing, the sections were incubated with streptavidin–biotin conjugated with horseradish peroxidase, and the peroxidase reaction was developed with 3,3′-diaminobenzidine tetrahydrochloride. Counterstaining with hematoxylin was performed and the sections were dehydrated in ethanol before mounting.

Two independent blinded investigators examined all tumor slides randomly. Five views were examined per slide, and 100 cells were observed per view at a 400x magnification. According to a previous report, immunostaining of Rsf-1 was scored on a semi-quantitative scale by evaluating the percentage of immunoreactive tumor cells and staining intensity [2]. The intensity and percentage of Rsf-1 positive cells in lung cancers were significantly higher than in normal lung tissues. Nuclear immunostaining in tumor cells was considered positive staining. According to previous reports, the staining intensity was categorized as follows: 0, negative or weak; 1, moderate; 2, strong. The percentage of stained tumor cells was scored as 0, 0%; 1, 1–5%; 2, 6–25%; 3, 26–75% and 4, 76–100%. The scores of each tumor sample were multiplied to give a final score of 0–8, and the tumor samples with a final score of 4–8 were finally determined to represent Rsf-1 overexpression.

2.4. Cell culture and small interfering RNA treatment

H1299 and H460 cell lines were obtained from American Type Culture Collection (Manassas, VA, USA). The cells were cultured in RPMI 1640 (Invitrogen, Carlsbad, CA, USA) containing 10% fetal calf serum (Invitrogen), 100 IU/ml penicillin (Sigma, St. Louis, MO, USA), and 100 μg/ml streptomycin (Sigma). Cells were grown on sterile tissue culture dishes and were passaged every 2 days using 0.25% trypsin (Invitrogen).

On-TargetPlus SMARTpool siRNA for Rsf-1 (L-020374-01-0005) and ON-TARGETplus Non-targeting siRNA #1 (D-001810-01-05) were purchased from Dharmacon. For transfections, cells were seeded in a 24-well plate 24 h before the experiment. Cells were transfected with siRNA using DharmaFECT 1 (0.20 μL/well; ThermoFisher Scientific) according to the manufacturer's protocol. Following transfection, mRNA and protein levels were assessed 48 h later.

Table 1
Distribution of Rsf-1 status in NSCLC according to clinicopathological characteristics.

Characteristics	Number of patients	Rsf-1 absent to weak	Rsf-1 overexpression	*P*
Age				
<60	37	13	24	0.3744
⩾60	53	14	39	
Gender				
Male	66	18	48	0.3491
Female	24	9	15	
Histology				
Adenocarcinoma	46	17	29	0.1409
Squamous cell carcinoma	44	10	34	
Differentiation				
Well	18	11	7	0.0013
Moderate- Poor	72	16	56	
TNM stage				
I	37	16	21	0.0220
II + III	53	11	42	
Tumor status				
T1	17	6	11	0.5969
T2 T3 T4	73	21	52	
Nodal status				
N0	42	16	26	0.1170
N1 N2 N3	48	11	37	

2.5. Western blot analysis

Total proteins from cells were extracted in lysis buffer (Pierce; Rockford, IL) and quantified using the Bradford method. Samples of 50 μg of protein were separated by SDS–PAGE. Samples were transferred to polyvinylidene fluoride membranes (Millipore, Billerica, MA, USA) and incubated overnight at 4 °C with antibody against Rsf-1 (1:1000; Upstate), p-ERK, p-AKT, cyclin D1, cyclin E, CDK4, CDK6 (1:1000; Cell Signaling, USA), and β-actin (1:500; Santa Cruz, USA). After incubation with peroxidase-coupled antimouse IgG (Santa Cruz) at 37 °C for 2 h, bound proteins were visualized using ECL (Pierce) and detected using a BioImaging System (UVP Inc., Upland, CA, USA). Relative protein levels were quantified using β-actin as a loading control.

2.6. Colony formation assays

H1299 and H460 cells were transfected with siRNA for 48 h and then plated into three 6-cm cell culture dishes (1000 per dish) and incubated for 12 days. Plates were washed with PBS and stained with Giemsa. The number of colonies with more than 50 cells was manually counted using a microscope.

2.7. Flow cytometry

Cells were seeded into 6-cm tissue culture dishes. Twelve hours later, cells were transfected with the indicated amounts of siRNA. At the indicated time points, cells were harvested, fixed in 1% paraformaldehyde, washed with phosphate-buffered saline (PBS), and stained in 5 mg/ml propidium iodide in PBS supplemented with RNase A (Roche, Indianapolis, IN) for 30 min at room temperature. Data were collected using BD systems.

For detection of apoptosis, adherent cells were both collected and resuspended in cold PBS for analysis. Cells were stained with Annexin V-FITC Apoptosis Kit (BD Pharmingen, USA) to monitor

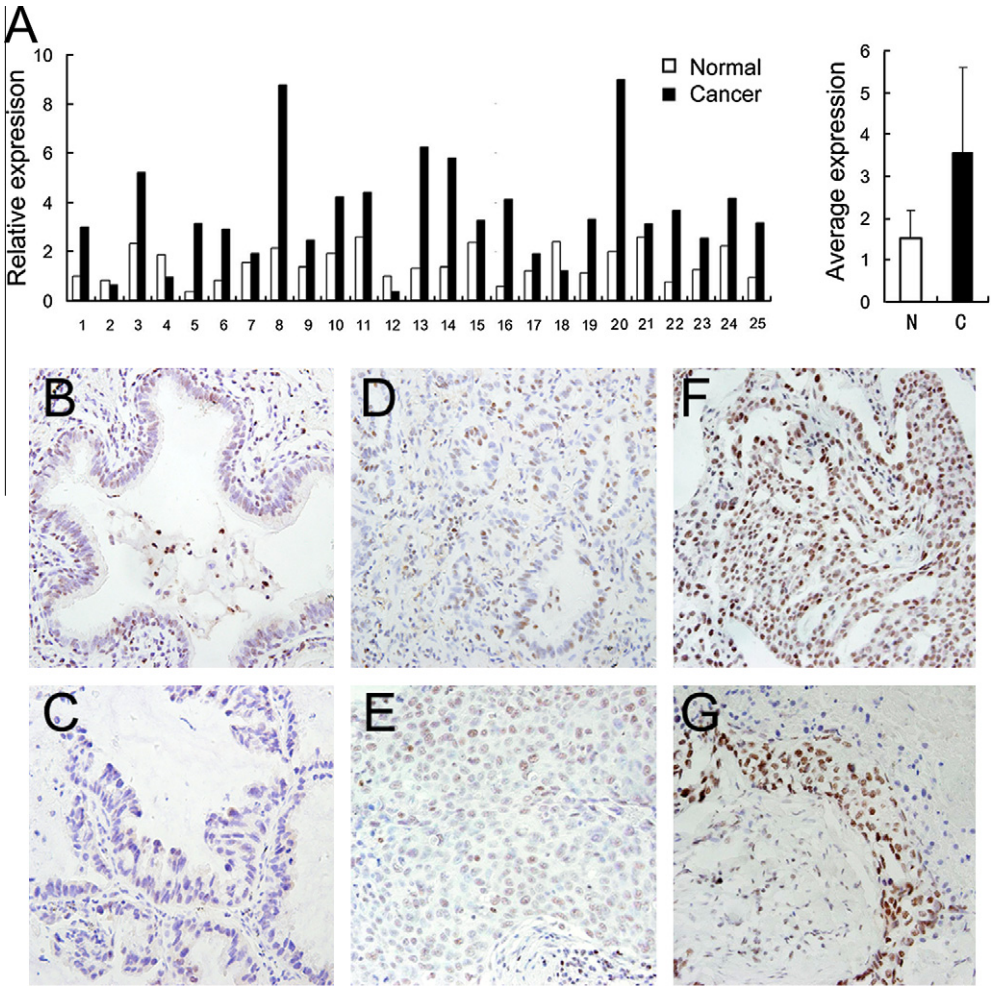

Fig. 1. Expression of Rsf-1 mRNA and protein in non-small cell lung cancer tissues. A. mRNA levels of Rsf-1 expression in 25 tumor samples with paired normal lung tissues. The average mRNA levels of Rsf-1 in tumor cases were 2.37 times higher than that in paired normal lung tissues. B. Weak nuclear staining of Rsf-1 in normal bronchial epithelium. C. Negative Rsf-1 expression in a case of well-differentiated adenocarcinoma. D and E. Moderate staining of Rsf-1 in well-differentiated adenocarcinoma (D) and squamous cell carcinoma (E). F and G. Strong nuclear immunostaining in poor differentiated adenocarcinoma (E) and squamous cell carcinoma (F).

apoptosis cells and propidium iodide (PI) to detect dead cells. Data were collected using BD systems.

2.8. Statistical analysis

SPSS version 11.5 for Windows was used for all statistical analyses. The χ^2 test was used to examine possible correlations between Rsf-1 expression and clinicopathologic factors. Student's *t*-test was used to compare densitometry data on focus numbers between control and Rsf-1-depleted cells. All p values were based on a two-sided statistical analysis, and $p < 0.05$ was considered to indicate statistical significance.

3. Results

3.1. Expression of Rsf-1 and its relationship with clinicopathological factors

Real-time PCR was employed to evaluate levels of Rsf-1 expression in a set of tumor samples with paired normal lung tissues from 25 patients. Compared to normal lung tissues, Rsf-1 overexpression was found in 20 of 25 paired tumor samples, which represented a significant statistical difference (Fig. 1A). The average mRNA levels of Rsf-1 in tumor cases were much higher than in paired normal lung tissues. We analyzed the expression of Rsf-1 in 90 NSCLC specimens and their corresponding normal tissues by immunohistochemistry. Rsf-1 expression was observed in the nuclear compartments of tumor cells, while normal lung tissues and the normal bronchial epithelia exhibited negative or weak expression (Fig. 1B). For 90 NSCLC tissues, negative and weak Rsf-1 expression (score < 4) was observed in 30% (27/90) of cases (Fig. 1C), while Rsf-1 overexpression (score ⩾ 4) was observed in 70% of cases (63/90) (Fig. 1D–G). We investigated the relationship between total Rsf-1 expression and the clinical parameters. As shown in Table 1, no statistical difference was found between Rsf-1 overexpression and age ($p = 0.3744$), gender ($p = 0.3491$), tumor histology ($p = 0.1409$), tumor status ($p = 0.5969$), and nodal status ($p = 0.1170$). Strong Rsf-1 expression correlated with poor differentiation ($p = 0.0013$) and patients with high Rsf-1 expression had advanced stage of NSCLC (I & II vs III, $p = 0.0220$).

3.2. Rsf-1 depletion inhibits proliferation in lung cancer cell lines

Rsf-1 expression was analyzed by Western blotting a panel of lung cancer cell lines. We found that levels of Rsf-1 were higher in lung cancer cell lines than in the normal bronchial cell line HBE. Extremely high expression of Rsf-1 in H1299 and H460 cells was observed (Fig. 2A). In order to explore the biological function of Rsf-1 in lung cancer, a pool consisting of three Rsf-1-targeting siRNAs was employed in these two cell lines and efficiently

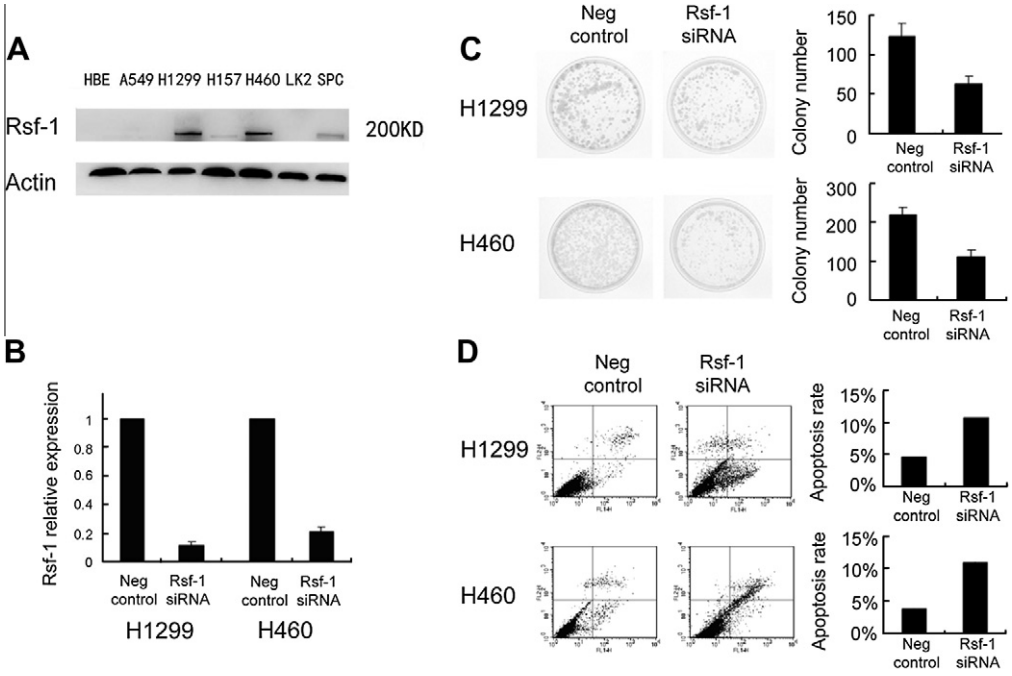

Fig. 2. Rsf-1 expression in a series of lung cancer cell line and Rsf-1 knockdown inhibited cell proliferation. (A) Endogenous expression of Rsf-1 in HBE and six lung cancer cell lines. (B) Realtime PCR analysis showed that siRNA treatment of Rsf-1 markedly decreases Rsf-1 levels in H1299 and H460 cells in comparison with cells transfected with negative control (NC). (C) Colony formation assay was performed in cells transfected with Rsf-1 siRNA, and control cells. A decrease in colony formation was seen in the groups with siRNA treatment in comparison with the controls. (D) Apoptotic cell death was determined by flow-cytometric analysis with Annexin V and PI staining. H1299 and H460 cells were transfected with Rsf-1 siRNA and control siRNA, and then subjected to apoptosis assay. The percentage of apoptosis, including early and late stage of apoptotic cell death in each group, is shown.

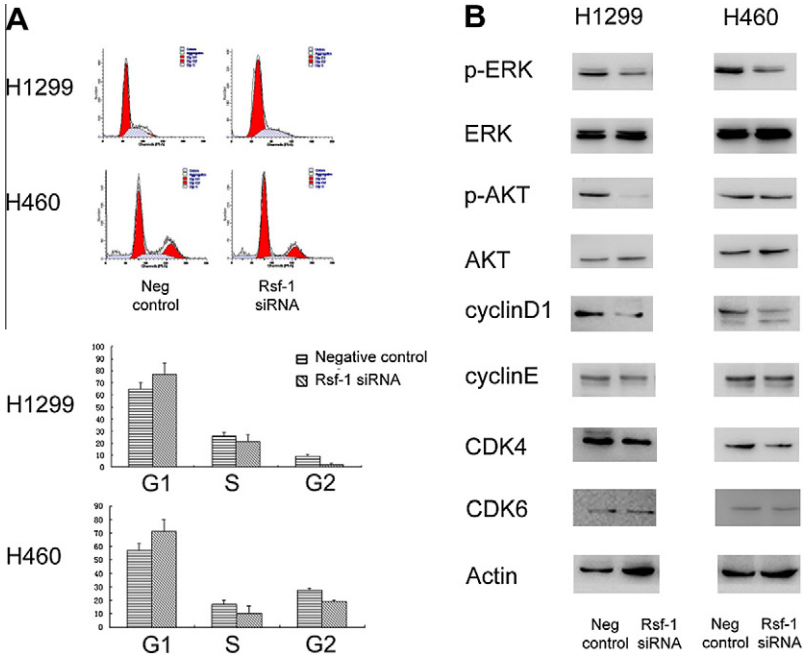

Fig. 3. Depletion of Rsf-1 inhibited cell cycle progression, decreased cyclinD1 expression and ERK activation in lung cancer cells. (A) Rsf-1 knockdown increased G1 phase cells and decreased S phase cells. (B) Western blot analysis revealed that knockdown of Rsf-1 decreased the protein levels of Cyclin D1 in both cell lines and resulted in a reduction in the levels of p-ERK.

blocked Rsf-1 expression 48 h after transfection (Fig. 2B). Next, we tested the effect of RNAi-mediated Rsf-1 repression on the growth of H1299 and H460 cells (Fig. 2C). The proliferation ability was determined by the colony formation assay. We found that treatment of Rsf-1-specific siRNA resulted in a significant decrease in proliferation compared to control siRNA. Colony formation assays showed that Rsf-1 knockdown in H1299 and H460 cells led to a strong reduction of focus numbers as well as sizes (H1299 control vs si Rsf-1: 123 ± 15 vs 64 ± 9; H460 control vs si Rsf-1: 218 ± 18 vs 112 ± 17; $p < 0.05$), suggesting that Rsf-1 modulates the proliferation of lung cancer cells. In addition, Annexin V kit was employed to characterize the death feature of H1299 and H460 cells with

Rsf-1 knockdown. Clearly, a significant population of early and late apoptosis (H1299: 10.8%; H460: 11.9) was observed in cells with Rsf-1 knockdown compared with scramble controls (H1299: 4.2%; H460: 3.1%), demonstrating that Rsf-1 knockdown results in apoptosis of the lung cancer cells.

3.3. Depletion of Rsf-1 affects the cell cycle and inhibits activation of ERK signaling in lung cancer cells

Cell cycle analyses by fluorescence activated cell sorting (FACS) were performed in cancer cells with or without Rsf-1 knockdown, and an increase in G1 populations and a concomitant decrease in S phase populations was found upon Rsf-1 repression. These results indicated that Rsf-1 depletion induced cell cycle arrest at the G1/S boundary to inhibit cell proliferation (Fig. 3A). To investigate the underlying mechanism inducing cell cycle arrest, we tested the effect of Rsf-1 knockdown on a series of cell cycle-related molecules. Western blotting analysis revealed that knockdown of Rsf-1 decreased cyclin D1 protein level in both cell lines (Fig. 3B). However, we did not observe remarkable changes in CDK4 and CDK6 expression. In addition, depletion of Rsf-1 resulted in a significant reduction in the levels of p-ERK in both cell lines. Rsf-1 depletion caused a decrease in the level of p-AKT in the H1299 cell line, but not in the H460 cell line. These results suggest that Rsf-1 affects lung cancer cell growth by regulating cyclin D1 expression and ERK signaling.

4. Discussion

The 11q13.5 amplification, which is present in a fraction of ovarian, breast, and head and neck carcinomas, has been proposed to contain a number of potential candidate drivers, including Rsf-1, EMSY, PAK1, TAOS1, Rad9, CCND1, FGF3, and FGF4 [9–13]. Previous research showed that Rsf-1 amplification exists in ovarian cancer and significantly correlates with the prognosis of patients. Depletion of Rsf-1 can reduce the proliferation ability of ovarian cancer cells, suggesting that it may be used as a marker of malignant tumor behavior in ovarian cancers [1,2]. Rsf-1 overexpression was also observed in breast cancer [3]. Due to 11q13 amplification in lung cancers [7,8], we speculated that Rsf-1 might also be overexpressed in lung cancer. Real-time PCR analysis in a set of tumor samples showed that Rsf-1 mRNA was overexpressed in lung cancer tissues. We also analyzed the expression of Rsf-1 in 90 NSCLC specimens by immunohistochemistry, and observed Rsf-1 overexpression in 63 cases. There was a significant association between Rsf-1 overexpression and pTNM stage and poor differentiation, suggesting that Rsf-1 correlates with the malignant behavior of lung cancer. Furthermore, we knocked down Rsf-1 in H1299 and H460 cells, which had high levels of endogenous Rsf-1 expression, and found that Rsf-1 depletion decreased the colony formation ability of lung cancer cells, suggesting that Rsf-1 can promote tumor growth of lung cancer. Furthermore, Rsf-1 knockdown induced apoptosis of H1299 and H460 cells and western blot suggested that apoptotic induction by silencing Rsf-1 could be partially due to blockage of the survival signal such as ERK1/2.

The precise mechanism by which Rsf-1 affects tumor progression has been unclear. A recent study suggested that the role of Rsf-1 in prompting cell proliferation is dependent upon formation of the Rsf-1/hSNF2H complex. The potential mechanism by which Rsf-1/hSNF2H complex regulates tumor progression at the molecular level remains ambiguous [14]. Previous studies using interaction network analyses showed that Rsf-1 expression is associated with changes in the expression of several genes involved in the NF-κB, ERK, and Akt pathways [14,15]. Therefore, we focused on the pathway regulated by Rsf-1/hSNF2H complex in order to explore the potential mechanism by which Rsf-1 induces tumor cell proliferation. In the present study, we found that in the lung cancer cell lines H1299 and H460, Rsf-1 knockdown inhibited cell cycle progression and down-regulated cyclin D1 expression. Cyclin D1 is associated with G1/S transition and is overexpressed in a variety of cancers including lung cancer [16,17]. Rsf-1 knockdown also decreased phospho-ERK levels, suggesting that Rsf-1 may modulate lung cancer cell growth through ERK activation. ERK signaling can activate AP-1, which plays an important role in cell proliferation, apoptosis, differentiation, and cancer cell invasion [18]. These results suggest that modulation of ERK activation by Rsf-1 may contribute to the malignant proliferation of lung cancer cells.

In conclusion, our study shows that Rsf-1 overexpression exists in lung cancer and correlates with pTNM stage and poor differentiation. Rsf-1 contributes to malignant cell growth, apoptosis and regulates cyclin D1 and ERK activity. Thus, Rsf-1 may qualify as a candidate therapeutic target in lung cancer.

References

[1] M. Shih Ie, J.J. Sheu, A. Santillan, K. Nakayama, M.J. Yen, R.E. Bristow, R. Vang, G. Parmigiani, R.J. Kurman, C.G. Trope, B. Davidson, T.L. Wang, Amplification of a chromatin remodeling gene, Rsf-1/HBXAP, in ovarian carcinoma, Proc. Natl. Acad. Sci. USA 102 (39) (2005) 14004–14009.
[2] B. Davidson, C.G. Trope, T.L. Wang, M. Shih Ie, Expression of the chromatin remodeling factor Rsf-1 is upregulated in ovarian carcinoma effusions and predicts poor survival, Gynecol. Oncol. 103 (3) (2006) 814–819.
[3] T.L. Mao, C.Y. Hsu, M.J. Yen, B. Gilks, J.J. Sheu, E. Gabrielson, R. Vang, L. Cope, R.J. Kurman, T.L. Wang, M. Shih Ie, Expression of Rsf-1, a chromatin-remodeling gene, in ovarian and breast carcinoma, Hum. Pathol. 37 (9) (2006) 1169–1175.
[4] F. M. Fang, C. F. Li, H. Y. Huang, M. T. Lai, C. M. Chen, I. W. Chiu, T. L. Wang, F. J. Tsai, M. Shih Ie, and J. J. Sheu, Overexpression of a chromatin remodeling factor, RSF-1/HBXAP, correlates with aggressive oral squamous cell carcinoma. Am. J. Pathol. 178 (5) p. 2407–2415.
[5] M. Schwab, Amplification of oncogenes in human cancer cells, Bioessays 20 (6) (1998) 473–479.
[6] H. C. Tai, H. Y. Huang, S. W. Lee, C. Y. Lin, M. J. Sheu, S. L. Chang, L. C. Wu, Y. L. Shiue, W. R. Wu, C. M. Lin, and C. F. Li, Associations of Rsf-1 overexpression with poor therapeutic response and worse survival in patients with nasopharyngeal carcinoma. J. Clin. Pathol.
[7] J. Xu, T. Tyan, E. Cedrone, N. Savaraj, N. Wang, Detection of 11q13 amplification as the origin of a homogeneously staining region in small cell lung cancer by chromosome microdissection, Genes, Chromosomes Cancer 17 (3) (1996) 172–178.
[8] T. Shibata, S. Uryu, A. Kokubu, F. Hosoda, M. Ohki, T. Sakiyama, Y. Matsuno, R. Tsuchiya, Y. Kanai, T. Kondo, I. Imoto, J. Inazawa, S. Hirohashi, Genetic classification of lung adenocarcinoma based on array-based comparative genomic hybridization analysis: its association with clinicopathologic features, Clin. Cancer Res. 11 (17) (2005) 6177–6185.
[9] L.A. Brown, J. Irving, R. Parker, H. Kim, J.Z. Press, T.A. Longacre, S. Chia, A. Magliocco, N. Makretsov, B. Gilks, J. Pollack, D. Huntsman, Amplification of EMSY, a novel oncogene on 11q13, in high grade ovarian surface epithelial carcinomas, Gynecol. Oncol. 100 (2) (2006) 264–270.
[10] B.T. Hennessy, M. Nanjundan, K.W. Cheng, L. Nolden, G.B. Mills, Identification of remodeling and spacing factor 1 (rsf-1, HBXAP) at chromosome 11q13 as a putative oncogene in ovarian cancer, Eur. J. Hum. Genet. 14 (4) (2006) 381–383.
[11] J. Bostner, M. Ahnstrom Waltersson, T. Fornander, L. Skoog, B. Nordenskjold, O. Stal, Amplification of CCND1 and PAK1 as predictors of recurrence and tamoxifen resistance in postmenopausal breast cancer, Oncogene 26 (49) (2007) 6997–7005.
[12] A. Rosen, P. Sevelda, M. Klein, K. Dobianer, C. Hruza, K. Czerwenka, H. Hanak, N. Vavra, H. Salzer, S. Leodolter, et al., First experience with FGF-3 (INT-2) amplification in women with epithelial ovarian cancer, Br. J. Cancer 67 (5) (1993) 1122–1125.
[13] C.K. Cheng, L.W. Chow, W.T. Loo, T.K. Chan, V. Chan, The cell cycle checkpoint gene Rad9 is a novel oncogene activated by 11q13 amplification and DNA methylation in breast cancer, Cancer Res. 65 (19) (2005) 8646–8654.
[14] J.J. Sheu, J.H. Choi, I. Yildiz, F.J. Tsai, Y. Shaul, T.L. Wang, M. Shih Ie, The roles of human sucrose nonfermenting protein 2 homologue in the tumor-promoting functions of Rsf-1, Cancer Res. 68 (11) (2008) 4050–4057.
[15] J.H. Choi, J.J. Sheu, B. Guan, N. Jinawath, P. Markowski, T.L. Wang, M. Shih Ie, Functional analysis of 11q13.5 amplicon identifies Rsf-1 (HBXAP) as a gene involved in paclitaxel resistance in ovarian cancer, Cancer Res. 69 (4) (2009) 1407–1415.
[16] O. Gautschi, D. Ratschiller, M. Gugger, D.C. Betticher, J. Heighway, Cyclin D1 in non-small cell lung cancer: a key driver of malignant transformation, Lung cancer 55 (1) (2007) 1–14.
[17] J.K. Kim, J.A. Diehl, Nuclear cyclin D1: an oncogenic driver in human cancer, J. Cell Physiol. 220 (2) (2009) 292–296.
[18] C. Montagut, J. Settleman, Targeting the RAF-MEK-ERK pathway in cancer therapy, Cancer Lett. 283 (2) (2009) 125–134.

Biochemical and Biophysical Research Communications 420 (2012) 11–16

Contents lists available at SciVerse ScienceDirect

Biochemical and Biophysical Research Communications

journal homepage: www.elsevier.com/locate/ybbrc

Mechanical loading prevents the stimulating effect of IL-1β on osteocyte-modulated osteoclastogenesis

Rishikesh N. Kulkarni, Astrid D. Bakker, Vincent Everts, Jenneke Klein-Nulend *

Department of Oral Cell Biology, Academic Centre for Dentistry Amsterdam (ACTA), University of Amsterdam and VU University Amsterdam, Research Institute MOVE, Amsterdam, The Netherlands

ARTICLE INFO

Article history:
Received 31 January 2012
Available online 27 February 2012

Keywords:
Interleukin-1β
Osteocytes
Osteoclastogenesis
Mechanical loading
Pulsating fluid flow

ABSTRACT

Inflammatory diseases such as rheumatoid arthritis are often accompanied by higher plasma and synovial fluid levels of interleukin-1β (IL-1β), and by increased bone resorption. Since osteocytes are known to regulate bone resorption in response to changes in mechanical stimuli, we investigated whether IL-1β affects osteocyte-modulated osteoclastogenesis in the presence or absence of mechanical loading of osteocytes.

MLO-Y4 osteocytes were pre-incubated with IL-1β (0.1–1 ng/ml) for 24 h. Cells were either or not subjected to mechanical loading by 1 h pulsating fluid flow (PFF; 0.7 ± 0.3 Pa, 5 Hz) in the presence of IL-1β (0.1–1 ng/ml). Conditioned medium was collected after 1 h PFF or static cultures. Subsequently mouse bone marrow cells were seeded on top of the IL-1β-treated osteocytes to determine osteoclastogenesis. Conditioned medium from mechanically loaded or static IL-1β-treated osteocytes was added to co-cultures of untreated osteocytes and mouse bone marrow cells. Gene expression of cysteine-rich protein 61 (CYR61/CCN1), receptor activator of nuclear factor kappa-B ligand (RANKL), and osteoprotegerin (OPG) by osteocytes was determined immediately after PFF.

Incubation of osteocytes with IL-1β, as well as conditioned medium from static IL-1β-treated osteocytes increased the formation of osteoclasts. However, conditioned medium from mechanically loaded IL-1β-treated osteocytes prevented osteoclast formation. Incubation with IL-1β upregulated RANKL and downregulated OPG gene expression by static osteocytes. PFF upregulated CYR61, RANKL, and OPG gene expression by osteocytes.

Our results suggest that IL-1β increases osteocyte-modulated osteoclastogenesis, and that mechanical loading of osteocytes may abolish IL-1β-induced osteoclastogenesis.

1. Introduction

Bones are subjected to a variety of mechanical loads during daily activities. Bone mass and architecture are continuously adapted to the daily mechanical loads. Osteocytes play an important role in the adaptation of bone to mechanical loading, by sensing the mechanical loads and orchestrating the activity of bone-forming osteoblasts and bone-resorbing osteoclasts [1–3]. Osteocytes are thought to regulate bone mass by orchestrating the balance between bone formation and resorption in response to mechanical loading [4]. Thus, any factor that alters the response of osteocytes to mechanical loading potentially affects bone mass.

Inflammatory diseases such as rheumatoid arthritis (RA) are often accompanied by higher plasma and synovial fluid levels of interleukin-1β (IL-1β) [5,6], and increased osteoclastic bone resorption [7]. Bone loss in patients with RA might be caused by the physiologic adaptation of bone to reduced physical activity, and/or by the use of corticosteroids by these patients. It could also be a direct effect of increased IL-1β levels. The relative importance of the proinflammatory cytokines IL-1 and TNF in the pathogenesis of RA is the subject of much debate. TNF is more important in inflammatory processes whereas IL-1 plays a more important role in joint destruction in a murine arthritis model [8]. The proinflammatory cytokine IL-1β facilitates osteoclastogenesis by inducing expression of receptor activator of nuclear factor kappa B (RANKL) by osteoblasts [9]. RANKL stimulates osteoclast precursors to commit to the osteoclastic phenotype whereas osteoprotegerin (OPG) inhibits RANKL activity [10]. Crockett et al. have shown that cysteine rich protein 61 (CYR61/CCN1) inhibits the formation of osteoclasts [11]. CYR61 is an extracellular matrix-associated signaling protein that belongs to the connective tissue growth factor (CCN) family of proteins. CYR61 stimulates osteoblast proliferation and

* Corresponding author at: Department of Oral Cell Biology, Academic Centre for Dentistry Amsterdam (ACTA), VU University Amsterdam, Gustav Mahlerlaan 3004, 1081 Amsterdam, LA, The Netherlands.
E-mail address: j.kleinnulend@acta.nl (J. Klein-Nulend).

0006-291X/$ - see front matter © 2012 Elsevier Inc. All rights reserved.
doi:10.1016/j.bbrc.2012.02.099

differentiation and is upregulated during fracture repair [12,13]. It is yet unknown whether IL-1β modulates CYR61 expression.

Several studies have shown that nitric oxide production by bone cells is rapidly increased in response to mechanical stress in vitro [14,15]. Nitric oxide mediates adaptive bone formation [16], and is essential for the inhibition of osteoclastogenesis by mechanically loaded MLO-Y4 osteocytes [17]. Bakker et al. have shown that both TNFα and IL-1β inhibit the upregulation of nitric oxide production after mechanical stimulation by PFF [18]. Therefore IL-1β might interfere with adaptive bone formation during inflammatory diseases by affecting osteocyte-modulated osteoclastogenesis. However, whether mechanical loading of osteocytes in the presence of IL-1β affects osteocyte-modulated osteoclastogenesis is unknown. Since IL-1β alters the mechano-response of osteocytes we aimed to investigate whether IL-1β affects osteocyte-modulated osteoclastogenesis in the presence or absence of mechanical loading of osteocytes.

2. Material and methods

2.1. Cell culture

MLO-Y4 osteocytes (kindly provided by Dr. L. Bonewald, San Antonio, TX, USA) [19] were cultured up to near-confluency in 75-cm^2 culture flasks using α-MEM supplemented with 5% fetal bovine serum (FBS; Gibco, Grand Island, NY), 5% calf serum (Gibco), 1.25 μg/ml fungizone (Gibco), 150 μg/ml penicillin (Sigma, St. Louis, MO), and 125 μg/ml streptomycin (Sigma) at 37 °C and 5% CO_2 in air.

Mouse bone marrow cells were used for the osteoclast formation assay. The animal committee of the VU University Amsterdam approved the use of mice in these experiments. Femurs and tibiae were harvested and soft tissue was removed as previously described in detail [20]. Cleaned femurs and tibiae were then ground in a mortar with α-MEM (Gibco) supplemented with 10% FBS, 150 μg/ml penicillin, 125 μg/ml streptomycin, 1.25 μg/ml fungizone, and heparin (170 IE/ml; Leo Pharmaceutical Products B.V., Weesp, The Netherlands). The resulting cell suspension was aspirated through a 21-gauge needle and filtered using a 100-μm pore size Cell Strainer filter (Falcon/Becton Dickinson, Franklin Lakes, NJ). Cells were then washed twice in culture medium, centrifuged for 10 min at 200*g*, and 1×10^6 cells/cm^2 were seeded on top of either or not IL-1β-treated (0.1, 0.5, or 1 ng/ml) MLO-Y4 osteocytes.

2.2. Pulsatile fluid flow (PFF)

MLO-Y4 osteocytes at passage 30 or 31 were harvested using 0.25% trypsin (Difco Laboratories, Detroit, MI) and 0.1% EDTA (Sigma) in PBS, and seeded at 2×10^4 cells/cm^2 on polylysine-coated (50 μg/ml; poly-L-lysine hydrobromide; Sigma) glass slides (15 cm^2) in α-MEM with 5% FBS, 5% calf serum, and antibiotics. Osteocytes were incubated with mouse recombinant IL-1β (0.1, 0.5, or 1 ng/ml) (Sigma) for 24 h before the start of the experiment. They were incubated overnight at 37 °C with 5% CO_2 in air, and subjected to mechanical loading for 1 h by PFF or kept under static control conditions in the presence or absence of IL-1β. PFF at 5 Hz pulse frequency was generated by pumping 13 ml of culture medium in a pulsatile manner through a parallel-plate flow chamber ($65 \times 24 \times 0.3$ mm) containing the bone cells [21]. The mean applied fluid shear stress was 0.7 Pa with a pulse amplitude of 0.3 Pa, and the estimated peak stress rate was 8.4 Pa/s [22,23]. Control cultures were kept under stationary conditions in a petri-dish containing 13 ml flow medium under similar conditions as the experimental cultures, i.e. at 37 °C in a humidified atmosphere of 5% CO_2 in air. Conditioned medium was collected after 1 h of PFF or static culture. After 1 h PFF the cells were lysed for total RNA isolation as described below.

2.3. Osteoclast formation

MLO-Y4 osteocytes were seeded at a density of 1×10^3 cells/well in 48-well tissue culture plates (Greiner Bio-One, Frickenhausen, Germany). After attachment the osteocytes were either or not pre-incubated for 24 h with 0.1, 0.5, or 1 ng/ml of mouse recombinant IL-1β. After this 24 h period, the medium containing IL-1β was removed, and 1×10^6 bone marrow cells/cm^2 were seeded on top of the IL-1β treated osteocytes. The cells were kept in co-culture in α-MEM (Gibco) supplemented with 10% FBS and antibiotics.

In another co-culture set-up, conditioned medium from mechanically loaded or static IL-1β treated osteocytes was added to co-cultures of untreated osteocytes and mouse bone marrow cells. Culture medium and osteocyte-conditioned medium were refreshed after 3 days. After 7 days of co-culture, cells were fixed in 4% formaldehyde in PBS for 10 min. Fixed cells were washed with PBS, and stained for tartrate-resistant acid phosphatase (TRACP) according to the manufacturer's instructions (Sigma). The number of TRACP-positive multinucleated (3 or more nuclei per cell) and mononuclear cells were counted using a Leica DM IL microscope (Leica, Wetzlar, Germany) equipped with a 20× objective.

2.4. Analysis of gene expression

Real-time polymerase chain reaction (PCR) was used to determine gene expression of CYR61, RANKL, OPG, and the housekeeping gene GAPDH (all primers from Applied Biosystems, Foster, CA). Total RNA was isolated using lysis buffer RA I (Macherey–Nagel, Düren, Germany) according to the manufacturer's instructions. cDNA synthesis was performed using 0.5–1 μg of total RNA in a 20 μl reaction mixture consisting of 5 units of Transcriptor Reverse Transcriptase (Roche Diagnostics, Mannheim, Germany), 0.08 A260 units of random primers (Roche Diagnostics), 1 mM of each dNTP (InVitrogen, Calrsbad, CA), and 1x concentrated Transcriptor RT reaction buffer (Roche Diagnostics). Real time PCR reactions were performed using Taq-Man® Gene Expression assays (TaqMan®, Applied Biosystems) in an ABI Prism 7700 DNA sequence detector (Applied Biosystems). Gene expression values were normalized for the housekeeping gene GAPDH.

2.5. Statistics

One way-ANOVA was performed to assess whether there was a significant difference in mRNA expression and osteoclast formation between groups. Bonferroni comparison between pairs of groups was used as a post hoc test. Two way-ANOVA with pairwise comparison was used to study the effect of IL-1β and PFF on mRNA expression and osteoclast formation. Differences were considered significant when $p < 0.05$.

3. Results

3.1. IL-1β increases osteocyte-modulated osteoclastogenesis

The effect of IL-1β on osteocyte-modulated osteoclastogenesis in co-cultures of IL-1β (0.1–1 ng/ml) treated osteocytes and mouse bone marrow cells was investigated. We found that IL-1β dose-dependently increased the number of osteoclasts, as assessed by counting the number of TRACP-positive mononuclear cells after 7 days of co-culture (Fig. 1).

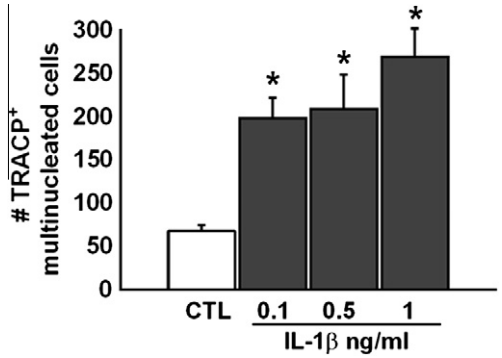

Fig. 1. Effect of IL-1β on osteocyte-modulated osteoclastogenesis. IL-1β at 0.1, 0.5, and 1 ng/ml upregulated the number of TRACP-positive multinucleated cells after 7 days of co-culture of MLO-Y4 osteocytes and mouse bone marrow cells. Values are mean ± SEM from six separate experiments. CTL, control. *Significant effect of IL-1β, $p < 0.05$.

3.2. IL-1β alters osteoclastogenesis-related gene expression by osteocytes

Since IL-1β increased the formation of osteoclasts, we investigated whether IL-1β alters osteoclastogenesis-related gene expression by osteocytes. IL-1β (0.5 and 1 ng/ml) upregulated RANKL gene expression by 3.7- to 4.0-fold (Fig. 2A). However, IL-1β (0.5 and 1 ng/ml) downregulated OPG gene expression by 1.2- to 1.7-fold (Fig. 2B). As a result IL-1β (0.5 and 1 ng/ml) upregulated RANKL/OPG ratio by 2.3- to 4.0-fold. IL-1β did not affect CYR61 gene expression (Fig. 2C).

3.3. Mechanical loading of osteocytes inhibits IL-1β stimulated osteoclastogenesis

Next, we determined whether mechanical loading of osteocytes in the absence or presence of IL-1β affects osteoclast formation in a co-culture system of MLO-Y4 osteocytes and bone marrow cells. We found that the conditioned medium from IL-1β-treated static osteocytes dose-dependently increased the number of osteoclasts (Fig. 3A). Conditioned medium from mechanically loaded osteocytes strongly inhibited the formation of osteoclasts (Fig. 3A and B). This inhibiting effect was seen in the absence and presence of different concentrations of IL-1β (Fig. 3A and B).

3.4. CYR61 is upregulated in mechanically stimulated osteocytes

To assess whether mechanical loading of osteocytes in the presence or absence of IL-1β affects CYR61, RANKL, and OPG gene expression, MLO-Y4 osteocytes were treated with or without 1 h PFF in the presence of IL-1β (0.1–1 ng/ml). PFF upregulated CYR61 gene expression by 1.3-fold in the absence of IL-1β (Fig. 4A). Addition of IL-1β (0.1–1 ng/ml) inhibited the upregulation of CYR61 gene expression after mechanical stimulation by PFF (Fig. 4A). PFF did not affect CYR61 gene expression in the presence of IL-1β (0.1–1 ng/ml) (Fig. 4A). PFF upregulated RANKL gene expression by 3.0-fold (Fig. 4B) and OPG gene expression by 1.4-fold in the absence of IL-1β (Fig. 4C). Addition of IL-1β (0.5 and 1 ng/ml) inhibited the upregulation of OPG gene expression after mechanical stimulation by PFF (Fig. 4C). PFF upregulated RANKL gene expression by 1.6-fold in the presence of IL-1β (0.1 ng/ml), but did not affect OPG gene expression in the presence of IL-1β (0.1–1 ng/ml).

4. Discussion

In the present study we found that IL-1β increases osteocyte-modulated osteoclastogenesis. These results are in accordance with data by others showing that IL-1β indirectly facilitates osteoclastogenesis by acting on osteoblasts or human periodontal ligament fibroblasts [24,25]. We found that IL-1β upregulates RANKL and inhibits OPG gene expression by osteocytes. Our results show that IL-1β probably stimulates osteoclastogenesis by modulating RANKL and OPG gene expression by osteocytes. Alternatively the

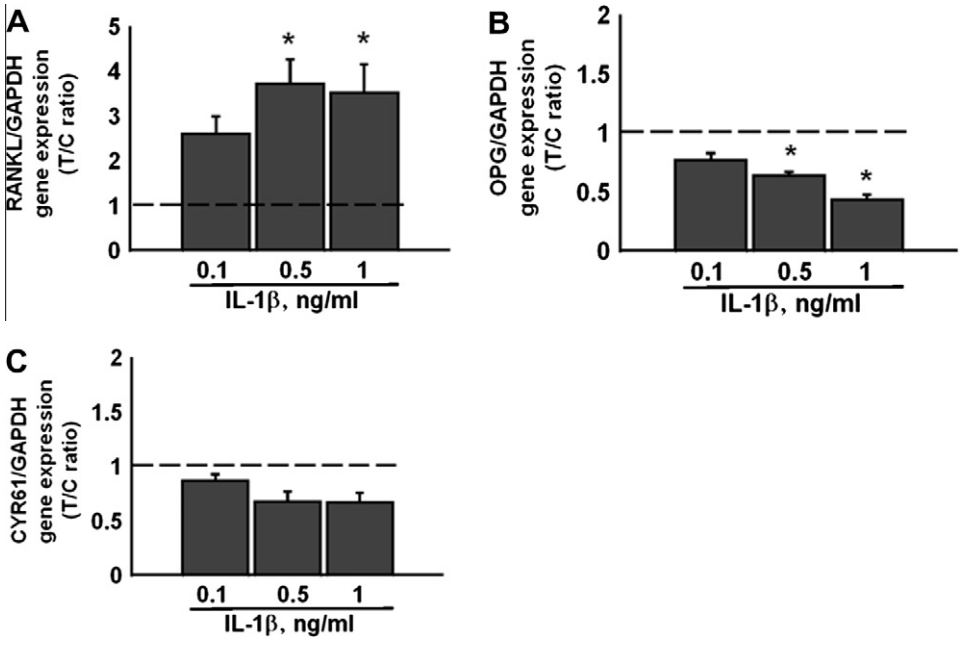

Fig. 2. Effect of IL-1β on RANKL, OPG, and CYR61 gene expression by MLO-Y4 osteocytes. Cells were incubated with IL-1β (0.1–1 ng/ml) for 24 h. (A) IL-1 β at 0.5 and 1 ng/ml upregulated RANKL gene expression. (B) IL-1 β at 0.5 and 1 ng/ml downregulated OPG gene expression. (C) IL-1 β did not affect CYR61 gene expression. Values are mean ± SEM of IL-1β treated-over-control ratios from five different experiments. Dashed line, $T/C = 1$ (no effect of IL-1β). *Significant effect of IL-1β, $p < 0.05$.

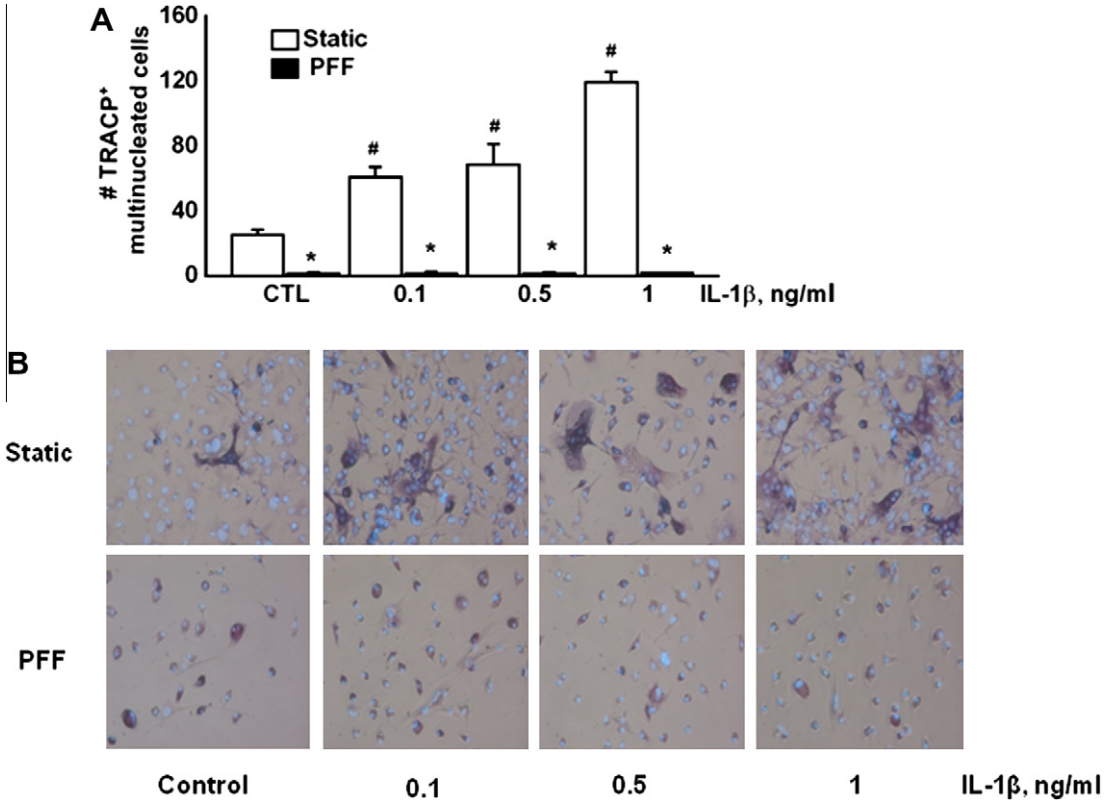

Fig. 3. Effect of conditioned medium obtained from static or mechanically stimulated osteocytes treated with or without IL-1β on osteocyte-modulated osteoclastogenesis. Cells were treated with IL-1β for 24 h before application of PFF. (A) Conditioned medium from static osteocytes treated with 0.1, 0.5, or 1 ng/ml IL-1β significantly upregulated the number of TRACP-positive multinucleated cells, whereas conditioned medium from mechanically stimulated osteocytes treated with 0.1, 0.5, or 1 ng/ml IL-1β significantly inhibited the number of TRACP-positive multinucleated cells. (B) Conditioned medium from mechanically stimulated osteocytes inhibited the formation of osteoclasts. Values are mean ± SEM from four separate experiments. PFF, pulsating fluid flow; static, static control conditions; CTL, control. *Significant effect of PFF, $p < 0.05$. #Significant effect of IL1-β, $p < 0.05$.

increased formation of osteoclast-like cells might have been due to osteocyte apoptosis [26].

Osteocytes extend their cell processes into bone marrow spaces [27], where osteoclast precursors are present. It is likely that osteocytes communicate with these osteoclast precursors present in the bone marrow space via their dendritic processes. Therefore we used a co-culture model of MLO-Y4 osteocytes and mouse bone marrow cells, which likely mimics the *in vivo* situation. Soluble factors released by mechanically loaded osteocytes inhibit osteoclastogenesis induced by stromal cells and osteocytes [28,29]. Therefore we investigated if conditioned medium from mechanically loaded and IL-1β-treated osteocytes does modulate osteoclastogenesis. We found that conditioned medium from static IL-1β-treated osteocytes dose-dependently increased the number of osteoclasts in co-cultures of osteocytes and bone marrow cells. Conversely conditioned medium from mechanically loaded IL-1β-treated osteocytes inhibited the formation of osteoclasts. To our knowledge we show for the first time that mechanical loading of osteocytes in the presence of IL-1β abolishes osteoclastogenesis. Since osteocytes are the most abundant bone cell type, vastly outnumbering the osteoblasts and osteoclasts in the bone, our findings provide important information related to the prevention of IL-1β-induced bone loss. Mechanically loaded osteocytes produce several factors which inhibit osteoclastogenesis. Osteocytes produce high levels of nitric oxide in response to mechanical stimulation [15,30], and nitric oxide mediates the inhibition of osteoclast activity by mechanically stimulated osteocytes [17]. Although IL-1β inhibits the upregulation of nitric oxide production after mechanical stimulation by PFF [18], we found that mechanical loading of osteocytes in the presence of IL-1β inhibits osteoclastogenesis. We propose that the inhibition of IL-β-induced osteoclastogenesis by mechanically loaded osteocytes is independent of nitric oxide.

Since a decrease in the RANKL/OPG ratio inhibits osteoclastogenesis, we also investigated whether mechanical loading of osteocytes in the presence of IL-1β modulates the RANKL/OPG ratio in osteocytes. We found that mechanical stimulation in the presence of IL-1β did not decrease the RANKL/OPG ratio in osteocytes. This suggests that mechanical loading of osteocytes in the presence of IL-1β might inhibit osteoclastogenesis in a RANKL/RANK/OPG independent manner. We then determined the effect of mechanical loading on CRY61 gene expression, a negative regulator of osteoclastogenesis [11], in osteocytes. Under these conditions we found an upregulation of CYR61 gene expression, which has not been shown before. Since CYR61 has been shown to inhibit osteoclastogenesis in a RANKL/RANK/OPG independent manner [11], this suggests that CYR61 might be a soluble factor produced after mechanical loading of osteocytes in the absence of IL-1β leading to the inhibition of osteoclastogenesis. However we found that IL-1β inhibits the upregulation of CYR61 gene expression after PFF. In spite of the inhibited expression of CYR61, conditioned medium from mechanically loaded IL-1β treated osteocytes still inhibited the formation of osteoclasts. Therefore CYR61 might not be involved in the inhibition of IL-1β-induced osteoclastogenesis. We also found that conditioned medium from mechanically loaded IL-1β-treated osteocytes inhibited clustering of osteoclast precursors (data not shown). This finding suggests the presence of factors in the conditioned medium that inhibit migration of osteoclast precursors towards each other to form osteoclasts.

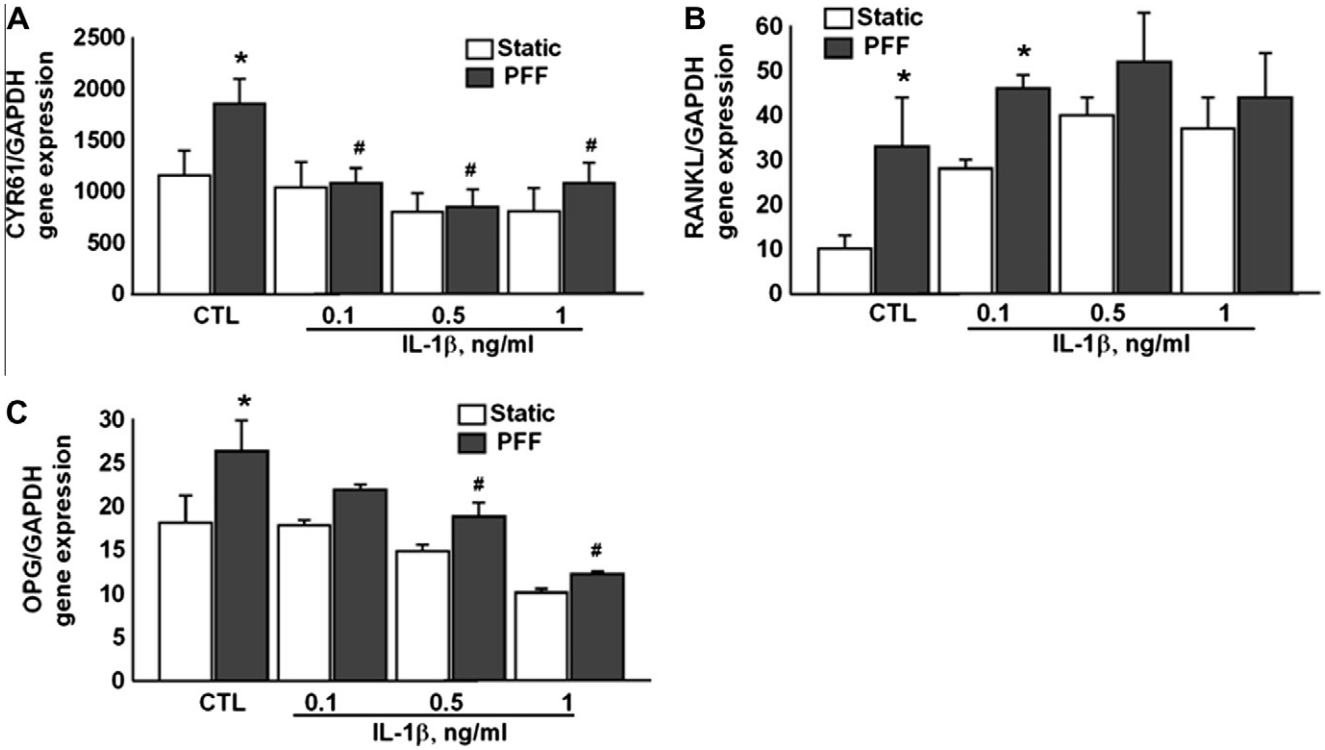

Fig. 4. Effect of 1 h PFF on CYR61, RANKL, and OPG gene expression by MLO-Y4 osteocytes in the presence or absence of IL-1β. (A) PFF upregulated CYR61 gene expression by osteocytes in the absence of IL-1β. (B) PFF upregulated RANKL gene expression by osteocytes in the absence and presence of 0.5 ng/ml IL-1β. (C) PFF upregulated OPG gene expression by osteocytes in the absence of IL-1β. Values are mean ± SEM from five different PFF experiments. PFF, pulsating fluid flow; static, static control conditions; CTL, control. *Significant effect of PFF, $p < 0.05$. #Significant effect of IL1-β, $p < 0.05$.

Further research focusing on the identification of the specific soluble factors produced after mechanical loading of IL-1β-treated osteocytes that inhibit osteoclastogenesis is warranted.

In conclusion, our results show that IL-1β increases osteocyte-modulated osteoclastogenesis, whereas mechanical loading of osteocytes inhibits IL-1β-induced osteoclastogenesis. Based on these findings we propose that in patients with RA, limited movement or disuse as a result of pain and presence of IL-1β might enhance bone loss, whereas mechanical loading of bone in these patients will hopefully, at least in part, alleviate the negative effects of IL-1β on bone mass.

Acknowledgments

The work of R.N. Kulkarni was supported by a Grant from the University of Amsterdam. The Research Institute MOVE of the VU University Amsterdam supported the work of A.D. Bakker. The authors thank J.M.A. Hogervorst for excellent help in performing mechanical loading experiments.

References

[1] T. Nakashima, M. Hayashi, T. Fukunaga, et al., Evidence for osteocyte regulation of bone homeostasis through RANKL expression, Nat. Med. 17 (2011) 1231–1234.

[2] P.S. Vezeridis, C.M. Semeins, Q. Chen, J. Klein-Nulend, Osteocytes subjected to pulsating fluid flow regulate osteoblast proliferation and differentiation, Biochem. Biophys. Res. Commun. 348 (2006) 1082–1088.

[3] J. Xiong, M. Onal, R.L. Jilka, et al., Matrix-embedded cells control osteoclast formation, Nat. Med. 17 (2011) 1235–1241.

[4] E.H. Burger, J. Klein-Nulend, Mechanotransduction in bone – role of the lacunocanalicular network, FASEB J. 13 (1999) S101–S112.

[5] J.A. Eastgate, J.A. Symons, N.C. Wood, et al., Correlation of plasma interleukin 1 levels with disease activity in rheumatoid arthritis, Lancet 24 (1988) 706–709.

[6] P. Kahle, J.G. Saal, K. Schaudt, et al., Determination of cytokines in synovial fluids: correlation with diagnosis and histomorphological characteristics of synovial tissue, Ann. Rheum. Dis. 51 (1992) 731–734.

[7] M. Bromley, D.E. Woolley, Chondroclasts and osteoclasts at subchondral sites of erosion in the rheumatoid joint, Arthritis Rheum. 27 (1984) 968–975.

[8] L.A. Joosten, M.M. Helsen, T. Saxne, et al., IL-1 alpha beta blockade prevents cartilage and bone destruction in murine type II collagen-induced arthritis, whereas TNF-alpha blockade only ameliorates joint inflammation, J. Immunol. 163 (1999) 5049–5055.

[9] S. Jurado, N. Garcia-Giralt, A. Díez-Pérez, et al., Effect of IL-1beta, PGE(2), and TGF-beta1 on the expression of OPG and RANKL in normal and osteoporotic primary human osteoblasts, J. Cell. Biochem. 15 (2010) 304–310.

[10] S. Teitelbaum, Osteoclasts: what do they do and how do they do it?, Am J. Pathol. 170 (2007) 427–435.

[11] J.C. Crockett, N. Schütze, D. Tosh, et al., The matricellular protein CYR61 inhibits osteoclastogenesis by a mechanism independent of alphavbeta3 and alphavbeta5, Endocrinology 148 (2007) 5761–5768.

[12] W. Si, Q. Kang, H.H. Luu, et al., CCN1/Cyr61 is regulated by the canonical Wnt signal and plays an important role in Wnt3A-induced osteoblast differentiation of mesenchymal stem cells, Mol. Cell. Biol. 26 (2006) 2955–2964.

[13] J. Lienau, H. Schell, D.R. Epari, et al., CYR61 (CCN1) protein expression during fracture healing in an ovine tibial model and its relation to the mechanical fixation stability, J. Orthop. Res. 24 (2006) 254–262.

[14] A.A. Pitsillides, S.C. Rawlinson, R.F. Suswillo, et al., Mechanical strain-induced NO production by bone cells: a possible role in adaptive bone (re)modeling?, FASEB J 9 (1995) 1614–1622.

[15] J. Klein-Nulend, C.M. Semeins, N.E. Ajubi, et al., Pulsating fluid flow increases nitric oxide (NO) synthesis by osteocytes but not periosteal fibroblasts-correlation with prostaglandin upregulation, Biochem. Biophys. Res. Commun. 217 (1995) 640–648.

[16] S.W. Fox, T.J. Chambers, J.W. Chow, Nitric oxide is an early mediator of the increase in bone formation by mechanical stimulation, Am. J. Physiol. 270 (1996) E955–E960.

[17] S.D. Tan, T.J. de Vries, A.M. Kuijpers-Jagtman, et al., Osteocytes subjected to fluid flow inhibit osteoclast formation and bone resorption, Bone 41 (2007) 745–751.

[18] A.D. Bakker, V.C. Silva, R. Krishnan, et al., Tumor necrosis factor alpha and interleukin-1beta modulate calcium and nitric oxide signaling in mechanically stimulated osteocytes, Arthritis Rheum. 60 (2009) 3336–3345.

[19] Y. Kato, J.J. Windle, B.A. Koop, et al., Establishment of an osteocyte-like cell line, MLO-Y4, J. Bone Miner. Res. 12 (1997) 2014–2023.

[20] T.J. de Vries, T. Schoenmaker, W. Beertsen, et al., Effect of CD44 deficiency on in vitro and in vivo osteoclast formation, J. Cell. Biochem. 94 (2005) 954–966.
[21] A.D. Bakker, K. Soejima, J. Klein-Nulend, E.H. Burger, The production of nitric oxide and prostaglandin E(2) by primary bone cells is shear stress dependent, J. Biomech. 34 (2001) 671–677.
[22] R.G. Bacabac, T.H. Smit, S.C. Cowin, et al., Dynamic shear stress in parallel-plate flow chambers, J. Biomech. 38 (2005) 159–167.
[23] J. Klein-Nulend, A. van der Plas, C.M. Semeins, et al., Sensitivity of osteocytes to biomechanical stress in vitro, FASEB J. 9 (1995) 441–445.
[24] T. Suda, N. Takahashi, N. Udagawa, et al., Modulation of osteoclast differentiation and function by the new members of the tumor necrosis factor receptor and ligand families, Endocr. Rev. 20 (1999) 345–357.
[25] V. Bloemen, T. Schoenmaker, T.J. de Vries, et al., IL-1β favors osteoclastogenesis via supporting human periodontal ligament fibroblasts, J. Cell. Biochem. 112 (2011) 1890–1897.
[26] G. Kogianni, V. Mann, B.S. Noble, Apoptotic bodies convey activity capable of initiating osteoclastogenesis and localized bone destruction, J. Bone Miner. Res. 23 (2008) 915–927.
[27] H. Kamioka, T. Honjo, T. Takano-Yamamoto, A three-dimensional distribution of osteocyte processes revealed by the combination of confocal laser scanning microscopy and differential interference contrast microscopy, Bone 28 (2001) 145–149.
[28] L. You, S. Temiyasathit, P. Lee, et al., Osteocytes as mechanosensors in the inhibition of bone resorption due to mechanical loading, Bone 42 (2008) 172–179.
[29] R.N. Kulkarni, A.D. Bakker, V. Everts, J. Klein-Nulend, Inhibition of osteoclastogenesis by mechanically loaded osteocytes: involvement of MEPE, Calcif. Tissue Int. 87 (2010) 461–468.
[30] G. Zaman, A.A. Pitsillides, S.C. Rawlinson, et al., Mechanical strain stimulates nitric oxide production by rapid activation of endothelial nitric oxide synthase in osteocytes, J. Bone Miner. Res. 14 (1999) 1123–1131.

Biochemical and Biophysical Research Communications 420 (2012) 17–23

Contents lists available at SciVerse ScienceDirect

Biochemical and Biophysical Research Communications

journal homepage: www.elsevier.com/locate/ybbrc

An involvement of SR-B1 mediated PI3K–Akt–eNOS signaling in HDL-induced cyclooxygenase 2 expression and prostacyclin production in endothelial cells

Qing-Hai Zhang [a,b], Xu-Yu Zu [a], Ren-Xian Cao [a], Jiang-Hua Liu [a], Zhong-Cheng Mo [b], Ying Zeng [b], Yuan-Bin Li [b], Sheng-Lin Xiong [b], Xing Liu [b], Duan-Fang Liao [c], Guang-Hui Yi [b,*]

[a] Clinical Research Institution, The First Affiliated Hospital, University of South China, Hengyang, Hunan 421001, China
[b] Institute of Cardiovascular Research, Key Laboratory for Atherosclerology of Hunan Province, University of South China, Hengyang, Hunan 421001, China
[c] Division of Stem Cell Regulation and Application, State Key Laboratory of Chinese Medicine Powder and Medicine Innovation in Hunan, Hunan University of Chinese Medicine, Changsha 410208, China

ARTICLE INFO

Article history:
Received 10 February 2012
Available online 27 February 2012

Keywords:
HDL
SR-B1
PI3K
eNOS
COX-2
PGI_2

ABSTRACT

It is well-known that sphingosine-1-phosphate (S1P), the phospholipid content of HDL, binding to S1P receptors can raise COX-2 expression and PGI_2 release through p38MAPK/CREB pathway. In the present study we assess the action of SR-B1 initiated PI3K–Akt–eNOS signaling in the regulation of COX-2 expression and PGI_2 production in response to HDL. We found that apoA1 could increase PGI_2 release and COX-2 expression in ECV 304 endothelial cells. Furthermore, SR-B1 was found to be involved in HDL induced up-regulation of COX-2 and PGI_2. Over-expressed SR-B1 did not significantly increase the expression of COX-2 and the PGI_2 levels, but knock-down of SR-B1 by siRNA could significantly attenuate COX-2 expression and PGI_2 release together with p38MAPK and CREB phosphorylation. Consistently, the declines of p-p38MAPK, p-CREB, COX-2 and PGI_2 were also observed after incubation with LY294002 (25 μmol/L; PI3K special inhibitor) or L-NAME (50 μmol/L; eNOS special inhibitor). In addition, we demonstrated the increases of PGI_2 release, COX-2 expression and p38MAPK phosphorylation, when nitric oxide level was raised through the incubation of L-arginine (10 or 20 nmol/L) in endothelial cells. Taking together, our data support that SR-B1 mediated PI3K–Akt–eNOS signaling was involved in HDL-induced COX-2 expression and PGI_2 release in endothelial cells.

1. Introduction

Prostacyclin (PGI_2) is a kind of vasoactive endothelial-derived lipid mediator which produced from arachidonic acid after a cascade reaction catalyzed by the cyclooxygenase (COX). Two decades ago, clinical studies found that there was a positive correlation between the plasma levels of HDL-C and PGI_2 [1,2]. Experiments *in vitro* had confirmed that different subtype of HDL, HDL_2 and HDL_3, could induce PGI_2 release in endothelial cells with a dose-dependent manner, which was significantly blocked by COX-2 inhibitor [3–5]. Furthermore, studies indicated that both lipid and protein moiety of HDL were required for induction of PGI_2. The lipid moiety of HDL could increase COX-2 expression and PGI_2 release through enriching arachidonate in smooth muscle cells or endothelial cells, however, neither HDL protein nor lipid moiety showed a more stimulation than native HDL in PGI_2 release [6–8]. Recently, the accumulating evidence has revealed that the phospholipid content of HDL, sphingosine-1-phosphate (S1P), binding to S1P receptors can raise COX-2 expression and PGI_2 release through p38MAPK/CREB pathway in vascular smooth muscle cells [9,10]. As a HMG-CoA reductase inhibitor, clinical dose of simvastatin can increase HDL-induced PGI_2 release in vascular smooth muscle cells, nevertheless, simvastatin treatment shows no significant modification in early MAPK phosphorylation or COX-2 up-regulation stimulated by HDL [11]. Apart from these, HDL_3 can upregulate the COX-2/PGIS activity and PGI_2 release via modulating the shuttling of PGIS and its coupling with COX-2 in a caveolin-dependent manner [12].

Scavenger receptor class B type 1 (SR-B1), a HDL physiological receptor, can specifically bind with the apoA1 and then mediate HDL-induced anti-inflammatory, anti-thrombosis, anti-oxidation and repairing endothelial injury [13,14]. HDL associated SR-B1 receptor can phosphorylate endothelial nitric oxide synthase (eNOS) to increase NO production and activate Rac to form pseudopodia, migrate and finally repair endothelial injury, which were

Abbreviations: HDL, high-density lipoprotein; apoA1, apolipoprotein A-1; SR-B1, scavenger receptor class B type 1; eNOS, endothelial nitric oxide synthase; p38MAPK, p38 mitogen activated protein kinase; CREB, cAMP-response element binding protein; PGIS, prostacyclin synthase; COX-2, cyclooxygenase 2; PGI_2, prostacyclin; S1P, sphingosine 1-phosphate.

* Corresponding author. Fax: +86 0734 8182293.
E-mail address: ghyi6108@163.com (G.-H. Yi).

0006-291X/$ - see front matter © 2012 Elsevier Inc. All rights reserved.
doi:10.1016/j.bbrc.2012.02.103

both dependent on the PI3K–Akt/MAPK signaling pathway[15,16]. However, whether SR-B1 plays a role in HDL induced PGI_2 synthesis still remains unclear to date. Therefore, we hypothesize that scavenger receptor SR-B1 mediated NO production in response to HDL may play a role in induction of COX-2 expression and PGI_2 synthesis in endothelial cells. In this study, we provided evidence that SR-B1 initiated PI3K–Akt–eNOS signaling was involved in HDL-induced COX-2 expression and PGI_2 release in endothelial cells. In addition, we further found an association between SR-B1–PI3K–Akt–eNOS signaling activation and p38MAPK-CREB phosphorylation which could be blunted by knock-down of SR-B1 or the inhibition of PI3K and eNOS activity.

2. Materials and methods

2.1. Materials

Apolipoprotein A1 and L-arginine were purchased from Sigma Chemical Co. (St. Louis, USA). The PI3K inhibitor, LY294002, and the eNOS specific inhibitor, L-NAME, were purchased from the Beyotime Institute of Biotechnology (Jiangsu, China).

2.2. Cell culture

ECV 304 endothelial cells were cultured in DMEM (Invitrogen Co.) supplemented with penicillin (100 U/ml), streptomycin (100 μg/ml) and 10% fetal calf serum (FCS; Sijiqing Ltd.) at 37 °C in 5% CO_2. After 3–4 days, cells were cultured to about 80% confluence and then incubated with fresh medium containing the above reagents for further incubation or with fresh medium containing free FCS for experiments.

2.3. Preparation of HDL

HDL were isolated from human plasma by sequential density ultracentrifugation as described previously [9] and dialyzed for 48 hours with PBS for eliminating EDTA. The HDL protein concentration was measured by the BCA protein assay™ (Pierce Co.). Then HDL were filtered by disposable filter (0.22 μm) and stored at 4 °C for the following experiments.

2.4. Cell transfection

The pcDNA3.1(−)-hSR-B1 recombined expression plasmid were finished in our previous study. The siRNA sequences of SR-B1 (sence: 5′-GGA CAA GUU CGG AUU AUU UdTdT-3′; antisence: 5′-AAA UAA UCC GAA CUU GUC CTdTd-3′) were designed and produced from Guangzhou Ribobio Co., Ltd., China. ECV304 endothelial cells were transfected with pcDNA3.1(−)-hSR-B1 plasmid or SR-B1 siRNA using Lipofectamine™ 2000 (Invitrogen Co.) when cells had been 50–70% confluent.

2.5. Polymerase chain reaction

Total RNA from cells was extracted using TRIzol reagent (Invitrogen Co.). After synthesized the first strand cDNA on Techne TC-412 Thermal Cycler according to the protocol of ReverAid™ First Strand cDNA Synthesis Kit (Fermentas Co.), 1 μl cDNA as template were subjected to polymerase chain reaction. COX-2 primers were 5′-TTC AAA TGA GAT TGT GGG AAA ATT GCT-3′ and 5′-AGA TCA TCT CTG CCT GAG TAT CTT-3′, which gives rise to 305 bp PCR products after 35 cycles of PCR. GAPDH Primers were 5′-CAA GGT CAT CCA TGA CAA CTT TG-3′ and 5′-GTC CAC CAC CCT GTT GCT GTA G-3′, which gives rise to 496 bp PCR products after 35 cycles of PCR. The relative mRNA level was calculated by densitometry using Labwords analysis software.

2.6. Western blot analysis

After treatment the cells were washed with phosphate-buffer saline (PBS), then equal amount of samples (cell lysates 20–50 μg) were subjected to western blot analysis. Antibodies used in this study were rabbit anti-COX-2 (Epitomics; 1:1000), anti-p38MAPK (Epitomics; 1:1000), anti-phospho-p38MAPK (Epitomics; 1:500), anti-CREB (Epitomics; 1:500), anti-phospho-CREB (Epitomics; 1:100), anti-β-actin (Epitomics; 1:2000), and HRP-conjugated goat anti-rabbit secondary antibody (Epitomics; 1:2000).

2.7. Prostacyclin production assay

PGI_2 was highly unstable and easy to metabolize to a stable metabolite 6-keto-$PGF_{1\alpha}$ Thus, PGI_2 in the culture medium was measured with an 6-keto-$PGF_{1\alpha}$ enzyme immunoassay kit (Cayman Co.). The assay was performed according to the manufacturer's instructions. The absorbance was read at 405 nm.

2.8. Nitric oxide production Assay

Nitric oxide (NO) *in vivo* is active, and it will metabolize into nitrite (NO_2^-) and nitrate (NO_3^-). The concentration of nitrite and nitrate can accurately represent the NO levels *in vivo*. Here we measured NO concentration of culture medium indirectly using NO assay kit (Nanjing Jiancheng Bioengineering Institute). The absorbance of samples was determined at 550 nm with a 722 spectrophotometer. The NO content (μmol/L) was calculated according to the formula: (the sample value − the blank value)/(the standard value − the blank value) × 100.

2.9. Immunohistochemistry

The COX-2 immunoreactivities in endothelial cells were verified with an Ultrasensitive™ S-P kit (MaiXin Ltd.). After treatment, the cells were washed three times with PBS (pH7.4) for 10 min, and incubated with 50 μl peroxidase blocking solution for 10 min at room temperature to block endogenous peroxidase activity. Subsequently, the cells were rinsed in PBS again and incubated with 50 μl normal non-immune serum for 10 min. After removed the serum and incubated with 50 μl COX-2 antibody (1:100) at 4 °C overnight, the cells were washed three times in PBS again. 50 μl biotinylated second antibody incubated for 10 min, PBS rinsed three times for 10 min and 50 μl streptavidin biotin–peroxidase solution incubated for 10 min at room temperature were performed in succession. Finally, 3,3′-diaminobenzidine tetrahydrochloride was used as the chromogen, and hematoxylin was used as the counterstain.

2.10. Statistical analysis

Data were expressed as means ± S.D. Results were analyzed by one-way ANOVA or Student's *t*-test, using SPSS 13.0 software. Significance is indicated when P values were less than 0.05.

3. Results

3.1. apoA1 increases PGI_2 release and COX-2 expression in ECV 304 endothelial cells

Some studies have confirmed that the S1P, phospholipid composition of HDL, can increase the release of PGI_2 in endothelial cells

[9–11], but whether apoA1, another important component of HDL, plays a role in HDL-induced PGI_2 release is still unclear. Here, we first observed the effect of apoA1 on PGI_2 release in ECV304 endothelial cells by enzyme-linked immunosorbent assay. As shown (Fig. 1), the PGI_2 generation was increased significantly after 30 μg/ml apoA1 incubated for 12 hours, and reached the peak at 24 hours (Fig. 1A). However, there was no significant difference among apoA1 treatment at the concentration of 30, 60 and 120 μg/ml (Fig. 1B).

HDL can concentration-dependently increase COX-2 expression in endothelial cells, and HDL-induced PGI_2 generation was dependent on COX-2 expression [7,9,11,12]. Therefore, the expression of COX-2 in endothelial cells after apoA1 treatment was examined. We found that COX-2 expression was up-regulated after treatment with 30 μg/ml apoA1 for 24 h at both transcriptional and translational levels (Fig. 1C and D). These results suggest that apoA1 can also play a role, at least in part, in HDL-induced PGI_2 release and COX-2 expression in endothelial cells.

3.2. SR-B1 is implicated in PGI_2 release and COX-2 expression induced by HDL

Scavenger receptor SR-B1 has been confirmed to mediate multiple functions of HDL through binding with apoA1. As shown above, we have suggested that apoA1 promoted PGI_2 production induced by HDL in endothelial cells. It may be supposed that SR-B1 also mediated HDL-induced PGI_2 release in endothelial cell. Here, we firstly modulated the expression of SR-B1 by transfection of recombinant human SR-B1 expression plasmid or SR-B1 siRNA in ECV 304 endothelial cells and the PGI_2 level in culture medium was observed after HDL treatment. Interestingly, the results showed that SR-B1 over-expression did not promote PGI_2 induction by HDL, but SR-B1 knock-down through RNA interference could significantly attenuate PGI_2 release by nearly half (Fig. 2A and B).

To confirm whether HDL up-regulated COX-2 expression could be mediated by SR-B1, RT-PCR and immunoassay were performed. As compared with HDL treatment alone, there was no significant increase in the expression of COX-2 mRNA and protein stimulated by HDL after over-expressing SR-B1 (Fig. 2C and E). However, A decline of COX-2 expression, both mRNA and protein levels, were observed dramatically when cells were transfected with SR-B1 siRNA (Fig. 2D and E). Those results were further confirmed by immunocytochemistry staining for COX-2 protein in ECV304 endothelial cells (Fig. 2F). These results above indicate that SR-B1 is required for HDL-induced COX-2 expression and PGI_2 production in endothelial cells.

3.3. PI3K–Akt–eNOS signaling pathway mediates PGI_2 release and COX-2 expression induced by HDL

As an important ligand of SR-B1, HDL enhanced eNOS activity via phosphorylating serine 1179 and increased nitric oxide production through SR-B1 mediated PI3K and Akt activation [15]. The former results indicate that SR-B1 involves in HDL-induced PGI_2 release and COX-2 expression. Hence, we attempt to define the role of PI3K/Akt/eNOS signaling pathway in HDL induced PGI_2 release and COX-2 expression. We treated ECV304 cells with LY294002 (25 μmol/L), a PI3K special inhibitor, or L-NAME (50 μmol/L), an eNOS special inhibitor, in the presence of HDL (30 μg/ml) for 24 h. Subsequently, the PGI_2 production and the COX-2 expression were determined. It was found that both PI3K inhibitor and eNOS inhibitor could impair HDL induced PGI_2 production and COX-2 expression (Fig. 3A–C); however, LY294002 showed more inhibition on HDL induced PGI_2 production and COX-2 expression than that with L-NAME.

The eNOS activation can catalyze L-arginine to generate NO, nevertheless inhibited eNOS can down-regulate the PGI_2 release and COX-2 expression stimulated by HDL. Then we further investigated whether NO play a role in HDL-induced COX-2 expression by co-treatment of HDL and L-arginine in ECV304 endothelial cells. As showed in Fig. 3D, HDL in combination with L-arginine (10 or 20 nmol/L) could promote NO generation. But when the concentration of L-arginine reached at 20 nmol/L, there was no significant rise

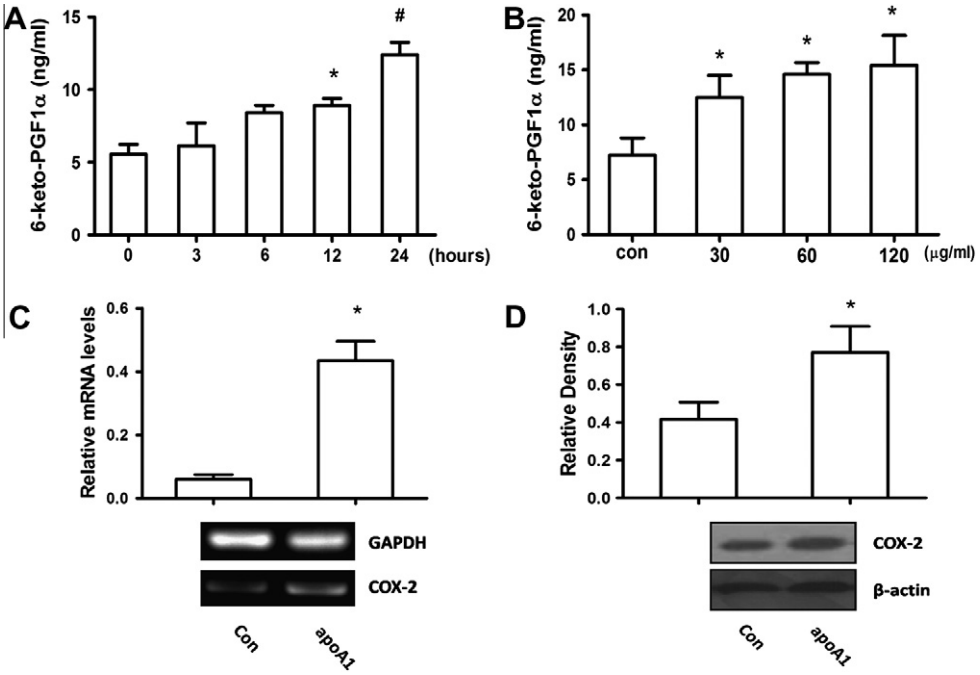

Fig. 1. apoA1 increases PGI_2 release and COX-2 expression in ECV 304 endothelial cells. (A) and (B) Cells incubated with 30 μg/ml apoA1 for different times (0, 3, 6, 12, 24 h) or with different concentration of apoA1(30, 60, 120 μg/ml) and 5 μl DMSO as control group for 24 h, respectively, then the PGI_2 levels of the medium was detected using ELISA kit. (C) and (D) COX-2 gene and protein expressions were measured by RT-PCR and western immunoblotting assays after incubation of 30 μg/ml apoA1 for 24 hours. All the results were expressed as mean ± S.D. from three independent experiments. $^{*}P < 0.05$ vs. 0 h or control group; $^{\#}P < 0.01$ vs. 0 h group.

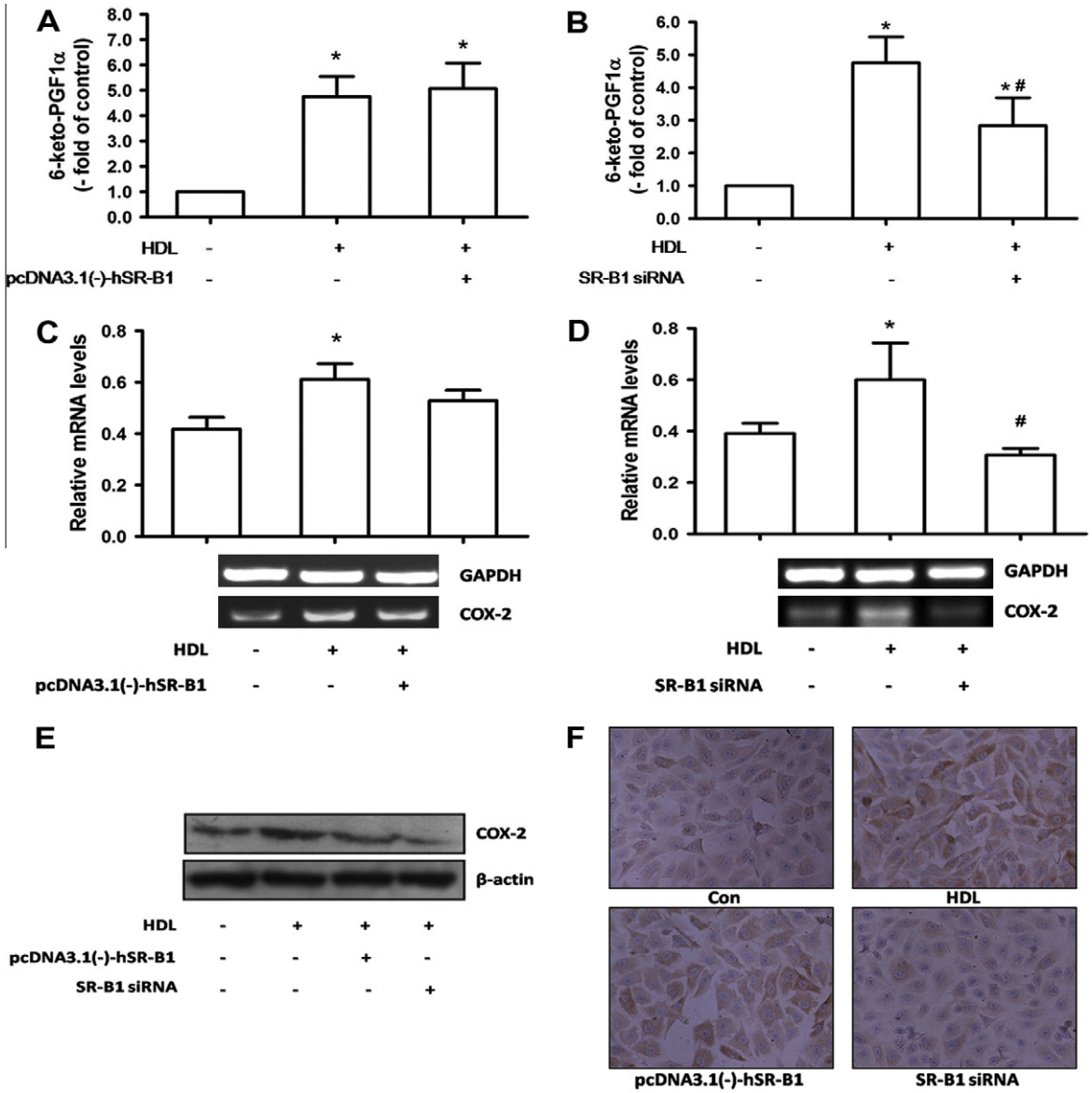

Fig. 2. SR-B1 mediates up-regulation of PGI_2 and COX-2 in response to HDL in ECV304 endothelia cells. (A) and (B) Cells were seeded in 6-well plates and incubated with 30 μg/ml HDL for 24 h, 5 μl DMSO as control group, in the absence or presence of pcDNA3.1(−)-hSR-B1 (4.0 μg per well) or SR-B1 siRNA (50 nmol per well) transfection, respectively, The PGI_2 levels were detected as described above. (C) and (D) RT-PCR determination of COX-2 mRNA levels. (E) Equal amounts of proteins (20 μg) were subjected to immunoblot analysis. (F) Similar results were showed by immunocytochemical stain (20×). Data were showed in mean ± S.D. which obtained in three independent experiments. $^{*}P < 0.05$ vs. control; $^{\#}P < 0.05$ vs. HDL group.

in the NO level compared with that at 10 nmol/L. Furthermore, we found that the PGI_2 release and the COX-2 expression were increased with the raising of NO level in endothelial cells (Fig. 3E and F).

3.4. SR-B1–PI3K–Akt–eNOS signaling pathway regulates p38MAPK and CREB activation

The expression of COX-2 was regulated by many transcription factors, such as CREB, NF-κB or AP-1[17]. However, studies have confirmed that HDL can increase the activation of CREB and subsequent COX-2 induction and PGI_2 release in endothelial or smooth muscle cells. Meanwhile, the phosphorylation of p38MAPK is implicated in this function of HDL. Next, we further investigate the phosphorylation of p38MAPK and CREB induced by HDL after modulation of SR-B1 expression or PI3K activity or eNOS activity. As previous studies showed, HDL could increase the phosphorylation of p38MAPK and CREB (Fig. 4). SR-B1 expression alteration showed no effect on the expression of p38MAPK and CREB, but the phosphorylation levels were both reduced by knock-down of SR-B1 gene expression (Fig. 4A).

In addition, using LY294002 to block PI3K/Akt activation could significantly decrease p38MAPK and CREB phosphorylation compared with HDL treatment alone (Fig. 4B), which was consistent with the former results (Fig. 3A and C). When endothelial cells were treated with eNOS inhibitor L-NAME, the HDL-induced activation of both p38MAPK and CREB were attenuated (Fig. 4B). On the contrary, increased NO generation by adding L-arginine could accelerate the phosphorylation of p38MAPK and CREB (Fig. 4C). Those results suggest that NO was implicated in HDL-stimulated p38MAPK activation and the follow-up CREB activation.

4. Discussion

It has been shown that the level of HDL-C is positively correlated to PGI_2 in plasma [1,2], and both HDL_2 and HDL_3 are able to

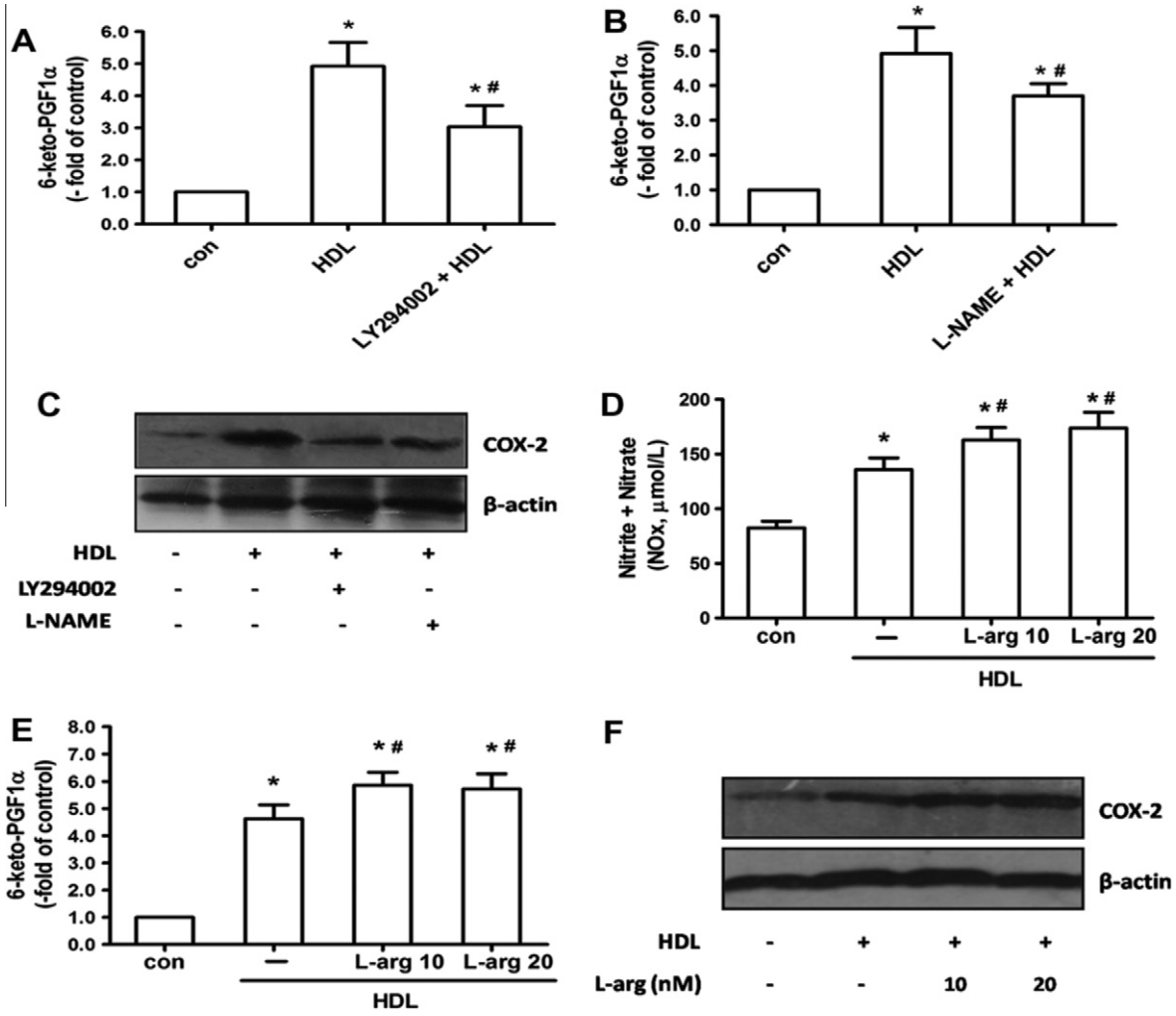

Fig. 3. PI3K–Akt–eNOS signaling pathway is required for up-regulation of HDL on PGI_2 release and COX-2 expression. (A) and (B) ECV304 endothelial cells were treated with 5 μl DMSO (as control group) or 30 μg/ml HDL or in combination with 25 μmol/L LY294002 (PI3K special inhibitor) or 50 μmol/L L-NAME (eNOS special inhibitor) for 24 h, respectively. The PGI_2 levels were determined via ELISA. (C) The COX-2 immunoactivity were determined via Western immunoblotting analysis. (D) The NO production of ECV304 cells after incubation of HDL combined with or without L-arginine (10 or 20 nmol/L). (E) and (F) An enhancing effect of L-arginine on induction of PGI_2 and COX-2 in response to HDL. Data were showed by mean ± S.D. from three independent experiments. $^{*}P < 0.05$ vs. control; $^{\#}P < 0.05$ vs. HDL group.

induce a dose-dependent release of PGI_2 in endothelial cells, which can be blocked by COX inhibitors [3–5]. Moreover, the phospholipid component of HDL, S1P, could increase PGI_2 release both in endothelial and smooth muscle cells [9,11]. In this study, we found apoA1 as the main protein component of HDL is able to significantly induce PGI_2 release and elevate COX-2 mRNA and protein levels in endothelial cells. The results given here are consistent with the latest study by Liu et al [18]. In addition, Pomerantz and Escudero et al. [6,7] had reported that lipid-poor HDL could significantly increase PGI_2 production which was weaker than the lipid-rich HDL stimulated. Thus, we can infer that apoA1 is definitely involved in HDL-induced PGI_2 synthesis and COX-2 expression in endothelial cells.

As a physiological receptor of HDL, SR-B1 can mediate HDL to exert multiple antiatherogenic functions including anti-inflammatory, antioxidant, anti-endothelial injury and antithrombosis [13,14]. It had been confirmed that HDL could up-regulate the expression of COX-2 to increase PGI_2 generation in endothelial or smooth muscle cells [7,9,11,12]. In the present study, we similarly showed an induction of HDL in PGI_2 release and COX-2 expression. Meanwhile, we demonstrated that knock-down of SR-B1 significantly reduced PGI_2 release and COX-2 expression, but there was no obvious increase of PGI_2 and COX-2 after over-expressing SR-B1. Apart from SR-B1, S1P receptors binding with S1P of HDL can also mediate PGI_2 generation [9–11]. Moreover, studies found that both scavenger receptor SR-B1 and S1P receptors were clustered in the caveolae/rafts region of plasma membrane in which phospholipids were rich [19,20]. Therefore, over-expressing SR-B1 in caveolae may spatially affect the part of S1P receptor-mediated function. Some evidence has indicated that S1P receptors mediated HDL induction in inhibiting NADPH activation to reduce the generation of reactive oxygen species and the expression of adhesion molecules was blocked in SR-B1 knockout mice, suggesting a functional synergy between S1P receptors and SR-B1 [21,22]. Combined with our results, we propose that SR-B1 is required for the PGI_2 release and COX-2 expression induced by HDL in endothelial cells.

Mineo and Shaul [15] have confirmed that HDL associated with SR-B1 could activate PI3K–Akt/MAPK signaling pathway, and then phosphorylate eNOS to increase NO production. In addition, apoA1 of HDL binding to SR-B1 could also activate Src kinase–PI3K/ERK-Rac pathway, leading to pseudopod formation, migration, and then repairing the endothelial injury [16]. NO is a highly unorthodox messenger molecule which is able to act as an important regulatory factor of COX-2 expression and activity [23]. A large

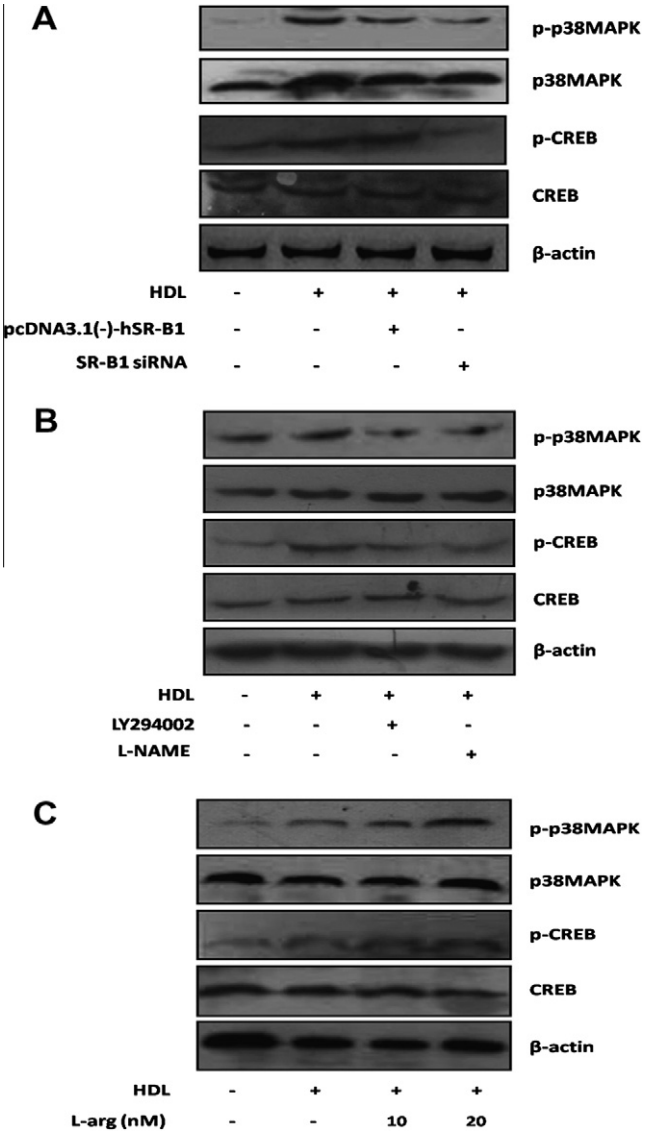

Fig. 4. The phosphorylation of p38MAPK and CREB mediated by SR-B1–PI3K–Akt–eNOS signaling. Cells were treated as demonstrated above respectively.

amount of evidence suggested that NO could increase or decrease the expression of COX-2 in a variety of cell types. But most past studies had shown that NO could up-regulate COX-2 expression or its activity [23–25]. Moreover, recent evidence demonstrates that oxidized steroids may increase COX-2 expression through the PI3K–Akt–eNOS pathway in human umbilical vein endothelial cells [26]. Thus, we observed whether the classical pathway mediated by SR-B1, PI3K–Akt–eNOS, plays a role in HDL-induced PGI_2 generation in endothelial cells. This paper provide evidence that both PI3K and eNOS inhibitor can significantly reduce COX-2 expression and PGI_2 generation induced by HDL. Meanwhile, to determine the exact role of NO in COX-2 expression and PGI_2 production caused by HDL, we further tested the effect of combination treatment with HDL and L-arginine on PGI_2 release and COX-2 expression. We found that both PGI_2 release and COX-2 expression was increased with the raising of NO production in endothelial cells. These results indicate that PI3K–Akt–eNOS signaling pathway plays a role in HDL induced PGI_2 and COX-2 production in endothelial cells.

The p38MAPK is activated by a wide range of factors. A series of studies have reported that NO could significantly activate p38MAPK via cGMP dependent and -independent mechanisms, contributing to regulate the mRNA stability and the expression of many genes, including COX-2, in monocytes/macrophages or endothelial cells [27–30]. Here, we report a role of SR-B1 and its associated PI3K–Akt–eNOS signaling in HDL induced p38MAPK and CREB activation. These results were highly consistent with the regulation of PI3K and eNOS on COX-2 expression and PGI_2 production. In the paper, although we have not investigated the specific mechanism between NO production and p38MAPK activation, it is suggested that increasing NO production is more likely to phosphorylate p38MAPK through autocrine/paracrine mechanisms, which contributes to trigger CREB activation and following induction of COX-2 expression and PGI_2 synthesis.

In summary, we can conclude that the SR-B1 initiated PI3K–Akt–eNOS signaling is required for HDL-induced COX-2 expression and PGI_2 release in endothelial cells. All these findings may help elucidate the mechanisms of antithrombotic effects of HDL. Certainly, how much of function does SR-B1 play or whether SR-B1 or S1P receptor plays a dominant role in HDL induction of PGI_2 synthesis needs to be further studied.

Acknowledgments

This work was supported by a Grant from the National Natural Sciences Foundation of China (30570958), and the Key Program of Research Foundation of Education Bureau of Hunan Province, China (09A078).

References

[1] R. Rauramaa, J.T. Salonen, K. Kukkonen-Harjula, et al., Effects of mild physical exercise on serum lipoproteins and metabolites of arachidonic acid: a controlled randomised trial in middle aged men, Br. Med. J. (Clin. Res. Ed.) 288 (1984) 603–606.
[2] J.D. Symons, Longitudinal and cross-sectional studies of the relationship between 6-keto PGF1 alpha and high density lipoproteins, Prostaglandins Leukot. Essent. Fatty Acids 39 (1990) 159–165.
[3] L.N. Fleisher, A.R. Tall, L.D. Witte, et al., Stimulation of arterial endothelial cell prostacyclin synthesis by high density lipoproteins, J. Biol. Chem. 257 (1982) 6653–6655.
[4] A.A. Spector, A.M. Scanu, T.L. Kaduce, et al., Effect of human plasma lipoproteins on prostacyclin production by cultured endothelial cells, J. Lipid Res. 26 (1985) 288–297.
[5] S. Oravec, K. Demuth, I. Myara, et al., The effect of high density lipoprotein subfractions on endothelial eicosanoid secretion, Thromb. Res. 92 (1998) 65–71.
[6] K.B. Pomerantz, L.N. Fleisher, A.R. Tall, et al., Enrichment of endothelial cell arachidonate by lipid transfer from high density lipoproteins: relationship to prostaglandin I2 synthesis, J. Lipid Res. 26 (1985) 1269–1276.
[7] I. Escudero, J. Martinez-Gonzalez, R. Alonso, et al., Experimental and interventional dietary study in humans on the role of HDL fatty acid composition in PGI2 release and Cox-2 expression by VSMC, Eur. J. Clin. Invest. 33 (2003) 779–786.
[8] M. Vinals, J. Martinez-Gonzalez, J.J. Badimon, et al., HDL-induced prostacyclin release in smooth muscle cells is dependent on cyclooxygenase-2 (Cox-2), Arterioscler. Thromb. Vasc. Biol. 17 (1997) 3481–3488.
[9] M. Gonzalez-Diez, C. Rodriguez, L. Badimon, et al., Prostacyclin induction by high-density lipoprotein (HDL) in vascular smooth muscle cells depends on sphingosine 1-phosphate receptors: effect of simvastatin, Thromb. Haemost. 100 (2008) 119–126.
[10] C. Rodriguez, M. Gonzalez-Diez, L. Badimon, et al., Sphingosine-1-phosphate: a bioactive lipid that confers high-density lipoprotein with vasculoprotection mediated by nitric oxide and prostacyclin, Thromb. Haemost. 101 (2009) 665–673.
[11] J. Martinez-Gonzalez, I. Escudero, L. Badimon, Simvastatin potenciates PGI(2) release induced by HDL in human VSMC: effect on Cox-2 up-regulation and MAPK signalling pathways activated by HDL, Atherosclerosis. 174 (2004) 305–313.
[12] G.D. Norata, E. Callegari, H. Inoue, et al., HDL3 induces cyclooxygenase-2 expression and prostacyclin release in human endothelial cells via a p38 MAPK/CRE-dependent pathway: effects on COX-2/PGI-synthase coupling, Arterioscler. Thromb. Vasc. Biol. 24 (2004) 871–877.
[13] M.A. Connelly, SR-BI-mediated HDL cholesteryl ester delivery in the adrenal gland, Mol. Cell. Endocrinol. 300 (2009) 83–88.
[14] C. Mineo, H. Deguchi, J.H. Griffin, et al., Endothelial and antithrombotic actions of HDL, Circ. Res. 98 (2006) 1352–1364.
[15] C. Mineo, P.W. Shaul, HDL stimulation of endothelial nitric oxide synthase: a novel mechanism of HDL action, Trends Cardiovasc. Med. 13 (2003) 226–231.

[16] D. Seetharam, C. Mineo, Gormley AK et al, High-density lipoprotein promotes endothelial cell migration and reendothelialization via scavenger receptor-B type I, Circ Res. 98 (2006) 63–72.
[17] J.S. Guo, C.H. Cho, J.Y. Wang, et al., Differential effects of selective and non-selective inhibition of nitric oxide synthase on the expression and activity of cyclooxygenase-2 during gastric ulcer healing, Eur. J. Pharmacol. 536 (2006) 301–308.
[18] D. Liu, L. Ji, X. Tong, et al., Human apolipoprotein A-I induces cyclooxygenase-2 expression and prostaglandin I-2 release in endothelial cells through ATP-binding cassette transporter A1, Am. J. Physiol. Cell Physiol. 301 (2011) C739–748.
[19] I.S. Yuhanna, Y. Zhu, B.E. Cox, et al., High-density lipoprotein binding to scavenger receptor-BI activates endothelial nitric oxide synthase, Nat. Med. 7 (2001) 853–857.
[20] J. Igarashi, T. Michel, Agonist-modulated targeting of the EDG-1 receptor to plasmalemmal caveolae. eNOS activation by sphingosine 1-phosphate and the role of caveolin-1 in sphingolipid signal transduction, J. Biol. Chem. 275 (2000) 32363–32370.
[21] T. Kimura, H. Tomura, C. Mogi, et al., Role of scavenger receptor class B type I and sphingosine 1-phosphate receptors in high density lipoprotein-induced inhibition of adhesion molecule expression in endothelial cells, J. Biol. Chem. 281 (2006) 37457–37467.
[22] M. Tolle, A. Pawlak, M. Schuchardt, et al., HDL-associated lysosphingolipids inhibit NAD(P)H oxidase-dependent monocyte chemoattractant protein-1 production, Arterioscler. Thromb. Vasc. Biol. 28 (2008) 1542–1548.
[23] D. Perez-Sala, S. Lamas, Regulation of cyclooxygenase-2 expression by nitric oxide in cells, Antioxid. Redox Signal. 3 (2001) 231–248.
[24] S. Honda, K. Migita, Y. Hirai, et al., Induction of COX-2 expression by nitric oxide in rheumatoid synovial cells, Biochem. Biophys. Res. Commun. 268 (2000) 928–931.
[25] S.W. Park, S.G. Lee, S.H. Song, et al., The effect of nitric oxide on cyclooxygenase-2 (COX-2) overexpression in head and neck cancer cell lines, Int. J. Cancer 107 (2003) 729–738.
[26] P.L. Liao, Y.W. Cheng, C.H. Li, et al., Cholesterol-3-beta,5-alpha,6-beta-triol induced PI(3)K–Akt–eNOS-dependent cyclooxygenase-2 expression in endothelial cells, Toxicol. Lett. 190 (2009) 172–178.
[27] A. Ptasinska, S. Wang, J. Zhang, et al., Nitric oxide activation of peroxisome proliferator-activated receptor gamma through a p38 MAPK signaling pathway, FASEB J. 21 (2007) 950–961.
[28] S. Wang, J. Zhang, Y. Zhang, et al., Nitric oxide-p38 MAPK signaling stabilizes mRNA through AU-rich element-dependent and -independent mechanisms, J. Leukoc. Biol. 83 (2008) 982–990.
[29] C.S. Boddupalli, S. Ghosh, S.S. Rahim, et al., Nitric oxide inhibits interleukin-12 p40 through p38 MAPK-mediated regulation of calmodulin and c-rel, Free Radic Biol Med. 42 (2007) 686–697.
[30] D.D. Browning, M.P. McShane, C. Marty, et al., Nitric oxide activation of p38 mitogen-activated protein kinase in 293T fibroblasts requires cGMP-dependent protein kinase, J. Biol. Chem. 275 (2000) 2811–2816.

Biochemical and Biophysical Research Communications 420 (2012) 24–28

Contents lists available at SciVerse ScienceDirect

Biochemical and Biophysical Research Communications

journal homepage: www.elsevier.com/locate/ybbrc

Targeting Werner syndrome protein sensitizes U-2 OS osteosarcoma cells to selenium-induced DNA damage response and necrotic death

Wen-Hsing Cheng [a,*], Ryan T.Y. Wu [a], Min Wu [a], Caroline R.B. Rocourt [a], Jose A. Carrillo [b], Jiuzhou Song [b], Christina T. Bohr [a], Tiffany J. Tzeng [a]

[a] Department of Nutrition and Food Science, University of Maryland, College Park, MD 20742, USA
[b] Department of Animal and Avian Sciences, University of Maryland, College Park, MD 20742, USA

ARTICLE INFO

Article history:
Received 17 February 2012
Available online 27 February 2012

Keywords:
Selenium
Werner syndrome
WRN
ATM
Cancer

ABSTRACT

Mutations in the Werner syndrome protein (WRN), a caretaker of the genome, result in Werner syndrome, which is characterized by premature aging phenotypes and cancer predisposition. Methylseleninic acid (MSeA) can activate DNA damage responses and is a superior compound to suppress tumorigenesis in mouse models of cancer. To test the hypothesis that targeting WRN can potentiate selenium toxicity in cancer cells, isogenic WRN small hairpin RNA (shRNA) and control shRNA U-2 OS osteosarcoma cells were treated with MSeA for 2 d, followed by recovery for up to 7 d. WRN deficiency sensitized U-2 OS cells to MSeA-induced necrotic death. Co-treatment with the ataxia-telangiectasia mutated (ATM) kinase inhibitor KU55933 desensitized the control shRNA cells, but not WRN shRNA cells, to MSeA treatment. WRN did not affect MSeA-induced ATM phosphorylation on Ser-1981 or H2A.X phosphorylation on Ser-139, but promoted recovery from the MSeA-induced DNA damage. Taken together, WRN protects U-2 OS osteosarcoma cells against MSeA-induced cytotoxicity, suggesting that oxidative DNA repair pathway is a promising target for improving the efficacy of selenium on tumor suppression.

1. Introduction

Cells respond to DNA damage by induction of cell cycle checkpoint, DNA repair, senescence and cell death. Werner syndrome, due to loss-of-function mutations in the *WRN* gene, is an autosomal recessive disorder characterized by premature aging and cancer predisposition [1,2]. The WRN protein exhibits helicase and exonuclease activities and is proposed to play essential roles in the maintenance of genomic stability, including telomere protection and DNA damage responses [3,4]. Excess reactive oxygen species (ROS) can induce oxidative DNA damage, which is converted to DNA breaks if left unrepaired [5]. Interestingly, oxidative modifications on proteins are prominent in cells isolated from Werner syndrome patients [6], and the aging phenotype in a mouse model of Werner syndrome can be reversed by dietary supplementation of vitamin C [7]. Indeed, WRN is involved in the repair of oxidative DNA damage [8–10], and oxidation on WRN protein suppresses its catalytic and base excision repair functions [11]. Another genome instability syndrome, ataxia-telangiectasia, is characterized by *ATM* mutations, neuronal degeneration and cancer predisposition [12]. In the response to DNA damage or oxidative stress [13,14], the ATM pathway is activated by phosphorylation of ATM on Ser-1981 (pATM Ser-1981).

Our recent publications demonstrate that MSeA-induced ROS formation differentially activates ATM-dependent DNA damage responses in cancerous and in non-cancerous cells [15,16]. Selenium mediates tumorigenesis through selenoproteins and low molecular weight selenium compounds [17,18], the latter of which represents up to 15% of total plasma selenium [19]. At nutritional level, selenium modulates tumorigenesis mainly through selenoproteins [17]. At supranutritional level, selenium metabolites and the resulting ROS account for much of the anti-carcinogenic effects of this element [18]. In principle, chemoprevention could reverse or prevent the initial phase of carcinogenesis or the progression from neoplastic through cancerous cells [20]. Although results of the Nutritional Prevention of Cancer (NPC) clinical trial implicate selenium chemoprevention in healthy individuals [21], the Selenium and Vitamin E Cancer Prevention Trial (SELECT) study did not demonstrate prostate cancer prevention by selenomethionine [22]. Nonetheless, orally administration of an acute dose of selenium inhibits angiogenesis in rats carrying carcinoma [23], and consumption of selenium-enriched broccoli suppresses the neoplastic

Abbreviations: ATM, ataxia-telangiectasia mutated; γH2A.X, H2A.X phosphorylation on Ser-139; MSeA, methylseleninic acid; MTT, 3-(4,5-dimethylthiazol-2-yl)-2,5-diphenyltetrazolium bromide; NPC, Nutritional Prevention of Cancer; pATM Ser-1981, phosphorylation of ATM on Ser-1981; ROS, reactive oxygen species; SELECT, Selenium and Vitamin E Cancer Prevention Trial; shRNA, small hairpin RNA; WRN, Werner syndrome protein.

* Corresponding author. Fax: +1 301 314 3313.
E-mail address: whcheng@umd.edu (W.-H. Cheng).

0006-291X/$ - see front matter © 2012 Elsevier Inc. All rights reserved.
doi:10.1016/j.bbrc.2012.02.104

polyps formation in a mouse model of colon cancer [24]. Altogether, selenium is proposed to play an inhibitory role against tumorigenesis in neoplastic and in cancerous cells.

Genome maintenance is a double-edged sword. DNA damage response protects normal cells against damage accumulation and senescence, but promotes the survival of cancer cells. In this regard, targeting DNA repair pathway [25] represents an appealing approach to improve the effect of selenium on tumor suppression. Interestingly, Brosh and colleagues [26] recently identified a small chemical inhibitor against WRN helicase that sensitized cancer cells to DNA-damaging agents. In this study, we tested the hypothesis that the efficacy of selenium toxicity on cancer cells can be improved by targeting WRN in U-2 OS osteosarcoma cells.

2. Materials and methods

2.1. Cell culture and chemicals

Based on proteomic analyses, the human osteosarcoma U-2 OS cells exhibit markers of early stage cancer and DNA damage [27]. The knockdown efficiency of WRN in U-2 OS cells is approximately 80–85% [28]. Because cancers found in Werner syndrome patients are mainly of mesenchymal origin [29,30], U-2 OS osteosarcoma cells were chosen to establish WRN knockdown. Selenium compounds and 3-(4,5-dimethylthiazol-2-yl)-2,5-diphenyltetrazolium bromide (MTT) were obtained from Sigma–Aldrich (St. Louis, MO) and all were dissolved in serum free cell culture medium. KU55933 was purchased from Tocris (Ellisville, MO) and was dissolved in DMSO.

2.2. Cell survival assay

Exponentially growing U-2 OS cells in 24-well plates were incubated with MSeA (0–10 μmol/l) for 48 h, followed by recovery for 7 d. Some cells were co-treated with KU55933 (10 μmol/l, Fig. 2). Because U-2 OS cells do not effectively form colonies under DNA-damaging agent exposure, a MTT assay was employed [31]. The MTT value in the cells without MSeA treatment was set as 100%.

2.3. Apoptosis, necrosis and senescence assay

The cells were plated and grown to 70% confluency and treated with MSeA (4 μmol/l) for 0–2 d, after which the cells were resuspended and incubated in a buffer containing annexin V-FITC and sytox green dye according to the manufacturer's instruction (Biovision K201-400, Mountain View, CA). The cells were then analyzed (Ex, 488 nm; Em, 530 nm in the FL1 channel) by using a BD FACSCanto II flow cytometer. Apoptotic cells were detected by annexin V staining. Sytox green dye penetrates and binds nucleic acids in necrotic cells, but is impermeable to healthy and apoptotic cells. Consequently, necrotic cells show a greater fluorescence signal than apoptotic cells, while healthy cells show little or no fluorescence. We detected the expression of senescence associated-β-galactosidase as described previously [16].

2.4. Immunofluorescence

Immunofluorescent analyses of pATM Ser-1981 were performed as described previously [15,16]. Cells were cultured on coverslips and treated with 4 μmol/l MSeA for 2 d, followed by recovery for 0–5 d. Because the level of H2A.X phosphorylation on Ser-139 (γH2A.X) is intrinsically high in U-2 OS cells, the expression level was quantified based on fluorescent intensity after deconvolution using AxioVision Release 4.7.2.0 coupled to a Zeiss Axio Observer Z1m fluorescence microscope (Zeiss, Thornwood, NY). Five pictures were randomly taken from each slide ($n = 3$). The γH2A.X signal was normalized with 4′,6-diamidino-2-phenylindole signal, and the level in control shRNA cells without MSeA treatment was set as 100%.

2.5. Statistics

In Figs. 1 and 2, two-group comparisons were analyzed using t test, assuming equal variance. In Tables 1 and 2, data were analyzed by General Linear Model of SAS (Cary, NC), and the Tukey's test was used for mean comparisons. In Table 2, the model used was: $y_{ijk} = \alpha_i + \beta_j + \gamma_{ij} + e_{ijk}$, where α_i = cell type, β_j = recovery time, γ_{ij} interactions, and e_{ijk} = errors of the observations. Linear regression was also applied in Tables 1 and 2.

3. Results

3.1. WRN ablation sensitized U-2 OS cells to MSeA exposure

WRN shRNA U-2 OS cells were more sensitive ($P < 0.05$) than control shRNA cells to MSeA treatment at 2–5 μmol/l (Fig. 1). Sub-

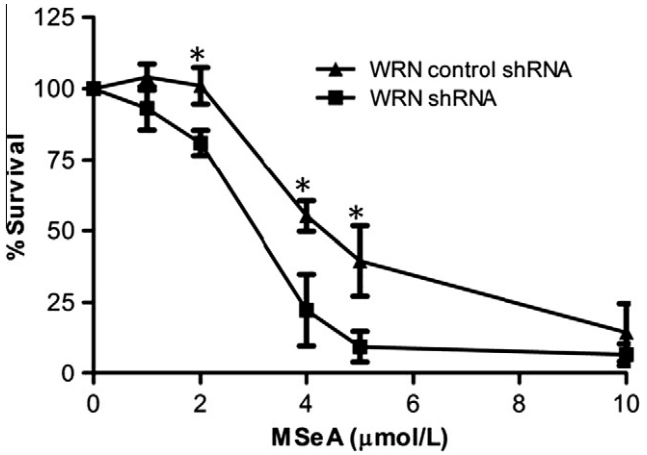

Fig. 1. Survival of WRN shRNA and control shRNA U-2 OS osteosarcoma cells incubated with various concentrations of MSeA. Values are means ± SEM, $n = 3$. *Different from control shRNA, $P < 0.05$.

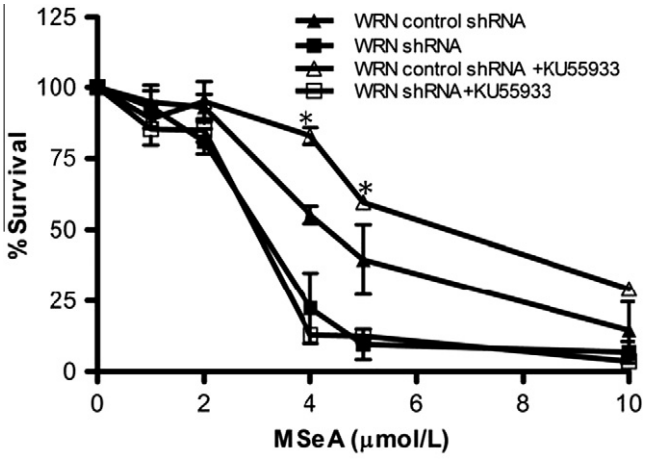

Fig. 2. Survival of WRN shRNA and control shRNA U-2 OS osteosarcoma cells incubated with KU55955 (10 μmol/l) and various concentrations of MSeA. Values are means ± SEM, $n = 3$. *Different from control shRNA cells without KU55933 treatment, $P < 0.05$.

Table 1
Flow cytometric analyses of the percent alive, apoptotic and necrotic WRN shRNA and control shRNA U-2 OS cells treated with MSeA (4 μmol/l).[1]

	Day		
	0	1	2
Living cells, %			
Control shRNA	90.3 ± 4.1	94.7 ± 1.4	81.5 ± 9.1
WRN shRNA[2]	86.6[a] ± 2.9	70.7[b,*] ± 7.8	58.1[b,*] ± 10.7
Apoptotic cells, %			
Control shRNA	5.8 ± 2.4	2.6 ± 0.9	10.6 ± 6.4
WRN shRNA	9.4 ± 2.3	12.1 ± 5.5	12.4 ± 5.7
Necrotic cells, %			
Control shRNA	2.9 ± 0.8	2.4 ± 0.2	7.6 ± 2.7
WRN shRNA[3]	3.6[a] ± 2.0	16.9[b,*] ± 3.9	28.1[b,*] ± 6.7

[1] Values are means ± SEM, $n = 3$. Within the same cell over time, means without a common letter differ, $P < 0.05$.
[2] Linear decrease ($P < 0.05$) 0–2 d.
[3] Linear increase ($P < 0.05$) 0–2 d.
[*] Different from control shRNA cells, $P < 0.05$. shRNA, small hairpin RNA; MSeA, methylseleninic acid.

sequent flow cytometric analyses demonstrated that WRN shRNA cells exhibited a linear increase ($P < 0.05$) in the incidence of necrotic death and a linear decrease ($P < 0.05$) in the percent of living cells after treatment with MSeA at 4 μmol/l (Table 1). As a result, there were greater necrotic WRN shRNA than control shRNA cells 1 and 2 d after MSeA treatment. In contrast, there were no WRN or time effects on percent apoptotic cells. U-2 OS cells did not show senescence associated-β-galactosidase expression 7 d after recovery from exposure to MSeA (1–5 μmol/l), Na_2SeO_3 (1–5 μmol/l), or methylselenocysteine (1–1000 μmol/l) (data not shown).

3.2. Role of WRN in MSeA-induced pATM Ser-1981 formation in U-2 OS cells

Because MSeA induces pATM Ser-1981 focus formation and the WRN-dependent ATM pathway activation exists [4,16], we tested a role for WRN in MSeA-induced DNA damage response. Immunofluorescent analyses demonstrated that pATM Ser-1981 focus formation was comparable between WRN shRNA and control shRNA U-2 OS cells 2 d after treatment with MSeA at 4 μmol/L (Table 2). Whereas the foci linearly subsided ($P < 0.05$) 0–5 d after recovery from the MSeA treatment in control shRNA cells, they linearly accumulated ($P < 0.05$) 0–3 d after recovery in WRN shRNA cells. As a result, pATM Ser-1981 foci were more prominent ($P < 0.05$) in WRN shRNA than in control shRNA U-2 OS cells at d 3. At d 5, the pATM Ser-1981 expression returned to a baseline level in both WRN shRNA and control shRNA cells. These results suggest that WRN is involved in the repair, but not formation, of MSeA-induced DNA damage in U-2 OS cells.

3.3. Role of WRN in MSeA-induced γH2A.X formation in U-2 OS cells

MSeA treatment (4 μmol/l, 2 d) did not significantly increase γH2A.X expression in WRN or control shRNA U-2 OS cells (Table 2). Whereas γH2A.X expression in WRN shRNA U-2 OS cells increased ($P < 0.05$) 1 and 3 d after recovery from the MSeA exposure, the expression decreased linearly 0–5 d after recovery in control shRNA U-2 OS cells. γH2A.X expression was greater ($P < 0.05$) in WRN shRNA than in control shRNA U-2 OS cells 1 and 3 d after the recovery. Therefore, WRN deficiency in U-2 OS cells stimulates γH2A.X focus formation during the recovery from MSeA treatment.

3.4. Differential effect of KU55933 on MSeA-induced proliferation suppression in WRN shRNA and control U-2 OS cells

Treatment of KU55933, an ATM kinase inhibitor, desensitized ($P < 0.05$) control shRNA, but not WRN shRNA U-2 OS cells to treatment with MSeA (4 and 5 μmol/l, Fig. 2). These results suggest that the kinase activity of ATM limits cell proliferation after MSeA treatment in a manner dependent on WRN.

4. Discussion

Available evidence indicates that selenium can counteract tumorigenesis at the initial phase of carcinogenesis [21,23]. In this study, we demonstrated a role for WRN in the repair of MSeA-induced DNA damage and the protection against the associated necrotic death in U-2 OS osteosarcoma cells. In contrast, deficiency in hMLH1, a DNA mismatch repair protein, does not sensitize cancer cells to selenium compounds [15]. Given the well documented role of WRN in the repair of oxidative and broken DNA damage, we propose that inactivation of WRN functions can increase selenium-induced DNA damage and cytotoxicity in neoplastic and in cancer cells.

Conclusions drawn from the two major selenium chemoprevention clinical studies, NPC [21] and SELECT [22], are not mutually supportive. Factors that affect the apparent discrepancy include the choice of selenium species and the body selenium status prior to entering the trials. Lu and colleagues [32] showed that, when administrated orally, MSeA is more efficacious than selenomethionine in the inhibition of tumor development in nude mice engrafted with prostate cancer cells. Furthermore, while the mean plasma selenium level was 1.7 μmol/l at the start of the SELECT trial, selenium supplementation effectively reduced prostate cancer

Table 2
Immunofluorescent analyses of pATM Ser-1981 and γH2A.X levels in WRN shRNA and control shRNA U-2 OS cells after recovery from treatment with MSeA (4 μmol/L) for 2 d.[1]

	NT	Recovery, d			
		0	1	3	5
pATM Ser-1981 positive cells,%					
Control shRNA[2]	3.1[a] ± 1.5	23.1[b] ± 3.4	15.3[ab] ± 1.3	15.3ab ± 2.4	5.4[a] ± 1.1
WRN shRNA[3]	2.4[a] ± 1.5	20.1[b] ± 3.7	24.3[bc] ± 1.5	30.8[c,*] ± 2.2	6.7[a] ± 2.4
γH2A.X intensity[4],%					
Control shRNA[2]	100 ± 2.4	106 ± 10.9	105 ± 6.4	95 ± 4.5	84 ± 3.7
WRN shRNA	100[a] ± 3.9	114[a] ± 5.0	158[b,*] ± 9.7	155[b,*] ± 13.4	113[a] ± 4.9

[1] Values are means ± SEM, $n = 6$. Within the same cell over time, means without a common letter differ, $P < 0.05$.
[2] Linear decrease ($P < 0.05$) 0–5 d after recovery.
[3] Linear increase ($P < 0.05$) 0–3 d after recovery.
[4] The expression level in the cells without MSeA treatment was set as 100%.
[*] Different from control shRNA cells, $P < 0.05$. pATM Ser-1981, ATM phosphorylation on Ser-1981; γH2A.X, H2A.X phosphorylation on Ser-139; shRNA, small hairpin RNA; MSeA, methylseleninic acid; NT, no treatment.

incidence only in men with plasma selenium concentration lower than 1.5 μmol/l in the NPC trial.

How does WRN protect U-2 OS cancer cells against MSeA-induced DNA damage? Instead of being involved in the initial DNA damage formation, WRN plays a role in the repair of MSeA-induced DNA damage (Table 2). Considering a role for WRN in resolving recombination intermediates [33], the unrepaired DNA in the MSeA-treated WRN shRNA cells is likely to be metabolized, forming secondary DNA breaks during DNA replication. Consistent with this view, DNA oxidation is greatly increased in cells deficient in WRN [34]. Moreover, the elevated DNA breaks in WRN shRNA U-2 OS cells may exceed the threshold for an ATM-dependent checkpoint response that would otherwise provide a time window for repairing the damaged DNA. This may explain why inactivation of ATM kinase activity desensitizes control shRNA, but not WRN shRNA, U-2 OS cells to incubation with MSeA.

Similar to our previous report employing PC-3 prostate cancer cells [16], the great extent of endogenous DNA breaks in U-2 OS osteosarcoma cells may limit γH2A.X focus induction by MSeA. In contrast, MSeA-induced pATM Ser-1981 formation is substantial in U-2 OS cells. These results suggest an interesting scenario, in which MSeA-induced ROS induction is coupled to persistent DNA breaks in the absence of WRN. Moreover, WRN is known to protect chronic myeloid leukemia cells against oxidative stress when WRN is phosphorylated and activated by the leukemia-specific BCR-ABL kinase [35]. However, c-Abl can phosphorylate and inhibit the catalytic activities of WRN [36]. Strikingly, the c-Abl tyrosine kinase can functionally and physically interact with the selenium-dependent glutathione peroxidase-1 in the response to ROS [37,38]. It is of future interest to study the interplay between MSeA-induced oxidative DNA breaks and WRN functions in cancer cells.

In conclusion, these studies suggest that the role of selenium in counteracting tumorigenesis can be affected by manipulating proteins that fix selenium-induced oxidative DNA damage. We propose a chemoprevention strategy that couples selenium administration to targeting WRN helicase. Functional WRN would otherwise protect neoplastic or cancer cells against selenium-induced cytotoxicity. Cautious evaluation, however, should take into consideration the physiological and practical issues. If applied to the whole body, the effective MSeA doses that sensitize WRN shRNA U-2 OS cells to death may not be physiological. Nonetheless, selenium compounds may be applied directly to precancerous and cancerous cells, in combination with strategies that inactivate WRN, to suppress tumorigenesis [26]. Indeed, selenium uptake may be elevated in neoplastic and cancer cells [39,40], and WRN is upregulated in immortalized lymphoblasts and can promote tumor cell growth [41]. The identification of WRN-dependent resistance to MSeA treatment in U-2 OS osteosarcoma opens up new horizons of research in tumorigenesis modulation through selenium by targeting oxidative DNA repair pathways.

References

[1] G.M. Martin, Genetic syndromes in man with potential relevance to the pathobiology of aging, Birth Defects Orig. Artic. Ser. 14 (1978) 5–39.
[2] C.E. Yu, J. Oshima, Y.H. Fu, E.M. Wijsman, F. Hisama, R. Alisch, S. Matthews, J. Nakura, T. Miki, S. Ouais, G.M. Martin, J. Mulligan, G.D. Schellenberg, Positional cloning of the Werner's syndrome gene, Science 272 (1996) 258–262.
[3] P.L. Opresko, W.H. Cheng, V.A. Bohr, Junction of RecQ helicase biochemistry and human disease, J. Biol. Chem. 279 (2004) 18099–18102.
[4] W.H. Cheng, D. Muftic, M. Muftuoglu, L. Dawut, C. Morris, T. Helleday, Y. Shiloh, V.A. Bohr, WRN is required for ATM activation and the S-phase checkpoint in response to interstrand cross-link-induced DNA double-strand breaks, Mol. Biol. Cell 19 (2008) 3923–3933.
[5] A. Barzilai, K. Yamamoto, DNA damage responses to oxidative stress, DNA Repair (Amst) 3 (2004) 1109–1115.
[6] C.N. Oliver, B.W. Ahn, E.J. Moerman, S. Goldstein, E.R. Stadtman, Age-related changes in oxidized proteins, J. Biol. Chem. 262 (1987) 5488–5491.
[7] L. Massip, C. Garand, E.R. Paquet, V.C. Cogger, J.N. O'Reilly, L. Tworek, A. Hatherell, C.G. Taylor, E. Thorin, P. Zahradka, D.G. Le Couteur, M. Lebel, Vitamin C restores healthy aging in a mouse model for Werner syndrome, FASEB J. 24 (2010) 158–172.
[8] A. Ghosh, M.L. Rossi, J. Aulds, D. Croteau, V.A. Bohr, Telomeric D-loops containing 8-oxo-2'-deoxyguanosine are preferred substrates for Werner and Bloom syndrome helicases and are bound by POT1, J. Biol. Chem. 284 (2009) 31074–31084.
[9] Z. Bukowy, J.A. Harrigan, D.A. Ramsden, B. Tudek, V.A. Bohr, T. Stevnsner, WRN Exonuclease activity is blocked by specific oxidatively induced base lesions positioned in either DNA strand, Nucleic Acids Res. 36 (2008) 4975–4987.
[10] A. Das, I. Boldogh, J.W. Lee, J.A. Harrigan, M.L. Hegde, J. Piotrowski, P.N. de Souza, W. Ramos, M.M. Greenberg, T.K. Hazra, S. Mitra, V.A. Bohr, The human Werner syndrome protein stimulates repair of oxidative DNA base damage by the DNA glycosylase NEIL1, J. Biol. Chem. 282 (2007) 26591–26602.
[11] J.A. Harrigan, J. Piotrowski, N.L. Di, R.L. Levine, V.A. Bohr, Metal-catalyzed oxidation of the Werner syndrome protein causes loss of catalytic activities and impaired protein–protein interactions, J. Biol. Chem. 282 (2007) 36403–36411.
[12] Y. Shiloh, M.B. Kastan, ATM: genome stability, neuronal development, and cancer cross paths, Adv. Cancer Res. 83 (2001) 209–254.
[13] C.J. Bakkenist, M.B. Kastan, DNA damage activates ATM through intermolecular autophosphorylation and dimer dissociation, Nature 421 (2003) 499–506.
[14] Z. Guo, S. Kozlov, M.F. Lavin, M.D. Person, T.T. Paull, ATM activation by oxidative stress, Science 330 (2010) 517–521.
[15] Y. Qi, N.W. Schoene, F.M. Lartey, W.H. Cheng, Selenium compounds activate ATM-dependent DNA damage response via the mismatch repair protein hMLH1 in colorectal cancer cells, J. Biol. Chem. 285 (2010) 33010–33017.
[16] M. Wu, M.M. Kang, N.W. Schoene, W.H. Cheng, Selenium compounds activate early barriers of tumorigenesis, J. Biol. Chem. 285 (2010) 12055–12062.
[17] D.L. Hatfield, M.H. Yoo, B.A. Carlson, V.N. Gladyshev, Selenoproteins that function in cancer prevention and promotion, Biochim. Biophys. Acta 1790 (2009) 1541–1545.
[18] H. Zeng, G.F. Combs Jr., Selenium as an anticancer nutrient: roles in cell proliferation and tumor cell invasion, J. Nutr. Biochem. 19 (2008) 1–7.
[19] R.F. Burk, Effect of dietary selenium level on Se binding to rat plasma proteins, Proc. Soc. Exp. Biol. Med. 143 (1973) 719–722.
[20] L. Zhang, X. Ren, E. Alt, X. Bai, S. Huang, Z. Xu, P.M. Lynch, M.P. Moyer, X.F. Wen, X. Wu, Chemoprevention of colorectal cancer by targeting APC-deficient cells for apoptosis, Nature 464 (2010) 1058–1061.
[21] L.C. Clark, G.F. Combs Jr., B.W. Turnbull, E.H. Slate, D.K. Chalker, J. Chow, L.S. Davis, R.A. Glover, G.F. Graham, E.G. Gross, A. Krongrad, J.L. Lesher Jr., H.K. Park, B.B. Sanders Jr., C.L. Smith, J.R. Taylor, Effects of selenium supplementation for cancer prevention in patients with carcinoma of the skin. A randomized controlled trial. Nutritional Prevention of Cancer Study Group, JAMA 276 (1996) 1957–1963.
[22] S.M. Lippman, E.A. Klein, P.J. Goodman, M.S. Lucia, I.M. Thompson, L.G. Ford, H.L. Parnes, L.M. Minasian, J.M. Gaziano, J.A. Hartline, J.K. Parsons, J.D. Bearden III, E.D. Crawford, G.E. Goodman, J. Claudio, E. Winquist, E.D. Cook, D.D. Karp, P. Walther, M.M. Lieber, A.R. Kristal, A.K. Darke, K.B. Arnold, P.A. Ganz, R.M. Santella, D. Albanes, P.R. Taylor, J.L. Probstfield, T.J. Jagpal, J.J. Crowley, F.L. Meyskens Jr., L.H. Baker, C.A. Coltman Jr., Effect of selenium and vitamin E on risk of prostate cancer and other cancers: the Selenium and Vitamin E Cancer Prevention Trial (SELECT), JAMA 301 (2009) 39–51.
[23] C. Jiang, W. Jiang, C. Ip, H. Ganther, J. Lu, Selenium-induced inhibition of angiogenesis in mammary cancer at chemopreventive levels of intake, Mol. Carcinog. 26 (1999) 213–225.
[24] C.D. Davis, H. Zeng, J.W. Finley, Selenium-enriched broccoli decreases intestinal tumorigenesis in multiple intestinal neoplasia mice, J. Nutr. 132 (2002) 307–309.
[25] H.E. Bryant, N. Schultz, H.D. Thomas, K.M. Parker, D. Flower, E. Lopez, S. Kyle, M. Meuth, N.J. Curtin, T. Helleday, Specific killing of BRCA2-deficient tumours with inhibitors of poly(ADP-ribose) polymerase, Nature 434 (2005) 913–917.
[26] M. Aggarwal, J.A. Sommers, R.H. Shoemaker, R.M. Brosh Jr., Inhibition of helicase activity by a small molecule impairs Werner syndrome helicase (WRN) function in the cellular response to DNA damage or replication stress, Proc. Natl. Acad. Sci. USA 108 (2011) 1525–1530.
[27] K.M. Niforou, A.K. Anagnostopoulos, K. Vougas, C. Kittas, V.G. Gorgoulis, G.T. Tsangaris, The proteome profile of the human osteosarcoma U2OS cell line, Cancer Genomics Proteomics 5 (2008) 63–78.
[28] W.H. Cheng, R. Kusumoto, P.L. Opresko, X. Sui, S. Huang, M.L. Nicolette, T.T. Paull, J. Campisi, M. Seidman, V.A. Bohr, Collaboration of Werner syndrome protein and BRCA1 in cellular responses to DNA interstrand cross-links, Nucleic Acids Res. 34 (2006) 2751–2760.
[29] Y. Tsuji, K. Kusuzaki, K. Kanemitsu, T. Matsumoto, Y. Ishikawa, Y. Hirasawa, Calcaneal osteosarcoma associated with Werner syndrome. A case report with mutation analysis, J. Bone Joint Surg. Am. 82 (2000) 1308–1313.
[30] Y. Ishikawa, R.W. Miller, R. Machinami, H. Sugano, M. Goto, Atypical osteosarcomas in Werner syndrome (adult progeria), Jpn. J. Cancer Res. 91 (2000) 1345–1349.
[31] W.H. Cheng, K.C. von Kobbe, P.L. Opresko, L.M. Arthur, K. Komatsu, M.M. Seidman, J.P. Carney, V.A. Bohr, Linkage between Werner syndrome protein and the Mre11 complex via Nbs1, J. Biol. Chem. 279 (2004) 21169–21176.
[32] G.X. Li, H.J. Lee, Z. Wang, H. Hu, J.D. Liao, J.C. Watts, G.F. Combs Jr., J. Lu, Superior in vivo inhibitory efficacy of methylseleninic acid against human prostate cancer over selenomethionine or selenite, Carcinogenesis 29 (2008) 1005–1012.

[33] A. Constantinou, M. Tarsounas, J.K. Karow, R.M. Brosh, V.A. Bohr, I.D. Hickson, S.C. West, Werner's syndrome protein (WRN) migrates Holliday junctions and co-localizes with RPA upon replication arrest, EMBO Rep. 1 (2000) 80–84.

[34] A. Bacolla, G. Wang, A. Jain, N.A. Chuzhanova, R.Z. Cer, J.R. Collins, D.N. Cooper, V.A. Bohr, K.M. Vasquez, Non-B DNA-forming Sequences and WRN deficiency independently increase the frequency of base substitution in human cells, J. Biol. Chem. 286 (2011) 10017–10026.

[35] A. Slupianek, T. Poplawski, S.K. Jozwiakowski, K. Cramer, D. Pytel, E. Stoczynska, M.O. Nowicki, J. Blasiak, T. Skorski, BCR/ABL stimulates WRN to promote survival and genomic instability, Cancer Res. 71 (2011) 842–851.

[36] W.H. Cheng, K.C. von Kobbe, P.L. Opresko, K.M. Fields, J. Ren, D. Kufe, V.A. Bohr, Werner syndrome protein phosphorylation by abl tyrosine kinase regulates its activity and distribution, Mol. Cell Biol. 23 (2003) 6385–6395.

[37] X. Sun, P. Majumder, H. Shioya, F. Wu, S. Kumar, R. Weichselbaum, S. Kharbanda, D. Kufe, Activation of the cytoplasmic c-Abl tyrosine kinase by reactive oxygen species, J. Biol. Chem. 275 (2000) 17237–17240.

[38] C. Cao, Y. Leng, W. Huang, X. Liu, D. Kufe, Glutathione peroxidase 1 is regulated by the c-Abl and Arg tyrosine kinases, J. Biol. Chem. 278 (2003) 39609–39614.

[39] S. Zhang, Y. Luo, H. Zeng, Q. Wang, F. Tian, J. Song, W.H. Cheng, Encapsulation of selenium in chitosan nanoparticles improves selenium availability and protects cells from selenium-induced DNA damage response, J. Nutr. Biochem. 22 (2011) 1137–1142.

[40] J. Lu, C. Jiang, Selenium and cancer chemoprevention: hypotheses integrating the actions of selenoproteins and selenium metabolites in epithelial and non-epithelial target cells, Antioxid. Redox. Signal. 7 (2005) 1715–1727.

[41] P.L. Opresko, J.P. Calvo, C. von Kobbe, Role for the Werner syndrome protein in the promotion of tumor cell growth, Mech. Ageing. Dev. 128 (2007) 423–436.

Biochemical and Biophysical Research Communications 420 (2012) 29–35

Contents lists available at SciVerse ScienceDirect

Biochemical and Biophysical Research Communications

journal homepage: www.elsevier.com/locate/ybbrc

Cyclin-dependent kinase inhibitor 3 is overexpressed in hepatocellular carcinoma and promotes tumor cell proliferation

Chunyang Xing [1], Haiyang Xie [1], Lin Zhou, Wuhua Zhou, Wu Zhang, Songming Ding, Bajin Wei, Xiaobo Yu, Rong Su, Shusen Zheng *

Key Lab of Combined Multi-Organ Transplantation, Ministry of Public Health, First Affiliated Hospital, School of Medicine, Zhejiang University, Hangzhou 310003, Zhejiang Province, China

ARTICLE INFO

Article history:
Received 7 February 2012
Available online 27 February 2012

Keywords:
CDKN3
p21
BIRC5
Oncomine
Co-expression

ABSTRACT

Cyclin-dependent kinase inhibitor 3 (CDKN3) belongs to the protein phosphatases family and has a dual function in cell cycling. The function of this gene has been studied in several kinds of cancers, but its role in human hepatocellular carcinoma (HCC) remains to be elucidated. In this study, we found that CDKN3 was frequently overexpressed in both HCC cell lines and clinical samples, and this overexpression was correlated with poor tumor differentiation and advanced tumor stage. Functional studies showed that overexpression of CDKN3 could promote cell proliferation by stimulating G1-S transition but has no impact on cell apoptosis and invasion. Microarray-based co-expression analysis identified a total of 61 genes co-expressed with CDKN3, with most of them involved in cell proliferation, and BIRC5 was located at the center of CDKN3 co-expression network. These results suggest that CDKN3 acts as an oncogene in human hepatocellular carcinoma and antagonism of CDKN3 may be of interest for the treatment of HCC.

1. Introduction

Hepatocellular carcinoma (HCC) is one of the most prevalent cancers worldwide, with an estimate of 748,300 new cases and 695,900 deaths annually, half of these cases and deaths occur in China [1]. Despite the recent advancement in diagnosis and treatment modalities, the prognosis of HCC patients remains dismal. Because current therapies are insufficient for most patients to achieve complete tumor eradication, it is essential to define the molecular mechanisms of HCC and identify novel targets to develop effective therapeutic approaches that will improve the clinical outcome of HCC patients.

Cyclin-dependent kinase inhibitor 3 (CDKN3) belongs to the protein phosphatases family and is involved in regulating the cell cycle [2,3]. It has a dual function in cell cycling. First, CDKN3 acts as a cyclin-dependent kinase inhibitor that selectively binds to CDK2 kinase [4,5] and reduces its capacity to phosphorylate the retinoblastoma protein (Rb) [6]. Non-phosphorylated Rb binds to transcription factor E2F1 and prevents the generation of proteins required for G1/S transition, thereby inhibiting G1/S transition [7–9]. Second, CDKN3 is also an Mdm2-binding protein. It could form a complex with Mdm2 and p53, therefore abolishing the induction of p21, a product of the p53 target gene, thus facilitates cell cycle progression [10]. Furthermore, this gene was reported to be deleted or overexpressed in several kinds of cancers [11–13], but the expression pattern and biological functions of CDKN3 in human hepatocellular carcinoma remain to be elucidated.

In this study, we aimed to assess the functional characteristics and molecular mechanisms of CDKN3 in HCC. We found that CDKN3 was frequently overexpressed in HCC, and its expression was correlated with poor clinical outcome. Overexpression of CDKN3 could stimulate the proliferation of HCC cell lines. Using microarray meta-analysis, a number of important cell cycle regulating molecules were found to be co-expressed with CDKN3, and BIRC5 appeared as the central node of the co-expression network.

2. Materials and methods

2.1. Patients

Fifty-six pairs of primary HCC and adjacent noncancerous liver tissues were collected from patients who underwent hepatic resection between 2005 and 2010 in our hospital (First Affiliated Hospital, Zhejiang University School of Medicine, Zhejiang, China). These patients included 41 males and 15 females with a mean age of 50.4 ± 11.0 y (range: 24–75). Written informed consent was obtained from all patients, and the study was approved by the local ethics committee.

* Corresponding author. Fax: +86 571 87236466.
E-mail address: shusenzheng@zju.edu.cn (S. Zheng).
[1] These authors contributed equally to this work.

0006-291X/$ - see front matter © 2012 Elsevier Inc. All rights reserved.
doi:10.1016/j.bbrc.2012.02.107

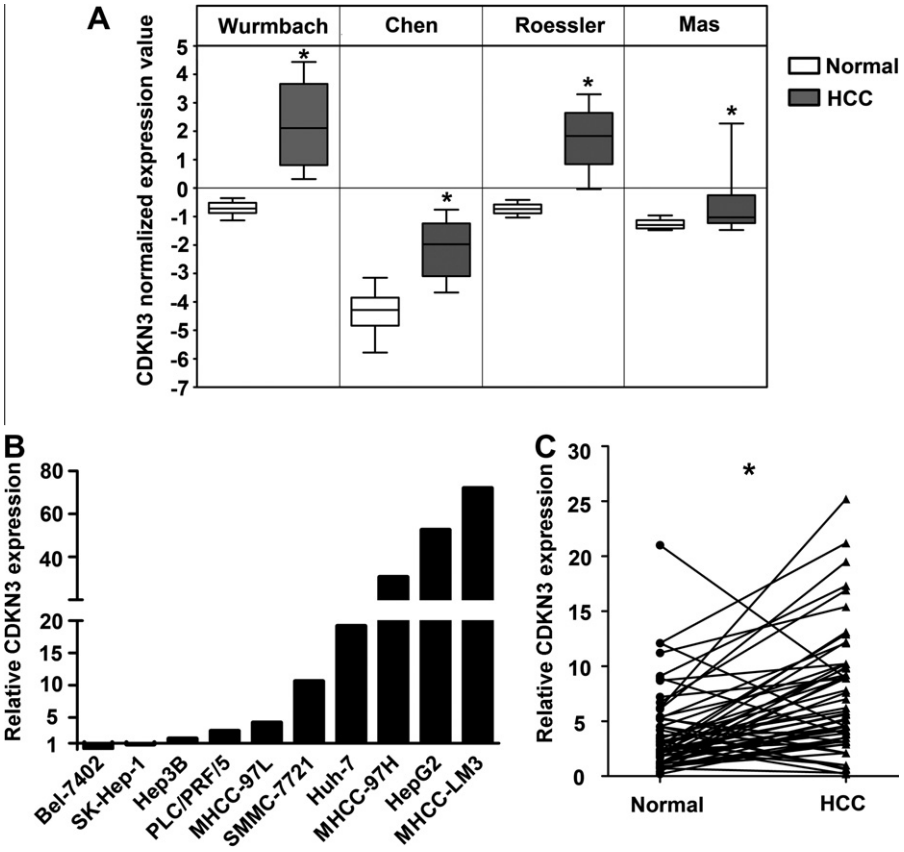

Fig. 1. CDKN3 is overexpressed in HCC. (A) Meta-analysis of HCC microarray data sets using Oncomine. Whiskers, 10th and 90th percentile; box boundaries, 75th and 25th percentile; line within box, median. *$p < 0.001$. (B) Relative CDKN3 expression in ten HCC cell lines compared with the mean value of two normal liver cell lines (L-02 and Chang liver). (C) Relative CDKN3 expression in HCC (right) and adjacent normal tissues (left). *$p < 0.001$.

2.2. Cell culture

Ten Human HCC cell lines (HepG2, Hep3B, Huh-7, Bel-7402, SK-Hep-1, PLC/PRF/5, SMMC-7721, MHCC-97L, MHCC-97H and MHCC-LM3) and two immortalized liver cell lines (L-02 and Chang liver) were cultured in Dulbecco's modified Eagle medium (DMEM, Gibco-Invitrogen, Carlsbad, CA) supplemented with 10% fetal bovine serum (SAFC Biosciences, Lenexa, KS), 100 units/mL penicillin and 100 mg/mL streptomycin (Sigma–Aldrich, St. Louis, MO).

2.3. Establishment of stable CDKN3-expressing cell lines

A human Full-length CDKN3 cDNA was cloned into XhoI and EcoRI sites of pEGFP-C1 (Clontech, Palo Alto, CA). The pEGFP-CDKN3 construct was verified by sequencing. HCC cells were transfected with pEGFP-CDKN3 and pEGFP-C1 as a negative control using Lipofectamine 2000. Transfected cells were selected by 400 μg/mL G418 (Gibco-Invitrogen) for 3 weeks.

2.4. Quantitative Real-time PCR analysis

Total RNA was extracted from whole cells using Trizol reagent (Invitrogen) and reverse-transcribed with TaqMan Reverse Transcription Kit (Applied Biosystems, Foster City, CA). Quantitative Real-time PCR (qRT-PCR) was carried out using SYBR Premix Ex Taq (TAKARA, Kusatsu, Japan) on an ABI 7500 Real Time PCR System (Applied Biosystems). All qRT-PCRs were performed in triplicate. The relative RNA expression was calculated using the delta-delta threshold cycle (ΔΔCT) method and normalized to GAPDH expression. PCR was performed with the following primers: 5′-CTCTCTGCTCCTCCTGTTCGAC-3′ and 5′-TGAGCGATGTGGCTCGGCT-3′ for GAPDH; 5′-CAGCGATGAAGCCGCCCAGT-3′ and 5′-TGACAGTTCCCCTCTGGTGCAG -3′ for CDKN3.

2.5. Western blotting analysis

Western blotting analysis was performed as previously described [14] with the following primary antibodies: monoclonal anti-CDKN3 (1:1000 dilution, Sigma–Aldrich, St. Louis, MO), monoclonal anti-p21 (1:1000 dilution, Epitomics, Burlingame, CA) and monoclonal anti-GAPDH (1:2000 dilution, Sigma–Aldrich, Saint Louis, MO).

2.6. Cell viability assay

Cell growth was determined by Cell Counting Kit-8 (CCK-8) cell viability assay (Dojindo Laboratories, Kumamoto, Japan) according to the manufacturer's instructions as previously described [15].

2.7. Cell proliferation analysis

Cell proliferation was measured using the EdU assay kit (Ribobio, Guangzhou, China) according to the manufacturers' instructions as previously described [16].

2.8. Cell cycle analysis

Cell cycle analysis was carried out as previously described [15].

Table 1
Correlations between CDKN3 expression and clinicopathological features.

Clinicopathologic variable	N	CDKN3		*p* value[b]
		High expression[a]	Low expression[a]	
Gender				
Male	41	12	29	0.524
Female	15	6	9	
Age (years)				
⩽50	24	8	16	1.000
>50	32	10	22	
Liver cirrhosis				
Absence	22	7	15	1.000
Presence	34	11	23	
Maximal tumor size (cm)				
⩽5	19	5	14	0.560
>5	37	13	24	
Capsular formation				
Absence	44	12	32	0.171
Presence	12	6	6	
Tumor nodule number				
Solitary	47	16	31	0.703
Multiple (⩾2)	9	2	7	
Tumor stage (AJCC)				
I–II	40	17	23	0.011
III–IV	16	1	15	
Vascular invasion				
Absence	33	8	25	0.155
Presence	23	10	13	
Tumor differentiation				
I–II	32	15	17	0.009
III–IV	24	3	21	
Serum AFP (ng/mL)				
⩽400	26	11	15	0.159
>400	30	7	23	
HBsAg				
Negative	9	2	7	0.703
Positive	47	16	31	
Anti-HCV				
Negative	54	18	36	1.000
Positive	2	0	2	

[a] CDKN3 low expressers ($n = 18$) and CDKN3 high expressers ($n = 38$) according to the mean relative expression of CDKN3 in adjacent nontumorous tissues.
[b] Fisher's exact test.

2.9. Cell apoptosis analysis

Cell apoptosis analysis was carried out as previously described [17].

2.10. Transwell invasion experiment

For transwell assay, 1×10^5 HepG2 cells or 5×10^5 MHCC-LM3 cells in serum-free DMEM were seeded into the upper chambers of each well (24-well insert, 8-mm pore size, Millipore, Billerica, MA) coated with Matrigel (BD Bioscience, San Jose, CA). DMEM containing 10% FBS was placed in the lower chambers as a chemoattractant. After 16 h of incubation, cells on the upper membrane surface were wiped off, and the cells that invaded across the Matrigel membrane were fixed with 100% methanol and stained with 0.2% crystal violet. The number of invasive cells was then counted (five randomly chosen high-power fields for each membrane) under a microscope.

2.11. Meta-analysis

The co-expression analysis of microarray data sets was performed with Oncomine database co-expression analysis tool (http://www.oncomine.org). The top 200 genes of each data set were extracted according to the co-expression score. The genes that appeared in three of these four data sets were defined as CDKN3 co-expressed genes. The Expression Analysis Systematic Explorer (EASE) software (http://david.abcc.ncifcrf.gov/ease/ease.jsp) was applied for Gene Ontology (GO) biological process enrichment analysis. Gene interaction network was constructed using the Genomatix Pathway System (GePS, http://www.genomatix.de/).

2.12. Statistical analysis

Pearson's chi-square test was applied to assess the correlation of CDKN3 expression with different clinicopathological parameters. Student's *t* test was used to analyze the differences between two groups. Statistical significance was accepted if $p < 0.05$. Statistical analysis was performed using SPSS 16.0 software (SPSS, Chicago, IL). Data are presented as mean ± SD.

3. Results

Overexpression of CDKN3 is frequent in HCC and is associated with poor clinical outcome.

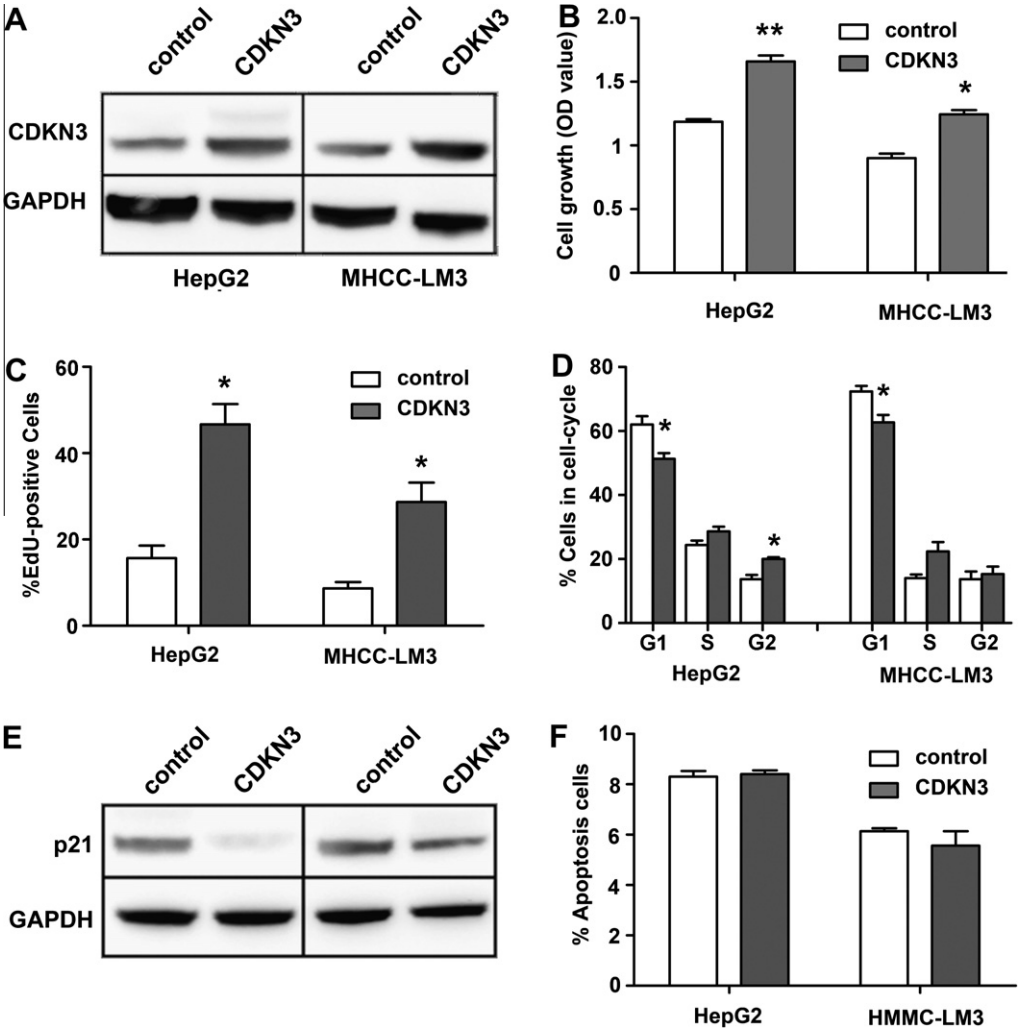

Fig. 2. Overexpression of CDKN3 promotes the proliferation of HCC cells. (A) HepG2 and MHCC-LM3 cells were stably transfected with pEGFP-CDKN3 (CDKN3) and pEGFP-C1 empty (control) vectors. Total cellular protein was extracted from the cells and CDKN3 expression was measured by western blotting. (B) Effects of CDKN3 on cell growth was assessed using CCK-8 assay kit ($n = 3$, $^{*}p = 0.002$, $^{**}p < 0.001$). (C) Cell proliferation was measured using EdU assay kit, the EdU-positive cells were counted in five randomly chosen high-power fields (400×) for each replicate ($n = 3$, $^{*}p < 0.05$). (D) Flow cytometry showing that overexpression of CDKN3 could promote G1/S phase transition ($n = 3$, $^{*}p < 0.05$). (E) Overexpression of CDKN3 downregulated the protein level of p21. (F) Effect of CDKN3 on cell apoptosis was assessed by flow cytometry using Annexin V/PI Apoptosis Kit ($n = 3$).

To determine the expression pattern of CDKN3 in HCC, Oncomine database [18] was used to analyze the microarray data sets from the studies of Wurmbach [19], Chen [20], Roessler [21] and Mas [22]. As seen in Fig. 1A, all of the four data sets showed a significantly higher level of CDKN3 in HCC compared with normal liver tissues. To validate this observation, qRT-PCR was then performed to evaluate the expression of CDKN3 in two immortalized liver cell lines (L-02 and Chang liver) and ten HCC cell lines (HepG2, Hep3B, Huh-7, Bel-7402, SK-Hep-1, PLC/PRF/5, MHCC-LM3, MHCC-97L, MHCC-97H and MHCC-LM3). Seven of these ten (70%) HCC cell lines, showed at least twofold overexpression of CDKN3 compared with the mean value of L-02 and Chang liver (Fig. 1B). Further analysis of 56 pairs of primary HCC and adjacent normal tissues confirmed this overexpression of CDKN3 ($p < 0.001$, Fig. 1C). Clinical association study demonstrated that the expression of CDKN3 was associated with poor tumor differentiation ($p = 0.009$) and advanced tumor stage ($p = 0.011$, Table 1).

3.1. Overexpression of CDKN3 promotes the proliferation HCC cells

To investigate the biological function of CDKN3 in HCC, a CDKN3 expression vector was established and stably transfected into HepG2 and MHCC-LM3 cells, (Fig. 2A). As shown in Fig. 2B, forced overexpression of CDKN3 resulted in a marked stimulation of cell growth in both HepG2 and MHCC-LM3 cells (up to 39.9% and 38.1%, respectively), which was based on the increase of proliferating cells (Fig. 2C) but had no effect on cell apoptosis (Fig. 2F). Cell cycle analysis revealed a major reduction of G1 cells by CDKN3 overexpression, along with a concomitant increase of cell population in S and G2 phase (Fig. 2D). It has been reported that CDKN3 could prevent the induction of p21 in breast cancer cells, thereby facilitating cell cycle progression [10], this report intrigued us to explore whether CDKN3 promotes cell cycle progression via the p53-p21 dependent pathway in HCC cells. As shown in Fig. 2E, the expression of p21 was lower in CDKN3 transfected cells compared with the control group.

3.2. Overexpression of CDKN3 has no effect on HCC cell invasion

Till now, most of the studies about CDKN3 focus mainly on its function of cell proliferation, and other functions of this gene are largely unknown. To determine whether CDKN3 is involved in cell invasion, transwell assay was then performed. The result showed no obviously changes of invasive ability in CDKN3 overexpressed cells (Fig. 3A and B).

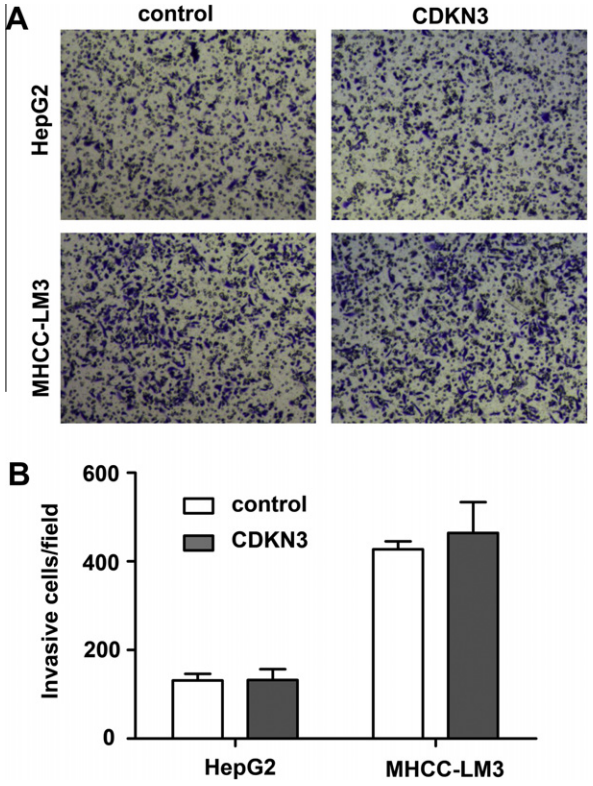

Fig. 3. Overexpression of CDKN3 has no effect on HCC cell invasion. (A) Representative pictures of transwell assay observed under light microscope. (B) The results of transwell assay were quantitated by counting invasive cells in five randomly chosen high-power fields (400×) for each replicate ($n = 3$).

3.3. Co-expression analysis of CDKN3 in different HCC microarray data sets

Genes that are co-expressed over a certain number of conditions suggests that these genes might be functionally related or even co-regulated [23]. Using the co-expression analysis of four microarray data sets from Oncomine [19–22], we found a total of 61 genes co-expressed with CDKN3 (Supplementary Table S1). Gene ontology analysis of theses co-expressed genes showed many of them were involved in biological processes relevant to cell proliferation, such as mitotic cell cycle and nuclear division (Fig. 4A).

To obtain insights into the functional connections of CDKN3 co-expressed genes, these 61 genes were uploaded into the Genomatix GePS software for network analysis. The network showed a dominance of BIRC5, which located at the center of this network and functionally linked to 38 genes (Fig. 4B). Some genes critically involved in cancer-relevant pathways were also highlighted as major nodes, such as CCNA2, CCNB1 and CDK1, suggesting that these genes might act as important regulators in CDKN3 co-expression network.

4. Discussion

CDKN3 was firstly identified as a co-repressor for zinc finger proteins containing KRAB repression domain [24–26]. CDKN3 can recruit and coordinate many complexes required for gene silencing (such as NuRD, N-CoR1 and SETDB) to inhibit the transcription of its target genes [27–29]. The main role of CDKN3 is cell cycle regulating, it functions differently in different types of cancers, either inhibits or stimulates cell proliferation. Though the function of CDKN3 has been studied in many other cancers, its role in HCC remains to be elucidated.

CDKN3 was reported to be upregulated in breast and prostate cancers [11]. Here, we found that CDKN3 was frequently overexpressed in HCC tissues and cell lines, and its expression was correlated with poor tumor differentiation and advanced tumor stage, suggesting that increased expression of CDKN3 is associated with HCC genesis and progression. The mechanisms of CDKN3 high expression may be the hypomethylation of its promoter region [30] and remains to be further studied. To better understand the biological function of CDKN3, we have then investigated whether overexpression of CDKN3 could promote the malignant phenotypes (such as cell proliferation, apoptotic resistance and invasion) in HCC cell lines.

The role of CDKN3 on cell proliferation has been well studied [3,31,32]. In human breast and colon cancer cells, CDKN3 could prevent the induction of p21, a p53 target gene, thereby inhibiting cell cycle progression [10]. It has been reported that p21 could interacted with cyclin/CDK complexes and PCNA to inhibit their kinase activities [33]. Besides, increased p21 could also cause a specific suppression of cell cycle progression genes, such as BUB1B and ORC1 [34]. In the case of HCC, we found that overexpression of CDKN3 could dramatically promote the proliferation of HepG2 and MHCC-LM3 cells through the induction of G1/S transition. In keeping with previous studies, the expression of p21 was inhibited in CDKN3 transfected HCC cells, suggesting that CDKN3 promotes HCC cell cycle progression, at least in part, via the p53-p21 dependent pathway.

Metastasis is a key event in tumor progression and is the most common cause of recurrence in HCC patients undergoing liver resection or transplantation [35,36]. The role of CDKN3 on cell metastasis is rarely reported and prompted us to investigate whether CDKN3 is of relationship with cell invasion. The functional study demonstrated that there were no different changes of cell invasion after CDKN3 transfection. This finding is coincident with our clinical data, as no significant correlation between the metastasis characterizes (such as venous invasion) and CDKN3 expression was observed, indicating CDKN3 could not affect the metastasis potential of HCC cells. To our knowledge, this is the first report of CDKN3 on tumor metastasis other than its proliferation functions.

To further investigate the molecular mechanism of CDKN3, co-expression analysis was used to identify possible partners of CDKN3 in HCC tissues. We identified 61 co-expression genes for CDKN3, most of them are related in the processes of cell cycling such as BIRC5, BUB1, PTTG1 and TOP2A (Supplementary Table S1). Functional network investigation of these co-expression genes highlighted BIRC5 to be the central node in the CDKN3 co-expression network, which exhibited the most interactions with other genes. BIRC5 is a member of the inhibitor of apoptosis (IAP) gene family, which encodes negative regulatory proteins that prevent apoptotic cell death [37,38]. In term of cell proliferation, BIRC5 acts as a component of the chromosomal passenger complex that facilitates chromosome segregation and cytokinesis [39,40]. Furthermore, BIRC5 could also increase nuclear accumulation of cyclin D and CDK4 thus increases the phosphorylation of Rb and subsequently facilitate G1/S progression [41]. These findings provide a more comprehensive insight into the molecular mechanisms of CDKN3 involved in HCC cell cycling.

In summary, our results have shown that CDKN3 is frequently up-regulated in hepatocellular carcinoma and is related to poor clinical outcome of HCC. The functional data strongly suggest that CDKN3 behaves as an oncogene in HCC, and overexpression of CDKN3 could promote HCC cell proliferation. Furthermore, our study also generates a list of potential partner genes of CDKN3,

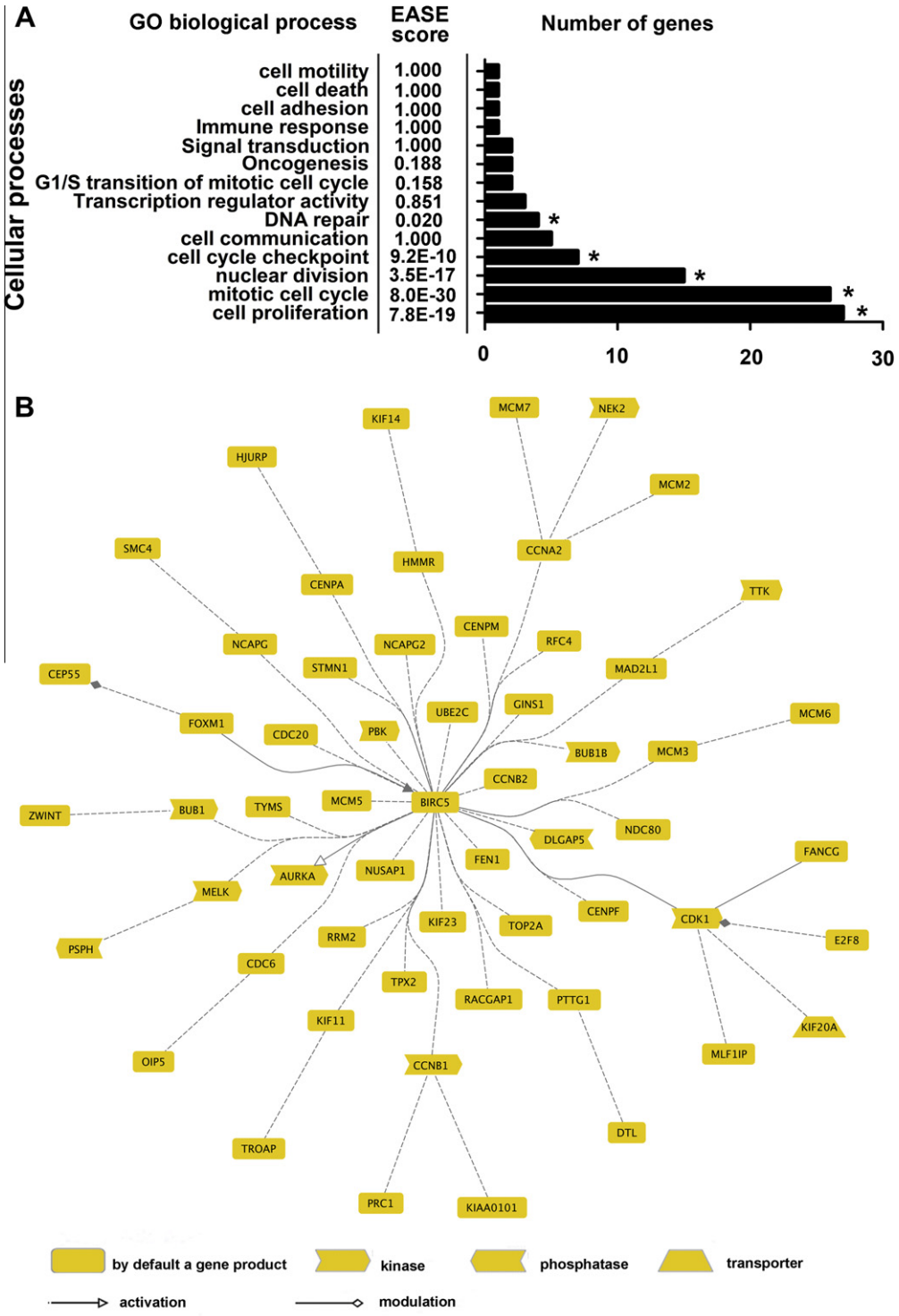

Fig. 4. Co-expression analysis of CDKN3. (A) Gene Ontology analysis of CDKN3 co-expressed genes. The bar indicates the number of genes involved in different biological processes. $^{*}p < 0.05$ (EASE score). (B) Bibliographic relationships for CDKN3 co-expressed gene profiles analyzed with GePS. The function of each gene is represented by its shapes for kinase, transporter and so on. The arrow direction indicates whether a gene works upstream or downstream of another. Dashed line: interaction between co-cited genes; solid line: interaction between genes with an expert curated connection. Genes that show no interaction with others are not displayed.

which provides valuable information for further investigation toward a comprehensive understanding of CDKN3.

Acknowledgments

This work was supported by Basic Research Fund of Zhejiang Provincial Education Department (Y201120248), National Science and Technology Major Project of China (2012ZX10002017) and the Foundation for Innovative Research Groups of the National Natural Science Foundation of China (81121002).

Appendix A. Supplementary data

Supplementary data associated with this article can be found, in the online version, at doi:10.1016/j.bbrc.2012.02.107.

References

[1] A. Jemal, F. Bray, M.M. Center, J. Ferlay, E. Ward, D. Forman, Global cancer statistics, CA Cancer J. Clin. 61 (2011) 69–90.
[2] G.J. Hannon, D. Casso, D. Beach, KAP: a dual specificity phosphatase that interacts with cyclin-dependent kinases, Proc. Natl. Acad. Sci. USA 91 (1994) 1731–1735.
[3] J. Gyuris, E. Golemis, H. Chertkov, R. Brent, Cdi1, a human G1 and S phase protein phosphatase that associates with Cdk2, Cell 75 (1993) 791–803.
[4] G.J. Hannon, D. Casso, D. Beach, Kap - a dual-specificity phosphatase that interacts with cyclin-dependent kinases, Proceedings of the National Academy of Sciences of the United States of America 91 (1994) 1731–1735.
[5] L.N. Johnson, E. De Moliner, N.R. Brown, H. Song, D. Barford, J.A. Endicott, M.E. Noble, Structural studies with inhibitors of the cell cycle regulatory kinase cyclin-dependent protein kinase 2, Pharmacol. Ther. 93 (2002) 113–124.
[6] N. Dyson, The regulation of E2F by pRB-family proteins, Genes Dev. 12 (1998) 2245–2262.
[7] F. Martelli, D.M. Livingston, Regulation of endogenous E2F1 stability by the retinoblastoma family proteins, Proc. Natl. Acad. Sci. USA 96 (1999) 2858–2863.
[8] M.J. Cecchini, F.A. Dick, The biochemical basis of CDK phosphorylation-independent regulation of E2F1 by the retinoblastoma protein, Biochem. J. 434 (2011) 297–308.
[9] E.J. Morris, J.Y. Ji, F. Yang, L. Di Stefano, A. Herr, N.S. Moon, E.J. Kwon, K.M. Haigis, A.M. Naar, N.J. Dyson, E2F1 represses beta-catenin transcription and is antagonized by both pRB and CDK8, Nature 455 (2008) 552–556.
[10] K. Okamoto, I. Kitabayashi, Y. Taya, KAP1 dictates p53 response induced by chemotherapeutic agents via Mdm2 interaction, Biochem. Biophys. Res. Commun. 351 (2006) 216–222.
[11] S.W. Lee, C.L. Reimer, L. Fang, M.L. Iruela-Arispe, S.A. Aaronson, Overexpression of kinase-associated phosphatase (KAP) in breast and prostate cancer and inhibition of the transformed phenotype by antisense KAP expression, Mol. Cell Biol. 20 (2000) 1723–1732.
[12] C.T. Yeh, S.C. Lu, T.C. Chen, C.Y. Peng, Y.F. Liaw, Aberrant transcripts of the cyclin-dependent kinase-associated protein phosphatase in hepatocellular carcinoma, Cancer Res. 60 (2000) 4697–4700.
[13] R. Jiang, Y. Xia, J. Li, L. Deng, L. Zhao, J. Shi, X. Wang, B. Sun, High expression levels of IKKalpha and IKKbeta are necessary for the malignant properties of liver cancer, Int. J. Cancer 126 (2010) 1263–1274.
[14] J. Cheng, L. Zhou, Q.F. Xie, H.Y. Xie, X.Y. Wei, F. Gao, C.Y. Xing, X. Xu, L.J. Li, S.S. Zheng, The impact of miR-34a on protein output in hepatocellular carcinoma HepG2 cells, Proteomics 10 (2010) 1557–1572.
[15] L.M. Wu, Z. Yang, L. Zhou, F. Zhang, H.Y. Xie, X.W. Feng, J. Wu, S.S. Zheng, Identification of histone deacetylase 3 as a biomarker for tumor recurrence following liver transplantation in HBV-associated hepatocellular carcinoma, PLoS One 5 (2010) e14460.
[16] J. Cheng, H.Y. Xie, X. Xu, J. Wu, X. Wei, R. Su, W. Zhang, Z. Lv, S. Zheng, L. Zhou, NDRG1 as a biomarker for metastasis, recurrence and of poor prognosis in hepatocellular carcinoma, Cancer Lett. 310 (2011) 35–45.
[17] Z. Yang, L. Zhou, L.M. Wu, M.C. Lai, H.Y. Xie, F. Zhang, S.S. Zheng, Overexpression of long non-coding RNA HOTAIR predicts tumor recurrence in hepatocellular carcinoma patients following liver transplantation, Ann. Surg. Oncol. 18 (2011) 1243–1250.
[18] D.R. Rhodes, J. Yu, K. Shanker, N. Deshpande, R. Varambally, D. Ghosh, T. Barrette, A. Pandey, A.M. Chinnaiyan, ONCOMINE: a cancer microarray database and integrated data-mining platform, Neoplasia 6 (2004) 1–6.
[19] E. Wurmbach, Y.B. Chen, G. Khitrov, W. Zhang, S. Roayaie, M. Schwartz, I. Fiel, S. Thung, V. Mazzaferro, J. Bruix, E. Bottinger, S. Friedman, S. Waxman, J.M. Llovet, Genome-wide molecular profiles of HCV-induced dysplasia and hepatocellular carcinoma, Hepatology 45 (2007) 938–947.
[20] X. Chen, S.T. Cheung, S. So, S.T. Fan, C. Barry, J. Higgins, K.M. Lai, J. Ji, S. Dudoit, I.O. Ng, M. Van De Rijn, D. Botstein, P.O. Brown, Gene expression patterns in human liver cancers, Mol. Biol. Cell 13 (2002) 1929–1939.
[21] S. Roessler, H.L. Jia, A. Budhu, M. Forgues, Q.H. Ye, J.S. Lee, S.S. Thorgeirsson, Z. Sun, Z.Y. Tang, L.X. Qin, X.W. Wang, A unique metastasis gene signature enables prediction of tumor relapse in early-stage hepatocellular carcinoma patients, Cancer Res. 70 (2010) 10202–10212.
[22] V.R. Mas, D.G. Maluf, K.J. Archer, K. Yanek, X. Kong, L. Kulik, C.E. Freise, K.M. Olthoff, R.M. Ghobrial, P. McIver, R. Fisher, Genes involved in viral carcinogenesis and tumor initiation in hepatitis C virus-induced hepatocellular carcinoma, Mol. Med. 15 (2009) 85–94.
[23] A.C. Fierro, F. Vandenbussche, K. Engelen, Y. Van de Peer, K. Marchal, Meta analysis of gene expression data within and across species, Curr. Genomics 9 (2008) 525–534.
[24] S.S. Kim, Y.M. Chen, E. O'Leary, R. Witzgall, M. Vidal, J.V. Bonventre, A novel member of the RING finger family, KRIP-1, associates with the KRAB-A transcriptional repressor domain of zinc finger proteins, Proc. Natl. Acad. Sci. USA 93 (1996) 15299–15304.
[25] J.R. Friedman, W.J. Fredericks, D.E. Jensen, D.W. Speicher, X.P. Huang, E.G. Neilson, F.J. Rauscher 3rd, KAP-1, a novel corepressor for the highly conserved KRAB repression domain, Genes Dev. 10 (1996) 2067–2078.
[26] Y. Agata, E. Matsuda, A. Shimizu, Two novel Kruppel-associated box-containing zinc-finger proteins, KRAZ1 and KRAZ2, repress transcription through functional interaction with the corepressor KAP-1 TIF1 beta/KRIP-1, J. Biol. Chem. 274 (1999) 16412–16422.
[27] D.C. Schultz, K. Ayyanathan, D. Negorev, G.G. Maul, F.J. Rauscher 3rd, SETDB1: a novel KAP-1-associated histone H3, lysine 9-specific methyltransferase that contributes to HP1-mediated silencing of euchromatic genes by KRAB zinc-finger proteins, Genes Dev. 16 (2002) 919–932.
[28] D.C. Schultz, J.R. Friedman, F.J. Rauscher 3rd, Targeting histone deacetylase complexes via KRAB-zinc finger proteins: the PHD and bromodomains of KAP-1 form a cooperative unit that recruits a novel isoform of the Mi-2alpha subunit of NuRD, Genes Dev. 15 (2001) 428–443.
[29] C. Underhill, M.S. Qutob, S.P. Yee, J. Torchia, A novel nuclear receptor corepressor complex, N-CoR, contains components of the mammalian SWI/SNF complex and the corepressor KAP-1, J. Biol. Chem. 275 (2000) 40463–40470.
[30] M.D. Niculescu, Y. Yamamuro, S.H. Zeisel, Choline availability modulates human neuroblastoma cell proliferation and alters the methylation of the promoter region of the cyclin-dependent kinase inhibitor 3 gene, J. Neurochem. 89 (2004) 1252–1259.
[31] M. Chinami, Y. Yano, X. Yang, S. Salahuddin, K. Moriyama, M. Shiroishi, H. Turner, T. Shirakawa, C.N. Adra, Binding of HTm4 to cyclin-dependent kinase (Cdk)-associated phosphatase (KAP). Cdk2.cyclin A complex enhances the phosphatase activity of KAP, dissociates cyclin A, and facilitates KAP dephosphorylation of Cdk2, J. Biol. Chem 280 (2005) 17235–17242.
[32] Y. Yu, X. Jiang, B.S. Schoch, R.S. Carroll, P.M. Black, M.D. Johnson, Aberrant splicing of cyclin-dependent kinase-associated protein phosphatase KAP increases proliferation and migration in glioblastoma, Cancer Res. 67 (2007) 130–138.
[33] J. Chen, P.K. Jackson, M.W. Kirschner, A. Dutta, Separate domains of p21 involved in the inhibition of Cdk kinase and PCNA, Nature 374 (1995) 386–388.
[34] B.D. Chang, K. Watanabe, E.V. Broude, J. Fang, J.C. Poole, T.V. Kalinichenko, I.B. Roninson, Effects of p21Waf1/Cip1/Sdi1 on cellular gene expression: implications for carcinogenesis, senescence, and age-related diseases, Proc. Natl. Acad. Sci. USA 97 (2000) 4291–4296.
[35] D.F. Schafer, M.F. Sorrell, Hepatocellular carcinoma, Lancet 353 (1999) 1253–1257.
[36] K. Shirabe, T. Kanematsu, T. Matsumata, E. Adachi, K. Akazawa, K. Sugimachi, Factors linked to early recurrence of small hepatocellular carcinoma after hepatectomy: univariate and multivariate analyses, Hepatology 14 (1991) 802–805.
[37] G.S. Salvesen, C.S. Duckett, IAP proteins: blocking the road to death's door, Nat. Rev. Mol. Cell Biol. 3 (2002) 401–410.
[38] G. Ambrosini, C. Adida, D.C. Altieri, A novel anti-apoptosis gene, survivin, expressed in cancer and lymphoma, Nat. Med. 3 (1997) 917–921.
[39] F. Li, G. Ambrosini, E.Y. Chu, J. Plescia, S. Tognin, P.C. Marchisio, D.C. Altieri, Control of apoptosis and mitotic spindle checkpoint by survivin, Nature 396 (1998) 580–584.
[40] A. Giodini, M.J. Kallio, N.R. Wall, G.J. Gorbsky, S. Tognin, P.C. Marchisio, M. Symons, D.C. Altieri, Regulation of microtubule stability and mitotic progression by survivin, Cancer Res. 62 (2002) 2462–2467.
[41] C.M. Connell, S.P. Wheatley, I.A. McNeish, Nuclear survivin abrogates multiple cell cycle checkpoints and enhances viral oncolysis, Cancer Res. 68 (2008) 7923–7931.

Biochemical and Biophysical Research Communications 420 (2012) 36–41

Contents lists available at SciVerse ScienceDirect

Biochemical and Biophysical Research Communications

journal homepage: www.elsevier.com/locate/ybbrc

Possible involvement of melanocortin-4-receptor and AMP-activated protein kinase in the interaction of glucagon-like peptide-1 and leptin on feeding in rats

Paul-Emile Poleni [a,1], Sayaka Akieda-Asai [a,1], Shuichi Koda [b], Maya Sakurai [a], Cho-Rong Bae [c], Kazuyo Senba [a], Youn-Soo Cha [c], Mayumi Furuya [b], Yukari Date [a,*]

[a] Frontier Science Research Center, University of Miyazaki, Miyazaki 889-1692, Japan
[b] Faculty of Pharmacology I, Asubio Pharma Co., Ltd., Kobe 650-0047, Japan
[c] Department of Food Science and Human Nutrition, Obesity Research Center, Chonbuk National University, Jeonju 561-756, Republic of Korea

ARTICLE INFO

Article history:
Received 18 January 2012
Available online 27 February 2012

Keywords:
GLP-1
Leptin
Feeding
MC4-R
AMPK

ABSTRACT

Glucagon-like peptide-1 (GLP-1) and leptin are anorectic hormones produced in the small intestine and white adipose tissue, respectively. Investigating how these hormones act together as an integrated anorectic signal is important to elucidate a mechanism to maintain energy balance. In the present study, coadministration of subthreshold GLP-1 and leptin dramatically reduced feeding in rats. Although coadministration of GLP-1 with leptin did not enhance leptin signal transduction in the hypothalamus, it significantly decreased phosphorylation of AMP-activated protein kinase (AMPK). In addition, coadministration of GLP-1 with leptin significantly increased proopiomelanocortin (POMC) mRNA levels. Considering that α-melanocortin stimulating hormone (α-MSH) is derived from POMC and functions through the melanocortin-4-receptor (MC4-R) as a key molecule involved in feeding reduction, the interaction of GLP-1 and leptin on feeding reduction may be mediated through the α-MSH/MC4-R system. As expected, the interaction of GLP-1 and leptin was abolished by intracerebroventricular preadministration of the MC4-R antagonists agouti-related peptide and SHU9119. Taken together, GLP-1 and leptin cooperatively reduce feeding at least in part via inhibition of AMPK following binding of α-MSH to MC4-R.

1. Introduction

The body weights of adult animals or humans are essentially maintained within a fixed range, even if the daily amount of food consumption is changed [1,2]. To sustain the body weight in this way, multiple signals such as nutrients or hormones must interact to efficiently regulate energy balance [3].

Leptin is produced by white adipose tissue and maintains energy balance by reducing feeding. It binds to its receptor, ob-Rb, and stimulates the Janus-activated kinase (JAK)/signal transducer and activator of transcription-3 (STAT3) signaling pathway. Many of the neuropeptides that regulate feeding are closely associated with the leptin signaling pathway in the hypothalamus [4,5]. Furthermore, leptin administration enhances the anorectic response to satiety signaling molecules such as cholecystokinin (CCK), bombesin, or amylin [6–8]. Williams et al. also demonstrated that a subthreshold dose of leptin enhances the feeding reduction and weight loss induced by glucagon-like peptide-1 (GLP-1) [9]. GLP-1 is a gastrointestinal hormone produced by L cells in the small intestine and is thought to function as a satiety signal. This hormone is released in response to meal intake [10] and acts on the GLP-1 receptor (GLP-1R) that is present in vagal afferents, pancreatic β-cells, and neurons in the central nervous system (CNS; see Refs. [11,12] for review).

In this study, we investigated whether GLP-1 and leptin have interactive effects on feeding using overnight fasted rats that were administered subthreshold doses of GLP-1 and leptin. Furthermore, we examined leptin signal transduction and the phosphorylation of AMP-activated protein kinase (AMPK) in the hypothalamus after coadministration of GLP-1 and leptin. We also evaluated mRNA expression of hypothalamic substances relative to feeding such as neuropeptide Y (NPY), agouti-related protein (AGRP), cocaine- and amphetamine-regulated transcript (CART), and proopiomelanocortin (POMC). To clarify molecular mechanisms in the hypothalamus

Abbreviations: AGRP, agouti-related protein; AMPK, AMP-activated protein kinase; α-MSH, α-melanocyte-stimulating hormone; CART, cocaine-and amphetamine-regulated transcript; CCK, cholecystokinin; CNS, central nervous system; GLP-1, glucagon-like peptide-1; GAPDH, glyceraldehyde 3-phosphate dehydrogenase; GLP-1R, GLP-1 receptor; ip, intraperitoneal or intraperitoneally; HRP, horseradish peroxidase; icv, intracerebroventricular or intracerebroventricularly; JAK, janus-activated kinase; MC4-R, melanocortin-4-receptor; NPY, neuropeptide Y; NTS, nucleus tractus solitarius; pAMPK, phosphorylated AMPK; POMC, proopiomelanocortin; pSTAT3, phosphorylated STAT3.

* Corresponding author. Address: Frontier Science Research Center, University of Miyazaki, Kiyotake, Miyazaki 889-1692, Japan.
E-mail address: dateyuka@med.miyazaki-u.ac.jp (Y. Date).

[1] These authors contributed equally to this work.

0006-291X/$ - see front matter © 2012 Elsevier Inc. All rights reserved.
doi:10.1016/j.bbrc.2012.02.109

involved in the interaction of GLP-1 and leptin, we investigated whether the interactive effect of these hormones on feeding is abolished in rats that were preadministered antagonists for hypothalamic substances.

2. Materials and methods

2.1. Experimental animals

Male Wistar rats (10 weeks old; Charles River Japan, Inc., Shiga, Japan), weighing 300–350 g, were used for all experiments. Rats were given standard laboratory chow and water *ad libitum* and housed individually in plastic cages at constant room temperature in a 12-h light/12-h dark cycle (0800–2000 h light). Anesthesia was performed with an ip injection of sodium pentobarbital (40 mg/kg; Abbot Laboratories, Chicago, IL, USA) before the following operations. For MC4-R blockade, we implanted intracerebroventricular (icv) cannulae into the lateral cerebral ventricles of rats after anesthesia. Proper placement of the cannula was verified by dye injection at the end of the experiment. Only animals exhibiting progressive weight gain after surgery were used in experiments. All procedures were performed in accordance with the Japanese Physiological Society's guidelines for animal care. This protocol was approved by the Ethics Review Committee for Animal Experimentation of the Faculty of Medicine, University of Miyazaki.

2.2. Feeding experiments

We evaluated the dose-dependency of GLP-1 and leptin on feeding. A solution of rat recombinant leptin (Sigma Aldrich, Saint Louis, MI, USA) dissolved in 0.9% saline (18.8–62.5 nmol/kg in a volume of 100 μL) was administered ip at 0930–1000 h to rats that had fasted overnight (n = 6–10). GLP-1 (7-36) amide (Peptide Institute, Inc., Osaka, Japan) was dissolved in 0.9% saline, and this solution (10–40 nmol/kg in a volume of 100 μL) was administered ip at 0930–1000 h to another set of rats fasted overnight (n = 6–10). After the injection, cumulative food intake was measured at 0.5, 1, and 2 h. Next, to evaluate the interaction of GLP-1 and leptin on feeding reduction, we used the dosage of 10 nmol/kg GLP-1 and 18.8 nmol/kg leptin, which individually did not decrease feeding of rats fasted over night. Rats fasted overnight were divided into four groups; a saline-injected group, a group injected with GLP-1 (10 nmol/kg), a group injected with leptin (18.8 nmol/kg), and a group coinjected with GLP-1 (10 nmol/kg) and leptin (18.8 nmol/kg). We measured the food intake of each group at 0.5, 1, and 2 h after injections.

To evaluate the contribution of MC4-R signaling to the interaction of the hormones, rats fasted overnight were administered icv vehicle alone (saline; n = 6), or the MC4-R antagonists, AGRP (16 μg/kg; n = 5; Peptide Institute, Osaka, Japan), or SHU9119 (1.2 μg/kg; n = 5; Sigma Aldrich) 1 h before peripheral coinjection of GLP-1 (10 nmol/kg) and leptin (18.8 nmol/kg). These doses of AGRP or SHU9119 are known to prevent feeding reduction caused by α-melanocyte stimulating hormone (α-MSH) [13,14]. GLP-1 + leptin or saline was administered ip to rats 1 h after preadministration of saline, AGRP, or SHU9119, and food intake was measured after 0.5, 1, and 2 h. The rats were fasted between the two injections.

2.3. Western blotting

The rats were decapitated and their hypothalami were rapidly removed 0.5 h after ip injection of saline, GLP-1, leptin, or GLP-1 + leptin into rats (n = 5–6 per group), and the amount of total protein was measured for each sample by the bicinchoninic acid method (Pierce Microplate BCA Protein Assay Kit, Thermo Scientific, Rockford, IL, USA). 30 μg of total proteins per sample were analyzed by SDS-PAGE (8% acrylamide) and electroblotted onto polyvinylidene difluoride membranes (Immobilon-P, Millipore, Tokyo, Japan). Membranes were then sequentially blocked in 5% (w/v) blocking buffer (5% (w/v) non-fat dry milk diluted in TBS Tween20), probed overnight at 4 °C with gentle shaking with primary antibody against Stat-3, phospho-Stat-3, AMPKα1 and 2, or phospho-AMPKα1 and 2 (Cell Signaling Technology, Inc., Danvers, MA, USA), and incubated for 1 h at room temperature with horseradish peroxidase (HRP)-conjugated secondary antibodies against the molecular weight standard (Biotinylated Protein Ladder, Cell Signaling Technology, Inc.) and an HRP labeled goat anti-rabbit IgG (H + L) antibody (Epitomics, Inc., Burlingame, CA, USA). Specific proteins were detected by chemiluminescence with the Phototope Detection system (Cell Signaling Technology, Inc.) in accordance with the manufacturer's instructions. Western blotting was quantified by densitometry relative to total STAT3 or AMPK by using NIH Image software (Image J).

2.4. Quantitative PCR

The hypothalami of rats fasted overnight were removed 1.5 h after ip injection of saline, GLP-1 (10 nmol/kg), leptin (18.8 nmol/kg), or GLP-1 (10 nmol/kg) and leptin (18.8 nmol/kg) (n = 10 in each group), and total RNAs were rapidly extracted with TRIzol® Reagent (Invitrogen Corp., Carlsbad, CA, USA). First-strand cDNA was synthesized from 1 μg total RNA using the commercially available Superscript® III First-Strand Synthesis System kit (Invitrogen Corp.), and the resulting samples were subjected to quantitative PCR. Quantitative PCR for NPY, AGRP, CART, and POMC was conducted on a LightCycler system (Roche Diagnostics GmbH, Mannheim, Germany) using the SYBR® Premix Ex Taq™ mix system (Takara Bio Inc., Shiga, Japan) with primer sets described elsewhere [15]. The relative abundance of all reaction products was normalized to the level of glyceraldehyde 3-phosphate dehydrogenase (GAPDH).

2.5. Statistical analysis

All data are expressed as mean ± standard error of the mean (SEM). Statistical significance was evaluated by a one-way or a two-way ANOVA. When ANOVA indicated a significant effect of the variable, differences between groups were analyzed using Dunnett's or Bonferroni's post hoc test. $P < 0.05$ was considered statistically significant.

3. Results

3.1. Interaction of GLP1 with leptin on food intake

We first tested various doses of leptin from 18.8 to 62.5 nmol/kg and of GLP-1 ranging from 10 to 40 nmol/kg in a feeding experiment using rats fasted overnight. An ip injection of 62.5 nmol/kg leptin significantly decreased food intake 2 h after injection, whereas neither 18.8 nmol/kg nor 35.7 nmol/kg leptin reduced feeding (Fig. 1A). An ip injection of 40 nmol/kg GLP-1 significantly decreased food intake by 0.5, 1, and 2 h after injection; however, neither 20 nmol/kg nor 10 nmol/kg GLP-1 reduced feeding (Fig. 1B). Therefore, we examined the interaction of GLP-1 and leptin on feeding using 18.8 nmol//kg leptin and 10 nmol/kg GLP-1. An ip coinjection of 10 nmol/kg GLP-1 and 18.8 nmol/kg leptin significantly reduced food intake of overnight fasted rats 0.5 and 1 h after injection compared to saline, 10 nmol/kg GLP-1, or 18.8 nmol/kg leptin injection (Fig. 1C).

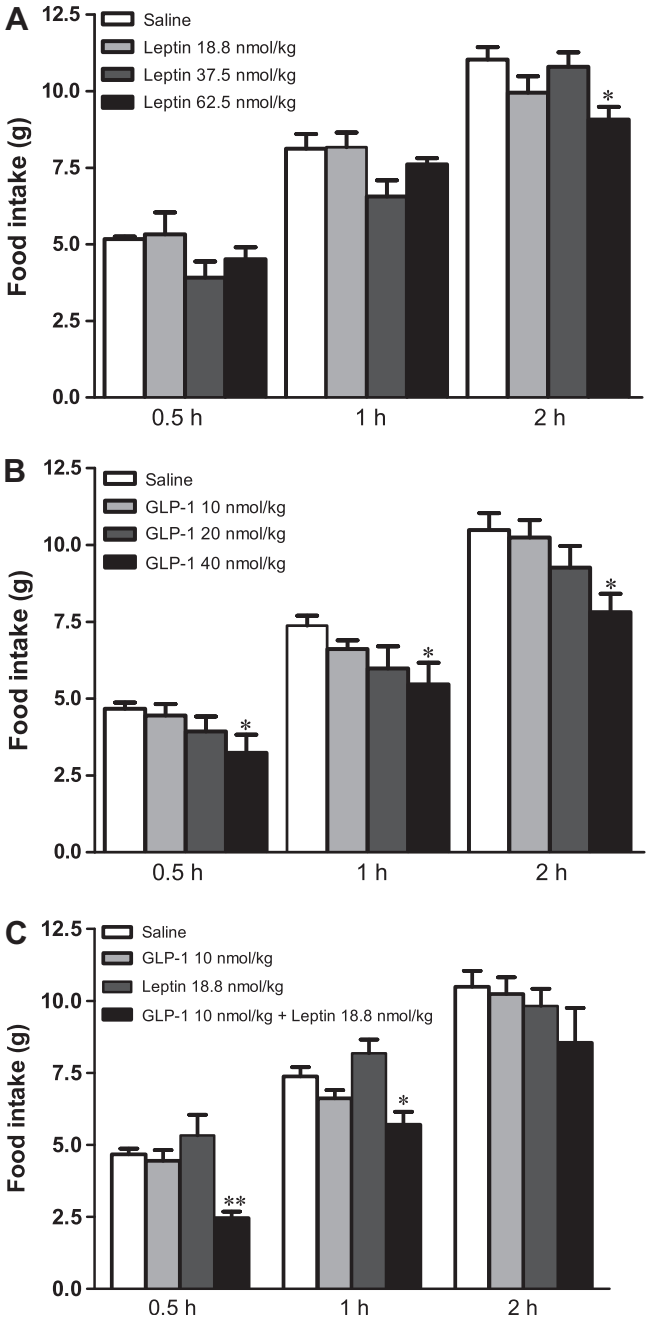

Fig. 1. The effect of ip administration of leptin, GLP-1, or leptin + GLP-1 on food intake in rats. Data represent mean ± SEM (n = 5–12 each). A, Food intake of rats fasted overnight after a single ip administration of leptin (18.8–62.5 nmol/kg). $^{*}P < 0.05$ *vs.* saline (one-way ANOVA followed by Dunnett's test). B, Food intake of rats fasted overnight after a single ip administration of GLP-1 (10–40 nmol/kg). $^{*}P < 0.05$ *vs.* saline (one-way ANOVA followed by Dunnett's test). C, Food intake of rats fasted overnight after a single ip administration of leptin (18.8 nmol/kg), GLP-1 (10 nmol/kg), or leptin (18.8 nmol/kg) + GLP-1 (10 nmol/kg). $^{*}P < 0.05$ *vs.* saline, $^{**}P < 0.01$ *vs.* saline (two-way ANOVA followed by Bonferroni's test).

3.2. Phosphorylation of STAT3 and AMPK in the hypothalamus after coinjection of GLP-1 and leptin

To investigate the molecular mechanism of the interaction between GLP-1 and leptin, we used Western blotting to examine the effect of coinjection of GLP-1 and leptin on phosphorylation of STAT3 and AMPK in the hypothalami of rats fasted overnight. There were no significant differences in the phosphorylation of STAT3 among the groups (Fig. 2A), but phosphorylation of AMPK in the hypothalami of rats was dramatically lower after coinjection of GLP-1 + leptin than after saline, GLP-1, or leptin injection (Fig. 2B).

3.3. mRNA expression

To examine the roles for anorectic or orexigenic substances produced in the hypothalamus in the interaction of GLP-1 and leptin, we used quantitative PCR to evaluate mRNA levels of NPY, AGRP, CART, and POMC after injection of saline, GLP-1, leptin, or GLP-1 + leptin into rats fasted overnight. There were no significant differences in NPY, AGRP, or CART mRNA levels among the groups (Fig. 3A–C). In contrast, the POMC mRNA level was significantly higher after coinjection of GLP-1 and leptin than after injection of saline, GLP-1, or leptin alone (Fig. 3D).

3.4. A role for MC4-R signaling in the interaction of GLP-1 and leptin

To investigate the relationship between MC4-R signaling and the interaction of GLP-1 and leptin, we evaluated the effects of AGRP and SHU9119 on the reduction in feeding induced by coinjection of GLP-1 and leptin to rats fasted overnight. An ip coinjection of GLP-1 and leptin significantly decreased 0.5-h food intake (Fig. 4A and B). However, when AGRP or SHU9119 was given prior to the coinjection of GLP-1 and leptin, the interaction on feeding was abrogated (Fig. 4A and B).

4. Discussion

In this study, we investigated the mechanism for interaction of GLP-1 and leptin on reducing feeding. GLP-1, a potent incretin hormone, is produced in the L cells of the ileum and colon and released in the response to nutrients including glucose, fatty acids, and dietary fiber [16,17]. GLP-1 augments insulin release in a glucagon-dependent manner, and drug targeting the GLP-1 pathway, such as DPP-IV inhibitors and GLP-1 receptor agonists, are used to treat type 2 diabetes [18–20]. GLP-1 itself reduces feeding when administered either centrally or peripherally [21–25]. Leptin, an adipose tissue-derived circulating hormone, also plays a key role in the regulation of feeding and energy homeostasis by conveying anorectic information to the brain.

We first examined the dose response for effects of ip leptin on food intake in fasted rats. Consistent with our preliminary examinations and a previous study [26], the present data showed that in fasted rats, ip injection of 62.5 nmol/kg leptin significantly decreased feeding, whereas leptin concentrations of 37.5 nmol/kg or less did not reduce feeding. We further showed that 40 nmol/kg GLP-1 reduced feeding in fasted rats, whereas 10 nmol/kg or 20 nmol/kg GLP-1 administered ip did not decrease feeding. However, in some studies ip injection of GLP-1 of 40 nmol/kg or less reduced food intake [9,27]. We performed all experiments using rats fasted overnight. As noted by Williams et al., it is hard to demonstrate that a low dose of GLP-1 reduces feeding in fasted rats, because several anorectic hormones that are expected to have some interaction with GLP-1 are decreased in the fasted state [9]. Thus, the doses of GLP-1 or leptin used here may be pharmacological not physiological. However, considering that overnight fasted rats have the conditions that influence of anorectic hormones can be reduced, the feeding experiment using fasted rats may be appropriate to merely evaluate the interaction of individual anorectic hormone. In a previous study, preinjection of 37.5 nmol/kg leptin not relative to feeding effects intensified the effect of GLP-1 (100 μg/kg, shown in the cited report to significantly decrease food intake) on feeding reduction [9]. In this

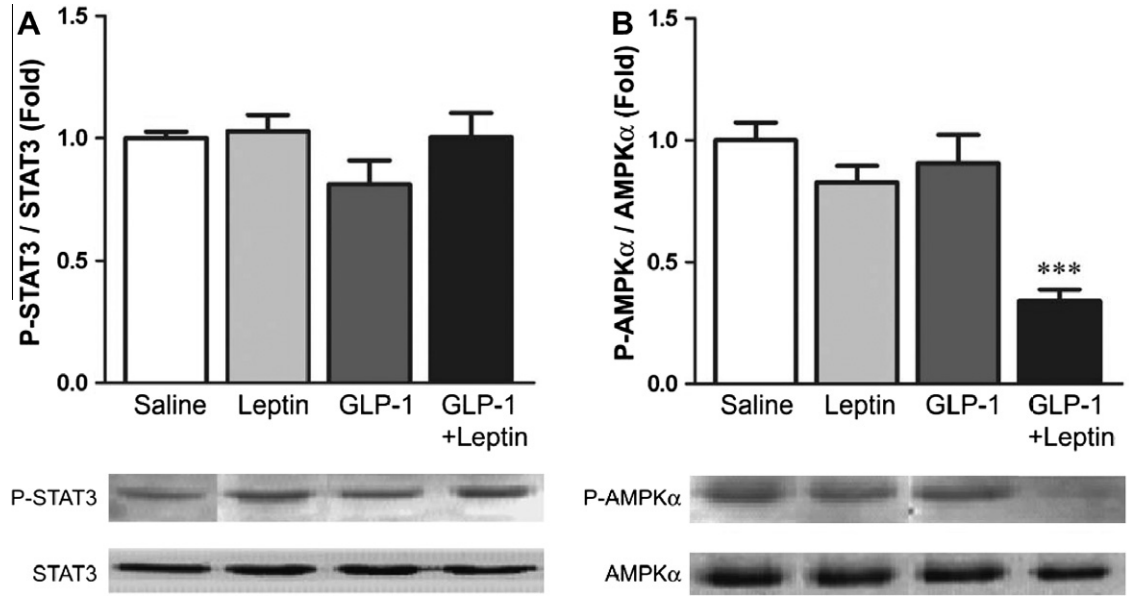

Fig. 2. Western blot analysis of phosphorylated STAT3 and AMPK (pSTAT3 and pAMPK) in the hypothalami of rats after an ip administration of saline, leptin (18.8 nmol/kg), GLP-1 (10 nmol/kg), or leptin (18.8 nmol/kg) + GLP-1 (10 nmol/kg). A, The protein level of pSTAT3 did not differ between the four groups. B, Coadministration of leptin with GLP-1 significantly decreased the protein level of pAMPK. The band intensity ratio of pSTAT3 and pAMPK to STAT3 or AMPK, respectively, in rats after saline administration was arbitrarily set to 1.0. Data represent mean ± SEM (n = 4–5 each). $^{***}P < 0.001$ *vs.* saline (two-way ANOVA followed by Bonferroni's test).

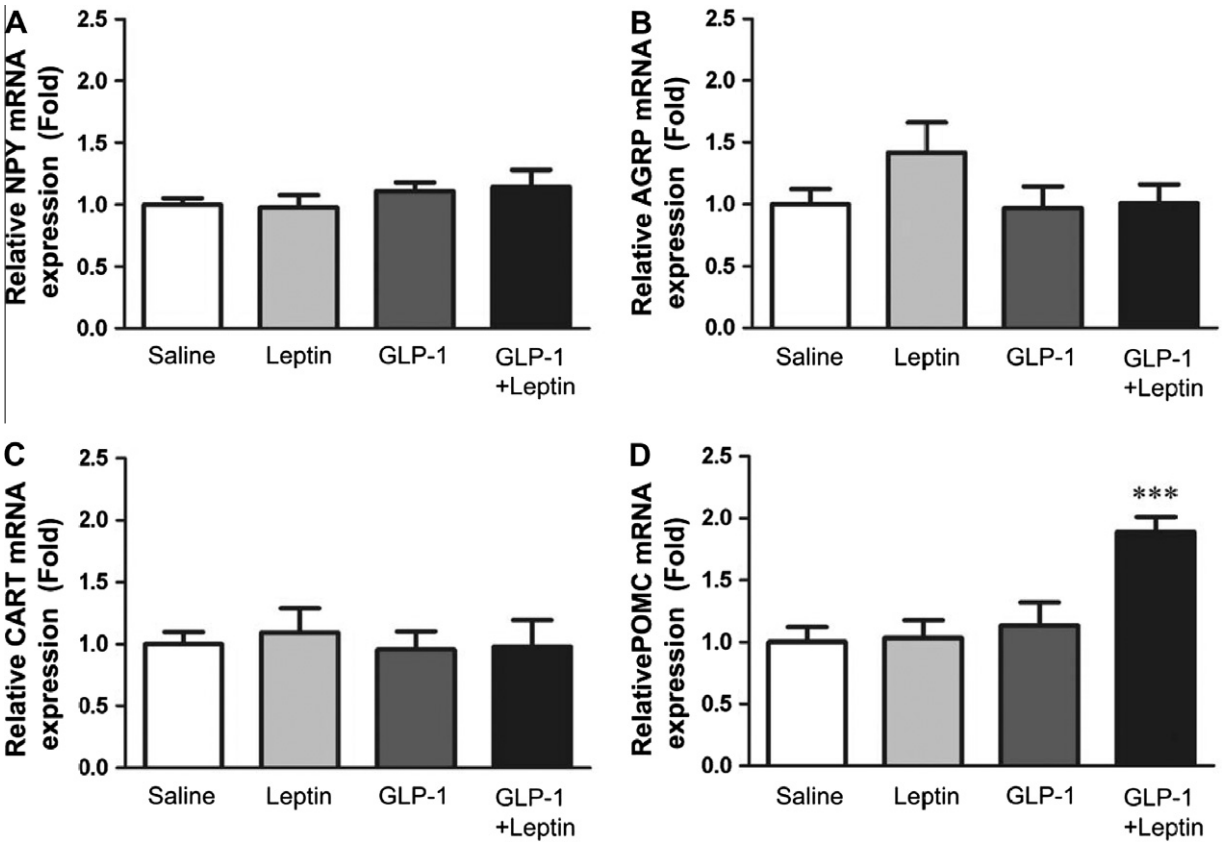

Fig. 3. Quantitative PCR analysis of NPY (A), AGRP (B), CART (C), and POMC (D) in the hypothalamus of rats fasted overnight after the ip administration of saline, leptin (18.8 nmol/kg), GLP-1 (10 nmol/kg), or leptin (18.8 nmol/kg) + GLP-1 (10 nmol/kg). Coadministration of leptin and GLP-1 significantly increased POMC mRNA levels. Data were normalized by the amount of GAPDH. Data represent mean ± SEM (n = 4–12 each). $^{***}P < 0.001$ *vs.* control (two-way ANOVA followed by Bonferroni's test).

study, we demonstrated that coinjection of even subthreshold doses of GLP-1 (10 nmol/kg) and leptin (18.8 nmol/kg) significantly decreased food intake. This finding suggests that anorectic information brought by coinjection of subthreshold doses of GLP-1 and leptin are integrated, contributing to the regulation of the neural circuit for feeding behavior.

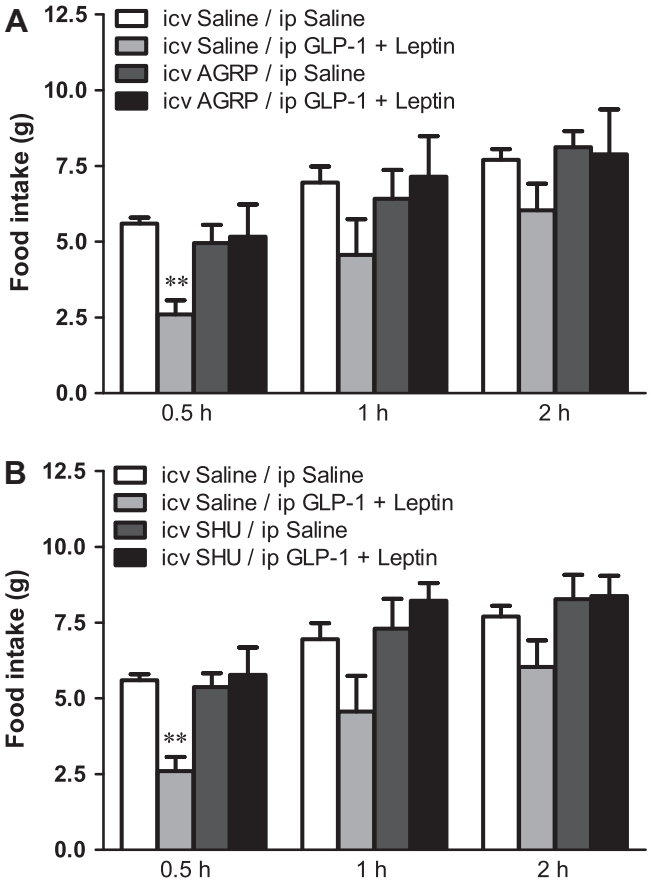

Fig. 4. The effect of AGRP (A) and SHU9119 (B) on the reduction in feeding reduction caused by leptin + GLP-1 in rats fasted overnight. Preadministration of AGRP or SHU9119 abolished the reduction in feeding induced by coadministration of leptin (18.8 nmol/kg) and GLP-1 (10 nmol/kg). Data represent mean ± SEM (n = 4–6 each). $^{**}P < 0.01$ *vs.* saline (two-way ANOVA followed by Bonferroni's test).

Very recently, Turek et al. presented data that amylin, an anorectic hormone produced in the islet, amplifies the phosphorylation of STAT3 in the arcuate nucleus that is induced by low-dose leptin [8]. They also showed that amylin/leptin coinfusion synergistically decreased food intake, body weight, and fat volume. In the present study, coinjection of GLP-1 and leptin did not increase phosphorylation of STAT3. These data indicate that the interactive effects of GLP-1 and leptin do not occur by intensifying leptin signaling in the hypothalamus.

AMPK has been considered to act as a general energy sensor and integrator of nutrient or hormonal signals in the hypothalamus [28,29]. Hypothalamic AMPK activity is reduced by anorectic hormones such as leptin, insulin, or GLP-1 [31–34]. Therefore, we examined phosphorylation of AMPK in the hypothalamus after coinjection of GLP-1 with leptin. Our data showed that GLP-1 or leptin alone did not influence phosphorylation of AMPK, whereas coinjection of GLP-1 with leptin dramatically decreased it. These data imply that GLP-1 and leptin act together on neural pathways that lead to the reduction of food intake by decreasing the phosphorylation of AMPK in the hypothalamus.

To investigate which system in the hypothalamus is involved in the suppression of AMPK activity, we examined mRNA expression of NPY, AGRP, CART, and POMC, which are hypothalamic substances related to feeding. Although subthreshold doses of GLP-1 and leptin to fasted rats did not affect mRNA expression of NPY, AGRP, or CART, it significantly increased POMC expression. POMC is the precursor for α-MSH, one of the key molecules involved in feeding regulation. α-MSH released from the axon terminals of POMC neurons binds to and activates MC4-R, reducing food intake and body weight [34]. Here we showed that even subthreshold doses of GLP-1 or leptin can significantly increase POMC expression when they are given together. Our data suggest that the POMC/MC4-R system at least in part plays an important role in the interaction between GLP-1 and leptin.

MC4-R is thought to be involved in the effect of leptin on AMPK activity in the hypothalamic periventricular nucleus [35]. It was also demonstrated that leptin does not inhibit AMPK activity in the PVN of MC4-R knockout mice [30]. These findings indicate that MC4-R signaling plays an important role in the control of AMPK activity, regulation of food intake, or energy metabolism. We have already shown that coinjection of GLP-1 and leptin increases POMC expression, probably leading to the suppression of AMPK activity via MC4-R signaling. We therefore investigated whether the interaction of GLP-1 and leptin is blocked in rats treated with MC4-R antagonists. As expected, the interactive effect of GLP-1 and leptin on feeding was abrogated by preadministration of AGRP or SHU9119, suggesting that POMC/MC4-R system plays a crucial role in the interaction of GLP-1 and leptin.

In this study, we showed that subthreshold amounts of GLP-1 and leptin significantly decrease food intake 0.5 and 1 h after coinjection, indicating that the interaction between GLP-1 and leptin is a fairly acute action. Considering that GLP-1 is extremely rapidly metabolized and inactivated by DPP-IV after secretion, signals of endogenous GLP-1 may be transmitted to the brain quickly. To fully understand the mechanism of the interaction of GLP-1 and leptin, we need to perform further studies, including identifying systems that integrate the signals of these two hormones or particular mechanisms in the hypothalamus that are involved in the decrease in the activity of AMPK.

5. Disclosure summary

The authors have nothing to disclose.

Acknowledgments

We thank A. Miyashita, Y. Aiboshi, T. Miyanaga (University of Miyazaki, Miyazaki, Japan) for their technical assistance and N. Murakami (University of Miyazaki) for helpful discussion. This study was supported in part by grants-in-aid from the Ministry of Education, Culture, Sports, Science and Technology of Japan; the Program for Promotion of Basic Research Activities for Innovative Bioscience (PROBRAIN); the Mitsubishi Foundation; the Naito Foundation; and the Takeda Science Foundation.

References

[1] G.A. Bray, Weight homeostasis, Annu. Rev. Med. 42 (1991) 205–216.
[2] R.E. Keesey, M.D. Hirvonen, Body weight set-points: determination and adjustment, J. Nutr. 127 (1997) 1875S–1883S.
[3] P.J. Havel, Peripheral signals conveying metabolic information to the brain: short-term and long-term regulation of food intake and energy homeostasis, Exp. Biol. Med. 226 (2001) 963–977.
[4] D.E. Cummings, M.W. Schwartz, Genetics and pathophysiology of human obesity, Annu. Rev. Med. 54 (2003) 453–471.
[5] S.P. Kalra, M.G. Dube, S. Pu, B. Xu, T.L. Horvath, P.S. Kalra, Interacting appetite-regulating pathways in the hypothalamic regulation of body weight, Endocr. Rev. 20 (1999) 68–100.
[6] M. Emond, G.J. Schwartz, E.E. Ladenheim, T.H. Moran, Central leptin modulates behavioral and neural responsivity to CCK, Am. J. Physiol. 276 (1999) R1545–R1549.
[7] E.E. Ladenheim, M. Emond, T.H. Moran, Leptin enhances feeding suppression and neural activation produced by systemically administered bombesin, Am. J. Physiol. Regul. Integr. Comp. Physiol. 289 (2005) R473–R477.
[8] V.F. Turek, J.L. Trevaskis, B.E. Levin, A.A. Dunn-Meynell, B. Irani, G. Gu, C. Wittmer, P.S. Griffin, C. Vu, D.G. Parkes, J.D. Roth, Mechanisms of amylin/leptin synergy in rodent models, Endocrinology 151 (2010) 143–152.

[9] D.L. Williams, D.G. Baskin, M.W. Schwartz, Leptin regulation of the anorexic response to glucagon-like peptide-1 receptor stimulation, Diabetes 55 (2006) 3387–3393.
[10] S. Mojsov, G. Heinrich, I.B. Wilson, M. Ravazzola, L. Orci, J.F. Habener, Preproglucagon gene expression in pancreas and intestine diversifies at the level of post-translational processing, J. Biol. Chem. 261 (1986) 11880–11889.
[11] M.R. Hayes, B.C. De Jonghe, S.E. Kanoski, Role of the glucagon-like-peptide-1 receptor in the control of energy balance, Physiol. Behav. 100 (2010) 503–510.
[12] J.J. Holst, The physiology of glucagon-like peptide 1, Physiol. Rev. 87 (2007) 1409–1439.
[13] M. Rossi, M.S. Kim, D.G. Morgan, C.J. Small, C.M. Edwards, D. Sunter, S. Abusnana, A.P. Goldstone, S.H. Russell, S.A. Stanley, D.M. Smith, K. Yagaloff, M.A. Ghatei, S.R. Bloom, A C-terminal fragment of agouti-related protein increases feeding and antagonizes the effect of alpha-melanocyte stimulating hormone in vivo, Endocrinology 139 (1998) 4428–4431.
[14] C.M. Edwards, C.R. Abbott, D. Sunter, M. Kim, C.L. Dakin, K.G. Murphy, S. Abusnana, S. Taheri, M. Rossi, S.R. Bloom, Cocaine- and amphetamine-regulated transcript, glucagon-like peptide-1 and corticotrophin releasing factor inhibit feeding via agouti-related protein independent pathways in the rat, Brain Res. 866 (2000) 128–134.
[15] Y. Date, M.S. Mondal, H. Kageyama, M. Ghamari-Langroudi, F. Takenoya, H. Yamaguchi, Y. Shimomura, M. Mori, N. Murakami, S. Shioda, R.D. Cone, M. Nakazato, Neuropeptide W: an anorectic peptide regulated by leptin and metabolic state, Endocrinology 151 (2010) 2200–2210.
[16] D.J. Drucker, Biological actions and therapeutic potential of the glucagon-like peptides, Gastroenterology 122 (2002) 531–544.
[17] H.C. Fehmann, R. Göke, B. Göke, Cell and molecular biology of the incretin hormones glucagon-like peptide-I and glucose-dependent insulin releasing polypeptide, Endocr. Rev. 16 (1995) 390–410.
[18] K. Nonaka, T. Kakikawa, A. Sato, K. Okuyama, G. Fujimoto, N. Kato, H. Suzuki, Y. Hirayama, T. Ahmed, M.J. Davies, P.P. Stein, Efficacy and safety of sitagliptin monotherapy in Japanese patients with type 2 diabetes, Diabetes Res. Clin. Pract. 7 (2008) 291–298.
[19] M. Kikuchi, N. Abe, M. Kato, S. Terao, N. Mimori, H. Tachibana, Vildagliptin dose-dependently improves glycemic control in Japanese patients with type 2 diabetes mellitus, Diabetes Res. Clin. Pract. 83 (2009) 233–240.
[20] Y. Seino, M.F. Rasmussen, M. Zdravkovic, K. Kaku, Dose-dependent improvement in glycemia with once-daily liraglutide without hypoglycemia or weight gain: a double-blind, randomized, controlled trial in Japanese patients with type 2 diabetes, Diabetes Res. Clin. Pract. 81 (2008) 161–168.
[21] M.D. Turton, D. O'Shea, I. Gunn, S.A. Beak, C.M. Edwards, K. Meeran, S.J. Choi, G.M. Taylor, M.M. Heath, P.D. Lambert, J.P. Wilding, D.M. Smith, M.A. Ghatei, J. Herbert, S.R. Bloom, A role for glucagon-like peptide-1 in the central regulation of feeding, Nature 379 (1996) 69–72.
[22] M. Tang-Christensen, P.J. Larsen, R. Göke, A. Fink-Jensen, D.S. Jessop, M. Møller, S.P. Sheikh, Central administration of GLP-1-(7-36) amide inhibits food and water intake in rats, Am. J. Physiol. 271 (1996) R848–856.
[23] M. Navarro, F. Rodriquez de Fonseca, E. Alvarez, J.A. Chowen, J.A. Zueco, R. Gomez, J. Eng, E. Blázquez, Colocalization of glucagon-like peptide-1 (GLP-1) receptors, glucose transporter GLUT-2, and glucokinase mRNAs in rat hypothalamic cells: evidence for a role of GLP-1 receptor agonists as an inhibitory signal for food and water intake, J. Neurochem. 67 (1996) 1982–1991.
[24] M. Szayna, M.E. Doyle, J.A. Betkey, H.W. Holloway, R.G. Spencer, N.H. Greig, J.M. Egan, Exendin-4 decelerates food intake, weight gain, and fat deposition in Zucker rats, Endocrinology 141 (2000) 1936–1941.
[25] F. Rodriquez de Fonseca, M. Navarro, E. Alvarez, I. Roncero, J.A. Chowen, O. Maestre, R. Gómez, R.M. Muñoz, J. Eng, E. Blázquez, Peripheral versus central effects of glucagon-like peptide-1 receptor agonists on satiety and body weight loss in Zucker obese rats, Metabolism 49 (2000) 709–717.
[26] C.M. Patterson, S.G. Bouret, A.A. Dunn-Meynell, B.E. Levin, Three weeks of postweaning exercise in DIO rats produces prolonged increases in central leptin sensitivity and signaling, Am. J. Physiol. Regul. Integr. Comp. Physiol. 296 (2009) R537–R548.
[27] E.B. Rüttimann, M. Arnold, J.J. Hillebrand, N. Geary, W. Langhans, Intrameal hepatic portal and intraperitoneal infusions of glucagon-like peptide-1 reduce spontaneous meal size in the rat via different mechanisms, Endocrinology 150 (2009) 1174–1181.
[28] B.B. Kahn, T. Alquier, D. Carling, D.G. Hardie, AMP-activated protein kinase: ancient energy gauge provides clues to modern understanding of metabolism, Cell Metab. 1 (2005) 15–25.
[29] S. Ramamurthy, G.V. Ronnett, Developing a head for energy sensing: AMP-activated protein kinase as a multifunctional metabolic sensor in the brain, J. Physiol. 574 (2006) 85–93.
[30] Y. Minokoshi, T. Alquier, N. Furukawa, Y.B. Kim, A. Lee, B. Xue, J. Mu, F. Foufelle, P. Ferré, M.J. Birnbaum, B.J. Stuck, B.B. Kahn, AMP-kinase regulates food intake by responding to hormonal and nutrient signals in the hypothalamus, Nature 428 (2004) 569–574.
[31] U. Andersson, K. Filipsson, C.R. Abbott, A. Woods, K. Smith, S.R. Bloom, D. Carling, C.J. Small, AMP-activated protein kinase plays a role in the control of food intake, J. Biol. Chem. 279 (2004) 12005–12008.
[32] M.S. Kim, J.Y. Park, C. Namkoong, P.G. Jang, J.W. Ryu, H.S. Song, J.Y. Yun, I.S. Namgoong, J. Ha, I.S. Park, I.K. Lee, B. Viollet, J.H. Youn, H.K. Lee, K.U. Lee, Anti-obesity effects of alpha-lipoic acid mediated by suppression of hypothalamic AMP-activated protein kinase, Nat. Med. 10 (2004) 727–733.
[33] S. Seo, S. Ju, H. Chung, D. Lee, S. Park, Acute effects of glucagon-like peptide-1 on hypothalamic neuropeptide and AMP activated kinase expression in fasted rats, Endocr. J. 55 (2008) 867–874.
[34] D. Huszar, C.A. Lynch, V. Fairchild-Huntress, J.H. Dunmore, Q. Fang, L.R. Berkemeier, W. Gu, R.A. Kesterson, B.A. Boston, R.D. Cone, F.J. Smith, L.A. Campfield, P. Burn, F. Lee, Targeted disruption of the melanocortin-4 receptor results in obesity in mice, Cell 88 (1997) 31–141.
[35] Y. Minokoshi, T. Shiuchi, S. Lee, A. Suzuki, S. Okamoto, Role of hypothalamic AMP-kinase in food intake regulation, Nutrition 24 (2008) 786–790.

Biochemical and Biophysical Research Communications 420 (2012) 42–47

Contents lists available at SciVerse ScienceDirect

Biochemical and Biophysical Research Communications

journal homepage: www.elsevier.com/locate/ybbrc

Molecular dynamics analysis of conformational change of paramyxovirus F protein during the initial steps of membrane fusion

Fernando Martín-García [a,b], Jesús Ignacio Mendieta-Moreno [a,b], Jesús Mendieta [a,b], Paulino Gómez-Puertas [a,*]

[a] Centro de Biología Molecular "Severo Ochoa" (CSIC/UAM), C/ Nicolás Cabrera, 1, Cantoblanco, 28049 Madrid, Spain
[b] Biomol-Informatics SL, Parque Científico de Madrid, C/ Faraday, 7, Cantoblanco, 28049 Madrid, Spain

ARTICLE INFO

Article history:
Received 1 February 2012
Available online 28 February 2012

Keywords:
Molecular dynamics
Fusion protein
Conformational change
Mechanical force

ABSTRACT

The fusion of paramyxovirus to the cell membrane is mediated by fusion protein (F protein) present in the virus envelope, which undergoes a dramatic conformational change during the process. Unlike hemagglutinin in orthomyxovirus, this change is not mediated by an alteration of environmental pH, and its cause remains unknown. Steered molecular dynamics analysis leads us to suggest that the conformational modification is mediated only by stretching mechanical forces once the transmembrane fusion peptide of the protein is anchored to the cell membrane. Such elongating forces will generate major secondary structure rearrangement in the heptad repeat A region of the F protein; from β-sheet conformation to an elongated coil and then spontaneously to an α-helix. In addition, it is proposed that the heptad repeat A region adopts a final three-helix coiled coil and that this structure appears after the formation of individual helices in each monomer.

1. Introduction

The *Paramyxoviridae* family is composed of enveloped, negative-stranded RNA viruses, many of which are human pathogens (e.g., the measles virus, human respiratory syncytial virus (RSV), Hendra and Nipah viruses and human metapneumovirus [1]). Their entry into target cells is mediated by two glycoproteins located on the viral membrane: the attachment (G) protein, that binds to heparin sulfate, and the fusion (F) protein [2,3]. The presence of both proteins and their interaction is usually necessary to drive the membrane fusion event [4–6]; however, both human and bovine RSV, as well as human metapneumovirus (MPV), are exceptions: their membranes can fuse in the absence of the viral G protein [7–10].

The F protein belongs to the class I viral fusion proteins, whose most important representative is from the influenza virus hemagglutinin (HA). Each monomer is initially synthesized as the F0 precursor and subsequently cleaved into the active F1 + F2 heterodimer by a trypsine-like protease. This cleavage releases a transmembrane fusion peptide (F peptide) with a length of 25–48 residues, located in the N-terminal end of F1 [11]. After binding to the host cell membrane, the trimeric F1 + F2 complex experiences a major multi-step structural change, mainly in the heptad repeat A (HRA) and heptad repeat B (HRB) domains, which results in a completely different post-fusion structure [12]. The change is irreversible; blocked by the energy barrier of the membrane fusion [13].

In the case of the *Paramyxoviridae* family, crystal structures have recently been published for both pre-fusion (parainfluenza virus 5; PDB ID: 2B9B [14]) and post-fusion (human parainfluenza virus 3; PDB ID: 1ZTM [15]) conformations of two viruses, and they illustrate this dramatic change. It has been suggested that other members of the family undergo the same structural modification, based on their sequence similarities. A multiple sequence alignment of domain III (DIII) of the F protein from some viruses in this family to illustrate their similarity is included as Supplementary material (Supp. Fig. S1). The HRA region of the protein undergoes major change in its secondary structure, and thus in its 3D structure. From an initial folded state composed of two beta strands in anti-parallel conformation, followed by a short α-helix segment (Supp. Fig. S1), the post-fusion arrangement of the HRA segment has a completely refolded structure. This post-fusion structure incorporates the residues that were formerly part of the 2beta + 1alpha region into a newly formed, completely extended all-alpha structure (Supp. Fig. S1) that interacts with the helix formed by the other two monomers, thus generating a three-helix coiled coil [15,16]. Although the rest of the structure of DIII is also altered,

Abbreviations: F protein, fusion protein; MD, molecular dynamics; HRA, heptad repeat A; HRB, heptad repeat B.

* Corresponding author. Fax: +34 91 196 4420.
E-mail address: pagomez@cbm.uam.es (P. Gómez-Puertas).

0006-291X/$ - see front matter © 2012 Elsevier Inc. All rights reserved.
doi:10.1016/j.bbrc.2012.02.112

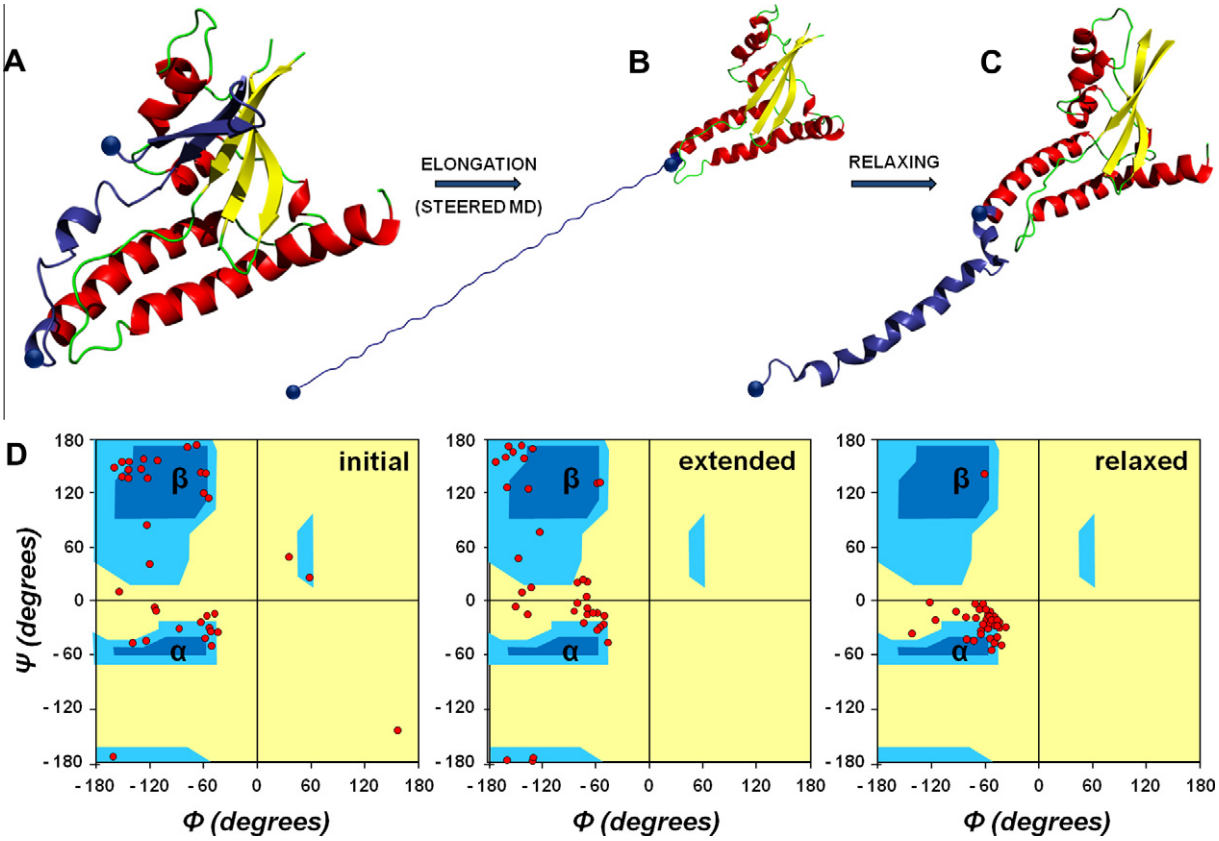

Fig. 1. Simulation of the conformational change in a single monomer. (A) Initial conformation of domain III structure of one monomer in the pre-folding state. Blue spheres indicate the position of the residues at the edge of the HRA region subjected to steered molecular dynamics process (residues 149–185). (B) Extended configuration of the same HRA region. (C) Final configuration after gradual relaxing of the extended shape; note the all-alpha refolded structure of the HRA segment. (D) Ramachandran plots corresponding to the initial (left), extended (center) and relaxed (right) states of the HRA segment represented above, during the MD simulation. Phi and psi angles vary from a beta + alpha conformation initially to an extended coil and then to all-alpha in the final plot. In the relaxed form, the only residue with phi and psi angles that correspond to a beta conformation corresponds to Pro-178. (For interpretation of the references to color in this figure legend, the reader is referred to the web version of this article.)

the changes are mainly related to accommodating the newly formed α-helix: they are less dramatic and do not involve changes in the secondary structure. In contrast to the well-known fusion event mechanism of orthomyxovirus [12], conformational change of paramyxovirus F protein is not dependent on pH [17] and unfortunately the published structures [14,15] provide no suitable clue as to the mechanism behind the event that triggers fusion. In order to understand the pathway that the HRA region follows in passing from one structure to another, we ran a series of simulations using the pre-fusion state of the F protein from parainfluenza virus 5 (PDB: 2B9B [14]) as the starting structure, analyzing the steps that allow the HRA region to convert from one structure to another, and proposing a mechanism that drives the whole structural change based only on mechanical forces.

2. Materials and methods

2.1. Protein structures

Coordinates for the pre-fusion and post-fusion states of the trimeric form of F protein were obtained from the Protein Bata Bank: PDB ID: 2B9B [14] and PDB ID: 1ZTM [15], respectively.

2.2. Steered molecular dynamics

Conformational change of F protein was simulated by steered MD procedures, using the SANDER module of the AMBER 10 package [18]. Generalized Born theory was applied to represent the solvent environment of the protein. All simulations were run taking Protein Data Bank entry 2B9B [14] as the starting structure. Disulfide bonds were assigned using the LEAP program. The steered MD process started with the adaptation of the initial structure to the AMBER force field through 5000 steps of energy minimization, using the conjugate gradient method combined with four initial steps of steepest descent in each iteration. This minimization was performed with no restrictions added to the initial structure. δt was 0.001 ps. The system was then heated over 10,000 steps of equilibration, also with δt = 0.001 ps, which raised the temperature from 0 to 300 K, while restraining the position of the Cα atoms. Finally, torsion restrictions were removed from the segment spanning residues Ala-149 to Cys-185, in order to start the MD. Three kinds of guide parameters were used to perform the steered MD: distance, angle and torsion between the Cα atoms of the residues. The values of these parameters in the simulation of one single monomer were as follows: (1) distance between Cα149 and Cα185, from 26 to 123 Å; (2) angle Cα149–Cα185–Cα47, from 24° to 156°; and (3) torsion values between axes formed by Cα149–Cα185 and Cα47–Cα204 from 28° to 4°. In all cases, the initial values corresponded to those of the pre-fusion structure 2B9B [14] and final values to those of the post-fusion structure 1ZTM [15]. Total simulation steps were 1.16×10^6. The force constant was 10 kcal mol^{-1} Å^{-2}. In this conditions, the energy added to the system in each computation step is lower than 2×10^{-6} kcal mol^{-1} To simulate the whole trimer structure, the values were similar (1.50×10^6 steps), only the respective angles for each monomer were varied to avoid atom collision during the elongation phase.

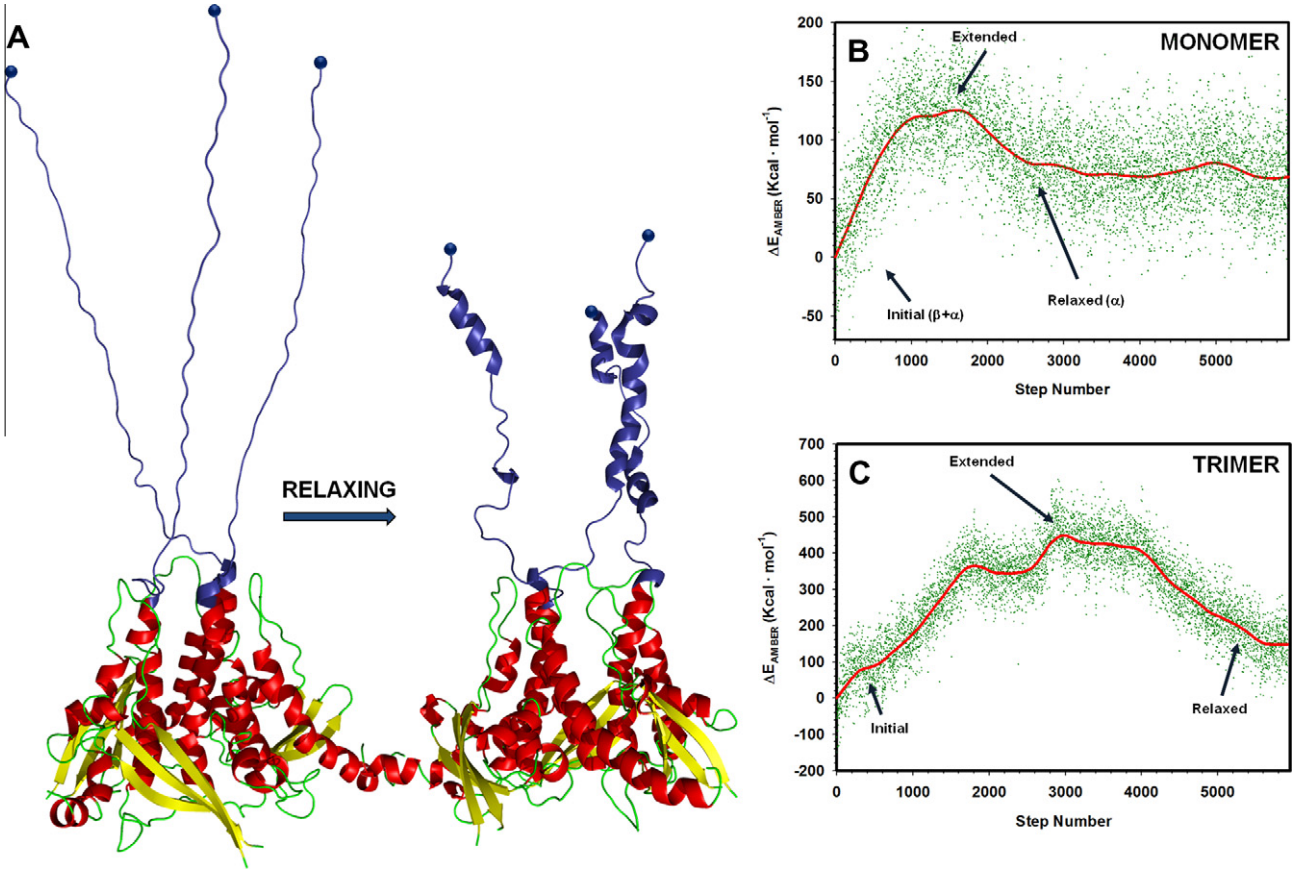

Fig. 2. Simulation of the conformational change in the trimeric domain. (A) Simulation of HRA region elongation and shortening of the trimer was performed using the same parameters as in the case of monomer simulation. (B and C) Energy variation (in kcal mol^{-1}) of the simulation system measured for one single monomer (upper panel) and the modeled trimer (lower panel). Approximate positions of the initial, extended and final relaxed states are indicated.

2.3. Coiled coil formation

To simulate the formation of the three-helix coiled coil, we performed a simple run of non-steered MD for 12 ns, using a trimerized model of the single monomer structure resulting from the steered MD procedures as the initial structure. To simulate the interaction of the three fusion peptides in the cell membrane, a force of 10 kcal mol^{-1} $Å^{-2}$ was applied during the initial steps to the distal end of each chain as a distance restriction, to avoid opening of the three helices. Distance control was removed after the first 0.2 ns of the run to allow the α-helices to interact without restrictions. Additional distance restrictions of the same value were applied to maintain the geometry between the Cα194, Cα55 and Cα206 atoms in the base of each monomer and thus to maintain the whole trimeric structure in the absence of the rest of the modeled protein.

3. Results and discussion

The behavior of the F protein trimer after the proteolytic event and subsequent binding of the three fusion peptides to the cell membrane was simulated using molecular dynamics (MD) techniques. In a first step, the individual change in the HRA region in DIII of one single monomer was simulated. Then, two alternative simulations were run taking into account the structure of DIII in the three monomers of the F protein, in order to analyze the formation of the coiled coil.

3.1. Simulation of the conformational change in a single monomer

In the first step, a simplified structure was used to explain the conformational change of HRA in a single monomer. Only DIII of PDB structure 2B9B [14] was used as the starting construct: residues 42–279 of 2B9B. A small fragment of HRA (residues 130–148, gray in Supp. Fig. 1), located immediately after the fusion peptide, was omitted from the MD simulation, as it does not undergo any conformational change during the protein fusion process and thus we were able to reduce the number of atoms in the system and reduce the computational cost of the subsequent simulation of the whole trimer (see below).

Unlike Orthomyxoviridae hemagglutinin protein, whose conformational change is caused by acidification in the endosome environment, no chemical variations, not even changes in pH [17], have been demonstrated to cause of the conformational change in paramyxovirus F protein. We hypothesized two possible triggering mechanisms. First, that the initial structure is synthesized in an unstable conformation that spontaneously changes to the pre-hairpin intermediate after the proteolytic process. In our hands, this hypothesis was initially ruled out as during unrestrained MD of DIII (and of the whole protein structure, see Supplementary Fig. S4) no substantial changes were observed, suggesting that the protein remains in a stable state, at least in the absence of external factors.

The second hypothesis is that an external force is the main cause of the structural change, driving the domain structure from the initial stable state to an unstable intermediate state (perhaps the extended intermediate state described previously [13]) and then to a subsequent stable state after the structural changes. As the fusion peptide was supposed to be included in the cell membrane, we hypothesized that, once attached, the random movement of the virus particles (in the target tissue or in the cell culture medium) would produce a putative stretching of the protein structure, and that this external mechanical force drives the structural rearrangement of DIII.

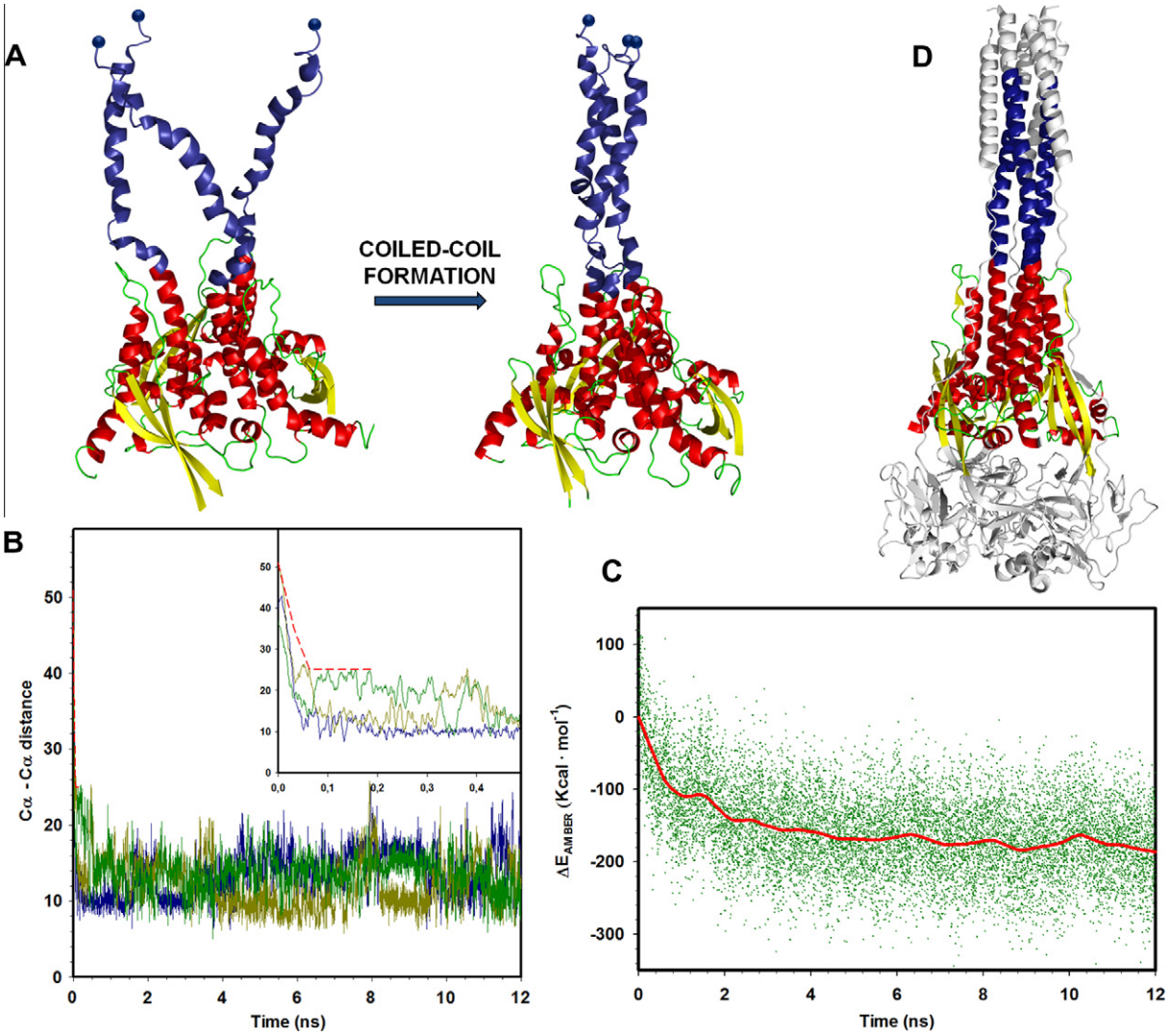

Fig. 3. Formation of the coiled coil structure. (A) Simulation of the formation of a stable coiled coil-like structure formed by the three single helical monomers of F protein after they individually refold. (B) Cα–Cα distances between the three Ala-149 residues (blue spheres) located in the N-terminal end of each monomer in the simulated trimer during coiled coil formation (simulation time: 12 ns). The dashed red line indicates the distance restrictions imposed on the system only during the first 0.2 ns of simulation to imitate the approach of F peptides inserted into the membrane. Insert: detail of the first 0.5 ns of simulation. (C) Energy variation (in kcal mol^{-1}) of the system measured during coiled coil formation. (D) Post-fusion structure of F protein from human parainfluenza virus 3 (PDB ID: 1ZTM); included for comparison with the structure obtained after molecular dynamics simulation (panel A). (For interpretation of the references to color in this figure legend, the reader is referred to the web version of this article.)

To study whether, under the conditions simulated, this latter hypothesis is plausible, the presence of a mechanical force was included in the simulation. Using steered MD, a force was applied to compel residues Ala-149 and Cys-185 to separate along their longitudinal axis (Fig. 1A and B, blue spheres). The mechanical force was only applied to these two residues because it is the region between them that experiences the greatest conformational change that differentiates the pre- and post-fusion structures (Supplementary Fig. S1, purple box). The MD parameters that steer the simulated conformational change are based on variations in distance, angle and torsion values between the Cα atoms of the Ala-47, Ala-149, Cys-185 and Thr-204 residues (see Section 2). The other residues that do not participate in the main structural change were maintained in their initial positions by imposing a restriction on the torsion values for their Cα atoms. The result of the elongation phase of the simulation, after increasing the distance between the Cα atoms of Ala-149 and Cys-185 from 26.05 to 135 Å, is shown in Fig. 1B; the initial structure of the HRA region (2 beta-strands plus 1 α-helix, PDB: 2B9B [14]) was reorganized into an extended coil. After the forced elongation phase, a subsequent step of slow relaxing (Fig. 1C) was simulated by reducing, stepwise, the distance between the Cα atoms of Ala-149 and Cys-185 from 135 to 64 Å. The most remarkable result from this phase was the spontaneous rearrangement of the extended coil into an all-α-helix structure, as observed in the crystallized post-fusion structure (1ZTM [15]). Ramachandran plots generated for the initial, elongated and final states of the HRA segment (Fig. 1D) illustrate the reorganization of the segment, where the phi and psi angles change from those of a beta-strand to those of a coil and then to an α-helix. These results indicate that, at least in one monomer, applying only a simulated mechanical force to the initial folded structure of the HRA region, this segment can completely change its beta + alpha configuration to an extended one and then, after relaxation, to an all-alpha structure, very similar to the actual post-fusion structure [15]. To analyze if the trajectory has reached an overall sufficient sampling, non-weighted covariance matrix of Cα atoms of the structure was calculated to obtain cosine content (c_i) [19] for the first principal components (Supplemental

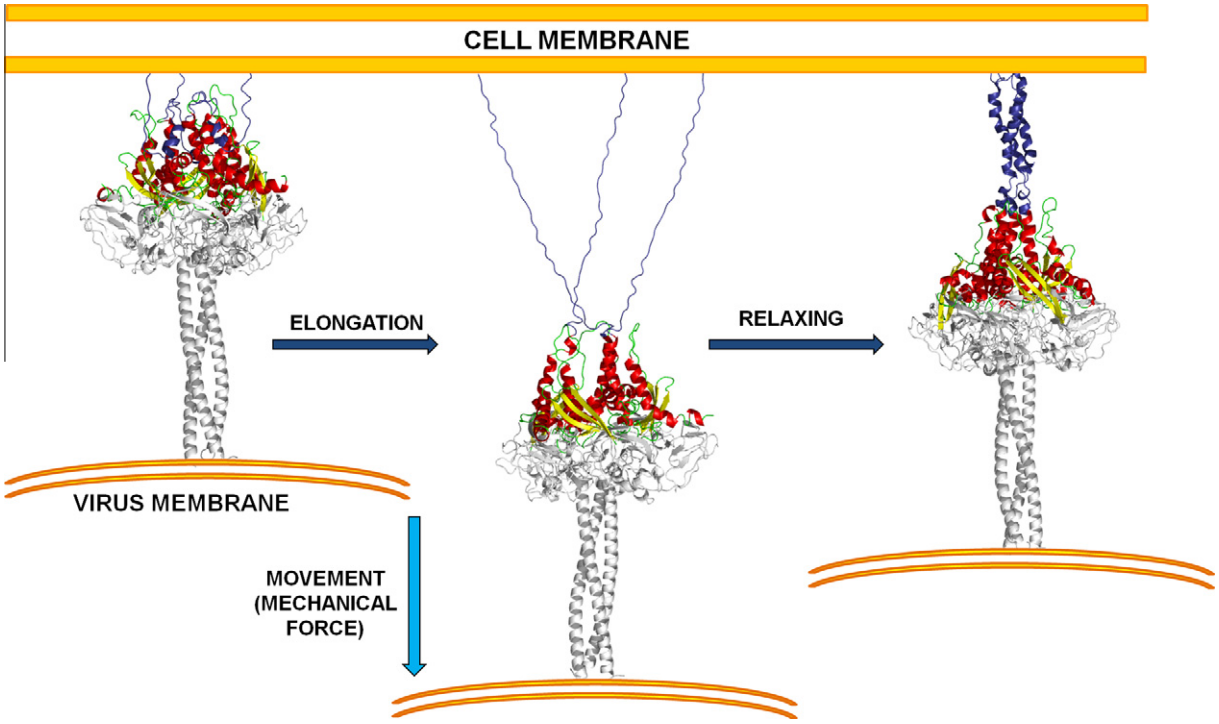

Fig. 4. Model of the initial steps of the F protein triggering event. Once the fusion peptides are inserted into the cell membrane, random virus movement will exert a mechanical force, compelling the HRA regions (in blue) of each monomer to reach an elongated state. After relaxing the mechanical force, the HRA regions will reorganize and spontaneously adopt an α-helix conformation and then a three-helix coiled coil structure, prior to rearrangement of the rest of the F protein structure (in gray). (For interpretation of the references to color in this figure legend, the reader is referred to the web version of this article.)

Table S1). This value ranges between 0 (no cosine) and 1 (perfect cosine). Values close to 1 are representative of random motion, and therefore, of insufficient sampling For our system, the c_i values indicated that the sampling of the performed conformational space is sufficient to observe a stable structural change. Detailed analysis of the steered-MD parameters is shown in Supplemental Fig. S2.

3.2. Simulation of the conformational change in the trimeric domain

Once the behavior of a single monomer had been analyzed, our next step was to analyze the performance of the native trimeric form of DIII. It is accepted, and it has previously been demonstrated for paramyxovirus using peptides that mimic regions HRA and HRB [20], that the formation of the pre-hairpin intermediate structure includes the generation of a three-helix coiled coil involving the three HRA regions before the formation of the definitive six-helix bundle, which is believed to appear only after the final membrane fusion event. In contrast, there is no evidence that indicates whether the formation of the three-HRA coiled coil occurs at the same time as or after the formation of each individual HRA α-helical structure. To analyze these two options, two different simulations were performed for the re-folding of the three HRA regions after the initial stretching step. The first approach consisted of simultaneously elongating the three peptides, in the same manner as described previously for a single monomer, and then relaxing the three extended coils at the same time, allowing them to reach equilibrium. The results, summarized in Fig. 2A, indicated that, although the three coils became rearranged into structures with a high percentage of α-helical segments, complete helical structures were not generated and that after the equilibrium at the final length was reached, there was no formation of the expected coiled coil.

Despite this, the MD procedure simulated the formation of α-helices in several continuous segments of the HRA region of the three monomers. Measurement of the variation of total energy values for the monomeric structure throughout the whole simulated trajectory (Fig. 2B) suggested the presence of an energy barrier, with a maximum in the extended conformation between the two folded states of the HRA region (pre- and post-fusion). The value of the measured energy barrier was around 180 kcal mol^{-1}. The values obtained during the MD simulation of the trimer (Fig. 2C) exhibit a very similar profile to those obtained in the simulation of the monomer. They are also self-consistent, as the values for the trimeric form are roughly threefold higher than those obtained for a single monomer. In agreement with this, the value of the energy barrier of the trimer was around 450 kcal mol^{-1}.

3.3. Coiled coil formation

Although the results of the first approach indicated the possibility of the formation of helical segments in the HRA region, the generation of stable coiled coils was not observed during the simulation. The second approach consisted of generating a trimeric form of DIII using as the starting structure the final relaxed form obtained in the simulation of the single monomer. The modeled trimer (Fig. 3A, left) was then subjected to MD. To simulate the interaction of the three fusion peptides in the cell membrane, a distance restriction was applied to the distal final end of each helical peptide (Fig. 3A, blue spheres) only during the initial steps of the MD. Continuous measurement of the distances between the Cα atoms of the three residues (Fig. 3B) indicated that after the first nanosecond (distance boundaries are indicated by a red line in Fig. 3B), the values settled into an equilibrium that was maintained without restrictions for the rest of the simulation. As expected, the measurement of the variation of energy values during the simulation process showed a continuous reduction towards a more stable level (Fig. 3C). The structure resulting from the MD (Fig. 3A, right) is consistent with a trimeric HRA coiled coil and it is remarkably

analogous (Fig. 3D) to the actual crystallized assembly of this segment in the structure of the post-fusion F protein of paramyxoviruses [15]. This result, compared to that presented in Fig. 2, suggests that, at least using MD simulation procedures, the formation of the three individual α-helices needs to be completed before the generation of the definitive coiled coil structure. Detailed analysis of the MD simulation parameters is shown in Supplemental Fig. S3. Also, as it was also measured for the monomer, the cosine content (c_i) [19] for the first principal components (Supplemental Table S1) indicated sufficient sampling of the conformational space.

In the present work, MD methods are used to devise a model of how conformational change of the HRA region of F protein is produced during the first steps of the fusion of viral and cell membranes in paramyxoviruses. The model suggests that the cause of the reorganization could be a mechanical force that elongates the HRA segment, followed by relaxation and refolding of the region into an all-alpha state. The two stable conformations are separated by an energy barrier that, in addition to the stabilization of the final coiled-coil structure, ensures the irreversibility of the process. Fig. 4 summarizes the proposed model. In the initial steps, the fusion peptide is inserted into the cell membrane. Once anchored, the stretching of the HRA region is triggered by the movement of the virus (i.e. during diffusive or drifting motions on the plasma membrane [21]) driving the conformational change to an extended coil structure. A second movement of the virus allows the HRA region to relax and to refold into three helical structures, forming the characteristic three-helix coiled coil of the pre-hairpin structure [12].

Acknowledgments

We thank Dr. Galo Ramírez for his continued scientific advice and encouragement. We are grateful to Toffa Evans for valuable assistance in the preparation of the manuscript. We thank Dr. Elena Papaleo for her constructive help in the analysis of the MD trajectories. This study was supported by: the Spanish *Ministerio de Ciencia e Innovación* through Grants SAF2007-61926, IPT2011-0964-900000 and SAF2011-13156-E; the Madrid regional authority through Grant S-BIO-0260/2006-COMBACT; and the European Commission through Grants FP7 HEALTH-F3-2009-223431 (EU Project "Divinocell") and FP7 HEALTH-2011-278603 (EU Project "Dorian"). Support from the "Fundación Ramón Areces" is acknowledged. We also thank the *Centro de Computación Científica* "CCC-UAM" for computational support. Work at Biomol-Informatics was partially financed by the European Social Fund.

Appendix A. Supplementary data

Supplementary data associated with this article can be found, in the online version, at doi:10.1016/j.bbrc.2012.02.112.

References

[1] P.L. Collins, J.E. Crowe, Respiratory syncytial virus and meta-pneumovirus, in: D.M. Knipe, P.M. Howley, D.E. Griffin, R.A. Lamb, M.A. Martin, B. Roizman, S.E. Straus (Eds.), Fields Virology, Lippincott Williams and Wilkins, Philadelphia, PA, 2007. pp. 1601–1646.
[2] R.A. Lamb, T.S. Jardetzky, Structural basis of viral invasion: lessons from paramyxovirus F, Curr. Opin. Struct. Biol. 17 (2007) 427–436.
[3] R.A. Lamb, R.G. Paterson, T.S. Jardetzky, Paramyxovirus membrane fusion: lessons from the F and HN atomic structures, Virology 344 (2006) 30–37.
[4] C.K. Navaratnarajah, N. Oezguen, L. Rupp, L. Kay, V.H. Leonard, W. Braun, R. Cattaneo, The heads of the measles virus attachment protein move to transmit the fusion-triggering signal, Nat. Struct. Mol. Biol. 18 (2011) 128–134.
[5] R.K. Plemper, M.A. Brindley, R.M. Iorio, Structural and mechanistic studies of measles virus illuminate paramyxovirus entry, PLoS Pathog. 7 (2011) e1002058.
[6] K. Tanabayashi, R.W. Compans, Functional interaction of paramyxovirus glycoproteins: identification of a domain in Sendai virus HN which promotes cell fusion, J. Virol. 70 (1996) 6112–6118.
[7] L. Gonzalez-Reyes, M.B. Ruiz-Arguello, B. Garcia-Barreno, L. Calder, J.A. Lopez, J.P. Albar, J.J. Skehel, D.C. Wiley, J.A. Melero, Cleavage of the human respiratory syncytial virus fusion protein at two distinct sites is required for activation of membrane fusion, Proc. Natl. Acad. Sci. USA 98 (2001) 9859–9864.
[8] J. Rawling, O. Cano, D. Garcin, D. Kolakofsky, J.A. Melero, Recombinant Sendai viruses expressing fusion proteins with two furin cleavage sites mimic the syncytial and receptor-independent infection properties of respiratory syncytial virus, J. Virol. 85 (2011) 2771–2780.
[9] R.M. Schowalter, S.E. Smith, R.E. Dutch, Characterization of human metapneumovirus F protein-promoted membrane fusion: critical roles for proteolytic processing and low pH, J. Virol. 80 (2006) 10931–10941.
[10] G. Zimmer, L. Budz, G. Herrler, Proteolytic activation of respiratory syncytial virus fusion protein. Cleavage at two furin consensus sequences, J. Biol. Chem. 276 (2001) 31642–31650.
[11] M.L. Bissonnette, J.E. Donald, W.F. DeGrado, T.S. Jardetzky, R.A. Lamb, Functional analysis of the transmembrane domain in paramyxovirus F protein-mediated membrane fusion, J. Mol. Biol. 386 (2009) 14–36.
[12] S.C. Harrison, Viral membrane fusion, Nat. Struct. Mol. Biol. 15 (2008) 690–698.
[13] M. Porotto, C.C. Yokoyama, G. Orefice, H.S. Kim, M. Aljofan, B.A. Mungall, A. Moscona, Kinetic dependence of paramyxovirus entry inhibition, J. Virol. 83 (2009) 6947–6951.
[14] H.S. Yin, X. Wen, R.G. Paterson, R.A. Lamb, T.S. Jardetzky, Structure of the parainfluenza virus 5 F protein in its metastable, prefusion conformation, Nature 439 (2006) 38–44.
[15] H.S. Yin, R.G. Paterson, X. Wen, R.A. Lamb, T.S. Jardetzky, Structure of the uncleaved ectodomain of the paramyxovirus (hPIV3) fusion protein, Proc. Natl. Acad. Sci. USA 102 (2005) 9288–9293.
[16] X. Zhao, M. Singh, V.N. Malashkevich, P.S. Kim, Structural characterization of the human respiratory syncytial virus fusion protein core, Proc. Natl. Acad. Sci. USA 97 (2000) 14172–14177.
[17] S. Herfst, V. Mas, L.S. Ver, R.J. Wierda, A.D. Osterhaus, R.A. Fouchier, J.A. Melero, Low-pH-induced membrane fusion mediated by human metapneumovirus F protein is a rare, strain-dependent phenomenon, J. Virol. 82 (2008) 8891–8895.
[18] D.A. Case, T.E. Cheatham 3rd, T. Darden, H. Gohlke, R. Luo, K.M. Merz Jr., A. Onufriev, C. Simmerling, B. Wang, R.J. Woods, The Amber biomolecular simulation programs, J. Comput. Chem. 26 (2005) 1668–1688.
[19] B. Hess, Convergence of sampling in protein simulations, Phys. Rev. E: Stat. Nonlin. Soft Matter Phys. 65 (2002) 031910.
[20] M. Magro, D. Andreu, P. Gomez-Puertas, J.A. Melero, C. Palomo, Neutralization of human respiratory syncytial virus infectivity by antibodies and low-molecular-weight compounds targeted against the fusion glycoprotein, J. Virol. 84 (2010) 7970–7982.
[21] C.J. Burckhardt, U.F. Greber, Virus movements on the plasma membrane support infection and transmission between cells, PLoS Pathog. 5 (2009) e1000621.

Biochemical and Biophysical Research Communications 420 (2012) 48–53

Contents lists available at SciVerse ScienceDirect

Biochemical and Biophysical Research Communications

journal homepage: www.elsevier.com/locate/ybbrc

Structural insights into the dual-targeting mechanism of Nutlin-3

Jae-Sun Shin [a], Ji-Hyang Ha [a], Fahu He [b], Yutaka Muto [b], Kyoung-Seok Ryu [c], Ho Sup Yoon [d], Sunghyun Kang [a], Sung Goo Park [a], Byoung Chul Park [a], Sang-Un Choi [e,*], Seung-Wook Chi [a,*]

[a] Medical Proteomics Research Center, KRIBB, Daejeon 305-806, Republic of Korea
[b] RIKEN Systems and Structural Biology Center, 1-7-22 Suehiro-cho, Tsurumi-ku, Yokohama 230-0045, Japan
[c] Division of Magnetic Resonance, Korea Basic Science Institute, Chungcheongbuk-Do 363-883, Republic of Korea
[d] Division of Structural Biology and Biochemistry, School of Biological Sciences, Nanyang Technological University, 60 Nanyang Drive, Singapore 637511, Singapore
[e] Research Center for Drug Discovery Technology, Division of Drug Discovery Research, Korea Research Institute of Chemical Technology, PO Box 107, Daejeon 305-600, Republic of Korea

ARTICLE INFO

Article history:
Received 15 February 2012
Available online 28 February 2012

Keywords:
Apoptosis
Multi-targeting drug
NMR
Nutlin-3
Bcl-2 family proteins

ABSTRACT

Multi-targeting therapy is an emerging strategy of drug discovery to improve therapeutic efficacy, safety and resistance profiles. In this study, we monitored the binding of a potent MDM2 inhibitor Nutlin-3 with anti-apoptotic Bcl-2 family proteins using NMR spectroscopy. Our results showed the universal binding of Nutlin-3 with diverse anti-apoptotic Bcl-2 family proteins. Taken together with the binding data for Nutlin-3 analogs, the structural model of the Bcl-X_L/Nutlin-3 complex showed that the binding mode of Nutlin-3 resembles that of the Bcl-X_L/Bcl-2 inhibitors, suggesting the molecular mechanism of transcription-independent mitochondrial apoptosis by Nutlin-3. Finally, our structural comparison provides structural insights into the dual-targeting mechanism of how Nutlin-3 can bind to two different target proteins, MDM2 and anti-apoptotic Bcl-2 family proteins in a similar manner.

1. Introduction

Multi-target-based therapy is an emerging strategy of drug development to improve therapeutic efficacy, safety and resistance profiles [1–3]. Many human diseases such as cancer arise from various factors, and thus single target-directed therapeutics show lower than desired clinical efficacies. Multi-targeting is based on the rekindled concept of "poly-pharmacology" in which one drug can bind to more than one target proteins [4]. Noteworthy examples of clinically successful multi-targeting drugs are anti-cancer multi-kinase inhibitors sorafenib, sunitnib, dasatinib and lapatinib [4,5]. Recently, targeting multiple arms of the apoptotic regulatory machinery could also provide new opportunities for apoptosis-promoting cancer therapy [6].

Nutlin-3 is one of the most potent MDM2 antagonists that serves as a competitive inhibitor of p53–MDM2 interaction [7,8]. Currently, Nutlins are being evaluated as cancer therapeutics in clinical trials. As an imidazoline-based compound, the structure of Nutlin mimics the structure of p53 transcriptional activation domain (p53TAD) peptide bound to MDM2 [9]. Initially, anti-cancer activity of Nutlin was thought to be attributed only to the inhibition of MDM2 function by blocking the p53–MDM2 interaction. However, Kojima et al. demonstrated that high levels of MDM2 do not prevent Nutlin from inducing apoptosis and that Nutlin exerts its effect not only in a transcription-dependent pathway but also a transcription-independent pathway for inducing p53-mediated apoptosis [10]. More recently, it was shown that the transcription-independent apoptotic mechanism of p53 provides an alternative pathway contributing to the Nutlin-induced apoptosis in tumor cells [11,12]. However, the detailed molecular mechanism underlying the transcription-independent mitochondrial apoptosis by Nutlin remains unclear.

In our previous studies, we showed that MDM2 and anti-apoptotic Bcl-2 family proteins share a remarkably similar mode of binding to p53TAD [13–15]. Based on this finding, we hypothesized that a p53TAD-mimetic MDM2 antagonist can directly bind to anti-apoptotic Bcl-2 family proteins in a manner analogous to that with p53TAD. Through NMR binding experiments, we provided a "proof-of-concept" evidence that the MDM2 antagonist Nutlin-3 binds to the anti-apoptotic Bcl-2 family proteins Bcl-X_L and Bcl-2 [14]. As Bcl-2 is an essential player in the apoptotic regulation, frequently overexpressed in many type of cancers, and is closely associated with the tumor progression and resistance to chemotherapeutic agents, targeting the anti-apoptotic Bcl-2 family of proteins is an attractive strategy for cancer therapy [16,17]. An inhibitor of Bcl-2 family proteins, ABT-737, was shown to induce regression of solid tumors [18]. However, ABT-737 can bind to only a few Bcl-2 family members such as Bcl-2 and Bcl-X_L, which confers resistance to apoptosis induced by ABT-737 [19,20]. Thus, neutralization of multiple anti-apoptotic Bcl-2 family proteins is required for efficient cancer therapy.

* Corresponding authors. Fax: +82 42 861 4246 (S.-U. Choi), +82 42 879 8596 (S.-W. Chi).
E-mail addresses: suchoi@krict.re.kr (S.-U. Choi), swchi@kribb.re.kr (S.-W. Chi).

0006-291X/$ - see front matter © 2012 Elsevier Inc. All rights reserved.
doi:10.1016/j.bbrc.2012.02.113

To test whether the Nutlin-3 binding is common to multiple anti-apoptotic Bcl-2 family proteins, we performed NMR-based binding assays of Nutlin-3 with other anti-apoptotic Bcl-2 family proteins (Bcl-w and Kaposi sarcoma-associated herpes virus (KSHV) Bcl-2). Our results provided direct evidence of universal interaction between Nutlin-3 and diverse anti-apoptotic Bcl-2 family proteins. Taken together with the binding assay data of Nutlin-3 analogs, the refined structural model of the Bcl-X_L/Nutlin-3 complex showed that Nutlin-3 binds to the anti-apoptotic Bcl-X_L in a manner similar to BH3-mimetic inhibitors, suggesting the molecular mechanism of transcription-independent mitochondrial apoptosis by Nutlin-3. Finally, our results will contribute to the development of a dual-target-based cancer therapies against MDM2 and anti-apoptotic Bcl-2 family proteins.

2. Materials and methods

2.1. Preparation of proteins and compounds

Truncated Bcl-X_L, Bcl-2 [21], Bcl-w (1–157) [22], and KSHV Bcl-2 (1–146, N67D/V117A) [23] were expressed and purified for NMR experiments as previously reported. Nutlin-3, Caylin-1 and Caylin-2 were purchased from Cayman Chemical Inc.

2.2. NMR spectroscopy

All the NMR data were acquired using Bruker Avance II 800 and 900 spectrometers equipped with cryogenic probe at the Korea Basic Science Institute. The 2D ^{15}N–^{1}H HSQC spectra of the anti-apoptotic Bcl-2 family proteins (Bcl-X_L, Bcl-2, Bcl-w and KSHV Bcl-2) were obtained at 25 °C in the absence or presence of Nutlin-3, Caylin-1 and Caylin-2. The NMR samples of Bcl-2 and KSHV Bcl-2 were prepared in 20 mM Tris–HCl (pH 7.8), 5 mM DTT and 90% H_2O/10% D_2O, and the NMR sample of Bcl-w was prepared in 20 mM sodium phosphate (pH 7.3), 50 mM NaCl, 0.5 mM EDTA, 3 mM DTT and 90% H_2O/10% D_2O. For the chemical shift perturbation experiments with the anti-apoptotic Bcl-2 family proteins, aliquots of concentrated Nutlin-3, Caylin-1, or Caylin-2 stock solution were added to the ^{15}N-labeled Bcl-2 family proteins during titration and ^{15}N–^{1}H HSQC spectra were collected at 25 °C for Bcl-2 or 30 °C for Bcl-w. All the NMR data were processed and analyzed using an NMRPipe/NMRDraw [24] and SPARKY [25] software.

2.3. Structure calculation

The structure of the Bcl-X_L/Nutlin-3 complex was calculated using the Crystallography and NMR system solve (CNS) within the HADDOCK 2.1 program [26]. Ambiguous interaction restraints (AIRs) were defined on the basis of the NOESY spectrum and chemical shift perturbation data. The ''active'' residues of Bcl-X_L were defined as those showing a significant exchange broadening effect and a chemical shift perturbation value with relative per-residue solvent accessibility larger than 50% for either side-chain or main-chain atoms. All the surrounding surface residues near the active residues were defined as ''passive'' residues. The parameter and topology files for Nutlin-3 were prepared using PRODRG [27]. Starting from the structure of the Bcl-X_L [21], 1000 rigid-body docking solutions were obtained. The best 200 structures were chosen for semi-flexible refinement and finally refined in explicit water. The clustering was performed using a 3 Å cut-off, and the complex models were selected for visualization by root mean square deviation from the best energy structure and HADDOCK energy score. Figures of the complex model were drawn using the PyMOL software package [28].

3. Results and discussion

3.1. The MDM2 antagonist Nutlin-3 binds to diverse anti-apoptotic Bcl-2 family proteins

Based on close mimicry between MDM2 and Bcl-2 family proteins in p53TAD recognition, we previously demonstrated that the MDM2 antagonist Nutlin-3 binds to anti-apoptotic Bcl-X_L and Bcl-2 [14]. Is the Nutlin-3 binding specific to Bcl-X_L and Bcl-2 or common to multiple anti-apoptotic Bcl-2 family proteins with conserved three-dimensional structural folds? To address this question, we monitored the binding of Nutlin-3 to Bcl-w and KSHV Bcl-2 by using NMR spectroscopy. Fig. 1A shows the overlaid ^{15}N–^{1}H HSQC spectra of anti-apoptotic Bcl-2 family proteins in the absence or presence of Nutlin-3. During the binding titration, we found that significant line-broadening and chemical shift changes of several ^{15}N–^{1}H crosspeaks in Bcl-w and KSHV Bcl-2 occurred upon the addition of Nutlin-3 [29], indicating the direct interaction of Nutlin-3 with both the anti-apoptotic Bcl-2 family proteins. Moreover, the NMR chemical shift perturbation induced by binding to Nutlin-3 was localized to a long hydrophobic groove surrounded by the Bcl-2 homology (BH) 1, BH2 and BH3 domains of Bcl-w and KSHV Bcl-2, which are in good agreement with those observed during the binding of Nutlin-3 to Bcl-X_L and Bcl-2 (Fig. 1B). Collectively, these results indicate that Nutlin-3 is universally involved in specific binding to diverse anti-apoptotic Bcl-2 family proteins and its binding site is highly conserved. Thus, Nutlin-3 may inhibit multiple anti-apoptotic Bcl-2 family proteins at the same time, which may be useful for developing apoptosis-promoting strategies in cancer therapy.

3.2. Structural basis of the interaction between Bcl-X_L and Nutlin-3

To shed light on the molecular mechanism of transcription-independent mitochondrial apoptosis of Nutlin-3, we calculated a refined structural model for the complex between Nutlin-3 and Bcl-X_L using HADDOCK 2.1 program [15]. Ambiguous interaction restraints (AIRs) for Bcl-X_L were derived from NOESY-based interaction restraints and NMR chemical shift perturbation. The ensemble of the six most energetically favorable structures showed a root mean square deviation of 0.44 ± 0.22 Å (Supplementary Table S1). As shown in Fig. 2A, Nutlin-3 binds to the central hydrophobic cleft of Bcl-X_L, which is essentially the same site that is occupied by the BH3 peptides of pro-apoptotic Bcl-2 family proteins Bak, Bad and Bim. Within the binding pocket, Nutlin-3 is surrounded by the hydrophobic side chains of Phe97, Tyr101, Phe105, Leu108, Leu112, Val126, Val127 and Leu130 of Bcl-X_L (Fig. 2A). The overall binding mode of Nutlin-3 is reminiscent of the complex between pro-apoptotic Bim BH3 peptide and Bcl-X_L, where the interaction of Bim BH3 peptide with anti-apoptotic Bcl-X_L/Bcl-2 is mainly mediated through the hydrophobic interactions of the BH3 peptide side-chains (i, i + 4, i + 7 and i + 11) in four discrete sub-binding sites within the binding groove [30].

3.3. Nutlin-3 analogs show differential binding patterns to anti-apoptotic Bcl-X_L

To validate our structural model of the Bcl-X_L/Nutlin-3 complex, we conducted NMR-binding experiments for Bcl-X_L with Nutlin-3 analogs, Caylin-1 and Caylin-2. The chemical structures of the Caylins are identical to that of the Nutlin-3, except that Caylin-1 contains additional chlorine groups (di-chlorophenyl rings), and Caylin-2 has trifluoromethyl groups instead of chlorine groups on the two phenyl ring moieties. Although more Bcl-X_L crosspeaks disappeared on Caylin-1 binding because of exchange broadening,

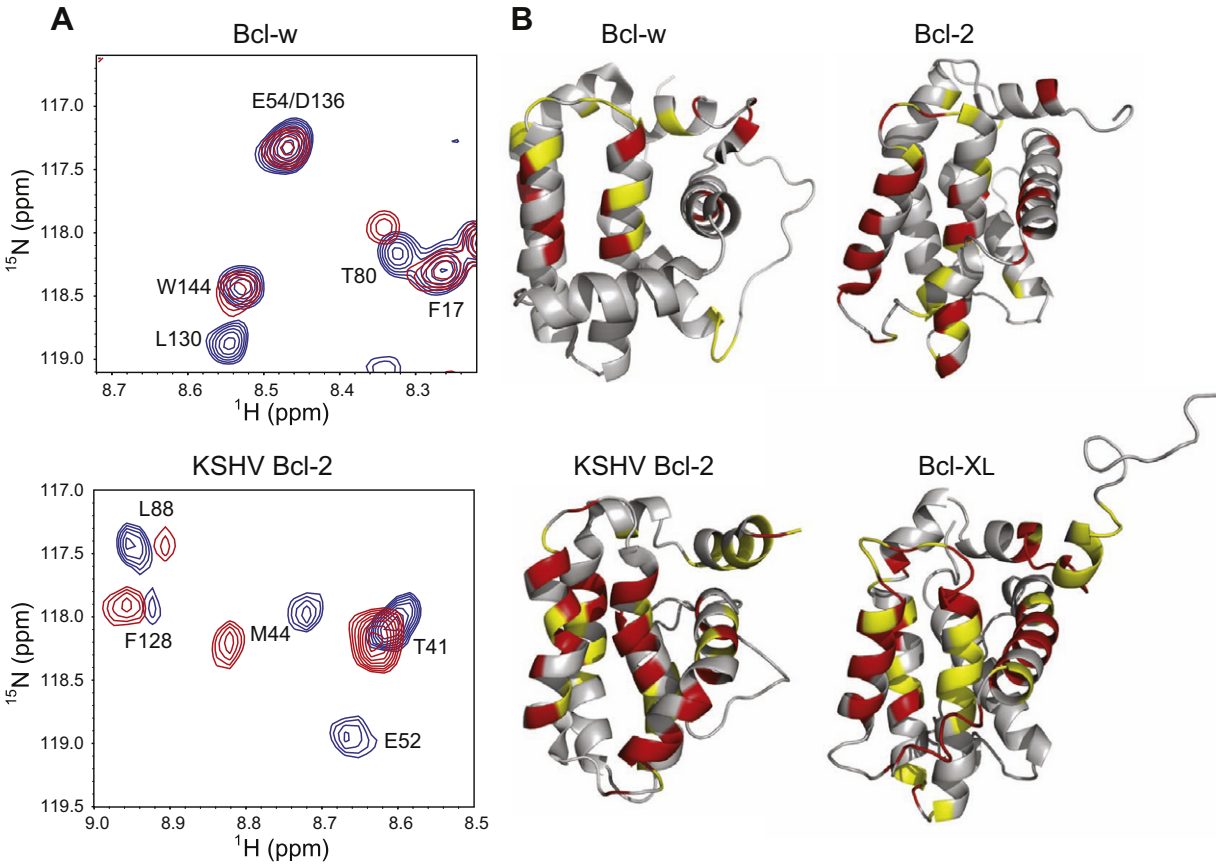

Fig. 1. Binding of Nutlin-3 to anti-apoptotic Bcl-2 family proteins. (A) The overlaid 2D ^{1}H–^{15}N HSQC spectra for ^{15}N-labeled Bcl-w and KSHV Bcl-2 in the absence (blue) or presence of Nutlin-3 (red). (B) Nutlin-3-binding site mapping on the structure of the anti-apoptotic Bcl-2 family proteins. The residues showing chemical shift changes of $\Delta CS > 0.08$ ppm and the disappeared residues are colored in red. The residues showing the chemical shift changes of 0.03 ppm $< \Delta CS < 0.08$ ppm are colored in yellow. The binding site mapping on the structures of Bcl-2 and Bcl-X_L is based on the previously observed chemical shift perturbations [14]. (For interpretation of the references to color in this figure legend, the reader is referred to the web version of this article.)

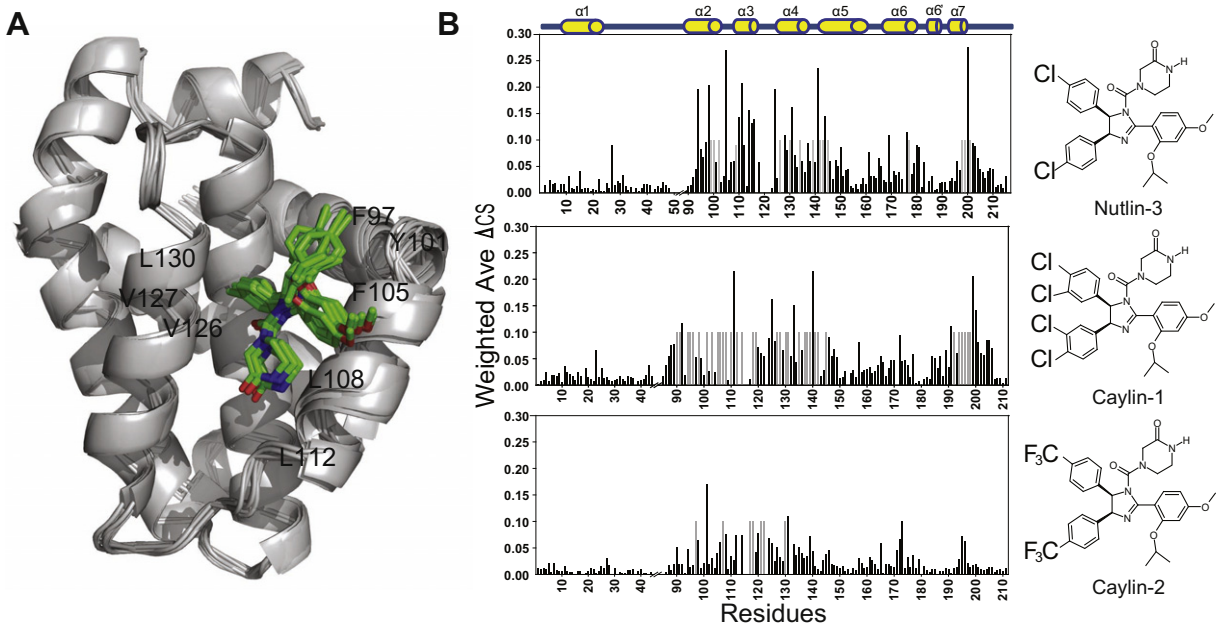

Fig. 2. Structural model of the Bcl-X_L/Nutlin-3 complex. (A) The overlay of the six best-energy structural models of the complex. Hydrophobic Bcl-X_L residues within the Nutlin-3 binding site are labeled and Nutlin-3 is colored in green. (B) Chemical shift perturbations of the Bcl-X_L residues upon binding to Nutlin-3 and its analogs Caylin-1 and Caylin-2. Resonances that disappeared on binding are shown as gray bars. The chemical formula of each inhibitor is displayed beside the box. (For interpretation of the references to color in this figure legend, the reader is referred to the web version of this article.)

the chemical shift perturbations in Bcl-X_L induced by Nutlin-3 and Caylin-1 were almost the same (Fig. 2B), indicating that they share the same binding sites in Bcl-X_L. In addition, the structural model of the Bcl-X_L/Caylin-1 complex showed that Caylin-1 binds to Bcl-X_L in a manner analogous to that observed with Nutlin-3 (Supplementary Fig. S1). It seems that the additional chlorine groups in Caylin-1 do not interfere with binding to Bcl-X_L, because the hydrophobic binding groove of Bcl-X_L is large enough to accommodate the di-chlorophenyl ring moiety of Caylin-1. However, the substitution of chlorine groups with trifluoromethyl groups in Caylin-2 substantially diminished the chemical shift perturbations seen in the presence of Nutlin-3 (Fig. 2B), suggesting that the bulky charged trifluoromethyl group of Caylin-2 would collide with the hydrophobic groove of Bcl-X_L. Consistent with the structural model, the NMR-binding data for the Nutlin-3 analogs showed that the chlorophenyl ring moiety of Nutlin-3 is a key binding determinant for Bcl-X_L, which is in good agreement with what was observed in the binding of Nutlin-2 with MDM2 [8].

3.4. Structural comparison of the Bcl-X_L/small molecule antagonist complexes

A comparison between the structure of the Bcl-X_L/Nutlin-3 complex and the structures of Bcl-X_L complexes with Bcl-2/Bcl-X_L small molecule inhibitors ABT-737 [18] and tetrahydroisoquinoline amide substituted phenyl pyrazole (THIQ-PP) [31] showed that Nutlin-3 binds to Bcl-X_L in a similar fashion to what was observed in the binding of the BH3-mimetic inhibitors (Fig. 3). Like BH3-mimetic inhibitors, Nutlin-3 can compete with the pro-apoptotic BH3 peptides to occupy the same binding site, because the bound Nutlin-3 would undergo steric overlap with the pro-apoptotic BH3 peptides. This may explain how Nutlin-3 could inhibit the function of anti-apoptotic Bcl-2 family proteins, inducing mitochondrial apoptosis in cancer cells independent of the transcriptional activity of p53 or of MDM2 status. Based on our results, we speculate that, at the mitochondria, Nutlin-3 directly targets multiple anti-apoptotic Bcl-2 family proteins, sequestering pro-apoptotic Bak/Bax from the complexes and finally inducing mitochondrial apoptosis in a transcription-independent fashion Although the binding of Nutlin-3 to Bcl-X_L occurs at the same binding sites for ABT-737 and THIQ-PP, there was a noticeable difference in the occupied sub-binding site, depending on the small molecule antagonist. The pro-apoptotic BH3 peptide-binding groove of Bcl-X_L comprises four discrete sub-binding sites (i, i + 4, i + 7 and i + 11 sites), which are filled up by the side-chains of the pro-apoptotic BH3 peptide [30]. ABT-737 occupies three of the four sub-binding sites (namely, i + 4, i + 7 and i + 11 sites), whereas both Nutlin-3 and THIQ-PP occupy two (i and i + 4 sites; Fig. 3).

3.5. Structural basis for the dual-targeting mechanism of Nutlin-3

Our structural model of the Bcl-X_L/Nutlin-3 complex can provide structural insights into the dual-targeting mechanism of how Nutlin-3 can target two different proteins MDM2 and Bcl-X_L. It should be noted that MDM2 and Bcl-X_L adopt quite different global folds, although their hydrophobic binding grooves are similar. Interestingly, our structural comparison between the Bcl-X_L/Nutlin-3 complex and the MDM2/Nutlin-2 complex revealed a remarkably close mimicry between MDM2 and Bcl-X_L in the binding mode of Nutlin (Fig. 4). First, the imidazoline scaffold of Nutlin-3 mimics the helical backbones of both the pro-apoptotic Bim BH3 and p53TAD(15–29) peptides [8,30]. Second, the ring moieties of Nutlin-3 enter the sub-binding sites occupied by the bulky hydrophobic side-chains of MDM2 and Bcl-X_L. In particular, one of the chlorophenyl rings of Nutlin-3 fits deeply into the hydrophobic grooves of both MDM2 and Bcl-X_L, making the largest contribution to forming the complexes. However, there is a subtle difference in the number of sub-binding sites occupied. Nutlin-3 binds to two sub-binding sites occupied by the hydrophobic side-chains of Ile90 and Leu94 (i and i + 4) in Bim (Fig. 4A). On the other hand, Nutlin-2 interacts with three sub-binding sites occupied by the hydrophobic side-chains of Phe19, Trp23 and Leu26 (i, i + 4 and i + 7) in p53TAD (Fig. 4B) [8,30]. Overall, the mode of Nutlin-3 binding to Bcl-X_L is quite similar to that observed in the binding of Nutlin-2 to MDM2.

MDM2 and anti-apoptotic Bcl-2 family proteins are well-known and promising anti-cancer targets that are associated with apoptosis signaling in different cellular compartments [32]. The Bcl-2/Bcl-X_L inhibitor ABT-737 predominantly induces apoptosis in G_1 cells, while the MDM2 inhibitor Nutlin-3 induces p53-mediated apoptosis mainly in S and G_2/M cells. Simultaneous inhibition of MDM2 and Bcl-2 results in apoptosis in a notably synergistic manner in acute myeloid leukemia (AML) [33]. In addition, sensitivity to apoptosis in cells with high MDM2 levels is enhanced by combined treatment with Nutlin-3 and ABT-737 to activate the pro-apoptotic Bcl-2 family protein Bax [34]. Thus, to inhibit MDM2 and anti-apoptotic Bcl-2 family proteins at the same time might provide an effective dual-target-based strategy to induce apoptosis in cancer cells. Taken together with the previous finding that the Bcl-2 family inhibitor BH3I potently inhibits the p53–MDM2 interaction [35], our results suggest the possibility to design a dual-targeting anti-cancer agent that can induce simultaneous inhibition of MDM2 and anti-apoptotic Bcl-2 family proteins. Our structural informa-

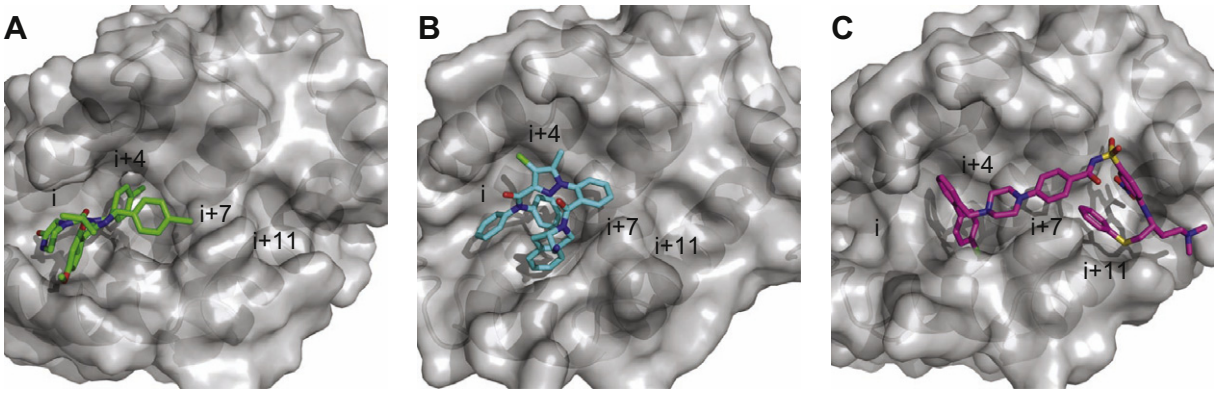

Fig. 3. Structural comparison between the Bcl-X_L/Nutlin-3 complex and BH3 mimetic inhibitor complexes. Structures of the Bcl-X_L/Nutlin-3 complex (A), Bcl-X_L/THIQ-PP complex (PDB code: 2W3L) (B) and Bcl-X_L/ABT-737 complex (PDB code: 2YXJ) (C) are compared. The pro-apoptotic BH3 binding sub-sites (i, i + 4, i + 7 and i + 11) are labeled on the molecular surface of Bcl-X_L.

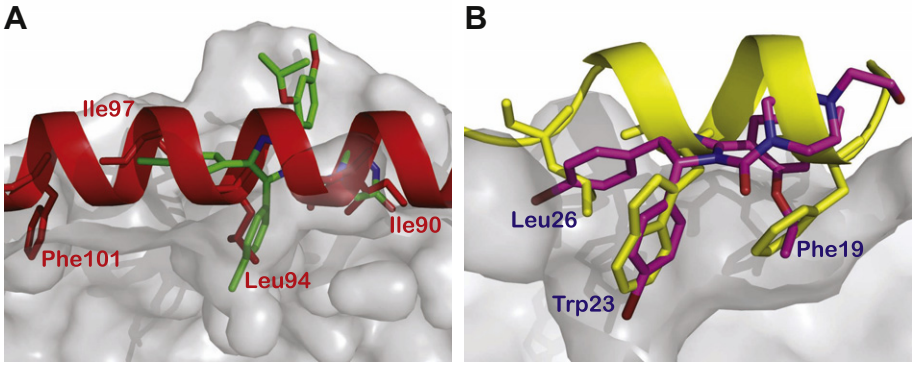

Fig. 4. Mimicry between Bcl-X_L and MDM2 in the binding of Nutlin. (A) The overlay of Nutlin-3 and Bim BH3 peptide (PDB code: 3FDL) on the surface of the Bcl-X_L structure. Nutlin-3 and Bim BH3 peptide are colored in green and red, respectively. (B) The overlay of Nutlin-2 (PDB code: 1RV1) and p53TAD(15–29) peptide (PDB code: 1YCR) on the surface of the MDM2 structure. Nutlin-2 and p53TAD peptide are colored in magenta and yellow, respectively. (For interpretation of the references to color in this figure legend, the reader is referred to the web version of this article.)

tion will be helpful for the design and further optimization of dual-targeting anti-cancer therapeutics.

In conclusion, we showed the universal interactions of a potent MDM2 inhibitor Nutlin-3 with multiple anti-apoptotic Bcl-2 family proteins, which may be important for transcription-independent apoptosis of Nutlin-3 and its application to cancer therapy. Interestingly, our structural studies provided structural insights into the dual-targeting mechanism of how Nutlin-3 can bind to two different target proteins, MDM2 and anti-apoptotic Bcl-2 family proteins in a similar manner, which might have important implications in multi-target based cancer therapy.

Acknowledgments

We sincerely thank Prof. Byong-Seok Choi for providing NMR machine time. This work was supported by a grant of the Korean Health Technology R&D Project, Ministry for Health and Welfare, Republic of Korea (A100089).

Appendix A. Supplementary data

Supplementary data associated with this article can be found, in the online version, at doi:10.1016/j.bbrc.2012.02.113.

References

[1] X.H. Ma, Z. Shi, C. Tan, Y. Jiang, M.L. Go, B.C. Low, Y.Z. Chen, In-silico approaches to multi-target drug discovery: computer aided multi-target drug design, multi-target virtual screening, Pharm Res 27 (2010) 739–749.
[2] A.L. Hopkins, J.S. Mason, J.P. Overington, Can we rationally design promiscuous drugs? Curr Opin Struct Biol 16 (2006) 127–136.
[3] J.P. Overington, B. Al-Lazikani, A.L. Hopkins, How many drug targets are there?, Nat Rev Drug Discovery 5 (2006) 993–996
[4] A.L. Hopkins, Network pharmacology: the next paradigm in drug discovery, Nat Chem Biol 4 (2008) 682–690.
[5] Y. Dai, S. Grant, Targeting multiple arms of the apoptotic regulatory machinery, Cancer Res 67 (2007) 2908–2911.
[6] Z. Shi, X.H. Ma, C. Qin, J. Jia, Y.Y. Jiang, C.Y. Tan, Y.Z. Chen, Combinatorial support vector machines approach for virtual screening of selective multi-target serotonin reuptake inhibitors from large compound libraries, J Mol Graph Model (2011).
[7] S.W. Fesik, Promoting apoptosis as a strategy for cancer drug discovery, Nat Rev Cancer 5 (2005) 876–885.
[8] L.T. Vassilev, B.T. Vu, B. Graves, D. Carvajal, F. Podlaski, Z. Filipovic, N. Kong, U. Kammlott, C. Lukacs, C. Klein, N. Fotouhi, E.A. Liu, In vivo activation of the p53 pathway by small-molecule antagonists of MDM2, Science 303 (2004) 844–848.
[9] P.H. Kussie, S. Gorina, V. Marechal, B. Elenbaas, J. Moreau, A.J. Levine, N.P. Pavletich, Structure of the MDM2 oncoprotein bound to the p53 tumor suppressor transactivation domain, Science 274 (1996) 948–953.
[10] K. Kojima, M. Konopleva, T. McQueen, S. O'Brien, W. Plunkett, M. Andreeff, Mdm2 inhibitor Nutlin-3a induces p53-mediated apoptosis by transcription-dependent and transcription-independent mechanisms and may overcome Atm-mediated resistance to fludarabine in chronic lymphocytic leukemia, Blood 108 (2006) 993–1000.
[11] A.V. Vaseva, N.D. Marchenko, U.M. Moll, The transcription-independent mitochondrial p53 program is a major contributor to Nutlin-induced apoptosis in tumor cells, Cell Cycle 8 (2009) 1711–1719.
[12] M.N. Saha, H. Jiang, H. Chang, Molecular mechanisms of Nutlin-induced apoptosis in multiple myeloma: evidence for p53-transcription-dependent and -independent pathways, Cancer Biol Ther 10 (2010) 567–578.
[13] N. Bharatham, S.W. Chi, H.S. Yoon, Molecular basis of Bcl-X(L)–p53 interaction: insights from molecular dynamics simulations, PLoS One 6 (2011) e26014.
[14] J.H. Ha, E.Y. Won, J.S. Shin, M. Jang, K.S. Ryu, K.H. Bae, S.G. Park, B.C. Park, H.S. Yoon, S.W. Chi, Molecular mimicry-based repositioning of Nutlin-3 to anti-apoptotic Bcl-2 family proteins, J Am Chem Soc 133 (2011) 1244–1247.
[15] H. Xu, H. Ye, N.E. Osman, K. Sadler, E.Y. Won, S.W. Chi, H.S. Yoon, The MDM2-binding region in the transactivation domain of p53 also acts as a Bcl-X(L)-binding motif, Biochemistry 48 (2009) 12159–12168.
[16] M.H. Kang, C.P. Reynolds, Bcl-2 inhibitors: targeting mitochondrial apoptotic pathways in cancer therapy, Clin Cancer Res 15 (2009) 1126–1132.
[17] G. Lessene, P.E. Czabotar, P.M. Colman, BCL-2 family antagonists for cancer therapy, Nat Rev Drug Discovery 7 (2008) 989–1000.
[18] T. Oltersdorf, S.W. Elmore, A.R. Shoemaker, R.C. Armstrong, D.J. Augeri, B.A. Belli, M. Bruncko, T.L. Deckwerth, J. Dinges, P.J. Hajduk, M.K. Joseph, S. Kitada, S.J. Korsmeyer, A.R. Kunzer, A. Letai, C. Li, M.J. Mitten, D.G. Nettesheim, S. Ng, P.M. Nimmer, J.M. O'Connor, A. Oleksijew, A.M. Petros, J.C. Reed, W. Shen, S.K. Tahir, C.B. Thompson, K.J. Tomaselli, B. Wang, M.D. Wendt, H. Zhang, S.W. Fesik, S.H. Rosenberg, An inhibitor of Bcl-2 family proteins induces regression of solid tumours, Nature 435 (2005) 677–681.
[19] M. Konopleva, R. Contractor, T. Tsao, I. Samudio, P.P. Ruvolo, S. Kitada, X. Deng, D. Zhai, Y.X. Shi, T. Sneed, M. Verhaegen, M. Soengas, V.R. Ruvolo, T. McQueen, W.D. Schober, J.C. Watt, T. Jiffar, X. Ling, F.C. Marini, D. Harris, M. Dietrich, Z. Estrov, J. McCubrey, W.S. May, J.C. Reed, M. Andreeff, Mechanisms of apoptosis sensitivity and resistance to the BH3 mimetic ABT-737 in acute myeloid leukemia, Cancer Cell 10 (2006) 375–388.
[20] M.F. van Delft, A.H. Wei, K.D. Mason, C.J. Vandenberg, L. Chen, P.E. Czabotar, S.N. Willis, C.L. Scott, C.L. Day, S. Cory, J.M. Adams, A.W. Roberts, D.C. Huang, The BH3 mimetic ABT-737 targets selective Bcl-2 proteins and efficiently induces apoptosis via Bak/Bax if Mcl-1 is neutralized, Cancer Cell 10 (2006) 389–399.
[21] A.M. Petros, A. Medek, D.G. Nettesheim, D.H. Kim, H.S. Yoon, K. Swift, E.D. Matayoshi, T. Oltersdorf, S.W. Fesik, Solution structure of the antiapoptotic protein Bcl-2, Proc Natl Acad Sci USA 98 (2001) 3012–3017.
[22] A.Y. Denisov, M.S. Madiraju, G. Chen, A. Khadir, P. Beauparlant, G. Attardo, G.C. Shore, K. Gehring, Solution structure of human Bcl-w: modulation of ligand binding by the C-terminal helix, J Biol Chem 278 (2003) 21124–21128.
[23] Q. Huang, A.M. Petros, H.W. Virgin, S.W. Fesik, E.T. Olejniczak, Solution structure of a Bcl-2 homolog from Kaposi sarcoma virus, Proc Natl Acad Sci U S A 99 (2002) 3428–3433.
[24] F. Delaglio, S. Grzesiek, G.W. Vuister, G. Zhu, J. Pfeifer, A. Bax, NMRPipe: a multidimensional spectral processing system based on UNIX pipes, J Biomol NMR 6 (1995) 277–293.
[25] T.D., Goddard, D.G. Kneller, SPARKY 3, University of California, San Francisco.
[26] C. Dominguez, R. Boelens, A.M. Bonvin, HADDOCK: a protein–protein docking approach based on biochemical or biophysical information, J Am Chem Soc 125 (2003) 1731–1737.
[27] A.W. Schuttelkopf, D.M. van Aalten, PRODRG: a tool for high-throughput crystallography of protein–ligand complexes, Acta Crystallogr D Biol Crystallogr 60 (2004) 1355–1363.
[28] W.L. DeLano, The PyMOL Molecular Graphics System, PyMOL, DeLano Scientific, 2002.

[29] J. Ha, E. Won, H. Yoon, S. Kang, K. Bae, S. Park, B. Park, B. Choi, J. Lee, S. Chi, Molecular interaction between a Bcl-2 homolog from Kaposi sarcoma virus and p53, Notes 30 (2009) 1655.
[30] E.F. Lee, J.D. Sadowsky, B.J. Smith, P.E. Czabotar, K.J. Peterson-Kaufman, P.M. Colman, S.H. Gellman, W.D. Fairlie, High-resolution structural characterization of a helical alpha/beta-peptide foldamer bound to the anti-apoptotic protein Bcl-X_L, Angew Chem Int Ed Engl 48 (2009) 4318–4322.
[31] J. Porter, A. Payne, B. de Candole, D. Ford, B. Hutchinson, G. Trevitt, J. Turner, C. Edwards, C. Watkins, I. Whitcombe, J. Davis, C. Stubberfield, Tetrahydroisoquinoline amide substituted phenyl pyrazoles as selective Bcl-2 inhibitors, Bioorg Med Chem Lett 19 (2009) 230–233.
[32] L.T. Vassilev, MDM2 inhibitors for cancer therapy, Trends Mol Med 13 (2007) 23–31.
[33] K. Kojima, M. Konopleva, I.J. Samudio, W.D. Schober, W.G. Bornmann, M. Andreeff, Concomitant inhibition of MDM2 and Bcl-2 protein function synergistically induce mitochondrial apoptosis in AML, Cell Cycle 5 (2006) 2778–2786.
[34] M. Wade, L.W. Rodewald, J.M. Espinosa, G.M. Wahl, BH3 activation blocks Hdmx suppression of apoptosis and cooperates with Nutlin to induce cell death, Cell Cycle 7 (2008) 1973–1982.
[35] J.R. Porter, M.R. Helmers, P. Wang, J.L. Furman, S.T. Joy, P.S. Arora, I. Ghosh, Profiling small molecule inhibitors against helix–receptor interactions: the Bcl-2 family inhibitor BH3I-1 potently inhibits p53/hDM2, Chem Commun (Camb) 46 (2010) 8020–8022.

Biochemical and Biophysical Research Communications 420 (2012) 54–60

Contents lists available at SciVerse ScienceDirect

Biochemical and Biophysical Research Communications

journal homepage: www.elsevier.com/locate/ybbrc

Protein tyrosine nitration of mitochondrial carbamoyl phosphate synthetase 1 and its functional consequences ☆

Hideo Takakusa [a,d,*], Isaac Mohar [b], Terrance J. Kavanagh [b], Edward J. Kelly [c], Rüdiger Kaspera [a], Sidney D. Nelson [a]

[a] Department of Medicinal Chemistry, University of Washington, Seattle, WA 98195, USA
[b] Department of Environmental and Occupational Health Sciences, University of Washington, Seattle, WA 98195, USA
[c] Department of Pharmaceutics, University of Washington, Seattle, WA 98195, USA
[d] Drug Metabolism and Pharmacokinetics Research Laboratories, Daiichi Sankyo Co. Ltd., Tokyo 140-8710, Japan

ARTICLE INFO

Article history:
Received 2 February 2012
Available online 28 February 2012

Keywords:
Protein tyrosine nitration
Carbamoyl phosphate synthetase 1
Peroxynitrite
LC–ESI–MS/MS
Homology modeling
Mitochondria

ABSTRACT

Mitochondria are the primary locus for the generation of reactive nitrogen species including peroxynitrite and subsequent protein tyrosine nitration. Protein tyrosine nitration may have important functional and biological consequences such as alteration of enzyme catalytic activity. In the present study, mouse liver mitochondria were incubated with peroxynitrite, and the mitochondrial proteins were separated by 1D and 2D gel electrophoresis. Nitrotyrosinylated proteins were detected with an anti-nitrotyrosine antibody. One of the major proteins nitrated by peroxynitrite was carbamoyl phosphate synthetase 1 (CPS1) as identified by LC–MS protein analysis and Western blotting. The band intensity of nitration normalized to CPS1 was increased in a peroxynitrite concentration-dependent manner. In addition, CPS1 activity was decreased by treatment with peroxynitrite in a peroxynitrite concentration- and time-dependent manner. The decreased CPS1 activity was not recovered by treatment with reduced glutathione, suggesting that the decrease of the CPS1 activity is due to tyrosine nitration rather than cysteine oxidation. LC–MS analysis of in-gel digested samples, and a Popitam-based modification search located 5 out of 36 tyrosine residues in CPS1 that were nitrated. Taken together with previous findings regarding CPS1 structure and function, homology modeling of mouse CPS1 suggested that nitration at Y1450 in an α-helix of allosteric domain prevents activation of CPS1 by its activator, *N*-acetyl-L-glutamate. In conclusion, this study demonstrated the tyrosine nitration of CPS1 by peroxynitrite and its functional consequence. Since CPS1 is responsible for ammonia removal in the urea cycle, nitration of CPS1 with attenuated function might be involved in some diseases and drug-induced toxicities associated with mitochondrial dysfunction.

1. Introduction

Protein tyrosine nitration is a post-translational modification which occurs in the presence of reactive nitrogen species [1]. One of the reactive nitrogen species is peroxynitrite ($ONOO^-$) which is formed by the reaction of a superoxide radical anion (O_2^-) with nitric oxide (NO) [2]. Tyrosine nitration can alter protein structure due to a shift in pKa from 10.1 to 7.2 of the tyrosine hydroxyl group, as well as the addition of bulkiness to the tyrosine residue [3]. The structural changes may have important functional and biological consequences such as alteration of enzyme catalytic activity, modulation of the tyrosine phosphorylation cascade and induction of immune responses [1]. Peroxynitrite can be formed intramitochondrially through the generation of reactive oxygen species by complexes I–III of the mitochondrial respiratory chain [4]. Due to the rather short-lived nature of these reactive species, it is conceivable that mitochondrial proteins are the primary targets of protein tyrosine nitration. One of the best-studied examples is nitration and inactivation of manganese superoxide dismutase (MnSOD) [5]. A normal function of MnSOD is to decrease peroxynitrite formation by dismutating superoxide to hydrogen peroxide and molecular oxygen. However, recent studies have shown that MnSOD can be inactivated by tyrosine nitration, resulting in increased peroxynitrite formation and further oxidative/nitrative stress. Decreases in MnSOD activity due to nitrative stress in mitochondria has been observed in animal models of renal

Abbreviations: CPS1, carbamoyl phosphate synthetase 1; MnSOD, manganese superoxide dismutase; NAG, *N*-acetyl-L-glutamate; GSH, glutathione.

☆ This work was performed while H.T. was a visiting scholar at the University of Washington.

* Corresponding author at: Drug Metabolism and Pharmacokinetics Research Laboratories, Daiichi Sankyo Co. Ltd., 1-2-58, Hiromachi, Shinagawa-ku, Tokyo 140-8710, Japan. Fax: +81 3 5436 8567.
E-mail address: takakusa.hideo.yb@daiichisankyo.co.jp (H. Takakusa).

0006-291X/$ - see front matter © 2012 Elsevier Inc. All rights reserved.
http://dx.doi.org/10.1016/j.bbrc.2012.02.114

ischemia/reperfusion [6] and in drug-induced liver injury caused by toxic doses of acetaminophen [7].

Protein tyrosine nitration demonstrates a degree of selectivity for proteins and specific tyrosine residues within those proteins [8,9]. There is no specific or preferred consensus sequence that promotes tyrosine nitration, however, the protein secondary structure and local environment of the tyrosine residues seem to be important for reactivity and accessibility of reactive nitrogen species to the tyrosine residue [8,9]. Therefore, the identification of tyrosine nitrated proteins and the sites of nitrated tyrosine residues is key to understanding the link between protein tyrosine nitration and its biological consequences.

In the present study, we have examined tyrosine nitration of mouse liver mitochondrial proteins after treatment with peroxynitrite followed by 1D and 2D SDS gel electrophoresis, Western blot analysis using an anti-nitrotyrosine antibody, and LC–MS/MS analysis of in-gel tryptic digests of the nitrated protein samples. Several algorithms such as Sequest and Popitam were utilized to identify proteins and search post-translational modifications, including tyrosine nitration, based on tandem mass spectrometry data (MS/MS spectra) and peptide sequence databases [10]. On the basis of our initial findings, we focused on the tyrosine nitration of carbamoyl phosphate synthetase 1 (CPS1) in mouse mitochondria. CPS1 is the mitochondrial enzyme that catalyzes the first and rate-limiting step of the urea cycle and responsible for the detoxification of excess ammonia [11]. *N*-acetyl-L-glutamate (NAG) is an allosteric activator of CPS1, playing a key role in controlling the flow of nitrogen through the urea cycle [12]. Here, we report tyrosine nitration of CPS1 with functional changes by treatment with peroxynitrite and possible involvement of a nitrated tyrosine residue as a functional consequence.

2. Materials and methods

2.1. Chemicals and reagents

Peroxynitrite was purchased from Cayman Chemical (Ann Arbor, MI). Pyruvate kinase, lactate dehydrogenase, phosphoenolpyruvate, NADH, ATP, NAG, glutathione (GSH) and glycylglycine were purchased from Sigma–Aldrich (St. Louis, MO). Mouse anti-nitrotyrosine antibody (clone 2A8.2) was purchased from Millipore Corporation (Temecula, CA). Rabbit anti-CPS1 antibody was obtained from Abcam Inc. (Cambridge, MA). Secondary antibodies were obtained from Li-Cor Biosciences (Lincoln, NE).

2.2. Preparation of mouse mitochondrial fractions

Mouse liver samples were collected from male C57BL/6 mice ($n = 3$), which were obtained form Jackson Labs (Bar Harbor, ME). The animal experiments were conducted with approval by the IACUC for the University of Washington. Preparation of mitochondrial fractions was based on a previously published protocol [13].

2.3. 1D and 2D gel electrophoresis

For 1D gel electrophoresis, the mitochondrial fractions (10 μg protein each) collected from three mice were individually incubated with each concentration of peroxynitrite (0, 0.1 and 1.0 mM) at 37 °C for 10 min in an aqueous solution containing 50 mM glycylglycine. Each reaction mixture was resolved using 7% SDS–polyacrylamide gels. For 2D gel electrophoresis, the mitochondrial fractions from three mice were pooled. The reaction mixtures (20 μL) including 100 μg protein of the pooled mitochondrial fractions, 50 mM glycylglycine, and peroxynitrite (0 or 1.0 mM) were incubated at 37 °C for 10 min. Each reaction mixture was separated by pH 3–10 isoelectric focusing as previously described [14].

2.4. Western blot analysis

Proteins were transferred to nitrocellulose membranes, which were blocked in a 1:1 ratio of phosphate buffered saline (pH 7.4) and Li-Cor Blocking Buffer for 1 h at room temperature. Membranes were incubated overnight at 4 °C with anti-nitrotyrosine antibody (1:500, mouse IgG) and anti-CPS1 antibody (1:10000, rabbit IgG). Membranes were then incubated with secondary anti-mouse IRDye 800CW antibody (1:5000, goat IgG) and anti-rabbit IRDye 680LT antibody (1:10000, donkey IgG) for 1 h at room temperature. Detection and quantification of the immunofluorescence bands was accomplished using the Odyssey Infrared Imaging System and Software ver. 2.1 (Li-Cor).

2.5. CPS1 activity assay

The mitochondrial fractions (5 μg protein, $n = 3$) were incubated with different concentrations of peroxynitrite at 37 °C for 10 min, or incubated with 1.0 mM peroxynitrite at 37 °C for different time periods. The assay mixtures contained 5 μg protein of the mitochondrial fractions after peroxynitrite treatment, 2.5 mM phosphoenolpyruvate, 0.2 mM NADH, 10 mM NH_4Cl, 100 mM $KHCO_3$, 5 mM ATP, 10 mM $MgSO_4$, 10 mM NAG, 10 U/ml pyruvate kinase, 12.5 U/ml of lactate dehydrogenase, and 50 mM glycylglycine. For (−) NAG assays, NAG was omitted. CPS1 activity was calculated from the initial velocity of NADH oxidation (absorbance at 340 nm). For the reversibility assay, the mitochondrial fractions were incubated with 1.0 mM peroxynitrite at 37 °C for 10 min and subsequently incubated with or without 5.0 mM GSH at 37 °C for 10 min, followed by the CPS1 activity assay with 10 mM NAG.

2.6. Detection and characterization of nitrated peptides by LC–MS/MS

The Coomassie blue-stained 1D gel bands and 2D gel spots that correspond to nitrated CPS1 were excised, and proteins were subjected to in-gel tryptic digestion. The peptides obtained were analyzed using a nano-HPLC (nanoAcquity systems; Waters, Milford, MA) coupled to a hybrid linear ion trap Orbitrap (LTQ-Orbitrap) mass spectrometer (Thermo Scientific, San Jose, CA). Peptide separation was performed with a laser-pulled 75 μm i.d. capillary packed with 15 cm of 100 Å (5 μm) Magic C18 particles (C18AQ; Michrom). Peptides were eluted using an acetonitrile gradient flowing at 250 nL/min in a mobile phase consisting of the following: A, water, 0.1% formic acid; B, acetonitrile, 0.1% formic acid. Peptides were analyzed in the positive ion mode with an MS survey scan acquired over a full m/z range of 400–2000 with the Orbitrap at a resolution of 60,000. The seven most intense precursor ions were sequentially isolated using a data-dependent mode and subjected to collision induced dissociation before a tandem mass spectrum was obtained with the Orbitrap at a resolution of 15,000. The Sequest (version 27) algorithm was applied to search the MS data against the IPI mouse database (ipi.MOUSE.fasta.v3.68). Additionally, the raw data was searched utilizing the open-modification search engine Popitam (freely accessible at www.expasy.ch/tools/popitam/).

2.7. Homology modeling of mouse CPS1

The crystal structures deposited in the PDB as 1JDB [15] and 2YVQ [16], corresponding to the whole structure of *Escherichia coli* CPS and the NAG binding domain of human CPS1 (residues 1343–1478), respectively, were used as the templates. Homology

modeling of mouse CPS1 was performed in the SWISS-MODEL Workspace [17]. Figures depicting protein structures were prepared with PyMOL (ver. 1.1, DeLano Scientific).

3. Results and discussion

3.1. Western blots of nitrated proteins in mouse liver mitochondria

The mitochondrial fractions isolated from mouse liver ($n = 3$) were incubated with different concentrations of peroxynitrite for 10 min, followed by 1D SDS gel electrophoresis and Western blot analysis using an anti-nitrotyrosine antibody (Fig. 1A). Many bands corresponding to nitrated proteins were observed and the most intense band was determined to be that at around 170 kDa by densitometry analysis. This band was subjected to in-gel tryptic digestion, LC–MS/MS analysis and a Sequest search, which showed that the band contained CPS1 (accession number: Q8C196; sequence coverage: 29%; number of unique peptides assigned to the protein: 60). The blot probed with anti-CPS1 antibody represented the bands at around 170 kDa corresponding to CPS1 in all samples (Fig. 1B). The band intensity of nitrotyrosine corresponding to CPS1 was normalized to that of CPS1, demonstrating that nitration of CPS1 increases in a peroxynitrite concentration-dependent manner (Fig. 1C). However, the bands at 170 kDa corresponding to nitrated CPS1 could include some other nitrated proteins because the 1D Western blots, especially for 1 mM peroxynitrite treatment, showed numerous bands of nitrated proteins without sufficient resolution. To further examine the nitration of CPS1, the mitochondrial fractions after incubation with 1.0 mM peroxynitrite were also subjected to 2D gel electrophoresis, followed by Western blot analysis using anti-nitrotyrosine and anti-CPS1 antibodies (Fig. 1D). CPS1 was detected as multiple serial spots, a so-called "charge-train", at around 170 kDa, which is consistent with previously reported findings [18]. The spots of nitrated proteins at around 170 kDa were largely overlapped with those of CPS1, as represented by yellow spots in Fig. 1D. This observation confirms that CPS1 is one of the major targets of tyrosine nitration in mitochondria and the calculation of nitrated CPS1 from 1D Western blot shown in Fig. 1C presents the peroxynitrite concentration dependency of CPS1 nitration, even though it is not rigorously quantitative. In the present study, SDS–PAGE analysis was performed on gels containing a relatively low concentration of acrylamide in order to resolve high molecular weight proteins including CPS1. In this case, however, small molecular weight proteins including mitochondrial MnSOD (25 kDa), which is well known to be nitrated, migrated at the buffer-front and, therefore, nitrated MnSOD was not detected. In preliminary experiments on gels containing higher concentrations of acrylamide, Western blots showed a nitrated protein band at 25 kD which probably corresponds to nitrated MnSOD (data not shown).

3.2. Effects of peroxynitrite treatment on CPS1 activity

The mitochondrial fractions were incubated with 1.0 mM peroxynitrite for different time periods, followed by measuring their CPS1 activities in the presence of NAG, an allosteric activator of CPS1 (Fig. 2A). The CPS1 activity was quickly and significantly decreased by treatment with peroxynitrite in a time-dependent manner (47% decrease in 1 min and 60% decrease in 10 min). The CPS1 activities after 10-min incubations with different concentrations of peroxynitrite were also examined (Fig. 2B). In the presence of NAG, CPS1 activity was decreased in a peroxynitrite concentration-dependent fashion. Significant decreases in the activity were observed for the samples treated by 0.1 mM or higher concentrations of peroxynitrite. In the absence of NAG, CPS1 activity without treatment with peroxynitrite was approximately half of that in the presence of NAG, which is consistent with the previous findings that NAG activates CPS1 by increasing the affinities of ATP,

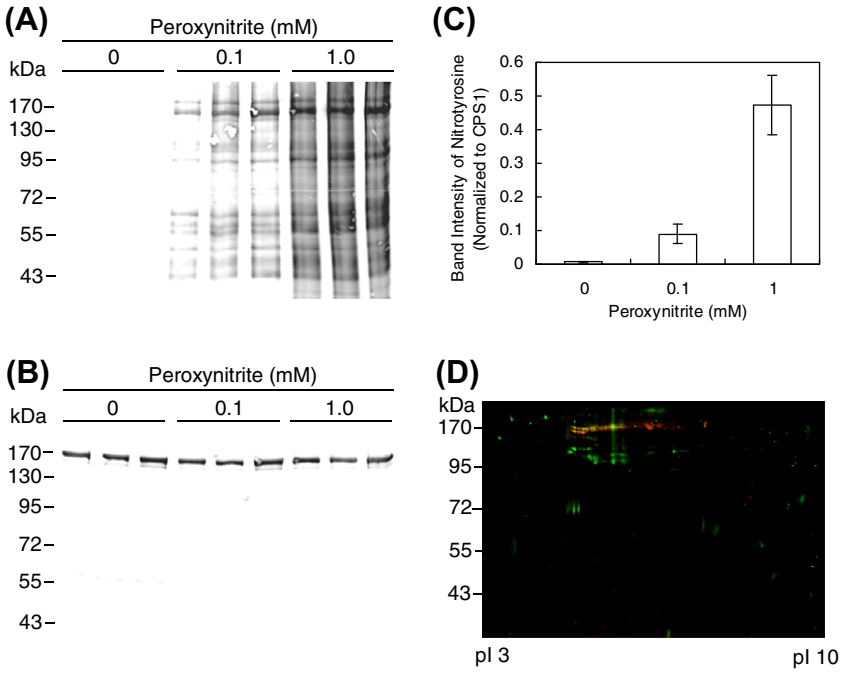

Fig. 1. Western blot analysis of mouse mitochondrial proteins after treatment with peroxynitrite. (A) The mitochondrial fractions collected from three mice were individually incubated with each concentration of peroxynitrite (0, 0.1 and 1.0 mM) at 37 °C for 10 min and subjected to 1D SDS gel electrophoresis. The blots were probed with antibodies to nitrotyrosine. (B) The blots were probed with antibodies to CPS1. (C) Densitometry analysis of nitration to CPS1 was performed using the Odyssey Infrared Imaging System. (D) The mitochondrial proteins pooled from three mice were incubated with 1.0 mM peroxynitrite at 37 °C for 10 min and subjected to 2D gel electrophoresis. The blots of nitrated proteins (green) were superimposed with those of CPS1 (red). The overlap is represented by yellow. (For interpretation of the references to colour in this figure legend, the reader is referred to the web version of this article.)

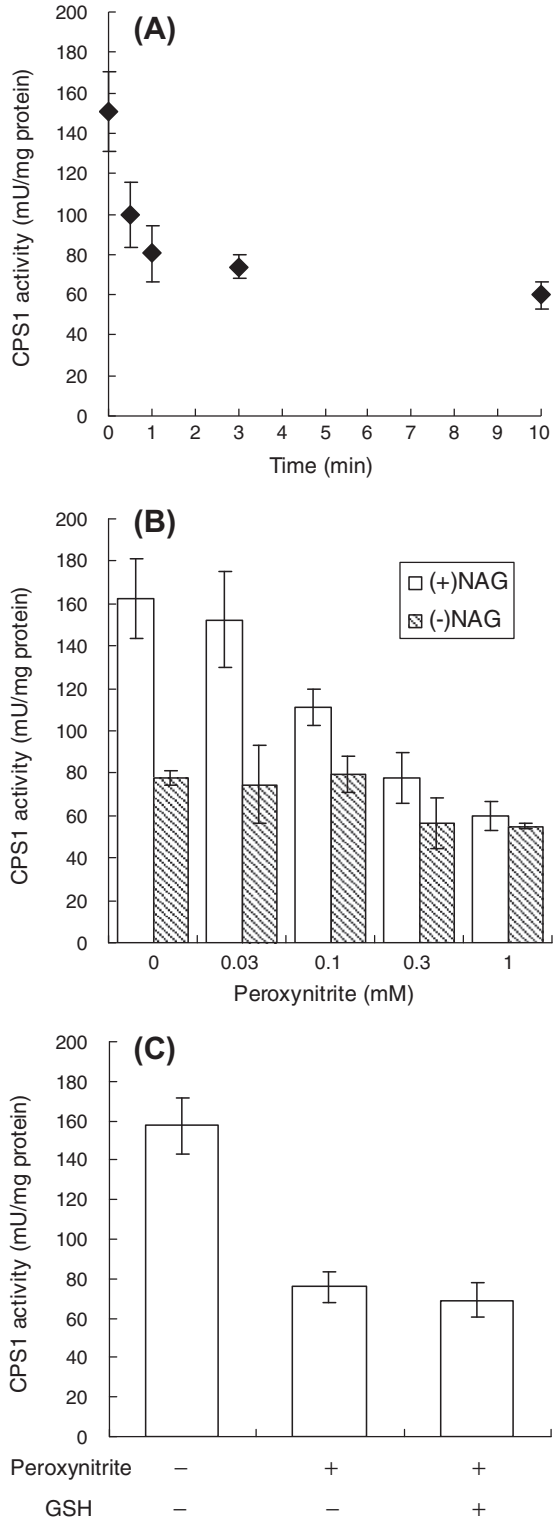

Fig. 2. The effects of peroxynitrite treatment on CPS1 activity in mouse mitochondrial fractions. (A) The mitochondrial fractions were incubated with 1.0 mM peroxynitrite at 37 °C for different time periods and subjected to the CPS1 activity assay. (B) The mitochondrial fractions were incubated with different concentrations of peroxynitrite at 37 °C for 10 min and subjected to the CPS1 activity assay with or without 10 mM NAG. (C) The mitochondrial fractions were incubated with 1.0 mM peroxynitrite at 37 °C for 10 min and subsequently incubated with or without 5.0 mM GSH at 37 °C for 10 min, followed by the CPS1 activity assay with 10 mM NAG.

Mg^{2+} and K^{+} to CPS1 [12]. Treatment with increasing concentrations of peroxynitrite did not have significant effects on CPS1 activity in the absence of NAG as shown in Fig. 2B. CPS1 activities after treatment with 1.0 mM peroxynitrite were comparable between in the presence and absence of NAG. These observations suggest that tyrosine nitration decreases CPS1 activity by affecting the interaction of CPS1 with NAG. In addition to tyrosine nitration, peroxynitrite can oxidize thiol groups of cysteines. The contribution of thiol oxidation to the decrease of CPS1 activity can be evaluated because thiol oxidation is reversible in the presence of the reducing agents such as GSH and dithiothreitol [19]. CPS1 activity decreased by peroxynitrite was not recovered by treatment with reduced GSH as shown in Fig. 2C, suggesting that the decrease of the CPS1 activity is due to tyrosine nitration rather than cysteine oxidation.

3.3. Determination of nitrated tyrosine residues by LC–MS/MS and Popitam analysis

Mouse CPS1 consists of 1500 amino acids including 36 tyrosine residues (NCBI protein database, Accession No. AAI26970). In order to determine the target tyrosine residues of nitration, the 1D gel bands and 2D gel spots corresponding to nitrated CPS1 were excised, followed by in-gel tryptic digestion of the proteins and LC–MS/MS of the digested peptides. LC–MS/MS spectra were analyzed using Popitam, which is an algorithm designed to identify mutations and modifications to peptides based on MS/MS spectral data. The Popitam-based modification search of the mouse CPS1 sequence identified five peptides that could contain nitrotyrosine (Table 1). The observed mass number of the precursor ions was close to the theoretical mass number for all candidate peptides (mass errors <3.1 ppm). The structures of the five nitrated peptides were verified by their MS/MS spectra. Representative MS/MS spectra and assignments of *b* and *y* ions are shown in Fig. 3. The mass difference of 208 Da corresponding to nitration (+45 Da) of tyrosine (163 Da) was observed in *y* ions and *b* ions. Previous studies reported that most nitrated tyrosines are found in loop structures with turn-inducing residues, proline or glycine, in the vicinity (from −5 to +5 residues around nitrated tyrosines) [8]. The proximity of a negative charge of acidic amino acids (i.e., aspartate and glutamate) is also beneficial [8]. All five nitrated tyrosines have acidic amino acid residue(s) in their proximal sequences (Table 2), which is consistent with the previous findings mentioned above. The tyrosines Y_{120}, Y_{162}, Y_{529} and Y_{1305} have turn-inducing residue(s) in their proximity, suggesting that they are located in loop structures.

3.4. Homology modeling of mouse CPS1 and location of nitrated tyrosine residues

Since a crystal structure of mouse CPS1 has not been solved, we created its model based on *E. coli* CPS (PDB file: 1JDB) [15] by homology modeling on SWISS-MODEL Workspace [17]. The created model of mouse CPS1 superimposed with the template structure is shown in Fig. 4A. The model mostly covered the sequence of mouse CPS1, whereas some parts of the protein, such as the allosteric domain, were not modeled because of poor homology of the sequence. Four out of five nitrated tyrosine residues (Y_{120}, Y_{162}, Y_{529} and Y_{1305}) were included in the created model of mouse CPS1 as shown in Fig. 4A. They appear to be located in or close to loop structures, which is consistent with the findings in primary sequences. Also, all these nitrated tyrosine residues are positioned on the protein surface, which can be explained by their accessibility to reactive nitrogen species. According to previous studies regarding the crystal structure of CPS from *E. coli*, there is a molecular tunnel for the transport of reaction intermediates between remotely located active sites (Fig. 4A) [15]. The superimposed image of mouse CPS1 indicates that those four tyrosine residues are located away from

Table 1
Nitrated peptides of mouse CPS1 detected by LC–MS/MS and Popitam analysis.

Peptide no.	Sequence	Calculated m/z[a]	Observed m/z[a] (mass error: ppm)	
			Sample from 1D gel	Sample form 2D gel
1	^{113}DELGLNKY*M#ESDGIK^{127}	886.9045	886.9055 (1.1)	886.9046 (0.1)
2	^{158}VPAIY*GVDTR^{167}	568.2914	568.2917 (0.5)	568.2917 (0.5)
3	^{524}GVLKEY*GVK^{532}	519.2855	519.2855 (0)	N.D.
4	^{1293}LPTLEQPIIPSDY*VAIK^{1309}	971.5309	971.5339 (3.1)	971.5311 (0.2)
5	^{1445}FVHDNY*VIR^{1453}	604.2969	604.2974 (0.8)	604.2975 (1.0)

[a] Numbers show m/z of doubly protonated molecular ions. Y* and M# represent nitrotyrosine and oxidized (+O) methionine, respectively. N.D. represents "not detected".

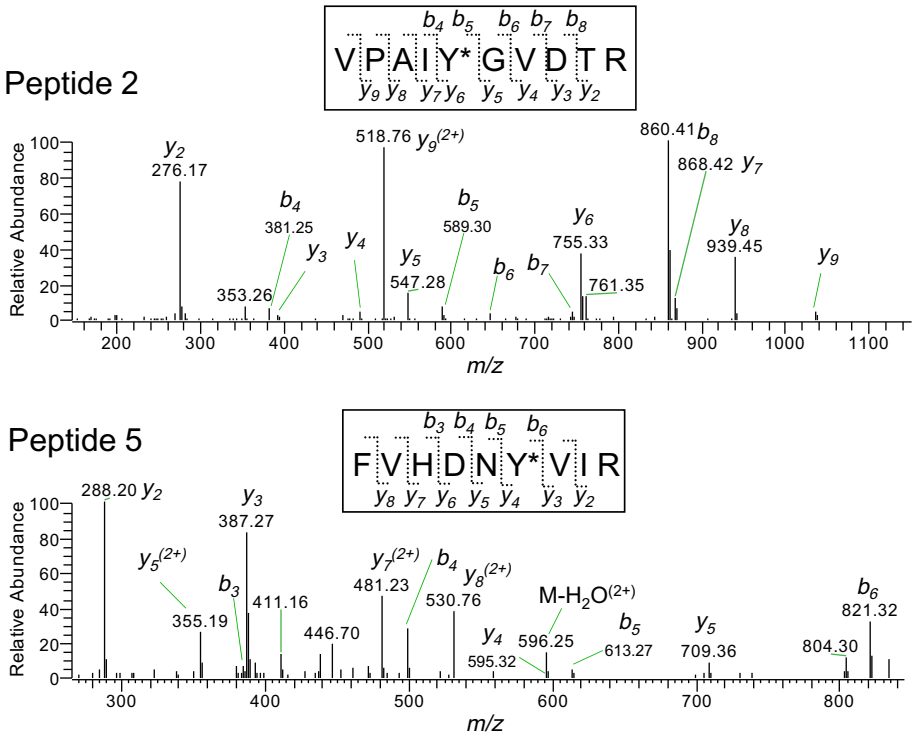

Fig. 3. Representative LC–MS/MS spectra and assignments of the sequence-specific fragment ions of the nitrated peptides. The sequence-specific fragment ions are labeled as y and b ions on the spectra. For the peptide 2, the mass difference of 208 detected between b_4 and b_5 and between y_5 and y_6 corresponds to nitrated tyrosine residue (163 (Tyr) + 45 (nitration)). For the peptide 5, the mass difference of 208 detected between b_5 and b_6 and between y_3 and y_4 corresponds to nitrated tyrosine residue.

Table 2
Proximal amino acids of nitrated tyrosine residues.

No.	Sequence from −5 to +5 amino acids relative to the nitrated tyrosine
1	L **G** L N K Y_{120}* M E S D **G**
2	K V **P** A I Y_{162}* **G** V D T R
3	**G** V L K E Y_{529}* **G** V K V L
4	I I **P** S D Y_{1305}* V A I K A
5	F V H D N Y_{1450}* V I R R T

Turn-inducing residues, proline and glycine, are shown in bold. Negatively-charged residues, aspartate and glutamate, are underlined. Y* represents nitrotyrosine.

active sites and the molecular tunnel, suggesting that they are unlikely to be involved in the nitration-mediated decrease in CPS1 activity. The other tyrosine residue, Y_{1450}, was considered to be located in the allosteric domain which interacts with the activator, NAG. Recently, the crystal structure of the NAG binding domain of human CPS1 (residues 1343–1478, PDB file: 2YVQ) has been solved and NAG-interacting residues were characterized [16]. We created the NAG binding domain of mouse CPS1 using the three-dimensional structure of human CPS1 as a template (Fig. 4B). Since the sequence of the domain is highly conserved among species including human and mouse, the created model is almost identical to the template. The tyrosine Y_{1450} is located in an α-helix, which is considered to directly contribute to NAG binding via an electrostatic interaction with N_{1449} and by hydrophobic interactions with F_{1445} and I_{1452} [16]. The primary amino acid sequence of this α-helix, including Y_{1450}, is strictly conserved as shown in Fig. 4C. The importance of this α-helical structure for CPS1 activity has also been demonstrated by CPS1 mutations found in CPS1 deficient patients. It was reported that the mutations R1453Q and R1453W, which were found in severe CPS1 deficiency, inactivated CPS1. Since R_{1453} does not interact with NAG directly, CPS1 inactivation by the mutations to R_{1453} was considered to be due to distortion of the α-helical structure [20]. Similarly, nitration to Y_{1450} could elicit a structural change of the α-helix and decrease the binding affinity to NAG, which is a possible mechanism for the decrease in CPS1 activity by peroxynitrite. This interpretation seems to be consistent with the finding that the peroxynitrite-dependent decrease in CPS1 activity was more significant in the presence of NAG than in its absence as shown in Fig. 2B. Even though most nitrated tyrosine residues are found in flexible loop regions, as mentioned above, functionally critical tyrosine nitration tends to be found in α-helices, such as Y_{34} in MnSOD [21] and Y_{97} and Y_{74} in cytochrome

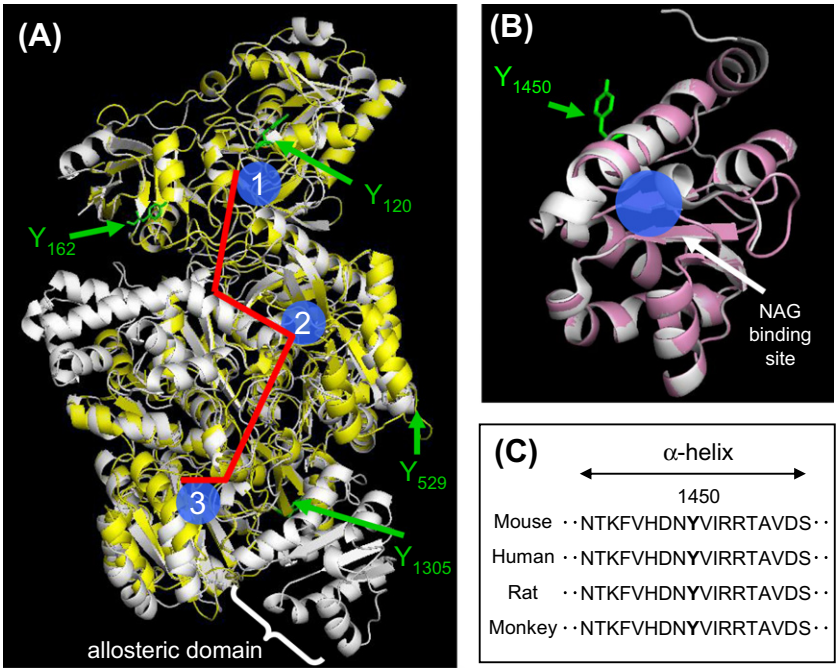

Fig. 4. Homology modeling of mouse CPS1. (A) The superimposed image of the created model of mouse CPS1 (yellow) with the template structure for the *E. coli* CPS (white, PDB file: 1JDB). Three active sites are shown in blue (1) glutamine binding site, (2) bicarbonate binding site, and (3) carbamoyl phosphate binding site) and the molecular tunnel is shown in red. (B) The superimposed image of the created model of the mouse NAG binding domain (pink) with the template structure for the human NAG binding domain (white, PBD file: 2YVQ). (C) The sequences (residues 1442–1459) in NAG binding domain of CPS1s from mouse (*Mus musculus*), human (*Homo sapiens*), rat (*Rattus norvegicus*) and monkey (*Macaca mulatta*), were obtained from the NCBI protein database. (For interpretation of the references to colour in this figure legend, the reader is referred to the web version of this article.)

c [22]. Also, a recent study demonstrated that the content of the α-helical structure of insulin was reduced by nitration to a tyrosine residue in an α-helix [23]. These findings support our results and interpretation. Future studies such as mutation analysis will be needed to clarify a mechanistic link between the nitration to Y_{1450} and loss of NAG binding.

In conclusion, our study for the first time revealed that CPS1 is one of the major targets of tyrosine nitration in mitochondria after treatment with peroxynitrite, and the functional consequence is the decrease in its enzymatic activity in the presence of NAG. Since CPS1 is responsible for the detoxification of excess ammonia, nitration of CPS1 with attenuated function may result in hyperammonemia and subsequent mitochondrial dysfunction in in vivo situations. Future in vivo studies will be required to investigate the relevance of these findings to some diseases and drug-induced toxicities.

Acknowledgments

This work was supported in part by National Institutes of Health Grant [GM32165] and support to H.T. from Daiichi Sankyo Co. Ltd. (Tokyo, Japan).

References

[1] N. Abello, H.A. Kerstjens, D.S. Postma, R. Bischoff, Protein tyrosine nitration: selectivity, physicochemical and biological consequences, denitration, and proteomics methods for the identification of tyrosine-nitrated proteins, J. Proteome. Res. 8 (2009) 3222–3238.
[2] C. Szabó, H. Ischiropoulos, R. Radi, Peroxynitrite: biochemistry, pathophysiology and development of therapeutics, Nat. Rev. Drug Discov. 6 (2007) 662–680.
[3] M. Sokolovsky, J.F. Riordan, B.L. Vallee, Conversion of 3-nitrotyrosine to 3-aminotyrosine in peptides and proteins, Biochem. Biophys. Res. Commun. 27 (1967) 20–25.
[4] R. Radi, A. Cassina, R. Hodara, C. Quijano, L. Castro, Peroxynitrite reactions and formation in mitochondria, Free Radic. Biol. Med. 33 (2002) 1451–1464.
[5] L.A. MacMillan-Crow, J.P. Crow, J.D. Kerby, J.S. Beckman, J.A. Thompson, Nitration and inactivation of manganese superoxide dismutase in chronic rejection of human renal allografts, Proc. Natl. Acad. Sci. USA 93 (1996) 11853–11858.
[6] D.L. Cruthirds, L. Novak, K.M. Akhi, P.W. Sanders, J.A. Thompson, L.A. MacMillan-Crow, Mitochondrial targets of oxidative stress during renal ischemia/reperfusion, Arch. Biochem. Biophys. 412 (2003) 27–33.
[7] R. Agarwal, L.A. MacMillan-Crow, T.M. Rafferty, H. Saba, D.W. Roberts, E.K. Fifer, L.P. James, J.A. Hinson, Acetaminophen-induced hepatotoxicity in mice occurs with inhibition of activity and nitration of mitochondrial manganese superoxide dismutase, J. Pharmacol. Exp. Ther. 337 (2011) 110–116.
[8] J.M. Souza, E. Daikhin, M. Yudkoff, C.S. Raman, H. Ischiropoulos, Factors determining the selectivity of protein tyrosine nitration, Arch. Biochem. Biophys. 371 (1999) 169–178.
[9] H. Ischiropoulos, Biological selectivity and functional aspects of protein tyrosine nitration, Biochem. Biophys. Res. Commun. 305 (2003) 776–783.
[10] P. Hernandez, R. Gras, J. Frey, R.D. Appel, Popitam: towards new heuristic strategies to improve protein identification from tandem mass spectrometry data, Proteomics 3 (2003) 870–878.
[11] D. Haussinger, Nitrogen metabolism in liver: structural and functional organization and physiological relevance, Biochem. J. 267 (1999) 281–290.
[12] V. Rubio, H.G. Britton, S. Grisolia, Mitochondrial carbamoyl phosphate synthetase activity in the absence of *N*-acetyl-L-glutamate. Mechanism of activation by this cofactor, Eur. J. Biochem. 134 (1983) 337–343.
[13] P. Zhao, T.F. Kalhorn, J.T. Slattery, Selective mitochondrial glutathione depletion by ethanol enhances acetaminophen toxicity in rat liver, Hepatology 36 (2002) 326–335.
[14] P.H. O'Farrell, High resolution two-dimensional electrophoresis of proteins, J. Biol. Chem. 250 (1975) 4007–4021.
[15] J.B. Thoden, H.M. Holden, G. Wesenberg, F.M. Raushel, I. Rayment, Structure of carbamoyl phosphate synthetase: a journey of 96 Å from substrate to product, Biochemistry 36 (1997) 6305–6316.
[16] S. Pekkala, A.I. Martinez, B. Barcelona, J. Gallego, E. Bendala, I. Yefimenko, V. Rubio, J. Cervera, Structural insight on the control of urea synthesis: identification of the binding site for *N*-acetyl-L-glutamate, the essential allosteric activator of mitochondrial carbamoyl phosphate synthetase, Biochem. J. 424 (2009) 211–220.
[17] K. Arnold, L. Bordoli, J. Kopp, T. Schwede, The SWISS-MODEL Workspace. A web-based environment for protein structure homology modeling, Bioinformatics 22 (2006) 195–201.
[18] A. Craig, J. Sidaway, E. Holmes, T. Orton, D. Jackson, R. Rowlinson, J. Nickson, R. Tonge, I. Wilson, J. Nicholson, Systems toxicology: integrated genomic,

proteomic and metabonomic analysis of methapyrilene induced hepatotoxicity in the rat, J. Proteome Res. 5 (2006) 1586–1601.
[19] J. Murray, S.W. Taylor, B. Zhang, S.S. Ghosh, R.A. Capaldi, Oxidative damage to mitochondrial complex I due to peroxynitrite: identification of reactive tyrosines by mass spectrometry, J. Biol. Chem. 278 (2003) 37223–37230.
[20] S. Pekkala, A.I. Martínez, B. Barcelona, I. Yefimenko, U. Finckh, V. Rubio, J. Cervera, Understanding carbamoyl-phosphate synthetase I (CPS1) deficiency by using expression studies and structure-based analysis, Hum. Mutat. 3 (2010) 801–808.
[21] F. Yamakura, H. Taka, T. Fujimura, K. Murayama, Inactivation of human manganese-superoxide dismutase by peroxynitrite is caused by exclusive nitration of tyrosine 34 to 3-nitrotyrosine, J. Biol. Chem. 273 (1998) 14085–14089.
[22] C. Batthyany, J.M. Souza, R. Duran, A. Cassina, C. Cervenansky, R. Radi, Time course and site(s) of cytochrome c tyrosine nitration by peroxynitrite, Biochemistry 44 (2005) 8038–8046.
[23] Y. Wang, Y. Luo, R. Zhong, D. Gao, S. Cui, Identification of site(s) of insulin nitration by peroxynitrite and characterization of its structural change, Protein Pept. Lett. 15 (2008) 1063–1067.

Biochemical and Biophysical Research Communications 420 (2012) 61–65

Contents lists available at SciVerse ScienceDirect

Biochemical and Biophysical Research Communications

journal homepage: www.elsevier.com/locate/ybbrc

Histone demethylase JMJD5 is essential for embryonic development

Sangphil Oh, Ralf Janknecht *

Department of Cell Biology, University of Oklahoma Health Sciences Center, Oklahoma City, OK 73104, USA

ARTICLE INFO

Article history:
Received 13 February 2012
Available online 28 February 2012

Keywords:
Embryonic development
Gene knockout
Histone demethylase
JMJD5
p21
p53

ABSTRACT

Histone lysine methylation is pivotal in regulating chromatin structure and thus profoundly affects the transcriptome. JMJD5 (jumonji C domain-containing 5) is a histone demethylase that specifically removes methyl moieties from dimethylated lysine 36 on histone H3 and exerts a pro-proliferative effect on breast cancer cells. Here, we generated JMJD5 knockout mice in order to study the physiological significance of this enzyme. Whereas heterozygous knockout mice displayed no overt phenotype, homozygous JMJD5 knockouts died around day 10 of embryonal development. JMJD5$^{-/-}$ embryos showed delayed development already at E8.5 and were actively resorbed at E10.5. While strong JMJD5 expression was observed only in the yolk sac at E8.5, JMJD5 was robustly expressed in E10.5 embryos at several sites, including the heart and eye. Lack of JMJD5 resulted in transcriptional upregulation of the tumor suppressor p53. Concurrently, the cell cycle inhibitor p21 and the pro-apoptotic molecule Noxa, both of which are prominent p53 target genes, became strongly upregulated in JMJD5$^{-/-}$ embryos. Collectively, our data indicate that JMJD5 is essential during embryonal development and a repressor of p53 expression. The latter suggests that JMJD5 has oncogenic activity and accordingly JMJD5 is upregulated in leukemias and breast cancer.

1. Introduction

Epigenetic changes are crucial during development and inappropriate occurrence in adults can cause various diseases, including cancer. Histone methylation has emerged as a major player in epigenetics [1,2] and the enzymes governing this dynamic post-translational modification, the histone methyltransferases and demethylases, are regarded as exciting new drug targets [3]. However, particularly very little is hitherto known about the normal and pathological functions of histone demethylases, most of which belong to the family of jumonji C domain-containing (JMJD) proteins consisting of 30 members in humans [4,5].

One only recently discovered histone demethylase is JMJD5, which is capable of demethylating dimethylated histone H3 on lysine 36 [6]. The function of dimethylated H3K36 is currently not fully understood, but this posttranslational modification mainly occurs within the coding region of genes to suppress aberrant transcription initiation and has also been implicated in the repair of DNA double-strand breaks [7]. Moreover, downregulation of JMJD5 resulted in reduced proliferation of MCF7 breast cancer cells [6] and shortened the circadian rhythm in *Arabidopsis thaliana* and human osteosarcoma cells [8,9]. Despite its apparent importance in various processes, it remains unknown if and how JMJD5 affects development and tumor formation in mammals. Therefore, we investigated here the consequences of JMJD5 ablation in a mouse model.

2. Materials and methods

2.1. Mouse work

The Sanger International Gene Trap Center embryonic stem (ES) cell line AZ0518 was obtained from the Mutant Mouse Regional Resource Center at UC Davis. ES cells were injected into mouse blastocysts and resulting embryos transferred into pseudopregnant mice at the Mayo Clinic Knockout Mouse Core Facility. Chimeric males were bred with C57BL/6 females and germ line transmission in progeny confirmed by Southern blotting and PCR genotyping. Thereafter, JMJD5 heterozygous knockout mice were bred for at least two generations with C57BL/6 wild-type mice. All animal work was approved by the respective Institutional Animal Care and Use Committees.

2.2. PCR genotyping

Mouse tail-clip DNA or yolk sac DNA was isolated and subjected to amplification with the GoTaq Green Master PCR kit (Promega) and the following primers: JMJD5/10269Fw (5′-ATACGGAAGTAACAGCCAAGGTTA-3′; located within JMJD5 intron 2), JMJD5/10668Rv

Abbreviations: E, embryonal day; ES, embryonic stem; β-geo, β-galactosidase/neomycin; JMJD, jumonji C domain-containing.

* Corresponding author. Address: University of Oklahoma Health Sciences Center, 975 NE 10th Street, BRC-1464, Oklahoma City, OK 73104, USA. Fax: +1 405 2713548.
E-mail address: ralf-janknecht@ouhsc.edu (R. Janknecht).

0006-291X/$ - see front matter © 2012 Elsevier Inc. All rights reserved.
doi:10.1016/j.bbrc.2012.02.115

(5′-GACTTACAAGTGGCCAAGAGAGA-3′; located within JMJD5 intron 3) and pGT01xr/317Rv (5′-CTTCACATCCATGCTGAGGA-3′; located within the EN2 sequence of the genetrap vector). The PCR program utilized was: 95 °C for 4 min; 30 cycles of 94 °C for 30 s, 58 °C for 30 s, 72 °C for 30 s; 72 °C for 2 min. Resultant PCR products were resolved on agarose gels and visualized by staining with ethidium bromide [10].

2.3. RT-PCR

RNA from AZ0518 ES cells was prepared with Trizol (Invitrogen) as described [11]. Reverse transcription and amplification of cDNA was performed with the Access Quick RT-PCR system (Promega) utilizing the following PCR program [12]: 48 °C for 45 min; 96 °C for 2 min; 31 repeats of 96 °C for 30 s, 56 °C for 45 s, and 68 °C for 1 min; followed by a final extension at 68 °C for 4 min. The primers used were JMJD5 exon2A (5′-GCTGATCATGTCAGAGGACACCAC-3′) and RACE-geo-1 (5′-AGTATCGGCCTCAGGAAGATCG-3′). This was followed by a second PCR utilizing iProof polymerase (BioRad) and the following PCR program: 98 °C for 2 min; 30 cycles of 98 °C for 30 s, 56 °C for 30 s, 72 °C for 1 min (+1 s/cycle); 72 °C for 5 min. The primers employed were JMJD5 exon2B (5′-GCACCCTCTGGAAGGAGCTCAGG-3′) and RACE-geo-1. Resultant PCR products were then subjected to standard DNA sequencing. Similarly, RNA was isolated from E8.5 embryos and employed for RT-PCR with JMJD5 exon2A and JMJD5 exon4rev (5′-CAGCAATCTCCTGGATGTACTGC-3′) primers followed by nested PCR with JMJD5 exon2B and JMJD5 exon4rev primers. Amplified cDNA was then visualized on ethidium-stained agarose gels [13].

In addition, the following mouse p53, p21, Puma, Noxa and GAPDH primer pairs were utilized for RT-PCR (20 cycles of amplification) followed by a second PCR for 10–20 cycles [14]: mP53-RT-fw1233 (5′-GCAGGGCTCACTCCAGCTACCT-3′) and mP53-RT-rv1565 (5′-GGTGCCAGGGTCCAACAACTGG-3′); mP21-RT-fw102 (5′-ATGTCCAATCCTGGTGATGTC-3′) and mP21-RT-rv572 (5′-TCTCTTGCAGAAGACCAATC-3′); mPuma-RT-fw582 (5′-CCTGTCACCAGCCCAGCAGC-3′) and mPuma-RT-rv910 (5′-AAGTCTCCGACGTCCCCCGG-3′); mNoxa-RT-fw197 (5′-CCAACGCGGGCAGAGCTACC-3′) and mNoxa-RT-rv536 (5′-GGCATTTCCATCAACCGGCGGA-3′); mGAPDH-for (5′-CGTAGACAAAATGGTGAAGGTC-3′) and mGAPDH-rev (5′-GTGAAGACACCAGTAGACTCC-3′).

2.4. β-galactosidase staining

Embryos were fixed in Fix-buffer (0.2% glutaraldehyde, 5 mM EGTA, 2 mM $MgCl_2$, 0.1 M phosphate buffer pH 7.3) at room temperature for 15–30 min depending on the size of the embryo. Then, embryos were washed three times in Wash-buffer (2 mM $MgCl_2$, 0.01% sodium deoxycholate, 0.02% NP-40, 0.1 M phosphate buffer pH 7.3) for 30 min and incubated in Wash-buffer plus 5 mM potassium ferricyanide, 5 mM potassium ferrocyanide, 1 mg/ml X-gal at 37 °C for 48 h in the dark. After washing briefly, embryos were treated with Fix-buffer at room temperature for 30 min, cleared in a graded glycerol series (15%, 30%, 50%, 70%, 80%, 90% in phosphate-buffered saline and finally 100%) and then photographed under a dissecting microscope.

2.5. Western blotting

Protein extracts were prepared according to standard procedures [15]. Thereafter, proteins were electrophoresed on SDS polyacrylamide gels and subjected to Western blotting [16]. Detection of proteins was by enhanced chemiluminescence [17] using the following antibodies: p21 (Santa Cruz Biotechnology sc-756),

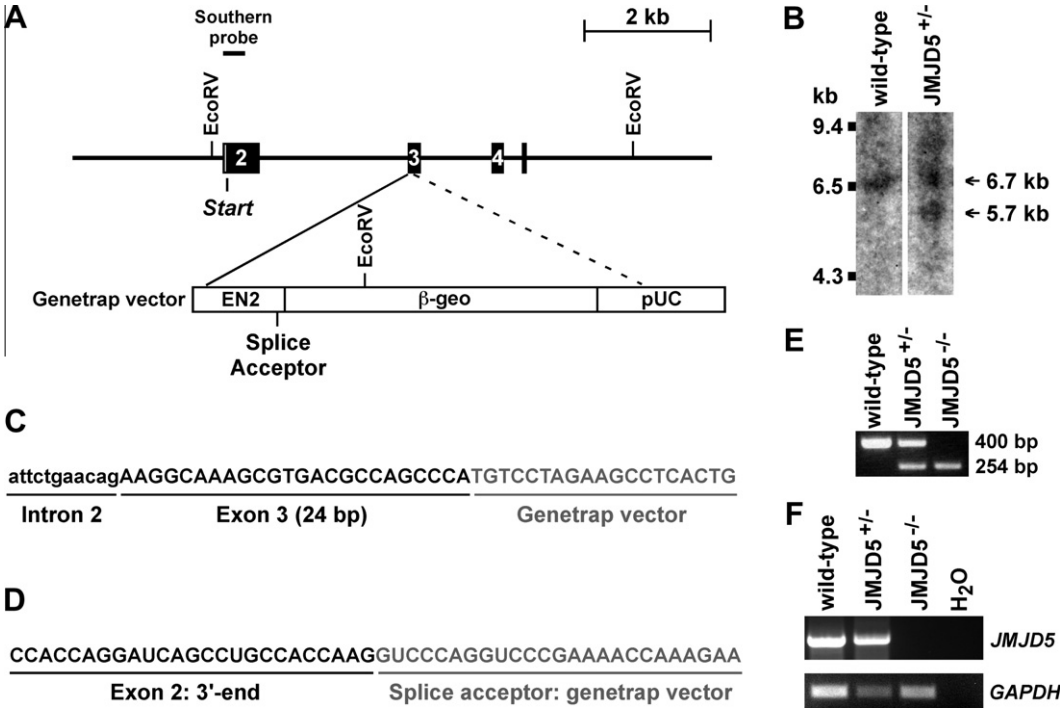

Fig. 1. Generation of JMJD5 knockout mice. (A) Scheme of the genetrap vector and mouse JMJD5 genomic DNA depicting exons 2–5. Start denotes the beginning of the JMJD5 open reading frame. (B) Southern blot of EcoRV-digested DNA derived from wild-type and heterozygous JMJD5 knockout mice. The probe used for hybridization encompassed nucleotides 3–361 of JMJD5 exon 2. The expected size for the wild-type or knockout allele is 6.7 or 5.7 kb, respectively. (C) DNA sequence at the junction between JMJD5 genomic DNA and the genetrap vector. The first 234 bp of the genetrap vector were deleted upon integration. (D) RT-PCR on JMJD5$^{+/-}$ ES cells with subsequent DNA sequencing to elucidate the nature of the JMJD5–β-geo fusion transcript. Shown is the thereby determined RNA sequence at the junction of JMJD5 and genetrap vector derived nucleotides. (E) PCR genotyping of indicated E8.5 embryos. Expected sizes for wild-type and knockout alleles are 400 and 254 bp, respectively. (F) RT-PCR on RNA isolated from E8.5 embryos. Amplification of JMJD5 and GAPDH mRNA is shown.

cleaved caspase 3 (Cell Signaling #9661), pRb-S780 (Cell Signaling #9307), cyclin D1 (Cell Signaling #2926), IκBα (Cell Signaling #4814), dimethylated H3K36 (Upstate 07-369) and actin (Sigma A2066).

3. Results and discussion

3.1. Generation of JMJD5 knockout mice

To study the *in vivo* significance of JMJD5, we made use of the Sanger International Gene Trap Center to obtain ES cells, in which the mouse JMJD5 gene has been inactivated due to the insertion of a β-galactosidase/neomycin (β-geo) fusion gene (Fig. 1A). Respective ES cells were utilized to generate heterozygous JMJD5 knock-out mice. Southern blotting as well as DNA sequencing of genomic DNA confirmed the integration of the β-geo gene after the first 24 bp of JMJD5 exon 3 (Fig. 1B and C). To determine if a JMJD5–β-geo fusion transcript would be generated, RNA from ES cells was isolated, RT-PCR performed and resultant cDNA analyzed by DNA sequencing. This showed that the fusion transcript consists of JMJD5 exons 1 and 2 followed by the β-geo gene (Fig. 1D). Thus, the splice acceptor site at the beginning of JMJD5 exon 3 is supplanted by the very strong one in front of β-geo leading to the exclusion of both intron 2 and the first 24 bp of exon 3 in the JMJD5–β-geo fusion transcript.

We then intercrossed JMJD5$^{+/-}$ mice and noted that no JMJD5$^{-/-}$ mice were born, whereas wild-type and JMJD5$^{+/-}$ mice were obtained at the expected 1:2 ratio. Moreover, JMJD5$^{+/-}$ mice did not display any obvious different phenotype compared to wild-type littermates up to six months after birth. While this manuscript was in preparation, another report also demonstrated that JMJD5 knockout mice are not viable [18]. Only a few other proven JMJD histone demethylases have been studied in mouse knockout models. In the majority of cases, a knockout did not result in embryonic lethality: JMJD1A$^{-/-}$ mice were viable with defects in spermatogenesis, JARID1A$^{-/-}$ mice also lived to adulthood with minor hematopoietic deficiencies, and JMJD2D$^{-/-}$ mice showed no obvious phenotype [19–21]. However, JARID1B$^{-/-}$ mice died between embryonal day (E) 4.5 and E7.5 [22]. Thus, both JARID1B and JMJD5 are required for embryonal development, yet perform non-overlapping functions as JMJD5$^{-/-}$ embryos survive beyond E7.5 (see below).

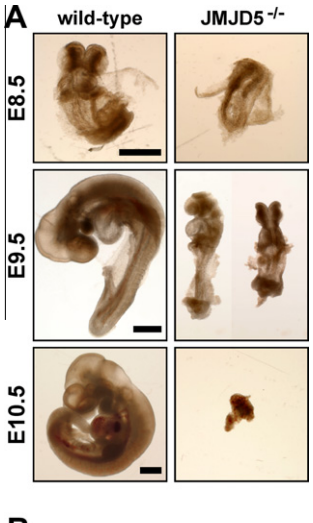

B

	wild-type	JMJD5$^{+/-}$	JMJD5$^{-/-}$	total
E8.5	17 (18)	36	21 (18)	74
E9.5	11 (9)	18	8 (9)	37
E10.5	2 (4)	9	3 (4)	14

Fig. 2. Embryonic lethality of JMJD5 knockouts. (A) JMJD5$^{+/-}$ mice were intercrossed and E8.5, E9.5 and E10.5 embryos isolated. Shown are respective wild-type and JMJD5$^{-/-}$ embryos. All embryos were genotyped by PCR utilizing yolk sac DNA. Scale bars are 500 μm long. (B) Number of genotypes observed. In brackets are the numbers of expected wild-type and JMJD5$^{-/-}$ embryos assuming Mendelian ratios.

3.2. JMJD5 knockout embryos

To uncover when JMJD5$^{-/-}$ embryos die during development, we first isolated 8.5 day embryos from JMJD5$^{+/-}$ intercrosses. PCR genotyping confirmed that E8.5 JMJD5$^{-/-}$ embryos were present (Fig. 1E) and RT-PCR corroborated the loss of JMJD5 expression (Fig. 1F). Of note, E8.5 JMJD5$^{-/-}$ embryos already showed delayed development and were smaller (Fig. 2A, top panels). However, a Mendelian ratio of wild-type, JMJD5$^{+/-}$ and JMJD5$^{-/-}$ embryos was observed (Fig. 2B), indicating that JMJD5 is not required for the first 8 days of embryogenesis.

Next, we isolated E9.5 and E10.5 embryos from JMJD5$^{+/-}$ intercrosses. At day 9.5, JMJD5$^{-/-}$ embryos were even more delayed in development and displayed failure of embryo turning and open neural tubes (Fig. 2A, middle panels). Moreover, E10.5 embryos were already in the process of being resorbed (Fig. 2A, bottom panels). In contrast, we did not observe any differences between wild-type and JMJD5$^{+/-}$ embryos (not shown), consistent with our above noted observation that JMJD5$^{+/-}$ mice were born at the expected Mendelian ratio and displayed no apparent developmental defects up to 6 months of age. In conclusion, loss of JMJD5 leads to lethality at around day 10 of embryonic development.

The design of the genetrap vector resulted in the expression of a JMJD5–β-geo fusion transcript (see Fig. 1), whose expression

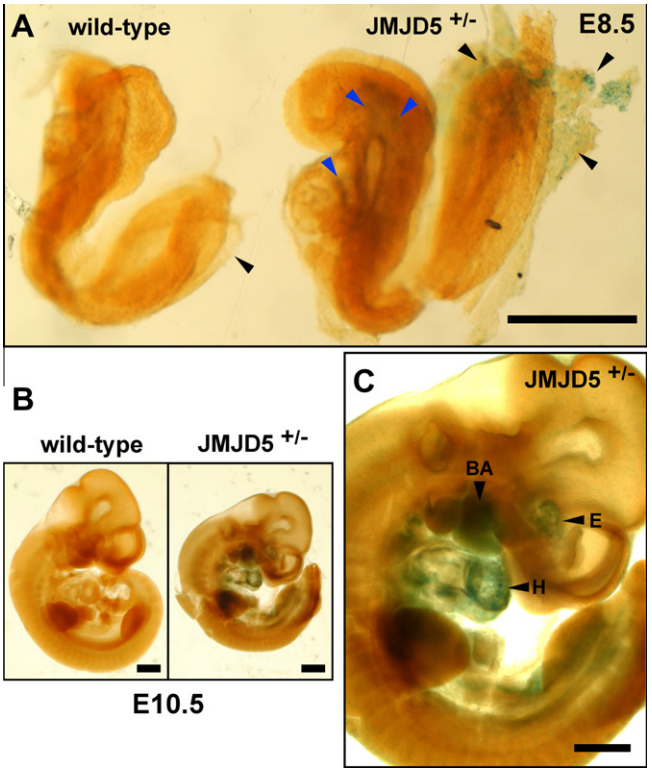

Fig. 3. Staining of embryos for β-galactosidase activity. Scale bars are 500 μm long. (A) Wild-type and JMJD5$^{+/-}$ embryos at E8.5. Black arrows point to yolk sac. Blue arrows indicate some sites of weak β-galactosidase activity within the JMJD5$^{+/-}$ embryo. (B) E10.5 embryos. (C) Enlarged view of the E10.5 JMJD5$^{+/-}$ embryo. BA, branchial arch; E, eye; H, heart. (For interpretation of the references to color in this figure legend, the reader is referred to the web version of this article.)

should be governed by the same control elements as the genuine JMJD5 mRNA. Furthermore, the JMJD5–β-geo fusion transcript gives rise to the expression of a β-galactosidase/neomycin fusion protein, thus allowing to probe for JMJD5 gene expression by measuring the activity of β-galactosidase in JMJD5$^{+/-}$ embryos. As shown in Fig. 3A, strong β-galactosidase activity was only observable in the yolk sac (black arrows), whereas weak, yet significant, β-galactosidase activity was noticeable at many sites within JMJD5$^{+/-}$ E8.5 embryos (e.g., blue arrows in Fig. 3A). However, at E10.5 robust β-galactosidase activity was detected at several locations within the JMJD5$^{+/-}$ embryo (Fig. 3B and C), including the developing branchial arch, eye and heart. Thus, it is conceivable that the lethality of JMJD5$^{-/-}$ embryos is a consequence of defective development in multiple organs, including the essential heart.

Altogether, the facts that JMJD5 is essential for embryonic development and expressed in various developing organs point out the crucial role of this histone demethylase at the organismal level. Future studies with conditional knockout mice are needed to explore the role of JMJD5 during later stages of embryonal development and in adults.

3.3. JMJD5 affects p53 expression

To uncover mechanistically how JMJD5 ablation may lead to embryonic lethality, we isolated RNA from E8.5 embryos and probed for the presence of p53, a tumor suppressor and key player in both cell proliferation and apoptosis [23]. Notably, p53 mRNA levels were increased in homozygous JMJD5 knockouts compared to wild-type littermates (Fig. 4A), whereas heterozygotes did not differ from wild-type mice (not shown). Prominent target genes of p53 are the cell cycle inhibitor p21 and the pro-apoptotic molecules Puma and Noxa [24]. Concurrently with p53 upregulation, transcription of p21 and Noxa was robustly enhanced upon JMJD5 knockout, whereas Puma mRNA levels were slightly increased (Fig. 4A). The significant induction of p21 and Noxa provides a possible explanation why JMJD5$^{-/-}$ embryos are delayed in development and eventually die through potentially both a blockade in cell cycling and increased cell death.

To further corroborate that JMJD5 affects the p53 pathway, we analyzed protein expression in E9.5 embryos, the earliest stage at which reasonable protein amounts were obtainable for Western blot analyses. Again, no difference was observable between wild-type and JMJD5$^{+/-}$ mice (not shown), but expectedly p21 protein levels were increased in homozygous JMJD5$^{-/-}$ mice (Fig. 4B). We also attempted to blot for p53, Puma and Noxa, but all three proteins were expressed below our detection level. However, as one would predict upon upregulation of Puma and Noxa, we observed in JMJD5$^{-/-}$ embryos higher levels of cleaved caspase 3, one hallmark of apoptosis.

In contrast to the high overexpression of the cell cycle inhibitor p21, two other markers of cell proliferation, the phosphorylation of the retinoblastoma tumor suppressor (pRb-S780) and the expression of cyclin D1, were only slightly, if at all, reduced upon complete JMJD5 knockout (Fig. 4B), suggesting that JMJD5 ablation blocks cell cycle progression predominantly through the p53–p21 axis. Similarly, there was no change in IκBα levels, indicating that the NFκB-regulated cell survival pathway is not affected by JMJD5 (Fig. 4B). This supports the notion that the absence of JMJD5 primarily induces apoptosis through the p53-Noxa axis. Surprisingly, there was no global change of H3K36 dimethylation upon JMJD5 knockout (Fig. 4B), suggesting that JMJD5 is not the major active H3K36 demethylase in mouse embryos. In fact, several other

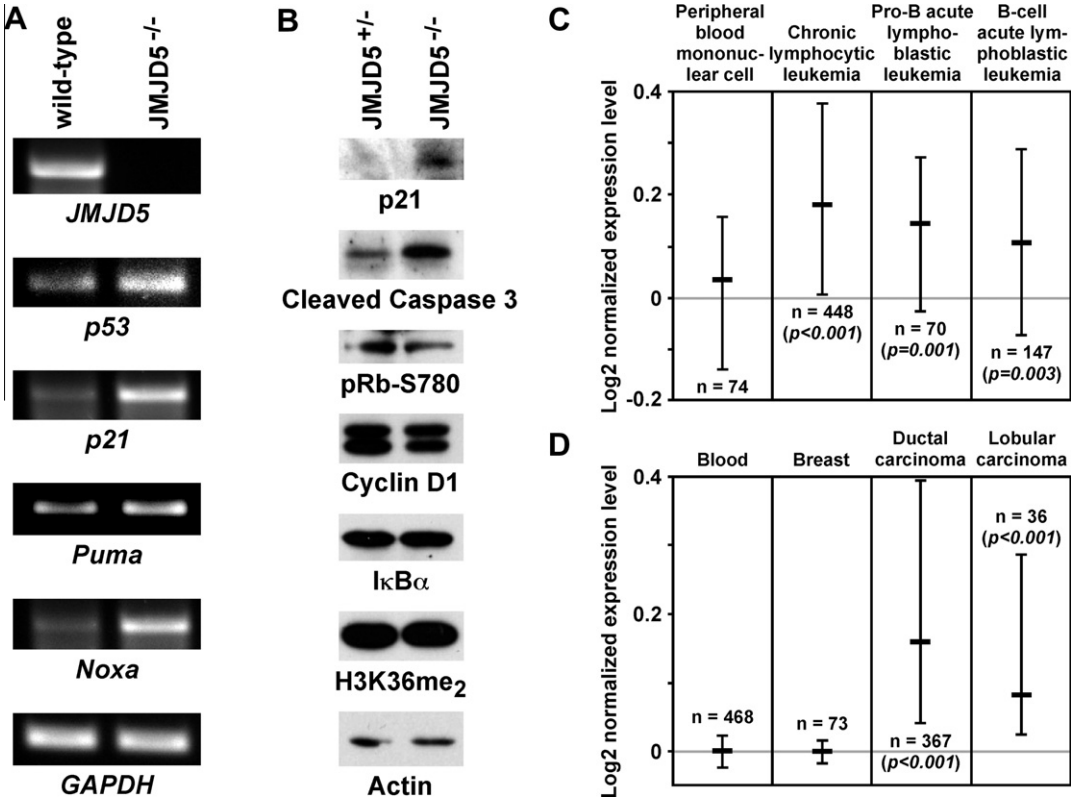

Fig. 4. (A) RT-PCR on RNA isolated from E8.5 embryos. (B) Western blots of protein extracts derived from E9.5 embryos. (C) Expression levels of JMJD5 mRNA in peripheral blood mononuclear cells and indicated leukemias. Depicted are median values with 25–75 percentile ranges. Number of patients in each cohort and statistical significance (Student's *t* test) is indicated in the graph. Microarray data were obtained from the publication of Haferlach et al. [26]. (D) Analogous for invasive ductal and invasive lobular breast carcinomas compared to normal blood cells and breast tissue. Microarray data were obtained from the cancer genome atlas at the National Cancer Institute.

demethylases, including JMJD2A, JMJD2C and KDM2A, can attack dimethylated H3K36 and may vastly outnumber JMJD5 [25]. However, this does not exclude that JMJD5 ablation changes H3K36me$_2$ levels at specific loci such as the p53 gene.

Our results suggest that JMJD5 may perform an oncogenic function by suppressing p53 expression, thereby relieving p53-imposed breaks on cell cycling and survival. Since many oncogenes are upregulated in human tumors, we analyzed JMJD5 mRNA expression with the Oncomine webtool (www.oncomine.org) in various matching normal and cancer tissues. Two types of cancer were thereby identified that show significant upregulation of JMJD5 mRNA: leukemia and breast cancer. Compared to normal peripheral blood mononuclear cells, JMJD5 mRNA was upregulated in chronic lymphocytic, pro-B and B-cell acute lymphoblastic leukemia (Fig. 4C). Similarly, significant upregulation of JMJD5 mRNA was observed in invasive ductal and invasive lobular breast carcinomas when compared to normal breast tissue or blood cells (Fig. 4D). Thus, this upregulation of JMJD5 may contribute to cancer formation by stimulating cell growth, and consistently MCF7 breast cancer cells were shown to require JMJD5 for maximal proliferation [6]. If indeed JMJD5 is a driver of tumorigenesis, small molecules blocking the catalytic center of JMJD5 hold promise in cancer therapy.

References

[1] P.A. Cloos, J. Christensen, K. Agger, K. Helin, Erasing the methyl mark: histone demethylases at the center of cellular differentiation and disease, Genes Dev. 22 (2008) 1115–1140.

[2] P. Chi, C.D. Allis, G.G. Wang, Covalent histone modifications – miswritten, misinterpreted and mis-erased in human cancers, Nat. Rev. Cancer 10 (2010) 457–469.

[3] A. Spannhoff, A.T. Hauser, R. Heinke, W. Sippl, M. Jung, The emerging therapeutic potential of histone methyltransferase and demethylase inhibitors, ChemMedChem 4 (2009) 1568–1582.

[4] R.J. Klose, Y. Zhang, Regulation of histone methylation by demethylimination and demethylation, Nat. Rev. Mol. Cell Biol. 8 (2007) 307–318.

[5] Y. Shi, J.R. Whetstine, Dynamic regulation of histone lysine methylation by demethylases, Mol. Cell 25 (2007) 1–14.

[6] D.A. Hsia, C.G. Tepper, M.R. Pochampalli, E.Y. Hsia, C. Izumiya, S.B. Huerta, M.E. Wright, H.W. Chen, H.J. Kung, Y. Izumiya, KDM8, a H3K36me2 histone demethylase that acts in the cyclin A1 coding region to regulate cancer cell proliferation, Proc. Natl. Acad. Sci. USA 107 (2010) 9671–9676.

[7] E.J. Wagner, P.B. Carpenter, Understanding the language of Lys36 methylation at histone H3, Nat. Rev. Mol. Cell Biol. 13 (2012) 115–126.

[8] M.A. Jones, M.F. Covington, L. DiTacchio, C. Vollmers, S. Panda, S.L. Harmer, Jumonji domain protein JMJD5 functions in both the plant and human circadian systems, Proc. Natl. Acad. Sci. U. S. A. 107 (2010) 21623–21628.

[9] M.A. Jones, S. Harmer, JMJD5 Functions in concert with TOC1 in the *Arabidopsis circadian* system, Plant Signaling Behav. 6 (2011) 445–448.

[10] S. Shin, K.L. Rossow, J.P. Grande, R. Janknecht, Involvement of RNA helicases p68 and p72 in colon cancer, Cancer Res. 67 (2007) 7572–7578.

[11] S. Shin, T.D. Kim, F. Jin, J.M. van Deursen, S.M. Dehm, D.J. Tindall, J.P. Grande, J.M. Munz, G. Vasmatzis, R. Janknecht, Induction of prostatic intraepithelial neoplasia and modulation of androgen receptor by ETS variant 1/ETS-related protein 81, Cancer Res. 69 (2009) 8102–8110.

[12] B.S. Goueli, R. Janknecht, Regulation of telomerase reverse transcriptase gene activity by upstream stimulatory factor, Oncogene 22 (2003) 8042–8047.

[13] J. Kim, S. Shin, M. Subramaniam, E. Bruinsma, T.D. Kim, J.R. Hawse, T.C. Spelsberg, R. Janknecht, Histone demethylase JARID1B/KDM5B is a corepressor of TIEG1/KLF10, Biochem. Biophys. Res. Commun. 401 (2010) 412–416.

[14] A. Goel, R. Janknecht, Acetylation-mediated transcriptional activation of the ETS protein ER81 by p300, P/CAF, and HER2/Neu, Mol. Cell. Biol. 23 (2003) 6243–6254.

[15] S.M. Mooney, A. Goel, A.B. D'Assoro, J.L. Salisbury, R. Janknecht, Pleiotropic effects of p300-mediated acetylation on p68 and p72 RNA helicase, J. Biol. Chem. 285 (2010) 30443–30452.

[16] S. Papoutsopoulou, R. Janknecht, Phosphorylation of ETS transcription factor ER81 in a complex with its coactivators CREB-binding protein and p300, Mol. Cell. Biol. 20 (2000) 7300–7310.

[17] T.D. Kim, S. Shin, R. Janknecht, Repression of Smad3 activity by histone demethylase SMCX/JARID1C, Biochem. Biophys. Res. Commun. 366 (2008) 563–567.

[18] A. Ishimura, K. Minehata, M. Terashima, G. Kondoh, T. Hara, T. Suzuki, Jmjd5, an H3K36me2 histone demethylase, modulates embryonic cell proliferation through the regulation of Cdkn1a expression, Development (Cambridge, U. K.) 139 (2012) 749–759.

[19] Y. Okada, G. Scott, M.K. Ray, Y. Mishina, Y. Zhang, Histone demethylase JHDM2A is critical for Tnp1 and Prm1 transcription and spermatogenesis, Nature 450 (2007) 119–123.

[20] R.J. Klose, Q. Yan, Z. Tothova, K. Yamane, H. Erdjument-Bromage, P. Tempst, D.G. Gilliland, Y. Zhang, W.G. Kaelin Jr., The retinoblastoma binding protein RBP2 is an H3K4 demethylase, Cell 128 (2007) 889–900.

[21] N. Iwamori, M. Zhao, M.L. Meistrich, M.M. Matzuk, The testis-enriched histone demethylase, KDM4D, regulates methylation of histone H3 lysine 9 during spermatogenesis in the mouse but is dispensable for fertility, Biol. Reprod. 84 (2011) 1225–1234.

[22] S. Catchpole, B. Spencer-Dene, D. Hall, S. Santangelo, I. Rosewell, M. Guenatri, R. Beatson, A.G. Scibetta, J.M. Burchell, J. Taylor-Papadimitriou, PLU-1/JARID1B/KDM5B is required for embryonic survival and contributes to cell proliferation in the mammary gland and in ER+ breast cancer cells, Int. J. Oncol. 38 (2011) 1267–1277.

[23] N. Rivlin, R. Brosh, M. Oren, V. Rotter, Mutations in the p53 tumor suppressor gene: important milestones at the various steps of tumorigenesis, Genes Cancer 2 (2011) 466–474.

[24] T. Riley, E. Sontag, P. Chen, A. Levine, Transcriptional control of human p53-regulated genes, Nat. Rev. Mol. Cell Biol. 9 (2008) 402–412.

[25] M.T. Pedersen, K. Helin, Histone demethylases in development and disease, Trends Cell Biol. 20 (2010) 662–671.

[26] T. Haferlach, A. Kohlmann, L. Wieczorek, G. Basso, G.T. Kronnie, M.C. Bene, J. De Vos, J.M. Hernandez, W.K. Hofmann, K.I. Mills, A. Gilkes, S. Chiaretti, S.A. Shurtleff, T.J. Kipps, L.Z. Rassenti, A.E. Yeoh, P.R. Papenhausen, W.M. Liu, P.M. Williams, R. Foa, Clinical utility of microarray-based gene expression profiling in the diagnosis and subclassification of leukemia: report from the International Microarray Innovations in Leukemia Study Group, J. Clin. Oncol. 28 (2010) 2529–2537.

Biochemical and Biophysical Research Communications 420 (2012) 66–71

Contents lists available at SciVerse ScienceDirect

Biochemical and Biophysical Research Communications

journal homepage: www.elsevier.com/locate/ybbrc

Endothelial RIG-I activation impairs endothelial function

Tobias Asdonk [a,*], Inga Motz [a], Nikos Werner [a], Christoph Coch [b], Winfried Barchet [b], Gunther Hartmann [b], Georg Nickenig [a], Sebastian Zimmer [a]

[a] Department of Medicine/Cardiology, University of Bonn, Sigmund-Freud-Str. 25, 53105 Bonn, Germany
[b] Institute for Clinical Chemistry and Clinical Pharmacology, University of Bonn, Sigmund-Freud-Str. 25, 53105 Bonn, Germany

ARTICLE INFO

Article history:
Received 17 February 2012
Available online 28 February 2012

Keywords:
Endothelial biology
RIG-I
Atherosclerosis
Inflammation
Innate immune system

ABSTRACT

Background: Endothelial dysfunction is a crucial part of the chronic inflammatory atherosclerotic process and is mediated by innate and acquired immune mechanisms. Recent studies suggest that pattern recognition receptors (PRR) specialized in immunorecognition of nucleic acids may play an important role in endothelial biology in a proatherogenic manner. Here, we analyzed the impact of endothelial retinoic acid inducible gene I (RIG-I) activation upon vascular endothelial biology.

Methods and results: Wild type mice were injected intravenously with 32.5 μg of the RIG-ligand 3pRNA (RNA with triphosphate at the 5′end) or polyA control every other day for 7 days. In 3pRNA-treated mice, endothelium-depended vasodilation was significantly impaired, vascular oxidative stress significantly increased and circulating endothelial microparticle (EMP) numbers significantly elevated compared to controls. To gain further insight in RIG-I dependent endothelial biology, cultured human coronary endothelial cells (HCAEC) and endothelial progenitor cells (EPC) were stimulated *in vitro* with 3pRNA. Both cells types express RIG-I and react with receptor upregulation upon stimulation. Reactive oxygen species (ROS) formation is enhanced in both cell types, whereas apoptosis and proliferation is not significantly affected in HCAEC. Importantly, HCAEC release significant amounts of proinflammatory cytokines in response to RIG-I stimulation.

Conclusion: This study shows that activation of the cytoplasmatic nucleic acid receptor RIG-I leads to endothelial dysfunction. RIG-I induced endothelial damage could therefore be an important pathway in atherogenesis.

1. Introduction

Atherosclerosis is a chronic inflammation of the vessel wall [1] and the leading cause of death worldwide. The main clinical manifestations are myocardial infarction, consecutive ischemic heart failure, stroke and peripheral artery disease leading to profound mortality and morbidity burden [2]. Both the innate and acquired immune systems significantly contribute to the development of these diseases. Immune cells such as macrophages, lymphocytes and dendritic cells invade and accumulate in the vessel wall and drive the atherosclerotic process in all stages by production of proinflammatory cytokines and growth factors [3]. Mechanisms of the acquired immune system have been studied extensively, but medical science today is just starting to reveal the secrets of innate immunity and to disclose its profound impact on chronic inflammatory diseases. Innate immune mechanisms encompass both cellular components including macrophages/monocytes or granulocytes and humoral components such as the complement system, defensines and, importantly, pattern recognition receptors (PRR).

PRR are highly conserved receptors and are expressed in various cell types of all tissues. PRR are specialized in detecting danger associated molecular patterns (DAMP) which represent distinctive classes of environmental ‘foreign’ pathogens, for instance fragments of microorganisms [4] but also endogenous molecules of necrotic/apoptotic cells such as nucleic acids [5]. They thereby trigger an instantaneous innate immune response independent of immunogenic experience and further initiate an activation of the acquired immune system as a second step in the human immune defense system.

Among the nucleic acid detecting PRR, toll-like receptor 3 (TLR3) and melanoma differentiation associated gene 5 (MDA5) bind long double-stranded RNA [6,7], toll-like receptor 9 (TLR9) targets CpG motifs [8], DNA-dependent activator of IFN-regulatory factors (DAI) recognizes double-strand DNA [9], toll-like receptor 7/8 (TLR7/8) is activated by single strand RNA containing certain sequence motifs [10] and retinoic acid inducible gene I (RIG-I) is stimulated by RNA with triphosphate at the 5′end [11,12]. These DAMP

* Corresponding author. Address: Medizinische Klinik und Poliklinik II Universitätsklinikum Bonn Sigmund-Freud-Str. 25, D-53105 Bonn, Germany. Fax: +49 (0) 228 287 51482.
E-mail address: tobias.asdonk@ukb.uni-bonn.de (T. Asdonk).

0006-291X/$ - see front matter © 2012 Elsevier Inc. All rights reserved.
doi:10.1016/j.bbrc.2012.02.116

induce, via complex intracellular signaling cascades, the production of proinflammatory cytokines such as type I interferon [13].

RIG-I is a cytoplasmic receptor consisting of 2 N-terminal caspase recruitment domains (CARD), a DExD/box helicase domain and a C-terminal repression domain (RD). It is expressed in macrophages, dendritic cells and fibroblasts. Down stream signaling mechanisms involve virus induced signaling adaptor (VISA), CARD adaptor inducing IFN-β (Cardif), interferon regulatory factor (IRF3) and nuclear factor 'kappa-light-chain-enhancer' of activated B-cells (NF-κB), resulting in production of proinflammatory cyto- and chemokine-like Interferon-β, Interleukin-1β (IL-1β) and Interleukin-6/8/28 (IL-6/8/28) [14].

Endothelial integrity is inalienable for vascular homeostasis, balance of coagulation, fibrinolysis, and regulation of vascular tension. It is crucial for the immune system by regulating diapedesis of circulating immune cells to inflammatory sites through expression of adhesion molecules. In atherosclerosis endothelial dysfunction is a central finding and persists over all stages [15]. It is now well known that endothelial damage is not only restored by adjacent mature endothelial cells but also by circulating endothelial progenitor cells (EPC) able to home to and renew endothelial lesions. They are mobilized from the bone marrow and can directly differentiate into endothelial cells or support regeneration via paracrine mechanisms [16,17].

The mechanisms of PRR related innate immune mechanisms affecting both endothelial and endothelial progenitor cells in a setting of atherosclerosis remain poorly understood. We therefore studied the endothelial response to specific RIG-I stimulation by 3pRNA both *in vivo* and *in vitro*.

2. Material & methods

2.1. In vitro EPC

Mononuclear cells were isolated from human buffy coats utilizing density Ficoll gradients and circulating angiogenic cells (CAC) were cultured using endothelium cell basal medium-2 (EBM-2, Clonetics), as previously described [18]. Experiments were performed on day seven after isolation. For stimulation cells were incubated with 3pRNA or vehicle polyA in concentrations of 1 μg/ml. For transfection Lipofectamine 2000 (Invitrogen) was used according to manufactures instructions.

2.2. In vitro HCAEC

Human coronary artery cells (HCAEC) (Lonza, Basel, Switzerland) were cultured at 37 °C and 5% CO_2 atmospheric concentration. Endothelial cell growth medium (MU, Dromo Cell) was renewed every 2 days and cells grown to 80% confluence. For stimulation cells were incubated with 3pRNA or vehicle polyA with 1 μg/ml. For transfection Lipofectamine 2000 (Invitrogen) was used according to manufactures instructions.

2.3. In vivo treatment

Eight to twelve weeks old wild type mice (C 57BL/6J, Charles River, Sulzfeld, Germany) were kept at 22 °C in a 12 h day/night rhythm and received food and water ad libitum. Mice were injected intravenously with either 3pRNA or polyA respectively at doses of 32.5 μg suspended in 200 ml 0.9% NaCl solution every other day for 7 days. Transfection was accomplished with JetPei agent (Polyplus Transfection). Aortic segments and blood were collected immediately after sacrifice. All animal experiments were performed in accordance with institutional guidelines and the German animal protection law.

2.4. Measurement of reactive oxygen species (ROS) ex vivo

ROS release in intact aortic segments was determined by L-012 chemiluminescence, as previously described [19]. Aortic segments were carefully excised and placed in chilled, modified Krebs-HEPES buffer. Connective tissue was removed and aortas were cut into 2 mm segments. Chemiluminescence of aortic segments was assessed in scintillation vials containing Krebs-HEPES buffer with 100 μmol/l L-012 over 15 min in a scintillation counter (Lumat LB 9501, Berthold, Bad Wildbad, Germany) in 1 min intervals. The vessel segments were then dried and dry weight was determined. ROS release is calculated as relative chemiluminescence per mg aortic tissue and as percent of control.

2.5. Measurement of reactive oxygen species In vitro

For analysis of cellular ROS production HCAEC and EPC were cultured as described above. Experiments were performed after 2 h stimulation. Cells were then trypsinated, pelleted, resuspended in Krebs-HEPES buffer with 100 μmol/l L-012 and immediately placed in the scintillation counter.

2.6. Immunohistochemistry

Cells were grown in 24-well plates on glass slides. For detection of RIG-I expression, immunohistochemical stains were performed. Briefly, cells were fixed with acetone at −20 °C. They were then washed twice in PBS plus 0.025% Triton X-100 for 5 min and subsequently incubated in 1% BSA with PBS for 2 h at room temperature. Next, the primary antibody (Rabbit polyclonal DDX58 antibody, ab45428, Abcam) was diluted 1:1000 in 1% BSA with PBS and the slides allowed to incubated overnight at 4 °C. Immunodetection was accomplished using an TRITC conjugated goat anti-rabbit secondary antibody (1:1000 dilution). The nuclei were stained with DAPI mounting medium.

2.7. Cytokine quantification

HCAEC were incubated with 3pRNA for 24 h and the concentration of IL-6 and interferon gamma-induced protein 10 (IP-10) was then quantified by ELISA in the supernatant medium. Commercially available kits for human IL-6 and IP-10 (R&D Systems) were used according to the manufactures protocols.

2.8. Real-time PCR

For analysis of gene expression in cultured HCAEC and EPC, cells were lysed using a 10G needle and homogenized with a motorized homogenizer. RNA was isolated with peqGOLD RNA-Pure (peqLAB Biotechnology). RNA concentration and quality was verified with a spectrophotometer. Then, 1 μg of the isolated total RNA was reversely transcribed using Omniscript RT Kit (Qiagen) according to the manufactures protocol. The single stranded cDNA was amplified by real-time quantitative reverse transcription-polymerase chain reaction (RT-PCR) with the TaqMan System (ABI-7500 fast PCR System) using SYBR-Green dye (RIG-I sense 5′GGA CGT GGC AAA ACA AAT CAG 3′, RIG-I antisense 5′ GCA ATG TCA ATG CCT TCA ACG 3′). For quantification, RIG-I mRNA expression were normalized to endogenous 18s rRNA.

2.9. Apoptosis

To determine HCAEC and EPC apoptosis, the Cell Death Detection ELISA Kit (Roche) was used according to manufacturer's instructions. The results are shown in relative proportion to the control group.

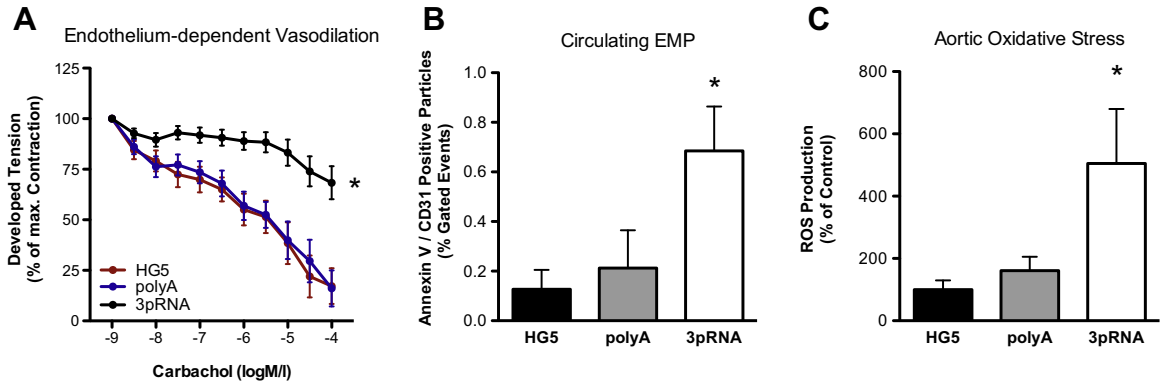

Fig. 1. RIG-I activation impairs endothelial function *in vivo*. (A) Endothelium-dependent vasodilation was significantly impaired in mice treated with 3pRNA indicating endothelial dysfunction and (B) the number of circulating EMP significantly increased suggesting endothelial damage. (C) RIG-I stimulation was also associated with a significant increase in vascular oxidative stress.

2.10. Proliferation

HCAEC proliferation was assessed by detection of bromodeoxyuridine (BrdU) incorporation after a 24 h incubation with 3pRNA and BrdU. BrdU positive nuclei were determined using an anti-BrdU antibody (Abcam) and the total number of cells using DAPI staining.

2.11. Flow cytometry

Murine blood samples were analyzed as described previously [20]. Following red cell lysis, the viable lymphocyte population was analyzed for Sca-1 (Becton Dickinson) and flk-1 (Becton Dickinson) to measure endothelial microparticles (EPC) and AnnexinV (Becton Dickinson) and CD 31 (Becton Dickinson) to measure EMP. Isotype identical antibodies and unstained samples served as controls in every experiment (Becton Dickinson). Cell fluorescence was measured immediately after staining using a FACS Calibur instrument (Becton Dickinson). Data were analyzed using CellQuest software (Becton Dickinson). Units of all measured components are specific events obtained after measuring 50.000 events (EPC) and 20.000 events (EMP) in a pre-specified gate during FACS analysis.

2.12. Aortic ring preparations and tension recording

Vasodilation and vasoconstriction of isolated aortic ring preparations were determined in organ baths filled with oxygenated modified Tyrode buffer (37 °C), as previously described [19,21]. Adventitial tissue was carefully removed, and 3 mm segments of

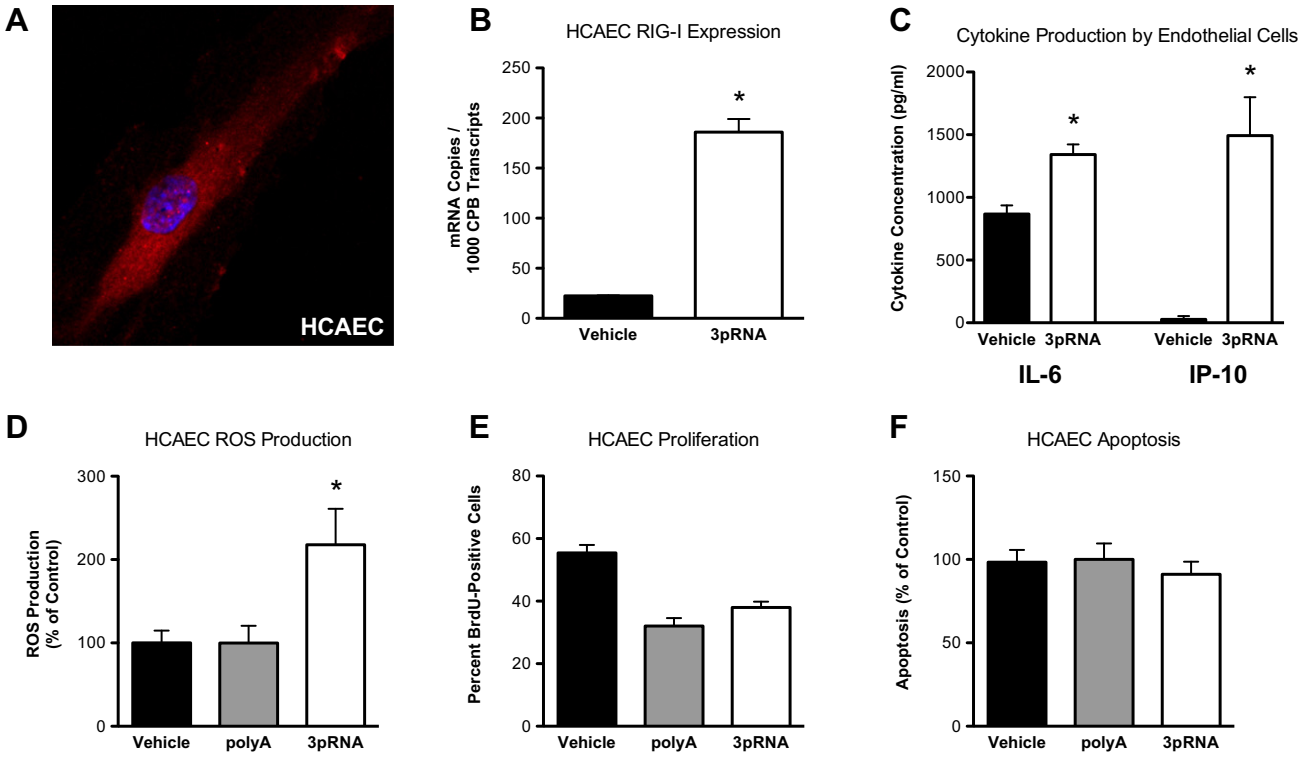

Fig. 2. RIG-I activation alters HCAEC biology *in vitro*. (A, B) HCAEC express RIG-I and specific stimulation with 3pRNA induces a receptor upregulation. (C) Upon RIG-I stimulation the proinflammatory cytokines IL-6 and IP-10 are released by HCAEC. (D) RIG-I stimulation also enhances ROS formation. (E) In contrast, proliferation and apoptosis (F) were not significantly affected by 3pRNA.

the thoracic aorta were investigated. A resting tension of 10 mN was maintained throughout the experiment. Drugs were added in increasing concentrations in order to obtain cumulative concentration–response curves: KCl 20 and 40 mmol/l, phenylephrine 1 nmol/l to 10 μmol/l, carbachol 10 nmol/l to 100 μmol/l (assessment of endothelium-dependent vasodilation after precontraction with phenylephrine), and nitroglycerin 1 nmol/l to 10 μmol/l (assessment of endothelium-independent vasodilation after precontraction with phenylephrine). The drug concentration was increased when vaso-constriction or -relaxation was completed. Drugs were washed out before the next substance was added.

2.13. Statistical analysis

Data are presented as mean ± standard error of mean (SEM). For statistical analysis, 2-tailed, unpaired Student's *t*-test and ANOVA for multiple comparisons were employed where applicable. $p < 0.05$ indicates statistical significance.

3. Results

3.1. RIG-I activation induces endothelial dysfunction in wild type mice

To investigate if specific stimulation of RIG-I with 3pRNA affects endothelial biology, wild type mice were injected intravenously with 32.5 μg 3pRNA or polyA (control RNA) supplemented with JetPEI transfection agent, or vehicle (HG5%) every other day for 7 days. No adverse events or signs of side effects were observed. Food and water intake as well as body weight remained unchanged. We first assessed vessel function of aortic rings in organ chamber experiments. Phenylephrine induced vasoconstriction did not differ between the groups (data not shown). Neither did endothelium-independent vasodilation in reaction to nitroglycerine (data not shown), indicating an intact and functional smooth muscle cell response. Endothelium-dependent vasodilation however was significantly impaired in mice treated with 3pRNA indicating endothelial dysfunction (Fig. 1A, vehicle 17.22 ± 7.79%, polyA 16.07 ± 7.62%, 3pRNA 68.34 2.73%, $n = 5$, $p < 0.05$).

Because endothelial dysfunction is often mediated by direct endothelial damage and cell apoptosis/death, we next studied the number of circulating endothelial microparticles in these mice. Stressed and dying endothelial cells release microparticles that can be measured by flow cytometry and correlate with the degree of endothelial damage. Specific RIG-I activation with 3pRNA significantly increased the number of circulating EMP compared to control mice (Fig. 1B, vehicle 0.13 ± 0.09%, polyA 0.21 ± 0.15%, 3pRNA 0.69 ± 0.18%, $n = 5$, $p < 0.05$).

In response to invading pathogens, activation of the innate immune system often induces the formation of reactive oxygen species. These radicals not only harm pathogens, but increased vascular oxidative stress also leads to endothelial damage/dysfunction and is associated with many proatherogenic mechanisms. We therefore measured the ROS production of isolated aortic rings in these mice by L-012-chemiluminescence. Here, *in vivo* RIG-I stimulation was associated with a significant increase in vascular oxidative stress (Fig. 1C, vehicle 100 ± 38.01%, polyA 97.83 ± 20.44%, 3pRNA 358.7 ± 118.9%, $n = 5$, $p < 0.05$). Together these *in vivo* data demonstrate that stimulation of RIG-I significantly impairs endothelial/vessel biology.

3.2. 3pRNA induced immune response in HCAEC effects cellular function

Our *in vivo* data highlight that vessel function is affected by RIG-I stimulation, specifically endothelial function seems to be the primary target. We therefore analyzed RIG-I activation in cultured human coronary artery endothelial cells. Receptor regulation is a widely used tool in signaling cascades allowing regulatory reactions to stimulation with specific ligands. HCAEC express RIG-I and stimulation leads to a receptor upregulation (Fig. 2A, B, vehicle 22.50 ± 0.50/1000 CPB transcripts, 3pRNA 186.00 ± 13.00/1000 CPB transcripts, $n = 5$, $p < 0.05$).

To test if HCAEC are immune competent we measured cytokine production upon RIG-I stimulation. HCAEC respond to stimulation with a significant release of IL-6 (Fig. 2C, vehicle 866.80 ± 69.71 pg/ml, 3pRNA 1342.00 ± 80.48 pg/ml, $n = 5$, $p < 0.05$) and IP-10 (Fig. 2C, vehicle 27.04 ± 27.04 pg/ml, 3pRNA 1493 ± 306.9 pg/ml, $n = 5$, $p < 0.05$). Vascular oxidative stress and apoptosis are essential aspects of inflammatory processes in the vessel wall. We therefore analyzed ROS formation and cell growth. RIG-I stimulation with 3pRNA leads to enhanced formation of ROS in HCAEC

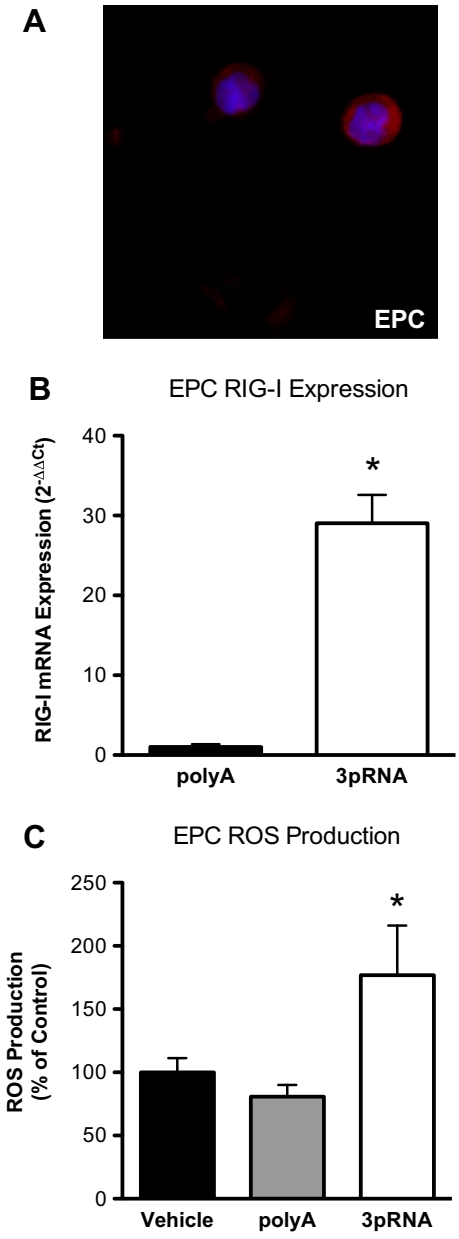

Fig. 3. EPC function is affected by RIG-I stimulation *in vitro*. (A, B) EPC express RIG-I and stimulation leads to significant receptor upregulation. (C) As with HCAEC, RIG-I stimulation also enhances ROS formation in EPC.

(Fig. 2D, vehicle 100 ± 14.82%, polyA 100 ± 20.5%, 3pRNA 217 ± 43.11%, $n = 5$, $p < 0.05$). In contrast, proliferation (Fig. 2E, vehicle 55.44 ± 2.539%, polyA 32.06 ± 2.54%, 3pRNA 37.98 ± 1.88%, $n = 5$, p = n.s.) and apoptosis (Fig. 2F, vehicle 98.33 ± 7.39%, polyA 100 ± 9.57%, 3pRNA 91.07 ± 7.54%, $n = 5$, p = n.s.) were not significantly affected by RIG-I activation.

3.3. Endothelial progenitor cell function is affected by RIG-I stimulation

Endothelial lesions are not only rejuvenated by healthy adjacent mature endothelial cells, but circulating EPC also contribute to endothelial healing. We therefore studied the number of circulating EPC in our mice treated with 3pRNA. Here, RIG-I activation did not substantially alter EPC numbers (vehicle 0.73 ± 0.17%, polyA 0.68 ± 0.18%, 3pRNA 0.80 ± 0.20%, $n = 5$, p = n.s.). Nevertheless, we studied whether EPC function may be affected *in vitro*. EPC express RIG-I and stimulation leads to significant receptor upregulation (Fig. 2A, B, poly A 1.16 ± 0.19 $2^{-\Delta\Delta Ct}$ vs. 3pRNA 33.84 ± 2.07 $2^{-\Delta\Delta Ct}$, $n = 5$, $p < 0.05$). Importantly, RIG-I stimulation also enhances ROS formation in EPC (Fig. 3B, vehicle 100 ± 11.1%, poly A 80.78 ± 9.92%, 3pRNA 176.8 ± 39.29%, $n = 5$, $p < 0.05$).

4. Discussion

The endothelium and specialized cells of the immune system such as macrophages/monocytes, dendritic cells and lymphocytes primarily drive the inflammatory atherosclerotic process. Recent evidence suggests that endothelial damage is not only mediated by cofactors but that endothelial cells themselves contribute to the vascular injury by overwhelming activation [22]. Which mechanisms induce this endothelial-mediated endothelial dysfunction are poorly understood. Here, we provide evidence that activation of the cytoplasmatic nucleic acid receptor RIG-I leads to endothelial dysfunction. RIG-I induced endothelial damage could therefore be an important pathway in atherogenesis.

RIG-I is generally known to mediate inflammation by detecting viral nucleic acids. However, there is rising evidence that beyond its function as an intracellular virus-sensor it is involved in chronic inflammatory processes such as rheumatoid arthritis, lupus nephritis and atherosclerosis. It has been reported, that RIG-I is highly expressed in intimal macrophages of atherosclerotic lesions, suggesting that RIG-I may be involved in the activation of macrophages during vascular inflammation [23]. Although viral fragments have been detected in atherosclerotic lesions [24] it seems unlikely that recurrent or chronic viral infections solely mediate atherogenesis. Evidence however suggests that besides double and single stranded viral RNA, also LPS, TNFα, interferons, Il-1β, oxidized cholesterol and even DNA from damaged senescent cells up-regulate RIG-I expression [14]. These protagonists of atherogenesis could therefore provide a fertile ground for viral RNA to aggravate vascular inflammation.

Our data show that RIG-I mediates endothelial damage and dysfunction directly and is associated with increased oxidative stress in both endothelial cells and endothelial progenitor cells. Interestingly, RIG-I had no profound effect on endothelial apoptosis although RIG-I was shown to enhance apoptosis in hepatoma [25] and melanoma cells [26]. This could be attributed to distinctive effects in different cell types. Furthermore RIG-I did not significantly alter numbers of circulating CAC whereas TLR3 recently was shown to cause both elevated endothelial apoptosis and to increase circulating EPC numbers [22]. Different PRR must therefore have distinctive impact on endothelial biology and we assume that the number of involved nucleic acid receptors is not restricted to TLR3 and RIG-I (i.e. MDA5 also impairs endothelial function, unpublished data of our group).

TLR3 and RIG-I activation leads to a release of proinflammatory cytokines, which enhance atherosclerotic processes and affect other cell types. TLR3 activation leads to elevated levels of IFN and RIG-I can be induced by IFN-γ in endothelial cells [27]. Interferons therefore may be considered a link between different PRR to mediate proinflammatory effects. IP-10 is released by monocytes, endothelial cells and fibroblasts in response to type I IFN [28]. IP-10 demonstrably has proatherosclerotic effects and IP-10 knockout mice display decreased atherosclerotic plaque formation [29]. Il-6 also is a player in the atherosclerotic cascade causing plaque development and plaque destabilization i.e. by oxidation of lipoproteins, release of prothrombic mediators and the activation of metalloproteinases [30].

Senescence is a major risk factor for atherosclerosis and oxidative stress is not only an important proatherosclerotic mechanism but also causes DNA damage. It has recently been demonstrated that RIG-I is induced by senescence associated DNA damage resulting in release of proinflammatory cytokines IL-6/8. This could be inhibited by the anti-aging protein Klotho by prohibiting the multimerization of the RIG-I CARD domain [31]. Therefore, anti-aging or anti-senescence therapies targeting the RIG-I pathways could be beneficial for vascular biology.

In summary, this study extends our knowledge on the immunological contribution of endothelial cells in vascular inflammation. Specific RIG-I activation greatly impairs endothelial function and could therefore become a target in the search for direct atherosclerotic treatment options. Further investigations are necessary to uncover the specific molecular mechanisms involved.

5. Funding sources

This study was supported by the medical faculty of the Rheinische Friedrich-Wilhelms-University Bonn (BONFOR).

6. Disclosures

None.

Acknowledgments

The excellent technical assistance of Catharina Peseke, Isabel Paez-Maletz, and Kathrin Paul is greatly appreciated.

References

[1] R. Ross, Atherosclerosis – an inflammatory disease, N. Engl. J. Med. 340 (1999) 115–126.
[2] C.J. Murray, A.D. Lopez, Alternative projections of mortality and disability by cause 1990–2020: global burden of disease study, Lancet 349 (1997) 1498–1504.
[3] G.K. Hansson, P. Libby, U. Schonbeck, Z.Q. Yan, Innate and adaptive immunity in the pathogenesis of atherosclerosis, Circ. Res. 91 (2002) 281–291.
[4] M.S. Lee, Y.J. Kim, Pattern-recognition receptor signaling initiated from extracellular, membrane, and cytoplasmic space, Mol. Cells 23 (2007) 1–10.
[5] Y. Shi, J.E. Evans, K.L. Rock, Molecular identification of a danger signal that alerts the immune system to dying cells, Nature 425 (2003) 516–521.
[6] L. Liu, I. Botos, Y. Wang, J.N. Leonard, J. Shiloach, D.M. Segal, D.R. Davies, Structural basis of toll-like receptor 3 signaling with double-stranded RNA, Science 320 (2008) 379–381.
[7] A. Pichlmair, O. Schulz, C.P. Tan, J. Rehwinkel, H. Kato, O. Takeuchi, S. Akira, M. Way, G. Schiavo, C. Reis e Sousa, Activation of MDA5 requires higher-order RNA structures generated during virus infection, J. Virol. 83 (2009) 10761–10769.
[8] H. Hemmi, O. Takeuchi, T. Kawai, T. Kaisho, S. Sato, H. Sanjo, M. Matsumoto, K. Hoshino, H. Wagner, K. Takeda, S. Akira, A Toll-like receptor recognizes bacterial DNA, Nature 408 (2000) 740–745.
[9] A. Takaoka, Z. Wang, M.K. Choi, H. Yanai, H. Negishi, T. Ban, Y. Lu, M. Miyagishi, T. Kodama, K. Honda, Y. Ohba, T. Taniguchi, DAI (DLM-1/ZBP1) is a cytosolic DNA sensor and an activator of innate immune response, Nature 448 (2007) 501–505.

[10] F. Heil, H. Hemmi, H. Hochrein, F. Ampenberger, C. Kirschning, S. Akira, G. Lipford, H. Wagner, S. Bauer, Species-specific recognition of single-stranded RNA via toll-like receptor 7 and 8, Science 303 (2004) 1526–1529.

[11] V. Hornung, J. Ellegast, S. Kim, K. Brzozka, A. Jung, H. Kato, H. Poeck, S. Akira, K.K. Conzelmann, M. Schlee, S. Endres, G. Hartmann, 5′-Triphosphate RNA is the ligand for RIG-I, Science 314 (2006) 994–997.

[12] M. Schlee, A. Roth, V. Hornung, C.A. Hagmann, V. Wimmenauer, W. Barchet, C. Coch, M. Janke, A. Mihailovic, G. Wardle, S. Juranek, H. Kato, T. Kawai, H. Poeck, K.A. Fitzgerald, O. Takeuchi, S. Akira, T. Tuschl, E. Latz, J. Ludwig, G. Hartmann, Recognition of 5' triphosphate by RIG-I helicase requires short blunt double-stranded RNA as contained in panhandle of negative-strand virus, Immunity 31 (2009) 25–34.

[13] M.S. Lee, Y.J. Kim, Signaling pathways downstream of pattern-recognition receptors and their cross talk, Annu. Rev. Biochem. 76 (2007) 447–480.

[14] F. Liu, J. Gu, Retinoic acid inducible gene-I more than a virus sensor, Protein Cell 2 351-357.

[15] V. Schachinger, M.B. Britten, A.M. Zeiher, Prognostic impact of coronary vasodilator dysfunction on adverse long-term outcome of coronary heart disease, Circulation 101 (2000) 1899–1906.

[16] S. Wassmann, N. Werner, T. Czech, G. Nickenig, Improvement of endothelial function by systemic transfusion of vascular progenitor cells, Circ. Res. 99 (2006) e74–83.

[17] D.P. Sieveking, A. Buckle, D.S. Celermajer, M.K. Ng, Strikingly different angiogenic properties of endothelial progenitor cell subpopulations: insights from a novel human angiogenesis assay, J. Am. Coll. Cardiol. 51 (2008) 660–668.

[18] K. Walenta, E.B. Friedrich, F. Sehnert, N. Werner, G. Nickenig, *In vitro* differentiation characteristics of cultured human mononuclear cells-implications for endothelial progenitor cell biology, Biochem. Biophys. Res. Commun. 333 (2005) 476–482.

[19] S. Wassmann, M. Stumpf, K. Strehlow, A. Schmid, B. Schieffer, M. Bohm, G. Nickenig, Interleukin-6 induces oxidative stress and endothelial dysfunction by overexpression of the angiotensin II type 1 receptor, Circ. Res. 94 (2004) 534–541.

[20] N. Werner, J. Priller, U. Laufs, M. Endres, M. Bohm, U. Dirnagl, G. Nickenig, Bone marrow-derived progenitor cells modulate vascular reendothelialization and neointimal formation: effect of 3-hydroxy-3-methylglutaryl coenzyme a reductase inhibition, Arterioscler. Thromb. Vasc. Biol. 22 (2002) 1567–1572.

[21] F. Custodis, M. Baumhakel, N. Schlimmer, F. List, C. Gensch, M. Bohm, U. Laufs, Heart rate reduction by ivabradine reduces oxidative stress, improves endothelial function, and prevents atherosclerosis in apolipoprotein E-deficient mice, Circulation 117 (2008) 2377–2387.

[22] S. Zimmer, M. Steinmetz, T. Asdonk, I. Motz, C. Coch, E. Hartmann, W. Barchet, S. Wassmann, G. Hartmann, and G. Nickenig, Activation of endothelial toll-like receptor 3 impairs endothelial function. Circ. Res. 108 1358–1366.

[23] T. Imaizumi, N. Yagihashi, K. Kubota, H. Yoshida, H. Sakaki, S. Yagihashi, H. Kimura, K. Satoh, Expression of retinoic acid-inducible gene-I (RIG-I) in macrophages: possible involvement of RIG-I in atherosclerosis, J. Atheroscler. Thromb. 14 (2007) 51–55.

[24] M.G. Hendrix, M.M. Salimans, C.P. van Boven, C.A. Bruggeman, High prevalence of latently present cytomegalovirus in arterial walls of patients suffering from grade III atherosclerosis, Am. J. Pathol. 136 (1990) 23–28.

[25] S. Peng, J. Geng, R. Sun, Z. Tian, H. Wei, Polyinosinic-polycytidylic acid liposome induces human hepatoma cells apoptosis which correlates to the up-regulation of RIG-I like receptors, Cancer Sci. 100 (2009) 529–536.

[26] M. Pan, S. Geng, S. Xiao, J. Ren, Y. Liu, X. Li, Z. Li, Z. Peng, Apoptosis induced by synthetic retinoic acid CD437 on human melanoma A375 cells involves RIG-I pathway, Arch. Dermatol. Res. 301 (2009) 15–20.

[27] T. Imaizumi, M. Hatakeyama, K. Yamashita, H. Yoshida, A. Ishikawa, K. Taima, K. Satoh, F. Mori, K. Wakabayashi, Interferon-gamma induces retinoic acid-inducible gene-I in endothelial cells, Endothelium 11 (2004) 169–173.

[28] A.D. Luster, J.C. Unkeless, J.V. Ravetch, Gamma-interferon transcriptionally regulates an early-response gene containing homology to platelet proteins, Nature 315 (1985) 672–676.

[29] E.A. Heller, E. Liu, A.M. Tager, Q. Yuan, A.Y. Lin, N. Ahluwalia, K. Jones, S.L. Koehn, V.M. Lok, E. Aikawa, K.J. Moore, A.D. Luster, R.E. Gerszten, Chemokine CXCL10 promotes atherogenesis by modulating the local balance of effector and regulatory T cells, Circulation 113 (2006) 2301–2312.

[30] H. Schuett, M. Luchtefeld, C. Grothusen, K. Grote, B. Schieffer, How much is too much? Interleukin-6 and its signalling in atherosclerosis, Thromb. Haemost. 102 (2009) 215–222.

[31] F. Liu, S. Wu, H. Ren, J. Gu, Klotho suppresses RIG-I-mediated senescence-associated inflammation. Nat. Cell. Biol. 13 254–262.

Biochemical and Biophysical Research Communications 420 (2012) 72–77

Contents lists available at SciVerse ScienceDirect

Biochemical and Biophysical Research Communications

journal homepage: www.elsevier.com/locate/ybbrc

Interleukin-17 deficiency reduced vascular inflammation and development of atherosclerosis in Western diet-induced apoE-deficient mice

Fumitake Usui [a], Hiroaki Kimura [a], Taichi Ohshiro [b], Kazuki Tatsumi [a], Akira Kawashima [a], Akiyo Nishiyama [a], Yo-ichiro Iwakura [c], Shun Ishibashi [b], Masafumi Takahashi [a,*]

[a] Division of Bioimaging Sciences, Center for Molecular Medicine, Japan
[b] Division Endocrine and Metabolism, Jichi Medical University, Tochigi, Japan
[c] Institute of Medical Science, University of Tokyo, Tokyo, Japan

ARTICLE INFO

Article history:
Received 14 February 2012
Available online 28 February 2012

Keywords:
Atherosclerosis
Cytokines
Diet
Inflammation
Macrophages

ABSTRACT

Objective: Several reports describe the role of interleukin (IL)-17 in the development of atherosclerosis; however, its precise role remains controversial. We generated double-deficient mice for apolipoprotein E (apoE) and IL-17 (apoE$^{-/-}$IL-17$^{-/-}$ mice) and investigated the effect of IL-17 deficiency on vascular inflammation and atherosclerosis.

Methods and results: Atherosclerotic plaque areas in apoE$^{-/-}$IL-17$^{-/-}$ mice fed a Western diet (WD) were significantly reduced compared with those in apoE$^{-/-}$ mice. No significant differences in plasma lipid profiles were observed between apoE$^{-/-}$ and apoE$^{-/-}$IL-17$^{-/-}$ mice. The number of infiltrated macrophages in the plaques was significantly decreased in WD-fed apoE$^{-/-}$IL-17$^{-/-}$ mice compared with WD-fed apoE$^{-/-}$ mice, whereas vascular smooth muscle cell content was not altered by IL-17 deficiency. Expression of inflammatory cytokines (MCP-1, IL-1β, IL-6, IFN-γ, and IL-12 p40) and scavenger receptors (Msr-1, Scarb1, and Olr1) in the plaques was inhibited in WD-fed apoE$^{-/-}$IL-17$^{-/-}$ mice. Furthermore, expression of inducible nitric oxide (M1 marker) and arginase-1 (M2 marker) was inhibited in WD-fed apoE$^{-/-}$IL-17$^{-/-}$ mice.

Conclusion: Our results indicate that IL-17 deficiency reduces vascular inflammation and atherosclerosis and that modulation of IL-17 could be a potential target for prevention and treatment of atherosclerosis.

1. Introduction

Atherosclerosis is a chronic inflammatory disease characterized by plaques containing lipid deposition, leukocyte infiltration, and vascular smooth muscle cell (VSMC) proliferation. The most prominent cells in the plaques are macrophages, but a substantial number of T cells are also detected. When these cells infiltrate into the plaques, they can secrete a number of inflammatory cytokines and participate in the various phases of immune and inflammatory responses in the pathogenesis of atherosclerosis. A new subset of effector CD4$^+$ T cells that produce interleukin (IL)-17 (named Th17 cells) was recently identified and characterized [1–4]. Thus far, 6 IL-17 family members have been identified as IL-17A through IL-17F. Of these, IL-17A (hereafter referred to as IL-17) is the most widely investigated. Much attention has been given to IL-17 and Th17 cells involved in multiple forms of inflammatory and autoimmune diseases.

The presence of IL-17 has been demonstrated in human and experimental atherosclerotic plaques, and IL-17 could play a role in the pathogenesis of atherosclerosis [5–7]. For instance, several investigations reported that IL-17 inhibition with neutralizing antibody reduced atherosclerotic plaques in mice, concluding that IL-17 is an atherogenic factor [5–9]. Conversely, Taleb et al. [10] unexpectedly observed an atheroprotective role of IL-17. Although the reason for this discrepancy is unclear, it may have been caused by the experimental models and methods of IL-17 inhibition [11]. Thus, the distinct role of IL-17 in the development of atherosclerosis is still controversial. Apolipoprotein E-deficient (apoE$^{-/-}$) mice exhibit severe hypercholesterolemia and are an excellent model of human atherosclerosis [12]. In the present study, we generated mice double-deficient for apoE and IL-17 (apoE$^{-/-}$IL-17$^{-/-}$ mice) and investigated the effect of IL-17 deficiency on the development of atherosclerosis and vascular inflammation. We showed that IL-17 deficiency reduced the extent of atherosclerotic plaques in apoE$^{-/-}$ mice fed a Western diet (WD). The findings obtained from this study demonstrate the critical role played by IL-17 in the development of moderate atherosclerosis and provide a new insight into the role of IL-17 in the pathogenesis of atherosclerosis.

* Corresponding author. Address: Division of Bioimaging Sciences, Center for Molecular Medicine, Jichi Medical University, 3311-1 Yakushiji, Shimotsuke, Tochigi 329-0498, Japan. Fax: +81 285 44 5365.
E-mail address: masafumi2@jichi.ac.jp (M. Takahashi).

0006-291X/$ - see front matter © 2012 Elsevier Inc. All rights reserved.
doi:10.1016/j.bbrc.2012.02.117

2. Materials and methods

2.1. Experimental animals and development of mild and moderate atherosclerotic plaques

All experiments in this study were performed in accordance with the Jichi Medical University Guide for Laboratory Animals. C57BL/6 mice (male, 8 weeks old) and apoE$^{-/-}$ mice (C57BL/6 background) were purchased from Clea Japan (Tokyo, Japan) and The Jackson Laboratory (Bar Harbor, ME), respectively. IL-17$^{-/-}$ mice (C57BL/6 background) were generated as previously described [1], and double-deficient (apoE$^{-/-}$IL-17$^{-/-}$) mice were generated from the mating of these mice. The mice were fed and watered, and maintained on a 12-h light and dark cycle. Mild, moderate, and severe atherosclerotic plaques were developed when the apoE$^{-/-}$ mice (male, 8 weeks old) were fed a standard diet (SD; CE-2, Clea Japan), WD (0.21% cholesterol without sodium cholate; D12079B, Research Diets, NJ), and Paigen diet (PD; 1.25% cholesterol with 0.5% sodium cholate; D12336, Research Diets) [13], respectively, for 12 weeks.

2.2. Plasma lipid analyses

Plasma levels of total cholesterol (TC), triglycerides (TGs), and nonesterified fatty acids (NEFA) after a 16-h fast were determined using colorimetric enzyme assay kits (Kyowa Medex Co., Ltd. for TC, and Wako Chemicals [Osaka, Japan] for TG and NEFA), according to the manufacturers' instructions.

2.3. Assessment of atherosclerosis in the aortas and aortic sinus

After the mice were euthanized, the aortas were excised and adventitial fat was removed. Aortas were the fixed in phosphate-buffered saline (PBS) containing 10% (w/v) formalin (Wako Chemicals). Whole aortas were opened longitudinally from the aortic arch to the iliac bifurcation, mounted *en face*, and stained for lipids with Sudan IV (Wako Chemicals) as previously described [14]. The extent of atherosclerotic areas was expressed as the percentage of lesion area in the entire aortic surface area. The hearts, perfused with PBS containing 10% (w/v) formalin, were embedded in Tissue-Tek O.C.T. compound (Sakura Finetechnical Co., Ltd., Tokyo, Japan), and 6-μm thick serial sections were cut using a cryostat (Leica CM1850; Leica Microsystems, Germany). The cross-sections of the aortic sinus were stained with Oil Red O (Sigma) and hematoxylin (Wako Chemicals). Quantification of average lesion area was performed from 10 sections stained with Oil Red O from each mouse. Images for atherosclerotic plaque areas were captured using the Leica Application Suite software (ver. 3.4.1, Leica Microsystems) and analyzed with the Adobe Photoshop CS4 software (Adobe Systems Inc., CA).

To assess macrophage infiltration and VSMC content, immunohistochemical analysis was performed. Briefly, the sections were incubated with primary antibody to mouse macrophage marker MOMA-2 (AbD Serotec, Raleigh, NC) and smooth muscle cell marker α-smooth muscle actin (α-SMA; clone 1A4, Sigma, St. Louis, MO) [15]. This was followed by incubation with biotin-conjugated secondary antibodies. Next, the sections were washed and treated with avidin–peroxidase (ABC kit; Vector Laboratories, Burlingame, CA). The reaction was developed using a DAB substrate kit (Vector Laboratories). The sections were then counterstained with hematoxylin. No signals were detected when an irrelevant IgG (Vector Laboratories) was used instead of the primary antibody as a negative control. All measurements were conducted in a double-blind manner by two independent researchers.

2.4. Real-time reverse transcription-polymerase chain reaction

Total RNA was prepared from the aortas using ISOGEN (Nippon Gene Co., Ltd., Toyama, Japan), according to the manufacturer's instructions. Real-time reverse transcription-polymerase chain reaction (RT-PCR) analysis was performed using the Takara TP960 PCR Thermal Cycler Dice Detection System (Takara Bio Inc., Shiga, Japan) to detect mRNA expression of IL-1β, IL-6, IL-12 p40, interferon (IFN)-γ, monocyte chemoattractant protein-1 (MCP-1, also known as CC chemokine ligand [CCL] 2), macrophage inflammatory protein-1β (MIP-1β, also known as CCL4), macrophage scavenger receptor 1 (Msr1, also known as SR-A, Scara1, and CD204), scavenger receptor class B member 1 (Scarb1, also known as SR-BI and CD36L1), oxidized low-density lipoprotein receptor (LDL-R)-1 (Olr-1, also known as LOX-1), inducible nitric oxide synthase (iNOS), arginase-1 (Arg-1), and β-actin [16]. Primers used in this study are described in Supplementary Table I. Expression levels of each target gene were normalized by subtracting the corresponding β-actin threshold cycle (CT) values; normalization was carried out using the $\Delta\Delta C_T$ comparative method.

2.5. In vitro experiments

Murine RAW264.7 macrophage cells were obtained from RIKEN Gene Bank (Tsukuba, Japan) and cultured in Dulbecco's modified Eagle's medium (Sigma) supplemented with 10% fetal bovine serum (Dainippon Pharmaceutical Co., Osaka, Japan). After serum starvation for 16 h, the cells were treated with or without recombinant murine IL-17 (PeproTech Inc., Rocky Hill, NJ) for 4 h and analyzed.

2.6. Statistical analyses

Data are expressed as mean ± standard error of the mean (SEM). An unpaired *t* test was used to compare two groups. For comparisons between multiple groups, the significance of differences between group means was determined by 1-way analysis of variance (ANOVA) combined with the Turkey–Kramer test. All analyses were performed using the GraphPad Prism Software (ver. 4, San Diego, CA). A *p*-value of <0.05 was considered to be statistically significant.

3. Results

3.1. Effect of IL-17 deficiency on development of mild and moderate atherosclerosis

We investigated whether IL-17 deficiency could influence development of mild (apoE$^{-/-}$ mice fed SD), moderate (apoE$^{-/-}$ mice fed WD), and severe atherosclerosis (apoE$^{-/-}$ mice fed Paigen diet). Sudan IV staining demonstrated that atherosclerotic plaque areas in whole aortas of WD-fed apoE$^{-/-}$IL-17$^{-/-}$ mice were significantly reduced compared with those in WD-fed apoE$^{-/-}$ mice ($p < 0.0003$) (Fig. 1A and B). Plaque areas of SD-fed apoE$^{-/-}$IL-17$^{-/-}$ mice also tended to be reduced compared with those in SD-fed apoE$^{-/-}$ mice. In the mice were fed Paigen diet, severe atherosclerotic plaques were observed. Furthermore, there was no significant difference of plaque areas between PD-fed apoE$^{-/-}$ and apoE$^{-/-}$IL-17$^{-/-}$ mice (Fig. 1A and B). Cross-sections of aortic sinuses stained with Oil Red O showed a significant reduction of plaques in WD-fed apoE$^{-/-}$ IL-17$^{-/-}$ mice compared with WD-fed apoE$^{-/-}$ mice ($p < 0.0001$) (Fig. 1C and D).

Progression of atherosclerosis is affected by lipid metabolism. We therefore determined the plasma levels of TC, NEFA, and TG. Although the concentration of plasma TC (but neither NEFA nor TG) was considerably increased in WD-fed apoE$^{-/-}$ mice compared

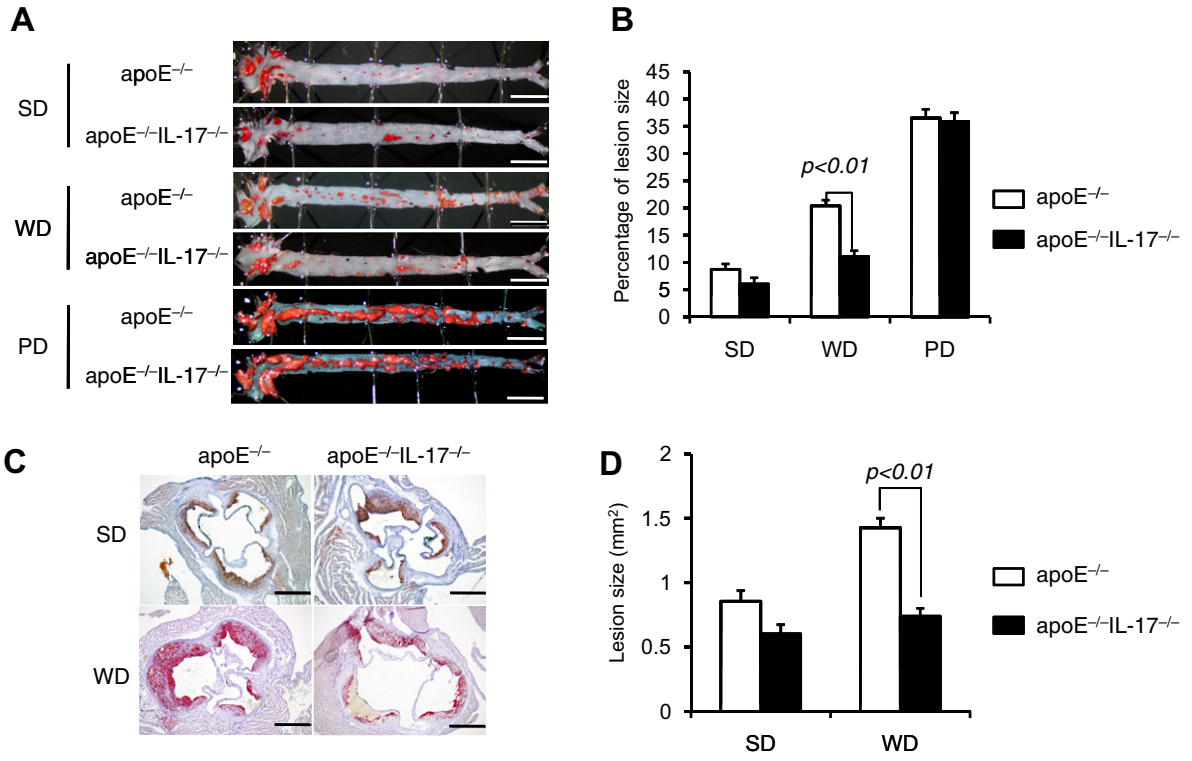

Fig. 1. Effect of IL-17 deficiency on development of mild and moderate atherosclerosis. ApoE$^{-/-}$ and apoE$^{-/-}$IL-17$^{-/-}$ mice were fed a SD, WD, and PD for 12 weeks. (A and B) Whole aortas were stained with Sudan IV. Representative photographs (A) and percentage (B) of atherosclerotic plaque areas are shown. Data are expressed as mean ± SEM (SD, $n = 9$; WD, $n = 11$; PD, $n = 10$ for each). (C and D) Cross-sections of aortic sinuses were stained with Oil Red O. Representative photographs (C) and quantitative plaque areas (D) are shown. Data are expressed as mean ± SEM ($n = 5$ for each).

with SD-fed apoE$^{-/-}$ mice (apoE$^{-/-}$ mice: TC in SD-fed, 359.0 ± 112.6 mg/dL, and TC in WD-fed, 959.8 ± 57.6 mg/dL, $p < 0.0001$; NEFA and TG, data not shown), there were no significant differences in the plasma TC level between apoE$^{-/-}$ and apoE$^{-/-}$IL-17$^{-/-}$ mice (apoE$^{-/-}$IL-17$^{-/-}$ mice: TC in SD-fed, 340.1 ± 57.2 mg/dL, TC in WD-fed, 1170.1 ± 305.7 mg/dL; n.s. vs apoE$^{-/-}$ mice).

3.2. Effect of IL-17 deficiency on macrophage infiltration and VSMC content

We next examined the effect of IL-17 deficiency on macrophage infiltration (MOMA-2) and VSMC content (αSMA) in plaques by immunohistochemical analysis. Marked infiltration of macrophages was detected in the plaques of WD-fed apoE$^{-/-}$ mice (Fig. 2A and B). However, infiltration was significantly reduced in WD-fed apoE$^{-/-}$IL-17$^{-/-}$ mice compared with WD-fed apoE$^{-/-}$ mice ($p < 0.0001$). Furthermore, there was no significant difference in the VSMC content of the plaques between apoE$^{-/-}$ and apoE$^{-/-}$IL-17$^{-/-}$ mice (Fig. 2C and D).

3.3. Effect of IL-17 deficiency on inflammatory cytokine expression

Infiltrated macrophages in plaques secrete inflammatory cytokines that contribute to the development of atherosclerosis. Quantitative RT-PCR analysis revealed that expression of MCP-1 (CCL2), IL-1β, IL-6, IFN-γ, and IL-12 p40, but not MIP-1β (CCL4), was significantly inhibited in the plaques of WD-fed apoE$^{-/-}$ IL-17$^{-/-}$ mice compared with WD-fed apoE$^{-/-}$ mice (MCP-1, $p < 0.0001$; IL-1β, $p = 0.0006$; IL-6, $p = 0.0055$; IFN-γ, $p = 0.0070$; IL-12 p40, $p = 0.0016$) (Fig. 3A). In particular, complete inhibition of IL-12 p40 expression was detected in the plaques of apoE$^{-/-}$ IL-17$^{-/-}$ mice. *In vitro* experiments using murine RAW 264.7 macrophages expressing IL-17 receptor (data not shown) showed that IL-17 stimulated the expression of IL-12 p40 and IL-6, but it do not stimulate the expression of IL-1β and MCP-1 (Fig. 3B).

3.4. Effect of IL-17 deficiency on SR expression and M1/M2 polarization

To further explore the possible role of IL-17 in macrophage function in atherosclerotic plaques, we examined the expression of SRs and M1/M2 polarization. Expression of Msr-1, Scarb1, and Olr1 was significantly inhibited in the plaques of WD-fed apoE$^{-/-}$IL-17$^{-/-}$ mice compared with WD-fed apoE$^{-/-}$ mice (Msr-1, $p = 0.0029$; Scarb1, $p = 0.0076$; and Olr1, $p = 0.0036$) (Fig. 4A). Similarly, expression of both iNOS (M1 marker) and Arg-1 (M2 marker) was significantly inhibited in the plaques of WD-fed apoE$^{-/-}$IL-17$^{-/-}$ mice (iNOS, $p = 0.0002$; Arg-1, $p < 0.0001$) (Fig. 4B). In addition, the expression ratio of M2/M1 was almost completely decreased in apoE$^{-/-}$IL-17$^{-/-}$ mice.

4. Discussion

The major findings of this study are as follows: (1) IL-17 deficiency reduced the extent of atherosclerotic plaques in apoE$^{-/-}$ mice fed the WD (moderate atherosclerosis), but not in apoE$^{-/-}$ mice fed the PD (severe atherosclerosis); (2) no significant differences in plasma lipid levels were observed between apoE$^{-/-}$ and apoE$^{-/-}$IL-17$^{-/-}$ mice; (3) IL-17 deficiency reduced macrophage infiltration but not VSMC content in plaques in apoE$^{-/-}$ mice fed the WD; (4) IL-17 deficiency inhibited expression of MCP-1, IL-1β, IL-6, IFN-γ, and IL-12 p40, but not MIP-1β, in plaques; (5) *in vitro* experiments using a murine macrophage cell line showed that IL-17 induced the expression of IL-12 p40 and IL-6; (6) IL-17 deficiency inhibited the expression of SRs (Msr-1, Scarb1, and

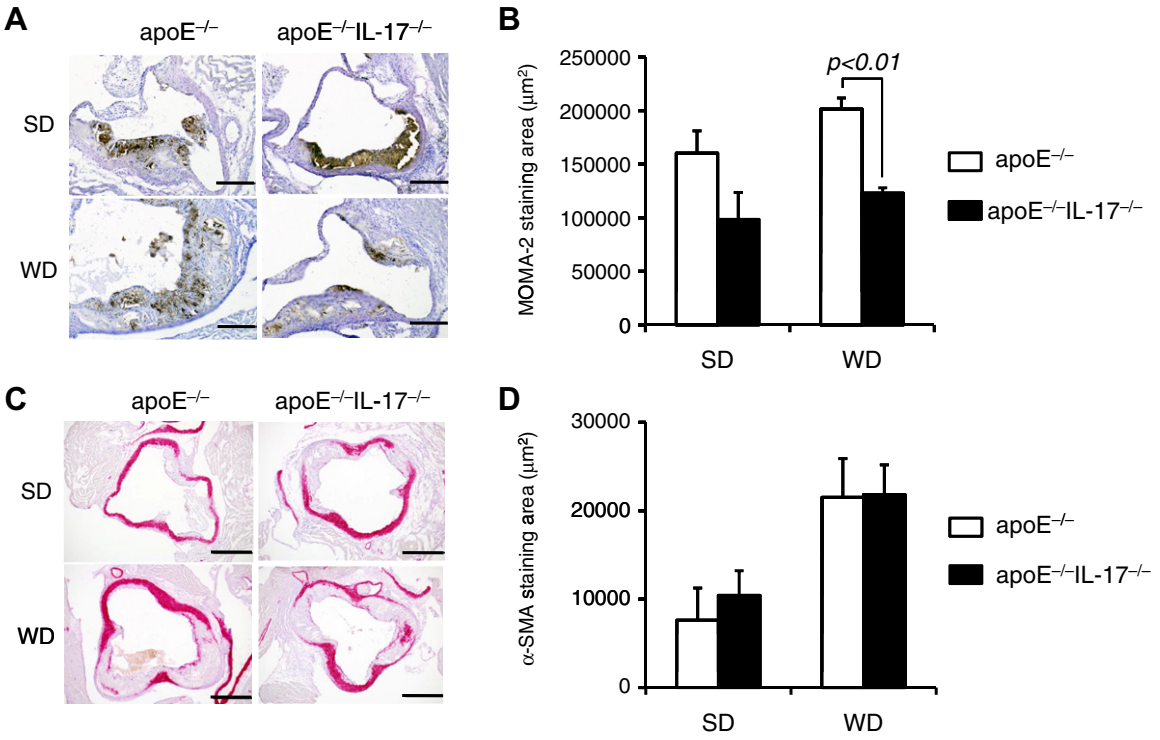

Fig. 2. Effect of IL-17 deficiency on macrophage infiltration and VSMC content. ApoE$^{-/-}$ and apoE$^{-/-}$IL-17$^{-/-}$ mice were fed SD and WD for 12 weeks. Cross-sections of aortic sinuses were immunochemically stained to identify macrophages (MOMA-2) and VSMCs (α-SMA). Representative photographs of infiltrated macrophages (A) and VSMC content (C) are shown. Quantitative analyses were performed ((B) for macrophages and (D) for VSMCs). Data are expressed as mean ± SEM (n = 5 for each).

Olr1), iNOS (M1 marker), and Arg-1 (M2 marker). These findings suggest that IL-17 plays inflammatory and atherogenic roles in a murine model of atherosclerosis induced by hypercholesterolemia. Despite the fact that several reports have described the role of IL-17 in the pathogenesis of atherosclerosis, its precise role remains unclear. Therefore, the findings of this study provide new insight into the role of IL-17 in vascular inflammation and atherosclerosis.

While IL-17 is known to be an inflammatory cytokine; it has been shown to exert pleiotropic effects and has been implicated in autoimmune and inflammatory diseases [2,4]. IL-17 has been extensively studied in experimental models of inflammatory bowel disease and is suggested to have protective and promotional roles in inflammatory responses in the intestine [17–19]. Similarly, the role of IL-17 in the development of atherosclerosis remains controversial. Recent investigations in which IL-17 was blocked suggested that inhibition of IL-17 induced atherosclerosis to a lesser extent in apoE$^{-/-}$ mice [6,7,9]. In contrast, Taleb et al. [10] recently reported that administration of recombinant IL-17 inhibited formation of atherosclerotic plaques in LDLR$^{-/-}$ mice, whereas administration of neutralizing antibody against IL-17 did not alter plaque formation. Furthermore, during preparation of this manuscript, Madhur et al. [11] reported that IL-17 deficiency had no effect on atherosclerotic plaque areas in apoE$^{-/-}$ mice fed a high-fat diet for 3 months, whereas it decreased inflammatory responses determined by macrophages and T cells. They further showed that IL-17 deficiency had no effect on plaque formation induced by angiotensin II infusion and carotid ligation in apoE$^{-/-}$ mice. Although an experimental model similar to ours, their results differed from those of the present study, which showed inhibition of plaque formation by IL-17 deficiency. The difference between our study and Madhur's study is diet: we used a WD that contained 0.21% cholesterol without sodium cholate and that is widely used with apoE$^{-/-}$ mice, whereas Madhur et al. [11] used a highly atherogenic diet, known as PD [13], that contained 1.25% high cholesterol and 0.5% sodium cholate. Therefore, we hypothesized that the diet used in each study may influence the anti-atherogenic effect of IL-17 deficiency. To confirm this idea, we examined the effect of IL-17 deficiency on atherosclerotic plaques in the PD-fed apoE$^{-/-}$ mice. Consistent with Madhur's study, IL-17 deficiency could not prevent the development of atherosclerotic plaques. In fact, Lichtman et al. [20] reported that the LDLR$^{-/-}$ mice fed the PD for 3 months showed a greater amount of atherosclerotic plaques than did mice fed the WD. Thus, we speculate that the protective effects of IL-17 on atherosclerosis are masked by severe atherosclerotic conditions and that the discrepancy in atherosclerotic development is mainly due to differences in the diet. In support of this idea, Madhur et al. [11] demonstrated that, similar to our study, IL-17 deficiency clearly inhibited infiltration of leukocytes into plaques. Taken together, IL-17 contributes to the development of atherosclerosis, but its effect depends on the states of immune and inflammatory responses as well as specific disease models.

We showed that IL-17 deficiency decreased expression of inflammatory cytokines, such as MCP-1, IL-1β, IL-6, IFN-γ, and IL-12 p40, in atherosclerotic plaques. The *in vitro* experiments revealed that IL-17 induced expression of IL-12 p40 and IL-6, suggesting that IL-17 might act as an upstream molecule for IL-12 and IL-6. In particular, previous studies demonstrated that IL-12 played a key role in progression of atherosclerosis in apoE$^{-/-}$ mice and that IL-12 produced by macrophages in plaques is important for both preferential Th1 differentiation of T cells and humoral responses by switching of the immunoglobulin isotype [21,22]. This suggests that the atherogenic effect of IL-17 in apoE$^{-/-}$ mice is mediated through IL-12. We also showed that IL-17 deficiency decreased expression of SRs and influenced M1/M2 polarization in plaque macrophages. It is widely accepted that uptake of modified lipoproteins by SRs plays a crucial role in foam cell formation in plaque

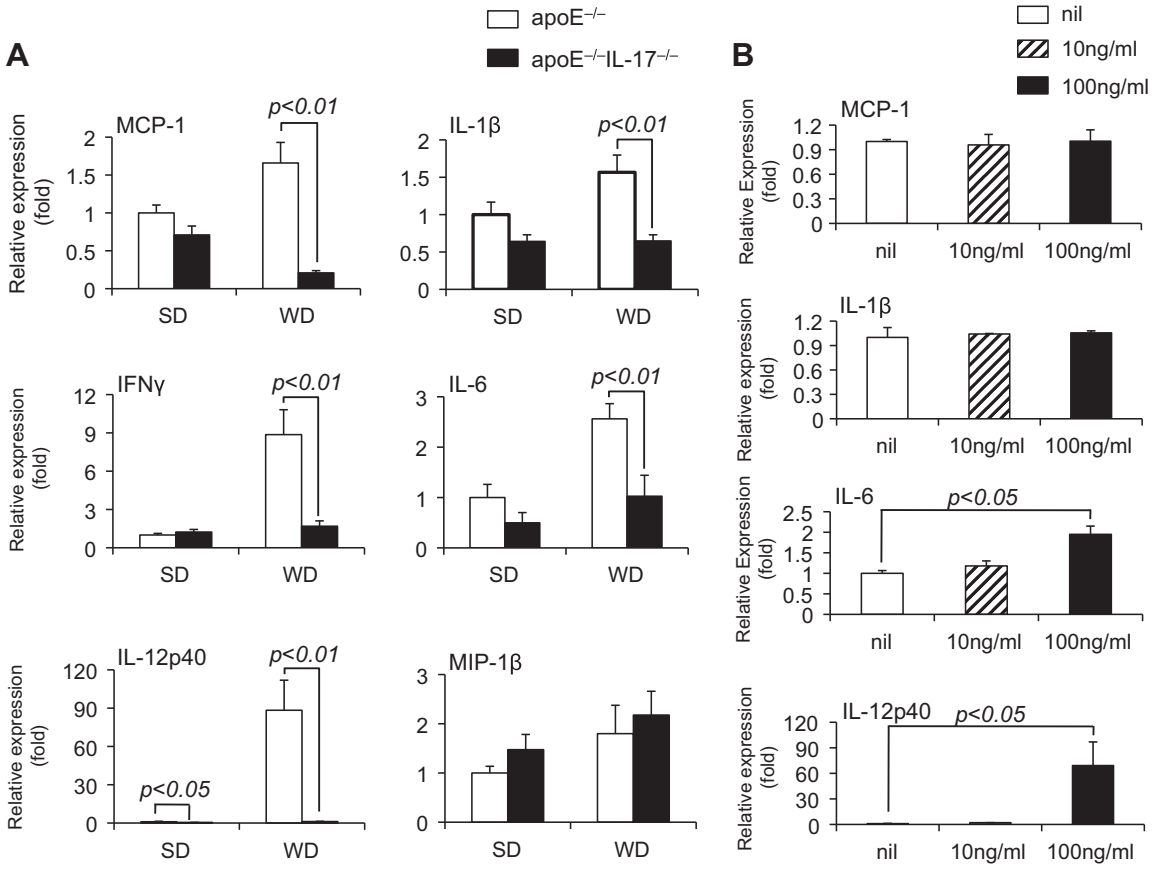

Fig. 3. Effect of IL-17 deficiency on inflammatory cytokine expression. ApoE$^{-/-}$ and apoE$^{-/-}$IL-17$^{-/-}$ mice were fed a SD and WD for 12 weeks. (A) Total RNA was prepared from atherosclerotic aortas and analyzed by real-time RT-PCR to determine mRNA expression levels of MCP-1, IL-1β, IL-6, IFN-γ, IL-12 p40, and MIP-1β. Quantitative analyses were performed. Data are expressed as mean ± SEM (n = 4 for apoE$^{-/-}$ and n = 5 for apoE$^{-/-}$IL-17$^{-/-}$ mice). (B) Murine RAW264.7 macrophage cells were treated with IL-17 for 4 h at the concentration indicated. Total RNA was prepared and analyzed by real-time RT-PCR. Quantitative analyses of mRNA expression levels of MCP-1, IL-1β, IL-6, and IL-12 p40 were performed. Data are expressed as mean ± SEM (n = 3 for each).

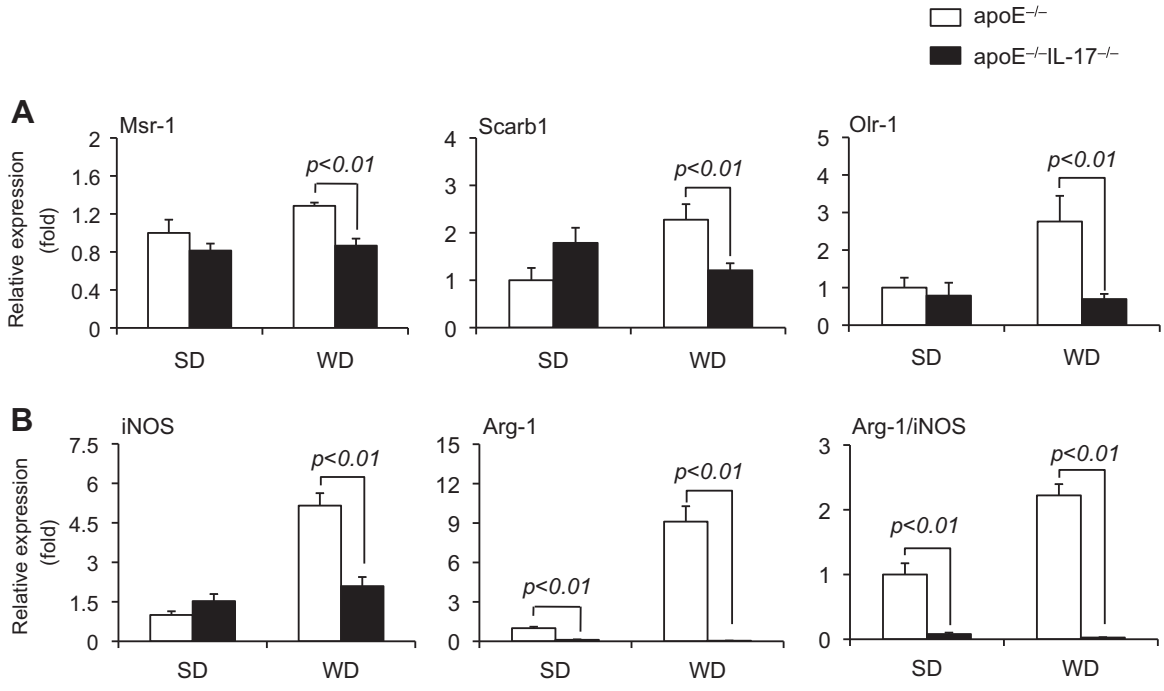

Fig. 4. Effect of IL-17 deficiency on SR expression and M1/M2 polarization. apoE$^{-/-}$ and apoE$^{-/-}$IL-17$^{-/-}$ mice were fed a SD and WD for 12 weeks. Total RNA was prepared from atherosclerotic aortas and analyzed by real-time RT-PCR to determine mRNA expression levels of SRs (A: Msr-1, Scarb1, and Olr-1) and M1/M2 markers (B: iNOS for M1 and Arg-1 for M2). Quantitative analyses were performed. Data are expressed as mean ± SEM (n = 4 for apoE$^{-/-}$ and n = 5 for apoE$^{-/-}$IL-17$^{-/-}$ mice).

macrophages [23]. Furthermore, Khallou-Laschet et al. [24] reported that an M2 macrophage phenotype that favors proliferation of VSMCs was predominant in the early stages (20 weeks) of plaques in apoE$^{-/-}$ mice. In the present study, IL-17 deficiency decreased the ratio of M2/M1 macrophages in apoE$^{-/-}$ mice, suggesting that IL-17 has a potential role in M1/M2 polarization in macrophages. Taken together, IL-17 shows a pleiotropic function as previously described and contributes to the development of atherosclerosis. Further, investigations are required to elucidate the precise mechanisms underlying the role of IL-17 in the development of atherosclerosis.

In conclusion, we have demonstrated that IL-17 deficiency reduced infiltration of macrophages, expression of inflammatory cytokines, and progression of atherosclerosis in apoE$^{-/-}$ mice fed WD. There are conflicting data on whether IL-17 exerts pro-atherogenic or athero-protective effects in the development of atherosclerosis. In particular, our data revealed that contribution of IL-17 to atherosclerotic plaque development could be considerably affected by diet. Our results indicate the importance of IL-17 in the pathogenesis of atherosclerosis and that modulation of IL-17 could possibly be a potential target for prevention and treatment of atherosclerosis.

5. Conflict of Interest

None.

Acknowledgments

We thank Sumiyo Watanabe, Masako Sakurai, Yumi Ohde, and Namiko Nakada for their excellent technical assistance. This study was granted by the Japan Society for the Promotion of Science (JSPS) through the "Funding Program for Next Generation World-Leading Researchers (NEXT Program)," initiated by the Council for Science and Technology Policy (CSTP) (to M.T.), the Vehicle Racing Commemorative Foundation (to M.T.), the Daiichi-Sankyo Foundation of Life Science (to M.T.), and Grant-in-Aid for Research Activity Start-up (to F.U.) and Banyu Life Science Foundation International (to F.U.).

Appendix A. Supplementary data

Supplementary data associated with this article can be found, in the online version, at doi:10.1016/j.bbrc.2012.02.117.

References

[1] S. Nakae, Y. Komiyama, A. Nambu, K. Sudo, M. Iwase, I. Homma, K. Sekikawa, M. Asano, Y. Iwakura, Antigen-specific T cell sensitization is impaired in IL-17-deficient mice, causing suppression of allergic cellular and humoral responses, Immunity 17 (2002) 375–387.
[2] T. Korn, E. Bettelli, M. Oukka, V.K. Kuchroo, IL-17 and Th17 Cells, Annu Rev Immunol 27 (2009) 485–517.
[3] T. Hata, M. Takahashi, S. Hida, M. Kawaguchi, Y. Kashima, F. Usui, H. Morimoto, A. Nishiyama, A. Izawa, J. Koyama, Y. Iwakura, S. Taki, U. Ikeda, Critical role of Th17 cells in inflammation and neovascularization after ischaemia, Cardiovasc Res 90 (2011) 364–372.
[4] Y. Iwakura, H. Ishigame, The IL-23/IL-17 axis in inflammation, J Clin Invest 116 (2006) 1218–1222.
[5] R.E. Eid, D.A. Rao, J. Zhou, S.F. Lo, H. Ranjbaran, A. Gallo, S.I. Sokol, S. Pfau, J.S. Pober, G. Tellides, Interleukin-17 and interferon-gamma are produced concomitantly by human coronary artery-infiltrating T cells and act synergistically on vascular smooth muscle cells, Circulation 119 (2009) 1424–1432.
[6] E. Smith, K.M. Prasad, M. Butcher, A. Dobrian, J.K. Kolls, K. Ley, E. Galkina, Blockade of interleukin-17A results in reduced atherosclerosis in apolipoprotein E-deficient mice, Circulation 121 (2010) 1746–1755.
[7] Q. Gao, Y. Jiang, T. Ma, F. Zhu, F. Gao, P. Zhang, C. Guo, Q. Wang, X. Wang, C. Ma, Y. Zhang, W. Chen, L. Zhang, A critical function of Th17 proinflammatory cells in the development of atherosclerotic plaque in mice, J Immunol 185 (2010) 5820–5827.
[8] S. Chen, K. Shimada, W. Zhang, G. Huang, T.R. Crother, M. Arditi, IL-17A is proatherogenic in high-fat diet-induced and *Chlamydia pneumoniae* infection-accelerated atherosclerosis in mice, J Immunol 185 (2010) 5619–5627.
[9] C. Erbel, L. Chen, F. Bea, S. Wangler, S. Celik, F. Lasitschka, Y. Wang, D. Bockler, H.A. Katus, T.J. Dengler, Inhibition of IL-17A attenuates atherosclerotic lesion development in apoE-deficient mice, J Immunol 183 (2009) 8167–8175.
[10] S. Taleb, M. Romain, B. Ramkhelawon, C. Uyttenhove, G. Pasterkamp, O. Herbin, B. Esposito, N. Perez, H. Yasukawa, J. Van Snick, A. Yoshimura, A. Tedgui, Z. Mallat, Loss of SOCS3 expression in T cells reveals a regulatory role for interleukin-17 in atherosclerosis, J Exp Med 206 (2009) 2067–2077.
[11] M.S. Madhur, S.A. Funt, L. Li, A. Vinh, W. Chen, H.E. Lob, Y. Iwakura, Y. Blinder, A. Rahman, A.A. Quyyumi, D.G. Harrison, Role of interleukin 17 in inflammation atherosclerosis and vascular function in apolipoprotein E-deficient mice, Arterioscler Thromb Vasc Biol (2011).
[12] S.H. Zhang, R.L. Reddick, J.A. Piedrahita, N. Maeda, Spontaneous hypercholesterolemia and arterial lesions in mice lacking apolipoprotein E, Science 258 (1992) 468–471.
[13] B. Paigen, A. Morrow, C. Brandon, D. Mitchell, P. Holmes, Variation in susceptibility to atherosclerosis among inbred strains of mice, Atherosclerosis 57 (1985) 65–73.
[14] T. Ohshiro, D. Matsuda, K. Sakai, C. Degirolamo, H. Yagyu, L.L. Rudel, S. Omura, S. Ishibashi, H. Tomoda, Pyripyropene a, an acyl-coenzyme a:cholesterol acyltransferase 2-selective inhibitor, attenuates hypercholesterolemia and atherosclerosis in murine models of hyperlipidemia, Arterioscler Thromb Vasc Biol 31 (2011) 1108–1115.
[15] Y. Shiba, M. Takahashi, T. Yoshioka, N. Yajima, H. Morimoto, A. Izawa, H. Ise, K. Hatake, K. Motoyoshi, U. Ikeda, M-CSF accelerates neointimal formation in the early phase after vascular injury in mice. The critical role of the SDF-1-CXCR4 system, Arterioscler Thromb Vasc Biol 27 (2007) 283–289.
[16] H. Morimoto, M. Takahashi, A. Izawa, H. Ise, M. Hongo, P.E. Kolattukudy, U. Ikeda, Cardiac overexpression of monocyte chemoattractant protein-1 in transgenic mice prevents cardiac dysfunction and remodeling after myocardial infarction, Circ Res 99 (2006) 891–899.
[17] M. Leppkes, C. Becker, Ivanov, II, S. Hirth, S. Wirtz, C. Neufert, S. Pouly, A.J. Murphy, D.M. Valenzuela, G.D. Yancopoulos, B. Becher, D.R. Littman, M.F. Neurath, ROR gamma-expressing Th17 cells induce murine chronic intestinal inflammation via redundant effects of IL-17A and IL-17F, Gastroenterology 136 (2009) 257–267.
[18] W. O'Connor Jr., M. Kamanaka, C.J. Booth, T. Town, S. Nakae, Y. Iwakura, J.K. Kolls, R.A. Flavell, A protective function for interleukin 17A in T cell-mediated intestinal inflammation, Nat Immunol 10 (2009) 603–609.
[19] K. Ivanov II, N. Atarashi, E.L. Manel, T. Brodie, U. Shima, D. Karaoz, K.C. Wei, C.A. Goldfarb, S.V. Santee, T. Lynch, A. Tanoue, K. Imaoka, K. Itoh, Y. Takeda, K. Umesaki, D.R. Honda, Littman, induction of intestinal Th17 cells by segmented filamentous bacteria, Cell 139 (2009) 485–498.
[20] A.H. Lichtman, S.K. Clinton, K. Iiyama, P.W. Connelly, P. Libby, M.I. Cybulsky, Hyperlipidemia and atherosclerotic lesion development in LDL receptor-deficient mice fed defined semipurified diets with and without cholate, Arterioscler Thromb Vasc Biol 19 (1999) 1938–1944.
[21] T.S. Lee, H.C. Yen, C.C. Pan, L.Y. Chau, The role of interleukin 12 in the development of atherosclerosis in ApoE-deficient mice, Arterioscler Thromb Vasc Biol 19 (1999) 734–742.
[22] P. Davenport, P.G. Tipping, The role of interleukin-4 and interleukin-12 in the progression of atherosclerosis in apolipoprotein E-deficient mice, Am J Pathol 163 (2003) 1117–1125.
[23] K.J. Moore, M.W. Freeman, Scavenger receptors in atherosclerosis: beyond lipid uptake, Arterioscler Thromb Vasc Biol 26 (2006) 1702–1711.
[24] J. Khallou-Laschet, A. Varthaman, G. Fornasa, C. Compain, A.T. Gaston, M. Clement, M. Dussiot, O. Levillain, S. Graff-Dubois, A. Nicoletti, G. Caligiuri, Macrophage plasticity in experimental atherosclerosis, PLoS One 5 (2010) e8852.

Biochemical and Biophysical Research Communications 420 (2012) 78–83

Contents lists available at SciVerse ScienceDirect

Biochemical and Biophysical Research Communications

journal homepage: www.elsevier.com/locate/ybbrc

A pro-inflammatory role of deubiquitinating enzyme cylindromatosis (CYLD) in vascular smooth muscle cells

Shuai Liu [a,b], Jiaju Lv [c], Liping Han [b], Tomonaga Ichikawa [b], Wenjuan Wang [b], Siying Li [b], Xing Li Wang [a], Dongqi Tang [d,*], Taixing Cui [b,*]

[a] Shandong University Qilu Hospital Research Center for Cell Therapy, Key Laboratory of Cardiovascular Remodeling and Function Research, Qilu Hospital of Shandong University, Jinan 250012, China
[b] Department of Cell Biology and Anatomy, University of South Carolina School of Medicine, Columbia, SC 29208, USA
[c] Department of Urology, Shandong Provincial Hospital, Shandong University, Jinan 250021, China
[d] Department of Pathology, Immunology, and Laboratory Medicine, University of Florida College of Medicine, Gainesville, FL 32610-0275, USA

ARTICLE INFO

Article history:
Received 16 February 2012
Available online 1 March 2012

Keywords:
CYLD
Vascular smooth muscle cells
TNFα
Inflammation
MAPK
NF-κB

ABSTRACT

CYLD, a deubiquitinating enzyme (DUB), is a critical regulator of diverse cellular processes, ranging from proliferation and differentiation to inflammatory responses, via regulating multiple key signaling cascades such as nuclear factor kappa B (NF-κB) pathway. CYLD has been shown to inhibit vascular lesion formation presumably through suppressing NF-κB activity in vascular cells. However, herein we report a novel role of CYLD in mediating pro-inflammatory responses in vascular smooth muscle cells (VSMCs) via a mechanism independent of NF-κB activity. Adenoviral knockdown of Cyld inhibited basal and the tumor necrosis factor alpha (TNFα)-induced mRNA expression of pro-inflammatory cytokines including monocyte chemotactic protein-1 (Mcp-1), intercellular adhesion molecule (Icam-1) and interleukin-6 (Il-6) in rat adult aortic SMCs (RASMCs). The CYLD deficiency led to increases in the basal NF-κB transcriptional activity in RASMCs; however, did not affect the TNFα-induced NF-κB activity. Intriguingly, the TNFα-induced IκB phosphorylation was enhanced in the CYLD deficient RASMCs. While knocking down of Cyld decreased slightly the basal expression levels of IκBα and IκBβ proteins, it did not alter the kinetics of TNFα-induced IκB protein degradation in RASMCs. These results indicate that CYLD suppresses the basal NF-κB activity and TNFα-induced IκB kinase activation without affecting TNFα-induced NF-κB activity in VSMCs. In addition, knocking down of Cyld suppressed TNFα-induced activation of mitogen activated protein kinases (MAPKs) including extracellular signal-activated kinases (ERK), c-Jun N-terminal kinase (JNK), and p38 in RASMCs. TNFα-induced RASMC migration and monocyte adhesion to RASMCs were inhibited by the Cyld knockdown. Finally, immunochemical staining revealed a dramatic augment of CYLD expression in the injured coronary artery with neointimal hyperplasia. Taken together, our results uncover an unexpected role of CYLD in promoting inflammatory responses in VSMCs via a mechanism involving MAPK activation but independent of NF-κB activity, contributing to the pathogenesis of vascular disease.

1. Introduction

Cardiovascular disease is a leading cause of disability and mortality in the United States, and the majority of cardiovascular disorders results from complications of vascular diseases [1]. While it is still far from a comprehensive understanding of molecular and cellular mechanisms leading to vascular diseases, a preponderance of evidence supports a notion that inflammation plays a critical role in a wide range of vascular complications and dysfunctions [2–7]. Vascular inflammation is a complex process involving endothelial dysfunction, leukocyte recruitment, inflammatory activation of VSMCs, and malfunction of inflammatory mediators including both anti-inflammatory and pro-inflammatory cytokines. Of note, the inflammatory activation of VSMCs which exhibit a phenotypic switch characterized by loss of contractility, increased migration, proliferation, apoptosis, and production of extracellular matrix and cytokines, or foam-cell-like transition, plays a key role in vascular lesion formation and disease progression. However, the molecular mechanism of the inflammatory phenotypic switch of VSMCs remains partly understood.

Since ubiquitin (Ub) was discovered in the early 1970s, the protein quality control by the ubiquitin proteasome system (UPS) that involve specific enzyme proteins of Ub-activating enzyme (E1), Ub-conjugating (E2), Ub-ligating (E3), proteasome and

* Corresponding authors.
E-mail addresses: tangdq@pathology.ufl.edu (D. Tang), taixing.cui@uscmed.sc.edu (T. Cui).

0006-291X/$ - see front matter © 2012 Elsevier Inc. All rights reserved.
doi:10.1016/j.bbrc.2012.02.118

deubiquitinating enzymes (DUBs) has emerged as a critical regulatory process in virtually all aspects of cell biology [8–15]. The process of ubiquitination is catalyzed by the sequential actions of E1, E2, and E3. The removal and processing of ubiquitin are mediated by DUBs. Human genome encodes approximately 100 functional DUBs. Relative to the other components of UPS, less is known about the DUBs. Nevertheless, emerging evidence has revealed that DUBs act as crucial regulators in diverse biological processes such as proliferation, migration, apoptosis, and inflammatory responses [10,16–18]. Importantly, a potential role of DUBs in the pathogenesis of vascular diseases was highlighted by the inhibitory role of DUB A20 (also called TNFα-induced protein 3 or Tnfaip3) in vascular lesion formation [19–21]. We and others have found that other DUBs of ubiquitin carboxyl-terminal hydrolase-L1 (UCH-L1) and CYLD may serve as endogenous inhibitors of vascular lesion formation [22–24]. At a molecular level, these DUB-mediated deubiquitination of IκB kinase γ (IKKγ), IκBα, or TNF receptor associated factor 2 (TRAF2) that leads to suppression of NF-κB activity [25–27] has been considered to resolve vascular inflammatory responses thus inhibiting vascular injury [19,22,23]. Because the DUB-mediated deubiquitination has been proposed to be non-selective, these findings seem quite predictable. However, several lines of evidence have recently revealed that DUBs are often found as part of large multiple protein complexes that functions to regulate their localization, substrate availability, and activity in cellular processes, and the association of DUBs with substrate adaptors, scaffolds, and inhibitors results in regulatory interactions driving specificity [28]. These results suggest that DUBs might be a unique class of molecules for the determination of biological consequences of diverse signaling cascades at differential pathological settings such as maladaptive vascular remodeling and dysfunction. However, precise role of DUBs in the vasculature remains to be further determined.

In the present study, we explored a role of CYLD in regulating inflammatory responses in primary culture of RASMCs by Cyld gene loss-of-function approach. Our results uncover an unexpected mediator role of CYLD in pro-inflammatory activation of VSMCs via a mechanism independent of NF-κB activation, highlighting functional significance of CYLD splicing variants in the pathogenesis of vascular disease.

2. Material and methods

2.1. Animals and treatment

Male ICR/sv129 mice at age of 8 weeks were treated subcutaneously with vehicle saline or infused with angiotensin II (Ang II) (Sigma–Aldrich) at a rate of 1.4 μg/kg/min for 2 weeks by osmotic minipumps as previously reported [29]. All of the animal procedures were conducted in accordance with the NIH Guide for Care and Use of Laboratory Animals and were approved by the Institutional Animal Care and Use Committee at University of South Carolina, USA.

2.2. Immunohistochemistry

Hearts were harvested and immunohistochemistry were performed as previously described [30]. Primary antibodies included a goat CYLD polyclonal antibody (Abcam Inc.) and a rabbit tropomyosin I antibody (Abcam Inc.). Cardiomyocytes were stained with anti-tropomycin I antibody. Nuclei were labeled with 4′, 6-diamidino-2-phenylindole (DAPI; Sigma–Aldrich).

2.3. Cell culture, adenoviral infection, transfection and NF-κB reporter assay

RASMCs were isolated from thoracic aorta of adult Spraque–Dawley rats and cultured as previously described [24]. Subconfluent RASMCs were infected with adenovirus of control scramble shRNA (Ad-cont sh) or Cyld shRNA (Ad-Cyld sh) (Welgen Inc.) in serum free Dulbecco's Modified Eagle's Medium (DMEM) for 48 h. Transfection and NF-kB reporter assay were performed as previously described [31].

2.4. Cell migration assay

TNFα-induced RASMC migration was assessed by measuring wound closure rate as previously described [32]. Briefly, RASMCs were infected with adenovirus of scramble shRNA or Cyld shRNA in serum free DMEM for 48 h, and then split into 6-well plates to reach approximately 100% confluence. The monolayer of RASMCs was further scratched with a plastic tip (200 μl), and followed with or without the treatment of TNFα (5 ng/ml) in serum free DMEM for 24 h. The wound area was calculated by tracing along the border of wound using image analysis software (Image ProPlus 6.0), and the percentage wound closure was calculated using the following equation: Wound closure rate = [wound area (0 h) − wound area (24 h)]/wound area (0 h).

2.5. Monocyte adhesion assay

Adhesion of monocyte to RASMCs was assessed utilizing fluorescein labeled THP-1 cells as previously described [33].

2.6. Quantitative real time reverse transcription-polymerase chain reaction (Q-PCR)

Total RNA purification, reverse transcription (RT) reaction, and Q-PCR were performed as described previously [30]. Primers that were used for Q-PCR are as follows: rat Cyld, forward primer (5′-GCAGTGTAACAGACAAACAGACACA-3′) and reverse primer (5′-TTGCCTTTAGCAGAAGGAACT-3′); rat Icam-1, forward primer (5′-AGAAGGACTGCTTGGGGAA-3′) and reverse primer (5′-CCTCTGGCGGTAATAGGTG-3′); rat Mcp-1, forward primer (5′-ATGCAGGTCTCTGTCACG-3′) and reverse primer (5′-CTAGTTCTCTGTCATACT-3′); rat Il-6, forward primer (5′-TGTTCTCAGGGAGATCTTGG-3′) and reverse primer (5′-TCCAGGTAGAAACGGAACTC-3′); rat glyceraldehyde-3-phosphate dehydrogenase (Gapdh), forward primer (5′-ACCACAGTCCATGCCATCAC-3′) and reverse primer (5′-TCCACCACCCTGTTGCTGTA-3′).

2.7. Western blot

Cell lysates were subjected to immunoblot analysis as described elsewhere [30] using antibodies of anti-phospho-IκBα (Ser32/36), anti-phospho-ERK, anti-phospho-p38 and anti-phospho-JNK (Cell Signaling Technology), as well as anti-IκBα, IκBβ, anti-IκBε, anti-ERK, anti-JNK, anti-p38 and anti-α-tubulin (Santa Cruz Biotechnology).

2.8. Statistical analysis

Data are expressed as mean ± s.d. Comparison between groups was done by two-sample *t*-test. A p value of <0.05 was considered significant. Statistical analysis was performed with Statistical Package for Social Sciences version 13.0 (SPSS, Inc.).

3. Results

3.1. Knocking down of Cyld suppresses TNFα-induced pro-inflammatory cytokine expression in RASMCs

Considering the inhibitory effect of over-expression of CYLD on NF-κB activity and its downstream inflammatory gene expression

in A7r5 VSMCs as well as neointimal formation in rat carotid artery after balloon injury [23], we hypothesized that CYLD deficiency in VSMCs could exaggerate vascular inflammatory responses, thereby leading to progressive vascular lesion formation. To test this hypothesis, we applied Cyld RNA interference (RNAi) approach to determine a pathophysiological significance of CYLD deficiency in the regulation of vascular lesion formation *in vitro* utilizing primarily cultured RASMCs. Adenoviral over-expression of Cyld shRNA dose-dependently inhibited Cyld mRNA expression with an efficacy of >80% knockdown of endogenous Cyld mRNA expression at dose of 50 multiplicity of infection (MOI) in RASMCs (Fig. 1A). Adenoviral over-expression of Cyld shRNA (50 MOI) resulted in suppression of >90% CYLD protein expression (Fig. 1A). We did not observe any apparent cytotoxic effects of the adenoviral infection in RASMCs (data not shown). Thus, Cyld RNAi approach was established in RASMCs. Surprisingly, the Cyld knockdown suppressed both basal and TNFα-induced expression of Mcp-1, Icam-1, and Il-6 mRNAs in RASMCs (Fig. 1B), suggesting a pro-inflammatory role of CYLD in VSMCs.

Knocking down of Cyld increases basal NF-κB activity without affecting TNFα-induced NF-κB activity and inhibits TNFα-induced activation of MAPKs in RASMCs.

Because Mcp-1, Icam-1 and Il-6 are well-documented downstream genes of NF-κB, a key regulator of vascular inflammatory responses and lesion formation [34,35], we examined the effect of CYLD deficiency on NF-κB signaling in RASMCs. Knocking down of Cyld led to an enhancement of the basal NF-κB transcriptional activity; however, did not affect TNFα-induced NF-κB transcriptional activity (Fig. 2A), suggesting that endogenous CYLD negatively regulates constitutive rather than induced NF-κB activity in VSMCs. Intriguingly, the TNFα-induced IκB phosphorylation was enhanced in the CYLD deficient RASMCs (Fig. 2B), indicating an inhibitory role of endogenous CYLD in suppressing the induced activation of IκB upstream kinases such as IKKs that phosphorylate IκBs leading to NF-κB activation [27] in VSMCs. While the CYLD deficiency slightly decreased the basal expression levels of IκBα and IκBβ proteins, it did not affect the basal expression of IκBε in RASMCs (Fig. 2B). In addition, it did not alter the kinetics of TNFα-induced IκB protein degradation in RASMCs (Fig. 2B). These results reveal that endogenous CYLD constitutively stabilizes the basal IκBα and IκBβ proteins thereby suppressing NF-κB activity [27] in VSMCs. Moreover, endogenous CYLD suppresses the activity of kinases for IκB phosphorylation; however, this suppression probably contributes to the basal IκB degradation rather than induced IκB degradation leading to NF-κB activation in VSMCs.

To further dissect the underlying molecular mechanisms of CYLD-mediated pro-inflammatory responses in VSMCs, we determined whether Cyld knockdown affects the TNFα-induced activation of MAPKs including ERK, JNK, and p38, a group of key signaling molecules in the regulation of inflammatory responses [36–39] in RASMCs. In fact, a critical role of ERK, JNK or p38 in mediating TNFα-induced expression of Mcp-1, Icam-1, or Il-6 has been established in rat or mouse VSMCs [40,41]. Interestingly, not the basal but TNFα-induced phosphorylation/activation of ERK, JNK, and p38 was attenuated by knocking down of Cyld in RASMCs (Fig. 3), indicating a mediator role of endogenous CYLD in inducing activation of MAPKs in VSMCs at a setting of inflammation.

3.2. Knocking down of Cyld inhibits TNFα-induced RASMC migration and monocyte adhesion to TNFα-inflamed RASMCs

To establish a functional link between CYLD deficiency and inflammatory responses in VSMCs, we determined effect of Cyld knockdown on TNFα-induced RASMC migration and monocyte adhesion to TNFα-inflamed RASMCs *in vitro* reflecting inflammatory activation of VSMCs [6]. In consistent with the inhibitory effect of Cyld knockdown on inflammatory cytokine expression, Cyld knockdown inhibited TNFα-induced RASMC migration and

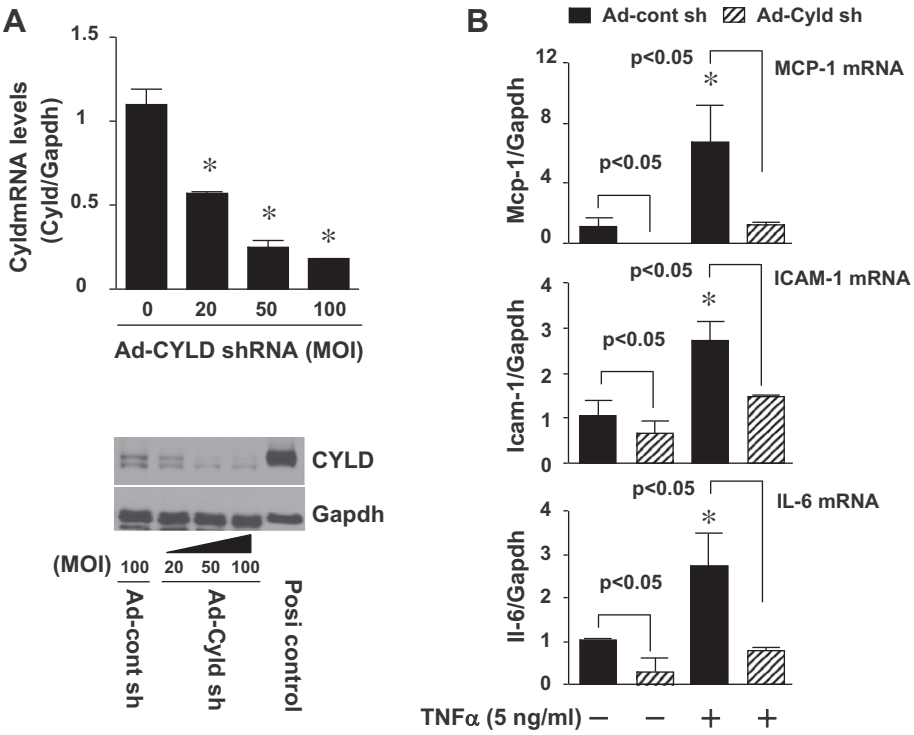

Fig. 1. Effect of Cyld knockdown on TNFα-induced inflammatory cytokine expression in RASMCs. (A) Efficacy of adenoviral knockdown of Cyld in RASMCs. Upper: Cyld mRNA expression. $^{*}p < 0.05$ vs. control (0), $n = 4$. Lower: Results are representative of three independent Western blot analysis of CYLD in infected RASMCs. Cell lysates from human 293 cells transfected with pDEST-HA-hCyld (Addgene) were used as positive (Posi) control. (B) Q-PCR analysis of Mcp-1, Icam-1 and Il-6 mRNA expression. $^{*}p < 0.05$ vs. Ad-cont sh (−), $n = 4$.

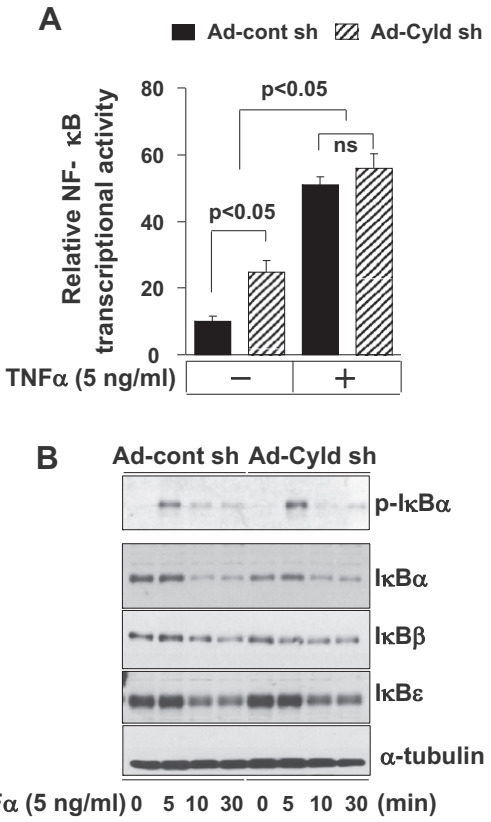

Fig. 2. Effect of Cyld knockdown on NF-κB signaling in RASMCs. (A) RASMCs infected with Ad-cont sh (50 MOI) or Ad-Cyld sh (50 MOI) were treated with or without TNFα (5 ng/ml) for 6 h. ns; non-significant. (B) RASMCs infected with Ad-cont or Ad-Cyld sh as described in (A) were stimulated with TNFα (5 ng/ml) as indicated. Results are representatives of three independent experiments.

adhesion of monocyte sto TNFα-activated RASMCs (Fig. 4A and B), revealing a critical role of CYLD in pro-inflammatory phenotypic switch of VSMCs leading to vascular lesion formation.

3.3. CYLD is up-regulated in the injured coronary artery with neointimal hyperplasia at a setting of sustained Ang II stimulation

To further establish a pathophysiological relevance of the CYLD-mediated pro-inflammatory activation of VSMCs, we examined CYLD expression in injured coronary arteries caused by sustained stimulation of Ang II that exhibits significant pro-inflammatory actions in the vessel wall via inducing the production of inflammatory cytokines and adhesion molecules, recruitment of inflammatory cells, and activation of VSMCs, culminating in vascular lesion formation with adverse clinical outcome [42]. As shown in Fig. 4C, CYLD was dramatically up-regulated in the small intramural coronary arteries (50–100 μm internal diameter) associated with neointimal hyperplasia that was induced by sustained Ang II infusion for 2 weeks.

4. Discussion

CYLD was originally identified as a tumor suppressor gene of human familial cylindromatosis (CYLD) [43]. Rapid growing evidence has demonstrated that CYLD plays a critical role in immunity, lipid metabolism, spermatogenesis, osteoclastogenesism antimicrobial defense, and inflammation predominantly via regulating NF-κB and JNK pathways [16–18]. To date, the majority of characterized CYLD targets are involved in the signaling transduction mediating NF-κB activation. CYLD has been considered as a negative regulator of IKK complex thereby suppressing NF-κB-driven pro-inflammatory signaling in diverse organ systems including vasculature [23]. However, our current study demonstrates for the first time that CYLD acts as a positive mediator of pro-inflammatory activation of VSMCs, potentially contributing to coronary arterial lesion formation. Mechanistically, CYLD mediates the pro-inflammatory phenotypic switch of VSMCs via a mechanism involving MAPK activation but independent of NF-κB activity.

Our findings are unexpected; however, raise several intriguing issues which need further investigation: Firstly, the signaling function of CYLD is complex and varies among different cell types and

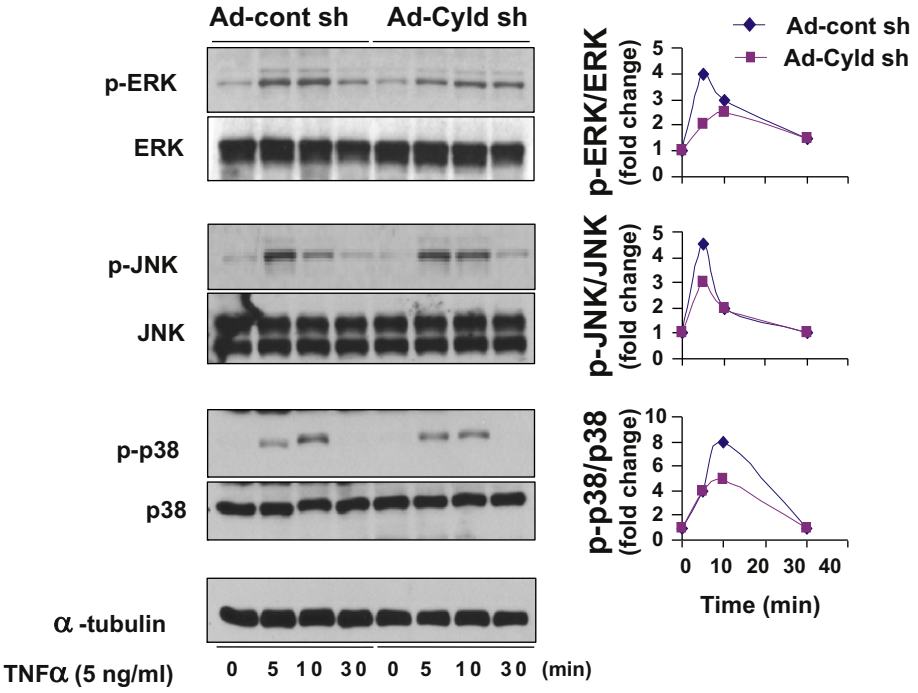

Fig. 3. Effect of Cyld knockdown on activation of MAPK in RASMCs. Infected RASMCs were treated with TNFα (5 ng/ml) as indicated. Results are representatives of three independent experiments. Left panel is the semi-quantification of ERK, JNK, and p38 activities.

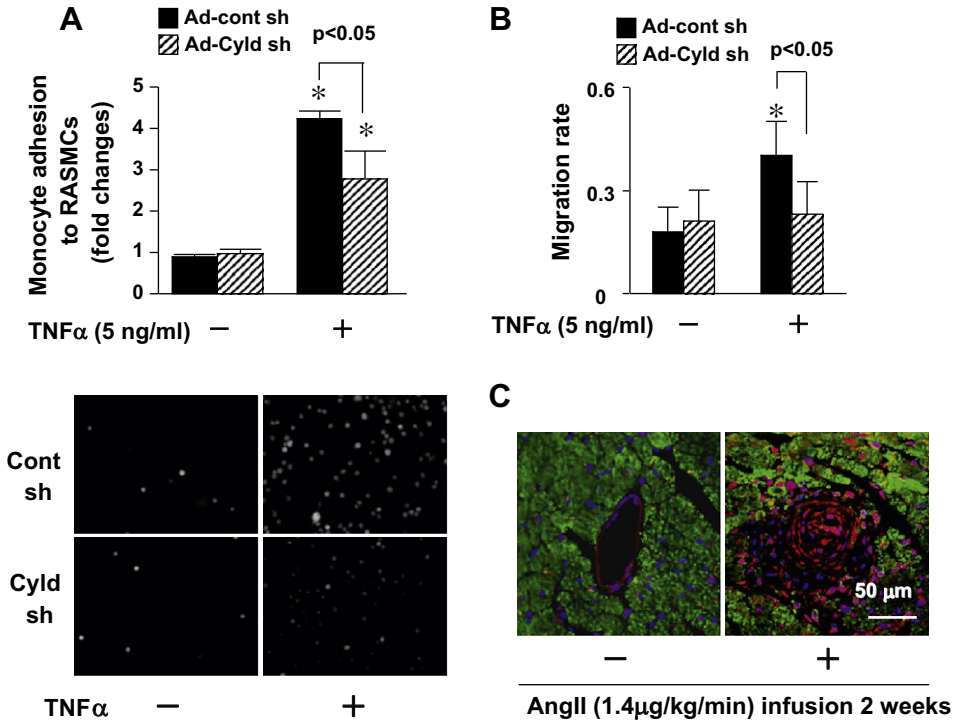

Fig. 4. Effect of Cyld knockdown on monocyte adhesion to RASMCs (A) and RASMC migration (B). Images are representatives of three independent experiments $^{*}p < 0.05$ vs. TNFα (−), $n = 4$. (C) Ang II-induced CYLD expression in murine coronary artery of right ventricle. Green indicates cardiomyocytes. Red is CYLD. Blue is nuclei.

pathological settings. Activation of IKK, NF-κB, ERK, JNK, and p38 induced by Toll-like receptors and TNF receptors is normal in Cyld deficient macrophages; however, activation of ERK and JNK is diminished in Cyld deficient thymocytes [44]. We have demonstrated that loss of Cyld function does not affect NF-κB activity but enhances JNK activity in renal tubular epithelial cells contributing the tubulointerstitial inflammation of IgA nephropathy [33]. Notably, truncation of deubiquitinating domain of CYLD specifically in myelomonocytic cells suppresses the development of lethal LPS-induced endotoxic shock and the accumulation of thioglycollate-elicited peritoneal macrophages with hyperactivation of NF-κB [45]. Because the over-expression of exogenous CYLD may cover the endogenous function of CYLD in VSMCs [23], aforementioned, we believe that results obtained by Cyld loss-of-function RNAi approach reflects more precisely the intrinsic function of CYLD in VSMCs. Thus, our data uncovers a novel role of CYLD in mediating pro-inflammatory responses in VSMCs probably via activating MAPKs. Secondly, TNFα exerts either pro- or anti-inflammatory effects in the vasculature [46,47]. In addition, protein ubiquitination cascades have recently been illustrated to play a critical role in TNF receptor signaling and account for spatial and temporal separation of IKK and MAPK signaling cascades thereby determining biological specificity and outcome [48]. Since CYLD has implicated into the deubiquitinating of TRAFs, IKKγ, Bcl3, TGFβ-activated kinase (TAK), receptor-interacting protein 1 (RIP1) and other molecules that are critical for TNF receptor-mediated IKK and MAPK signaling [17,18,48], it is possible that CYLD may deubiquitinate the putative molecules coupling with the TNFα-mediated pro-inflammatory responses specifically in VSMCs. Finally, it is worthy to note that CYLD can both positively and negative regulate NF-κB signaling, depending on the expression of CYLD splicing variants. A splicing variant of CYLD which lacks the TRAF2 and IKKγ binding sites increases basal rather than anti-IgM-induced NF-κB activity and enhances LPS-induced MAPK p38 activation in B cells [49]. Moreover, this shorter CYLD (sCYLD) enhances NF-κB activity accompanied by an increased nuclear translocation of the IκB molecule Bcl-3, along with nuclear p50 and p65 leading to a pro-inflammatory phenotype in dendritic cells [50]. Considering the similarities between these previous finding and ours, such as the increased basal rather induced NF-κB activity or the enhanced p38 activity in both Cyld deficient VSMCs and Cyld deficient with sCyld overexpressing B or dendritic cells, it is possible that sCYLD is responsible for pro-inflammatory activation of VSMCs whereas full-length CYLD is a negative regulator of inflammatory responses in diverse organ systems including vasculature. Therefore, our results highlight a pathophysiological significance of the splicing variants of CYLD at least in vasculature.

In summary, we have demonstrated that endogenous CYLD is critical for the pro-inflammatory activation of VSMCs via mechanism of activating MAKP independent of NF-κB. Importantly, our findings also reveal a potential role of CYLD splicing variants in the control of NF-κB and MAPK pathways leading to biological specificity and outcome of inflamed VSMCs. Further investigation of the precise role of CYLD splicing variants in the vasculature is warranted in future.

Acknowledgments

This work was supported by Grants from American Heart Association (10GRNT4020019) and National Institution of Health (P20 GM103499).

References

[1] W. Rosamond, K. Flegal, K. Furie, A. Go, K. Greenlund, N. Haase, S.M. Hailpern, M. Ho, V. Howard, B. Kissela, S. Kittner, D. Lloyd-Jones, M. McDermott, J. Meigs, C. Moy, G. Nichol, C. O'Donnell, V. Roger, P. Sorlie, J. Steinberger, T. Thom, M. Wilson, Y. Hong, Heart disease and stroke statistics–2008 update: a report from the American Heart Association Statistics Committee and Stroke Statistics Subcommittee, Circulation 117 (2008) e25–146.

[2] R. Ross, Atherosclerosis – an inflammatory disease, N. Engl. J. Med. 340 (1999) 115–126.
[3] V.J. Dzau, R.C. Braun-Dullaeus, D.G. Sedding, Vascular proliferation and atherosclerosis: new perspectives and therapeutic strategies, Nat. Med. 8 (2002) 1249–1256.
[4] I.F. Charo, M.B. Taubman, Chemokines in the pathogenesis of vascular disease, Circ. Res. 95 (2004) 858–866.
[5] G.K. Hansson, P. Libby, The immune response in atherosclerosis: a double-edged sword, Nat. Rev. Immunol. 6 (2006) 508–519.
[6] A.C. Doran, N. Meller, C.A. McNamara, Role of smooth muscle cells in the initiation and early progression of atherosclerosis, Arterioscler. Thromb. Vasc. Biol. 28 (2008) 812–819.
[7] R. Kleemann, S. Zadelaar, T. Kooistra, Cytokines and atherosclerosis: a comprehensive review of studies in mice, Cardiovasc. Res. 79 (2008) 360–376.
[8] M.H. Glickman, A. Ciechanover, The ubiquitin-proteasome proteolytic pathway: destruction for the sake of construction, Physiol. Rev. 82 (2002) 373–428.
[9] K. Haglund, I. Dikic, Ubiquitylation and cell signaling, EMBO J. 24 (2005) 3353–3359.
[10] S.M. Nijman, M.P. Luna-Vargas, A. Velds, T.R. Brummelkamp, A.M. Dirac, T.K. Sixma, R. Bernards, A genomic and functional inventory of deubiquitinating enzymes, Cell 123 (2005) 773–786.
[11] T. Kodadek, D. Sikder, K. Nalley, Keeping transcriptional activators under control, Cell 127 (2006) 261–264.
[12] D. Mukhopadhyay, H. Riezman, Proteasome-independent functions of ubiquitin in endocytosis and signaling, Science 315 (2007) 201–205.
[13] K. Hochrainer, J. Lipp, Ubiquitylation within signaling pathways in- and outside of inflammation, Thromb. Haemost. 97 (2007) 370–377.
[14] G.N. Demartino, T.G. Gillette, Proteasomes: machines for all reasons, Cell 129 (2007) 659–662.
[15] B.A. Schulman, J.W. Harper, Ubiquitin-like protein activation by E1 enzymes: the apex for downstream signalling pathways, Nat. Rev. Mol. Cell Biol. 10 (2009) 319–331.
[16] G. Courtois, Tumor suppressor CYLD: negative regulation of NF-kappaB signaling and more, Cell Mol. Life Sci. 65 (2008) 1123–1132.
[17] P.W. Blake, J.R. Toro, Update of cylindromatosis gene (CYLD) mutations in Brooke–Spiegler syndrome: novel insights into the role of deubiquitination in cell signaling, Hum. Mutat. 30 (2009) 1025–1036.
[18] S.C. Sun, CYLD: a tumor suppressor deubiquitinase regulating NF-kappaB activation and diverse biological processes, Cell Death Differ. 17 (2010) 25–34.
[19] V.I. Patel, S. Daniel, C.R. Longo, G.V. Shrikhande, S.T. Scali, E. Czismadia, C.M. Groft, T. Shukri, C. Motley-Dore, H.E. Ramsey, M.D. Fisher, S.T. Grey, M.B. Arvelo, C. Ferran, A20, a modulator of smooth muscle cell proliferation and apoptosis, prevents and induces regression of neointimal hyperplasia, FASEB J. 20 (2006) 1418–1430.
[20] S. Daniel, V.I. Patel, G.V. Shrikhande, S.T. Scali, H.E. Ramsey, E. Csizmadia, N. Benhaga, M.D. Fisher, M.B. Arvelo, C. Ferran, The universal NF-kappaB inhibitor A20 protects from transplant vasculopathy by differentially affecting apoptosis in endothelial and smooth muscle cells, Transplant. Proc. 38 (2006) 3225–3227.
[21] S. Wolfrum, D. Teupser, M. Tan, K.Y. Chen, J.L. Breslow, The protective effect of A20 on atherosclerosis in apolipoprotein E-deficient mice is associated with reduced expression of NF-kappaB target genes, Proc. Natl. Acad. Sci. USA 104 (2007) 18601–18606.
[22] Y. Takami, H. Nakagami, R. Morishita, T. Katsuya, T.X. Cui, T. Ichikawa, Y. Saito, H. Hayashi, Y. Kikuchi, T. Nishikawa, Y. Baba, O. Yasuda, H. Rakugi, T. Ogihara, Y. Kaneda, Ubiquitin carboxyl-terminal hydrolase L1, a novel deubiquitinating enzyme in the vasculature, attenuates NF-kappaB activation, Arterioscler. Thromb. Vasc. Biol. 27 (2007) 2184–2190.
[23] Y. Takami, H. Nakagami, R. Morishita, T. Katsuya, H. Hayashi, M. Mori, H. Koriyama, Y. Baba, O. Yasuda, H. Rakugi, T. Ogihara, Y. Kaneda, Potential role of CYLD (cylindromatosis) as a deubiquitinating enzyme in vascular cells, Am. J. Pathol. 172 (2008) 818–829.
[24] T. Ichikawa, J. Li, X. Dong, J.D. Potts, D.Q. Tang, D.S. Li, T. Cui, Ubiquitin carboxyl terminal hydrolase L1 negatively regulates TNFalpha-mediated vascular smooth muscle cell proliferation via suppressing ERK activation, Biochem. Biophys. Res. Commun. 391 (2010) 852–856.
[25] A. Kovalenko, C. Chable-Bessia, G. Cantarella, A. Israel, D. Wallach, G. Courtois, The tumour suppressor CYLD negatively regulates NF-kappaB signalling by deubiquitination, Nature 424 (2003) 801–805.
[26] C. Mauro, F. Pacifico, A. Lavorgna, S. Mellone, A. Iannetti, R. Acquaviva, S. Formisano, P. Vito, A. Leonardi, ABIN-1 binds to NEMO/IKKgamma and co-operates with A20 in inhibiting NF-kappaB, J. Biol. Chem. 281 (2006) 18482–18488.
[27] M.S. Hayden, S. Ghosh, Shared principles in NF-kappaB signaling, Cell 132 (2008) 344–362.
[28] F.E. Reyes-Turcu, K.H. Ventii, K.D. Wilkinson, Regulation and cellular roles of ubiquitin-specific deubiquitinating enzymes, Annu. Rev. Biochem. 78 (2009) 363–397.
[29] J. Li, C. Zhang, Y. Xing, J.S. Janicki, M. Yamamoto, X.L. Wang, D.Q. Tang, T. Cui, Up-regulation of p27(kip1) contributes to Nrf2-mediated protection against angiotensin II-induced cardiac hypertrophy, Cardiovasc. Res. 90 (2011) 315–324.
[30] J. Li, T. Ichikawa, L. Villacorta, J.S. Janicki, G.L. Brower, M. Yamamoto, T. Cui, Nrf2 protects against maladaptive cardiac responses to hemodynamic stress, Arterioscler. Thromb. Vasc. Biol. 29 (2009) 1843–1850.
[31] T. Ichikawa, J. Li, P. Nagarkatti, M. Nagarkatti, L.J. Hofseth, A. Windust, T. Cui, American ginseng preferentially suppresses STAT/iNOS signaling in activated macrophages, J. Ethnopharmacol. 125 (2009) 145–150.
[32] K.P. Goetsch, C.U. Niesler, Optimization of the scratch assay for in vitro skeletal muscle wound healing analysis, Anal. Biochem. 411 (2011) 158–160.
[33] T.G. Cui, T. Ichikawa, M. Yang, X. Dong, J. Li, T. Cui, An emerging role of deubiquitinating enzyme cylindromatosis (CYLD) in the tubulointerstitial inflammation of IgA nephropathy, Biochem. Biophys. Res. Commun. 390 (2009) 307–312.
[34] C. Monaco, E. Paleolog, Nuclear factor kappaB: a potential therapeutic target in atherosclerosis and thrombosis, Cardiovasc. Res. 61 (2004) 671–682.
[35] A.R. Brasier, The nuclear factor-kappaB-interleukin-6 signalling pathway mediating vascular inflammation, Cardiovasc. Res. 86 (2010) 211–218.
[36] K. Ono, J. Han, The p38 signal transduction pathway: activation and function, Cell Signal. 12 (2000) 1–13.
[37] A.M. Manning, R.J. Davis, Targeting JNK for therapeutic benefit: from junk to gold?, Nat Rev. Drug Discov. 2 (2003) 554–565.
[38] P.K. Mehta, K.K. Griendling, Angiotensin II cell signaling: physiological and pathological effects in the cardiovascular system, Am. J. Physiol. Cell Physiol. 292 (2007) C82–C97.
[39] J.R. Bradley, TNF-mediated inflammatory disease, J. Pathol. 214 (2008) 149–160.
[40] Y.M. Chen, W.C. Chiang, S.L. Lin, K.D. Wu, T.J. Tsai, B.S. Hsieh, Dual regulation of tumor necrosis factor-alpha-induced CCL2/monocyte chemoattractant protein-1 expression in vascular smooth muscle cells by nuclear factor-kappaB and activator protein-1: modulation by type III phosphodiesterase inhibition, J. Pharmacol. Exp. Ther. 309 (2004) 978–986.
[41] K.W. Choi, H.J. Park, D.H. Jung, T.W. Kim, Y.M. Park, B.O. Kim, E.H. Sohn, E.Y. Moon, S.H. Um, D.K. Rhee, S. Pyo, Inhibition of TNF-alpha-induced adhesion molecule expression by diosgenin in mouse vascular smooth muscle cells via downregulation of the MAPK, Akt and NF-kappaB signaling pathways, Vascul. Pharmacol. 53 (2010) 273–280.
[42] V.J. Dzau, Theodore cooper lecture: tissue angiotensin and pathobiology of vascular disease: a unifying hypothesis, Hypertension 37 (2001) 1047–1052.
[43] G.R. Bignell, W. Warren, S. Seal, M. Takahashi, E. Rapley, R. Barfoot, H. Green, C. Brown, P.J. Biggs, S.R. Lakhani, C. Jones, J. Hansen, E. Blair, B. Hofmann, R. Siebert, G. Turner, D.G. Evans, C. Schrander-Stumpel, F.A. Beemer, A. van Den Ouweland, D. Halley, B. Delpech, M.G. Cleveland, I. Leigh, J. Leisti, S. Rasmussen, Identification of the familial cylindromatosis tumour-suppressor gene, Nat. Genet. 25 (2000) 160–165.
[44] W.W. Reiley, M. Zhang, W. Jin, M. Losiewicz, K.B. Donohue, C.C. Norbury, S.C. Sun, Regulation of T cell development by the deubiquitinating enzyme CYLD, Nat. Immunol. 7 (2006) 411–417.
[45] A. Tsagaratou, D.L. Kontoyiannis, G. Mosialos, Truncation of the deubiquitinating domain of CYLD in myelomonocytic cells attenuates inflammatory responses, PLoS One 6 (2011) e16397.
[46] L. Zhang, K. Peppel, P. Sivashanmugam, E.S. Orman, L. Brian, S.T. Exum, N.J. Freedman, Expression of tumor necrosis factor receptor-1 in arterial wall cells promotes atherosclerosis, Arterioscler. Thromb. Vasc. Biol. 27 (2007) 1087–1094.
[47] L. Zhang, P. Sivashanmugam, J.H. Wu, L. Brian, S.T. Exum, N.J. Freedman, K. Peppel, Tumor necrosis factor receptor-2 signaling attenuates vein graft neointima formation by promoting endothelial recovery, Arterioscler. Thromb. Vasc. Biol. 28 (2008) 284–289.
[48] M. Karin, E. Gallagher, TNFR signaling: ubiquitin-conjugated TRAFfic signals control stop-and-go for MAPK signaling complexes, Immunol. Rev. 228 (2009) 225–240.
[49] N. Hovelmeyer, F.T. Wunderlich, R. Massoumi, C.G. Jakobsen, J. Song, M.A. Worns, C. Merkwirth, A. Kovalenko, M. Aumailley, D. Strand, J.C. Bruning, P.R. Galle, D. Wallach, R. Fassler, A. Waisman, Regulation of B cell homeostasis and activation by the tumor suppressor gene CYLD, J. Exp. Med. 204 (2007) 2615–2627.
[50] C.C. Srokowski, J. Masri, N. Hovelmeyer, A.K. Krembel, C. Tertilt, D. Strand, K. Mahnke, R. Massoumi, A. Waisman, H. Schild, Naturally occurring short splice variant of CYLD positively regulates dendritic cell function, Blood 113 (2009) 5891–5895.

Biochemical and Biophysical Research Communications 420 (2012) 84–90

Contents lists available at SciVerse ScienceDirect

Biochemical and Biophysical Research Communications

journal homepage: www.elsevier.com/locate/ybbrc

4-Hydroxy-2-nonenal induces chronic obstructive pulmonary disease-like histopathologic changes in mice

Takayuki Takimoto *, Mitsuhiro Yoshida, Haruhiko Hirata, Yozo Kashiwa, Yoshito Takeda, Sho Goya, Takashi Kijima, Toru Kumagai, Isao Tachibana, Ichiro Kawase

Department of Respiratory Medicine, Allergy and Rheumatic Diseases, Osaka University Graduate School of Medicine, Suita, Osaka 565-0871, Japan

ARTICLE INFO

Article history:
Received 22 February 2012
Available online 3 March 2012

Keywords:
Chronic obstructive pulmonary disease (COPD)
Oxidative stress
4-Hydroxy-2-nonenal (4-HNE)
Inflammation
Matrix metalloprotease (MMP)
Apoptosis

ABSTRACT

The α,β-unsaturated aldehyde 4-hydroxy-2-nonenal (4-HNE) is an endogenous product of oxidative stress that is found at increased levels in the lungs of patients with chronic obstructive pulmonary disease (COPD) and animal models of this lung disorder. In the present study, levels of 4-HNE adducts were increased in two different mouse models of COPD. Challenging lungs with 4-HNE enlarged the airspace and induced goblet cell metaplasia of the airways in mice, two characteristics of COPD. 4-HNE induced the accumulation of inflammatory cells expressing high levels of MMP-2 and MMP-9. Our results indicate that 4-HNE production during oxidative stress is a key pathway in the pathogenesis of COPD.

1. Introduction

Chronic obstructive pulmonary disease (COPD) is an inflammatory lung disease that is elicited by noxious particles or gases, resulting in progressive and at least partially nonreversible airflow limitations [1]. COPD afflicts more than 210 million adults and is currently the fourth leading cause of death in the world [1,2]. The prevalence of this disease and associated mortality are predicted to further increase in the coming decades. Existing pharmacologic therapies, however, are inadequate, and long-term oxygen therapy is the only treatment modality that prolongs the survival of patients with COPD. Therefore, a better understanding of the precise mechanisms of COPD is urgently required to guide the development of more effective treatment strategies.

Oxidative stress is elevated in the lungs of patients with COPD [3]. Cigarette smoke—a major risk factor for COPD—contains an estimated 10^{14} oxidant molecules [4]. Other factors, such as air pollutants, infections, and occupational dust, also oxidatively stress the lungs of these patients. Activated inflammatory cells, such as alveolar macrophages and neutrophils, contribute to the oxidant burden by releasing reactive oxygen species. The pathogenic effects of oxidative stress are also evident in numerous animal models of COPD [5–11]. Furthermore, epidemiologic studies have revealed a positive correlation between dietary intake of antioxidants and lung function [12,13]. These data support a pivotal role for the oxidant–antioxidant imbalance theory in the pathogenesis of COPD.

An expanding evidence base indicates that reactive aldehydes generated via oxidative stress and peroxidation of membrane lipids are involved in the development of several diseases, such as atherosclerosis, diabetes mellitus, and Alzheimer's disease. Among these compounds, the α,β-unsaturated aldehyde 4-hydroxy-2-nonenal (4-HNE)—a major product of lipid peroxidation—contributes to several biologic processes, including signal transduction, gene expression, and cell proliferation and survival [14–16]. 4-HNE results in Micheal adduct protein formation, altering the functions of the native proteins [15]. A recent study demonstrated a net increase in 4-HNE protein adduct levels in the lungs of patients with COPD [17], and 4-HNE adduct levels in alveolar epithelium inversely correlated with pulmonary function. In addition, cigarette smoke inhalation or vascular endothelial growth factor receptor blockade resulted in more 4-HNE adducts in alveolar macrophages and epithelia of the terminal bronchiole in rats [6,7]. These results suggest that 4-HNE contributes to the pathogenesis of COPD.

Yet the precise roles of 4-HNE in COPD have not been clearly elucidated. In the present study, we immunohistochemically investigated the levels and localization of 4-HNE in the lungs of two different animal models of COPD: elastase-treated mice and surfactant protein D (SP-D)-deficient mice. Additionally, we challenged mouse lungs intratracheally with 4-HNE to investigate the potential contributions of 4-HNE to COPD, lung inflammation, and metalloproteinase expression.

* Corresponding author. Fax: +81 6 6879 3839.
E-mail address: takataka2003@mail.goo.ne.jp (T. Takimoto).

0006-291X/$ - see front matter © 2012 Elsevier Inc. All rights reserved.
doi:10.1016/j.bbrc.2012.02.119

2. Materials and methods

2.1. 4-HNE administration to mice

A solution of 4-HNE in ethanol (Cayman Chemical Co., Ann Arbor, MI) was concentrated to 50 mg/ml and stored at −80 °C. The stock solution was diluted with saline to two concentrations (20 mM or approximately 8 mg/kg; 30 mM or approximately 12 mg/kg). Eight-week-old C57BL6 J male mice (Clea Japan, Tokyo, Japan) were anesthetized with pentobarbital and intratracheally challenged with 100 μl of the 4-HNE solution. Mice were sacrificed at 3 h, 1, 3, 5, or 7 days after the mice were challenged with 4-HNE. For bronchoalveolar lavage, the trachea was cannulated and the lungs were lavaged three times with 0.5 ml of PBS. Inflammatory cells were counted using a hemocytometer. Counts of morphologically different cell types were performed after Diff-Quik staining (International Reagents, Hyogo, Japan) to classify the infiltrating cells as monocytes/macrophages, lymphocytes, neutrophils, or eosinophils. Supernatant was stored at −80 °C until the experiments. Mice were maintained in a specific pathogen-free facility, and all animal procedures were performed in accordance with Osaka University guidelines on animal care.

2.2. COPD models

Eight-week-old C57BL6J male mice were anesthetized with pentobarbital and intratracheally challenged with porcine pancreatic elastase (Elastin Products Company, Owensville, MO) solution (1.2 U/100 μl of saline) as reported previously [18] and sacrificed after 3 weeks. SP-D-deficient mice were kindly provided by Jeffrey A. Whitsett (Cincinnati Children's Hospital Medical Center, Cincinnati, OH) [11].

2.3. Morphometry

Lungs were inflation-fixed (25 cm H_2O) with 10% formalin in PBS for 1 min and immersed in the same fixative for 18 h at 4 °C. Samples were then processed according to standard methods for paraffin-embedded blocks. Sections (5-μm thick) were stained with hematoxylin and eosin and the alveolar space size was quantified by measuring the mean chord length using previously described NIH image software [19]. Briefly, 20 randomly selected fields from the left lung of each mouse were examined using Scion Image (Scion, Frederick, MD). Images were manipulated with processing software. At least 200 measurements per field were performed. The lengths of lines overlying the airspace air were averaged as the mean chord length.

2.4. Histologic analysis

Five-micrometer lung sections were stained with hematoxylin and eosin and Periodic acid-Schiff (PAS) to detect mucin-producing cells. Immunohistochemistry was performed on paraffin sections (5-μm thick). Primary antibodies were specific for 4-HNE protein adducts (1:50, Calbiochem, Darmstadt, Germany), matrix metalloproteinase (MMP)-2 (1:100, goat polyclonal, Santa Cruz Biotechnologies, Santa Cruz, CA), MMP-9 (1:100, goat polyclonal, Santa Cruz Biotechnologies), and Mucin 5AC (MUC5AC) (1:50, mouse monoclonal, Abcam, Cambridge, UK). After incubation with biotinized secondary antibodies, signals were visualized with Vectastain ABC Kit reagents (Vector Laboratories, Burlingame, CA). TdT-mediated dUTP nick end labeling (TUNEL) staining was performed using an In Situ Cell Death Detection Kit (Roche, Mannheim, Germany).

2.5. Bronchoalveolar lavage fluid (BALF) analysis

Protein concentrations in BALF were measured using the Lowry method. MMP activity in BALF was determined using gelatin zymography as described previously [20]. Briefly, 10 μl of BALF supernatant was incubated with nonreducing sample buffer and subjected to electrophoresis on 10% zymogram gelatin gels (Novex, Carlsbad, CA). Gels were washed twice in 2.5% Triton X-100;

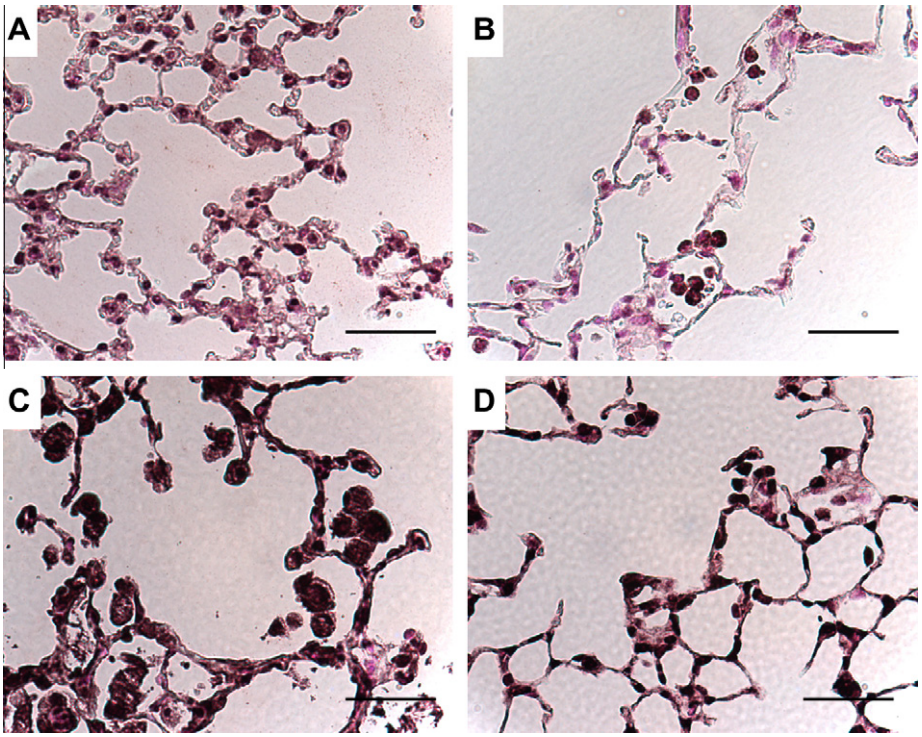

Fig. 1. 4-HNE in animal models of COPD. Immunostaining for 4-HNE adducts in lungs from naïve control mice (A), elastase-treated mice at 14 days (B), SP-D-deficient mice at 6 months (C), and 4-HNE-challenged mice at 3 h (D). Scale bar = 50 μm.

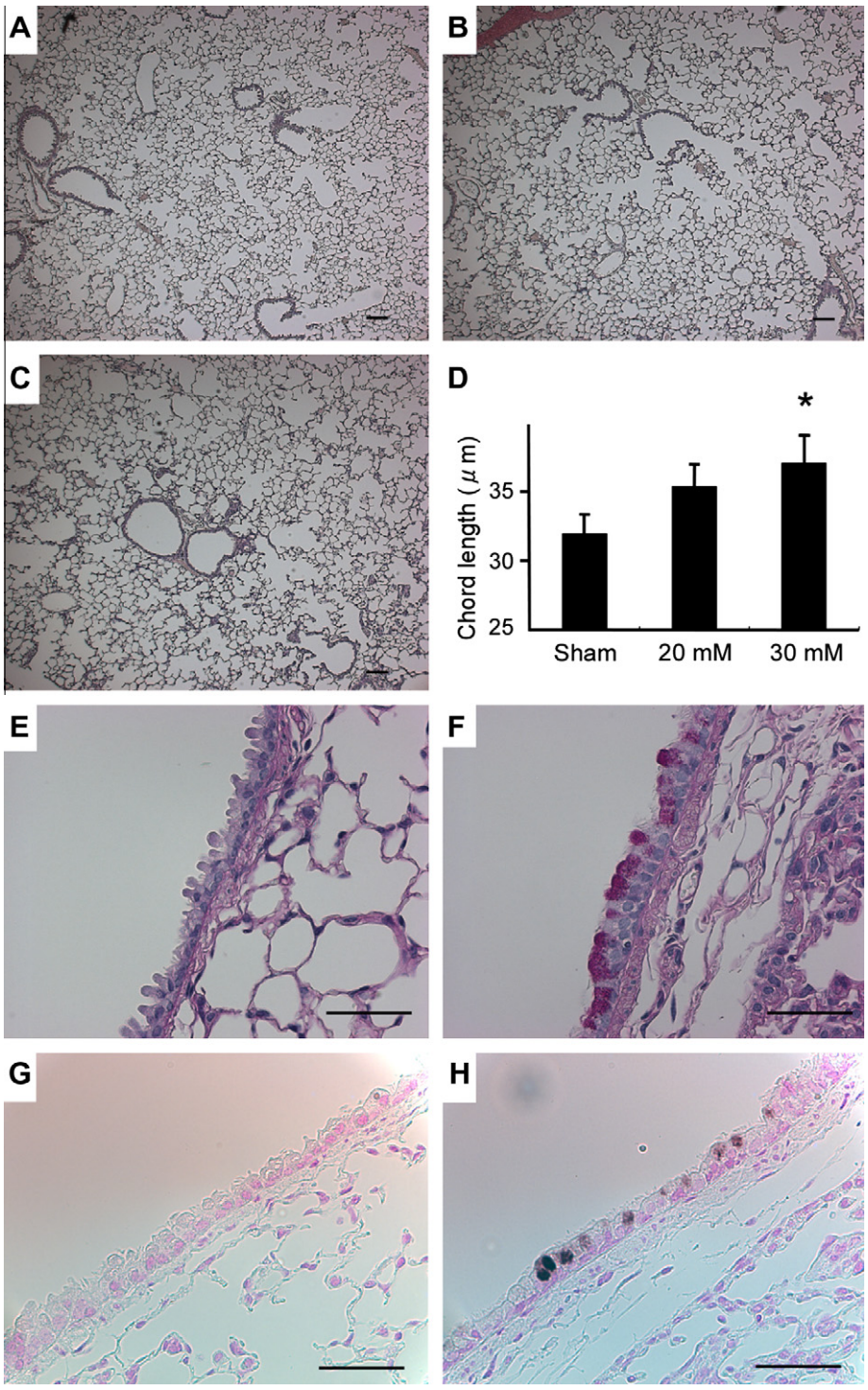

Fig. 2. Intratracheal administration of 4-HNE induces COPD-like changes in mice. Representative histologic changes in peripheral lungs after 1 week in sham-treated mice (A), and mice challenged with 20 mM (B) or 30 mM (C) 4-HNE (n = 5/group). Scale bar = 50 μm. (D) Chord length in the airspace was calculated from photomicrographs of lung parenchyma from sham-treated and 4-HNE-challenged mice. Values are means ± SEM. *Significant difference between the sham-treated and 4-HNE-challenged groups. Representative histologic changes after 1 week in airways from sham-treated mice (E, G) and 4-HNE-challenged mice (F, H). Mucous cell metaplasia was visualized using PAS staining (E, F) and MUC5AC immunostaining (G, H) (n = 5/group). Scale bar = 50 μm.

incubated for 24 h with 40 mM Tris/HCl (pH 7.5), 10 mM $CaCl_2$, and 1 M $ZnCl_2$; and stained with Coomassie Blue. Gelatinolytic activities were quantified on a FluorChem system (Alpha Innotech, San Leandro, CA) using AlphaEase software.

2.6. Statistical analysis

Data are expressed as means ± SEM. Differences between two groups were evaluated using two-sided Student's t-tests. Differences

between multiple groups were evaluated using one-factor ANOVA followed by Tukey–Kramer test for post hoc analysis. *P* values < 0.05 were considered statistically significant.

3. Results

3.1. 4-HNE levels were elevated in animal models of COPD

To examine whether 4-HNE contributes to the pathogenesis of COPD, we immunohistochemically examined 4-HNE adducts in two different mouse models of COPD. Elastase-induced emphysema is frequently used to model COPD based on the protease–antiprotease imbalance hypothesis [18]. We observed significantly higher levels of 4-HNE adducts in inflammatory cells accumulating in the alveolar space of elastase-treated mouse lungs (Fig. 1B). We also performed immunohistochemistry for 4-HNE adducts in SP-D-deficient mice, in which inflammatory cell accumulation and emphysematous changes in the peripheral lungs are observed beginning 3 weeks after birth and progress thereafter [11]. Our results showed that 4-HNE adduct-positive cells were localized in the enlarged airspaces of the lungs of 6-month-old SP-D-deficient mice (Fig. 1C). Together with previous studies identifying 4-HNE-positive cells in the lungs of patients with COPD [17] and other COPD animal models [6,7,21], our data suggest that 4-HNE contributes to the pathogenesis of human and animal COPD.

3.2. 4-HNE induced COPD-like changes in mice

Next, we examined if 4-HNE produced COPD-like change in the lungs of the mice. Two concentrations of 4-HNE were intratracheally injected into 8-week-old mice. Immunohistochemistry showed that 4-HNE was widely distributed throughout the airway and alveolar regions 3 h after injection (Fig. 1D). Morphometric analysis of the chord length showed that 4-HNE injection caused significant airspace enlargement compared with sham treatment 7 days after the injection (Fig. 2D). The change in the alveolar size was dependent on the injected 4-HNE dose. PAS staining and immunohistochemistry for MUC5AC occasionally revealed goblet cell metaplasia accompanied by subepithelial inflammation in the airway walls of the 4-HNE-challenged mice, which was never found in sham-treated mice (Fig. 2E–H).

Apoptosis of alveolar septal cells has been implicated in the pathogenesis of COPD [5,22,23]. TUNEL staining, however, failed to detect positive cells in the alveolar septa, suggesting that apoptosis does not markedly contribute to the development of the emphysematous phenotype in this model. In contrast, TUNEL-positive cells were seen in the airway epithelia as early as 2 h after mice were challenged with 4-HNE (data not shown).

3.3. 4-HNE induced lung inflammation and upregulation of MMP expression

To characterize the COPD-like changes after 4-HNE administration, we analyzed BALF. The total cell count in BALF was significantly elevated 1 and 3 days after intratracheal injection of 4-HNE (Fig. 3A). Neutrophil infiltration into airspaces peaked 1 day after the injection and remained elevated for the next 4 days. More macrophages were observed in BALF from 4-HNE-challenged mice, peaking 3 days after 4-HNE administration (Fig. 3B). Similarly, total BALF protein concentrations—an indicator of lung vascular permeability—were also significantly increased at 1 and 3 days (Fig. 3C). These results indicate that 4-HNE injection caused severe pulmonary inflammation. We next examined proteolytic activities in BALF using gelatin zymography. The activities of MMP-2 and MMP-9 in BALF increased 1 day after injection (Fig. 4A and B). High expression levels of these MMPs were detected in alveolar inflammatory cells from 4-HNEchallenged mice (Fig. 4C–F). Taken together, the data show that that 4-HNE administration induced lung inflamma-

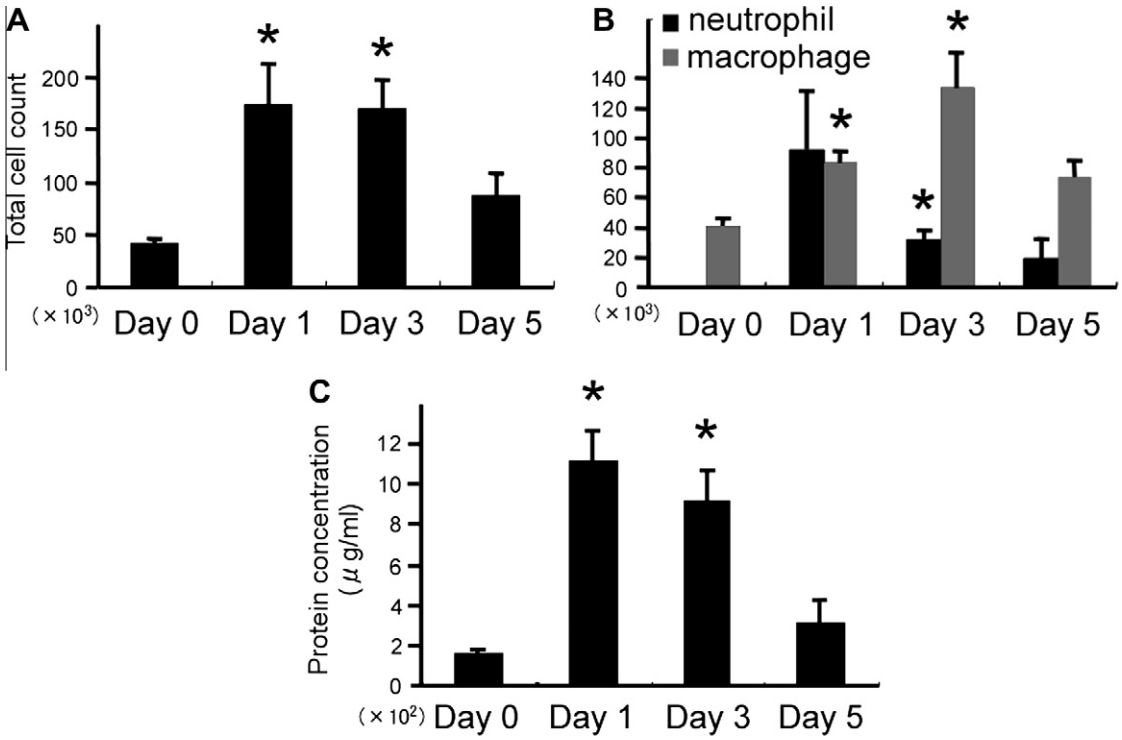

Fig. 3. Intratracheal administration of 4-HNE induces lung inflammation. Bronchoalveolar lavage was performed 0, 1, 3, or 5 days after 4-HNE administration (n = 6/group). Total cell count (A), neutrophil and macrophage numbers (B), and protein concentrations (C) were measured in BALF samples. Values are means ± SEM. *Significant difference between the naïve control and 4-HNE-challenged groups.

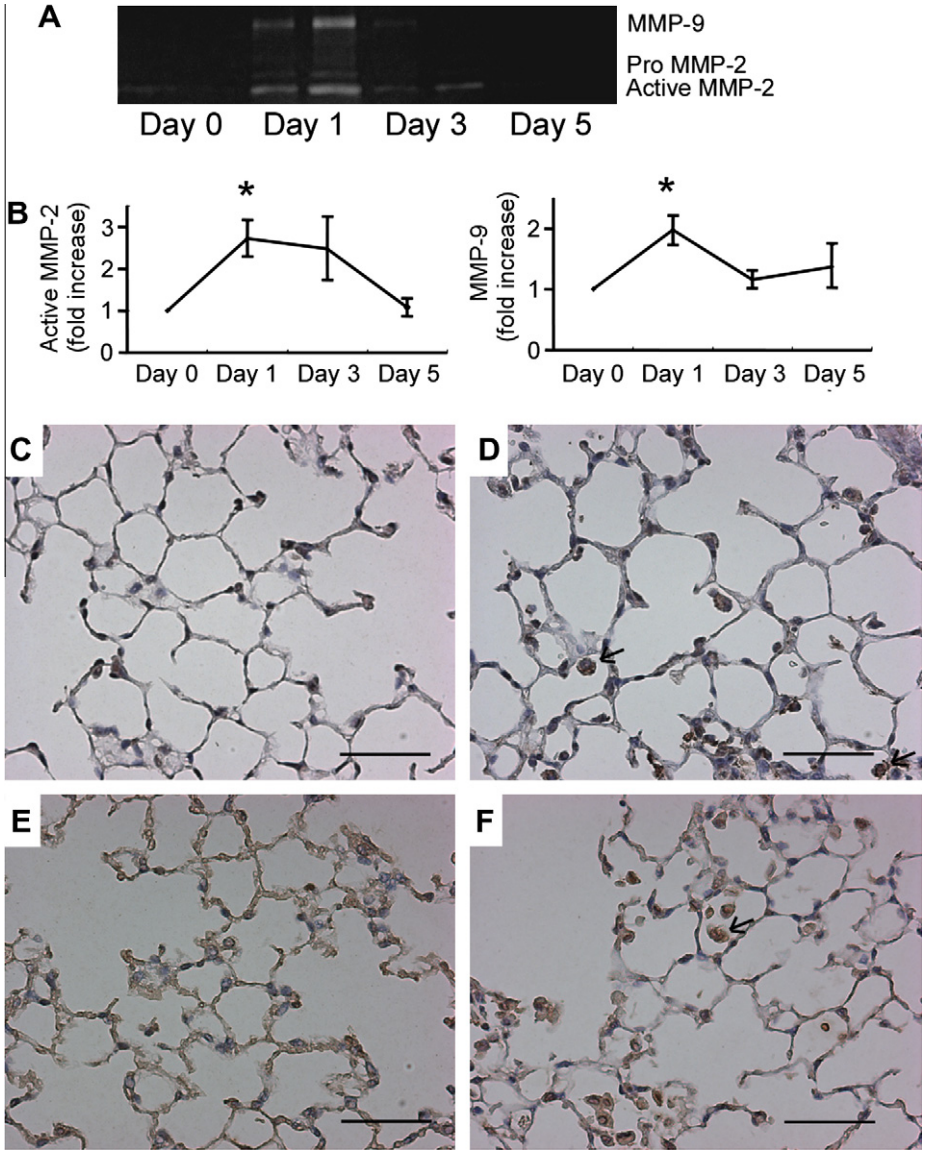

Fig. 4. Intratracheal administration of 4-HNE induces MMP activation in lungs. MMP-2 and MMP-9 activities were examined using gelatin zymography and BALF supernatants obtained 0, 1, 3, or 5 days after 4-HNE administration (n = 4/group). (A) Representative zymographic results. (B) Densitometric analysis of zymograms. Values are presented as means ± SEM. *Significant difference between the sham-treated and 4-HNE-challenged groups. Representative results of immunohistochemical staining for MMP-2 (C, D) and MMP-9 (E, F) in the lungs from sham-treated mice (C, E) and 4-HNEchallenged mice 1 day after injection (D, F). Scale bar = 50 μm.

tion and increased MMP expression, suggesting that airspace enlargement in the 4-HNEchallenged mice was due to protease–antiprotease imbalance.

4. Discussion

We have investigated the role of 4-HNE in the pathogenesis of COPD. In addition to previous reports, we have demonstrated that 4-HNE adduct levels were increased in two different COPD models: elastase-treated mice and SP-D-deficient mice. Challenging lungs with 4-HNE enlarged the airspace and induced mucus metaplasia of the airways in mice, two characteristics of COPD. Neutrophils and macrophages also accumulated. These inflammatory cells expressed high levels of MMP-2 and MMP-9, suggesting that protease–antiprotease imbalance contributes to the development of these histopathologic changes.

This is the first report to demonstrate 4-HNE-induced structural changes in airways and lung parenchyma that resemble the effects of COPD. These changes were 4-HNE concentration-dependent and were observed after only one injection. Because 4-HNE is endogenously generated by oxidative stress, the presence of 4-HNE suggests a role for oxidative stress in COPD. Our study therefore supports the oxidant–antioxidant imbalance theory in the pathogenesis of COPD.

One drawback of our model is a lack of precise information about 4-HNE concentrations in the respiratory fluid. Previous data demonstrated that 4-HNE accumulated in certain tissues to concentrations of 1 μM to 5 mM in response to oxidative insults [16,17]; yet the concentration of this aldehyde in the respiratory lining fluid of patients with COPD has not been reported. Another limitation is that our model is an acute model with a single 4-HNE challenge, whereas COPD is a chronic progressive disease. The chronic progressive symptoms of COPD, however, are thought to occur as a result of repeated acute insults [24–26], and repeated exposure to relatively low concentrations of 4-HNE may induce similar histopathologic changes that mimic the effects observed in the lungs of patients with COPD.

The present study demonstrated that 4-HNE elicited an influx of neutrophils and macrophages into mouse lungs. *In vivo* studies have shown that 4-HNE causes inflammation at the site of injection [27,28]; the underlying mechanism has been reported to be upregulated expression of chemokines (e.g., monocyte chemoattractant protein-1 [29] and interleukin-8 [30]), destruction of the endothelial barrier [31], or structural modification of collagen by 4-HNE [32]. A recent study revealed reduced levels of protein deacetylases, including histone deacetylases (HDACs) [33] and sirtuin (SIRT) proteins [34], in peripheral lungs of patients with COPD. Cigarette smoke increases 4-HNE-mediated modifications of HDAC2 and SIRT1, decreasing the activities of these enzymes [34–36]. These findings imply that decreases in the levels or activities of protein deacetylases may contribute to 4-HNE-induced inflammation.

Of note, we observed that the infiltrating inflammatory cells expressed elevated levels of MMP-2 and MMP-9. These data were supported by other reports demonstrating a link between oxidative stress, inflammation, and activation of proteases in the pathogenesis of COPD [8,10,11,37,38]. Furthermore, our observation was consistent with previous data showing that 4-HNE enhanced MMP production in murine macrophages [39]. 4-HNE has also been shown to activate latent forms of proenzymes [40].

Unexpectedly, in our animal study, the number of apoptotic alveolar septal cells did not significantly increase in 4-HNE-challenged mice compared with sham-treated mice. In contrast, a number of apoptotic bronchial epithelial cells were observed. It has been previously demonstrated that 4-HNE exerts cytotoxic effects for a variety of cells *in vitro* [41,42] and induces apoptosis of lung structural cells *ex vivo* [43], supporting our observation of apoptosis in bronchial epithelial cells. One explanation of the discrepancy between the alveolar and airway regions may be the local concentration of 4-HNE, which was likely lower in the alveolar region than in the airway region owing to removal mechanisms and/or differences in the surface areas.

In conclusion, 4-HNE, an end-product of oxidative stress, induced accumulation of inflammatory cells expressing high levels of MMPs, leading to such histopathologic hallmarks of COPD as airspace enlargement and goblet cell metaplasia. Our results indicate that 4-HNE plays an important role in the development of COPD, and further supports the oxidant–antioxidant imbalance theory in the pathogenesis of COPD.

Acknowledgments

We thank R. Inoue for technical assistance, Y. Habe for secretarial assistance, and Y. Tomita and S. Furue (Shionogi & Co., Osaka, Japan) for assistance with chord length measurements. This study was supported by a Grant-in Aid for Scientific Research from the Ministry of Education, Culture, Sports, Science and Technology of Japan.

References

[1] R.A. Pauwels, A.S. Buist, P.M. Calverley, C.R. Jenkins, S.S. Hurd, Global strategy for the diagnosis, management, and prevention of chronic obstructive pulmonary disease. NHLBI/WHO Global Initiative for Chronic Obstructive Lung Disease (GOLD) Workshop summary, Am. J. Respir. Crit. Care Med. 163 (2001) 1256–1276.

[2] J.B. Soriano, R. Rodriguez-Roisin, Chronic obstructive pulmonary disease overview: epidemiology, risk factors, and clinical presentation, Proc. Am. Thorac. Soc. 8 (2011) 363–367.

[3] W. MacNee, Pathogenesis of chronic obstructive pulmonary disease, Proc. Am. Thorac. Soc. 2 (2005) 258–266 (discussion 290–251).

[4] S. Rajendrasozhan, H. Yao, I. Rahman, Current perspectives on role of chromatin modifications and deacetylases in lung inflammation in COPD, COPD 6 (2009) 291–297.

[5] I. Petrache, V. Natarajan, L. Zhen, T.R. Medler, A.T. Richter, C. Cho, W.C. Hubbard, E.V. Berdyshev, R.M. Tuder, Ceramide upregulation causes pulmonary cell apoptosis and emphysema-like disease in mice, Nat. Med. 11 (2005) 491–498.

[6] C.S. Stevenson, C. Docx, R. Webster, C. Battram, D. Hynx, J. Giddings, P.R. Cooper, P. Chakravarty, I. Rahman, J.A. Marwick, P.A. Kirkham, C. Charman, D.L. Richardson, N.R. Nirmala, P. Whittaker, K. Butler, Comprehensive gene expression profiling of rat lung reveals distinct acute and chronic responses to cigarette smoke inhalation, Am. J. Physiol. Lung Cell. Mol. Physiol. 293 (2007) L1183–1193.

[7] R.M. Tuder, L. Zhen, C.Y. Cho, L. Taraseviciene-Stewart, Y. Kasahara, D. Salvemini, N.F. Voelkel, S.C. Flores, Oxidative stress and apoptosis interact and cause emphysema due to vascular endothelial growth factor receptor blockade, Am. J. Respir. Cell Mol. Biol. 29 (2003) 88–97.

[8] R.F. Foronjy, O. Mirochnitchenko, O. Propokenko, V. Lemaitre, Y. Jia, M. Inouye, Y. Okada, J.M. D'Armiento, Superoxide dismutase expression attenuates cigarette smoke- or elastase-generated emphysema in mice, Am. J. Respir. Crit. Care Med. 173 (2006) 623–631.

[9] M.L. Rubio, M.C. Martin-Mosquero, M. Ortega, G. Peces-Barba, N. Gonzalez-Mangado, Oral N-acetylcysteine attenuates elastase-induced pulmonary emphysema in rats, Chest 125 (2004) 1500–1506.

[10] T. Rangasamy, C.Y. Cho, R.K. Thimmulappa, L. Zhen, S.S. Srisuma, T.W. Kensler, M. Yamamoto, I. Petrache, R.M. Tuder, S. Biswal, Genetic ablation of Nrf2 enhances susceptibility to cigarette smoke-induced emphysema in mice, J. Clin. Invest. 114 (2004) 1248–1259.

[11] S.E. Wert, M. Yoshida, A.M. LeVine, M. Ikegami, T. Jones, G.F. Ross, J.H. Fisher, T.R. Korfhagen, J.A. Whitsett, Increased metalloproteinase activity, oxidant production, and emphysema in surfactant protein D gene-inactivated mice, Proc. Natl. Acad. Sci. USA 97 (2000) 5972–5977.

[12] B.K. Butland, A.M. Fehily, P.C. Elwood, Diet, lung function, and lung function decline in a cohort of 2512 middle aged men, Thorax 55 (2000) 102–108.

[13] P. Kirkham, I. Rahman, Oxidative stress in asthma and COPD: antioxidants as a therapeutic strategy, Pharmacol. Ther. 111 (2006) 476–494.

[14] G. Leonarduzzi, F. Robbesyn, G. Poli, Signaling kinases modulated by 4-hydroxynonenal, Free Radic. Biol. Med. 37 (2004) 1694–1702.

[15] D.R. Petersen, J.A. Doorn, Reactions of 4-hydroxynonenal with proteins and cellular targets, Free Radic. Biol. Med. 37 (2004) 937–945.

[16] M.U. Dianzani, 4-Hydroxynonenal from pathology to physiology, Mol. Aspects Med. 24 (2003) 263–272.

[17] I. Rahman, A.A. van Schadewijk, A.J. Crowther, P.S. Hiemstra, J. Stolk, W. MacNee, W.I. De Boer, 4-Hydroxy-2-nonenal, a specific lipid peroxidation product, is elevated in lungs of patients with chronic obstructive pulmonary disease, Am. J. Respir. Crit. Care Med. 166 (2002) 490–495.

[18] T. Kinoshita, T. Hoshino, H. Imaoka, H. Ichiki, M. Okamoto, T. Kawayama, J. Yodoi, S. Kato, H. Aizawa, Thioredoxin prevents the development and progression of elastase-induced emphysema, Biochem. Biophys. Res. Commun. 354 (2007) 712–719.

[19] T. Zheng, Z. Zhu, Z. Wang, R.J. Homer, B. Ma, R.J. Riese Jr., H.A. Chapman Jr., S.D. Shapiro, J.A. Elias, Inducible targeting of IL-13 to the adult lung causes matrix metalloproteinase- and cathepsin-dependent emphysema, J. Clin. Invest. 106 (2000) 1081–1093.

[20] Y. Takeda, P. He, I. Tachibana, B. Zhou, K. Miyado, H. Kaneko, M. Suzuki, S. Minami, T. Iwasaki, S. Goya, T. Kijima, T. Kumagai, M. Yoshida, T. Osaki, T. Komori, E. Mekada, I. Kawase, Double deficiency of tetraspanins CD9 and CD81 alters cell motility and protease production of macrophages and causes COPD-like phenotype in mice, J. Biol. Chem. 283 (2008) 26089–26097.

[21] H. Yao, I. Edirisinghe, S. Rajendrasozhan, S.R. Yang, S. Caito, D. Adenuga, I. Rahman, Cigarette smoke-mediated inflammatory and oxidative responses are strain-dependent in mice, Am. J. Physiol. Lung Cell. Mol. Physiol. 294 (2008) L1174–1186.

[22] Y. Kasahara, R.M. Tuder, L. Taraseviciene-Stewart, T.D. Le Cras, S. Abman, P.K. Hirth, J. Waltenberger, N.F. Voelkel, Inhibition of VEGF receptors causes lung cell apoptosis and emphysema, J. Clin. Invest. 106 (2000) 1311–1319.

[23] I.K. Demedts, T. Demoor, K.R. Bracke, G.F. Joos, G.G. Brusselle, Role of apoptosis in the pathogenesis of COPD and pulmonary emphysema, Respir. Res. 7 (2006) 53.

[24] B.D. Gelbman, A. Heguy, T.P. O'Connor, J. Zabner, R.G. Crystal, Upregulation of pirin expression by chronic cigarette smoking is associated with bronchial epithelial cell apoptosis, Respir. Res. 8 (2007) 10.

[25] J.C. Hogg, F. Chu, S. Utokaparch, R. Woods, W.M. Elliott, L. Buzatu, R.M. Cherniack, R.M. Rogers, F.C. Sciurba, H.O. Coxson, P.D. Pare, The nature of small-airway obstruction in chronic obstructive pulmonary disease, N. Engl. J. Med. 350 (2004) 2645–2653.

[26] J.C. Hogg, Pathophysiology of airflow limitation in chronic obstructive pulmonary disease, Lancet 364 (2004) 709–721.

[27] T. Kumagai, N. Matsukawa, Y. Kaneko, Y. Kusumi, M. Mitsumata, K. Uchida, A lipid peroxidation-derived inflammatory mediator: identification of 4-hydroxy-2-nonenal as a potential inducer of cyclooxygenase-2 in macrophages, J. Biol. Chem. 279 (2004) 48389–48396.

[28] I. Boldogh, A. Bacsi, B.K. Choudhury, N. Dharajiya, R. Alam, T.K. Hazra, S. Mitra, R.M. Goldblum, S. Sur, ROS generated by pollen NADPH oxidase provide a signal that augments antigen-induced allergic airway inflammation, J. Clin. Invest. 115 (2005) 2169–2179.

[29] M. Nitti, C. Domenicotti, C. d'Abramo, S. Assereto, D. Cottalasso, E. Melloni, G. Poli, F. Biasi, U.M. Marinari, M.A. Pronzato, Activation of PKC-beta isoforms mediates HNE-induced MCP-1 release by macrophages, Biochem. Biophys. Res. Commun. 294 (2002) 547–552.

[30] F. Facchinetti, F. Amadei, P. Geppetti, F. Tarantini, C. Di Serio, A. Dragotto, P.M. Gigli, S. Catinella, M. Civelli, R. Patacchini, Alpha, beta-unsaturated aldehydes in cigarette smoke release inflammatory mediators from human macrophages, Am. J. Respir. Cell Mol. Biol. 37 (2007) 617–623.
[31] P.V. Usatyuk, N.L. Parinandi, V. Natarajan, Redox regulation of 4-hydroxy-2-nonenal-mediated endothelial barrier dysfunction by focal adhesion, adherens, and tight junction proteins, J. Biol. Chem. 281 (2006) 35554–35566.
[32] P.A. Kirkham, G. Spooner, C. Ffoulkes-Jones, R. Calvez, Cigarette smoke triggers macrophage adhesion and activation: role of lipid peroxidation products and scavenger receptor, Free Radic. Biol. Med. 35 (2003) 697–710.
[33] K. Ito, M. Ito, W.M. Elliott, B. Cosio, G. Caramori, O.M. Kon, A. Barczyk, S. Hayashi, I.M. Adcock, J.C. Hogg, P.J. Barnes, Decreased histone deacetylase activity in chronic obstructive pulmonary disease, N. Engl. J. Med. 352 (2005) 1967–1976.
[34] S. Rajendrasozhan, S.R. Yang, V.L. Kinnula, I. Rahman, SIRT1, an antiinflammatory and antiaging protein, is decreased in lungs of patients with chronic obstructive pulmonary disease, Am. J. Respir. Crit. Care Med. 177 (2008) 861–870.
[35] J.A. Marwick, P.A. Kirkham, C.S. Stevenson, H. Danahay, J. Giddings, K. Butler, K. Donaldson, W. Macnee, I. Rahman, Cigarette smoke alters chromatin remodeling and induces proinflammatory genes in rat lungs, Am. J. Respir. Cell Mol. Biol. 31 (2004) 633–642.
[36] F.M. Moodie, J.A. Marwick, C.S. Anderson, P. Szulakowski, S.K. Biswas, M.R. Bauter, I. Kilty, I. Rahman, Oxidative stress and cigarette smoke alter chromatin remodeling but differentially regulate NF-kappaB activation and proinflammatory cytokine release in alveolar epithelial cells, FASEB J. 18 (2004) 1897–1899.
[37] T. Iizuka, Y. Ishii, K. Itoh, T. Kiwamoto, T. Kimura, Y. Matsuno, Y. Morishima, A.E. Hegab, S. Homma, A. Nomura, T. Sakamoto, M. Shimura, A. Yoshida, M. Yamamoto, K. Sekizawa, Nrf2-deficient mice are highly susceptible to cigarette smoke-induced emphysema, Genes Cells 10 (2005) 1113–1125.
[38] M. Yoshida, T.R. Korfhagen, J.A. Whitsett, Surfactant protein D regulates NF-kappa B and matrix metalloproteinase production in alveolar macrophages via oxidant-sensitive pathways, J. Immunol. 166 (2001) 7514–7519.
[39] S.J. Lee, C.E. Kim, M.R. Yun, K.W. Seo, H.M. Park, J.W. Yun, H.K. Shin, S.S. Bae, C.D. Kim, 4-Hydroxynonenal enhances MMP-9 production in murine macrophages via 5-lipoxygenase-mediated activation of ERK and p38 MAPK, Toxicol. Appl. Pharmacol. 242 (2010) 191–198.
[40] B. Morquette, Q. Shi, P. Lavigne, P. Ranger, J.C. Fernandes, M. Benderdour, Production of lipid peroxidation products in osteoarthritic tissues: new evidence linking 4-hydroxynonenal to cartilage degradation, Arthritis Rheum. 54 (2006) 271–281.
[41] W. Liu, M. Kato, A.A. Akhand, A. Hayakawa, H. Suzuki, T. Miyata, K. Kurokawa, Y. Hotta, N. Ishikawa, I. Nakashima, 4-Hydroxynonenal induces a cellular redox status-related activation of the caspase cascade for apoptotic cell death, J. Cell Sci. 113 (Pt 4) (2000) 635–641.
[42] T. Takimoto, M. Yoshida, H. Hirata, M. Suzuki, M. Yanagita, Y. Kashiwa, K. Inoue, Y. Yano, S. Hoshino, Y. Takeda, S. Goya, T. Kijima, T. Kumagai, T. Osaki, I. Tachibana, I. Kawase, 4-Hydroxy-2-nonenal induces endothelial cell injury via PKCδ and biphasic JNK activation, EXCLI J. 7 (2008) 71–78.
[43] C.N. Compton, A.P. Franko, M.T. Murray, L.N. Diebel, S.A. Dulchavsky, Signaling of apoptotic lung injury by lipid hydroperoxides, J. Trauma 44 (1998) 783–788.

Biochemical and Biophysical Research Communications 420 (2012) 91–95

Contents lists available at SciVerse ScienceDirect

Biochemical and Biophysical Research Communications

journal homepage: www.elsevier.com/locate/ybbrc

DACH1 regulates cell cycle progression of myeloid cells through the control of *cyclin D*, *Cdk 4/6* and $p21^{Cip1}$

Jae-Woong Lee [a], Hyeng-Soo Kim [a], Seonggon Kim [a], Junmo Hwang [a], Young Hun Kim [a], Ga Young Lim [a], Wern-Joo Sohn [b], Suk-Ran Yoon [c], Jae-Young Kim [b], Tae Sung Park [d], Kwon Moo Park [e], Zae Young Ryoo [a], Sanggyu Lee [a,*]

[a] School of Life Science and Biotechnology, Kyungpook National University, Daegu 702-701, Republic of Korea
[b] Department of Biochemistry, School of Dentistry, IHBR, Kyungpook National University, Daegu 700-412, Republic of Korea
[c] Cell Therapy Research Center, Korea Research Institute of Bioscience and Biotechnology, Yuseong-gu, Daejeon 305-806, Republic of Korea
[d] Department of Laboratory Medicine, Kyung Hee University School of Medicine, 1 Hoegi-dong, Dongdaemun-gu, Seoul 130-702, Republic of Korea
[e] Department of Anatomy, Kyungpook National University School of Medicine, Daegu 700-422, Republic of Korea

ARTICLE INFO

Article history:
Received 7 February 2012
Available online 3 March 2012

Keywords:
DACH1
Myeloid leukemia
CCND
$p21^{Cip1}$
MLL-AF9

ABSTRACT

The cell-fate determination factor *Dachshund*, a component of the Retinal Determination Gene Network (RDGN), has a role in breast tumor proliferation through the repression of *cyclin D1* and several key regulators of embryonic stem cell function, such as *Nanog* and *Sox2*. However, little is known about the role of *DACH1* in a myeloid lineage as a cell cycle regulator. Here, we identified the differential expression levels of extensive cell cycle regulators controlled by *DACH1* in myeloid progenitor cells. The forced expression of *DACH1* induced $p27^{Kip1}$ and repressed $p21^{Cip1}$, which is a pivotal characteristic of the myeloid progenitor. Furthermore, *DACH1* significantly increased the expression of *cyclin D1, D3, F,* and *Cdk 1, 4,* and *6* in myeloid progenitor cells. The knockdown of *DACH1* blocked the cell cycle progression of HL-60 promyeloblastic cells through the decrease of *cyclin D1, D3, F,* and *Cdk 1, 4,* and *6* and increase in $p21^{Cip1}$, which in turn decreased the phosphorylation of the Rb protein. The expression of *Sox2, Oct4,* and *Klf4* was significantly up-regulated by the forced expression of *DACH1* in mouse myeloid progenitor cells.

1. Introduction

Cell cycle regulation is critically important for both proper hematopoiesis for the production of various lineages of mature blood cells and leukemogenesis. Abnormal expression of cell cycle regulators results in the development of many hematologic malignancies [1]. The expression level of *cyclin D1* in bone marrow cells is significantly increased in the accelerated phase of common myeloid leukemia [2], and the inhibition of proliferation is associated with increased $p21^{Cip1}$ gene expression in myeloid leukemia cells [3]. Moreover, high $p27^{Kip1}$ expression was significantly associated with shorter overall survival as well as event-free survival in myeloid malignancies [4]. In addition, direct transcriptional control of *cyclin D3* by MEIS1 promotes hematopoietic and leukemic stem cell proliferation by modulating G1-to-S phase progression [5]. However, the transcription factor that extensively regulates the expression of genes associated with cell cycle progression in hematopoietic cells is poorly understood.

The *Drosophila dachshund* (*dac*) gene is a member of the retinal determination gene network (RDGN) that regulates retinal cell fate determination. Recently, *DACH1* was shown to suppress growth of tumor cells and spheroid formation. *DACH1* also regulates bFGF-mediated tumor-initiating activity of glioma cells [6]. *DACH1* inhibits its oncogene-mediated breast cancer epithelial cell DNA synthesis and contact-independent growth of human breast cancer cells *in vivo*. *DACH1* also inhibits DNA synthesis induced by NeuT, Ras/ErbB2, and c-Myc, in which *cyclin D1* and $p21^{Cip1}$ are involved in the process [7]. Furthermore, *DACH1* reduces oncogene-induced expression of *cyclin D1* through direct binding to the *cyclin D1* promoter region, which results in a reduction of cell proportions distributed within the S phase of the cell cycle [7]. *DACH1* acts as a suppressor of *Nanog* and *Sox2* which blocks mammary tumor growth and inhibits properties involved in stem cell expansion in Met-1 breast cancer cells [8]. However, our previous study identified that *DACH1* is significantly up-regulated in myeloid progenitor cells from AML M5 patients harboring t(9;11) [9] and little is known about the role of *DACH1* in leukemogenesis.

In this study, we initially identified the role of *DACH1* in myeloid cells associated with cell cycle regulation and examined the

* Corresponding author.
E-mail address: slee@knu.ac.kr (S. Lee).

0006-291X/$ - see front matter © 2012 Elsevier Inc. All rights reserved.
doi:10.1016/j.bbrc.2012.02.120

expression of *DACH1* in various leukemia cells. Our study provides novel insight into the role of *DACH1* as a cell cycle regulator in myeloid cells.

2. Materials and methods

2.1. Cell lines

Various human leukemia cells were grown in RPMI 1640 medium containing 10% fetal bovine serum (FBS) and 1% penicillin/streptomycin (Gibco). Human embryonic kidney (HEK) 293 cells were grown in DMEM containing 10% fetal bovine serum (FBS) and 1% penicillin/streptomycin (Gibco).

2.2. Plasmids

MLL-AF9 was amplified from a total cDNA library prepared from the myeloid progenitor cells of an AML-M5 patient and digested with EcoRI/XhoI, followed by ligation into pcDNA3.1/myc/hisA (Invitrogen). The human *DACH1* (NM_080759) was cloned into pcDNA3.1/myc/hisA. All constructs were confirmed by sequencing.

2.3. Retroviral transformation assays

A human *DACH1* cDNA fragment was cloned into the BglII/XhoI sites of the retroviral pMIG (MSCV-IRES-GFP) vector. The retrovirus was produced by Fugene HD transfection of Plat-E cells. The virus was harvested 48 h after transfection, filtered, and used to infect mouse bone marrow mononuclear cells. Bone marrow mononuclear cells were harvested from the femurs and tibiae of 6-week-old C57Bl/6 mice and isolated using Ficoll-Paque™ PLUS (GE Healthcare). The mononuclear cells were activated in IMDM containing 15% FBS, IL-3, IL-6, and SCF for 48 h and transduced with retroviral supernatants in RetroNectin (TaKaRa)-coated well plates. 1.0×10^4 cells were cultured in MeholCult M3234 methylcellulose medium (Stem Cell Technologies) in IMDM, 15% FBS, IL-3, IL-6, and GM-CSF, all at 10 ng/mL and SCF at 100 ng/mL. Cell growth, colony morphology, and numbers were measured after serial replating of the methylcellulose cultures.

2.4. RNA isolation, quantitative RT-PCR

For real-time RT-PCR, equal numbers of induced HEK 293 cells were lysed and RNA was purified according to the manufacturer's instructions (RNeasy Mini kit, Qiagen). A total of 3 μg of RNA was reverse-transcribed to cDNA with M-MLV Reverse Transcriptase according to the manufacturer's protocol (Invitrogen). The levels of gene expression were measured using SYBR green reagents (TaKaRa) using the following sets of primers (Supplementary Table 1). The reactions were performed in an ABI StepOne Plus machine (Applied Biosystems) and analyzed with StepOne software (Applied Biosystems). All reactions were performed in triplicate.

2.5. shRNA

pSUPER expression vectors for small interfering RNAs against *DACH1* were designed with following sense strands of the short hairpin sequence (sh*DACH1*_1: 5′-GATCCCCGCACTTGAGTTTGAGACGATTCAAGAGATCGTCTCAAACTCAAGTGCTTTTTA-3′; sh*DACH1*_2: 5′-GATCCCCCTGTTGAAAGTTGCCATAGTTCAAGAGACTATGGCAACTTTCAACAGTTTTTA-3′; sh*DACH1*_3: 5′-GATCCCCCTGTTTGTTATGTGGATTATTCAAGAGATAATCCACATAACAAACAGTTTTTA-3′ sh*DACH1*_4: 5′-GATCCCCCTGTTGAAAGTTGCCATAGTTCAAGAGACTATGGCAACTTTCAACAGTTTTTA-3′). The vectors were transfected into cells using the FuGENE HD Transfection Reagent (Promega) according to the manufacturer's instructions.

2.6. Western blot analysis

Western blot analysis with antibodies to tubulin α (Bioworld Technology) and phosphorylated pRB (residue amino acid Ser^{780}) (SCBT) were performed as previously described [10].

2.7. Flow cytometric analysis

For cell cycle analysis, 1.0×10^5 cells were harvested and washed with PBS. Cells fixed with 70% ethanol were resuspended in 500 ul of propidium iodide staining solution (50 μg/ml propidium iodide, 2.5% formaldehyde, 0.1% NP40, 50 μg/ml RNase A in PBS), and incubated for 15 min. DNA contents of the cells for cycle distribution were analyzed by a FACS caliber (BD Bioscience). For apoptosis analysis, 1.0×10^5 cells were stained with annexin-V-Cy5 (Biovision), according to the manufacturer's instructions and analyzed using a FACS caliber (BD Bioscience).

2.8. Data analysis and statistics

Data are presented as the mean values ± standard error of the mean. All experiments were performed in triplicate.

Other materials and methods are given in the Supplementary data.

3. Results and discussion

3.1. Molecular regulation of the cell cycle machinery in mouse myeloid progenitor cells by the forced expression of DACH1

To gain insights into the regulation of cell cycle machinery by *DACH1* in myeloid cells, IL-3, IL-6, and SCF-activated mouse myeloid progenitor cells isolated from mouse bone marrow mononuclear cells were transduced with retroviral pMIG or pMIG-*DACH1* and sorted by FACS using the expression of the green fluorescent protein (GFP) (Fig. 1A). Following that, the expression levels of various components of the cell cycle machinery in the transduced mouse myeloid progenitor cells were analyzed by qRT-PCR (Fig. 1B–E). As a result of that, the expression levels of *cyclin D1* and *D3, cyclin E2*, and *Cdk 1, 4,* and *6*, all positive regulators of G_1-phase progression, were elevated in *DACH1* transduced myeloid progenitor cells. Differentiation of long-term HSC (LT-HSC) into multipotent progenitor (MPP) was specifically correlated with increased expression of *cyclin D1*. However, *cyclin D1* should be down-regulated for further proper differentiation of MPP into GMP (granulo-monocytic progenitor) or MEP (megakaryocyte/erythroid progenitor) [11]. It implies that the sustained high expression of *cyclin D1* by the abnormal expression of *DACH1* in myeloid cells may cause abnormal cell cycle progression (Fig. 1B–E).

The expression of *cyclin F* was also increased by *DACH1* (Fig. 1C) [12]. Interestingly, *cyclin F* is required for proper mitosis and genome integrity and predominantly is expressed in GMP including myeloid progenitor, which is one of the most actively proliferative cell populations among the hematopoietic lineages [11]. Therefore, the specific role of *cyclin F* associated with the up-regulation of *DACH1* in myeloid leukemia cells harboring t(9;11) needs to be elucidated.

Moreover, *DACH1* transduced myeloid progenitor cells displayed high levels of $p15^{Ink4b}$ and $p27^{Kip1}$ and low levels of $p16^{Ink4a}$ and $p21^{Cip1}$ (Fig. 1D). In particular, the reduced level of $p21^{Cip1}$ and increased level of $p27^{Kip1}$ by forced expression of *DACH1* was consistent with the specific status of the cell cycle machinery of the

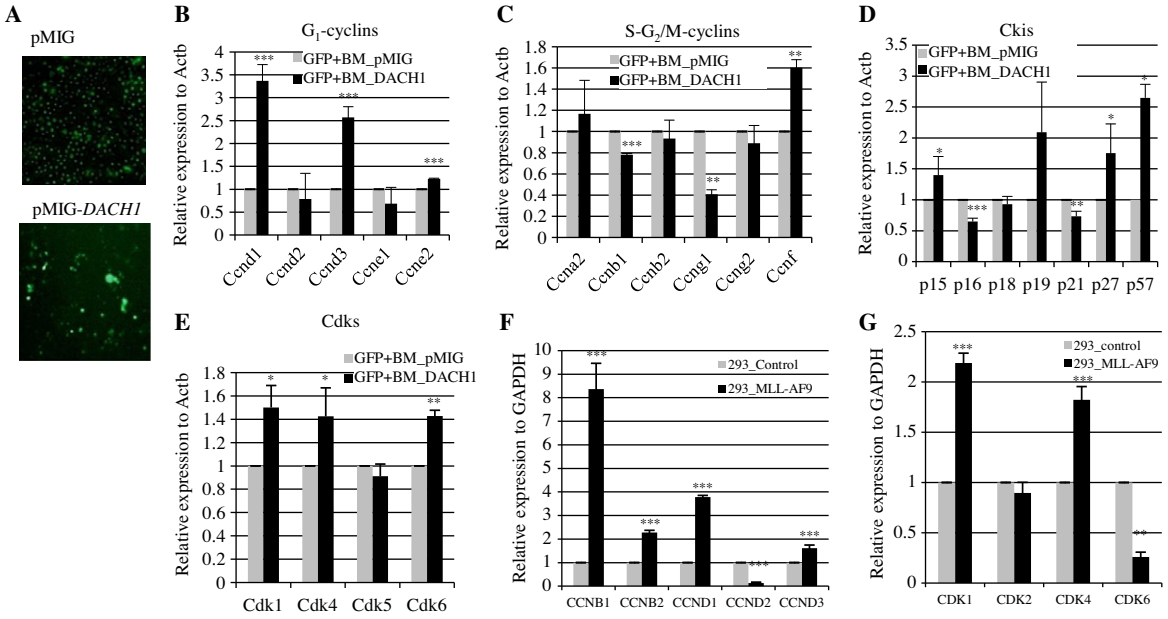

Fig. 1. (A) Isolation of GFP positive mouse bone marrow cells. GFP positive mouse myeloid progenitor cells infected with retrovirus pMIG or pMIG-*DACH1* were analyzed and isolated by FACSAria (BD) (B–E) investigation of the quantitative relative transcript levels of cell cycle regulators in GFP positive mouse myeloid progenitor cells transduced with retrovirus pMIG or pMIG-*DACH1*. The relative expression level was obtained by normalization to that of *ACTB*. (F and G) Differential mRNA expression level of cell cycle regulators. The expression level was determined by real-time PCR analysis in *MLL-AF9*-transfected HEK 293 cells. (mean ± SD, $^{*}P < 0.05$, $^{**}P < 0.01$, $^{*}P < 0.001$, compared with control cells.)

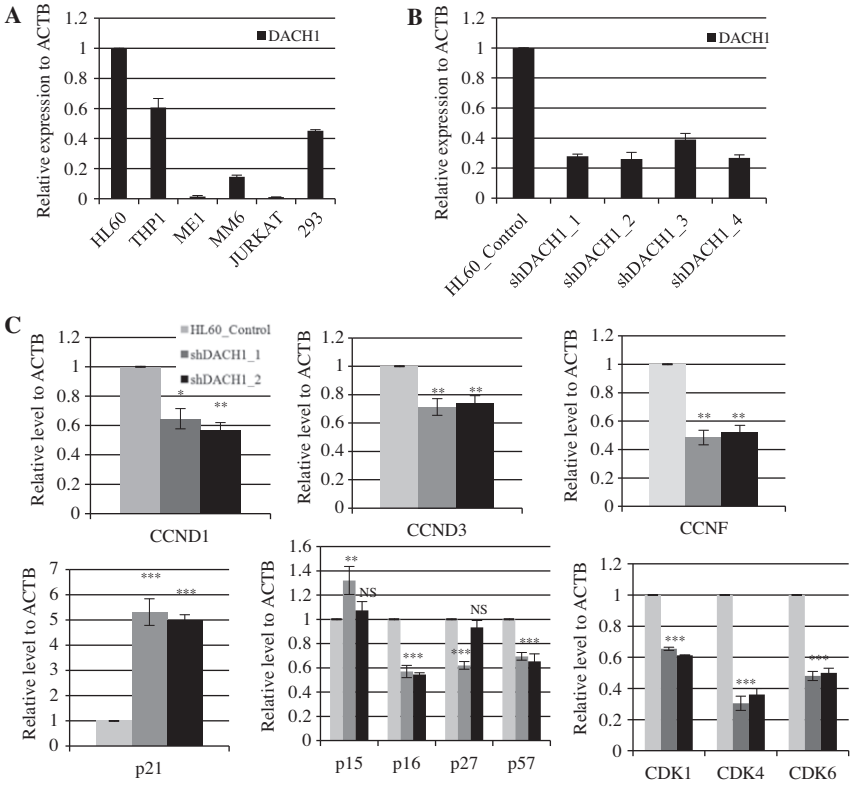

Fig. 2. (A) Differential mRNA expression level of *DACH1* in various leukemic and HEK 293 cells. The expression level was determined by real-time PCR analysis. (B) Knockdown of *DACH1* by transfection of 4 different shRNA constructs targeting different regions of *DACH1*. (C) qRT-PCR. Knockdown of *DACH1* repressed the expression of cell cycle regulators in HL-60. (mean ± SD, $^{*}P < 0.05$, $^{**}P < 0.01$, $^{*}P < 0.001$, compared with control cells.)

GMP population [11]. The expression level of $p57^{Kip2}$ was also significantly increased by the forced expression of *DACH1* (Fig. 1D). It was reported that the deletion of $p57^{Kip2}$, which is the most abundant family member ($p21^{Cip1}$, $p27^{Kip1}$, and $p57^{Kip2}$) in HSCs, results in a decreased number of adult HSCs as well as the abrogation of the self-renewal capacity of the HSCs caused by the exit from

quiescence and entry into apoptosis of the HSCs [13]. In particular, it was identified that the predominant expression of $p57^{Kip2}$ in the HSC compartment is down-regulated during differentiation toward mature myeloid cells [11]. Interestingly, the predominant expression of *DACH1* in the HSC compartment was consistent with the expression of $p57^{Kip2}$ [14]. Therefore, abnormally increased $p57^{Kip2}$ expression by *DACH1* may be associated with maintaining the self-renewal capacity and survival advantage in myeloid leukemia cells harboring t(9;11).

MLL rearrangements affect cell cycle progression and apoptosis, which result in the abnormal regulation of proliferation and differentiation of myeloid cells [15,16]. *MLL-AF9* is one of the most frequent rearrangements that were identified mainly in acute monocytic leukemia [17]. HEK 293 cells transfected with *MLL-AF9* also displayed a significantly increased expression level of *cyclin D1* and *D3*, and *Cdk 1* and *4*, similar to the *DACH1* transduced myeloid progenitor cells (Fig. 1F and G). Although the cell fate determination factor *DACH1* was significantly increased in CD15 + myeloid progenitor cells harboring *MLL-AF9* [9], the specific role of *DACH1* associated with cell cycle regulation has been poorly understood. The current study suggests that *DACH1* may contribute to the abnormal regulation of cell cycle progression in *MLL-AF9* mediated myeloid leukemia.

3.2. Knockdown of DACH1 in HL-60 cells down-regulates cyclin D1, D3, and F, and Cdk 1, 4, and 6 expression and up-regulates the expression of $p21^{Cip1}$

To investigate the differential expression level of *DACH1* in various leukemia cells, we performed qRT-PCR using total mRNA from HL-60, THP-1, ME1, MM6, and Jurkat cells (Fig. 2A). The expression of *DACH1* was most abundant in acute promyelocytic leukemia HL-60 cells, which were arrested at the promyelocytic differentiation stage [18]. Moreover, a human myelomonocytic leukemia ME1 cells derived from eosinophilia (M4E0) showed a lower expression level of *DACH1* relative to THP-1 and MM6 acute monocytic leukemia cells (M5) harboring t(9;11). Interestingly, expression of *DACH1* was negligible in T lymphocytic Jurkat cells harboring t(4;11), which could be a result of the lineage restricted expression of *DACH1* in the monocytic fraction.

To investigate the role of *DACH1* associated with cell cycle regulation in myeloid leukemia cells, short hairpin RNA (shRNA) targeting four different mRNA regions of *DACH1* were used to knock down the expression of endogenous *DACH1* in HL-60 cells (Fig. 2B). From the results of the qRT-PCR using the mRNA from the HL-60 cells transfected with sh*DACH1*, the expression levels of *cyclin D1* and *D3* were significantly reduced and the expression levels of *Cdk 1, 4,* and *6* were also repressed (Fig. 2C). These data suggest that *cyclin D-Cdk 4/6* is the major downstream target of *DACH1* in myeloid leukemia cells. Moreover, expression of *cyclin F,* which is a positive regulator of mitosis, was significantly repressed by the knockdown of *DACH1* (Fig. 2C). This data indicates that increased expression of *cyclin F* by abnormal up-regulation of *DACH1* may have a critical role in cell cycle progression in myeloid leukemia cells.

In addition, $p21^{Cip1}$ expression was significantly increased by knockdown of *DACH1* (Fig. 2C). $p21^{Cip1}$, which is known to have negative effects on the cell cycle machinery, arrests proliferation and inhibits *Cdk* 2 and 4 activities, and suppresses retinoblastoma phosphorylation in human myeloid leukemia cells [19]. However, the specific transcription factor that regulates the expression of $p21^{Cip1}$ in both primary myeloid and leukemia cells was poorly identified. These data suggests that the expression of $p21^{Cip1}$ as well as *cyclin D-Cdk 4/6* has a pivotal role in the *DACH1* mediated regulation of cell cycle progression.

3.3. Knockdown of DACH1 blocks cell cycle progression of HL-60 cells

To evaluate the effect of the abnormally regulated cell cycle machinery by knockdown of *DACH1*, cell cycle distribution was analyzed by PI staining (Fig. 3A). The knockdown of *DACH1* significantly induced the block of G_1 phase with a reduced proportion of the cells undergoing mitotic division. Since the tumor suppressor protein retinoblastoma (Rb) is the major regulator of the G_1/S transition, the level of phosphorylated Rb ser 780 was analyzed. As expected, immunoblot analysis using HL-60 cells transfected with sh*DACH1* showed that down-regulation of *DACH1* inhibited the phosphorylation status of Rb ser 780 (Fig. 3B).

3.4. Forced expression of DACH1 induces the expression of genes associated with embryonic stem cell function

Transcription factors *Oct4, Sox2, Klf4, Nanog,* and *c-Myc* are the key regulator for embryonic stem cell (ESC) self-renewal and pluripotency [20]. Recently, it was reported that *DACH1* represses the expression of *Klf4, Sox2,* and *Nanog* through direct interaction of *DACH1* in the promoter region of the target genes in Met-1 cells, which inhibits mammosphere formation and the $CD44^{+}/CD24^{-}$ cancer stem cell phenotype [8]. To confirm the opposite role of *DACH1* in myeloid cells, the expression of the critical reprogramming factors *Nanog, Oct4, Sox2, Klf4,* and *Lin28* was analyzed using mRNA from the primary mouse myeloid progenitor cells transduced with retroviral control or *DACH1* (Fig. 4). Interestingly,

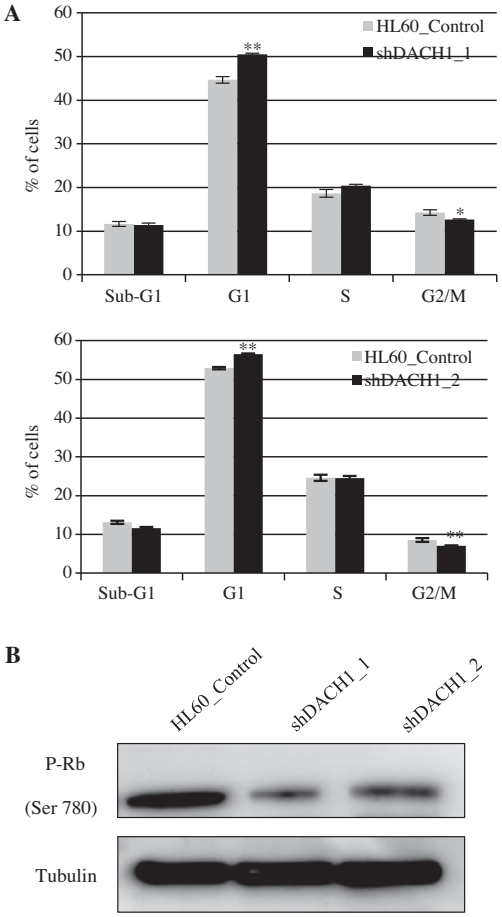

Fig. 3. *DACH1* knockdown induces cell cycle arrest and apoptosis. (A) Cell cycle distribution analysis of HL-60 cells transfected with empty or sh*DACH1* by flow cytometry (mean ± SD, $^{*}P < 0.05$, $^{**}P < 0.01$, $^{*}P < 0.001$, compared with control cells.) (B) immunoblots of Rb phosphorylation at Ser 780.

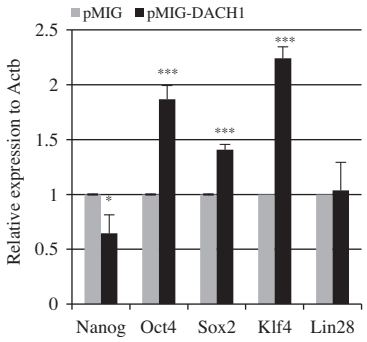

Fig. 4. qRT-PCR analysis using GFP-sorted mouse bone marrow progenitor cells transduced with either control vector or *DACH1* retroviral vector expressing GFP. (mean ± SD $^{*}P < 0.05$, $^{***}P < 0.001$, compared with control cells).

qRT-PCR analysis showed a significant increased expression of *Oct4, Sox2*, and *Klf4* by forced expression of *DACH1*. These data indicates the consistent opposite role of *DACH1* in myeloid progenitor cells against cells originating from other tissues. In particular, the transcription factors Oct4, Sox2, and Klf4 form a self-regulatory complex through direct interaction, which controls a wide range of downstream genes involved in somatic cell reprogramming [21,22]. Therefore, these data imply that simultaneous up-regulation of *Oct4*, *Sox2*, and *Klf4* by *DACH1* could provide the 'gain-of-function' associated with embryonic or induced pluripotent stem cells such as the stemness or self-renewal capacity of myeloid progenitor cells. Thus, further studies will be required to identify the precise effect of Klf4 with the Oct4 and Sox2 triple complex in hematopoietic cells or leukemia stem cells.

3.5. Concluding remarks

It has been reported that *DACH1* inhibits the expression of *cyclin D1*, *Sox2*, *Nanog*, and *Klf4* and increases the expression of $p21^{Cip1}$ in breast cancer cells. Hence, *DACH1* has a role as a tumor suppressor in breast cancer by regulating cell cycle progression and stem cell reprogramming factors. However, our study demonstrated the opposite roles of *DACH1* associated with the regulation of the cell cycle machinery and expression of reprogramming factors in myeloid cells. Therefore, the effect of *DACH1* associated with cell fate determination and tumorigenesis has to be differentially considered in hematopoietic lineages.

Acknowledgments

This research was supported by a Korea Science and Engineering Foundation (KOSEF) grant funded by the government of Korea (MEST) (2011-0011163).

Appendix A. Supplementary data

Supplementary data associated with this article can be found, in the online version, at doi:10.1016/j.bbrc.2012.02.120.

References

[1] V. Zolota, C. Sirinian, M. Melachrinou, A. Symeonidis, D.S. Bonikos, Expression of the regulatory cell cycle proteins p21, p27, p14, p16, p53, mdm2, and cyclin E in bone marrow biopsies with acute myeloid leukemia. Correlation with patients' survival, Pathol. Res. Pract. 203 (2007) 199–207.
[2] J.H. Liu, C.C. Yen, Y.C. Lin, J.P. Gau, M.H. Yang, T.C. Chao, L.T. Hsiao, W.S. Wang, Y.C. Tsai, P.M. Chen, Overexpression of *cyclin D1* in accelerated-phase chronic myeloid leukemia, Leuk. Lymphoma 45 (2004) 2419–2425.
[3] S. Rodriguez, A. Khabir, C. Keryer, C. Perrot, M. Drira, A. Ghorbel, R. Jlidi, A. Bernheim, A. Valent, P. Busson, Conventional and array-based comparative genomic hybridization analysis of nasopharyngeal carcinomas from the Mediterranean area, Cancer Genet. Cytogenet. 157 (2005) 140–147.
[4] C. Haferlach, U. Bacher, A. Kohlmann, S. Schindela, T. Alpermann, W. Kern, S. Schnittger, T. Haferlach, CDKN1B, encoding the cyclin-dependent kinase inhibitor 1B (p27), is located in the minimally deleted region of 12p abnormalities in myeloid malignancies and its low expression is a favorable prognostic marker in acute myeloid leukemia, Haematologica 96 (2011) 829–836.
[5] B. Argiropoulos, E. Yung, P. Xiang, C.Y. Lo, F. Kuchenbauer, L. Palmqvist, C. Reindl, M. Heuser, S. Sekulovic, P. Rosten, A. Muranyi, S.L. Goh, M. Featherstone, R.K. Humphries, Linkage of the potent leukemogenic activity of Meis1 to cell-cycle entry and transcriptional regulation of *cyclin D3*, Blood 115 (2010) 4071–4082.
[6] A. Watanabe, H. Ogiwara, S. Ehata, A. Mukasa, S. Ishikawa, D. Maeda, K. Ueki, Y. Ino, T. Todo, Y. Yamada, M. Fukayama, N. Saito, K. Miyazono, H. Aburatani, Homozygously deleted gene DACH1 regulates tumor-initiating activity of glioma cells, Proc. Natl. Acad. Sci. USA 108 (2011) 12384–12389.
[7] K. Wu, A. Li, M. Rao, M. Liu, V. Dailey, Y. Yang, D. Di Vizio, C. Wang, M.P. Lisanti, G. Sauter, R.G. Russell, A. Cvekl, R.G. Pestell, DACH1 is a cell fate determination factor that inhibits *cyclin D1* and breast tumor growth, Mol. Cell Biol. 26 (2006) 7116–7129.
[8] K. Wu, X. Jiao, Z. Li, S. Katiyar, M.C. Casimiro, W. Yang, Q. Zhang, N.E. Willmarth, I. Chepelev, M. Crosariol, Z. Wei, J. Hu, K. Zhao, R.G. Pestell, Cell fate determination factor Dachshund reprograms breast cancer stem cell function, J. Biol. Chem. 286 (2011) 2132–2142.
[9] S. Lee, J. Chen, G. Zhou, R.Z. Shi, G.G. Bouffard, M. Kocherginsky, X. Ge, M. Sun, N. Jayathilaka, Y.C. Kim, N. Emmanuel, S.K. Bohlander, M. Minden, J. Kline, O. Ozer, R.A. Larson, M.M. LeBeau, E.D. Green, J. Trent, T. Karrison, P.P. Liu, S.M. Wang, J.D. Rowley, Gene expression profiles in acute myeloid leukemia with common translocations using SAGE, Proc. Natl. Acad. Sci. USA 103 (2006) 1030–1035.
[10] E. Kim, J.W. Lee, D.C. Baek, S.R. Lee, M.S. Kim, S.H. Kim, C.S. Kim, Z.Y. Ryoo, H.S. Kang, K.T. Chang, Processing and subcellular localization of ADAM2 in the Macaca fascicularis testis and sperm, Anim. Reprod. Sci. 117 (2010) 155–159.
[11] E. Passegue, A.J. Wagers, S. Giuriato, W.C. Anderson, I.L. Weissman, Global analysis of proliferation and cell cycle gene expression in the regulation of hematopoietic stem and progenitor cell fates, J. Exp. Med. 202 (2005) 1599–1611.
[12] V. D'Angiolella, V. Donato, S. Vijayakumar, A. Saraf, L. Florens, M.P. Washburn, B. Dynlacht, M. Pagano, SCF(Cyclin F) controls centrosome homeostasis and mitotic fidelity through CP110 degradation, Nature 466 (2010) 138–142.
[13] A. Matsumoto, S. Takeishi, T. Kanie, E. Susaki, I. Onoyama, Y. Tateishi, K. Nakayama, K.I. Nakayama, P57 is required for quiescence and maintenance of adult hematopoietic stem cells, Cell Stem Cell 9 (2011) 262–271.
[14] E.C. Forsberg, S.S. Prohaska, S. Katzman, G.C. Heffner, J.M. Stuart, I.L. Weissman, Differential expression of novel potential regulators in hematopoietic stem cells, PLoS Genet. 1 (2005) e28.
[15] A. Pession, V. Martino, R. Tonelli, C. Beltramini, F. Locatelli, G. Biserni, M. Franzoni, F. Freccero, L. Montemurro, L. Pattacini, G. Paolucci, MLL-AF9 oncogene expression affects cell growth but not terminal differentiation and is downregulated during monocyte-macrophage maturation in AML-M5 THP-1 cells, Oncogene 22 (2003) 8671–8676.
[16] C. Caslini, A. Serna, V. Rossi, M. Introna, A. Biondi, Modulation of cell cycle by graded expression of MLL-AF4 fusion oncoprotein, Leukemia 18 (2004) 1064–1071.
[17] Z. Mikulasova, D. Ilencikova, T. Slamka, D. Durovcikova, Acute myeloblastic leukaemia with alternations of MLL proto-oncogene protein (11q23/MLL+ AML), Klin. Onkol. 23 (2010) 401–407.
[18] A. Chen, J.D. Licht, Y. Wu, N. Hellinger, W. Scher, S. Waxman, Retinoic acid is required for and potentiates differentiation of acute promyelocytic leukemia cells by nonretinoid agents, Blood 84 (1994) 2122–2129.
[19] M.J. Munoz-Alonso, J.C. Acosta, C. Richard, M.D. Delgado, J. Sedivy, J. Leon, $P21^{Cip1}$ and p27Kip1 induce distinct cell cycle effects and differentiation programs in myeloid leukemia cells, J. Biol. Chem. 280 (2005) 18120–18129.
[20] J.C. Heng, Y.L. Orlov, H.H. Ng, Transcription factors for the modulation of pluripotency and reprogramming, Cold Spring Harb. Symp. Quant. Biol. 75 (2010) 237–244.
[21] N. Xu, T. Papagiannakopoulos, G. Pan, J.A. Thomson, K.S. Kosik, MicroRNA-145 regulates OCT4, SOX2, and KLF4 and represses pluripotency in human embryonic stem cells, Cell 137 (2009) 647–658.
[22] Z. Wei, Y. Yang, P. Zhang, R. Andrianakos, K. Hasegawa, J. Lyu, X. Chen, G. Bai, C. Liu, M. Pera, W. Lu, Klf4 interacts directly with Oct4 and Sox2 to promote reprogramming, Stem Cells 27 (2009) 2969–2978.

Biochemical and Biophysical Research Communications 420 (2012) 96–101

Contents lists available at SciVerse ScienceDirect

Biochemical and Biophysical Research Communications

journal homepage: www.elsevier.com/locate/ybbrc

The receptor for advanced glycation endproducts and its ligands in patients with myasthenia gravis

Bernhard Moser [a,*], Christine Bekos [a], Fritz Zimprich [b], Stefanie Nickl [a,c], Walter Klepetko [a], Jan Ankersmit [a,c]

[a] Department of Thoracic Surgery, Division of Surgery, Medical University Vienna, Währinger Gürtel 18-20, 1090 Vienna, Austria
[b] Department of Neurology, Medical University Vienna, Währinger Gürtel 18-20, 1090 Vienna, Austria
[c] Christian Doppler laboratory for Cardiac and Thoracic Diagnosis and Regeneration, Währinger Gürtel 18-20, 1090 Vienna, Austria

ARTICLE INFO

Article history:
Received 22 February 2012
Available online 3 March 2012

Keywords:
Myasthenia gravis
Receptor for advanced glycation endproducts
RAGE ligands
Autoimmunity

ABSTRACT

Objective: Myasthenia gravis (MG) is a T- and B-cell mediated autoimmune disorder affecting the neuromuscular junction. The receptor for advanced glycation endproducts (RAGE) plays a role in the amplification of chronic inflammatory disorders and autoimmune diseases. We sought to investigate the role of RAGE and its ligands in the pathophysiology of MG.

Methods: In this cross-sectional study we enrolled 42 patients with MG and 36 volunteers. We employed enzyme-linked immunosorbent assays to determine the concentration of soluble RAGE (sRAGE) and high mobility group box 1 (HMGB1) in serum of patients and volunteers. In a subpopulation of patients we measured the serum levels of endogenous secretory (es) RAGE and various RAGE ligands, such as S100B, S100A8 and advanced glycation endproducts (AGE-CML). Reported are means and standard error mean.

Results: We found significantly reduced levels of the soluble receptors sRAGE and esRAGE in patients with MG compared to volunteers without MG (sRAGE [pg/ml] 927.2 ± 80.8 vs. 1400.1 ± 92.4; $p < 0.001$; esRAGE [pg/ml] 273.5 ± 24.6 vs. 449.0 ± 22.4; $p < 0.001$). Further categorization of patients with MG according to the distribution of muscle involvement revealed the following sRAGE concentrations: generalized MG 999.4 ± 90.8 and ocular MG 696.1 ± 161.8 (vs. control; One-way ANOVA: $p < 0.001$; *Post hoc* analysis: generalized vs. ocular MG: $p = 0.264$, generalized MG vs. control: $p = 0.008$, ocular MG vs. control: $p = 0.001$). In patients with detectable antibodies specific for acetylcholine receptors (Anti-AChR positive) the sRAGE concentration was 970.0 ± 90.2 compared to those without (seronegative) 670.6 ± 133.1 (vs. control; One-way ANOVA: $p < 0.001$; *Post hoc* analysis: Pos vs. Neg.: $p = 0.418$, Pos vs. control: $p = 0.003$, Neg. vs. control: $p = 0.008$). We next investigated the role of RAGE ligands in MG. The concentrations of RAGE ligands in patients with MG and controls were as follows: (HMGB1 [ng/ml] 1.7 ± 0.1 vs. 2.1 ± 0.2; $p = 0.058$; S100B [pg/ml] 22.5 ± 22.5 vs. 14.4 ± 9.2; $p = 0.698$; S100A8 [pg/ml] 107.0 ± 59.3 vs. 242.5 ± 103.6; $p = 0.347$; and AGE-CML [ng/ml] 1100.8 ± 175.1 vs. 1399.8 ± 132.8; $p = 0.179$).

Conclusions: Our data suggest a role for the RAGE pathway in the pathophysiology of MG. Further studies are warranted to elucidate more about this immunological axis in patients with MG.

1. Introduction

Myasthenia gravis (MG) is a rare neurological disorder with an estimated prevalence of 20/100,000 people [1]. It is an autoimmune disorder characterized by autoantibodies against the acetylcholine receptor (AChR) or other proteins of the neuromuscular junction. Functional loss of AChR ultimately leads to impaired neuromuscular transmission and results in a characteristic fluctuating muscle weakness pathognomonic for MG [2].

The receptor for advanced glycation endproducts (RAGE), a multiligand member of the immunoglobulin superfamily, interacts with proinflammatory advanced glycation endproducts (AGEs), the products of nonenzymatic glycation and oxidation of proteins [3]; high-mobility group box 1 (HMGB1), also known as amphoterin [4–6]; S100/calgranulins, S100B and S100A8 [7,8], and others to amplify inflammation and tissue injury.

Soluble (s) RAGE is the extracellular domain of RAGE that binds RAGE ligands and acts as a ligand decoy [9]. Endogenous secretory (es) RAGE is an alternative splice variant of the RAGE gene that is actively secreted, whereas sRAGE results from proteolytic cleavage of the cell surface bound full-length RAGE receptor [10]. We have

* Corresponding author. Fax: +43 1 40400 6977.
E-mail addresses: bernhard.moser@meduniwien.ac.at (B. Moser), n0840363@students.meduniwien.ac.at (C. Bekos), friedrich.zimprich@meduniwien.ac.at (F. Zimprich), stefanie.nickl@meduniwien.ac.at (S. Nickl), walter.klepetko@meduniwien.ac.at (W. Klepetko), hendrik.ankersmit@meduniwien.ac.at (J. Ankersmit).

0006-291X/$ - see front matter © 2012 Elsevier Inc. All rights reserved.
doi:10.1016/j.bbrc.2012.02.121

shown that blockade of RAGE suppresses alloimmune reactions in vitro and delays allograft rejection in murine heart transplantation [11]. RAGE expressed on T cells is required for efficient priming of T cells and RAGE engagement has critical roles for cognate dendritic cell–T cell interactions [12].

RAGE and its ligands have been implicated in various autoimmune disorders. For instance, RAGE/ligand interactions are involved in the differentiation of T cells to a pathogenic phenotype during the late stages of autoimmune diabetes [13]. Patients with rheumatoid arthritis have reduced levels of sRAGE compared to patients with non-inflammatory joint diseases [14]. HMGB1 is a nuclear protein binding DNA. When released from cells it functions as an alarmin and is associated with disease activity and is a potential therapeutic target in patients with systemic lupus erythematosus [15,16]. AGE N^{ε}-carboxymethyllysine (CML) adducts are chemically modified amino acids derived *in vivo* from lipid- and carbohydrate precursors [17]. CML are markers of tissue injury and oxidative stress. AGE accumulation *in vivo* is involved in the pathogenesis of various disease processes [18]. Autoantibodies to AGE-modified low density lipoproteins (AGE-LDL) were isolated from human type 1 diabetic patients [19]. Various members of the S100 family of related calcium-binding proteins have been shown to interact with RAGE. S100B has been shown to act as a chemoattractant enhancing the infiltration of RAGE-expressing encephalitogenic T-cells into the central nervous system in a model of experimental autoimmune encephalomyelitis, mimicking human multiple sclerosis [20]. S100A8 forms a heterodimer with S100A9, is released from activated phagocytes and mediates the recruitment of leukocytes during inflammatory conditions [21]. Recently a role for RAGE and its ligand S100B has been shown in an animal model for MG, experimental autoimmune myasthenia gravis (EAMG) [22].

There is no information in the published literature about the RAGE axis in human patients with MG. The present study sought to investigate a role for the RAGE pathway in human patients with the autoimmune disorder MG.

2. Materials and methods

2.1. Subjects

For this observational study with cross-sectional design we enrolled 42 patients with MG. The diagnosis of MG was established by a neurologist specialized in the diagnosis and treatment of patients with MG in every case. Briefly, the diagnosis of MG was based on disease specific clinical findings of fluctuating weakness of voluntary muscles that is exacerbated by effort and improved by rest and either a temporary reversal by acetylcholine inhibitors or electrophysiological decremented response of more than 10% in negative peak amplitude of the compound muscle action potential upon supramaximal repetitive (2 or 3 Hz) stimulation.

Among patients with MG, only one patient was without medical therapy. Acetylcholinesterase inhibitor therapy in the form of pyridostigmine was prescribed to 71.4% of patients. Orally administered steroids were prescribed to 47.6% of patients. Fifty percent of patients were treated with immunosuppressant therapy other than steroids: of those 80.9% were taking azathioprine, 14.3% were taking mycophenolate mofetil and 4.8% methotrexate.

Patients were classified according to the pattern of involved muscles: there were 23.8% of patients that presented with purely ocular manifestations of disease (ocular MG) and 76.2% of patients with generalized symptoms (generalized MG). When categorized according to age at diagnosis (disease onset of MG), there were 47.6% of patients with early onset MG (less than 40 years old at onset of disease, EOMG) and 52.4% of patients with late onset MG (40 years or older at disease onset, LOMG). The majority of patients were seropositive for acetylcholine receptor antibodies (AChR Ab; seropositive MG, 85.7%).

When patients were classified according to the Myasthenia Gravis Foundation of America (MGFA) MG clinical score, the majority of patients were in classes I–III (MGFA class I 47.6%, II 42.9%, III 21.4%, IV 2.4% and V 0%). In our patient cohort 73.8% of patients had a history of thymectomy and 21.4% a history of thymoma. At the time of entry into this study all of the patients with thymoma had previously undergone surgical resection of their tumors and were without any signs of recurrence. There were three patients with additional autoimmune diseases: one with hashimoto thyroiditis, one with scleroderma and one with autoimmune gastritis. The characteristics of patients with MG are summarized in Table 3.

We have compared the serum samples of MG patients with 44 age- and sex-matched volunteering control subjects. The age of patients with MG and healthy volunteers ranged from 16 to 85 and 22 to 83 years. None of the 44 control subjects studied had any evidence or suspicion of MG, malignancies or infectious conditions at the time of entry into this study. There was only one patient included with another autoimmune disease (psoriasis). None of the volunteers received acetylcholinesterase inhibitor therapy, steroids or other immunosuppressant medications.

Ethical approval was obtained from our institutional review board on human research. Written informed consent was obtained from all patients and volunteers participating in this study.

2.2. Detection of serum proteins

Serum concentrations of the indicated proteins in patients with MG and healthy volunteers were quantified by enzyme-linked immunosorbent assays (ELISA). All ELISA tests were commercially available and performed according to the manufacturers' instructions. The employed quantitative sandwich immunoassays were purchased as follows: sRAGE (RnD Systems, Minneapolis, MN, USA), esRAGE (B-Bridge International Inc., CA, USA), S100B (BioVendor GmbH, Czech Republic), HMGB1 (IBL International GmbH, Hamburg, Germany) and S100A8 (BMA Biomedicals, Augst, Switzerland). The competitive AGE-CML ELISA Kit was purchased from MicroCoat Biotechnologie GmbH (Bernfried, Germany).

Researchers performing the laboratory work and data analyses were blinded to the groups associated with each sample.

2.3. Statistical methods

Statistical analysis of data was performed using SPSS software (version 17; SPSS Inc., IL, USA). The concentrations of proteins in serum of patients with MG were compared to those of healthy volunteers using Student's *t* test or One-way ANOVA and are reported as mean (median) ± standard deviation (and standard error mean). *Post hoc* comparisons were computed with the Tukey correction. The level of statistical significance was set at <0.05 (two-tailed *p*-values).

3. Results

There was no statistically significant difference in age and sex between patients with MG and volunteers (Table 1).

3.1. Reduced levels of sRAGE in MG

To test the hypothesis that RAGE is involved in disease processes of MG, we employed an ELISA for the detection of sRAGE in the serum of patients with MG and healthy volunteers. We found significantly reduced levels of sRAGE in patients with MG

Table 1
Given are the basic characteristics of patients with MG and healthy volunteers together with serum concentrations of sRAGE. Reported is mean (median) ± standard deviation (standard error mean).

	Total MG patients (n = 42)	Controls (n = 36)	p value
Age in years, mean (median) ± standard deviation (SEM), [range]	50.6 (48.0) ± 18.1 (2.8), [16–85]	48.3 (46.5) ± 15.8 (2.6), [22–83]	0.548
F:M ratio n (%)	24:18 (57:43)	23:13 (64:36)	0.644
sRAGE [pg/ml]	927.2 (866.4) ± 523.6 (80.8)	1400.1 (1370.4) ± 554.2 (92.4)	<0.001

MG, myasthenia gravis; n number of patients; F:M ratio, female to male ratio; sRAGE, soluble receptor for advanced glycation endproducts; esRAGE, endogenous secretory receptor for advanced glycation endproducts.

compared to healthy volunteers (sRAGE [pg/ml] 927.2 ± 80.8 vs. 1400.1 ± 92.4; $p < 0.001$; Fig. 1(A) and Table 1).

3.2. The splice variant esRAGE was reduced in MG

Next we measured a splice variant of RAGE, esRAGE, in a randomly selected subgroup of MG patients and healthy volunteers. The actively secreted esRAGE was significantly lower in serum of patients with MG compared to controls (esRAGE [pg/ml] 273.5 ± 24.6 vs. 449.0 ± 22.4; $p < 0.001$; Fig. 1(B) and Table 2).

3.3. No influence of pharmacological therapy on sRAGE

Patients with MG typically receive pharmacological therapy from three distinct groups of substances: acetylcholinesterase inhibitors, steroids, and other immunosuppressant therapy. The choice of substance or combination of substances is dependent on the severity of disease. Current treatments of our patients at the time of entry into the study are listed in Table 3.

Briefly, neither acetylcholinesterase inhibitors, steroids, nor other immunosuppressant therapy had an influence on the serum expression of RAGE (sRAGE [pg/ml] acetylcholinesterase inhibitors (yes) 994.9 ± 98.0 vs. (no) 758.0 ± 135.1, $p = 0.402$; steroids (yes) 957.3 ± 135.9 vs. (no) 899.9 ± 95.2, $p = 0.937$; other immunosuppressant therapy (yes) 962.3 ± 111.5 vs. (no) 892.2 ± 119.2, $p = 0.907$; see Fig. 2(A)–(C) and Table 3), respectively.

3.4. Clinical presentation of disease was not associated with differing sRAGE concentrations

When patients whose myasthenic weakness remained localized to the ocular muscles were compared to those with generalized myasthenic involvement of muscles, we found no significant difference in protein concentrations of sRAGE [pg/ml]: ocular MG 696.1 ± 161.8 vs. generalized MG 999.4 ± 90.8, $p = 0.264$, respectively. Both subdivisions of MG, ocular and generalized, showed highly significant differences compared to control, $p = 0.001$ and 0.008; see Fig. 3(A) and Table 3, respectively.

3.5. Age at onset of disease did not parallel different sRAGE levels

Furthermore we did not find differences in the levels of sRAGE in patients with different disease onset of MG. Patients with LOMG showed lower levels of sRAGE than those with EOMG (sRAGE [pg/ml] EOMG 1048.7 ± 111.6, LOMG 816.8 ± 113.5, $p = 0.344$; see Fig. 2), respectively. LOMG vs. control reached statistical significance ($p < 0.001$), while EOMG vs. control did not ($p = 0.054$); see Fig. 3(B) and Table 3, respectively.

3.6. Detection of antibodies specific to AChR was not associated with serum RAGE expression

Patients seropositive for AChR antibodies did not significantly differ from seronegative patients (sRAGE [pg/ml] AChR pos. 970.0 ± 90.2 vs. AChR neg. 670.6 ± 133.1, $p = 0.418$; see Fig. 2), respectively. Seropositive as well as seronegative patients showed highly significant differences in comparison to control, $p = 0.003$ and 0.008; see Fig. 3(C) and Table 3, respectively.

3.7. Expression of RAGE ligands in MG

After obtaining the above described results for the soluble receptors of RAGE, sRAGE and esRAGE, we focused on the determination of RAGE ligands in MG. The serum level of RAGE ligand HMGB1 was not significantly different in patients with MG from that of controls ([ng/ml] 1.7 ± 0.1 vs. 2.1 ± 0.2; $p = 0.058$). There were also no statistically significant differences in the concentrations of other ligands between MG patients and volunteers (S100B [pg/ml] 22.5 ± 22.5 vs. 14.4 ± 9.2; $p = 0.698$; S100A8 [pg/ml] 107.0 ± 59.3 vs. 242.5 ± 103.6; $p = 0.347$; and AGE-CML [ng/ml] 1100.8 ± 175.1 vs. 1399.8 ± 132.8; $p = 0.179$). Please see also Table 4 for a more detailed analysis.

4. Discussion

Our findings are the first demonstration of a role for RAGE in human patients with the autoimmune disorder MG.

In a previous study, the exacerbation of experimental autoimmune myasthenia gravis (EAMG) via activation of RAGE was shown [22]. In this animal model, rats were immunized with peptide

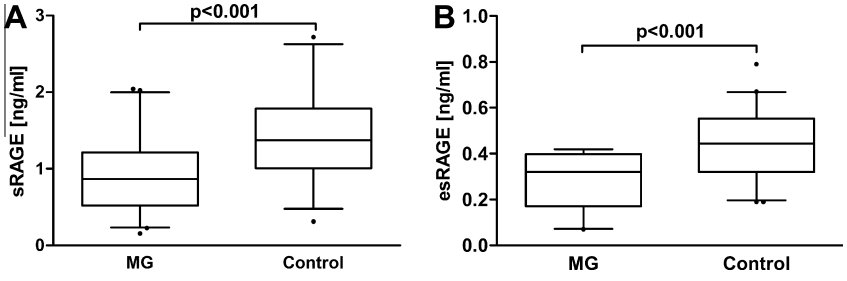

Fig. 1. Serum concentrations of sRAGE (A) and esRAGE (B) in patients with MG and control subjects. Two-sided Student's t-test; MG, myasthenia gravis.

Table 2
Basic characteristics of patients with MG and healthy volunteers together with serum concentrations of esRAGE. Reported is mean (median) ± standard deviation (standard error mean).

	Total MG patients (n = 24)	Controls (n = 44)	p value
Age in years, mean (median) ± standard deviation (SEM), [range]	52.0 (48.0) ± 18.6 (3.8), [22–85]	44.7 (43.5) ± 13.3 (2.0), [22–80]	0.065
F:M ratio n (%)	12:12 (50/50)	24:20 (54.5/45.5)	0.802
esRAGE [pg/ml]	273.5 (318.0) ± 120.6 (24.6)	449.0 (445.2) ± 144.9 (22.4)	<0.001

MG, Myasthenia gravis; n, number of patients; F:M ratio, female to male ratio; sRAGE, soluble receptor for advanced glycation endproducts; esRAGE, endogenous secretory receptor for advanced glycation endproducts.

Table 3
Characterization and categorization of patients with MG according to type of therapy, clinical disease manifestation and autoantibody status with the corresponding concentration of sRAGE. Reported is mean (median) ± standard deviation (standard error mean).

Concentratin of sRage [pg/ml]: mean (median) ± standard deviation (SEM)			One-way ANOVA[a] p value
Patients with MG – categories		Control patients	
AChE Inh therapy[b]			
Yes (n = 30)	No. (n = 12)	Control (n = 36)	0.001
994.9 (1054.8) ± 536.6 (98.0)	758.0 (645.8) ± 467.9 (135.1)	1400.1 (1370.4) ± 554.2 (92.4)	
Immunosuppression			
incl. steroids			
Yes (n = 33)	No. (n = 9)		0.001
938.2 (824.0) ± 525.4 (91.5)	886.8 (908.9) ± 546.5 (182.2)		
excl. Steroids			
Yes (n = 21)	No (n = 21)		0.001
962.3 (824.0) ± 511.1 (111.5)	892.2 (908.9) ± 546.1 (119.2)		
Steroids			
Yes (n = 20)	No (n = 22)		0.001
957.3 (884.1) ± 607.8 (135.9)	899.9 (866.5) ± 446.6 (95.2)		
Clinical Manifestation			
Generalized MG (n = 32)	Ocular MG (n = 10)		<0.001
999.4 (1065.7) ± 513.8 (90.8)	696.1 (577.1) ± 511.6 (161.8)		
Disease onset			
EOMG (n = 20)	LOMG (n = 22)		<0.001
1048.7 (1109.7) ± 498.7 (111.6)	816.8 (652.1) ± 532.2 (113.5)		
Anti-AChR			
Positive (n = 36)	Negative (n = 6)		0.001
970.0 (1025.2) ± 541.1 (90.2)	670.6 (584.6) ± 326.0 (133.1)		

SEM, standard error of the mean; AChE Inh, actylcholinesterase inhibitor therapy; MG, myasthenia gravis; n, number of patients; EOMG, early-onset MG; LOMG, late-onset MG; Anti-AChR, seropositive serum autoantibody status (antibodies against the acetylcholine receptor).
[a] *Post hoc* analysis: please see corresponding figures.
[b] Actylcholinesterase inhibitor therapy: pyridostigmine was used in all patients.

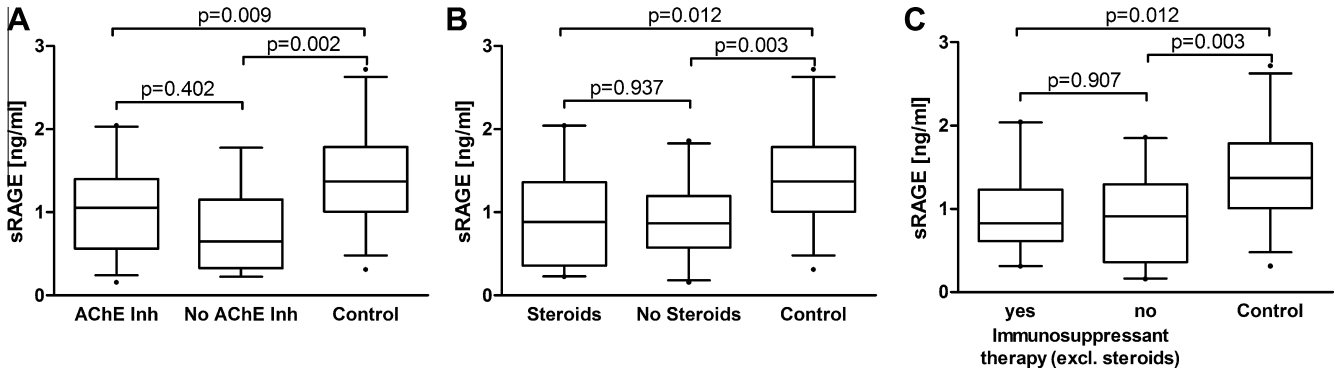

Fig. 2. The influence of MG specific medications is shown: acetylcholinesterase inhibitor therapy (A), steroid therapy (B), and immunosuppressant therapy excluding steroids (C), compared to control subjects. *Post hoc* comparisons with the Tukey correction are shown. AChE Inh, acetylcholinesterase inhibitor therapy; MG, myasthenia gravis.

corresponding to the 97–116 region of the rat acetylcholine receptor (AChR). *In vivo* blockade of the RAGE axis could markedly reduce disease severity. Increased expression of RAGE on CD4+ T cells and S100B in serum of rats with EAMG *in vivo,* as well as heightened peptide-specific in vitro proliferation of T cells from lymph nodes in the presence of S100B, could be demonstrated. After in vitro incubation with S100B, the disequilibrium of helper T cells (Th) towards a raise in Th1, Th17 cells and a reduction in foxp3+ regulatory T cells was further altered. There was an increased number of RAGE positive splenocytes in animals with EAMG. S100b stimulated cyclooxygenase-2 (COX-2) expression in EAMG rats. These experimental data corroborate our findings in human patients, although we could not detect an increase of the RAGE ligand S100B in our patient population. The reasons for this might be attributable to intrinsic immunological mechanisms of the above described murine model of EAMG. None of the tested

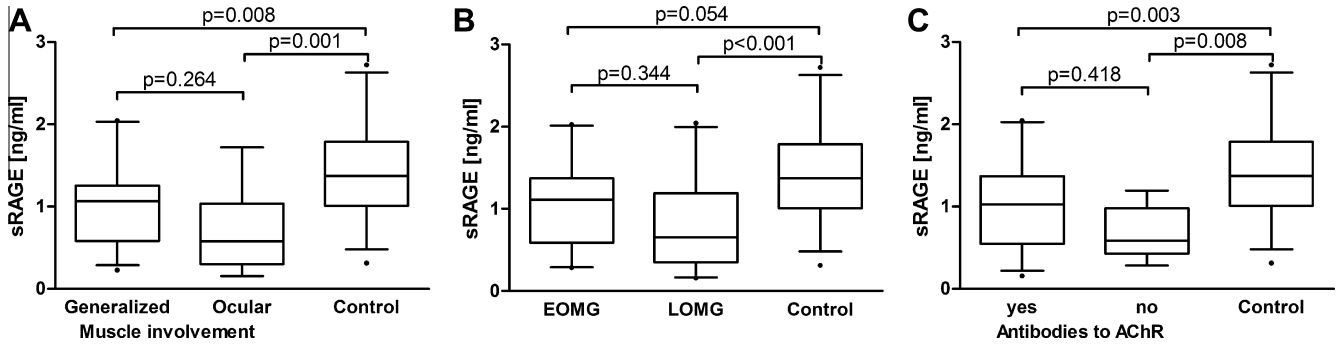

Fig. 3. Patients with MG are categorized according to clinical disease manifestation (A), onset of disease (B) and autoantibody status (C), and compared to control subjects. *Post hoc* comparisons with the Tukey correction are shown. EOMG, early-onset MG; LOMG, late-onset MG; Antibodies to AChR, serum autoantibody status (antibodies against the acetylcholine receptor).

Table 4
Serum concentrations of RAGE ligands in patients with MG and controls. Reported is mean (median) ± standard deviation (standard error mean).

	MG patients	Controls	*p* value
S100B [pg/ml][a]	22.5 (0) ± 110.2 (22.5)	14.4 (0) ± 59.3 (9.2)	0.698
S100A8 [pg/ml][a]	107.0 (0) ± 290.7 (59.3)	242.5 (0) ± 663.1 (103.6)	0.347
AGE-CML [ng/ml][a]	1100.8 (722.6) ± 857.6 (175.1)	1399.8 (989.3) ± 860.4 (132.8)	0.179
HMGB1 [ng/ml][b]	1.6 (1.6) ± 0.8 (0.1)	2.1 (1.6) ± 1.3 (0.2)	0.058

MG, Myasthenia gravis; HMGB1, high-mobility group box 1; S100B and S100A8, members of the S100/calgranulin family of proteins; AGE-CML, advanced glycation endproducts carboxymethyllysine adducts.
[a] The patient characteristics for the S100B, S100A8 and AGE/CML immunoassay are reported in Table 1.
[b] The patient characteristics for the HMGB1 immunoassay are reported in Table 2.

RAGE ligands in this study were upregulated in patient serum. We speculate that there might be unidentified ligands in serum of patients or that the composition of ligands in the microenvironment at the neuromuscular junction could be misbalanced.

Two forms of soluble receptor of RAGE were reduced in patients with MG. One that is proteolytically cleaved from the cell surface, called sRAGE, and one that is alternatively spliced; containing unique amino acids not present in membrane bound RAGE [10]. Both soluble forms of RAGE act as decoy receptors that are able to scavenge diverse ligands, and thus control RAGE-dependent signaling. It was proposed that in chronic disorders the binding of ligands, such as AGEs, to cell bound RAGE leads to the sustained activation of transcription factor nuclear factor kappa B [23]. The reduced levels of soluble forms of RAGE could reflect less protection from activating proinflammatory ligands, as was shown for other autoimmune and inflammatory disorders [14,16]. If sRAGE and esRAGE have different regulatory roles in patients with MG remains open for future study.

The reduced concentrations of sRAGE in serum of patients with MG were not due to the administration of symptom relieving pharmacological therapy or immunosuppressant therapy. In the above described animal model of MG, the administration of RAGE blocking RAGE-Fc to rats with EAMG could markedly reduce disease severity of EAMG [22]. Similarly, we have previously shown that blockade of RAGE by administration of sRAGE in a murine model of heterotopic cardiac transplantation delayed allograft rejection [11]. Taken together, RAGE blockade in animal models gives promising results. Current immunosuppressive medications administered to patients with MG do not seem to block a possible effect of the RAGE axis on MG development or progression.

Several clinical subtypes of MG can be distinguished by clinical presentation, age at onset of disease and autoantibody profile. None of these subtypes showed significant differences in the sRAGE serum concentrations. Worth mentioning is that only in patients with LOMG a significantly lower sRAGE level was observed ($p < 0.001$) while there was only a not significant trend towards lower sRAGE in patients with EOMG ($p = 0.054$). The proposition of LOMG as a pathophysiologically different entity of MG is widely accepted [24]. If the findings with RAGE in this regard will be of clinical value remains unclear and open for future study.

The findings of the current study raise new questions that have to be addressed in future research. Is the RAGE–RAGE ligand axis involved in the development or progression of MG? Can sRAGE, esRAGE or a yet not identified RAGE ligand be used as helpful biomarker for diagnosis or treatment surveillance? Can pharmacological RAGE blockade ameliorate disease processes of patients with MG?

Taken together, we suggest that the RAGE axis is involved in the pathophysiology of patients with MG and further studies are warranted to elucidate the relationship between RAGE, possibly its ligands and the immunological pathogenesis of MG. We hope that basic science and clinical research on RAGE and ligands will translate into better understanding of MG, thus improving diagnosis, therapy and eventually better outcome for patients.

Conflict of interest

The authors declare that there is no conflict of interest.

References

[1] L.H. Phillips II, The epidemiology of myasthenia gravis, Ann. N.Y. Acad. Sci. 998 (2003) 407–412.
[2] A. Vincent, Unravelling the pathogenesis of myasthenia gravis, Nat. Rev. Immunol. 2 (10) (2002) 797–804.
[3] A.M. Schmidt, M. Vianna, M. Gerlach, et al., Isolation and characterization of two binding proteins for advanced glycosylation end products from bovine lung which are present on the endothelial cell surface, J. Biol. Chem. 267 (21) (1992) 14987–14997.
[4] A. Taguchi, D.C. Blood, G. del Toro, et al., Blockade of RAGE-amphoterin signalling suppresses tumour growth and metastases, Nature 405 (6784) (2000) 354–360.
[5] R.E. Voll, V. Urbonaviciute, B. Fürnrohr, et al., The role of high-mobility group box 1 protein in the pathogenesis of autoimmune diseases, Curr. Rheumatol. Rep. 10 (5) (2008) 341–342.

[6] U. Andersson, H.E. Harris, The role of HMGB1 in the pathogenesis of rheumatic disease, Biochim. Biophys. Acta 1799 (1–2) (2010) 141–148 (Review).
[7] E. Leclerc, E. Sturchler, S.W. Vetter, The S100B/RAGE axis in Alzheimer's disease, Cardiovasc. Psychiatry Neurol. 2010 (2010) 539581.
[8] A.J. Halayko, S. Ghavami, S100A8/A9: a mediator of severe asthma pathogenesis and morbidity? Can. J. Physiol. Pharmacol. 87 (10) (2009) 743–755 (Review).
[9] B. Moser, B.I. Hudson, A.M. Schmidt, Soluble RAGE: a hot new biomarker for the hot joint? Arthritis Res Ther. 7 (4) (2005) 142–144.
[10] A.Z. Kalea, A.M. Schmidt, B.I. Hudson, Alternative splicing of RAGE: roles in biology and disease, Front Biosci. 1 (17) (2011) 2756–2770.
[11] B. Moser, M.J. Szabolcs, H.J. Ankersmit, et al., Blockade of RAGE suppresses alloimmune reactions in vitro and delays allograft rejection in murine heart transplantation, Am. J. Transplant. 7 (2) (2007) 293–302 (Erratum in Am. J. Transplant. 7 (5) (2007) 1318).
[12] B. Moser, D.D. Desai, M.P. Downie, et al., Receptor for advanced glycation end products expression on T cells contributes to antigen-specific cellular expansion in vivo, J. Immunol. 179 (12) (2007) 8051–8058.
[13] Y. Chen, S.S. Yan, J. Colgan, et al., Blockade of late stages of autoimmune diabetes by inhibition of the receptor for advanced glycation end products, J. Immunol. 173 (2) (2004) 1399–1405.
[14] R. Pullerits, M. Bokarewa, L. Dahlberg, et al., Decreased levels of soluble receptor for advanced glycation endproducts in patients with rheumatoid arthritis indicating deficient inflammatory control, Arthritis Res. Ther. 7 (2005) R817–R824.
[15] C.Y. Ma, Y.L. Jiao, J. Zhang, et al., Elevated plasma level of HMGB1 is associated with disease activity and combined alterations with IFN-alpha and TNF-alpha in systemic lupus erythematosus, Rheumatol. Int. 32 (2) (2012) 395–402.
[16] V. Urbonaviciute, R.E. Voll, High-mobility group box 1 represents a potential marker of disease activity and novel therapeutic target in systemic lupus erythematosus, J. Intern. Med. 270 (4) (2011) 309–318.
[17] M.U. Ahmed, S.R. Thorpe, J.W. Baynes, Identification of N epsilon-carboxymethyllysine as a degradation product of fructoselysine in glycated protein, J. Biol. Chem. 261 (1986) 4889–4894.
[18] M. Vlassara, R. Bucala, L. Striker, Pathogenetic effects of advanced glucosylation: biochemical, biologic and clinical implications for diabetes and aging, Lab. Invest. 70 (1994) 138–151.
[19] G. Virella, S.R. Thorpe, N.L. Alderson, et al., Autoimmune response to advanced glycosylation end-products of human LDL, J. Lipid Res. 44 (3) (2003) 487–493.
[20] S.S. Yan, Z.Y. Wu, H.P. Zhang, et al., Suppression of experimental autoimmune encephalomyelitis by selective blockade of encephalitogenic T-cell infiltration of the central nervous system, Nat. Med. 9 (3) (2003) 287–293.
[21] D. Foell, H. Wittkowski, T. Vogl, et al., S100 proteins expressed in phagocytes: a novel group of damage-associated molecular pattern molecules, J. Leukoc. Biol. 81 (1) (2007) 28–37 (Review).
[22] L. Mu, Y. Zhang, B. Sun, et al., Activation of the receptor for advanced glycation end products (RAGE) exacerbates experimental autoimmune myasthenia gravis symptoms, Clin. Immunol. 141 (2011) 36–48.
[23] A. Bierhaus, S. Schiekofer, M. Schwaninger, et al., Diabetes-associated sustained activation of the transcription factor nuclear factor-kappaB, Diabetes 50 (12) (2001) 2792–2808.
[24] J.A. Aarli, Late-onset myasthenia gravis: a changing scene, Arch. Neurol. 56 (1) (1999) 25–27.

Biochemical and Biophysical Research Communications 420 (2012) 102–107

Contents lists available at SciVerse ScienceDirect

Biochemical and Biophysical Research Communications

journal homepage: www.elsevier.com/locate/ybbrc

Regulation of P2X7-dependent inflammatory functions by P2X4 receptor in mouse macrophages

Ayumi Kawano [a,1], Mitsutoshi Tsukimoto [a,*,1], Daisuke Mori [a], Taisei Noguchi [a], Hitoshi Harada [b], Takato Takenouchi [c], Hiroshi Kitani [c], Shuji Kojima [a]

[a] Department of Radiation Biosciences, Faculty of Pharmaceutical Sciences, Tokyo University of Science, 2641 Yamazaki, Noda-shi, Chiba, Japan
[b] Faculty of Pharmaceutical Sciences, Suzuka University of Medical Science, 3500-3 Minamitamagaki-cho, Suzuka-shi, Mie, Japan
[c] Animal Immune and Cell Biology Research Unit, Division of Animal Sciences, National Institute of Agrobiological Sciences, 1-2 Ohwashi, Tsukuba-shi, Ibaraki, Japan

ARTICLE INFO

Article history:
Received 22 February 2012
Available online 1 March 2012

Keywords:
P2X7 receptor
P2X4 receptor
HMGB1
IL-1β
LC3-II
Reactive oxygen species
Extracellular ATP

ABSTRACT

Activation of the P2X7 receptor of macrophages plays an important role in inflammation. We recently reported that co-expression of P2X4 receptor with P2X7 receptor facilitates P2X7 receptor-mediated cell death via Ca^{2+} influx. However, it remained unclear whether P2X4 receptor is involved in P2X7 receptor-mediated inflammatory responses, such as cytokine production. Here, we present evidence that P2X4 receptor modulates P2X7 receptor-dependent inflammatory functions. Treatment of mouse macrophage RAW264.7 cells with 1 mM ATP induced high mobility group box 1 (HMGB1) release and IL-1β production via activation of P2X7 receptor. Knockdown of P2X4 receptor or removal of extracellular Ca^{2+} suppressed ATP-induced release of both HMGB1 and IL-1β. On the other hand, knockdown of P2X4 receptor or removal of extracellular Ca^{2+} enhanced P2X7-dependent LC3-II expression (an index of autophagy), suggesting that P2X4 receptor suppresses P2X7-mediated autophagy. Since LC3-II expression was inhibited by pretreatment with antioxidant and NADPH oxidase inhibitor, we examined P2X7-mediated production of reactive oxygen species (ROS). We found that activation of P2X7 receptor-mediated production of ROS was significantly facilitated in P2X4-knockdown cells, suggesting that co-expression of P2X4 receptor with P2X7 receptor may suppress anti-inflammatory function-related autophagy via suppression of ROS production. We conclude that co-expression of P2X4 receptor with P2X7 receptor enhances P2X7-mediated inflammation through both facilitation of release of cytokines and suppression of autophagy.

1. Introduction

The purinergic P2X7 receptor belongs to the family of purinoreceptors for ATP. P2X7 receptor is unique among the P2X receptors in that it requires high concentrations (millimolar) of ATP to be activated. In addition, P2X7 receptor is sensitive to the synthetic ATP analog 2′&3′-O-(4-benzoyl) benzoyl-ATP (BzATP), and thus BzATP is often used to study P2X7 action. P2X7 receptor in unactivated macrophages shows little or no functional activity, but is upregulated and become functional in response to lipopolysaccharide (LPS) and other inflammatory stimuli [1,2]. Activation of P2X7 receptor results in Ca^{2+} influx [3], the formation of a non-selective pore [4], the production of reactive oxygen species (ROS) via NADPH oxidase activation [5,6], IL-1β release [7], and cell death [8]. These activities have been proposed to contribute to the regulation of macrophage survival and inflammatory responses.

High mobility group box 1 protein (HMGB1) is a 215-amino-acid protein with a highly conserved sequence among species [9]. HMGB1 has been shown to have an extracellular role in promoting tumor metastasis and inflammation [10,11]. When immune cells are activated, the nuclear HMGB1 is actively translocated into cytoplasm, and then released by exocytosis [12]. Macrophage cell lines have also been shown to release HMGB1 during necrosis [13]. Once released, HMGB1 induces production of several pro-inflammatory cytokines by macrophages, thereby sustaining prolonged inflammation [14]. Subsequent studies showed that HMGB1 is present at high levels in the serum of septic patients [15] and in the joints of rheumatoid arthritis patients [16]. These

Abbreviations: BAPTA-AM, 1,2-bis(2-aminophenoxy)ethane-*N*,*N*,*N*,*N*-tetraacetic acid acetoxymethyl ester; BzATP, 2′&3′-O-(4-benzoyl)benzoyl-ATP; DPI, diphenyleneiodonium; H_2DCF-DA, 2′,7′-dichlorodihydrofluorescein diacetate; HMGB1, high mobility group box 1; L-NMMA, N^G-monomethyl-L-arginine; NAC, N-acetylcysteine; ROS, reactive oxygen species.

* Corresponding author. Address: Department of Radiation Biosciences, Faculty of Pharmaceutical Sciences, Tokyo University of Science, 2641 Yamazaki, Noda-shi, Chiba 278-8510, Japan. Fax: +81 (0) 4 7121 3613.
E-mail address: tsukim@rs.noda.tus.ac.jp (M. Tsukimoto).

[1] These authors are contributed equally to this work, and share the first authorship.

0006-291X/$ - see front matter © 2012 Elsevier Inc. All rights reserved.
doi:10.1016/j.bbrc.2012.02.122

observations fueled the idea that HMGB1 is a prototypical endogenous danger signal, which is released from activated macrophages and necrotic cells. It has been reported that ATP induces HMGB1 release in murine thymocytes [17] and a murine macrophage-like cell line [18] through activation of P2X7 receptor.

Autophagy is a highly conserved homeostatic process for sequestration and degradation of cytosolic macromolecules, damaged organelles and some pathogens [19–21]. When autophagy is initiated, cytoplasmic constituents are sequestered into autophagosomes, which are closed double-membrane vacuoles. The autophagosome eventually fuses with a lysosome, forming an autolysosome, in which the contents are degraded and the degradation products are recycled for protein synthesis [22]. It was recently reported that inhibition of autophagy in macrophages by knockdown of autophagy-related genes promoted the secretion of IL-1β in response to LPS [23] and also that autophagy controlled IL-1β secretion in macrophages [24]. These reports indicate that autophagy has an important role in regulating inflammation. Targeted administration of autophagy-inducing compounds might offer new remedies for inflammatory conditions such as sepsis [24] and Crohn's disease [25,26]. There have also been reports indicating that the P2X7 receptor signaling pathway leads to autophagy in microglia [27] and human monocytes/macrophages [28].

P2X4 receptor, which is highly permeable to calcium [29], is more homologous to P2X7 receptor than are the other P2X receptor subtypes. Recent evidence has indicated structural interactions between P2X7 and P2X4 receptors [30,31]. Moreover, we have shown that decreased P2X4 expression results in suppression of the initial ATP-induced Ca^{2+} influx and P2X7 receptor-mediated cell death [32]. Therefore, we considered that co-expression of P2X4 receptor with P2X7 receptor might be important in the regulation of immune function-related processes in RAW 264.7 macrophages.

In this study, we focused on the role of P2X4 receptor in P2X7 receptor-mediated inflammatory functions, such as release of HMGB1 and IL-1β, and anti-inflammatory functions, such as autophagy. We found that suppression of intracellular Ca^{2+} concentration or decrease of P2X4 expression resulted in suppression of ATP-induced HMGB1 and IL-1β release, but up-regulation of ROS production and autophagy. These findings indicated that P2X4 receptor has a role in the regulation of P2X7-mediated inflammatory functions.

2. Materials and methods

2.1. Cell culture

Macrophage-like RAW264.7 cells were routinely maintained in D-MEM (Wako Pure Chemical, Osaka, Japan) supplemented with 10% heat-inactivated FBS (Biowest, Nuaille, France), 100 U/mL penicillin, 100 μg/mL streptomycin. Cells were preincubated for 4 h with 1 μg/mL LPS. The conditioned medium was replaced with RPMI1640-based buffer [8] before experiments.

2.1.1. Short Hairpin RNA (shRNA) plasmid stable transfection

shRNA for P2X4 receptor-transfected RAW 264.7 cells was obtained in the previous study [32]. Briefly, stable transfection with shRNA was performed using the SureSilencing™ shRNA Plasmid Kit for Mouse P2X4 (SABiosciences, Frederick, MD). Two shRNA plasmid targeting P2X4 (clone ID: red and yellow) or the negative control shRNA plasmid (scramble) was transfected by lipofection using FuGENE 6 Transfection Reagent (Roche Applied Science). The transfected cells were selected in hygromycin-containing (100 μg/mL) culture medium for 2 weeks. In cells transfected with P2X4-shRNA, P2X4 receptor mRNA and protein expression levels were decreased to <50% of that in scramble shRNA-transfected cells (negative control) [32]. This transfection did not affect P2X7 receptor expression [32]. We used these stable transfectants in some experiments.

2.2. Immunoblotting

The culture supernatant or equal amounts of cell lysates were mixed with 2× sample buffer (50% glycerin, 2% SDS, 125 mM Tris, 10 mM DTT) and incubated at 95 °C for 10 min. Aliquots of samples containing protein were analyzed by 15% SDS–PAGE and bands were transferred to PVDF membranes. The blots were incubated for 2 h at room temperature in TBST (0.1% Tween-20, 10 mM Tris–HCl, 0.1 M NaCl) with 1% bovine serum albumin (BSA), then further incubated overnight at 4 °C with anti-HMGB1 antibody (1:1000) (Cell Signaling Technology Inc., Beverly, MA) or LC3B antibody (1:1000) (Novus Biologicals, LLC, Southpark Way, Littleton CO, USA), or mouse anti-β-actin antibody (1:1000) (Santa Cruz Biotechnology Inc., Santa Cruz, CA, USA) to confirm equal loading. Blots were washed with TBST, incubated with goat horseradish peroxidase (HRP)-conjugated anti-rabbit IgG antibody (1:20,000) (Cell Signaling Technology) or goat HRP-conjugated anti-mouse IgG antibody (1:10,000) (Santa Cruz Biotechnology) for 1.5 h, and washed again with TBST. Specific proteins were visualized by using ECL Prime Western blotting detection reagents (GE Healthcare, Piscataway, NJ).

2.3. Determination of IL-1β production

Culture supernatant was harvested, and IL-1β was measured by ELISA. A 96-well plate was coated with purified anti-mouse IL-1β mAb (1:250) (R&D Systems Inc., Minneapolis, MN, USA) and incubated overnight at 4 °C. The wells were washed with PBS containing 0.05% Tween-20, and nonspecific binding was blocked with PBS containing 1% bovine serum albumin for 1 h at room temperature. The plate was washed, culture supernatant was added, and incubation was continued for 2 h at room temperature. The plate was washed again, and anti-mouse biotin-conjugated IL-1β mAb

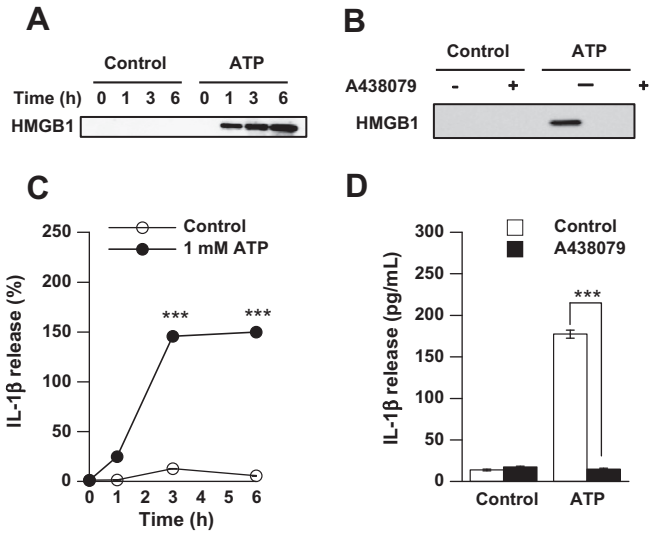

Fig. 1. ATP-induced inflammatory reaction through P2X7 receptor activation (A, C) RAW 264.7 cells were incubated with 1 mM ATP for the indicated times. (B, D) Cells were preincubated with 50 μM A438079 for 30 min, and incubated with vehicle (control) or 1 mM ATP for 6 h. (A, B) At the end of incubation, supernatants were collected and HMGB1 was detected by immunoblotting as described in Section 2. (C, D) The culture supernatant was harvested for determination of IL-1β. Concentrations of IL-1β in the culture supernatants were measured as described in Section 2. Error bars indicate ±SE ($n = 3$). Significant differences between indicated groups are indicated with $^{***}(p < 0.001)$.

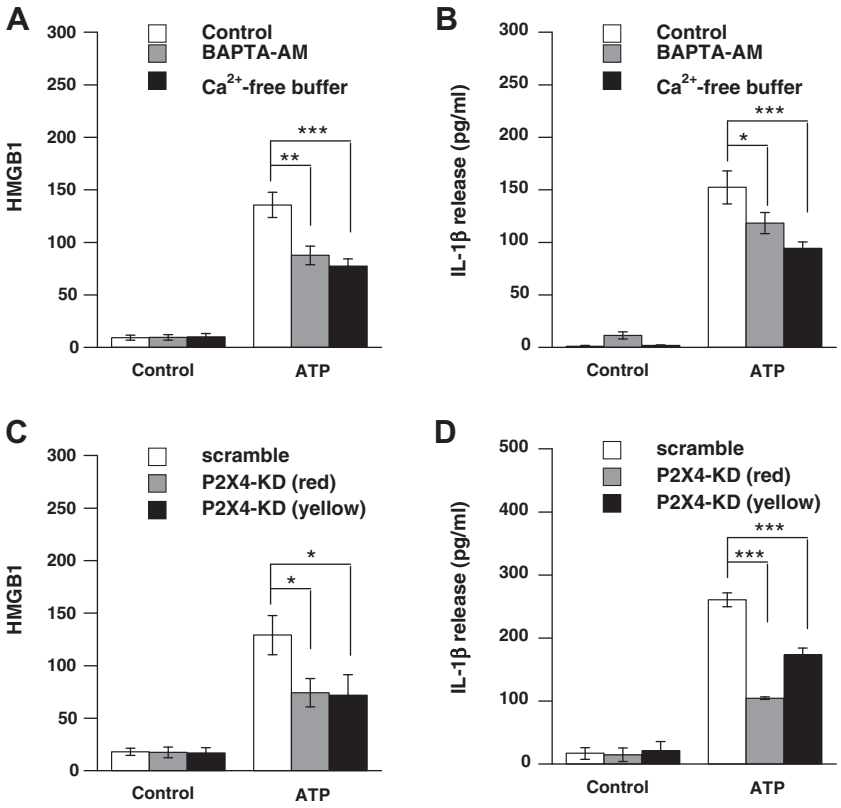

Fig. 2. Involvement of elevation of intracellular Ca^{2+} and P2X4 receptor in ATP-induced inflammation (A, B) Cells were incubated with vehicle (control) or 1 mM ATP for 6 h in RPMI1640 buffer, Ca^{2+}-free RPMI1640 buffer or RPMI1640 buffer containing BAPTA-AM (10 μM). (C, D) Cells were transfected with shRNA targeting P2X4 (clone ID: red or yellow) or negative control shRNA (scramble shRNA). Transfectants were incubated with vehicle (control) or 1 mM ATP for 6 h. (A, C) At the end of incubation, supernatants were collected and HMGB1 was detected by immunoblotting as described in Section 2. Values are expressed as ratios of HMGB1, and are means ± SE of three independent experiments. Statistically significant differences between groups are indicated by $^{***}(p < 0.001)$, $^{**}(p < 0.01)$ or $^{*}(p < 0.05)$. (B, D) The culture supernatant was harvested for determination of IL-1β. Concentrations of IL-1β in the culture supernatants were measured as described in Section 2. Error bars indicate ±SE ($n = 4$). Significant differences between groups are indicated with $^{***}(p < 0.001)$ and $^{*}(p < 0.05)$.

(1:250) (R&D Systems Inc.) was added for 1 h at room temperature. The plate was further washed, and avidin-horseradish peroxidase (Sigma) was added. The plate was incubated for 30 min at room temperature, then washed, and 3,3′,5,5′-tetramethylbenzidine was added. The reaction was stopped by adding 5 N H_2SO_4, and the absorption at 450 nm was measured with an ImmunoReader NJ-2000 (Nihon InterMed, Tokyo, Japan). A standard curve was established with recombinant mouse IL-1β (R&D Systems Inc.), and the concentration of IL-1β was estimated by interpolation.

2.4. Measurement of reactive oxygen species production

Intracellular ROS levels were monitored by using the fluorescent dye 2′,7′-dichlorodihydrofluorescein diacetate (H_2DCF-DA) (Invitrogen, Carlsbad, CA). Cells were incubated with H_2DCF-DA (10 μM) at 37 °C for 30 min. After the incubation, the supernatant was removed and the cells were washed twice with RPMI buffer. The cells were then re-suspended in RPMI buffer. The fluorescence of the stirred cell suspension (1.0×10^5 cells/mL) was measured (emission at 530 nm and excitation at 488 nm) using a fluorescence spectrophotometer (F-2500, Hitachi). In some experiments, DCF fluorescence was measured using a Wallac 1420 ARVO-SX multilabel counter (PerkinElmer, Yokohama, Japan; excitation/emission 485 nm/535 nm).

2.5. Statistics

Values are given as the mean ± SE. Comparison between two values was performed by means of the unpaired Student's *t*-test. Multiple groups were compared using ANOVA followed by pairwise comparisons with Bonferroni's *post hoc* analysis. Significance was defined as $p < 0.01$. Calculations were done using the Instat version 3.0 statistical package (GraphPad Software, San Diego, CA).

3. Results and discussion

3.1. Activation of P2X7 receptor induces release of HMGB1 and IL-1β

Activation of P2X7 receptor by treatment with 1 mM ATP can induce cell death in RAW 264.7 cells [32]. Since HMGB1 is released during necrotic cell death [13], we examined whether activation of P2X7 receptor induces HMGB1 release. As shown in Fig. 1A, release of HMGB1 in response to 1 mM ATP (Sigma) started within 1 h, and the amount of extracellular HMGB1 increased in a time-dependent manner. Next, the involvement of P2X7 receptor in ATP-induced HMGB1 release was examined. A438079 (a P2X7 receptor antagonist) (Tocris Bioscience, Bristol, UK) markedly abolished ATP-induced release of HMGB1 (Fig. 1B).

It has been reported that HMGB1 itself has only minimal proinflammatory properties, but it acquires much greater activity upon binding to IL-1β [33]. Therefore, the concentration of IL-1β in culture supernatant of cells incubated with 1 mM ATP was measured by ELISA. A significant increase of IL-1β production was observed from 3 h, reaching a plateau at 6 h post-treatment (Fig. 1C). ATP-induced IL-1β production was blocked by pretreatment with A438079 (Fig. 1D), suggesting that activation of P2X7 receptor induces production of IL-1β. These results indicated that activation of P2X7 receptor elicits inflammatory responses, such

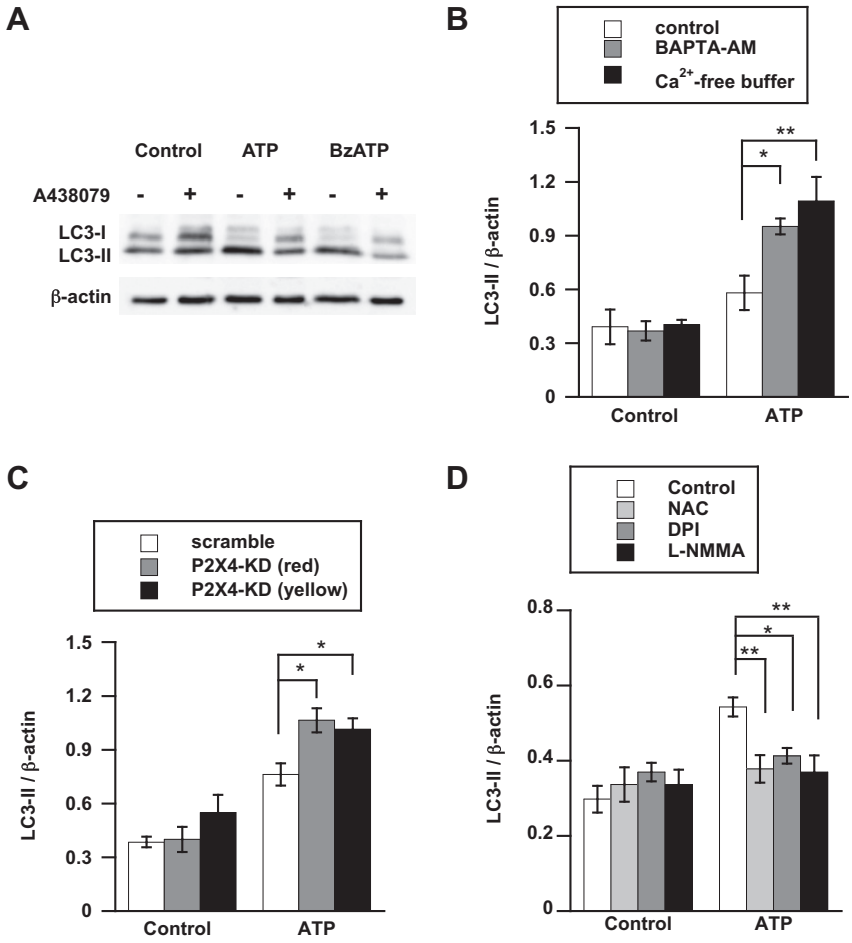

Fig. 3. Expression of LC3-II via multiple pathways (A) Cells were pretreated with vehicle (control) or A438079 for 30 min and then incubated with vehicle (control), 1 mM ATP or 200 μM BzATP for 3 h. (B) Cells were incubated with vehicle (control) or 1 mM ATP for 3 h in RPMI1640 buffer, Ca^{2+} free-RPMI1640 buffer or RPMI1640 buffer containing BAPTA-AM (10 μM). (C) Transfectants were incubated with vehicle (control) or 1 mM ATP for 3 h. (D) Cells were preincubated with vehicle (control), 5 mM NAC for 2 h, 10 μM DPI for 1.5 h, or 1 mM L-NMMA for 1 h, and incubated with vehicle (control) or 1 mM ATP for 3 h. Expression of LC3 was examined by immunoblotting, as described in Materials and Methods. Values are expressed as ratios of LC3-II/β-actin, and are means ± SE of three independent experiments. Significant differences between groups are indicated with $^{***}(p < 0.001)$, $^{**}(p < 0.01)$ and $^{*}(p < 0.05)$.

as release of HMGB1 and IL-1β, which are associated with induction of cell death.

3.2. Involvement of P2X4 receptor in P2X7-dependent inflammation through elevation of intracellular Ca^{2+}

It has been reported that Ca^{2+}-dependent HMGB1 secretion occurs in LPS-stimulated RAW264.7 cells [34]. Therefore, we investigated the effect of the removal of extracellular Ca^{2+} or pretreatment with an intracellular Ca^{2+} chelator, 1,2-bis(2-aminophenoxy)ethane-*N,N,N,N*-tetraacetic acid acetoxymethyl ester (BAPTA-AM) (Dojindo, Kumamoto, Japan) on ATP-induced HMGB1 release, in order to confirm the involvement of Ca^{2+} influx. As shown in Fig. 2A and B, HMGB1 release was decreased by suppression of elevation of intracellular Ca^{2+} concentration and IL-1β release was also diminished, indicating that elevation of intracellular Ca^{2+} is involved in P2X7-dependent inflammation.

We have shown that P2X4 receptor is involved in P2X7 receptor-dependent cell death via Ca^{2+} influx using P2X4-knockdowned RAW264.7 cells [32]. We therefore measured HMGB1 and IL-1β release in the stably P2X4-knockdowned RAW264.7 cells [32]. In addition to the effect on cell death, P2X4-knockdown cells showed suppression of HMGB1 and IL-1β release in response to ATP stimulation (Fig. 2C and D). These results indicated that Ca^{2+} influx via P2X4 receptor is involved in not only P2X7-mediated cell death, but also P2X7-mediated HMGB1 and IL-1β release.

3.3. Increased expression of LC3-II in response to P2X4 knockdown

Cytoplasmic LC3 associates with the membrane of autophagosomes. Because cytoplasmic LC3 (LC3-I) and autophagosome membrane-associated LC3 (LC3-II) exhibit different mobilities in immunoblot analysis, LC3-II can be used as a marker for autophagosome formation [35]. Thus, to determine whether activation of P2X7 receptor leads to autophagosome formation in RAW264.7 cells, cells were treated with ATP or BzATP (a P2X1, P2X7 receptor agonist) (Sigma) for 3 h, and the expression of LC3 was evaluated by Western blotting. Treatment of cells with ATP and BzATP resulted in an increase of LC3-II (16 kDa) and a decrease of LC3-I (18 kDa), compared to the expression levels in control cells. Moreover, A438079 inhibited accumulation of LC3-II (Fig. 3A), suggesting the involvement of P2X7 receptor in the ATP-induced increase in LC3-II expression.

Ca^{2+} influx through P2X7 receptor channels is involved in the ATP-induced increase of LC3-II [27,28]. Therefore, we examined the involvement of Ca^{2+} influx in ATP-induced LC3-II expression in RAW264.7 cells. Contrary to previous reports, we found that ATP-induced expression of LC3-II was increased when the elevation

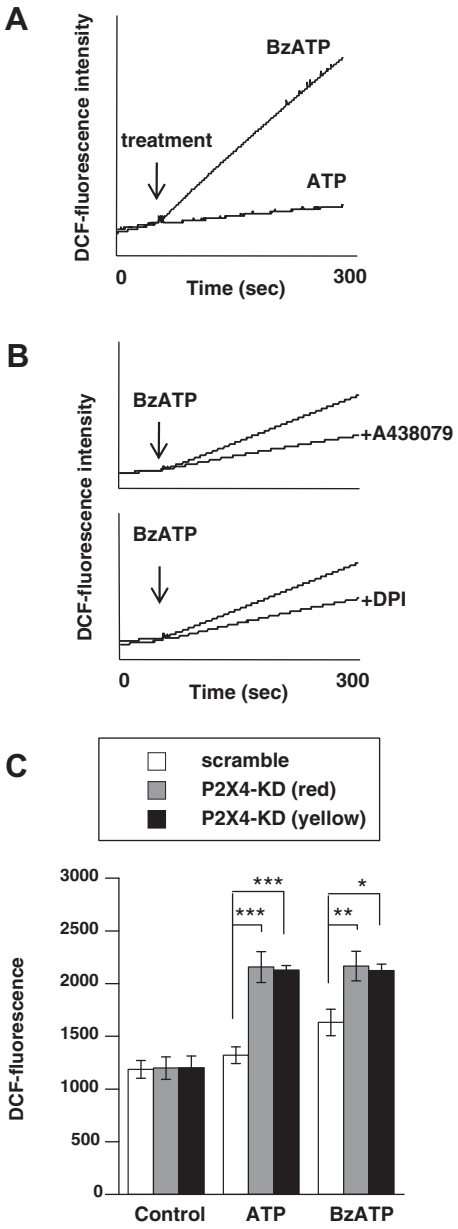

Fig. 4. Elevation of ROS generation by knockdown of P2X4 receptor (A) Cells loaded with H_2DCF-DA were stimulated with 1 mM ATP or 200 μM BzATP. (B) Cells loaded with H_2DCF-DA were preincubated with vehicle (control), 50 μM A438079, or 10 μM DPI for 5 min, and incubated with 1 mM ATP for 5 min. The fluorescence was analyzed with a fluorescence spectrometer. We obtained qualitatively similar results in three independent experiments, and typical data are presented. (D) Transfectants loaded with H_2DCF-DA were stimulated with 1 mM ATP or 200 μM BzATP. The fluorescence was monitored with a Wallac 1420 ARVO-SX multilabel counter. Error bars indicate ±SE (n = 5–6). Significant differences between groups are indicated with $^{***}(p < 0.001)$, $^{**}(p < 0.01)$ and $^{*}(p < 0.05)$.

of intracellular Ca^{2+} concentration was suppressed (Fig. 3B). Furthermore, decreased P2X4 expression resulted in increased expression of LC3-II (Fig. 3C). These results suggested that P2X4 receptor negatively controls P2X7-mediated induction of LC3-II expression via Ca^{2+} influx.

3.4. Effect of antioxidants on ATP-induced LC3-II expression

Reactive oxygen species can regulate autophagy under conditions of amino acid and serum starvation [36,37]. LPS-induced autophagy is also mediated by oxidative signaling and is associated with cytoprotection [38]. Therefore, the involvement of oxidative signaling in ATP-induced expression of LC3-II was examined. Preincubation with an antioxidant N-acetylcysteine (NAC) (Wako Pure Chemical), a NADPH oxidase inhibitor diphenyleneiodonium (DPI) (Sigma) or a nitric oxide synthase inhibitor N^G-monomethyl-L-arginine (L-NMMA) (Dojindo) blocked P2X7-mediated expression of LC3-II (Fig. 3D). In contrast, preincubation with DPI promoted ATP-induced release of lactate dehydrogenase, HMGB1 and IL-1β (data not shown). These results suggested that ROS generation up-regulates LC3-II induction but down-regulates inflammatory response associated with ATP.

3.5. Involvement of P2X4 receptor in ROS generation

It has already been reported that extracellular ATP stimulation promotes intracellular ROS generation [5,6]. Therefore, we finally examined whether P2X4 receptor regulates P2X7 receptor-mediated ROS generation. Fig. 4A shows ROS generation in response to stimulation of cells with BzATP; the magnitude of the response was higher in cells treated with BzATP than in those treated with ATP. These results are accord with findings in microglia [39]. BzATP-induced ROS generation is blocked by A438079 or DPI (Fig. 4B), suggesting that activation of P2X7 receptor triggers activation of NADPH oxidase and subsequent ROS production. Next, we examined the role of P2X4 receptor in P2X7 receptor-mediated ROS generation. Decreased P2X4 expression resulted in elevation of DCF fluorescence in response to ATP or BzATP (Fig. 4C). The elevation of ROS generation by knockdown of P2X4 receptor was blocked by pretreatment with A438079 (data not shown), suggesting that P2X4 receptor negatively regulates P2X7 receptor-mediated ROS production.

Since necrosis is known to induce inflammation, necrosis might be involved in diseases that feature chronic inflammation. Our results suggest that P2X4 receptor modulates multiple mechanisms of P2X7 receptor-mediated inflammation, including release of HMGB1 and IL-1β, which are associated with macrophage death. On the other hand, it is also known that activation of P2X7 receptor induces cell autophagy, and our results indicate that co-expression of P2X4 receptor with P2X7 receptor could negatively regulate P2X7 receptor-dependent expression of LC3-II via Ca^{2+} influx or ROS production. Since suppression of autophagy causes up-regulation of IL-1β production [23,24], we examined the effect of wortmannin or 3-methyladenine, both of which are known to inhibit autophagy, on ATP-induced LC3-II expression and release of IL-1β in RAW 264.7 cells. Pre-incubation with these autophagy inhibitors resulted in decreased expression of LC3-II, but promoted the release of IL-1β mediated by P2X7 receptor (data not shown). Therefore, attenuation of autophagy by P2X4 receptor might be one reason for the facilitation of IL-1β production by P2X4 receptor. This is the first demonstration that expression of P2X4 receptor modulates P2X7 receptor-dependent inflammation-related processes in macrophages. These results are consistent with the idea that co-expression of P2X7 and P2X4 receptors may play an important role in regulating the inflammatory responses associated with a variety of immunological and pathophysiological processes.

Acknowledgment

Parts of this work were supported by Grant-in-Aid for Young Scientists (B) (to M.T.) from the Ministry of Education, Culture, Sports, Science, and Technology of Japan.

References

[1] D. Ferrari, C. Pizzirani, E. Adinolfi, et al., The P2X7 receptor: a key player in IL-1 processing and release, J. Immunol. 176 (2006) 3877–3883.

[2] B.D. Humphreys, G.R. Dubyak, Modulation of P2X7 nucleotide receptor expression by pro- and anti-inflammatory stimuli in THP-1 monocytes, J. Leukoc. Biol. 64 (1998) 265–273.
[3] B.R. Bianchi, K.J. Lynch, E. Touma, et al., Pharmacological characterization of recombinant human and rat P2X receptor subtypes, Eur. J. Pharmacol. 376 (1999) 127–138.
[4] A. Surprenant, F. Rassendren, E. Kawashima, et al., The cytolytic P2Z receptor for extracellular ATP identified as a P2X receptor (P2X7), Science 272 (1996) 735–738.
[5] B.C. Suh, J.S. Kim, U. Namgung, et al., P2X7 nucleotide receptor mediation of membrane pore formation and superoxide generation in human promyelocytes and neutrophils, J. Immunol. 166 (2001) 6754–6763.
[6] T. Noguchi, K. Ishii, H. Fukutomi, et al., Requirement of reactive oxygen species-dependent activation of ASK1-p38 MAPK pathway for extracellular ATP-induced apoptosis in macrophage, J. Biol. Chem. 283 (2008) 7657–7665.
[7] P. Pelegrin, A. Surprenant, Pannexin-1 mediates large pore formation and interleukin-1beta release by the ATP-gated P2X7 receptor, EMBO J. 25 (2006) 5071–5082.
[8] M. Tsukimoto, M. Maehata, H. Harada, et al., P2X7 receptor-dependent cell death is modulated during murine T cell maturation and mediated by dual signaling pathways, J. Immunol. 177 (2006) 2842–2850.
[9] S. Muller, P. Scaffidi, B. Degryse, et al., New EMBO members' review: the double life of HMGB1 chromatin protein: architectural factor and extracellular signal, EMBO J. 20 (2001) 4337–4340.
[10] U. Andersson, H. Erlandsson-Harris, H. Yang, et al., HMGB1 as a DNA-binding cytokine, J. Leukoc. Biol. 72 (2002) 1084–1091.
[11] C.J. Czura, H. Wang, K.J. Tracey, Dual roles for HMGB1: DNA binding and cytokine, J. Endotoxin Res. 7 (2001) 315–321.
[12] H. Wang, J.M. Vishnubhakat, O. Bloom, et al., Proinflammatory cytokines (tumor necrosis factor and interleukin 1) stimulate release of high mobility group protein-1 by pituicytes, Surgery 126 (1999) 389–392.
[13] P. Scaffidi, T. Misteli, M.E. Bianchi, Release of chromatin protein HMGB1 by necrotic cells triggers inflammation, Nature 418 (2002) 191–195.
[14] U. Andersson, H. Wang, K. Palmblad, et al., High mobility group 1 protein (HMG-1) stimulates proinflammatory cytokine synthesis in human monocytes, J. Exp. Med. 192 (2000) 565–570.
[15] J. Sunden-Cullberg, A. Norrby-Teglund, A. Rouhiainen, et al., Persistent elevation of high mobility group box-1 protein (HMGB1) in patients with severe sepsis and septic shock, Crit. Care Med. 33 (2005) 564–573.
[16] N. Taniguchi, K. Kawahara, K. Yone, et al., High mobility group box chromosomal protein 1 plays a role in the pathogenesis of rheumatoid arthritis as a novel cytokine, Arthritis Rheum. 48 (2003) 971–981.
[17] R. Auger, I. Motta, K. Benihoud, et al., A role for mitogen-activated protein kinase (Erk1/2) activation and non-selective pore formation in P2X7 receptor-mediated thymocyte death, J. Biol. Chem. 280 (2005) 28142–28151.
[18] L.M. Thomas, R.D. Salter, Activation of macrophages by P2X7-induced microvesicles from myeloid cells is mediated by phospholipids and is partially dependent on TLR4, J. Immunol. 185 (2010) 3740–3749.
[19] V. Deretic, Autophagy in infection, Curr. Opin. Cell Biol. 22 (2010) 252–262.
[20] I. Monastyrska, D.J. Klionsky, Autophagy in organelle homeostasis: peroxisome turnover, Mol. Aspects Med. 27 (2006) 483–494.
[21] K. Moreau, S. Luo, D.C. Rubinsztein, Cytoprotective roles for autophagy, Curr. Opin. Cell Biol. 22 (2010) 206–211.
[22] A.M. Cuervo, Autophagy: in sickness and in health, Trends Cell Biol. 14 (2004) 70–77.
[23] T. Saitoh, N. Fujita, M.H. Jang, et al., Loss of the autophagy protein Atg16L1 enhances endotoxin-induced IL-1beta production, Nature 456 (2008) 264–268.
[24] J. Harris, M. Hartman, C. Roche, et al., Autophagy controls IL-1beta secretion by targeting pro-IL-1beta for degradation, J. Biol. Chem. 286 (2011) 9587–9597.
[25] N.J. Prescott, S.A. Fisher, A. Franke, et al., A nonsynonymous SNP in ATG16L1 predisposes to ileal Crohn's disease and is independent of CARD15 and IBD5, Gastroenterology 132 (2007) 1665–1671.
[26] J.D. Rioux, R.J. Xavier, K.D. Taylor, et al., Genome-wide association study identifies new susceptibility loci for Crohn disease and implicates autophagy in disease pathogenesis, Nat. Genet. 39 (2007) 596–604.
[27] T. Takenouchi, M. Nakai, Y. Iwamaru, et al., The activation of P2X7 receptor impairs lysosomal functions and stimulates the release of autophagolysosomes in microglial cells, J. Immunol. 182 (2009) 2051–2062.
[28] D. Biswas, O.S. Qureshi, W.Y. Lee, et al., ATP-induced autophagy is associated with rapid killing of intracellular mycobacteria within human monocytes/macrophages, BMC Immunol. 9 (2008) 35.
[29] T.M. Egan, B.S. Khakh, Contribution of calcium ions to P2X channel responses, J. Neurosci. 24 (2004) 3413–3420.
[30] W. Ma, A. Korngreen, S. Weil, et al., Pore properties and pharmacological features of the P2X receptor channel in airway ciliated cells, J. Physiol. 571 (2006) 503–517.
[31] O.S. Qureshi, A. Paramasivam, J.C. Yu, et al., Regulation of P2X4 receptors by lysosomal targeting, glycan protection and exocytosis, J. Cell Sci. 120 (2007) 3838–3849.
[32] A. Kawano, M. Tsukimoto, T. Noguchi, et al., Involvement of P2X4 receptor in P2X7 receptor-dependent cell death of mouse macrophages, Biochem. Biophys. Res. Commun 419 (2012) 374–380.
[33] Y. Sha, J. Zmijewski, Z. Xu, et al., HMGB1 develops enhanced proinflammatory activity by binding to cytokines, J. Immunol. 180 (2008) 2531–2537.
[34] Y.J. Oh, J.H. Youn, Y. Ji, et al., HMGB1 is phosphorylated by classical protein kinase C and is secreted by a calcium-dependent mechanism, J. Immunol. 182 (2009) 5800–5809.
[35] N. Mizushima, T. Yoshimori, How to interpret LC3 immunoblotting, Autophagy 3 (2007) 542–545.
[36] Y. Chen, M.B. Azad, S.B. Gibson, Superoxide is the major reactive oxygen species regulating autophagy, Cell Death Differ. 16 (2009) 1040–1052.
[37] R. Scherz-Shouval, E. Shvets, E. Fass, et al., Reactive oxygen species are essential for autophagy and specifically regulate the activity of Atg4, EMBO J. 26 (2007) 1749–1760.
[38] H. Yuan, C.N. Perry, C. Huang, et al., LPS-induced autophagy is mediated by oxidative signaling in cardiomyocytes and is associated with cytoprotection, Am. J. Physiol. Heart Circ. Physiol. 296 (2009) H470–H479.
[39] L.K. Parvathenani, S. Tertyshnikova, C.R. Greco, et al., P2X7 mediates superoxide production in primary microglia and is up-regulated in a transgenic mouse model of Alzheimer's disease, J. Biol. Chem. 278 (2003) 13309–13317.

Biochemical and Biophysical Research Communications 420 (2012) 108–113

Contents lists available at SciVerse ScienceDirect

Biochemical and Biophysical Research Communications

journal homepage: www.elsevier.com/locate/ybbrc

Chondroregulatory action of prolactin on proliferation and differentiation of mouse chondrogenic ATDC5 cells in 3-dimensional micromass cultures

Dutmanee Seriwatanachai [a], Nateetip Krishnamra [a,b], Narattaphol Charoenphandhu [a,b,*]

[a] Center of Calcium and Bone Research (COCAB), Faculty of Science, Mahidol University, Bangkok, Thailand
[b] Department of Physiology, Faculty of Science, Mahidol University, Bangkok, Thailand

ARTICLE INFO

Article history:
Received 21 February 2012
Available online 3 March 2012

Keywords:
Bone elongation
Chondrocyte
Micromass
Mineralizing nodule
Prolactin
Proteoglycans

ABSTRACT

A recent investigation in lactating rats has provided evidence that the lactogenic hormone prolactin (PRL) increases endochondral bone growth and bone elongation, presumably by accelerating apoptosis of hypertrophic chondrocytes in the growth plate and/or subsequent chondrogenic matrix mineralization. Herein, we demonstrated the direct chondroregulatory action of PRL on proliferation, differentiation and apoptosis of chondrocytes in 3-dimensional micromass culture of mouse chondrogenic ATDC5 cell line. The results showed that ATDC5 cells expressed PRL receptor (PRLR) transcripts, and responded typically to PRL by downregulating PRLR expression. Exposure to a low PRL concentration of 10 ng/mL, comparable to the normal levels in male and non-pregnant female rats, increased chondrocyte viability, differentiation, proteoglycan accumulation, and mRNA expression of several chondrogenic differentiation markers, such as Sox9, ALP and Hspg2. In contrast, high PRL concentrations of $\geqslant$100 ng/mL, comparable to the levels in pregnancy or lactation, decreased chondrocyte viability by inducing apoptosis, with no effect on chondrogenic marker expression. It could be concluded that chondrocytes directly but differentially responded to non-pregnant and pregnant/lactating levels of PRL, thus suggesting the stimulatory effect of PRL on chondrogenesis in young growing individuals, and supporting the hypothesis of hypertrophic chondrocyte apoptosis in the growth plate of lactating rats.

1. Introduction

The growth and maintenance of the mammalian skeleton is a product of developmental and postnatal processes that occur throughout life. After being derived from mesenchymal progenitors, chondrocytes proliferate and differentiate in the growth plate at the cartilage–bone interface. This dynamic region therefore determines longitudinal growth of long bones through the multiplication and hypertrophy of chondrocytes, followed by apoptosis of hypertrophic chondrocytes and chondrogenic matrix calcification. A number of humoral and transcriptional factors, such as parathyroid hormone-related peptide and SRY (sex determining region Y)-box (Sox)-9, respectively, act in concert to regulate normal growth plate development [1,2]. We recently reported in lactating rats that the lactogenic hormone prolactin (PRL) could modulate chondrogenic activity in the growth plate, leading to a decrease in hypertrophic zone height, increased endochondral bone growth and bone elongation [3]. The underlying mechanism of growth plate changes in lactating rats remains unknown, but it is possible that elevated plasma PRL levels during pregnancy and lactation ($\geqslant$100 ng/mL; normal non-pregnant levels ~7–10 ng/mL) could induce apoptosis of hypertrophic chondrocytes [3]. The presence of PRL receptor (PRLR) in the growth plate and articular chondrocytes also suggested the direct effects of PRL on chondrocyte proliferation, differentiation and function [3–5].

PRL has been recognized as an important calciotropic hormone that provides additional calcium for fetal growth and milk production during pregnancy and lactation, respectively [6]. To accomplish this task, PRL stimulates intestinal calcium absorption and osteoclast-mediated bone resorption throughout the lactating period [7,8]. However, the outcomes of PRL actions regarding bone and calcium metabolism are dependent on various factors, such as age and plasma PRL concentration. For example, PRL increases bone calcium accretion in young growing animals, but induces bone loss in mature adults and lactating mothers [8–10]. Moreover, PRL responses in several cell types, e.g., intestinal epithelial cells and Leydig cells, are biphasic, i.e., low and high doses have opposite actions [11,12].

The main objective of this study was to investigate the effect of PRL on chondrocyte proliferation, differentiation and apoptosis by using micromass culture of mouse chondrogenic ATDC5 cell line. This micromass culture is a reliable in vitro model for investigating temporal modulation of factors that coordinate chondrocyte differentiation and chondrogenesis [13].

* Corresponding author at: Department of Physiology, Faculty of Science, Mahidol University, Rama VI Road, Bangkok 10400, Thailand. Fax: +66 2 354 7154.
E-mail address: naratt@narattsys.com (N. Charoenphandhu).

0006-291X/$ - see front matter © 2012 Elsevier Inc. All rights reserved.
http://dx.doi.org/10.1016/j.bbrc.2012.02.123

2. Materials and methods

2.1. Micromass culture

Mouse chondrogenic ATDC5 cells (RIKEN Cell Bank, Tsukuba, Japan; 1×10^5 cells/cm^2) were cultured until confluent (~3 days) in maintenance medium containing 1:1 Dulbecco's modified Eagle medium (DMEM)/F-12 medium (Sigma, St. Louis, MO, USA), supplemented with 5% fetal bovine serum (FBS), 100 U/mL penicillin, 100 μg/mL streptomycin (Gibco, Grand Island, NY, USA), 1% L-glutamine (Gibco). After reaching 100% confluent, cells were centrifuged to obtain a density of 2×10^7 cells/mL. Cell suspension (10 μL) was then placed in 12-well plates (Corning, NY, USA) at the center of each well for 2–3 h before adding chondrogenic differentiation medium (maintenance medium plus 10 μg/mL insulin, 10 μg/mL transferrin and 30 nmol/L sodium selenite), which allowed cells to form 3-dimensional (3D) micromass [14]. All cultures were maintained at 37 °C in a humidified 5% CO_2 incubator. The medium was changed every other day.

2.2. Cell viability assay

ATDC5 cells were grown in a 96-well culture plate (3000 cells/well) until 70% confluent. After being incubated with vehicle (1 mg/mL bovine serum albumin in 0.004 N HCl; control group), 10, 50, 100 or 600 ng/mL recombinant human PRL (catalog no. 682-PL; >97% purity, R&D Systems, Minneapolis, MN, USA) for 24 h, culture media were replaced with 3-(4,5-dimethylthiazol-2-yl)-2,5-diphenyltetrazolium bromide (MTT) reagent (Sigma). After 3-h MTT incubation at 37 °C, the absorbance of each well was spectrometrically determined at 540 nm by a microplate reader (model Multiscan EX; Thermo Labsystems, Cergy-Pontoise, France) as described previously [15]. The absorbance of control wells was normalized to 1. The relative values of PRL-exposed cells were presented as fold change compared to the control group.

2.3. Cell proliferation assay

ATDC5 cell proliferation was quantified by 5-bromo-2-deoxyuridine (BrdU) colorimetric kit (Roche, Indianapolis, IN, USA), according to the manufacturer's instruction. Briefly, 3-day micromass nodules were incubated with 10 μmol/L BrdU for 16 h. Thereafter, vehicle, 10, 100, or 600 ng/mL PRL were added and then incubated for 24 h before cells were fixed and later incubated with anti-BrdU-peroxidase antibody to detect BrdU-incorporated cells. Substrate solution containing tetramethylbenzidine was added for color development. Optical density was quantified by a microplate reader at 370 nm. The absorbance of control cells was normalized to 1. Relative proliferation of PRL-exposed cells was presented as fold change compared to the control group.

2.4. Quantitative real-time PCR (qRT-PCR)

ATDC5 micromass nodules (3 days) were incubated with vehicle, 10 or 100 ng/mL PRL for 24 h or 7 days. Thereafter, total RNA was extracted and quantified as described previously [7]. One microgram of total RNA was reverse-transcribed by iScript kit (Bio-rad, Hercules, CA, USA). Four-microliter aliquots were used for cDNA amplification by MiniOpticon real-time PCR system (Bio-rad) with iQ SYBR Green Supermix (Bio-rad). Forward and reverse primers used in the present study were: glyceraldehyde 3-phosphate dehydrogenase (GAPDH), 5′-ACTGAGGACCAGGTTGTC-3′, 5′-TGCTGTAGCCGTATTCATTG-3′; PRLR, 5′-GAGAAGGGCAAGTCTGAAGAAC-3′, 5′-GGGATGGCATTAGCCGCTC-3′; cyclin D1, 5′-CAG AAGTGCGAAGAGGAGGTC-3′, 5′-TCATCTTAGAGGCCACGAACAT-3′; heparan sulfate proteoglycan (Hspg)-2, 5′-GATGGCCTTTCCCTCCCTG-3′, 5′-GTACTCAATGGACCGCGTAAA-3′; Sox9, 5′-GAGCCGGATCTGAAGAGGGA-3′, 5′-GCTTGACGTGTGGCTTGTTC-3′; collagen (Col)-10, 5′-TTCTGCTGCTAATGTTCTTGACC-3′, 5′-GGGATGAAGTATTGTGTCTTGGG-3′; and alkaline phosphatase (ALP), 5′-ACTGATGTGGAATACGAACTGGATGAGAAGG-3′, 5′-CAGTCAGGTTGTTCCGATTCAATTCATACTGC-3′. GAPDH was a housekeeping gene for normalization. Relative mRNA expression was calculated from the threshold cycle (C_t) by using $2^{-\Delta C_t}$ method.

2.5. TUNEL assay for cell apoptosis

Apoptotic cells were determined by the in situ cell death detection kit (Roche), based on labeling DNA strand breaks [terminal deoxynucleotidyl transferase-mediated deoxyuridine triphosphate nick end labeling (TUNEL) technology]. ATDC5 cells were cultured in differentiation medium for 24 h to form micromass. After being treated with vehicle, 10, or 100 ng/mL of PRL for another 24 h, cells were fixed at 4 °C overnight with 4% formaldehyde in phosphate buffer saline (PBS), and then permeabilized with 0.1% Triton X-100 in 0.1% wt/vol sodium citrate on ice for 2 min. Fixed cells were later incubated at 37 °C for 60 min with FITC-conjugated dUTP in a terminal deoxynucleotidyl transferase (TdT)-catalyzed reaction in a humidified atmosphere, and washed three times with PBS at room temperature. Finally, the TUNEL-labeled apoptotic cells from three independent experiments were randomly counted in five microscopic fields per experiment. Fluorescent images were captured by a fluorescent microscope (model BX51TRF; Olympus, Tokyo, Japan) operated with Motic Images Plus 2.0 (Motic Instruments Inc., Richmond, Canada).

2.6. Quantification of proteoglycan accumulation and mineralizing nodule formation

Micromass nodules were cultured in vehicle, 10 or 100 ng/mL PRL-containing differentiation media before proteoglycan accumulation and mineralizing nodule formation were quantified on day 15 and 21, respectively. As previously described [16], the micromass nodules were washed twice with PBS and fixed overnight in cold 4% paraformaldehyde. They were then incubated with 1% alcian blue (Sigma) in 5% acetic acid for 2 h to stain proteoglycans, or 1% alizarin red S solution (Sigma) for 5 min to stain mineralizing nodules. After being destained with 6 mol/L guanidine–HCl, the optical density was determined at 650 nm (alcian blue) and 540 nm (alizarin red S) by standard spectrophotometric method.

2.7. Immunocytochemistry

ATDC5 cells were cultured on coverslips (50,000 cells/well in 6-well plate) in differentiation medium for 3 days, and fixed in cold 4% paraformaldehyde/PBS. Non-specific binding sites were blocked by 10% FBS for 30 min at room temperature. Thereafter, samples were incubated at 4 °C overnight with 1:300 polyclonal rabbit anti-mouse PRLR primary antibody (catalog no. sc-30225; Santa Cruz Biotechnology, Santa Cruz, CA, USA), and then with 1:200 biotinylated goat anti-rabbit secondary antibody, followed by 60-min incubation with streptavidin-conjugated horseradish peroxidase solution (Zymed, San Francisco, CA, USA) and 3,3′-diaminobenzidine chromogen. Regarding the negative control slides, cells were incubated without primary antibody. Images were captured by a light microscope.

2.8. Statistical analysis

Results are expressed as mean ± SE. Unless otherwise specified, multiple comparisons were performed by one-way analysis

of variance followed by Dunnett's post-test. The level of significance was $p < 0.05$. All data were analyzed by GraphPad Prism 5.0 for Mac OS X (GraphPad Software Inc., San Diego, CA, USA).

3. Results

3.1. PRLR expression during chondrocyte differentiation

The PRLR expression was first investigated in ATDC5 cells to confirm that this cell type could directly respond to PRL. As depicted in Fig. 1A, ATDC5 cells abundantly expressed PRLR proteins as determined by immunocytochemistry. The negative control slides (no primary antibody) showed no positive signal (data not shown). qRT-PCR revealed that PRLR mRNA expression in ATDC5 micromass was decreased on days 7 and 15, which represented the differentiating period (Fig. 1B). The typical downregulation of PRLR mRNA expression was also observed in the day-7 micromass exposed to 10 and 100 ng/mL PRL (Fig. 1C).

3.2. Viability and proliferation of PRL-exposed ATDC5 cells

MTT and BrdU assays were used to determine viability and proliferation of PRL-exposed ATDC5 cells. As shown in Fig. 1D, exposure to 10 ng/mL PRL for 24 h significantly increased cell viability, whereas 600 ng/mL PRL decreased cell viability compared with the control group, indicating that chondrocytes responded to PRL in a biphasic dose-dependent manner similar to that reported in the intestinal epithelial cells [11]. At 72 h exposure, 100 and 600 ng/mL PRL also decreased cell viability (data not shown). BrdU assay demonstrated that chondrocyte cell proliferation was decreased after a 24-h exposure to 600 ng/mL PRL (Fig. 1E).

3.3. Proteoglycan accumulation and mineralizing nodule formation in PRL-exposed micromass

After cell proliferation to form a micromass, chondrocytes became fully differentiated and synthesized extracellular matrix (proteoglycan accumulation) that finally underwent mineralization. After exposure to 10 ng/mL PRL for 15 days, proteoglycan accumulation was significantly increased when compared to the control group (Fig. 2A), whereas 100 ng/mL PRL decreased proteoglycan accumulation in this chondrocyte micromass (Fig. 2A). A 21-day exposure to 10 or 100 ng/mL PRL showed tendency to increase and decrease mineralizing nodule formation in chondrocyte micromass, respectively (Fig. 2B). Moreover, mineralizing nodule formation in the 100 ng/mL PRL-treated micromass was significantly less than that in the 10 ng/mL PRL-treated group (Fig. 2B).

3.4. Expression of chondrocyte differentiation markers in PRL-exposed ATDC5 micromass

Since PRL altered the functions of differentiated chondrocytes as indicated by proteoglycan accumulation, we further investigated the expression of genes responsible for chondrocyte differentiation, i.e., ALP, Sox9, Hspg2 and Col10. The results showed that 10 ng/mL, but not 100 ng/mL PRL markedly upregulated the mRNA expression of Sox9, ALP and Hspg2 in differentiated ATDC5 cells (day 7 of PRL incubation; Fig. 3). However, PRL had no effect on Col10 mRNA expression (data not shown). In addition, proliferating ATDC5 cells directly exposed for 24 h to 10 ng/mL PRL, but not 100 ng/mL PRL, upregulated the mRNA expression of cyclin D1 (Fig. 3D), a gene responsible for cell proliferation.

3.5. Apoptosis of PRL-exposed ATDC5 cells in micromass culture

As determined by TUNEL assay, 100 ng/mL PRL, but not 10 ng/mL PRL, apparently led to greater DNA fragmentation, an indicator

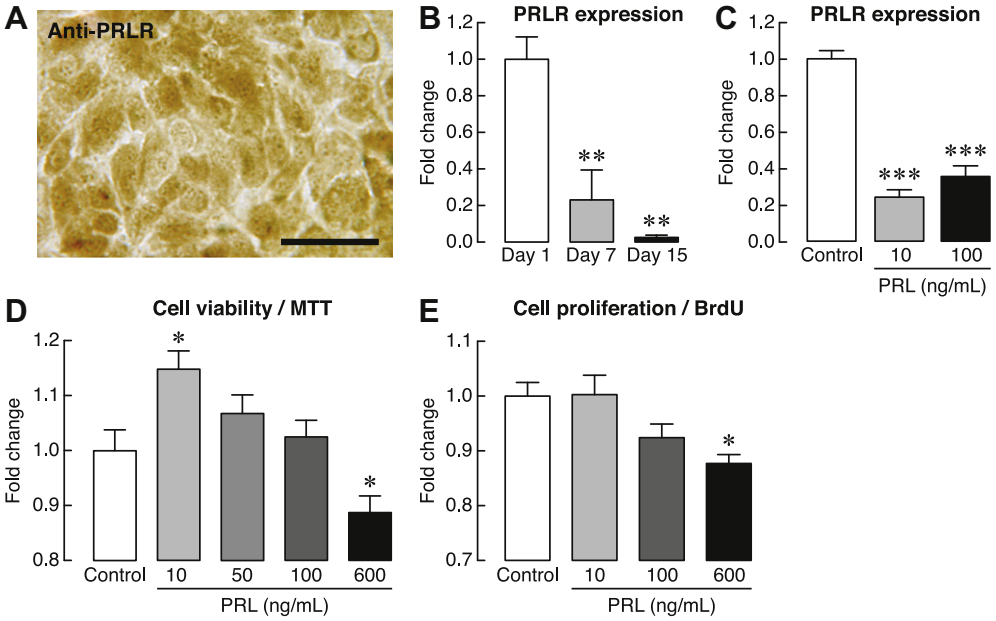

Fig. 1. (A) A representative photomicrograph shows PRLR protein expression (brownish color) in mouse chondrogenic ATDC5 cells, as determined by immunocytochemistry (magnification 200×). Cells were cultured in differentiating medium for 3 days before being stained with anti-PRLR antibody. Negative controls were performed by incubating cells in an absence of anti-PRLR (data not shown). Bar, 200 μm. (B) PRLR mRNA expression in ATDC5 cells as determined by qRT-PCR ($n = 3$ per group). Cells were harvested on days 1, 7 and 15 after being incubated in differentiating media. (C) PRLR mRNA expression in ATDC5 cells exposed to 0 (control), 10 or 100 ng/mL PRL for 7 days ($n = 3$ per group). (D) ATDC5 cell viability and (E) cell proliferation after exposure to 10–600 ng/mL PRL for 24 h, as determined by MTT ($n = 10$ per group) and BrdU assays ($n = 3$ per group), respectively. All experiments were performed at least in triplicate. $^{*}p < 0.05$, $^{**}p < 0.01$ and $^{***}p < 0.001$ compared with their corresponding control group (open bar).

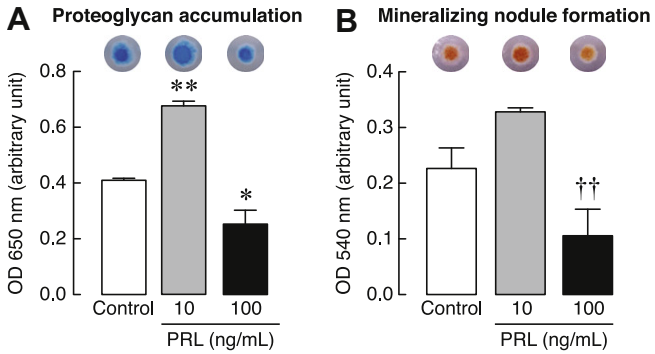

Fig. 2. (A) Proteoglycan accumulation (day 15 of PRL treatment; alcian blue staining), and (B) mineralizing nodule formation (day 21 of PRL treatment; alizarin red S staining) in 10 and 100 ng/mL PRL-treated ATDC5 micromass nodules ($n = 3$ per group), as represented by optical density (OD) at 650 and 540 nm, respectively. Representative culture plates are presented along with spectrophotometric data. $^{*}p < 0.05$, $^{**}p < 0.01$ compared with the corresponding control group (open bar). †† $p < 0.01$ compared with 10 ng/mL PRL-treated group (Tukey post-test).

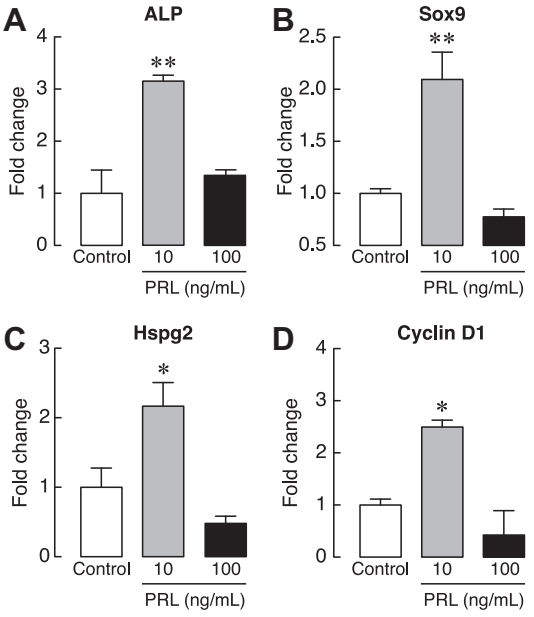

Fig. 3. Relative mRNA expression of genes responsible for chondrocyte proliferation and differentiation, i.e. (A) ALP, (B) Sox9, (C) Hspg2, and (D) cyclin D1, after being incubated with 10 or 100 ng/mL PRL for 24 h (cyclin D1 only) or 7 days ($n = 3$ per group). GAPDH was a housekeeping gene for normalization. $^{*}p < 0.05$, $^{**}p < 0.01$ compared with the corresponding control group (open bar).

of chondrocyte apoptosis (Fig. 4A; green signals). Therefore, the number of apoptotic chondrocytes was significantly higher in the 100 ng/mL PRL-treated group than the control group (Fig. 4B).

4. Discussion

Fetomaternal calcium homeostasis and bone metabolism during pregnancy and lactation are partly maintained by the PRL-enhanced intestinal calcium absorption [6]. In lactating humans and rodents with inadequate intestinal calcium supply (e.g., low calcium intake), PRL, in turn, enhanced a massive calcium release from bone to provide sufficient amount of free-ionized calcium for milk production, thereby resulting in trabecular bone loss in the metaphysis of long bones [8,10]. It was postulated that trabecular bone loss and perhaps reduced bone strength were compensated by the enhanced endochondral bone formation [3], which produced bone trabeculae and bone elongation.

Our previous investigation suggested that PRL is an important chondroregulatory hormone in lactation since administration of bromocriptine, an inhibitor of pituitary PRL release, completely prevented the lactation-induced reduction in the tibial growth plate height, which was decreased after PRL injection despite bromocriptine treatment [3]. PRL is also essential for proper chondrocyte function in fetal and neonatal rodents, the latter of which exhibit high plasma PRL levels of 140–500 ng/mL [4,17,18]. Since PRLR knockout mice manifested the absence of calvarial ossification and reduction in bone development and growth [4], one may hypothesize that chondrocytes was not committed into apoptotic phase, resulting in impaired endochondral bone formation. Furthermore, possible direct action of PRL on chondrocytes was supported by the previous reports of PRLR expression in hyaline cartilage, articular cartilage and growth plate cartilage of rodents [3,5,19,20]. In the present study, chondrogenic ATDC5 cells were also found to express PRLR mRNA and protein, with the levels of mRNA expression being decreased from early to late differentiation stages in 3D micromass culture. The typical PRL-induced downregulation of PRLR expression was also observed in both 10 and 100 ng/mL PRL-treated ATDC5 cells (Fig. 1C), similar to that reported in rat intestinal epithelial cells [21].

During endochondral bone formation, the apoptosis of fully differentiated hypertrophic chondrocytes warrants that chondrogenic matrix mineralization and subsequent osteoblast-mediated bone formation in the primary spongiosa do occur [22], otherwise the growth plate height could be abnormally increased, followed by deformity of the long bone as observed in vitamin D-deficient rickets [23]. Therefore, decreases in cell viability and proliferation as well as increased apoptosis observed in the PRL-treated ATDC5 cells could explain the enhanced endochondral bone formation and bone elongation in pregnant and lactating rats with elevated plasma PRL levels of $\geqslant$100 ng/mL (up to 600 ng/mL during suckling) [3,10]. A decrease in proteoglycan accumulation in 100 ng/mL PRL-treated micromass was consistent with the PRL-induced reduction in growth plate height, particularly the hypertrophic zone height, in lactating rats [3].

On the other hand, a lower PRL concentration of 10 ng/mL induced a number of positive effects on ATDC5 cells, such as increases in cell viability, proteoglycan accumulation and expression of differentiation marker transcripts. Since this PRL concentration is comparable to the plasma levels of male and non-pregnant female adult rodents [24,25], PRL is likely to promote chondrocyte differentiation and function in normal individuals. Although the present TUNEL assay did not show a significant anti-apoptotic effect of 10 ng/mL PRL on ATDC5 cells, a previous investigation in articular chondrocytes revealed a protective action of PRL against starvation-induced apoptosis [26]. However, unlike growth plate chondrocytes, the differentiated articular chondrocytes do not proceed to the hypertrophic differentiation stage [27]. Since 10 ng/mL PRL could also upregulate cyclin D1 (Fig. 3D), a positive regulator of cell cycle progression [28], normal levels of PRL in non-pregnant rodents might be essential for promoting the chondrocyte cell division, although its effect was not large enough to be detected by BrdU assay. In breast cancer cells, PRL has recently been reported to stimulate cyclin D1 promoter, thereby increasing cell proliferation [29].

Besides cell proliferation, 10 ng/mL PRL appeared to enhance chondrogenic differentiation by upregulating the mRNA expression of Sox9 (Fig. 3B), an essential transcription factor in chondrocyte lineage determination and differentiation [2]. Once ATDC5 cells became differentiated and formed a 3D micromass, they produced extracellular matrix molecules, e.g., aggrecan, chondroitin sulfate, Hspg2, and collagens (particularly Col10), similar to the hypertro-

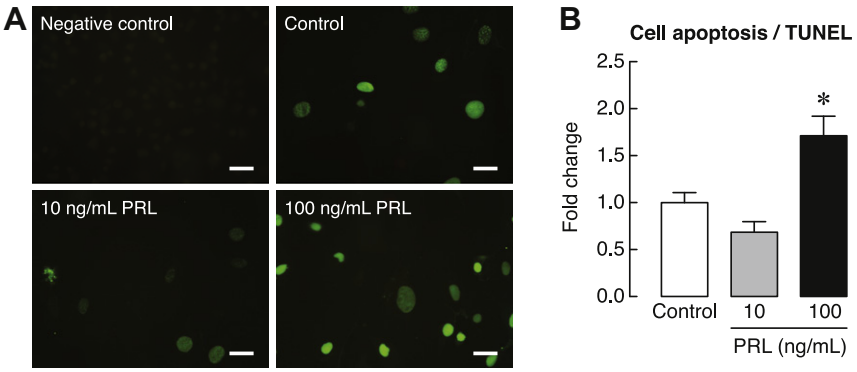

Fig. 4. (A) Representative fluorescent photomicrographs of apoptotic chondrocytes (green) as determined by TUNEL staining technique (magnification 200×). ATDC5 cells were incubated with 10 or 100 ng/mL PRL for 24 h. The negative control was performed in the absence of TUNEL. Scale bars, 200 μm. (B) Chondrocyte apoptosis after exposure for 24 h to 10 or 100 ng/mL PRL ($n = 3$ per group). Number of apoptotic cells in the control group was normalized to 1. All experiments were performed in quadruplicate. $^{*}p < 0.05$ compared with the corresponding control group (open bar). (For interpretation of the references to colour in this figure legend, the reader is referred to the web version of this article.)

phic chondrocytes in the growth plate [30,31]. Some extracellular matrix molecules, such as Hspg2, are essential for development of the cartilaginous framework during the embryonic and postnatal period [32]. In the present study, differentiated chondrocytes in a 3D micromass responded to 10 ng/mL PRL by increasing Hspg2 mRNA expression and proteoglycan accumulation, consistent to that observed in differentiated chondrocytes from human mesenchymal stem cells [5]. Differentiated chondrocytes, especially hypertrophic chondrocytes in the growth plate, also strongly expressed ALP, an enzyme essential for mineral deposition [33]. Thus, the upregulation of ALP by 10 ng/mL PRL not only indicated the PRL-induced chondrogenic differentiation, but also suggested that normal levels of PRL are essential for endochondral ossification and perhaps bone elongation in non-pregnant mammals.

In conclusion, the present study demonstrated the dose-specific chondroregulatory effect of PRL on chondrocyte proliferation and differentiation, which could explain the mechanism of the PRL-induced bone elongation in lactating rats, as well as a possible role of PRL in the regulation of chondrogenesis in male and non-pregnant female mammals. We found that high PRL concentrations ($\geqslant$100 ng/mL as in pregnancy and lactation) markedly decreased chondrocyte viability, proliferation and proteoglycan accumulation, and induced chondrocyte apoptosis, all of which are sequential processes leading to endochondral bone growth. These findings are also consistent with the PRL-induced decreases in the total growth plate height and hypertrophic zone height in the tibiae of lactating rats [3]. Furthermore, the different responses of chondrocytes to 10 ng/mL PRL, e.g., increases in chondrocyte viability, proteoglycan accumulation, and differentiation marker expression, suggested that basal circulating levels of PRL are also required for normal chondrogenesis in young growing mammals.

5. Conflict of interest

The authors declare no conflicts of interest.

Acknowledgments

We thank Jirawan Thongbunchoo for excellent technical assistance. This work was supported by grants from the Discovery-based Development Grant, National Science and Technology Development Agency (P-10-11281 to N. Charoenphandhu), the Mahidol University research grant of fiscal year 2012 (to N. Charoenphandhu), and the Faculty of Science, Mahidol University (to N. Charoenphandhu). D. Seriwatanachai is a postdoctoral fellow under supervision of N. Charoenphandhu.

References

[1] G. Karsenty, E.F. Wagner, Reaching a genetic and molecular understanding of skeletal development, Dev. Cell 2 (2002) 389–406.
[2] H.M. Kronenberg, Developmental regulation of the growth plate, Nature 423 (2003) 332–336.
[3] P. Suntornsaratoon, K. Wongdee, N. Krishnamra, N. Charoenphandhu, Possible chondroregulatory role of prolactin on the tibial growth plate of lactating rats, Histochem. Cell Biol. 134 (2010) 483–491.
[4] P. Clément-Lacroix, C. Ormandy, L. Lepescheux, P. Ammann, D. Damotte, V. Goffin, B. Bouchard, M. Amling, M. Gaillard-Kelly, N. Binart, R. Baron, P.A. Kelly, Osteoblasts are a new target for prolactin: analysis of bone formation in prolactin receptor knockout mice, Endocrinology 140 (1999) 96–105.
[5] S. Ogueta, J. Muñoz, E. Obregon, E. Delgado-Baeza, J.P. García-Ruiz, Prolactin is a component of the human synovial liquid and modulates the growth and chondrogenic differentiation of bone marrow-derived mesenchymal stem cells, Mol. Cell. Endocrinol. 190 (2002) 51–63.
[6] N. Charoenphandhu, K. Wongdee, N. Krishnamra, Is prolactin the cardinal calciotropic maternal hormone?, Trends Endocrinol Metab. 21 (2010) 395–401.
[7] N. Charoenphandhu, L.I. Nakkrasae, K. Kraidith, J. Teerapornpuntakit, K. Thongchote, N. Thongon, N. Krishnamra, Two-step stimulation of intestinal Ca^{2+} absorption during lactation by long-term prolactin exposure and suckling-induced prolactin surge, Am. J. Physiol. Endocrinol. Metab. 297 (2009) E609–E619.
[8] D. Seriwatanachai, K. Thongchote, N. Charoenphandhu, J. Pandaranandaka, K. Tudpor, J. Teerapornpuntakit, T. Suthiphongchai, N. Krishnamra, Prolactin directly enhances bone turnover by raising osteoblast-expressed receptor activator of nuclear factor κB ligand/osteoprotegerin ratio, Bone 42 (2008) 535–546.
[9] N. Krishnamra, J. Seemoung, Effects of acute and long-term administration of prolactin on bone ^{45}Ca uptake, calcium deposit and calcium resorption in weaned young and mature rats, Can. J. Physiol. Pharmacol. 74 (1996) 1157–1165.
[10] P. Suntornsaratoon, K. Wongdee, S. Goswami, N. Krishnamra, N. Charoenphandhu, Bone modeling in bromocriptine-treated pregnant and lactating rats: possible osteoregulatory role of prolactin in lactation, Am. J. Physiol. Endocrinol. Metab. 299 (2010) E426–E436.
[11] W. Jantarajit, N. Thongon, J. Pandaranandaka, J. Teerapornpuntakit, N. Krishnamra, N. Charoenphandhu, Prolactin-stimulated transepithelial calcium transport in duodenum and Caco-2 monolayer are mediated by the phosphoinositide 3-kinase pathway, Am. J. Physiol. Endocrinol. Metab. 293 (2007) E372–E384.
[12] P.R. Manna, T. El-Hefnawy, J. Kero, I.T. Huhtaniemi, Biphasic action of prolactin in the regulation of murine Leydig tumor cell functions, Endocrinology 142 (2001) 308–318.
[13] C.G. James, C.T. Appleton, V. Ulici, T.M. Underhill, F. Beier, Microarray analyses of gene expression during chondrocyte differentiation identifies novel regulators of hypertrophy, Mol. Biol. Cell 16 (2005) 5316–5333.
[14] C. Shukunami, C. Shigeno, T. Atsumi, K. Ishizeki, F. Suzuki, Y. Hiraki, Chondrogenic differentiation of clonal mouse embryonic cell line ATDC5 in vitro: differentiation-dependent gene expression of parathyroid hormone (PTH)/PTH-related peptide receptor, J. Cell Biol. 133 (1996) 457–468.
[15] T. Mosmann, Rapid colorimetric assay for cellular growth and survival: application to proliferation and cytotoxicity assays, J. Immunol. Methods 65 (1983) 55–63.
[16] D. Seriwatanachai, N. Krishnamra, J.P. van Leeuwen, Evidence for direct effects of prolactin on human osteoblasts: inhibition of cell growth and mineralization, J. Cell. Biochem. 107 (2009) 677–685.

[17] P. Hwang, H. Guyda, H. Friesen, A radioimmunoassay for human prolactin, Proc. Natl. Acad. Sci. USA 68 (1971) 1902–1906.
[18] Y.F. Smith, D.K. Mullon, M. Hamosh, J.W. Scanlon, P. Hamosh, Serum prolactin and respiratory distress syndrome in the newborn, Pediat. Res. 14 (1979) 93–95.
[19] S.J. Tzeng, D.I. Linzer, Prolactin receptor expression in the developing mouse embryo, Mol. Reprod. Dev. 48 (1997) 45–52.
[20] D. Coss, L. Yang, C.B. Kuo, X. Xu, R.A. Luben, A.M. Walker, Effects of prolactin on osteoblast alkaline phosphatase and bone formation in the developing rat, Am. J. Physiol. Endocrinol. Metab. 279 (2000) E1216–E1225.
[21] N. Charoenphandhu, K. Wongdee, J. Teerapornpuntakit, K. Thongchote, N. Krishnamra, Transcriptome responses of duodenal epithelial cells to prolactin in pituitary-grafted rats, Mol. Cell. Endocrinol. 296 (2008) 41–52.
[22] E.J. Mackie, Y.A. Ahmed, L. Tatarczuch, K.S. Chen, M. Mirams, Endochondral ossification: how cartilage is converted into bone in the developing skeleton, Int. J. Biochem. Cell Biol. 40 (2008) 46–62.
[23] M.Z. Mughal, Rickets, Curr. Osteoporos. Rep. 9 (2011) 291–299.
[24] L.S. Jacobs, I.K. Mariz, W.H. Daughaday, A mixed heterologous radioimmunoassay for human prolactin, J. Clin. Endocrinol. Metab. 34 (1972) 484–490.
[25] N. Bliesener, S. Albrecht, A. Schwager, K. Weckbecker, D. Lichtermann, D. Klingmuller, Plasma testosterone and sexual function in men receiving buprenorphine maintenance for opioid dependence, J. Clin. Endocrinol. Metab. 90 (2005) 203–206.
[26] C. Zermeño, J. Guzmán-Morales, Y. Macotela, G. Nava, F. López-Barrera, J.B. Kouri, C. Lavalle, G.M. de la Escalera, C. Clapp, Prolactin inhibits the apoptosis of chondrocytes induced by serum starvation, J. Endocrinol. 189 (2006) R1–R8.
[27] A.M. Bhosale, J.B. Richardson, Articular cartilage: structure injuries and review of management, Br. Med. Bull. 87 (2008) 77–95.
[28] G.F. Draetta, Mammalian G1 cyclins, Curr. Opin. Cell Biol. 6 (1994) 842–846.
[29] J. Tao, P. Oladimeji, L. Rider, M. Diakonova, PAK1-Nck regulates cyclin D1 promoter activity in response to prolactin, Mol. Endocrinol. 25 (2011) 1565–1578.
[30] F. Burdan, J. Szumiło, A. Korobowicz, R. Farooquee, S. Patel, A. Patel, A. Dave, M. Szumiło, M. Solecki, R. Klepacz, J. Dudka, Morphology and physiology of the epiphyseal growth plate, Folia Histochem. Cytobiol. 47 (2009) 5–16.
[31] S.M. Smith, C. Shu, J. Melrose, Comparative immunolocalisation of perlecan with collagen II and aggrecan in human foetal, newborn and adult ovine joint tissues demonstrates perlecan as an early developmental chondrogenic marker, Histochem. Cell Biol. 134 (2010) 251–263.
[32] E. Arikawa-Hirasawa, H. Watanabe, H. Takami, J.R. Hassell, Y. Yamada, Perlecan is essential for cartilage and cephalic development, Nat. Genet. 23 (1999) 354–358.
[33] Y. Ishikawa, W.B. Valhmu, R.E. Wuthier, Induction of alkaline phosphatase in primary cultures of epiphyseal growth plate chondrocytes by a serum-derived factor, J. Cell Physiol. 133 (1987) 344–350.

Biochemical and Biophysical Research Communications 420 (2012) 114–118

Contents lists available at SciVerse ScienceDirect

Biochemical and Biophysical Research Communications

journal homepage: www.elsevier.com/locate/ybbrc

Th2-inducing cytokines IL-4 and IL-33 synergistically elicit the expression of transmembrane TNF-α on macrophages through the autocrine action of IL-6

Hiromi Ogawa [a,1], Kaori Mukai [a,1,2], Yohei Kawano [a], Yoshiyuki Minegishi [a,b], Hajime Karasuyama [a,b,*]

[a] Department of Immune Regulation, Tokyo Medical and Dental University Graduate School, 1-5-45 Yushima, Bunkyo-ku, Tokyo 113-8519, Japan
[b] JST, CREST, Tokyo Medical and Dental University Graduate School, 1-5-45 Yushima, Bunkyo-ku, Tokyo 113-8519, Japan

ARTICLE INFO

Article history:
Received 21 February 2012
Available online 3 March 2012

Keywords:
Macrophage
TNF-α
IL-4
IL-6
IL-33
Inflammation

ABSTRACT

Tumor necrosis factor-α (TNF-α) is a potent proinflammatory cytokine produced predominantly by activated macrophages, and plays a central role in the protective immunity against intracellular pathogens and the pathogenesis of autoimmune and inflammatory diseases. While both the soluble and transmembrane forms of TNF-α (sTNF-α and tmTNF-α) are biologically functional, the latter but not the former acts as a receptor besides as a ligand, and transmit a retrograde signal in a cell-to-cell contact manner. The production of TNF-α by macrophages under Th2-type (allergic) inflammatory conditions has been ill defined, compared to that under Th1-type inflammatory conditions. Here we examined the effect of representative Th2-inducing cytokines IL-4 and IL-33 on the TNF-α expression in macrophages. IL-4 induced the production of neither sTNF-α nor tmTNF-α while IL-33 promoted the production of sTNF-α with no detectable tmTNF-α. Notably, the combination of IL-4 and IL-33 elicited the tmTNF-α expression on macrophages, in addition to the enhanced production of sTNF-α and IL-6. The IL-4/IL-33-elicited tmTNF-α expression was not observed in IL-6-deficient macrophages, suggesting the involvement of macrophage-derived IL-6 in the tmTNF-α expression. Indeed, the stimulation of macrophages with the combination of IL-4 and IL-6 induced the tmTNF-α expression with no detectable production of sTNF-α. Thus, IL-4 and IL-33 synergistically elicit the tmTNF-α expression on macrophages through the autocrine action of IL-6.

1. Introduction

TNF-α, one of the most abundant early mediators in inflamed tissues, is produced by many different types of cells, particularly macrophages [1,2]. TNF-α shows pleiotropic effects on various cell lineages and play crucial roles in the host defense against intracellular pathogens [3,4] and the pathogenesis of autoimmune and inflammatory disorders [5,6]. Indeed, several anti-TNF-α agents have been successfully introduced for treating rheumatoid arthritis and inflammatory bowel diseases such as Crohn's disease [5,6]. TNF-α is first generated as a type II transmembrane polypeptide (tmTNF-α) that is in turn processed by TNF-α-converting enzyme (TACE, also known as ADAM17) on the cell surface to release sTNF-α [7,8]. sTNF-α exerts its biological function through binding to two types of receptors (TNFR1 and TNFR2) expressed on targets cells [9]. Of note, it has been shown that tmTNF-α, in addition to sTNF-α, is involved in cytotoxicity and inflammatory responses, in a cell-to-cell contact manner [10–13]. tmTNF-α acts as a ligand by binding to TNF receptors on target cells as does sTNF-α. Moreover, tmTNF-α, in contrast to sTNF-α, functions as a receptor that transmits outside-to-inside (reverse) signals back into the tmTNF-α-expressing cells [14]. Although both sTNF-α and tmTNF-α can bind to TNFR1 and TNFR2, TNFR2, that is typically expressed by immune cells, can be fully activated only by tmTNF-α and not by sTNF-α [15]. Thus, tmTNF-α shows activities that are distinct from as well as overlapping with those displayed by sTNF-α [16].

Macrophages are distributed throughout many different tissues and organs, and play a central role in homeostasis, host defense, inflammatory reactions, and tissue remodeling [17]. They are heterogeneous in their phenotype and function, and can be polarized to various distinct subsets, depending on the microenvironment [17,18]. Polarized macrophages have been broadly classified as M1 or M2 macrophages. M1 macrophages are induced by microbial products such as lipopolysaccharide (LPS) and IFN-γ during Th1-type responses, and function as effector cells against microorganisms and tumor cells. M2 macrophages, in contrast,

Abbreviations: TNF-α, tumor necrosis factor-α; tmTNF-α, transmembrane TNF-α; sTNF-α, soluble TNF-α; TACE, TNF-α-converting enzyme; LPS, lipopolysaccharide; WT, wild-type.

* Corresponding author at: Department of Immune Regulation, Tokyo Medical and Dental University Graduate School, 1-5-45 Yushima, Bunkyo-ku, Tokyo 113-8519, Japan. Fax: +81 3 3814 7172.
E-mail address: karasuyama.mbch@tmd.ac.jp (H. Karasuyama).

[1] These authors contributed equally to this work.
[2] Current address: Department of Pathology, Stanford University School of Medicine, Stanford, CA, United States.

0006-291X/$ - see front matter © 2012 Elsevier Inc. All rights reserved.
doi:10.1016/j.bbrc.2012.02.124

are typically induced by Th2 cytokines such as IL-4 during Th2-type responses, including allergic reactions and parasitic infections [19,20]. IL-33, a recently-identified member of the IL-1 family of cytokines, has been shown to amplify the M2 polarization of macrophages, and promote the production of Th2 cytokines such as IL-4, IL-5 and IL-13 by innate-type lymphoid cells, basophils, mast cells, and Th2 cells [21–24].

The production of TNF-α by macrophages under Th2-type inflammatory conditions has been ill defined, compared to that under Th1-type inflammatory conditions. Therefore, in the present study, we examined the expression of tmTNF-α and sTNF-α by macrophages that were stimulated with Th2-inducing cytokines, IL-4 and IL-33, either alone or in combination. Whereas IL-4-stimulated macrophages, a prototype of M2 macrophages, produced no detectable TNF-α, regardless of a transmembrane or soluble form, the combinatorial stimulation of macrophages with IL-4 and IL-33 induced the tmTNF-α expression on the cell surface, even though IL-33 alone failed to do so. The IL-4/IL-33-elicited tmTNF-α expression turned out to be dependent on a proinflammatory cytokine IL-6 produced by macrophages, in contrast to the LPS-elicited tmTNF-α expression. Thus, Th2-inducing cytokines IL-4 and IL-33 synergistically elicit the tmTNF-α expression on macrophages through the autocrine action of IL-6.

2. Materials and methods

2.1. Mice

BALB/c and C57BL/6 mice (6–10 week old) were purchased from CLEA Japan (Tokyo, Japan). *Il6*$^{-/-}$ mice [25] were maintained in our animal facilities under specific pathogen-free conditions. All animal experiments were performed according to the guidelines of the Institutional Animal Care and Use Committees of the Tokyo Medical and Dental University. The protocols for animal experiments were approved by the Institutional Animal Care and Use Committees of the Tokyo Medical and Dental University.

2.2. Antibodies

FITC-conjugated anti-mouse F4/80 (BM8), anti-CD11b (M1/70) and control rat IgG1 and IgG2a, biotinylated control rat IgG1 and IgG2a were purchased from eBioscience (San Diego, CA). PE-conjugated anti-mouse F4/80 (BM8), Pacific Blue™ anti-mouse CD11b (M1/70), biotinylated anti-mouse TNF-α (MP6-XT22), APC-conjugated streptavidin were from BioLegend (San Diego, CA). Anti-CD16/32 (2.4G2) was prepared from hybridoma culture supernatants in our laboratory.

2.3. Preparation and stimulation of macrophages

Cells were harvested from the peritoneal cavity 4 days after mice were injected i.p. with 1.5 ml of 3% thioglycolate broth (BD Diagnostic Systems), and cultured at 37 °C for 2 h in RPMI 1640 containing 10% FCS, 2 mM L-glutamine, 1 mM sodium pyruvate, 100 μM nonessential amino acids, 0.05 M 2-ME, 100 U/ml penicillin, and 100 μg/ml streptomycin. Adherent cells (as peritoneal macrophages, 1×10^6 cells/1 ml/well) were stimulated with IL-4 (50 ng/ml, R&D), IL-6 (50 ng/ml, Peprotech), IL-33 (50 ng/ml, R&D), or LPS *Escherichia coli* 055:B5 (100 ng/ml, Sigma–Aldrich) individually or in combination for the indicated time periods.

2.4. Flow cytometric analysis

Cells were preincubated with anti-CD16/32 mAb and normal rat serum on ice for 15 min prior to incubation with the indicated combination of Abs in order to prevent the non-specific binding of irrelevant Abs. Stained cells were analyzed on a FACSCanto II machine (BD) using FACSDiva software (BD). Macrophages were identified as F4/80$^+$CD11b$^+$ cells.

2.5. Evaluation of cytokine production

The concentration of TNF-α and IL-6 in culture supernatants was determined by ELISA using Ready-SET-Go! (eBioscience) and Mouse IL-6 ELISA MAX™ Standard (BioLegend), respectively, according to the manufacturer's instructions.

2.6. Statistical analysis

Data were analyzed by unpaired Student *t* test to determine the difference between the samples. $P < 0.05$ was considered as significant.

3. Results

3.1. IL-4 and IL-33 synergistically induce the tmTNF-α expression on macrophages

Peritoneal macrophages isolated from BALB/c mice were stimulated with representative Th2-inducing cytokines, IL-4 and IL-33, either individually or in combination (Fig. 1). Neither IL-4 nor IL-33 alone induced any significant expression of tmTNF-α on macrophages during the 48 h culture. In contrast, the surface expression of tmTNF-α became detected 24 h and 48 h after the stimulation of macrophages with the combination of IL-4 and IL-33. LPS stimulation is well known to induce the TNF-α production. However, the LPS-elicited tmTNF-α expression on the cell surface was confined to the early phase (2–6 h) of the culture, and became undetectable at the late phase (24 h and 48 h) (Fig. 1). Thus, the tmTNF-α expression on macrophages can be induced even under Th2 conditions if both IL-4 and IL-33 coexist, although the timing of the tmTNF-α expression is much delayed compared to that observed in LPS-stimulated macrophages. The similar pattern of tmTNF-α expression was observed in macrophages isolated from C57BL/6 mice (as shown later in Fig. 3), even though they had a tendency to show lower levels of tmTNF-α expression compared to BALB/c macrophages.

IL-4 alone induced little or no production of sTNF-α in macrophages while IL-33 alone was sufficient for inducing the sTNF-α production (Fig. 2A). Notably, the combination of IL-4 and IL-33 stimulation significantly augmented the sTNF-α production compared to the stimulation with IL-33 alone (Fig. 2A). This was also true for the IL-6 production by macrophages, and the combination of IL-4 and IL-33 stimulation promoted the IL-6 production to the extent comparable to that induced by the LPS stimulation (Fig. 2B).

3.2. The IL-4/IL-33-elicited production of tmTNF-α but not sTNF-α is abolished in IL-6-deficient macrophages

To examine the possible influence of macrophage-derived IL-6 on the TNF-α production by macrophages, we compared the production of sTNF-α and tmTNF-α between macrophages derived from wild-type mice and those from IL-6-deficient mice, when stimulated with either LPS or IL-4 plus IL-33 (Fig. 3). Because the IL-6-deficient mice we obtained have the C57BL/6-type genetic background, C57BL/6 instead of BALB/c mice were used as wild-type control mice in this experiment. No significant difference in the sTNF-α production was observed between wild-type and IL-6-deficient macrophages when stimulated with the combination of IL4 and IL-33 (Fig. 3A). Intriguingly, however, the IL-4/IL-33-elic-

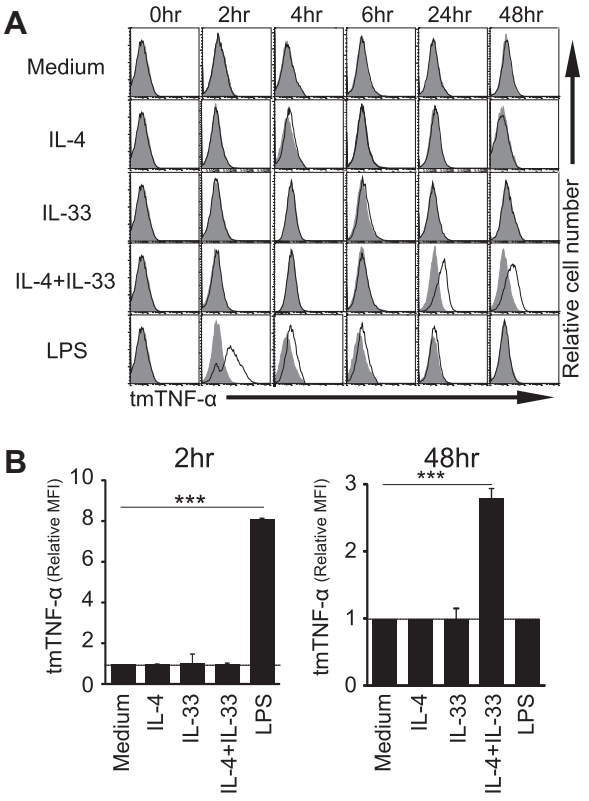

Fig. 1. IL-4 and IL-33 synergistically induce the tmTNF-α expression on macrophages. (A) Peritoneal macrophages isolated from BALB/c mice were cultured with either control medium, IL-4, IL-33 or LPS alone or in combination for the indicated time periods. Data shown are representative of the surface expression of tmTNF-α (open histograms) compared with control staining with an isotype-matched control antibody (filled histograms) at each time point. (B) The level of the tmTNF-α expression on macrophages that were stimulated as in A for 2 h (left panel) or 48 h (right panel) is shown as the relative mean fluorescence intensity (MFI), that is, the MFI of staining with the anti-TNF-α antibody/the MFI of control staining with the isotype-matched control antibody, in which 1 stands for no tmTNF-α expression. The mean ± SEM, $n = 5$ (2 h) and $n = 3$ (48 h). $^{***}P < 0.001$. Data shown in A and B are representative of five independent experiments.

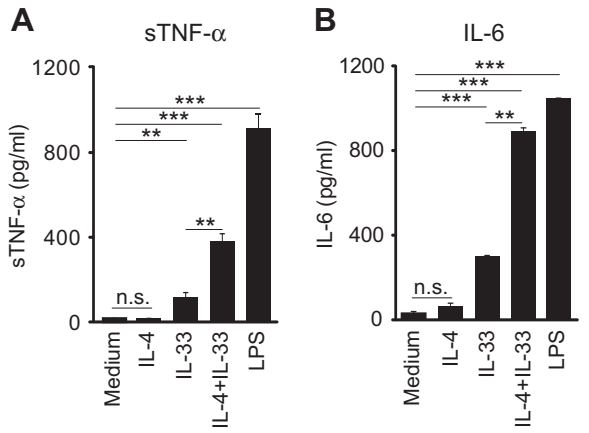

Fig. 2. IL-4 augments the production of sTNF-α and IL-6 by IL-33-stimulated macrophages. Peritoneal macrophages from BALB/c mice were cultured as in Fig. 1 for 48 h, and their culture supernatants were assayed for the production of sTNF-α (A) and IL-6 (B). Data shown are the mean ± SEM ($n = 4$ each) and representative of five independent experiments. $^{**}P < 0.01$; $^{***}P < 0.001$; n.s., not significant.

ited tmTNF-α expression (after the 48 h stimulation) was almost completely abolished in IL-6-deficient macrophages while the LPS-elicited tmTNF-α expression (after 2 h stimulation) remained intact even in the absence of IL-6 (Fig. 3B and C). This observation suggested that IL-6 is critically involved in the tmTNF-α expression induced by the stimulation with the IL-4 and IL-33 combination but not with LPS.

3.3. IL-4 and IL-6 cooperatively induce the tmTNF-α expression with no detectable sTNF-α production

The stimulation of macrophages with IL-6 alone induced little or no production of tmTNF-α (Fig. 4A and B) or sTNF-α (Fig. 4C) as did the IL-4 stimulation. In contrast, the combination of IL-4 and IL-6 stimulation elicited the tmTNF-α expression on macrophages at the late phase (24–48 h) but not early phase (2–6 h) of culture (Fig. 4A and B) as did the IL-4/IL-33 stimulation. Of note, no significant production of sTNF-α was detected in the IL-4/IL-6-stimulated macrophages (Fig. 4C) unlike in the IL-4/IL-33-stimulated ones (Fig. 2A). Thus, IL-4 and IL-6 cooperatively induced the production of tmTNF-α but not sTNF-α. The combination of IL-6 and IL-33 failed to induce the tmTNF-α expression (data not shown). These results suggested that the IL-4/IL-33-elicited tmTNF-α is mediated by the autocrine action of macrophage-derived IL-6 in combination with IL-4.

4. Discussion

M2 macrophages have been shown to produce little or no pro-inflammatory cytokines, including TNF-α, in contrast to M1 macrophages [19,20]. However, this may not reflect what happens *in vivo* under Th2-type inflammatory conditions such as allergic responses, because macrophages could be stimulated *in vivo* with typical Th2 cytokines, such as IL-4, in combination with other cytokines present in the microenvironment. Th2 cells, mast cells, and basophils are important players in Th2-type (allergic responses, and can produce an array of cytokines, including IL-4 and IL-6, upon activation [26–28]. In the present study, we demonstrated for the first time, to our knowledge, that IL-4 and IL-6 in combination but not individually elicit the tmTNF-α expression on macrophages with no detectable production of sTNF-α. This suggests that M2 macrophages differentiated under Th2-type inflammatory conditions can exert their function through tmTNF-α expressed on their surface.

The mechanism underlying the synergistic effect of IL-4 and IL-6 on the expression of tmTNF-α remains to be determined. Peritoneal macrophages used in the present study express IL-4 receptor (IL-4R) on their surface even without addition of exogenous cytokines, and the IL-6 stimulation showed little or no effect on the level of *Il4rα* mRNA or surface IL-4Rα expression (data not shown). Therefore, the synergy of IL-4 and IL-6 does not seem to be attributed to the IL-6-mediated induction or up-regulation of IL-4R on macrophages. The IL-4/IL-6-stimulated macrophages express tmTNF-α and produce no detectable sTNF-α. This phenotype is similar to that observed in iRhom2-deficient macrophages when stimulated with LPS [29,30]. iRhom2 is a member of the rhomboid family, and its expression is induced by LPS stimulation. iRhom2 promotes the intracellular trafficking and activation of TACE, leading to the conversion of tmTNF-α to sTNF-α [29,30]. Further studies are needed to clarify the mechanism by which IL-4 and IL-6 regulate the production and processing of TNF-α, including the involvement of iRhom2.

IL-33 has been recognized as one of the key cytokines enhancing Th2-type immune responses [21–24]. It amplifies the M2 polarization of macrophages, and promotes the production of Th2 cytokines such as IL-4, IL-5 and IL-13 by innate-type lymphoid cells, basophils, mast cells, and Th2 cells. Pretreatment of macrophages with IL-33 has been shown to enhance the LPS-induced

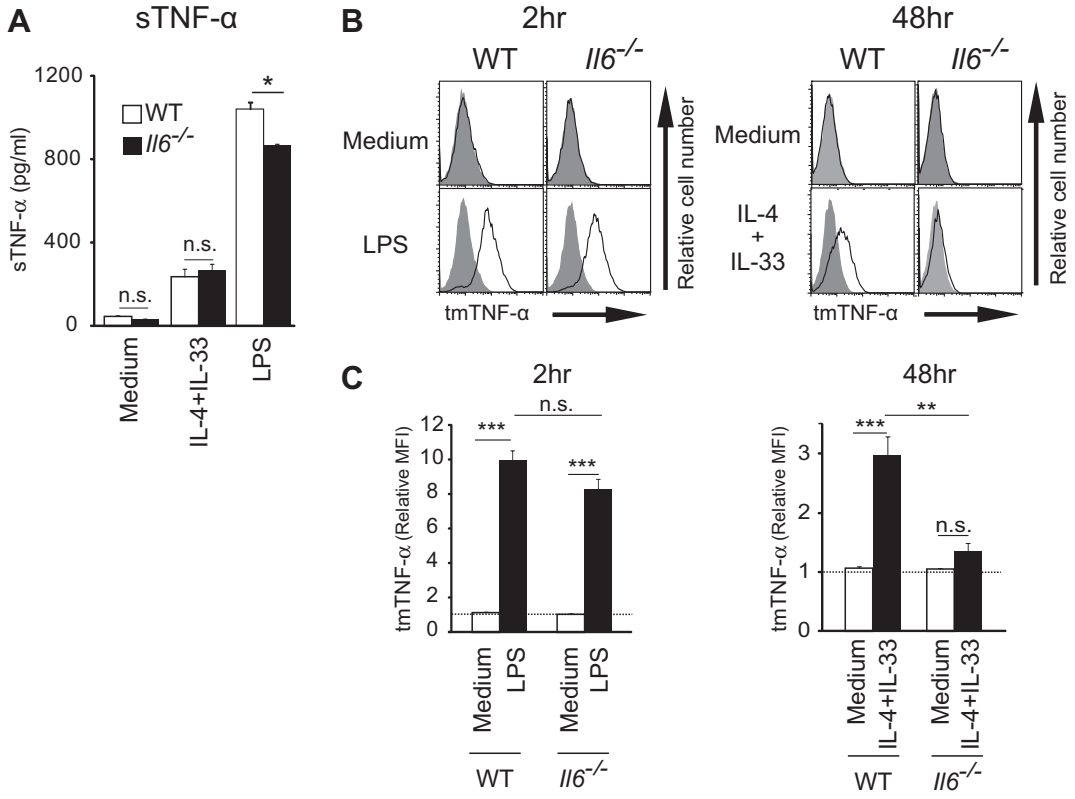

Fig. 3. The IL-4/IL-33-elicited production of tmTNF-α but not sTNF-α is abolished in IL-6-deficient macrophages. Peritoneal macrophages isolated from wild-type (WT) or *Il6*$^{-/-}$ C57BL/6 mice were stimulated with either LPS or IL-4 plus IL-33. (A) The sTNF-α production by WT (open bars) and *Il6*$^{-/-}$ (filled bars) macrophages during the 48 h-culture is shown (the mean ± SEM, $n = 3$ each). (B and C) Representative data of the tmTNF-α expression on macrophages stimulated with LPS for 2 h and those stimulated with IL-4 plus IL-33 for 48 h are shown in B, and all the data are summarized in C (displayed as in Fig. 1B, the mean ± SEM, $n = 3$ each). Data shown in A–C are representative of at least three independent experiments. $^{*}P < 0.05$; $^{**}P < 0.01$; $^{***}P < 0.001$; n.s., not significant.

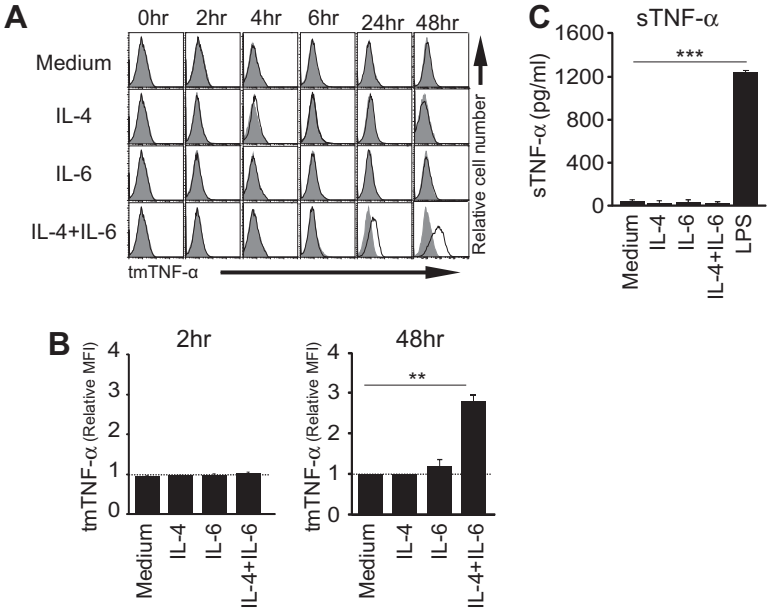

Fig. 4. IL-4 and IL-6 cooperatively induce the tmTNF-α expression with no detectable sTNF-α production. (A) Peritoneal macrophages from BALB/c mice were cultured with either control medium, IL-4, IL-6 or LPS alone or in combination for the indicated time periods. Data shown are representative of the surface expression of tmTNF-α (open histograms) compared with control staining with an isotype-matched control antibody (filled histograms) at each time point. (B) The level of the tmTNF-α expression on macrophages that were stimulated as in A for 2 h (left panel) or 48 h (right panel) is displayed as in Fig. 1B. The mean ± SEM, $n = 5$ (2 h) and $n = 3$ (48 h). (C) The sTNF-α production by macrophages during the 48 h-culture is shown (the mean ± SEM, $n = 3$ each). Data shown in A–C are representative of three independent experiments. $^{**}P < 0.01$; $^{***}P < 0.001$.

sTNF-α production by macrophages [31]. We found in the present study that while IL-4-elicited M2 macrophages produced little or no sTNF-α or IL-6, the combination of IL-4 and IL-33 stimulation significantly enhanced the production of sTNF-α and IL-6 above the level of production by IL-33-stimulated macrophages. This might be explained by the fact that Th2 cytokines enhance the

expression of an IL-33 receptor, ST2 [21]. Notably, IL-4 and IL-33 in combination, but not individually, induced the tmTNF-α expression on macrophages in an IL-6-dependent manner. Given that IL-4 and IL-6 synergistically induce the tmTNF-α expression, IL-6 produced by IL-4/IL-33-stimulated macrophages appears to act on macrophages, in combination with IL-4, leading to the tmTNF-α expression. Thus, Th2-inducing cytokines IL-4 and IL-33 can synergistically elicit the tmTNF-α expression on macrophages through the autocrine action of IL-6.

Taken together, the present study underscores the need for considering possible involvement of both tmTNF-α and sTNF-α even in Th2-type inflammatory responses, in addition to Th1-type responses, although it remains to be clarified whether they exert pro-inflammatory or anti-inflammatory functions under Th2 conditions.

Acknowledgments

This work was supported by research grants from JST, CREST, the Japanese Ministry of Education, Culture, Sports, Science and Technology, Takeda Science Foundation, the Mitsubishi Foundation, the Naito Foundation, and the Uehara Memorial Foundation.

References

[1] B. Beutler, A. Cerami, The biology of cachectin/TNF—a primary mediator of the host response, Annu. Rev. Immunol. 7 (1989) 625–655.
[2] P. Vassalli, The pathophysiology of tumor necrosis factors, Annu. Rev. Immunol. 10 (1992) 411–452.
[3] K. Pfeffer, T. Matsuyama, T.M. Kündig, A. Wakeham, K. Kishihara, A. Shahinian, K. Wiegmann, P.S. Ohashi, M. Krönke, T.W. Mak, Mice deficient for the 55 kd tumor necrosis factor receptor are resistant to endotoxic shock, yet succumb to *L. monocytogenes* infection, Cell 73 (1993) 457–467.
[4] J.L. Flynn, M.M. Goldstein, J. Chan, K.J. Triebold, K. Pfeffer, C.J. Lowenstein, R. Schreiber, T.W. Mak, B.R. Bloom, Tumor necrosis factor-alpha is required in the protective immune response against *Mycobacterium tuberculosis* in mice, Immunity 2 (1995) 561–572.
[5] M. Feldmann, Development of anti-TNF therapy for rheumatoid arthritis, Nat. Rev. Immunol. 2 (2002) 364–371.
[6] B.E. Sands, F.H. Anderson, C.N. Bernstein, W.Y. Chey, B.G. Feagan, R.N. Fedorak, M.A. Kamm, J.R. Korzenik, B.A. Lashner, J.E. Onken, D. Rachmilewitz, P. Rutgeerts, G. Wild, D.C. Wolf, P.A. Marsters, S.B. Travers, M.A. Blank, S.J. van Deventer, Infliximab maintenance therapy for fistulizing Crohn's disease, N. Engl. J. Med. 350 (2004) 876–885.
[7] R.A. Black, C.T. Rauch, C.J. Kozlosky, J.J. Peschon, J.L. Slack, M.F. Wolfson, B.J. Castner, K.L. Stocking, P. Reddy, S. Srinivasan, N. Nelson, N. Boiani, K.A. Schooley, M. Gerhart, R. Davis, J.N. Fitzner, R.S. Johnson, R.J. Paxton, C.J. March, D.P. Cerretti, A metalloproteinase disintegrin that releases tumour-necrosis factor-alpha from cells, Nature 385 (1997) 729–733.
[8] M.L. Moss, S.L. Jin, M.E. Milla, D.M. Bickett, W. Burkhart, H.L. Carter, W.J. Chen, W.C. Clay, J.R. Didsbury, D. Hassler, C.R. Hoffman, T.A. Kost, M.H. Lambert, M.A. Leesnitzer, P. McCauley, G. McGeehan, J. Mitchell, M. Moyer, G. Pahel, W. Rocque, L.K. Overton, F. Schoenen, T. Seaton, J.L. Su, J.D. Becherer, Cloning of a disintegrin metalloproteinase that processes precursor tumour-necrosis factor-alpha, Nature 385 (1997) 733–736.
[9] P. Vandenabeele, W. Declercq, R. Beyaert, W. Fiers, Two tumour necrosis factor receptors: structure and function, Trends Cell Biol. 5 (1995) 392–399.
[10] M. Kriegler, C. Perez, K. DeFay, I. Albert, S.D. Lu, A novel form of TNF/cachectin is a cell surface cytotoxic transmembrane protein: ramifications for the complex physiology of TNF, Cell 53 (1988) 45–53.
[11] C. Perez, I. Albert, K. DeFay, N. Zachariades, L. Gooding, M. Kriegler, A nonsecretable cell surface mutant of tumor necrosis factor (TNF) kills by cell-to-cell contact, Cell 63 (1990) 251–258.
[12] S.R. Ruuls, R.M. Hoek, V.N. Ngo, T. McNeil, L.A. Lucian, M.J. Janatpour, H. Körner, H. Scheerens, E.M. Hessel, J.G. Cyster, L.M. McEvoy, J.D. Sedgwick, Membrane-bound TNF supports secondary lymphoid organ structure but is subservient to secreted TNF in driving autoimmune inflammation, Immunity 15 (2001) 533–543.
[13] C. Mueller, N. Corazza, S. Trachsel-Løseth, H.P. Eugster, M. Bühler-Jungo, T. Brunner, M.A. Imboden, Noncleavable transmembrane mouse tumor necrosis factor-alpha (TNFalpha) mediates effects distinct from those of wild-type TNFalpha in vitro and in vivo, J. Biol. Chem. 274 (1999) 38112–38118.
[14] G. Eissner, W. Kolch, P. Scheurich, Ligands working as receptors: reverse signaling by members of the TNF superfamily enhance the plasticity of the immune system, Cytokine Growth Factor Rev. 15 (2004) 353–366.
[15] M. Grell, E. Douni, H. Wajant, M. Löhden, M. Clauss, B. Maxeiner, S. Georgopoulos, W. Lesslauer, G. Kollias, K. Pfizenmaier, P. Scheurich, The transmembrane form of tumor necrosis factor is the prime activating ligand of the 80 kDa tumor necrosis factor receptor, Cell 83 (1995) 793–802.
[16] T. Horiuchi, H. Mitoma, S. Harashima, H. Tsukamoto, T. Shimoda, Transmembrane TNF-alpha: structure, function and interaction with anti-TNF agents, Rheumatology (Oxford) 49 (2010) 1215–1228.
[17] P.J. Murray, T.A. Wynn, Protective and pathogenic functions of macrophage subsets, Nat. Rev. Immunol. 11 (2011) 723–737.
[18] S. Gordon, P.R. Taylor, Monocyte and macrophage heterogeneity, Nat. Rev. Immunol. 5 (2005) 953–964.
[19] T. Kreider, R.M. Anthony, J.F. Urban, W.C. Gause, Alternatively activated macrophages in helminth infections, Curr. Opin. Immunol. 19 (2007) 448–453.
[20] F.O. Martinez, L. Helming, S. Gordon, Alternative activation of macrophages: an immunologic functional perspective, Annu. Rev. Immunol. 27 (2009) 451–483.
[21] M. Kurowska-Stolarska, B. Stolarski, P. Kewin, G. Murphy, C.J. Corrigan, S. Ying, N. Pitman, A. Mirchandani, B. Rana, N. van Rooijen, M. Shepherd, C. McSharry, I.B. McInnes, D. Xu, F.Y. Liew, IL-33 amplifies the polarization of alternatively activated macrophages that contribute to airway inflammation, J. Immunol. 183 (2009) 6469–6477.
[22] K. Oboki, T. Ohno, N. Kajiwara, H. Saito, S. Nakae, IL-33 and IL-33 receptors in host defense and diseases, Allergol. Int. 59 (2010) 143–160.
[23] F.Y. Liew, N.I. Pitman, I.B. McInnes, Disease-associated functions of IL-33: the new kid in the IL-1 family, Nat. Rev. Immunol. 10 (2010) 103–110.
[24] J. Schmitz, A. Owyang, E. Oldham, Y. Song, E. Murphy, T.K. McClanahan, G. Zurawski, M. Moshrefi, J. Qin, X. Li, D.M. Gorman, J.F. Bazan, R.A. Kastelein, IL-33, an interleukin-1-like cytokine that signals via the IL-1 receptor-related protein ST2 and induces T helper type 2-associated cytokines, Immunity 23 (2005) 479–490.
[25] M. Kopf, H. Baumann, G. Freer, M. Freudenberg, M. Lamers, T. Kishimoto, R. Zinkernagel, H. Bluethmann, G. Köhler, Impaired immune and acute-phase responses in interleukin-6-deficient mice, Nature 368 (1994) 339–342.
[26] W.E. Paul, J. Zhu, How are T(H)2-type immune responses initiated and amplified?, Nat Rev. Immunol. 10 (2010) 225–235.
[27] S.J. Galli, M. Grimbaldeston, M. Tsai, Immunomodulatory mast cells: negative, as well as positive, regulators of immunity, Nat. Rev. Immunol. 8 (2008) 478–486.
[28] H. Karasuyama, K. Mukai, K. Obata, Y. Tsujimura, T. Wada, Nonredundant roles of basophils in immunity, Annu. Rev. Immunol. 29 (2011) 45–69.
[29] C. Adrain, M. Zettl, Y. Christova, N. Taylor, M. Freeman, Tumor necrosis factor signaling requires iRhom2 to promote trafficking and activation of TACE, Science 335 (2012) 225–228.
[30] D.R. McIlwain, P.A. Lang, T. Maretzky, K. Hamada, K. Ohishi, S.K. Maney, T. Berger, A. Murthy, G. Duncan, H.C. Xu, K.S. Lang, D. Häussinger, A. Wakeham, A. Itie-Youten, R. Khokha, P.S. Ohashi, C.P. Blobel, T.W. Mak, IRhom2 regulation of TACE controls TNF-mediated protection against Listeria and responses to LPS, Science 335 (2012) 229–232.
[31] Q. Espinassous, E. Garcia-de-Paco, I. Garcia-Verdugo, M. Synguelakis, S. von Aulock, J.M. Sallenave, A.N. McKenzie, J. Kanellopoulos, IL-33 enhances lipopolysaccharide-induced inflammatory cytokine production from mouse macrophages by regulating lipopolysaccharide receptor complex, J. Immunol. 183 (2009) 1446–1455.

Biochemical and Biophysical Research Communications 420 (2012) 119–123

Contents lists available at SciVerse ScienceDirect

Biochemical and Biophysical Research Communications

journal homepage: www.elsevier.com/locate/ybbrc

Temperature dependent *N*-glycosylation of plasma membrane heat shock protein Hsp30p in *Saccharomyces cerevisiae*

Ken'ichi Kamo [a,1], Akiko Takabatake [b,1], Yoshiharu Inoue [a], Shingo Izawa [b,*]

[a] *Laboratory of Molecular Microbiology, Graduate School of Agriculture, Kyoto University, Uji, Kyoto 611-0011, Japan*
[b] *Laboratory of Microbial Technology, Graduate School of Science and Technology, Kyoto Institute of Technology, Matsugasaki, Kyoto 606-8585, Japan*

ARTICLE INFO

Article history:
Received 17 February 2012
Available online 1 March 2012

Keywords:
N-glycosylation
Stress response
Heat shock protein
Hsp30p
Saccharomyces cerevisiae

ABSTRACT

The *HSP30* gene of the budding yeast *Saccharomyces cerevisiae* encodes a seven-transmembrane heat shock protein expressed in response to various types of stress including heat shock. Although Hsp30p contains a potential *N*-glycosylation consensus sequence (Asn^2-Asp^3-Thr^4), whether it is actually *N*-glycosylated has not been verified. Here we demonstrate that *N*-glycosylation is induced at Asn^2 of Hsp30p by severe heat shock, ethanol stress, and acetic acid stress. Mild heat shock and glucose depletion induced the expression but not *N*-glycosylation of Hsp30p, indicating the *N*-glycosylation to be dependent on temperature and environmental conditions. *N*-glycosylation did not affect on the intracellular localization of Hsp30p but its physiological role under severe heat shock conditions. Since limited information is available on stress-responsive or condition-induced *N*-glycosylation, our findings provide new insight into the regulation of cellular stress response in yeast.

1. Introduction

Hsp30p of *Saccharomyces cerevisiae* is a plasma membrane-bound heat shock protein with a role in tolerance to environmental stress. It has been reported that Hsp30p inhibits Pma1p, a H^+-ATPase of the plasma membrane, to conserve intracellular ATP reserves under stressed conditions [1], and a knockout mutant (hsp30Δ) was more sensitive to high temperature than the wild type [2]. The expression of Hsp30p is induced by various types of stress, including heat shock, ethanol stress, glucose limitation, and weak organic acid [3–5]. Hsp30p has seven predicted transmembrane domains and one potential *N*-glycosylation consensus sequence (Asn^2-Asp^3-Thr^4). However, the mechanisms responsible for the sorting and turnover of Hsp30p have not been clarified. Additionally, it is not clear whether Hsp30p is actually *N*-glycosylated.

N-linked core oligosaccharides are added to asparagine residues within the glycosylation consensus sequence (Asn-X-Ser/Thr, X ≠ Pro) in the endoplasmic reticulum (ER). An oligosaccharyltransferase (OST) scans the nascent polypeptide for the glycosylation consensus sequence and forms an *N*-glycoside bond between the core oligosaccharide ($Glc_3Man_9GlcNAc_2$) and the side chain nitrogen of the Asn residue [6–8]. The OST complex of *S. cerevisiae* consists of trans-membrane subunits (Ost1-6p, Stt3p, Swp1p, and Wbp1p). Ost3p and Ost6p have different protein substrate-specific activities at the level of individual glycosylation sites and define distinct OST isoforms [6,9,10].

N-glycosylation is one of the most widespread covalent modifications of membrane and secretory proteins in eukaryotic cells [11,12]. *N*-glycosylation plays pivotal roles in the quality control, folding, sorting, and secretion of glycoproteins. Additionally, *N*-glycosylation influences the stability, turnover, and biological functions of numerous proteins [8,12–16]. It has been reported that an absence of *N*-glycosylation severely affected the folding of a yeast acid phosphatase [17].

In this study, the *N*-glycosylation of Hsp30p and its physiological roles were investigated. We demonstrate that *N*-glycosylation is induced at Asn^2 of Hsp30p by severe heat shock, ethanol stress, and acetic acid stress. A defect in *N*-glycosylation at high temperature affected susceptibility to severe heat shock but not the transport of Hsp30p to the plasma membrane. Our findings indicate the *N*-glycosylation of Hsp30p to be essential for tolerance to severe heat shock.

2. Materials and methods

2.1. Yeast strains and media

S. cerevisiae W303-1A (*MAT***a** *his3-11, 15 leu2-3, 112 trp1-1 ade2-1 ura3-1 can1-100*) was used as a wild-type strain, and an isogenic *hsp30*Δ strain (*MAT***a** *his3-11, 15 leu2-3, 112 trp1-1 ade2-1 ura3-1 hsp30*Δ::*CgTRP1*) was constructed by the method of Kitada et al.

* Corresponding author. Fax: +81 75 724 7764.
E-mail address: thioredoxin@kit.ac.jp (S. Izawa).
[1] These authors contributed equally to this work.

0006-291X/$ - see front matter © 2012 Elsevier Inc. All rights reserved.
doi:10.1016/j.bbrc.2012.02.126

[18]. The DNA fragment (1.5 kbp) encoding the *hsp30*Δ::*CgTRP1* region was amplified using the plasmid pSHB1804 (containing the *TRP1* gene of *Candida glabrata)* as a template and 5′-AATCGTAACGAGGCTTTAGGGCTTAATCCACCACATGGCAGGTGGACTCTAGAGGATCC-3′ and 5′-AAGCAGTATCTTCGACAGCTTGCTCTGCTTCAGGTTCGGCACAGGAAACAGCTATGACC-3′ as primers [18]. BY4741 (*MAT***a** *his3*Δ*1 ura3*Δ*0 leu2*Δ*0 met15*Δ*0*) and its isogenic knockout mutants (*ost3*Δ and *ost6*Δ) were purchased from Open Biosystems (AL, USA). Cells were cultured in 50 ml of SD (synthetic dextrose) minimal medium (2% glucose and 0.67% yeast nitrogen base without amino acids) with appropriate amino acids and bases at 28 °C with reciprocal shaking in Erlenmeyer flasks (300 ml). Exponentially growing cells were harvested at A_{600} = 0.4–0.5.

2.2. Plasmids

A 0.8-kbp fragment encoding part of the ORF of *HSP30* was amplified using 5′-CAAGGGCTCTAGATTGACTAGATATGCCTTAGCTC-3′ and 5′-GCTGCCTCGAGCAGTATCTTCGACAGCTTGCTCTG-3′. The amplicon was digested with XbaI/XhoI and cloned into the XbaI/XhoI sites of pPS1630 [19] to construct YIp-*HSP30*-GFP. To integrate the HSP30-GFP gene at the chromosomal *HSP30* locus, YIp-*HSP30*-GFP was linearized by partial digestion with KpnI and introduced into yeast cells.

To estimate the protein levels of Hsp30p, an integrate-type plasmid YIp-*HSP30*-FLAG was constructed. This plasmid contains a FLAG tag sequence (encoded by 24 nt) immediately upstream of the stop codon and 3′-flanking region of *HSP30* [20]. A 0.8-kbp fragment encoding a FLAG tag sequence, a stop codon and the 3′-flanking region of *HSP30* was amplified using 5′-GGTTGCTCGAGTAGACTACAAGGATGACGATGACAAGTAGAGCAGCTTGAGATTGTCTTAAT-3′ and 5′-AGCTCAATGGATCCTGAAAGAGCTTACAAC-3′. The amplicon was digested with XhoI/BamHI respectively, and cloned into the XbaI/BamHI sites of YIp-*HSP30*-GFP to construct YIp-*HSP30*-FLAG. To integrate the *HSP30*-FLAG gene at the chromosomal *HSP30* locus, YIp-*HSP30*-FLAG was linearized by partial digestion with KpnI and introduced into yeast cells.

A SalI/BamHI fragment encoding the promoter region and *HSP30*-FLAG was cloned into the SalI/BamHI site of pRS316 [21] to construct pRS-*HSP30*^{WT}-FLAG. Substitution of Asn^2 with Gln (*hsp30*^{N2Q}) was carried out by replacement of the SalI/HindIII region of *HSP30*^{WT} with a *hsp30*^{N2Q} fragment, which was amplified using 5′-GCTATGTCGACCATATCCGTTTTGCATAAG-3′ and 5′-GTAAAAAGCTTGATAGCGTATCTTGCATTTGAAAT-3′ (underlined letters encode Gln), to construct pRS-*hsp30*^{N2Q}-FLAG. The SalI/XhoI fragments of pRS-*HSP30*^{WT}-FLAG or pRS-*hsp30*^{N2Q}-FLAG encoding the promoter region and ORF of the *HSP30* gene were cloned into the SalI/XhoI site of pAUR-*ZRC1*-GFP [22] to construct pAUR-*HSP30*^{WT}-GFP or pAUR-*hsp30*^{N2Q}-GFP, respectively. The plasmids, pAUR-*HSP30*^{WT}-FLAG and pAUR-*hsp30*^{N2Q}-FLAG, were constructed by replacement of the GFP region of pAUR-*HSP30*-GFP with the FLAG region of YIp-*HSP30*-FLAG. pAUR plasmids were linearized by digestion with StuI and introduced into yeast cells.

2.3. Microscopy

A Leica AF6500 (Leica Microsystems Vertrieb GmbH, Germany) fluorescence microscopic system with a thermo plate (MATS55AX-KAF20, Tokai Hit Co. Ltd., Shizuoka, Japan) was used to analyze the intracellular localization of Hsp30p-GFP. Since the chromophore's formation in the GFP is blocked at high temperature [23,24], Hsp30p-GFP generates faint fluorescence under conditions of severe heat shock. Hence we compared the localization of Hsp30p^{WT}-GFP and hsp30p^{N2Q}-GFP within a few minutes after the shift to 25 °C from severe heat shock treatment at 42 °C or 43 °C.

2.4. Western blot analysis

After the treatment of cells with various forms of stress in SD medium, the plasma membrane fraction was immediately prepared as follows: collected cells were disrupted with glass beads (diameter 0.4 mm) in a lysis buffer (50 mM Tris–HCl pH 7.5, 6.0 M Urea, and 5% SDS) using FastPrep FP100A (MP biomedicals, OH, USA) for 30 s at 4 °C. For the endoglycosidase H (Endo H) treatment, Triton X-100 (final concentration, 3%) was used instead of Urea and SDS in the lysis buffer. After the disruption, supernatant was collected by centrifugation (5000*g* for 10 min at 4 °C). Protein quantification was carried out using the RC DC protein assay (Bio-Rad laboratories). Forty micrograms of protein was applied to each lane for SDS–PAGE. The polyacrylamide (15%) gel, containing 6.0 M urea and 0.1% SDS, was prepared using acrylamide:*N*,*N*′- methylenebisacrylamide 37.5:1 (Wako 016-15915, Osaka, Japan). The monoclonal anti-FLAG M2 antibody (F3165-2MG) was purchased from Sigma–Aldrich (St. Louis, MO, USA). Endo H was purchased from New England Biolabs (MA, USA). Ponceau S (Sigma–Aldrich) staining was used to confirm equal protein loading.

2.5. Stress susceptibility assay

Cells cultivated in SD medium until A_{600} = 0.5 were harvested and resuspended in fresh SD medium to obtain an initial A_{600} value of 0.1. To examine their susceptibility to severe heat shock, the cells were incubated at 43 °C for 180 min or 44 °C for 120 min. They were then spotted on plates of YPD medium (2% glucose, 1% yeast extract, 2% peptone, and 2% agar pH 5.5) in 10-fold serial dilutions and incubated at 28 °C for 2 days.

3. Results

3.1. Severe heat shock induces N-glycosylation of Hsp30p

Although it has been reported that various stress treatments increase the levels of *HSP30* mRNA [5], limited information is available on the protein levels of Hsp30p. We therefore examined the effects of stress on levels of Hsp30p by Western blot analysis. As shown in Fig. 1A, heat shock treatment induced production of Hsp30p, but the protein was not detected at 28 °C (w/o stress). We verified that glucose depletion, ethanol stress, and acetic acid also induce the synthesis of Hsp30p (Fig. 1B).

Intriguingly, we detected another clear band on the higher molecular weight side at 42–44 °C (Fig. 1A). The upper band was also detected in the cells treated with ethanol and acetic acid (Fig. 1B). These findings suggested that severe heat shock (>42 °C), ethanol, and acetic acid stress induced the modification of Hsp30p. The upper band did not disappear on treatment with various phosphatases (data not shown), indicating that it did not represent the phosphorylation of Hsp30p.

Since Hsp30p contains a potential glycosylation consensus sequence (Asn^2-Asp^3-Thr^4), we next investigated whether *N*-glycosylation of Hsp30p was induced or not. Tunicamycin prevents *N*-linked glycosylation by inhibiting the synthesis of dolichol-diphosphate-GlcNAc and induces ER stress [25,26]. Pretreatment with tunicamycin (2.5 μg/ml for 30 min) prior to the severe heat shock at 42 °C or 43 °C blocked the appearance of the upper band of Hsp30p (Fig. 2A). Tunicamycin pretreatment also blocked the appearance of the upper band upon 7.5% ethanol stress and 20 mM acetic acid stress (data not shown). Furthermore, the upper band was disappeared following treatment with endoglycosidase H (Endo H) treatment (Fig. 2B). These results clearly indicate that the upper band represented the *N*-linked glycosylation of Hsp30p,

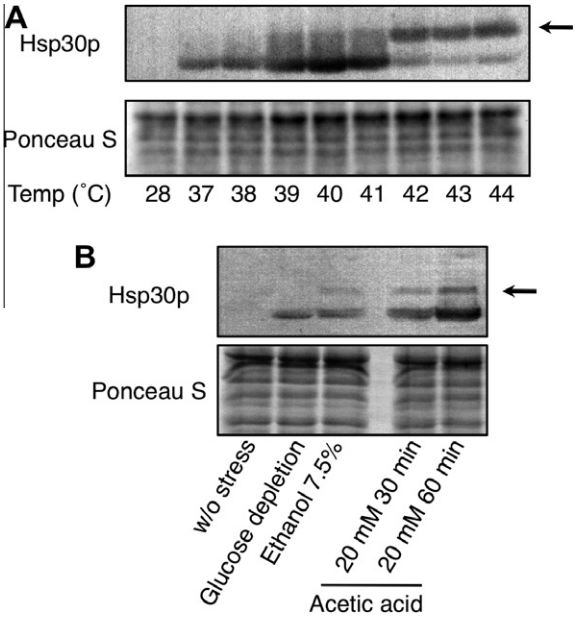

Fig. 1. Effects of various forms of stress on the expression of Hsp30p. Levels of Hsp30p-FLAG were determined by Western blot analysis using anti-FLAG antibody. Cells carrying YIp-*HSP30*-FLAG were cultured in SD medium until A_{600} = 0.5, and treated with heat shock at various temperatures (37–44 °C) for 30 min (A) or subjected to glucose depletion (30 min), ethanol stress (30 min), and acetic acid stress (30 or 60 min) (B). The plasma membrane fraction and SDS–PAGE samples were prepared using urea and SDS as described in Section 2. Ponceau S staining was used as a loading control.

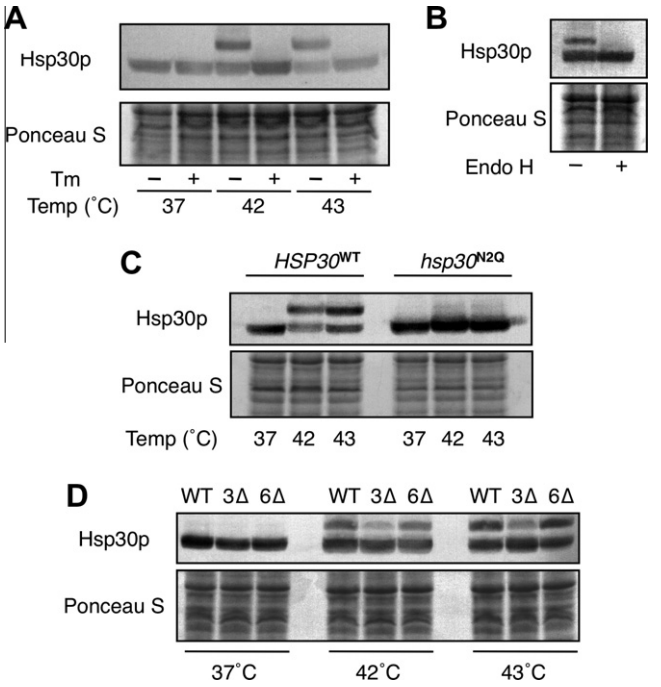

Fig. 2. Severe heat shock induces *N*-glycosylation of Hsp30p. (A) Pretreatment with tunicamycin (Tm) caused the disappearance of the upper band of Hsp30p-FLAG. Cells were treated with or without Tm (2.5 μg/ml) for 30 min prior to the treatment with heat shock (37 °C, 42 °C, and 43 °C) for 30 min. Hsp30p-FLAG was detected by Western blot analysis using anti-FLAG antibody. (B) The upper band of Hsp30p-FLAG disappeared after the treatment with endoglycosidase H (Endo H). Cells cultured in SD medium until A_{600} = 0.5 were exposed to heat shock at 43 °C for 60 min. The plasma membrane fraction was treated with or without Endo H for 30 min. (C) An amino-acid substitution of Asn^2 to Gln (N2Q) caused the disappearance of the upper band of Hsp30p-FLAG. Cells carrying pAUR-*HSP30*^{WT}-FLAG or pAUR-*hsp30*^{N2Q}-FLAG were cultured in SD medium until A_{600} = 0.5, and treated with heat shock (37 °C, 42 °C, or 43 °C) for 30 min. (D) The upper band of Hsp30p diminished in the *ost3*Δ cells. The wild-type cells and the *ost* mutant cells, *ost3*Δ (3Δ) and *ost6*Δ (6Δ), carrying YIp-*HSP30*-FLAG were cultured in SD medium until A_{600} = 0.5, and subjected to heat shock (37 °C, 42 °C, or 43 °C) for 30 min. Ponceau S staining was used as a loading control.

and that severe heat shock, ethanol, and acetic acid can induce the partial glycosylation of Hsp30p.

To verify the site of *N*-linked glycosylation of Hsp30p, we constructed a mutant with an amino acid substitution from Asn^2 to Gln (hsp30p^{N2Q}). Subsequently, only a single band was detected from cells expressing hsp30p^{N2Q} upon severe heat shock (Fig. 2C), indicating that the *N*-linked glycan was added to the Asn^2 residue within the glycosylation consensus sequence of Hsp30p.

We also investigated the effects of the oligosaccharyltransferase (OST) complex on the *N*-linked glycosylation of Hsp30p. Ost3p and Ost6p are alternative members of the OST complex and define functionally distinct OST isoforms [6,9,10,27]. We examined the glycosylation state of Hsp30p in the *ost3*Δ and *ost6*Δ deletion mutants. As shown in Fig. 2D, the *ost3*Δ cells showed a lower level of glycosylation of Hsp30p than the wild-type cells and *ost6*Δ cells, indicating that the OST complex with Ost3p rather than Ost6p preferentially catalyzes the glycosylation of Hsp30p.

3.2. N-glycosylation has little effect on the cellular localization of Hsp30p

We investigated the effects of *N*-glycosylation on the transport and intracellular localization of Hsp30p. Although little GFP signal was detected under non-stressed conditions at 28 °C, the expression of Hsp30p^{WT}-GFP was induced by mild heat shock (37 °C for 60 min) and its signal was detected in the plasma membrane (Fig. 3). It seems quite reasonable because Hsp30p is a plasma membrane-bound protein and has seven predicted transmembrane domains [1,4,5]. It should be noted that Hsp30p^{WT}-GFP spread out as small foci in the plasma membrane (Fig. 3, top view pictures). hsp30p^{N2Q}-GFP showed the same intracellular distribution as Hsp30p^{WT}-GFP at 37 °C.

We next examined the localization of Hsp30p under conditions that induce *N*-glycosylation of Hsp30p. After the treatment with severe heat shock at 42 °C for 60 min, Hsp30p^{WT}-GFP and hsp30p^{N2Q}-GFP showed the same intracellular distribution. Although the size of foci of Hsp30p-GFP in the plasma membrane was slightly bigger at 42 °C than at 37 °C, no significant difference was observed in the intracellular localization at 42 °C between Hsp30p^{WT} and hsp30p^{N2Q} (Fig. 3). Additionally, no significant difference in transport to the plasma membrane was observed between Hsp30p^{WT}-GFP and hsp30p^{N2Q}-GFP, i.e. hsp30p^{N2Q}-GFP did not show any delay in the appearance on the plasma membrane (data not shown). These results suggest that *N*-glycosylation affects neither the transport nor localization of Hsp30p.

3.3. N-glycosylation affects the function of Hsp30p under severe heat shock

To see whether *N*-glycosylation affects the function of Hsp30p, we investigated the susceptibility of cells expressing hsp30p^{N2Q} to severe heat shock. As reported previously [2], *hsp30*Δ cells were hypersensitive to severe heat shock stress at 43 °C and 44 °C (Fig. 4). The hypersensitivity to heat shock of *hsp30*Δ cells was suppressed by the expression of Hsp30p^{WT} but not hsp30p^{N2Q}. This finding indicates that *N*-glycosylation of Hsp30p is required for sufficient tolerance to severe heat shock stress.

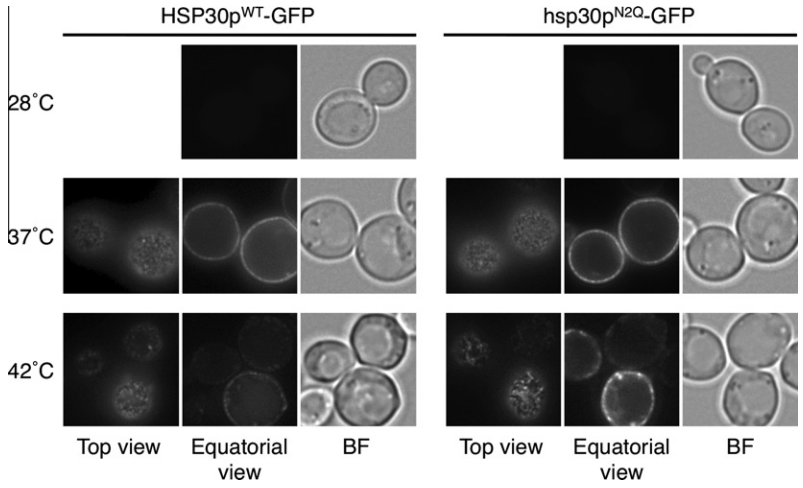

Fig. 3. Effects of *N*-glycosylation on the intracellular localization of Hsp30p. Cells carrying pAUR-*HSP30*^{WT}-GFP or pAUR-*hsp30*^{N2Q}-GFP were cultured in SD medium until A_{600} = 0.5, and treated without stress (28 °C) or with heat shock at 37 °C or 42 °C for 60 min. The exposure times were the same for each stress condition. For the top view, the focusing was done on the top of the cell. BF, bright field.

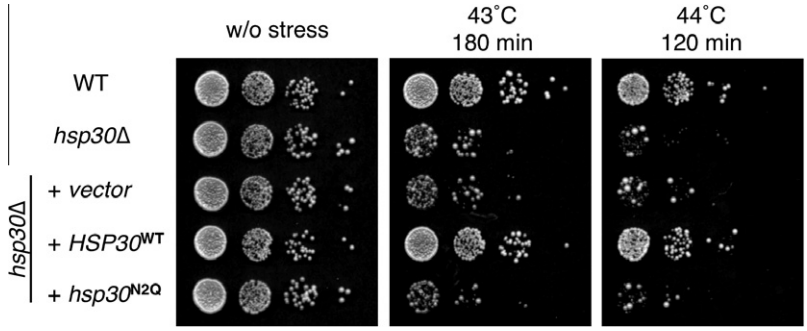

Fig. 4. Effects of *N*-glycosylation of Hsp30p on cellular tolerance to severe heat shock. Cells cultured in SD medium until A_{600} = 0.5 were treated with heat shock at 43 °C for 180 min or at 44 °C for 120 min, then spotted on plates of YPD medium in 10-fold serial dilutions and incubation at 28 °C for 2 days.

4. Discussion

It is well known that 41 °C is the upper limit for growth of most *Saccharomyces* strains, and high temperature conditions above 42 °C can be regarded as severe stress for yeast cells [28]. To adapt to severe heat shock at 42 °C rapidly and efficiently, yeast gene expression is strictly controlled not only by transcriptional regulation but also by the selective nuclear export of mRNAs [29,30]. We too have reported that *HSP* mRNAs were smoothly exported and translated at 42 °C, where the nuclear export of bulk poly $(A)^+$ mRNA was blocked [20,31]. Our results in this study confirmed that the expression of the *HSP30* gene as well as other *HSP* genes is preferentially conducted under severe heat shock stressed conditions (Figs. 1 and 3).

We also found that *N*-glycosylation of Hsp30p was induced by severe heat shock (Figs. 1 and 2), indicating that severe heat shock causes the modification of Hsp30p. This finding also indicates the *N*-glycosylation to be dependent on environmental conditions. Indeed, glucose depletion and mild heat shock at 37 °C did not induce the *N*-glycosylation of Hsp30p, but acetic acid stress and ethanol stress did (Fig. 1). In mammalian cells, the glycosylation of specific proteins has been shown to be induced by heat shock and other stress treatments [32–34]. It is widely believed that stress-induced protein glycosylation is a significant component of the cellular stress response [35,36]. Therefore, it is no great surprise that *N*-linked glycan is added to yeast Hsp30p upon severe heat shock. Since limited information is available on stress-responsive or conditional induction of *N*-glycosylation in yeast cells, our findings provide new insight into the regulation of the yeast stress response.

N-glycosylation affects the folding, functions, and stability of various proteins [8,12–15]. Glycosylation of the yeast invertase prevents its aggregation and thereby facilitates its correct refolding [37]. Additionally, *N*-glycosylation affects the cell surface transport and intracellular trafficking of proteins [38,39]. The fact that the *N*-glycosylation of Hsp30p was induced upon severe heat shock implies that the *N*-glycosylated Hsp30p might be an optimized form under high temperature conditions. Initially, we speculated that the *N*-glycosylation facilitates the folding and transport to the membrane of Hsp30p under severe heat shock conditions. However, we could not observe any significant differences between Hsp30p^{WT} and hsp30p^{N2Q} regarding their turnover (data not shown) and transport to the plasma membrane (Fig. 3). *N*-glycosylation presumably has little effect on the stability and transport of Hsp30p under stressed conditions.

However, an effect of *N*-glycosylation on the physiological function of Hsp30p was observed. Expression of Hsp30p^{WT} but not hsp30p^{N2Q} suppressed the hypersensitivity to severe heat shock of the *hsp30*Δ mutant (Fig. 4), indicating that *N*-glycosylated Hsp30p is required for tolerance to severe heat shock. *N*-glycosylation might be crucial for bringing out the function of Hsp30p under high temperature conditions. Conversely, such a modification of Hsp30p does not seem necessary for yeast cells to address mild heat shock. Currently, the function of Hsp30p is thought to exert through inhibition of Pma1p to reserve intracellular ATP under

stressed conditions [1]. Hence, it may be feasible that the *N*-glycosylated Hsp30p inhibits Pma1p more efficiently.

We also demonstrated that Hsp30p-GFP formed small foci and spread throughout the plasma membrane under stressed conditions (Fig. 3). Intriguingly, the localization pattern of Hsp30p was quite similar with that of Pma1p [40]. This is the first report demonstrating that Hsp30p forms foci in the plasma membrane, and our observation may suggest that Hsp30p functions in the limited area of the plasma membrane.

It is thought that the mammalian stress response includes stress-induced protein glycosylation, which appears essential and complementary to the role of HSPs [35,36]. This concept might be supported by the *N*-glycosylation of Hsp30p upon severe heat shock and applicable to the yeast stress response. Heat shock-induced glycosylation may occur in other yeast proteins. Identification of such proteins will provide further insight into the temperature-dependent *N*-glycosylation in the cellular stress response.

Acknowledgments

We thank Dr. A. Hosomi (RIKEN Advanced Science Institute, Japan) for valuable discussions. This study was supported by grants from the Japanese ministry of Education, Culture, Sports, Science and Technology.

References

[1] P.W. Piper, C. Oritz-Calderon, C. Holyoak, P. Coote, M. Cole, Hsp30, the integral plasma membrane heat shock protein of *Saccharomyces cerevisiae*, is a stress-inducible regulator of plasma membrane H^+-ATPase, Cell Stress Chaperones 2 (1997) 12–24.
[2] R.C. Meena, S. Thakur, A. Chakrabarti, Regulation of *Saccharomyces cerevisiae* plasma membrane H^+-ATPase (Pma1) by dextrose and Hsp30 during exposure to thermal stress, Indian J. Microbiol. 51 (2011) 153–158.
[3] B. Panaretou, P.W. Piper, The plasma membrane of yeast acquires a novel heat-shock protein (hsp30) and displays a decline in proton-pumping ATPase levels in response to both heat shock and the entry to stationary phase, Eur. J. Biochem. 206 (1992) 635–640.
[4] P.W. Piper, K. Talreja, B. Panaretou, P. Moradas-Ferreira, K. Byrne, U.M. Praekelt, P. Meacock, M. Recnacq, H. Boucherie, Induction of major heat-shock proteins of *Saccharomyces cerevisiae*, including plasma membrane Hsp30, by ethanol levels above a critical threshold, Microbiology 140 (1994) 3031–3038.
[5] I.J. Seymour, P.W. Piper, Stress induction of *HSP30*, the plasma membrane heat shock protein gene of *Saccharomyces cerevisiae*, appears not to use known stress-regulated transcription factors, Microbiology 145 (1999) 231–239.
[6] R. Knauer, L. Lehle, The oligosaccharyl transferase complex from yeast, Biochim. Biophys. Acta 1426 (1999) 259–273.
[7] L.W. Ruddock, M. Molinari, *N*-glycan processing in ER quality control, J. Cell Sci. 119 (2006) 4373–4380.
[8] J. Roth, C. Zuber, S. Park, I. Jang, Y. Lee, K.G. Kysela, V.L. Fourn, R. Santimaria, B. Guhl, J.W. Cho, Protein *N*-glycosylation, protein folding, and protein quality control, Mol. Cells 30 (2010) 497–506.
[9] M. Schwarz, R. Knauer, L. Lehle, Yeast oligosaccharyltransferase consists of two functionally distinct sub-complexes, specified by either the Ost3p or Ost6p subunit, FEBS Lett. 579 (2005) 6564–6568.
[10] B. Schulz, M. Aebi, Analysis of glycosylation site occupancy reveals a role for Ost3p and Ost6p in site-specific *N*-glycosylation efficiency, Mol. Cell. Proteomics 8 (2009) 357–364.
[11] L. Lehle, S. Strahl, W. Tanner, Protein glycosylation, conserved from yeast to man: a model organism helps elucidate congenital human diseases, Angew. Chem. Int. Ed. 45 (1997) 6802–6818.
[12] A. Helenius, M. Aebi, Intracellular functions of *N*-linked glycans, Science 291 (2001) 2364–2369.
[13] A. Helenius, M. Aebi, Role of *N*-linked glycans in the endoplasmic reticulum, Annu. Rev. Biochem. 73 (2004) 1019–1049.
[14] R. Golzman, T. Okiyoneda, C.M. Mulvihill, J.M. Rini, H. Barriere, G.L. Lukas, N-glycans are direct determinants of CFTR folding and stability in secretory and endocytic membrane traffic, J. Biol. Chem. 184 (2009) 847–862.
[15] S.S. Pinho, R. Seruca, F. Gärtner, Y. Yamaguchi, J. Gu, N. Taniguchi, C.A. Reis, Modulation of E-cadherin function and dysfunction by *N*-glycosylation, Cell. Mol. Life Sci. 68 (2011) 1011–1020.
[16] F. Scwarz, M. Aebi, Mechanisms and principles of *N*-linked protein glycosylation, Curr. Opin. Struct. Biol. 21 (2011) 576–582.
[17] M.A. Riederer, A. Hinnen, Removal of *N*-glycosylation sites of the yeast acid phosphatase severely affects protein folding, J. Bacteriol. 173 (1991) 3539–3546.
[18] K. Kitada, E. Yamaguchi, M. Arisawa, Cloning of the *Candida glabrata TRP1* and *HIS3* genes, and construction of their disruptant strains by sequential integrative transformation, Gene 165 (1995) 203–206.
[19] J.A. Kahana, G. Schlenstedt, D.M. Evanchuk, J.R. Geiser, M.A. Hoyt, P.A. Silver, The yeast dynactin complex is involved in portioning the mitotic spindle between mother and daughter cells during anaphase B, Mol. Biol. Cell 9 (1999) 1741–1756.
[20] S. Izawa, T. Kita, K. Ikeda, Y. Inoue, Heat shock and ethanol stress provoke distinctly different responses in 3′-processing and nuclear export of *HSP* mRNA in *Saccharomyces cerevisiae*, Biochem. J. 414 (2008) 111–119.
[21] R.S. Sikorski, P. Hieter, A system of shuttle vectors and yeast host strains designed for efficient manipulation of DNA in *Saccharomyces cerevisiae*, Gene 122 (1989) 19–27.
[22] K. Ikeda, S. Kitagawa, T. Tada, H. Iefuji, Y. Inoue, S. Izawa, Modification of yeast characteristics by soy peptides: cultivation with soy peptides represses the formation of lipid bodies, Appl. Microbiol. Biotechnol. 89 (2011) 1971–1977.
[23] C.R. Lim, Y. Kimata, M. Oka, K. Nomaguchi, K. Kohno, Thermosensitivity of green fluorescent protein fluorescence utilized to reveal novel nuclear-like compartments in a mutant nucleoporin Nsp1, J. Biochem. 118 (1995) 13–17.
[24] H. Ogawa, S. Inouye, F.I. Tsuji, K. Yasuda, K. Umesono, Localization, trafficking, and temperature-dependence of the Aequorea green fluorescent protein in cultured vertebrate cells, Proc. Natl. Acad. Sci. USA 92 (1995) 11899–11903.
[25] L. Lehle, W. Tanner, The specific site of tunicamycin inhibition in the formation of dolichol-bound *N*-acetylglucosamine derivatives, FEBS Lett. 72 (1976) 167–170.
[26] A. Herscovics, P. Orlean, Glycoprotein biosynthesis in yeast, FASEB J. 7 (1993) 540–550.
[27] A. Yan, E. Ahmed, W.J. Lennarz, New findings on interactions among the yeast oligosaccharyl transferase subunits using a chemical cross-linker, J. Biol. Chem. 278 (2003) 33078–33087.
[28] S. Benjaphokee, P. Koedrith, C. Auesukaree, T. Asvarak, M. Sugiyama, Y. Kaneko, C. Boonchird, S. Harashima, *CDC19* encoding pyruvate kinase is important for high-temperature tolerance in *Saccharomyces cerevisiae*, New Biotechnol. 29 (2011) 166–176.
[29] T. Tani, R.J. Derby, Y. Hiraoka, D.L. Spector, Nuclear accumulation of poly $(A)^+$ RNA in heat-shocked yeast cells: implication of nucleolar involvement in mRNA transport, Mol. Biol. Cell 6 (1995) 1515–1534.
[30] C. Saavedra, K.S. Tung, D.C. Amberg, A.K. Hopper, C.N. Cole, Regulation of mRNA export in response to stress in *Saccharomyces cerevisiae*, Genes Dev. 10 (1996) 1608–1620.
[31] S. Izawa, R. Takemura, Y. Inoue, Gle2p is essential to induce adaptation of the export of bulk poly$(A)^+$ mRNA to heat shock in *Saccharomyces cerevisiae*, J. Biol. Chem. 279 (2004) 35469–35478.
[32] K.J. Henle, W.A. Nagle, Inhibition of heat shock protein synthesis and protein glycosylation by stepdown heating, Exp. Cell Res. 196 (1991) 184–191.
[33] K.J. Henle, G.P. Kaushal, W.A. Nagle, G.T. Nolen, Prompt protein glycosylation during acute heat stress, Exp. Cell Res. 207 (1993) 245–251.
[34] S.M. Jethmalani, K.J. Henle, G.P. Kaushal, Heat shock-induced prompt glycosylation. Identification of P-SG67 as calreticulin, J. Biol. Chem. 269 (1994) 23603–23609.
[35] K.J. Henle, S.M. Jethmalani, W.A. Nagle, Heat stress-induced protein glycosylation in mammalian cells, Trends Glycosci. Glycotechnol. 7 (1995) 191–204.
[36] K.J. Henle, S.M. Jethmalani, W.A. Nagle, Stress proteins and glycoproteins, Int. J. Mol. Med. 1 (1998) 25–32.
[37] N. Schülke, F.X. Schmid, Effect of glycosylation on the mechanism of renaturation of invertase from yeast, J. Biol. Chem. 263 (1988) 8832–8837.
[38] Y. Hirai-Fujita, M. Yamamoto-Hino, O. Kanie, S. Goto, *N*-glycosylation of the *Drosophila* neural protein Chaoptin is essential for its stability, cell surface transport and adhesive activity, FEBS Lett. 582 (2008) 2572–2576.
[39] Y. Haga, K. Ishii, T. Suzuki, *N*-glycosylation is critical for the stability and intracellular trafficking of glucose transporter GLUT4, J. Biol. Chem. 286 (2011) 31320–31327.
[40] F. Fröhlich, K. Moreira, P.S. Aguilar, N.C. Hubner, M. Mann, P. Walter, T.C. Walther, A genome-wide screen for genes affecting eisosomes reveals Nce102 function in sphingolipid signaling, J. Cell Biol. 185 (2009) 1227–1242.

Biochemical and Biophysical Research Communications 420 (2012) 124–129

Contents lists available at SciVerse ScienceDirect

Biochemical and Biophysical Research Communications

journal homepage: www.elsevier.com/locate/ybbrc

ROCK inhibitor prevents the dedifferentiation of human articular chondrocytes

Emi Matsumoto, Takayuki Furumatsu *, Tomoko Kanazawa, Masanori Tamura, Toshifumi Ozaki

Department of Orthopaedic Surgery, Science of Functional Recovery and Reconstruction, Okayama University Graduate School of Medicine, Dentistry, and Pharmaceutical Sciences, 2-5-1 Shikatacho, Kitaku, Okayama 700-8558, Japan

ARTICLE INFO

Article history:
Received 18 February 2012
Available online 1 March 2012

Keywords:
Chondrocyte
Dedifferentiation
Redifferentiation
ROCK inhibitor
SOX9
Type II collagen

ABSTRACT

Chondrocytes lose their chondrocytic phenotypes in vitro. The Rho family GTPase ROCK, involved in organizing the actin cytoskeleton, modulates the differentiation status of chondrocytic cells. However, the optimum method to prepare a large number of un-dedifferentiated chondrocytes is still unclear. In this study, we investigated the effect of ROCK inhibitor (ROCKi) on the chondrogenic property of monolayer-cultured articular chondrocytes. Human articular chondrocytes were subcultured in the presence or absence of ROCKi (Y-27632). The expression of chondrocytic marker genes such as SOX9 and COL2A1 was assessed by quantitative real-time PCR analysis. Cellular morphology and viability were evaluated. Chondrogenic redifferentiation potential was examined by a pellet culture procedure. The expression level of SOX9 and COL2A1 was higher in ROCKi-treated chondrocytes than in untreated cells. Chondrocyte morphology varied from a spreading form to a round shape in a ROCKi-dependent manner. In addition, ROCKi treatment stimulated the proliferation of chondrocytes. The deposition of safranin O-stained proteoglycans and type II collagen was highly detected in chondrogenic pellets derived from ROCKi-pretreated chondrocytes. Our results suggest that ROCKi prevents the dedifferentiation of monolayer-cultured chondrocytes, and may be a useful reagent to maintain chondrocytic phenotypes in vitro for chondrocyte-based regeneration therapy.

1. Introduction

Articular cartilage has a poor intrinsic capacity for healing, and cartilage lesion from trauma or degeneration can result in morbidity and functional impairment [1]. Cartilage repair strategies that include arthroscopic debridement, bone marrow stimulation, osteochondral mosaicplasty, and autologous chondrocyte implantation are available for the treatment of symptomatic chondral and osteochondral lesions [2]. In chondrocyte-based approaches for the treatment of cartilage defects, several issues involved in a loss of chondrocytic phenotype during culture, which is called dedifferentiation, and requiring two surgeries (chondral tissue harvest and cultured cell implantation) are considered [3]. Monolayer-cultured articular chondrocytes leads to a process of dedifferentiation whereby the cells acquire a fibroblastic morphology and lose their chondrocytic properties [4–7]. The expression of chondrocyte-specific genes, such as α1(II) collagen (COL2A1), aggrecan, SRY-type high-mobility-group box (SOX) 9, and SOX 5/6, is gradually downregulated during cell multiplication in monolayer culture conditions [4–7]. Several authors have reported that three-dimensional culture systems, such as cultures in agarose, alginate beads, and the other scaffolds, recover the chondrogenic phenotype of dedifferentiated chondrocytes and induce their redifferentiation in vitro [4–6]. However, three-dimensional culture is not a cell-proliferating method to prepare a sufficient number of chondrocytes. Since primary chondrocytes that can be isolated from the native cartilage is limited, a monolayer culture technique that stimulates cellular proliferation without inducing their dedifferentiation or hypertrophic differentiation is important for a clinical application of chondrocyte-based therapy. Several biochemical factors such as fibroblast growth factor (FGF)-2, insulin, insulin-like growth factor, and bone morphogenetic protein (BMP)-2 synergistically promote chondrocyte proliferation in a three-dimensional atelocollagen gel culture [8,9]. After the cell number-increasing step (FGF-2/insulin-supplemented monolayer culture), the combination of BMP-2, insulin, and triiodothyronine has the optimal effect on chondrocyte redifferentiation in the sequential gel culture system [9]. However, ex vivo three-dimensional culture systems accompanied by continuous growth factor treatments are expensive and complicated. In this study, we investigated the effect of a reasonable reagent, ROCK inhibitor (ROCKi), on the status of cellular dedifferentiation, redifferentiation, and proliferation in monolayer-cultured human articular chondrocytes.

The Rho family GTPases including RhoA, Rac1, and Cdc42 are members of the Ras superfamily of small GTPases [10,11]. Rho GTPases regulate various biological functions such as cell motility and gene expression by organizing the actin cytoskeleton [12]. ROCK, one of the RhoA downstream effectors, has an important role in inducing stress fiber formation and assembly of focal adhesions

* Corresponding author. Fax: +81 86 223 9727.
E-mail address: matino@md.okayama-u.ac.jp (T. Furumatsu).

0006-291X/$ - see front matter © 2012 Elsevier Inc. All rights reserved.
doi:10.1016/j.bbrc.2012.02.127

[11,13]. However, the effect of RhoA/ROCK signaling is still controversial on chondrogenic property and cellular behavior of cultured chondrocytes. RCOK inhibition causes cortical actin organization and cell rounding, and reduces the number of actin fibers in chondrogenic ATDC5 cells [14]. In addition, ROCKi treatment increases glycosaminoglycan synthesis and the expression of chondrogenic marker genes, such as Col2a1, aggrecan, Sox9, and Sox5/6, in ATDC5 cells [14,15]. On the other hand, RhoA overexpression in ATDC5 cells results in increased proliferation and a delay of hypertrophic differentiation [16]. Inhibition of ROCK signaling partially rescues the effects of RhoA overexpression in chondrocytic cells [16]. In the present study, we investigated cellular behavior of ROCKi-treated articular chondrocytes and evaluated the role of ROCK signaling in chondrocyte dedifferentiation during monolayer culture condition.

2. Materials and methods

2.1. Cells and cell culture

Institutional Review Board approval and informed consent were obtained before beginning all experimental studies. Articular cartilage was obtained at notchplasty in patients suffering from anterior cruciate ligament injury ($n = 4$). Patients were 13, 18, 19, and 21 years of age. Articular chondrocytes were prepared by collagenase (Sigma, St. Louis, MO) digestion [17]. Attached cells (passage 0) were maintained with Dulbecco's modified Eagle's medium (DMEM, Wako, Osaka, Japan) containing 10% fetal bovine serum (HyClone, South Logan, UT), and penicillin/streptomycin (Sigma). Monolayer-cultured chondrocytes between passage 1 and 7 were used. ROCK inhibition was performed by a ROCK-specific inhibitor Y-27632 (Wako). ROCKi-supplemented media were changed every 3 days.

2.2. Cell proliferation assay

Cell proliferation assays were performed as described [18]. Cells were incubated in ROCKi-supplemented media for 48 h prior to addition of WST-1 (Roche, Mannheim, Germany). Untreated chondrocytes used as controls. The optical density (OD, 450–630 nm) was measured, and the mean value derived from 5 wells was evaluated.

2.3. RT-PCR and quantitative real-time PCR

RNA samples were obtained from monolayer- and pellet-cultured chondrocytes. Total cellular RNAs were isolated using ISOGEN reagent (Nippon Gene, Toyama, Japan). RNA samples (500 ng) were reverse-transcribed with ReverTra Ace (Toyobo, Osaka, Japan). The cDNAs underwent PCR amplification in the presence of specific primers using Taq DNA polymerase (TaKaRa, Ohtsu, Japan). For all the RT-PCR fragments, the reaction was allowed to proceed for 28–32 cycles. The following primer sets were used: COL2A1, aggrecan, SOX9, SOX5, SOX6, glyceraldehyde-3-phosphate dehydrogenase (G3PDH) [19–22], 5′-ccc ttt ttg ctg cta gta tcc ttg-3′ and 5′-cta cag ctg atg gtc ccg gt-3′ for α1(X) collagen (COL10A1). Quantitative real-time PCR analyses were performed using FastStart DNA Master SYBR Green I kit (Roche) [23]. The cycle number crossing the signal threshold was selected in the linear part of the amplification curve. Amplification data of G3PDH were used for normalization. These assays were run in triplicate, and relative mRNA levels were normalized with the level of untreated chondrocytes for every sample.

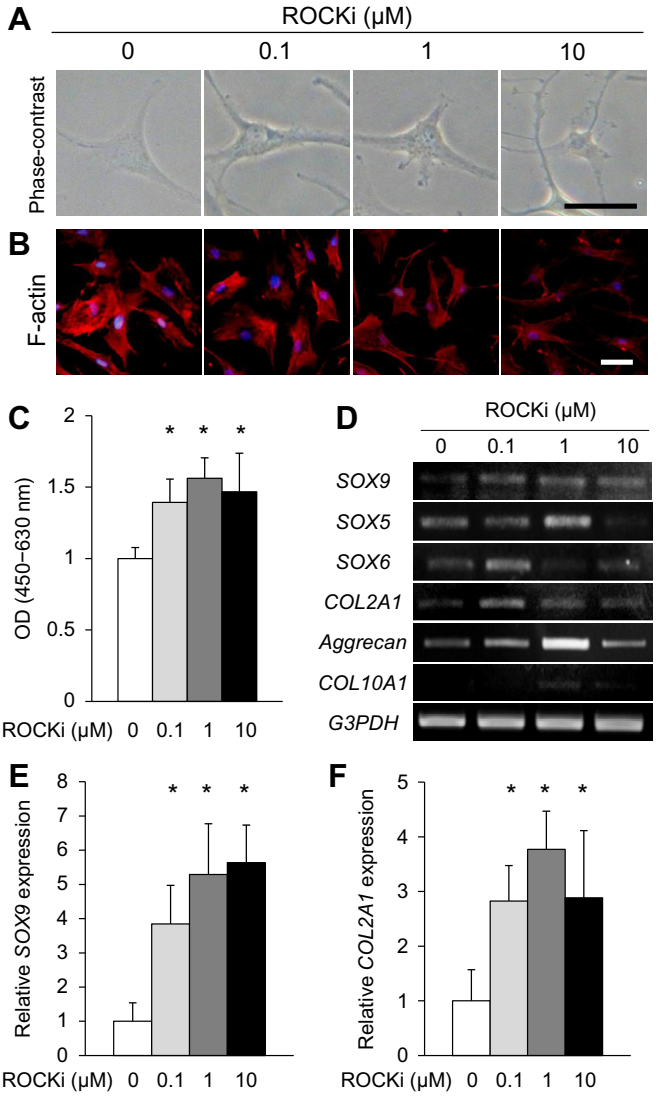

Fig. 1. ROCKi influences cellular morphology, proliferation, and gene expression of primary chondrocytes. (A) Phase-contrast microscopic images of human articular chondrocytes (passage 1) in the presence or absence of ROCKi (0, 0.1, 1, and 10 μM, 48 h). ROCK inhibition transformed cell shape to small and round, chondrocyte-like morphology. (B) Stress fibers were detected by phalloidin regents (F-actin, red). Cellular morphology and stress fiber formation were modified by ROCKi treatments (48 h). (C) Cellular proliferation was increased up to 1.5-fold levels of untreated chondrocytes by ROCKi treatments (0.1, 1, and 10 μM). OD (450–630 nm) was measured at 48 h after ROCKi administration. (D) Chondrogenic gene expressions of SOX9, SOX5/6, COL2A1, and aggrecan were affected by 1-week-treatment of ROCKi in monolayer-cultured chondrocytes (passage 1). The expression of COL10A1, a hypertrophic differentiation marker, was not influenced by ROCKi treatment. (E and F) Real-time PCR analyses revealed that ROCKi treatment increased the expression of SOX9 and COL2A1 in human articular chondrocytes. Bars, 50 μm. $^{*}p < 0.05$ compared with each untreated control. (For interpretation of the references to colour in this figure legend, the reader is referred to the web version of this article.)

2.4. Chondrocyte redifferentiation, histological analysis, and Western blot

To assess the redifferentiation ability of dedifferentiated chondrocytes after monolayer culture, pellet-cultured chondrocytes (5×10^5 cells/pellet) were maintained in ROCKi-free chondrogenic induction media [DMEM-high glucose supplemented with 10% FBS, dexamethasone (0.1 mM, Sigma), ascorbate (0.17 mM, Sigma), ITS Premix (1%, BD Biosciences, Bedford, MA), and transforming growth factor-β3 (10 ng/ml, R&D, Minneapolis, MN)] for 2 weeks

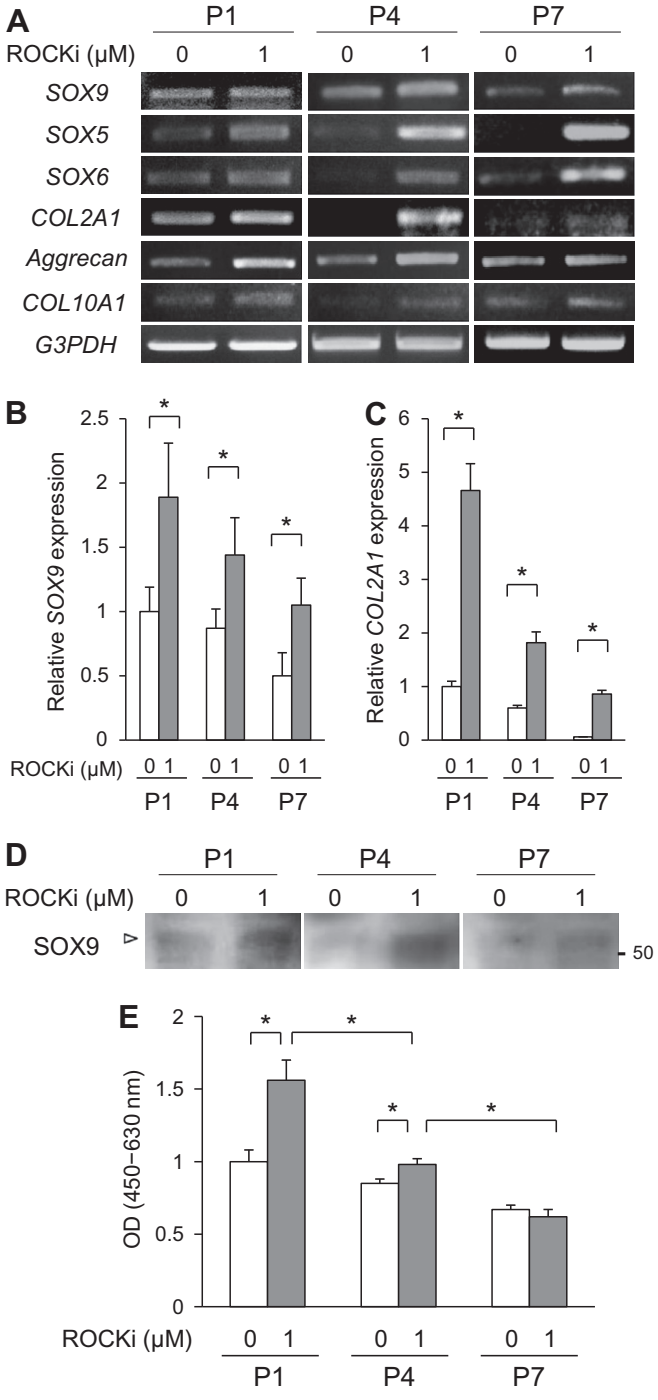

Fig. 2. ROCKi prevents the dedifferentiation of monolayer-cultured chondrocytes. (A) The expression of chondrogenic marker genes, such as SOX9, SOX5/6, COL2A1, and aggrecan, was higher in ROCKi-treated chondrocytes than in untreated cells during passaging procedures. (B and C) In real-time PCR analyses, ROCKi-supplemented condition maintained the expression of SOX9 and COL2A1 at a higher level in monolayer-cultured chondrocytes. (D) Western blot analysis revealed that the total amount of SOX9 protein (open arrowhead) was higher in ROCKi-treated chondrocytes compared with untreated cells. An indicated number denotes 50 kDa. (E) Continuous ROCKi treatment stimulated the proliferation of chondrocytes between passage 1 and 4. P, passage. $^{*}p < 0.05$.

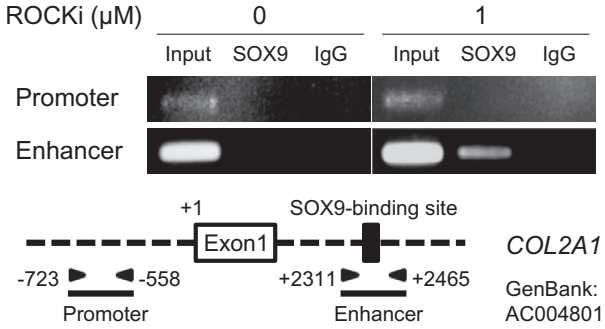

Fig. 3. ROCKi promotes the association between SOX9 and the COL2A1 enhancer on chromatin. Chromatin IP analysis revealed that ROCKi treatment (1 μM) increased the association between SOX9 and the conserved SOX9-binding site on the COL2A1 enhancer in monolayer-cultured articular chondrocytes (passage 7). No fragment was observed in the SOX9-IP fraction using the primer set for the COL2A1 promoter region contained no SOX9 recognition sequence. Mouse IgG was used as the control for chromatin IP (IgG). A scheme involving the human COL2A1 promoter, exon 1, and intron 1 is shown (dashed line). Filled box denotes the SOX9-binding site on the enhancer region of COL2A1 intron 1. Numbers indicate the distance from the transcription start site of the COL2A1 gene (GenBank, AC004801). Arrowheads denote the primer sets for chromatin IP.

[24,25]. The deposition of proteoglycans was evaluated by safranin O staining. The Bern pellet histology score (range, 0–9) was measured [26]. Type II collagen distribution was investigated using a mouse anti-collagen type II antibody (MP Biomedicals, Solon, OH) [22]. Signal density of type II collagen deposition was quantified by Image J 1.31 as described [23]. To evaluate the effect of ROCK inhibition on the actin cytoskeleton, F-actin fibers were visualized by Alexa Fluor 568 phalloidin (Invitrogen, Carlsbad, CA) [17]. Total amounts of SOX9 protein was investigated by Western blot using a mouse anti-SOX9 antibody (Sigma) [22,24]. Protein concentrations were measured by BCA protein assay kit (Bio-Rad, Hercules, CA). Equal amounts of proteins were applied (15 μg/lane).

2.5. Chromatin immunoprecipitation (Chromatin IP)

Chromatin IP assays were performed as described [22,24]. In brief, sonicated cell lysates were suspended in nuclear lysis buffer. The 10% volume of supernatant was stocked as an input sample. The half of each remaining sample was incubated for 2 h with anti-SOX9 antibody (1:200) and protein G beads. The remaining supernatant was incubated with mouse IgG and protein G beads as a control. Input fraction DNAs, DNA fragments immunoprecipitated with endogenous SOX9, and DNAs in IgG controls were purified. PCR reactions were performed using the primer sets to amplify specific regions of COL2A1 promoter [19] and SOX9-binding COL2A1 enhancer [24] and allowed to proceed for 30 cycles.

2.6. Statistical analysis

All experiments were repeated three times and similar results were obtained. Data were expressed as means with standard deviations. Mean values were compared with ANOVA. Post hoc comparisons were performed using the Tukey test. Significance was set at $p < 0.05$.

3. Results

3.1. ROCKi influences cellular morphology, proliferation, and gene expression of human articular chondrocytes

Chondrocyte morphology varied from a spreading form to a round shape in a ROCKi-dependent manner (Fig. 1A). Also, the stress fiber formation was influenced by ROCKi (Fig. 1B). In addition, ROCKi treatment stimulated the proliferation of monolayer-cultured primary chondrocytes (Fig. 1C). The expression of chondrogenic marker genes, such as SOX9, SOX5/6, COL2A1, and aggrecan, was affected by ROCKi (Fig. 1, D–F). ROCKi treatment (1 μM, for

1 week) increased the expression of SOX9 and COL2A1 up to 5.3- and 3.8-fold levels of untreated controls, respectively (Fig. 1, E and F). However, the expression of a hypertrophic differentiation marker, COL10A1, was not stimulated by ROCKi treatment (Fig. 1D).

3.2. ROCKi prevents the dedifferentiation of monolayer-cultured chondrocytes

The expression level of SOX9, SOX5/6, COL2A1, and aggrecan was higher in ROCKi-treated chondrocytes than in untreated cells during monolayer culturing periods (Fig. 2A). Expression of SOX5/6 was maintained in the presence of ROCKi (1 μM) even in high-passaged chondrocytes (Fig. 2A). ROCKi-supplemented condition maintained SOX9 gene expression at a higher level in monolayer-cultured chondrocytes (Fig. 2B). In addition, the total amount of SOX9 protein was higher in ROCKi-treated chondrocytes compared with untreated cells (Fig. 2D). ROCKi treatment prevented the decrease of COL2A1 expression during the middle-term culture periods (Fig. 2C, passage 1 and 4). Continuous ROCKi treatment stimulated the proliferation of chondrocytes at passage 1 and 4 (Fig. 2E). However, the proliferative effect of ROCKi was gradually diminished on a parallel with the decrease of cellular proliferation in untreated chondrocytes (Fig. 2E). Chromatin IP analysis revealed that ROCKi promoted the association between SOX9 and the COL2A1 enhancer, which contains the SOX9-binding sequence, on chromatin in monolayer-cultured chondrocytes (Fig. 3).

3.3. ROCKi pretreatment enhances the redifferentiation of pellet-cultured chondrocytes

ROCKi pretreatment (1 μM) during monolayer culture influenced the gene expression of SOX9 and COL2A1 in pellet-cultured

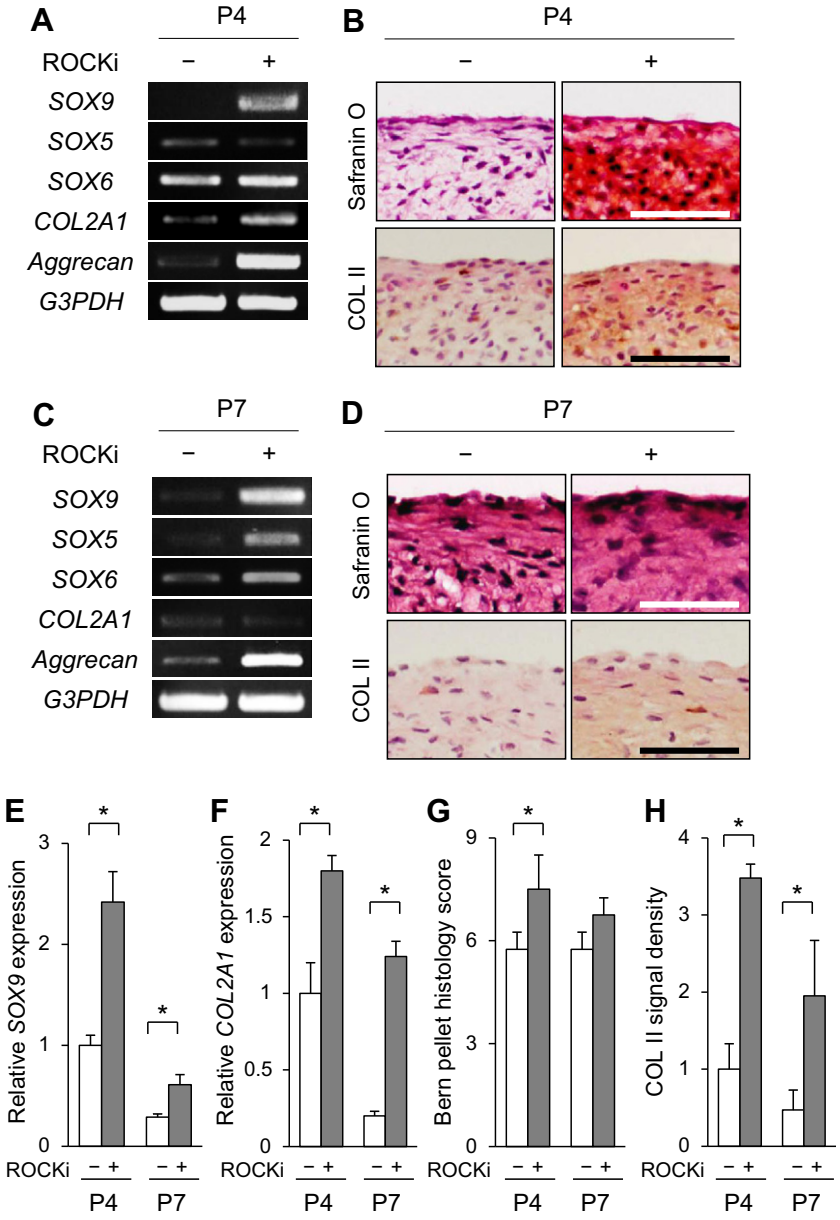

Fig. 4. ROCKi pretreatment enhances the redifferentiation of cultured chondrocytes. ROCKi pretreatment (1 μM) during monolayer culture enhanced the gene expression of SOX9 and COL2A1 in pellet-cultured chondrocytes (A, C, E, and F). The deposition of safranin O-stained proteoglycans (red) and type II collagen (COL II, brown) was highly observed in a pellet derived from ROCKi-pretreated chondrocytes (B and D). The Bern pellet histology score was higher in ROCKi-pretreated pellets than in untreated pellets (G, passage 4). Signal density of type II collagen deposition was also higher in ROCKi-pretreated pellets (H). Bars, 100 μm. $^{*}p < 0.05$. (For interpretation of the references to color in this figure legend, the reader is referred to the web version of this article.)

chondrocytes (Fig. 4, A, C, E, and F). Chondrogenic pellets derived from ROCKi-untreated chondrocytes showed a lower expression level of SOX9 and COL2A1 compared with those derived from ROCKi-pretreated chondrocytes (Fig. 4, A, C, E, and F). The deposition of safranin O-stained proteoglycans and type II collagen was highly detected in a pellet derived from ROCKi-pretreated chondrocytes (Fig. 4, B and D). The Bern pellet histology score was higher in ROCKi-pretreated cells than in untreated cells (Fig. 4G, passage 4). In addition, signal density of type II collagen deposition was higher in ROCKi-pretreated pellets compared with untreated pellets (Fig. 4H).

4. Discussion

The SOX E protein SOX9 regulates the expression of its target genes through association with the SOX9-binding DNA sequences (WWCAAWG) on promoters or enhancers of cartilage-specific genes such as COL2A1, α1(IX), α2(XI) collagen, aggrecan, cartilage link protein, and cartilage oligomeric matrix protein [27–29]. Heterozygous mutations in the SOX9 gene cause the congenital dwarfism syndrome, campomelic dysplasia [30]. On the other hand, Sox9 overexpression in chondrocytes also produces a phenotype of dwarfism [31]. These findings suggest that additional mechanisms such as SOX9-associating molecules and coactivators cooperatively regulate SOX9-dependent transcription during chondrogenesis, and that chondrocyte differentiation is not controlled by SOX9 alone [28,32]. The group D SOX5 and SOX6, which possess a leucine zipper and a coiled-coil domain, cooperate with SOX9 to activate the expression of COL2A1 and aggrecan genes [33]. The gene transactivation by SOX5/6 and SOX9 is much stronger than the activation by SOX9 alone, while SOX5 and SOX6 do not influence the activity of gene expression in the absence of SOX9. SOX5/6 may stabilize SOX9 on its binding site through the bending of DNA and thereby stimulate SOX9-regulated gene expression [28,34]. In our study, continuous ROCKi treatment stimulated the expression of SOX5/6 in high-passaged chondrocytes (Fig. 2A). In addition, COL2A1 expression was maintained at a higher level by ROCKi treatment in monolayer-cultured chondrocytes, compared with untreated chondrocytes (Fig. 2, A and C). These findings suggest that SOX9 and SOX5/6 cooperatively prevent the dedifferentiation of cultured chondrocytes, and positively regulate chondrogenic gene expression under the inhibition of ROCK signaling.

RhoA/ROCK signaling, which organizes the actin cytoskeleton, modulates the expression of SOX9 in several chondrocytic cells [14,15,35,36]. Sox9 expression is increased by ROCKi (Y-27632, 10 μM) in three-dimensional micromass cultures of mouse mesenchymal limb buds cells [14], whereas ROCKi decreases the Sox9 target gene expression including Col2a1 and aggrecan in micromass cultures via delayed and/or decreased phosphorylation of Sox9 [15]. ROCK inhibition (10 μM) in monolayer cultures of primary chondrocytes isolated from mouse embryonic growth plates enhances the expression of Col2a1 and aggrecan genes [15]. On the other hand, Sox9 expression is suppressed by 48-h-treatment of ROCKi (10 μM) in monolayer-cultured rat primary chondrocytes [37]. However, SOX9 phosphorylation and the activity of SOX9-related transcriptional complex under ROCK inhibition remain unclear in monolayer-cultured human articular chondrocytes. ROCKi (5 μM) prevents TGF-β-induced SOX9 phosphorylation and nuclear localization in human SW1353 chondrosarcoma cells [35]. In contrast, inhibition of RhoA/ROCK signaling by Rho antagonist C3 enhances the activity of Sox9-related transcriptional complex by increasing the expression of Sox9 and Sox5/6 in chicken embryo sternal chondrocytes [36]. We demonstrated that ROCK inhibition (1 μM) stimulated the expression of SOX9 and COL2A1 in monolayer-cultured human articular chondrocytes (Figs. 1 and 2). These findings suggest that the effects of ROCKi on SOX9 activation and chondrogenic gene expression may rely on the cellular context. In addition, several authors have reported that ROCK inhibition (Y-27632, 10 μM) reduces the proliferation of mouse ATDC5 cells (cultured for 10 days), rat chondrosarcoma cells (3 days), and 1-day-old rat primary chondrocytes (2 days) [16,37]. In our study, ROCKi treatment (0.1–10 μM, 48 h) stimulated the proliferation of human articular chondrocytes (Fig. 1C, passage 1). However, continuous ROCKi treatment (1 μM) did not affect cellular proliferation of high-passaged chondrocytes compared with untreated cells (Fig. 2E, passage 7). The discrepancy in cellular proliferation might be caused by the difference in cell species, ROCKi/serum concentration, and culture condition. Further investigations will be required to understand the precise mechanism of ROCK and other Rho GTPases in chondrocyte proliferation.

In conclusion, ROCKi treatment is a simple method that prevents chondrocyte dedifferentiation in the long-term monolayer culture, without inducing adverse effects such as hypertrophic differentiation and cell number reduction. ROCKi may be useful for preparation of sufficient number of articular cartilage-derived cells that maintain high chondrocytic properties in the application for cell-based clinical therapy and experimental research.

Declaration of interest

The authors have no conflicts of interest.

Acknowledgments

We thank Dr. Nobuhiro Abe and Ms. Aki Yoshida for their kind cooperation. This work was supported by Japan Society for the Promotion of Science (No. 20791040), JSPS Fujita Memorial Fund for Medical Research, Japan Orthopaedics and Traumatology Foundation (No. 225), and The Nakatomi Foundation.

References

[1] B.T. Bedi, R.J. Feeley, Williams 3rd, Management of articular cartilage defects of the knee, J. Bone Joint Surg. Am. 92 (2010) 994–1009.
[2] B.R. Mandelbau, J.E. Browne, F. Fu, et al., Articular cartilage lesions of the knee, Am. J. Sports Med. 26 (1998) 853–861.
[3] P.D. Gikas, W.J. Aston, T.W. Briggs, Autologous chondrocyte implantation: where do we stand now? J. Orthop. Sci. 13 (2008) 283–292.
[4] P.D. Benya, J.D. Shaffer, Dedifferentiated chondrocytes reexpress the differentiated collagen phenotype when cultured in agarose gels, Cell 30 (1982) 215–224.
[5] J. Bonaventure, N. Kadhom, L. Cohen-Solal, et al., Reexpression of cartilage-specific genes by dedifferentiated human articular chondrocytes cultured in alginate beads, Exp. Cell Res. 212 (1994) 97–104.
[6] D.G. Stokes, G. Liu, R. Dharmavaram, et al., Regulation of type-II collagen gene expression during human chondrocyte de-differentiation and recovery of chondrocyte-specific phenotype in culture involves Sry-type high-mobility-group box (SOX) transcription factors, Biochem. J. 360 (2001) 461–470.
[7] N. Takata, T. Furumatsu, N. Abe, et al., Comparison between loose fragment chondrocytes and condyle fibrochondrocytes in cellular proliferation and redifferentiation, J. Orthop. Sci. 16 (2011) 589–597.
[8] T. Takahashi, T. Ogasawara, J. Kishimoto, et al., Synergistic effects of FGF-2 with insulin or IGF-I on the proliferation of human auricular chondrocytes, Cell Transplant. 14 (2005) 683–693.
[9] G. Liu, H. Kawaguchi, T. Ogasawara, et al., Optimal combination of soluble factors for tissue engineering of permanent cartilage from cultured human chondrocytes, J. Biol. Chem. 282 (2007) 20407–20415.
[10] A.L. Bishop, A. Hall, Rho GTPases and their effector proteins, Biochem. J. 348 (2000) 241–255.
[11] K. Burridge, K. Wennerberg, Rho and Rac take center stage, Cell 116 (2004) 167–179.
[12] C.D. Nobes, A. Hall, Rho, rac, and cdc42 GTPases regulate the assembly of multimolecular focal complexes associated with actin stress fibers, lamellipodia, and filopodia, Cell 81 (1995) 53–62.
[13] P. Aspenström, Effectors for the Rho GTPases, Curr. Opin. Cell Biol. 11 (1999) 95–102.
[14] A. Woods, G. Wang, F. Beier, RhoA/ROCK signaling regulates Sox9 expression and actin organization during chondrogenesis, J. Biol. Chem. 280 (2005) 11626–11634.

[15] A. Woods, F. Beier, RhoA/ROCK signaling regulates chondrogenesis in a context-dependent manner, J. Biol. Chem. 281 (2006) 13134–13140.
[16] G. Wang, A. Woods, S. Sabari, et al., RhoA/ROCK signaling suppresses hypertrophic chondrocyte differentiation, J. Biol. Chem. 279 (2004) 13205–13214.
[17] H. Date, T. Furumatsu, Y. Sakoma, et al., GDF-5/7 and bFGF activate integrin α2-mediated cellular migration in rabbit ligament fibroblasts, J. Orthop. Res. 28 (2010) 225–231.
[18] Y. Miyake, T. Furumatsu, S. Kubota, et al., Mechanical stretch increases CCN2/CTGF expression in anterior cruciate ligament-derived cells, Biochem. Biophys. Res. Commun. 409 (2011) 247–252.
[19] T. Furumatsu, C. Shukunami, M. Amemiya-Kudo, et al., Scleraxis and E47 cooperatively regulate the Sox9-dependent transcription, Int. J. Biochem. Cell Biol. 42 (2010) 148–156.
[20] T. Furumatsu, T. Kanazawa, Y. Yokoyama, et al., Inner meniscus cells maintain higher chondrogenic phenotype compared with outer meniscus cells, Connect. Tissue Res. 52 (2011) 459–465.
[21] T. Tetsunaga, T. Furumatsu, N. Abe, et al., Mechanical stretch stimulates integrin αVβ3-mediated collagen expression in human anterior cruciate ligament cells, J. Biomech. 42 (2009) 2097–2103.
[22] T. Kanazawa, T. Furumatsu, M. Hachioji, et al., Mechanical stretch enhances COL2A1 expression on chromatin by inducing SOX9 nuclear translocalization in inner meniscus cells, J. Orthop. Res. 30 (2012) 468–474.
[23] K. Saiga, T. Furumatsu, A. Yoshida, et al., Combined use of bFGF and GDF-5 enhances the healing of medial collateral ligament injury, Biochem. Biophys. Res. Commun. 402 (2010) 329–334.
[24] T. Furumatsu, M. Tsuda, N. Taniguchi, et al., Smad3 induces chondrogenesis through the activation of SOX9 via CREB-binding protein/p300 recruitment, J. Biol. Chem. 280 (2005) 8343–8350.
[25] T. Furumatsu, M. Hachioji, K. Saiga, et al., Anterior cruciate ligament-derived cells have high chondrogenic potential, Biochem. Biophys. Res. Commun. 391 (2010) 1142–1147.
[26] S.P. Grogan, A. Barbero, V. Winkelmann, et al., Visual histological grading system for the evaluation of in vitro-generated neocartilage, Tissue Eng. 12 (2006) 2141–2149.
[27] Y. Kamachi, M. Uchikawa, H. Kondoh, Pairing SOX off: with partners in the regulation of embryonic development, Trends Genet. 16 (2000) 182–187.
[28] T. Furumatsu, H. Asahara, Histone acetylation influences the activity of Sox9-related transcriptional complex, Acta Med. Okayama 64 (2010) 351–357.
[29] T. Furumatsu, T. Ozaki, H. Asahara, Smad3 activates the Sox9-dependent transcription on chromatin, Int. J. Biochem. Cell Biol. 41 (2009) 1198–1204.
[30] T. Wagner, J. Wirth, J. Meyer, et al., Autosomal sex reversal and campomelic dysplasia are caused by mutations in and around the SRY-related gene SOX9, Cell 79 (1994) 1111–1120.
[31] H. Akiyama, J.P. Lyons, Y. Mori-Akiyama, et al., Interactions between Sox9 and β-catenin control chondrocyte differentiation, Genes Dev. 18 (2004) 1072–1087.
[32] T. Furumatsu, T. Ozaki, Epigenetic regulation in chondrogenesis, Acta Med. Okayama 64 (2010) 155–161.
[33] T. Ikeda, H. Kawaguchi, S. Kamekura, et al., Distinct roles of Sox5, Sox6, and Sox9 in different stages of chondrogenic differentiation, J. Bone Miner. Metab. 23 (2005) 337–340.
[34] M. Wegner, All purpose Sox: the many roles of Sox proteins in gene expression, Int. J. Biochem. Cell Biol. 42 (2010) 381–390.
[35] D.R. Haudenschild, J. Chen, N. Pang, et al., Rho kinase-dependent activation of SOX9 in chondrocytes, Arthritis Rheum. 62 (2010) 191–200.
[36] D. Kumar, A.B. Lassar, The transcriptional activity of Sox9 in chondrocytes is regulated by RhoA signaling and actin polymerization, Mol. Cell. Biol. 29 (2009) 4262–4273.
[37] C.T. Appleton, S.E. Usmani, J.S. Mort, et al., Rho/ROCK and MEK/ERK activation by transforming growth factor-α induces articular cartilage degradation, Lab. Invest. 90 (2010) 20–30.

Biochemical and Biophysical Research Communications 420 (2012) 130–135

Contents lists available at SciVerse ScienceDirect

Biochemical and Biophysical Research Communications

journal homepage: www.elsevier.com/locate/ybbrc

Methionine sulfoxide reductase B3 protects from endoplasmic reticulum stress in *Drosophila* and in mammalian cells

Geun-Hee Kwak [a], Do-Hwan Lim [b], Jee Yun Han [b], Young Sik Lee [b,*], Hwa-Young Kim [a,*]

[a] Department of Biochemistry and Molecular Biology, Yeungnam University College of Medicine, Daegu 705-717, Republic of Korea
[b] College of Life Sciences and Biotechnology, Korea University, Seoul 136-713, Republic of Korea

ARTICLE INFO

Article history:
Received 16 February 2012
Available online 3 March 2012

Keywords:
Methionine sulfoxide reductase
MsrB
ER stress
ER homeostasis
Unfolded protein response

ABSTRACT

Methionine sulfoxide reductase B3A (MsrB3A), which catalyzes the stereospecific reduction of methionine-*R*-sulfoxide to methionine, is localized to the endoplasmic reticulum (ER). Here, we report a critical role of the ER-targeted MsrB3 in protection against ER stress in *Drosophila* and in mammalian cells. Flies overexpressing human MsrB3A exhibited significantly increased resistance to ER stress induced by dithiothreitol. These flies also showed slightly enhanced resistance to tunicamycin-induced ER stress. In addition, overexpression of MsrB3A in mammalian cells increased resistance to dithiothreitol- and thapsigargin-induced ER stresses. However, MsrB3A overexpression had no effect on the resistance to tunicamycin-induced ER stress. Knockdown of MsrB3A in mammalian cells led to a significant decrease in the resistance to thapsigargin-induced ER stress, but had no effects on the resistance to either dithiothreitol- or tunicamycin-induced ER stress. Collectively, our data provide evidence that the ER-type of MsrB3 plays an important role in protection against ER stress, suggesting that MsrB3 may be involved in the regulation of ER homeostasis.

1. Introduction

Methionine sulfoxide reductases (Msrs) are oxidoreductases that catalyze the reduction of methionine sulfoxide to methionine [1–3]. Msrs are important enzymes repairing oxidatively damaged proteins. In addition, they play a critical defense role as antioxidants in scavenging reactive oxygen species (ROS). There are two Msr families with different substrate specificities for the reduction of oxidized methionine residues in proteins. MsrA is stereospecific for the reduction of methionine-*S*-sulfoxide, whereas MsrB only reduces the *R*-form.

In mammals, there is a single MsrA gene and its protein product is localized in mitochondria, cytosol, and nucleus [4–6]. By contrast, three MsrB genes (B1–B3) are expressed in mammals and each MsrB protein is targeted to different cellular compartments [7]. MsrB1 is present in the cytosol and nucleus. MsrB2 is targeted to mitochondria. In humans, there are two MsrB3 forms, MsrB3A and MsrB3B, generated by alternative splicing of the first exon. MsrB3A resides in the endoplasmic reticulum (ER), whereas MsrB3B is targeted to the mitochondria. However, in mice, no alternatively spliced forms of MsrB3 were found [8,9]. Mouse MsrB3 contains consecutive ER and mitochondrial targeting signals in the N-terminus, but the protein is targeted only to the ER [8]. The distinct cellular compartmentalization of Msr proteins in mammalian cells is suggested to maintain the methionine sulfoxide reduction system in different cellular compartments for repair of oxidatively damaged proteins, protection against oxidative stress, and regulation of protein function.

ER is an essential cellular compartment for protein folding. The perturbation of ER functions such as inhibition of glycosylation or disulfide bond formation leads to ER stress, which can result in accumulation of unfolded or misfolded proteins in the ER lumen [10]. An increase in ER stress can lead to the accumulation of intracellular ROS, which, in turn, contributes to accelerating ER stress [11,12]. The predominant localization of human MsrB3A to the ER raises the possibility of its potential function in a response to ER stress. In this work, we report that human MsrB3A in the ER has a protective function from ER stress in *Drosophila* and in mammalian cells, suggesting that MsrB3-catalyzed methionine sulfoxide reduction may be involved in the ER homeostasis.

2. Materials and methods

2.1. Drosophila strains

Two independent human MsrB3A (hMsrB3A) transgenic flies, *UAS-hMsrB3a[6A]* and *UAS-hMsrB3a[17C]*, were previously described [13]. *Daughterless* (*da*)-*GAL4* [*w**; *P{w*$^{+mW.hs}$ = *GAL4-da.G32}UH1*] and

* Corresponding authors. Addresses: College of Life Sciences and Biotechnology, Korea University, 145 Anam-ro, Seongbuk, Seoul 136-713, Republic of Korea. Fax: +82 2 926 9746 (Y.S. Lee), Department of Biochemistry and Molecular Biology, Yeungnam University College of Medicine, 170 Hyeonchungno, Namgu, Daegu 705-717, Republic of Korea. Fax: +82 53 654 6651 (H.-Y. Kim).
E-mail addresses: ys-lee@korea.ac.kr (Y.S. Lee), hykim@ynu.ac.kr (H.-Y. Kim).

0006-291X/$ - see front matter © 2012 Elsevier Inc. All rights reserved.
doi:10.1016/j.bbrc.2012.02.128

elav-GAL4 [*w*, *P{w*$^{+mW.hs}$ = *GawB}elav*^{C155}] driver lines were used to express the *UAS-hMsrB3a* transgene in the whole body and nervous system, respectively. The hMsrB3A transgenic and *GAL4* driver lines had been outcrossed six times to a w^{1118} strain obtained from the Bloomington Stock Center [13] and were used in this study. All experimental crosses were performed at 25 °C on standard cornmeal/agar media (6.3% cornmeal, 2.6% yeast, 6.3% molasses, 0.9% agar, 1.4% tegosept and 0.5% propionic acid) under non-crowded conditions.

2.2. ER stress tests in Drosophila

Each of the hMsrB3A transgenic lines was mated to isogenic *GAL4* drivers. Crosses were also made between isogenic *GAL4* drivers and the w^{1118} strain for a control. Progenies of the crosses were raised to adulthood at 25 °C. Flies of each genotype were collected in mixed-sex groups within 24 h of eclosion and aged at 29 °C until testing. Cohorts of 10-day-old male or female flies (20 per vial) were used for ER stress tests, each of which was repeated five times. Resistance to ER stress was assayed as described previously [14] with modifications. Flies of each genotype were first starved for 4 h in empty vials to avoid the variation arising from differential ingestion rates, and then transferred to a solid medium containing 1% agarose, 2% sucrose, and either 100 mM dithiothreitol (DTT) or 12 μM tunicamycin (all from Sigma–Aldrich). Survivors were counted periodically at 29 °C.

2.3. Construction of recombinant MsrB3A adenovirus

A coding region of hMsrB3A was PCR-amplified using p423-MsrB3A [15] as a template and inserted into *Sal*I/*Hind*III sites of pShuttle-CMV (Stratagene). The construct was verified by DNA sequencing and named pShuttle-HR3A. A recombinant MsrB3A adenovirus was generated with the construct pShuttle-HR3A using the AdEasy Adenoviral Vector System (Stratagene) according to the manufacturer's protocol [16]. The recombinant MsrB3A adenovirus was prepared using AD-293 cells (Stratagene) and was purified by CsCl density gradient centrifugation. The purified recombinant MsrB3A adenovirus was dialyzed against 10% glycerol in phosphate buffered saline (PBS) and stored at −80 °C until use. A control virus generated with pShuttle-CMV as described [16] was also prepared.

2.4. Mammalian cell culture

A549 and human dermal fibroblast (HDF) [17] cells were grown in RPMI and DMEM, respectively, supplemented with 10% fetal bovine serum and 100 U penicillin–streptomycin antibiotics at 37 °C in a 5% CO_2 incubator.

2.5. Virus infection

Cells were cultured for 16–20 h and the culture medium was replaced with a medium without antibiotics. Cells were infected with recombinant adenoviruses, unless noted otherwise, at a multiplicity of infection (MOI) of 100, and further incubated for 48 h.

2.6. siRNA-mediated knockdown of MsrB3

Cells were transfected with MsrB3 siRNA (sense, 5′-CUGGAAUUC GUAGGCUUCAdTdT-3′; antisense, 5′-UGAAGCCUACGAAUUCCAGdT dT-3′) using Lipofectamine 2000 (Invitrogen) according to the manufacturer's instructions. The transfected cells were cultured for additional 48 h. A control siRNA (sense, 5′-ACGUGACACGUUCGGAG AAUU-3′; antisense, 5′-UUCUCCGAACGUGUCACGUUU-3′) was also used.

2.7. MsrB activity assay

The reaction mixture (100 μl) for MsrB activity assay contained 50 mM sodium phosphate (pH 7.5), 50 mM NaCl, 20 mM DTT, 200 μM dabsyl-methionine-*R*-sulfoxide, and 200 μg crude protein. The reaction was carried out at 37 °C for 30 min and the product, dabsyl-Met, was analyzed by an established high-performance liquid chromatography (HPLC) procedure as described previously [18].

2.8. Western blot analysis

MsrB3 protein levels were analyzed using polyclonal anti-MsrB3 antibodies [8]. Glyceraldehyde 3-phosphate dehydrogenase (GAPDH) was used as a protein loading control.

2.9. Measurements of RNA levels by reverse transcription-PCR (RT-PCR)

Total RNA was extracted from cells with TRI-Solution (Bioscience) and quantified by measuring the absorbance at 260 nm. RT-PCR was performed using a Reverse Transcription Master Premix kit (ELPIS Biotech) containing the oligo-dT primer with the following primers: 5′-AACTGAGGAAGCGGCTAACA-3′ and 5′-ACAAGGCAG CCGAATTTATG-3′ for MsrB3, 5′-GATACTCATCTGGGTGGAGAAGAC-3′ and 5′-ACCATACGCTACAGCTTCATCTGG-3′ for BiP, and 5′-GGAGC CAAAAGGGTCATCAT-3′ and 5′-GTGATGGCATGGACTGTGGT-3′ for GAPDH. BiP was used for a marker of ER stress. GAPDH was used to normalize the amount of RNA in each sample. Quantitative analysis of mRNA levels was performed using the ImageJ software (NIH, USA).

2.10. ER stress tests in mammalian cells

The virus-infected or siRNA-transfected cells were treated with 0–1 mM DTT (MP Biomedicals) for 6 h, 0–5 μg/ml tunicamycin (Sigma–Aldrich) for 6 h, or 0–2 μM thapsigargin (Tocris Bioscience) for 24 h. Cell viability was analyzed using an established colorimetric 3-(4,5-dimethylthiazol-2-yl)-2,5-diphenyltetrazolium bromide (MTT)-based assay.

2.11. Oxidative stress test and measurement of protein–carbonyl content

The virus-infected A549 cells were treated with 0–300 μM H_2O_2 for 3 h. Cell viability was analyzed using the MTT assay. Protein–carbonyl content was measured using an OxyBlot protein oxidation detection kit (Chemicon International) according to the manufacture's protocol. The blot signals were quantified by densitometric analysis using the ImageJ software.

2.12. Statistical analyses

Survival curves of ER stress tests in *Drosophila* were analyzed with log-rank test. Viability of mammalian cells was analyzed using a Student's *t*-test. Prism 5 software (GraphPad) was used for the statistical analysis of data. A P value of <0.05 was considered significant.

3. Results

3.1. Overexpression of MsrB3A increases ER stress resistance in Drosophila

We have recently generated hMsrB3A transgenic flies and have shown that the hMsrB3A-overexpressing flies exhibited increased

resistance to paraquat-induced oxidative stress [13]. It should be noted that the *Drosophila* genome does not code for an ortholog of hMsrB3A [19]. Since hMsrB3A is predominantly localized to the ER in *Drosophila* cells [13], and oxidative stress can be linked to ER stress, we speculated potential functions of hMsrB3A in a response to ER stress. We first examined the resistance of hMsrB3A-overexpressing flies to ER stress induced by DTT, a strong reducing agent that causes the reductive state of the ER. Flies overexpressing hMsrB3A in the whole body displayed an increased resistance to DTT-induced ER stress in both males and females. The median survival of ubiquitously hMsrB3A-overexpressing flies was increased by 78% in males and by 43% in females, compared to the driver controls (Fig. 1A and B, and Table 1). Similarly, overexpression of hMsrB3A in neurons using the *elav-GAL4* driver increased the median survival of males and females by 24% and 16%, respectively, compared to the driver controls, in response to DTT-induced ER stress (Fig. 1C and D, and Table 1). In agreement with the ER localization of hMsrB3A in both *Drosophila* and human cells, these results suggest that hMsrB3A may have a protective function in response to increased unfolded or misfolded proteins generated by DTT-induced ER stress.

We further tested the effect of another ER stressor tunicamycin, a blocker of *N*-glycosylation of proteins, on the survival of flies. Overexpression of hMsrB3A in neurons led to a slightly but statistically significant increase in the resistance to tunicamycin-induced ER stress. The median survival of flies with neuron-specific hMsrB3A overexpression was increased by 7% in males and by 3% in females, compared to the driver controls (Supplementary Fig. S1 and Table 1).

3.2. Construction of MsrB3A-overexpressing adenovirus

To investigate the effects of MsrB3A on resistance to ER stress in mammalian cells, we generated an adenovirus-mediated hMsr B3A-overexpressing (Ad-MsrB3) construct. The overexpression of hMsrB3A mediated by Ad-MsrB3 in A549 cells was confirmed by Western blot analysis, compared with the MsrB3 level in the cells infected with the control virus (Ad-Con) (Fig. 2A). The expression levels of MsrB3A were increased along with increasing MOI of virus. Also, the functionality of hMsrB3A was confirmed by enzyme assay (Fig. 2B). Cells infected with Ad-MsrB3 showed increased MsrB activities up to threefold along with increasing MOI of virus at 48 h post-infection.

3.3. Overexpression of MsrB3A increases ER stress resistance in mammalian cells

To test the effect of hMsrB3A on resistance to ER stress, we chose A549 cells because the endogenous MsrB3 level was relatively low in these cells (the protein was hardly detectable by Western blot analysis as seen in Fig. 2A), when compared with other cell lines. Ad-MsrB3-infected cells had significantly increased resistance to DTT-induced ER stress compared with Ad-Con-infected cells (Fig. 3A). Overexpression of hMsrB3A enhanced the cell viability by 40% and 30% in the treatment of 0.5 and 1 mM DTT, respectively. However, hMsrB3A overexpression did not increase resistance to tunicamycin-induced ER stress (Fig. 3B). Thapsigargin is an ER stress agent that perturbs calcium homeostasis of the ER. We further tested whether hMsrB3A could protect cells from thapsigargin-induced ER stress. Interestingly, overexpression of hMsrB3A led to increased resistance to the ER stress (Fig. 3C). Collectively, the data showed that hMsrB3A overexpression enhances resistance to DTT- and thapsigargin-induced ER stresses in mammalian cells.

3.4. Overexpression of MsrB3A increases resistance to oxidative stress in mammalian cells

Next, we tested whether hMsrB3A overexpression in mammalian cells had a positive effect on resistance to oxidative stress.

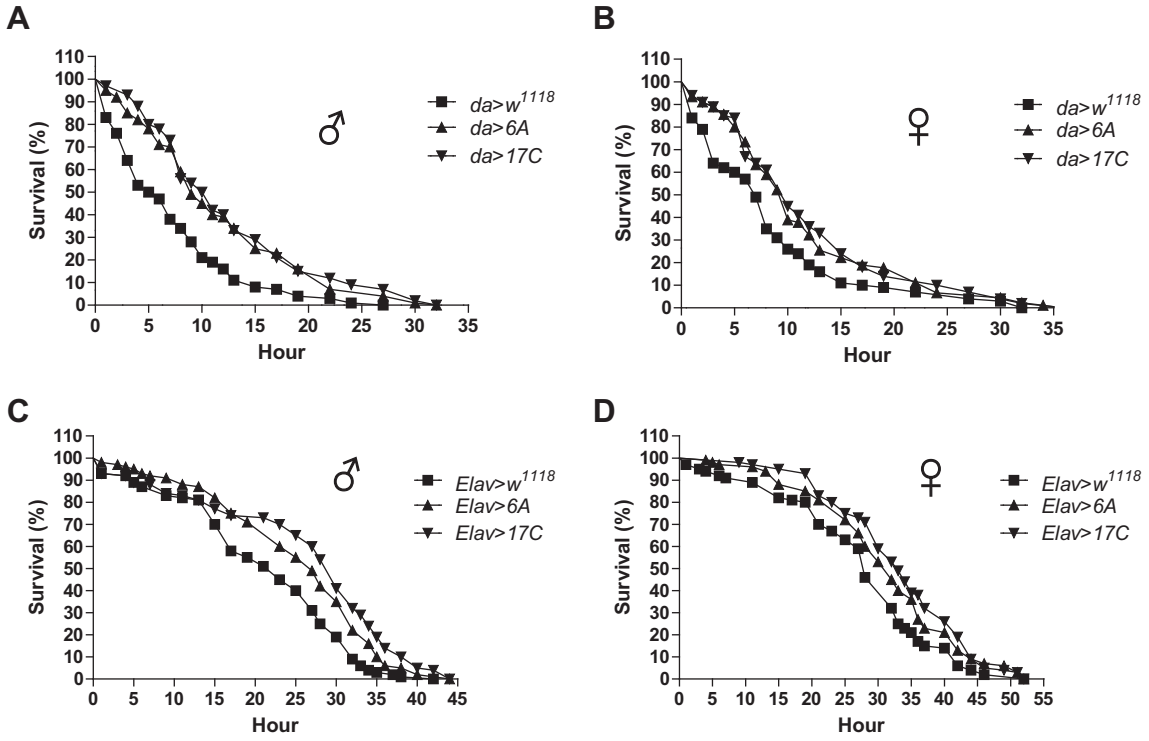

Fig. 1. Expression of hMsrB3A protects against DTT-induced ER stress in *Drosophila*. Ten-day-old male and female flies with ubiquitous (A and B) or neuronal (C and D) overexpression of hMsrB3A exhibit an increase in survival when fed with 100 mM DTT, compared with the age-matched driver control flies (n = 100/sex/genotype). Median survival for flies of each indicated genotype and statistical significance are indicated in Table 1.

Table 1
Statistical analysis of survival curves.

Stressor	Driver line		Median survival (h)			Statistical analysis (*P*-value)[a]	
			w^{1118}	[6A]	[17C]	[6A]	[17C]
DTT	*da-GAL4*	Male	5.5	9	10.5	<0.0001	<0.0001
		Female	7	10	10	0.0092	0.0020
	elav-GAL4	Male	23	27	30	0.0009	<0.0001
		Female	28	32	33	0.0372	0.0014
Tunicamycin	*elav-GAL4*	Male	119	126	128.5	0.0017	0.0004
		Female	107.5	111.5	110	0.0010	0.0011

[a] Statistical analysis using log-rank test.

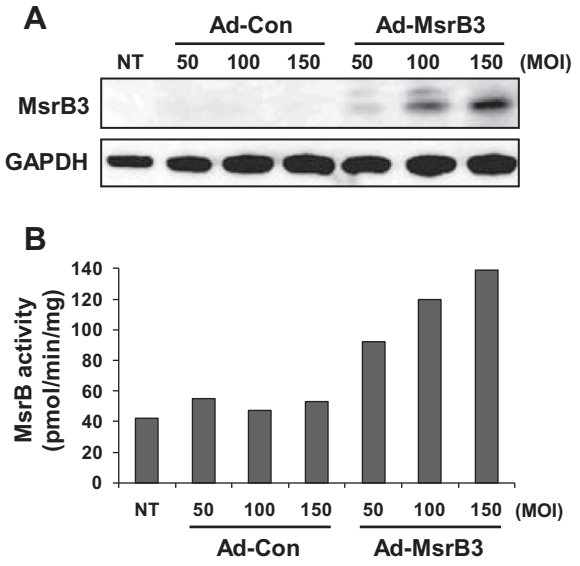

Fig. 2. Construction of MsrB3A-overexpressing adenovirus. A549 cells were infected with hMsrB3A-overexpressing (Ad-MsrB3) or control (Ad-Con) adenoviruses at the indicated MOI for 48 h. (A) Western blot analysis for MsrB3 protein levels. (B) MsrB activity assay. NT, not treated.

When treated with H_2O_2, Ad-MsrB3-infected A549 cells showed significantly increased viability, compared to the Ad-Con-infected cells (Supplementary Fig. S2A). These results suggest that hMsrB3A in the ER can protect against H_2O_2-induced oxidative stress. Protein–carbonyl content is generally used as a marker of oxidative stress. Accordingly, >twofold increase in the protein–carbonyl content was observed when treated with 300 μM H_2O_2 for 3 h (Supplementary Fig. S2B). Under this oxidative condition, however, the protein–carbonyl content was significantly lower in the Ad-MsrB3-infected cells compared with that in the Ad-Con-infected cells (Supplementary Fig. S2B), indicating that hMsrB3A overexpression reduced H_2O_2-induced oxidative stress.

3.5. Down-regulation of MsrB3 increases sensitivity to thapsigargin-induced ER stress

We also investigated the effect of MsrB3 deficiency on resistance to ER stress using siRNA-mediated knockdown. Efficiency of the siRNA-mediated MsrB3 knockdown in A549 cells was analyzed by RT-PCR because the MsrB3 protein was hardly detectable by Western blot analysis. Notably, the MsrB3-targeting siRNA (siMsrB3) used could affect the expression of both MsrB3A and MsrB3B forms. A significant decrease in a total of MsrB3 expression level was observed in siMsrB3-transfected A549 cells (Fig. 4A). As mentioned above, overexpression of hMsrB3A showed a positive effect on the resistance to DTT-induced ER stress in A549 cells. In contrast, MsrB3 knockdown had no negative effect on resistance to the same ER stress (Fig. 4B). Additionally, it did not affect resistance to tunicamycin-induced ER stress (Fig. 4C). However, the MsrB3 knockdown led to a significantly elevated sensitivity to thapsigargin-induced ER stress (Fig. 4D). We further observed that knockdown of MsrB3 in primary HDF cells also increased their sensitivity to thapsigargin-induced ER stress (Supplementary Fig. S3). Together, the data

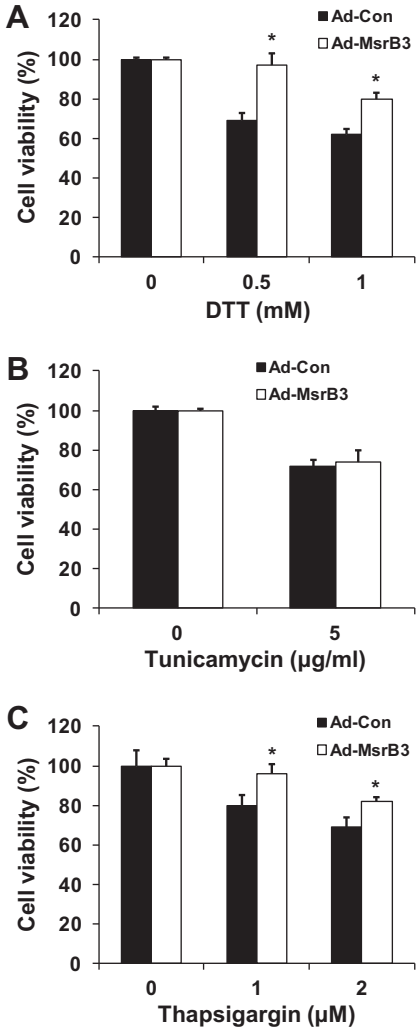

Fig. 3. Effects of MsrB3A overexpression on the resistance of A549 cells to ER stress. Cells were infected with recombinant adenoviruses at an MOI of 100 for 48 h. The virus-infected cells were then treated with DTT for 6 h (A), tunicamycin for 6 h (B), or thapsigargin for 24 h (C) at the indicated concentrations. Cell viability was analyzed by the MTT assay. Data are shown as mean ± SEM from three independent experiments (*$P < 0.05$ vs the control). Ad-Con, control virus; Ad-MsrB3, hMsrB3A-overexpressing virus.

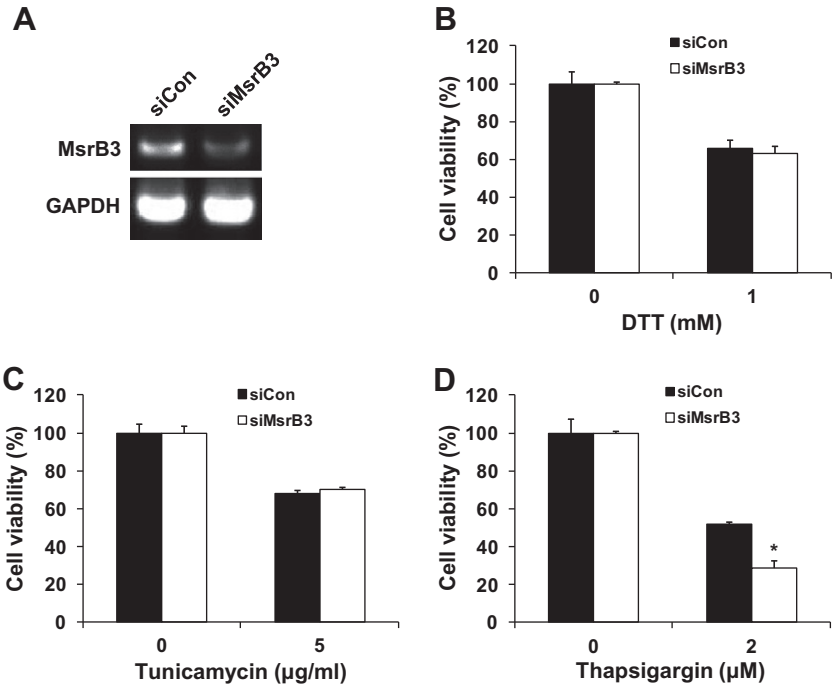

Fig. 4. Effects of MsrB3 knockdown on ER stress resistance in A549 cells. Cells were transfected with MsrB3-targeting (siMsrB3) or control (siCon) siRNAs for 48 h. MsrB3 mRNA levels were analyzed by RT-PCR (A). The cells at 48 h post-transfection were treated with DTT for 6 h (B), tunicamycin for 6 h (C), or thapsigargin for 24 h (D) at the indicated concentrations. Cell viability was analyzed by the MTT assay. Data are shown as mean ± SEM from three independent experiments (*$P < 0.05$ vs the control).

demonstrated that down-regulation of MsrB3 causes cells to be hypersensitive to ER stress induced by thapsigargin.

4. Discussion

MsrB functions as a protein repair enzyme that reduces methionine-*R*-sulfoxide residues and plays an antioxidant defense role in cells [15,20,21]. Here, to our best knowledge, we report for the first time that MsrB is involved in the ER functions. Given that hMsrB3A is targeted to the ER, and ER stress is associated with oxidative stress [12], we investigated a potential role of hMsrB3A in protection against ER stress in *Drosophila* and in mammalian cells. The hMsrB3A-expressing flies showed a significantly increased survival against DTT-induced ER stress. In addition, expression of hMsrB3A in *Drosophila* led to a slightly increased survival with statistical significance against tunicamycin-induced ER stress. Thus, our data demonstrated that hMsrB3A in the ER plays a protective function from ER stress in *Drosophila*.

In agreement with the positive effect of hMsrB3A on resistance to DTT-induced ER stress in *Drosophila*, overexpression of hMsrB3A in human A549 cells resulted in significantly increased viability against the same ER stress. However, there was no positive effect of hMsrB3A expression against tunicamycin-induced ER stress in these cells. Instead, hMsrB3A overexpression increased viability of A549 cells in response to thapsigargin-induced ER stress. In addition, we investigated the role of MsrB3 in protection against ER stress by knocking down its expression. Depletion of MsrB3 led to decreased viability of A549 cells under thapsigargin-induced ER stress condition, but did not affect cell viability in response to either DTT- or tunicamycin-induced ER stress. The negative effect of MsrB3 knockdown on viability was also observed in HDF cells under the thapsigargin-induced ER stress condition. Collectively, the data revealed that the ER-type MsrB3 protects mammalian cells from ER stresses induced by DTT and thapsigargin. Although MsrB3 may play an important role in repairing oxidized proteins that accumulate in the ER under stress conditions, further studies are needed to understand the molecular basis for the roles of MsrB3 in the ER functions.

DTT is a strong reducing agent that inhibits disulfide bond formation of proteins in the ER, tunicamycin blocks *N*-glycosylation of proteins in the ER, and thapsigargin blocks calcium influx into the ER. All these agents induce unfolded protein response (UPR). UPR is an essential adaptive response to ER stress, including translational attenuation of global protein synthesis, transcriptional induction of UPR genes such as molecular chaperones and folding enzymes, and ER-associated degradation of unfolded or misfolded proteins [10,11]. Our data suggest that the function of MsrB3 in the ER may be directly implicated in UPR.

Calcium homeostasis in the ER is essential for the ER functions including proper protein folding [11,22]. An accumulation of misfolded proteins in the ER can induce leak of calcium from the ER. As a result, calcium is concentrated in the mitochondria and causes disruption of mitochondrial membrane potential, leading to increasing ROS production. Presently, MsrB3 in mammalian cells had a protective effect against ER stress induced by thapsigargin, which perturbs calcium homeostasis of the ER. Therefore, our data also suggest that MsrB3 may be associated with regulation of calcium homeostasis in the ER.

Acknowledgments

This work was supported by the National Research Foundation of Korea Grants 2010-0001240 and 2010-0020596 (to H.-Y.K.), and by Mid-career Researcher Program through NRF grant funded by the MEST (2011-0016863 to Y.S.L.). D.H.L. was supported by Hi Seoul Science/Humanities Fellowship from Seoul Scholarship Foundation.

Appendix A. Supplementary data

Supplementary data associated with this article can be found, in the online version, at doi:10.1016/j.bbrc.2012.02.128.

References

[1] H.Y. Kim, V.N. Gladyshev, Methionine sulfoxide reductases: selenoprotein forms and roles in antioxidant protein repair in mammals, Biochem. J. 407 (2007) 321–329.

[2] J. Moskovitz, Methionine sulfoxide reductases: ubiquitous enzymes involved in antioxidant defense, protein regulation, and prevention of aging-associated diseases, Biochim. Biophys. Acta 1703 (2005) 213–219.

[3] X.H. Zhang, H. Weissbach, Origin and evolution of the protein-repairing enzymes methionine sulphoxide reductases, Biol. Rev. Camb. Philos. Soc. 83 (2008) 249–257.

[4] H.Y. Kim, V.N. Gladyshev, Role of structural and functional elements of mouse methionine-*S*-sulfoxide reductase in its subcellular distribution, Biochemistry 44 (2005) 8059–8067.

[5] G. Kim, N.B. Cole, J.C. Lim, H. Zhao, R.L. Levine, Dual sites of protein initiation control the localization and myristoylation of methionine sulfoxide reductase A, J. Biol. Chem. 285 (2010) 18085–18094.

[6] S. Vougier, J. Mary, B. Friguet, Subcellular localization of methionine sulphoxide reductase A (MsrA): evidence for mitochondrial and cytosolic isoforms in rat liver cells, Biochem. J. 373 (2003) 531–537.

[7] H.Y. Kim, V.N. Gladyshev, Methionine sulfoxide reduction in mammals: characterization of methionine-*R*-sulfoxide reductases, Mol. Biol. Cell 15 (2004) 1055–1064.

[8] H.Y. Kim, V.N. Gladyshev, Characterization of mouse endoplasmic reticulum methionine-*R*-sulfoxide reductase, Biochem. Biophys. Res. Commun. 320 (2004) 1277–1283.

[9] Z.M. Ahmed, R. Yousaf, B.C. Lee, S.N. Khan, S. Lee, K. Lee, T. Husnain, A.U. Rehman, S. Bonneux, M. Ansar, W. Ahmad, S.M. Leal, V.N. Gladyshev, I.A. Belyantseva, G. Van Camp, S. Riazuddin, T.B. Friedman, S. Riazuddin, Functional null mutations of MSRB3 encoding methionine sulfoxide reductase are associated with human deafness DFNB74, Am. J. Hum. Genet. 88 (2011) 19–29.

[10] C.Y. Liu, R.J. Kaufman, The unfolded protein response, J. Cell Sci. 116 (2003) 1861–1862.

[11] K. Zhang, R.J. Kaufman, From endoplasmic-reticulum stress to the inflammatory response, Nature 454 (2008) 455–462.

[12] J.D. Malhotra, R.J. Kaufman, Endoplasmic reticulum stress and oxidative stress: a vicious cycle or a double-edged sword?, Antioxid Redox Signaling 9 (2007) 2277–2293.

[13] D.H. Lim, JY. Han, J.R. Kim, Y.S. Lee, H.Y. Kim, Methionine sulfoxide reductase B in the endoplasmic reticulum is critical for stress resistance and aging in Drosophila, Biochem. Biophys. Res. Commun. 419 (2012) 20–26.

[14] I.E. Clark, M.W. Dodson, C. Jiang, J.H. Cao, J.R. Huh, J.H. Seol, S.J. Yoo, B.A. Hay, M. Guo, Drosophila pink1 is required for mitochondrial function and interacts genetically with parkin, Nature 441 (2006) 1162–1166.

[15] G.H. Kwak, J.R. Kim, H.Y. Kim, Expression, subcellular localization, and antioxidant role of mammalian methionine sulfoxide reductases in *Saccharomyces cerevisiae*, BMB Rep. 42 (2009) 113–118.

[16] S.H. Choi, H.Y. Kim, Methionine sulfoxide reductase A regulates cell growth through the p53–p21 pathway, Biochem. Biophys. Res. Commun. 416 (2011) 70–75.

[17] H.J. Kim, J.H. Cho, H. Quan, J.R. Kim, Down-regulation of Aurora B kinase induces cellular senescence in human fibroblasts and endothelial cells through a p53-dependent pathway, FEBS Lett. 585 (2011) 3569–3576.

[18] R.A. Kumar, A. Koc, R.L. Cerny, V.N. Gladyshev, Reaction mechanism evolutionary analysis and role of zinc in Drosophila methionine-*R*-sulfoxide reductase, J. Biol. Chem. 277 (2002) 37527–37535.

[19] H.Y. Kim, V.N. Gladyshev, Alternative first exon splicing regulates subcellular distribution of methionine sulfoxide reductases, BMC Mol. Biol. 7 (2006) 11.

[20] J. Moskovitz, E. Flescher, B.S. Berlett, J. Azare, J.M. Poston, E.R. Stadtman, Overexpression of peptide-methionine sulfoxide reductase in *Saccharomyces cerevisiae* and human T cells provides them with high resistance to oxidative stress, Proc. Natl. Acad. Sci. USA 95 (1998) 14071–14075.

[21] F. Cabreiro, C.R. Picot, M. Perichon, J. Castel, B. Friguet, I. Petropoulos, Overexpression of mitochondrial methionine sulfoxide reductase B2 protects leukemia cells from oxidative stress-induced cell death and protein damage, J. Biol. Chem. 283 (2008) 16673–16681.

[22] A. Gorlach, P. Klappa, T. Kietzmann, The endoplasmic reticulum: folding, calcium homeostasis, signaling, and redox control, Antioxid. Redox Signaling 8 (2006) 1391–1418.

Biochemical and Biophysical Research Communications 420 (2012) 136–140

Contents lists available at SciVerse ScienceDirect

Biochemical and Biophysical Research Communications

journal homepage: www.elsevier.com/locate/ybbrc

Peptide–surfactant interactions: Consequences for the amyloid-beta structure

Sandra Rocha [a,*], Joana A. Loureiro [a], Gerald Brezesinski [b], Maria do Carmo Pereira [a]

[a] LEPAE, Department of Chemical Engineering, Faculty of Engineering, University of Porto, Rua Roberto Frias, Porto, Portugal
[b] Max Planck Institute of Colloids and Interfaces, Science Park Potsdam-Golm, Potsdam, Germany

ARTICLE INFO

Article history:
Received 10 February 2012
Available online 3 March 2012

Keywords:
Conformation
Amyloid-beta peptide
Surfactants
Micelles
Sulfate monolayers
Electrostatic interactions
Hydrophobic effect

ABSTRACT

The conformation of amyloid-beta peptide (Aβ) determines if toxic aggregates are formed. The peptide structure by its turn depends on the environment and molecule–molecule interactions. We characterized the secondary structure of Aβ-(1–40) in surfactant solutions and interacting with monolayers. The peptide adopts β-sheet structure in solutions of ionic surfactants at sub-micelle concentrations and α-helix in the presence of ionic micelles. Uncharged micelles induce β-sheets. Aβ-(1–40) alters the critical micelle concentration value of the non-ionic surfactant, underlining hydrophobic interactions. At ionic monolayers the peptide forms β-sheets when its concentration at the surface is high enough. These results suggest that only electrostatic interactions of charged micelles that surround completely the peptide are able to induce non-aggregated α-helix structure.

1. Introduction

Secondary structure alterations and aggregation of amyloid beta-peptide (Aβ) are related to Alzheimer's disease (AD) [1]. The peptide is aggregated as amyloid fibrils within the neuritic plaques and vascular deposits that characterize the disease [2,3]. In this state Aβ is in a beta-sheet conformation, which is usually stabilized by protein aggregation since the hydrogen bonds are between CO and NH groups of different strands. Aβ is a normal metabolic product of enzymatic processing of a transmembranar protein, the amyloid precursor protein, resulting in two principal sequence lengths with 40 and 42 amino acids [4]. The sequence of 40 residues is normally the more abundantly produced by cells (concentration of secreted $A\beta_{42}$ is 10-fold lower that of $A\beta_{40}$) and its aggregation kinetic rate is much lower than that of the 42 ($A\beta_{40}$ at 20 μM is stable for 8 days or more whereas $A\beta_{42}$ aggregates immediately) [5,6]. The ratio $A\beta_{42}/A\beta_{40}$ has been related to the progression of AD as its increasing is associated to oligomerization of $A\beta_{42}$ and consequently neurotoxicity [7]. $A\beta_{40}$ monomers inhibit the aggregation of $A\beta_{42}/A\beta_{40}$ mixtures (in a concentration-dependent manner), whereas $A\beta_{40}$ fibrils accelerate their fibrillogenesis [8,9]. The $A\beta_{42}$ also affects the aggregation of the mixture by accelerating the process. The factors that lead to the *in vivo* aggregation of amyloid peptides can be numerous and are difficult to identify. An important feature is the conformation of soluble oligomers (smaller intermediates in the aggregation process) which is common for several different amyloid-prone synthetic protein [10]. Since $A\beta_{40}$ affects the aggregation of the more toxic sequence ($A\beta_{42}$) its structural changes need to be better understood and controlled. This work relates to the study of the structure of $A\beta_{40}$ in the presence of amphiphilic molecules. $A\beta_{40}$ adopts α-helix structure in solutions of negatively charged sodium dodecyl sulfate (SDS) micelles [11–13]. But if SDS concentrations are below the critical micelle concentration (CMC), the peptide forms β-sheets [13–16]. Notably, vesicles of negatively charged phospholipids have a concentration-dependence effect on $A\beta_{40}$ structure: they induce β-sheet at lipid-to-peptide ratios below 30, and helix at higher ratios [17]. We report the structure of $A\beta_{40}$ low molecular weight species when interacting with cationic, anionic perfluorinated and non-ionic surfactants (Fig. 1), and the effect of the peptide on their CMC. With this study, the influence of charged/non-ionic head group and of fluorinated chains is addressed to characterize the interaction forces that might be involved on the stabilization of $A\beta_{40}$ secondary structures by amphiphiles and to screen for molecules that can induce a non-aggregated stable state.

2. Materials and methods

2.1. $A\beta_{40}$ solution

$A\beta_{40}$ (amyloid-β peptide 1–40, purity 96%, MW 4329.90, Genic-Bio Limited) was dissolved in HFIP (1,1,1,3,3,3-hexafluoro-2-propanol, ⩾99.8%, Sigma–Aldrich) at a concentration of 1 mg/mL. This pre-treatment was performed to improve peptide solubility and disaggregate pre-formed agglomerates. HFIP was evaporated

* Corresponding author. Address: Faculty of Engineering, University of Porto, Rua, Dr. Roberto Frias, 4200-465 Porto, Portugal. Fax: +351 225081449.
E-mail address: sandra.rocha@fe.up.pt (S. Rocha).

0006-291X/$ - see front matter © 2012 Elsevier Inc. All rights reserved.
http://dx.doi.org/10.1016/j.bbrc.2012.02.129

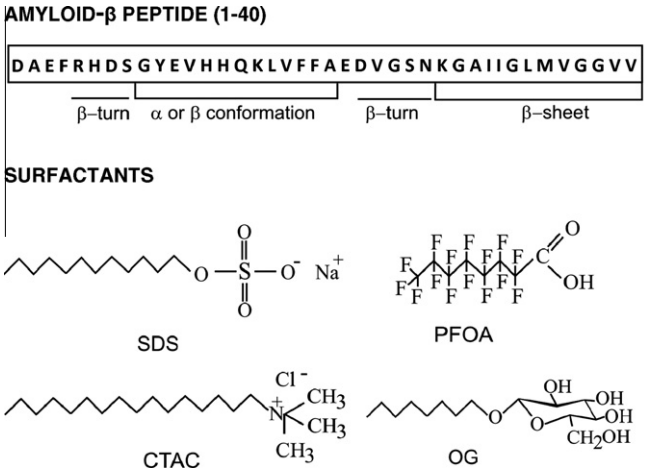

Fig. 1. The sequence of amyloid-β peptide (1–40) showing structure prediction [27] and the chemical structure of the surfactants used in this study.

with nitrogen flow and the peptide film was dissolved in Hepes buffer (10 mM, pH 7.4) at a concentration of 1 mg/mL.

2.2. Surfactants

Stock solutions of surfactants were prepared by dissolving CTAC (cetyltrimethylammonium chloride, 25 wt.% sol. in water, MW 320.01, Sigma–Aldrich); OG (octyl β-D-glucopyranoside, ⩾98%, MW 292.37, Sigma–Aldrich); SDS (sodium dodecyl sulfate, ⩾98.5%, MW 288.38, Sigma–Aldrich) or PFOA (pentadecafluorooctanoic acid, 96%, MW 414.06, Sigma–Aldrich) in Hepes buffer 10 mM, pH 7.4 (HEPES hemisodium salt, ⩾99%, Sigma–Aldrich). Arachidyl sulfate (AS, sodium salt, Sigma–Aldrich) was dissolved in chloroform–methanol (4:1 w/w) at a concentration of 1 mM.

2.3. Circular dichroism (CD) spectroscopy

CD spectra of $A\beta_{40}$ in solutions of different surfactant concentrations were recorded in a quartz cell of 0.05 cm path length at a temperature of 20 ± 1 °C with a Jasco spectropolarimeter (Model J-715). Spectra were obtained at 0.2 nm intervals from 190 to 260 nm by averaging 8–10 scans. All spectra were corrected by subtracting the buffer/surfactant baseline. The secondary structure content was estimated using the method CONTIN/LL [18].

2.4. Surface tension and conductivity measurements

The critical micelle concentration (CMC) of surfactants was determined at room temperature in the presence and absence of $A\beta_{40}$ by surface tension measurements (OG and CTAC) and conductivity (SDS and PFOA). The concentration of $A\beta_{40}$ was constant (46 μM). Surface tension method was carried out by the hanging drop method using an optical contact angle system (OCA 15 plus) and conductivity was measured using a Crison GLP 31 conductivimeter.

2.5. Infrared reflection absorption spectroscopy (IRRAS)

Langmuir monolayers of AS were prepared by spreading 40 μL of the stock solution at the buffer surface (Hepes pH 7.4, 100 mM NaCl). The chloroform was let to evaporate for at least 1 h. For $A\beta_{40}$ adsorption studies, the peptide was dissolved in the subphase (buffer) at a concentration of 0.185 μM. IRRA spectra were recorded on an IFS66 FTIR spectrometer (Bruker, Germany) fitted with a liquid nitrogen-cooled mercury cadmium telluride detector and the XA511 external reflection accessory. The angle of incidence of the infrared beam was 40° with respect to the surface normal and the IR beam was polarized by a BaF_2 polarizer. FTIR spectra were collected with s-polarized light (polariser perpendicular to the plane of incidence) at a resolution of 8 cm^{-1} with 200 scans and subtracted to the spectrum of the reference trough (filled with buffer).

3. Results

3.1. $A\beta_{40}$ in amphiphile solutions

The CMC of the surfactants dissolved in Hepes buffer is 6.9 mM for SDS, 12.2 mM for PFOA, 0.9 mM for CTAC and 22.4 mM for OG (Table 1). The presence of $A\beta_{40}$ does not change the CMC of charged surfactants (SDS, PFOA, CTAC) significantly but it increases the value of the non-ionic amphiphile (OG) to 28.2 mM. This variation was statistically significant as determined by *t*-Student test ($P < 0.01$).

In aqueous buffer, pH 7.4, $A\beta_{40}$ (46 μM) is mainly in unordered (49%) and β-sheet (34%) conformations, as determined by CD spectroscopy (Figs. 2 and 3). The CD spectrum of the peptide in ionic surfactant solutions is characteristic of β-sheet structure, if the surfactant concentrations are below the CMC (Fig. 2). At concentrations close to the CMC or above, the surfactants induce α-helix structure (Fig. 2). Quantitative analysis of the fraction of secondary structures shows substantial 45% of β-sheet structure induced by sub-micelle concentrations of SDS (1.7 mM), in contrast to 24% in the presence of micelles (Fig. 3). The increase of α-helix content by PFOA at micelle concentrations is more significant when compared to the effect of SDS and is due to a decrease of both random coil and β-sheet contents (Fig. 3). The cationic amphiphile CTAC induces changes on $A\beta_{40}$ at much lower concentrations when compared to the anionic surfactants (Figs. 2 and 3), which is explained by its lower CMC value owed to its longer hydrocarbon chain (Fig. 1). Non-ionic amphiphile at sub-micelle concentrations has no significant influence on $A\beta_{40}$. However, at concentrations above the CMC, spectra are characteristic of β-sheet conformation (Fig. 2). The β-sheet structure might be twisted since the spectrum has the $\pi\pi^*$ band near 195 nm much stronger than the $n\pi^*$ band [19]. Further increase of the concentration results in a small increase of the band intensities with a red shift. This might be due to either an increase of β-turn content (type II has a spectrum similar to the β-sheet shifted to the red) or an increase of the number of strands. The position of the $\pi\pi^*$ absorption band depends on the width of the sheet, strongly shifted to the blue in single or double strand sheet, but shifting to longer wavelengths with increasing number of strands [19]. Since the shift is observed mainly for the positive band near 195 nm, it is most likely that increasing the micelle concentration leads to an increase of the number of strands (Fig. 3).

3.2. $A\beta_{40}$ at amphiphile monolayers

The interaction of $A\beta_{40}$ with highly negatively charged monolayers was studied in saline buffer (Hepes pH 7.4, 100 mM NaCl)

Table 1
Critical micelle concentration of surfactants in Hepes buffer (10 mM) in the absence and presence of amyloid-β peptide (1–40) (46 μM).

	Surfactant (mM)	Surfactant + $A\beta_{40}$ (mM)
SDS	6.9 ± 0.3	6.4 ± 0.2
PFOA	12.2 ± 0.3	12.0 ± 0.2
CTAC	0.9 ± 0.2	0.8 ± 0.2
OG	22.4 ± 0.1	28.2 ± 0.9

SDS, sodium dodecyl sulfate; PFOA, pentadecafluorooctanoic acid; CTAC, cetyltrimethylammonium chloride; OG, octyl β-D-glucopyranoside.

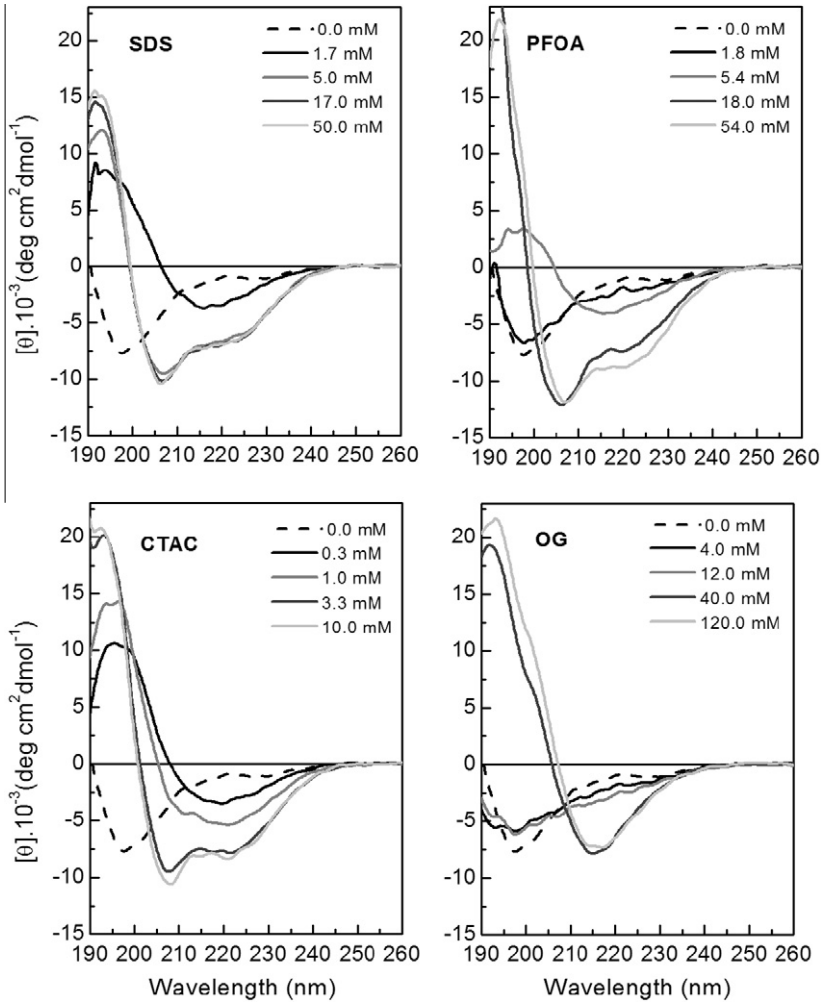

Fig. 2. Circular dichroism spectra of amyloid-β peptide (1–40) (46 μM) in surfactant solutions: SDS (sodium dodecyl sulfate), PFOA (pentadecafluorooctanoic acid), CTAC (cetyltrimethylammonium chloride) and OG (octyl β-D-glucopyranoside) at different concentrations.

by IRRAS to detect the peptide at the interface in moderate ionic strength conditions. During $A\beta_{40}$ adsorption to uncompressed arachidyl sulfate (AS) monolayer, the amide I (1700–1620 cm^{-1}) and amide II (1580–1520 cm^{-1}) bands appear (Fig. 4A). The amide I arises from coupled vibrational modes of C=O stretching of polypeptide backbone and is sensitive to the secondary structure. Amide II band results from C–N stretching and N–H bending vibrations. The most intense band in the amide I region is at 1624 cm^{-1} after 37 min adsorption time and shifts slightly to 1629 cm^{-1} after 4 h, with a shoulder at 1690 cm^{-1}, characteristic of antiparallel β-sheet conformation [20,21]. In the case of β-sheets the amide I splits into two components. The shift of the band at 1624 cm^{-1} to higher values with increasing adsorption time indicates stack beta-sheets [22]. A shoulder of the amide I in the 1648–1658 cm^{-1} region indicates small amount of unordered or α-helix and is more pronounced at the beginning of the adsorption. During Aβ adsorption, the surface pressure increases and reaches a final value of 18 mN m^{-1}, caused by the peptide penetration into the areas not occupied by the surfactant molecules and compression of the monolayer. If then the monolayer is compressed to 30 mN m^{-1}, the peptide is squeezed out and desorbs completely as indicated by the disappearance of the amide I and II bands (Fig. 4A). Similar behavior was described for zwitterionic and charged lipids that form condensed monolayers on saline buffer surface [20,21,23]. The interaction of $A\beta_{40}$ with lipid monolayers at high surface pressures ($\geqslant$30 mN m^{-1}) is however not prevented in the case of charged condensed monolayers if the ionic strength is low (water) or in the case of disordered fluid anionic monolayers independent of the ionic strength [20,23]. This stresses the importance of electrostatic and hydrophobic interactions between the peptide and charged surfactants. $A\beta_{40}$ is surface active and adsorbs to the pure air/water interface [24,25]. The spectrum of the peptide adsorbed at the monolayer after subtraction of the spectrum of the surfactant is very similar to that of $A\beta_{40}$ at the air/buffer interface and is characteristic of β-sheets (Fig. 4B).

4. Discussion

Structure prediction studies of Aβ indicate two β-turns between residues 5 and 8, and residues 23 and 27 [26,27]. The two hydrophobic domains, residues 17–21 and 30–40, may adopt both α-helix and β-sheet conformation depending on environmental conditions (Fig. 1). Most works, including nuclear magnetic resonance (NMR) studies, which are usually performed at low ionic strength, describe the structure of $A\beta_{40}$ monomers in aqueous solutions as unordered [26,28]. In saline solutions (e.g. 50 or 100 mM NaCl, pH 7) $A\beta_{40}$ monomers are partially helical, indicating that salt alters the conformational preferences of the peptide [29,30]. The changes in the $A\beta_{40}$ structure induced by different surfactants

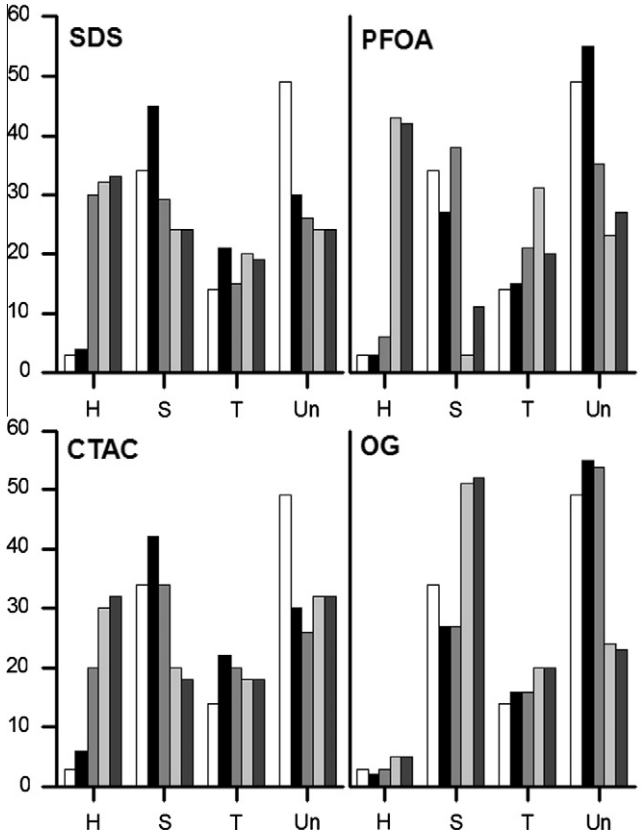

Fig. 3. Secondary structure motifs (in percentage) of amyloid-β peptide (1–40) in surfactant solutions estimated by deconvolution of circular dichroism spectra using the algorithm CONTIN/LL: α-helix (H); β-sheet (S); β-turn (T); unordered (Un). The concentration of surfactants increases from left (white column – 0 mM) to right (dark gray column) and is the same as shown in Fig. 1.

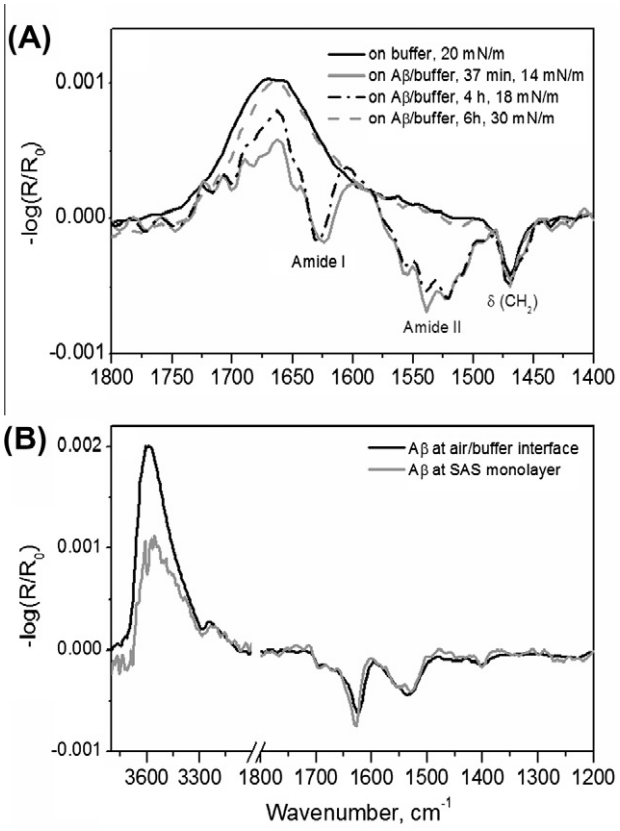

Fig. 4. (A) Infrared reflection absorption spectra of arachidyl sulfate monolayers on Hepes saline buffer and on the same buffer containing amyloid-β peptide (1–40). The amide I and II bands appear due to the peptide adsorption, which leads to surface pressure changes. After 6 h the monolayer was compressed to 30 mN m^{-1} and the amide bands disappeared (dashed gray line). (B) Infrared reflection absorption spectra of amyloid-β peptide (1–40) at arachidyl sulfate monolayers (18 mN m^{-1}) after subtraction of the surfactant spectrum and at air/buffer interface (15 mN m^{-1}).

were studied at low ionic strength and depend on their concentration and on whether the polar head group is charged. There is a concentration threshold for ionic surfactants, tested here or reported in the literature (SDS or LiDS), at which they are able to induce helical structure on soluble $A\beta_{40}$ [13]. A similar concentration-dependence effect has been described for negatively charged lipid vesicles [17]. The same binding steps proposed for globular proteins can explain the interaction of ionic surfactant monomers with $A\beta_{40}$: they bind trough electrostatic interactions to the charged side chains of the peptide and via hydrophobic binding to the nearby nonpolar regions [31]. This interaction efficiently solvates the peptide but on the other hand it removes water molecules from the peptide surface. Thus peptide segments will form hydrogen bonds with neighboring groups. Below the CMC, the hydrogen bonds are formed between different peptide molecules, as the ionic surfactant monomers cannot efficiently surround Aβ. At concentrations close to the CMC or above, the ionic micelles can coat the peptide and favor instead hydrogen bonds within the molecule as a result of the electrostatic interactions. The interaction with non-ionic surfactant OG at sub-CMC concentrations does not affect the peptide structure but above the CMC $A\beta_{40}$ adopts β-sheet conformation. According to the mechanism of action proposed for α-lactalbumin interacting with non-ionic surfactants, uncharged monomers cooperate with micelles to unfold the protein [31,32]. Unfolding occurs only close to and above the CMC but it is the binding to monomers that enables the interaction with the micelles [32]. Thus we hypothesize that $A\beta_{40}$ interacts with uncharged OG monomers through hydrophobic interactions, as denoted by the change on the surfactant CMC value in the presence of the peptide and uncharged micelles further unfold the peptide, resulting in β-sheet formation. Micelle formation is driven by the hydrophobic effect and the interactions between non-ionic surfactant monomers are usually stronger than that between ionic monomers due to the lack of electrostatic repulsion of the polar heads. The increase of the OG CMC induced by $A\beta_{40}$ indicates that the surfactant–peptide interactions are favorable enough to stabilize the non-ionic monomers in aqueous solutions. In the case of the ionic surfactants the number of sequestered monomers by the peptide is most likely to low to be detected by the techniques used to determine the CMC. Stabilization of aggregated β-sheet is attributed to intermolecular ion-pairing interactions, which cannot be prevented by uncharged micelles [12,33,34]. Molecular dynamics simulations of $A\beta_{42}$ bound to charged phospholipid bilayers demonstrated that the changes on the peptide secondary structure observed experimentally are due to peptide–peptide interactions, which are enhanced when Aβ binds to the bilayers [35]. The simulations revealed that there is no structure conversion of the monomeric peptide on the surface of the bilayer. This interaction mechanism is supported by the observation that $A\beta_{40}$ forms β-sheets at charged phospholipid or surfactant monolayers. The peptide is attracted to the monolayer by electrostatic interactions and when its concentration increases at the surface β-sheets are formed [20,23,25]. According to the calculated α-helix content of $A\beta_{40}$ in aqueous micelle solutions, it is possible to estimate that in SDS and CTAC micelle solutions 13 residues of the peptide form the helix, whereas in PFOA micelles 17 residues are involved. This

estimation is consistent with the predicted α-helix structure in solutions of charged micelles (two helices, residues 15–24 and residues 28–36, separated by a looped region), considering that at pH 7 the helical domain of residues 15–24 can be less structured [11,36,37]. The higher propensity for helix structure in fluorinated micelle solutions coincides with previous results on the effect of fluorinated nanoparticles on Aβ peptides [38,39]. The insertion of the strong electronegative trifluoromethyl group significantly increases the acidic nature of the carboxylic acid. As a consequence fluorinated particles or micelles can have higher charge surface densities than their hydrogenated analogs and bind strongly to the peptide molecule.

It has been proposed that transient intermediates of the aggregation process contain considerable amount of α-helix structure (up to 32%), which may then be converted into β-sheet depending on solution conditions [40,41]. If the α-helix structure is stable enough, amyloid fibrils are not formed. This means that fibrils are formed only if the conditions lower the energy barrier for helix formation without increasing significantly the energy for conversion to β-sheet. If a deep energy well is created for the α-helix structure then fibril formation is prevented [40]. The time-dependent changes on the peptide structure may also occur through an alternative pathway, which does not involve helix intermediates.

Acknowledgment

This work was supported by FCT Research Project PTDC/QUI-BIQ/102827/2008.

References

[1] J. Hardy, D.J. Selkoe, Medicine – the amyloid hypothesis of Alzheimer's disease: progress and problems on the road to therapeutics, Science 297 (2002) 353–356.
[2] D.A. Kirschner, C. Abraham, D.J. Selkoe, X-ray-diffraction from intraneuronal paired helical filaments and extraneuronal amyloid fibers in Alzheimer-disease indicates cross-beta conformation, Proc. Natl. Acad. Sci. USA 83 (1986) 503–507.
[3] D.J. Selkoe, Presenilins, beta-amyloid precursor protein and the molecular basis of Alzheimer's disease, Clin. Neurosci. Res. 1 (2001) 91–103.
[4] J. Kang, H.G. Lemaire, A. Unterbeck, J.M. Salbaum, C.L. Masters, K.H. Grzeschik, G. Multhaup, K. Beyreuther, B. Mullerhill, The precursor of Alzheimers-disease amyloid-A4 protein resembles a cell-surface receptor, Nature 325 (1987) 733–736.
[5] C. Haass, M.G. Schlossmacher, A.Y. Hung, C. Vigopelfrey, A. Mellon, B.L. Ostaszewski, I. Lieberburg, E.H. Koo, D. Schenk, D.B. Teplow, D.J. Selkoe, Amyloid beta-peptide is produced by cultured-cells during normal metabolism, Nature 359 (1992) 322–325.
[6] J.T. Jarrett, E.P. Berger, P.T. Lansbury, The carboxy terminus of the beta-amyloid protein is critical for the seeding of amyloid formation – implications for the pathogenesis of Alzheimers-disease, Biochemistry (US) 32 (1993) 4693–4697.
[7] C. Haass, D.J. Selkoe, Soluble protein oligomers in neurodegeneration: lessons from the Alzheimer's amyloid beta-peptide, Nat. Rev. Mol. Cell. Biol. 8 (2007) 101–112.
[8] A. Jan, O. Gokce, R. Luthi-Carter, H.A. Lashuel, The ratio of monomeric to aggregated forms of A beta 40 and A beta 42 is an important determinant of amyloid-beta aggregation, fibrillogenesis, and toxicity, J. Biol. Chem. 283 (2008) 28176–28189.
[9] I. Kuperstein, K. Broersen, I. Benilova, J. Rozenski, W. Jonekheere, M. Debulpaep, A. Vandersteen, I. Segers-Nolten, K. Van der Werf, V. Subramaniam, D. Braeken, G. Callewaert, C. Bartic, R. D'Hooge, I.C. Martins, F. Rousseau, J. Schymkowitz, B. De Strooper, Neurotoxicity of Alzheimer's disease A beta peptides is induced by small changes in the A beta(42) to A beta(40) ratio, EMBO J. 29 (2010) 3408–3420.
[10] R. Kayed, E. Head, J.L. Thompson, T.M. McIntire, S.C. Milton, C.W. Cotman, C.G. Glabe, Common structure of soluble amyloid oligomers implies common mechanism of pathogenesis, Science 300 (2003) 486–489.
[11] M. Coles, W. Bicknell, A.A. Watson, D.P. Fairlie, D.J. Craik, Solution structure of amyloid beta-peptide(1–40) in a water-micelle environment. Is the membrane-spanning domain where we think it is?, Biochemistry (US) 37 (1998) 11064–11077.
[12] K. Ma, E.L. Clancy, Y.B. Zhang, D.G. Ray, K. Wollenberg, M.G. Zagorski, Residue-specific p*K*(a) measurements of the beta-peptide and mechanism of pH-induced amyloid formation, J. Am. Chem. Soc. 121 (1999) 8698–8706.
[13] A. Wahlstrom, L. Hugonin, A. Peralvarez-Marin, J. Jarvet, A. Graslund, Secondary structure conversions of Alzheimer's A beta(1–40) peptide induced by membrane-mimicking detergents, FEBS J. 275 (2008) 5117–5128.
[14] V. Rangachari, D.K. Reed, B.D. Moore, T.L. Rosenberry, Secondary structure and interfacial aggregation of amyloid-beta(1–40) on sodium dodecyl sulfate micelles, Biochemistry (US) 45 (2006) 8639–8648.
[15] D.J. Tew, S.P. Bottomley, D.P. Smith, G.D. Ciccotosto, J. Babon, M.G. Hinds, C.L. Masters, R. Cappai, K.J. Barnham, Stabilization of neurotoxic soluble beta-sheet-rich conformations of the Alzheimer's disease amyloid-beta peptide, Biophys. J. 94 (2008) 2752–2766.
[16] J.M. Lin, T.L. Lin, U.S. Jeng, Z.H. Huang, Y.S. Huang, Aggregation structure of Alzheimer amyloid-beta(1–40) peptide with sodium dodecyl sulfate as revealed by small-angle X-ray and neutron scattering, Soft Matter 5 (2009) 3913–3919.
[17] E. Terzi, G. Holzemann, J. Seelig, Interaction of Alzheimer beta-amyloid peptide(1–40) with lipid membranes, Biochemistry (US) 36 (1997) 14845–14852.
[18] N. Sreerama, R.W. Woody, Estimation of protein secondary structure from circular dichroism spectra: comparison of CONTIN, SELCON, and CDSSTR methods with an expanded reference set, Anal. Biochem. 287 (2000) 252–260.
[19] G.D. Fasman, Circular dichroism and the conformational analysis of biomolecules, Plenum Publishing Corporation, New York, 1996.
[20] E. Maltseva, A. Kerth, A. Blume, H. Mohwald, G. Brezesinski, Adsorption of amyloid beta (1–40) peptide at phospholipid monolayers, ChemBioChem 6 (2005) 1817–1824.
[21] E. Maltseva, V.L. Shapovalov, H. Mohwald, G. Brezesinski, Ionization state and structure of L-1,2-dipalmitoylphosphatidylglycerol monolayers at the liquid/air interface, J. Phys. Chem. B 110 (2006) 919–926.
[22] E.L. Karjalainen, H.K. Ravi, A. Barth, Simulation of the amide I absorption of stacked beta-sheets, J. Phys. Chem. B 115 (2011) 749–757.
[23] G. Brezesinski, E. Maltseva, H. Mohwald, Adsorption of amyloid beta (1–40) peptide at liquid interfaces, Z. Phys. Chem. 221 (2007) 95–111.
[24] C. Schladitz, E.P. Vieira, H. Hermel, H. Mohwald, Amyloid-beta-sheet formation at the air–water interface, Biophys. J. 77 (1999) 3305–3310.
[25] E. Maltseva, G. Brezesinski, Adsorption of amyloid beta (1–40) peptide to phosphatidylethanolamine monolayers, ChemPhysChem 5 (2004) 1185–1190.
[26] L.M. Hou, H.Y. Shao, Y.B. Zhang, H. Li, N.K. Menon, E.B. Neuhaus, J.M. Brewer, I.J.L. Byeon, D.G. Ray, M.P. Vitek, T. Iwashita, R.A. Makula, A.B. Przybyla, M.G. Zagorski, Solution NMR studies of the A beta(1–40) and A beta(1–42) peptides establish that the met35 oxidation state affects the mechanism of amyloid formation, J. Am. Chem. Soc. 126 (2004) 1992–2005.
[27] L.C. Serpell, Alzheimer's amyloid fibrils: structure and assembly, BBA: Mol. Basis Dis. 1502 (2000) 16–30.
[28] N.D. Lazo, M.A. Grant, M.C. Condron, A.C. Rigby, D.B. Teplow, On the nucleation of amyloid beta-protein monomer folding, Protein Sci. 14 (2005) 1581–1596.
[29] S. Narayanan, B. Reif, Characterization of chemical exchange between soluble and aggregated states of beta-amyloid by solution-state NMR upon variation of salt conditions, Biochemistry (US) 44 (2005) 1444–1452.
[30] S. Vivekanandan, J.R. Brender, S.Y. Lee, A. Ramamoorthy, A partially folded structure of amyloid-beta(1–40) in an aqueous environment, Biochem. Biophys. Res. Commun. 411 (2011) 312–316.
[31] D. Otzen, Protein–surfactant interactions: a tale of many states, BBA: Proteins Proteom. 2011 (1814) 562–591.
[32] D.E. Otzen, P. Sehgal, P. Westh, Alpha-Lactalbumin is unfolded by all classes of surfactants but by different mechanisms, J. Colloid Interf. Sci. 329 (2009) 273–283.
[33] P.E. Fraser, D.R. Mclachlan, W.K. Surewicz, C.A. Mizzen, A.D. Snow, J.T. Nguyen, D.A. Kirschner, Conformation and fibrillogenesis of Alzheimer a-beta peptides with selected substitution of charged residues, J. Mol. Biol. 244 (1994) 64–73.
[34] C. Soto, E.M. Castano, B. Frangione, N.C. Inestrosa, The alpha-helical to beta-strand transition in the amino-terminal fragment of the amyloid beta-peptide modulates amyloid formation, J. Biol. Chem. 270 (1995) 3063–3067.
[35] C.H. Davis, M.L. Berkowitz, Structure of the amyloid-beta (1–42) monomer absorbed to model phospholipid bilayers: a molecular dynamics study, J. Phys. Chem. B 113 (2009) 14480–14486.
[36] M.G. Zagorski, C.J. Barrow, NMR-studies of amyloid beta-peptides – proton assignments, secondary structure, and mechanism of an alpha-helix–beta-sheet conversion for a homologous, 28-residue, N-terminal fragment, Biochemistry (US) 31 (1992) 5621–5631.
[37] H.Y. Shao, S.C. Jao, K. Ma, M.G. Zagorski, Solution structures of micelle-bound amyloid beta-(1–40) and beta-(1–42) peptides of Alzheimer's disease, J. Mol. Biol. 285 (1999) 755–773.
[38] S. Rocha, A.F. Thuneman, M.D. Pereira, M. Coelho, H. Mohwald, G. Brezesinski, Influence of fluorinated and hydrogenated nanoparticles on the structure and fibrillogenesis of amyloid beta-peptide, Biophys. Chem. 137 (2008) 35–42.
[39] A.M. Saraiva, I. Cardoso, M.C. Pereira, M.A.N. Coelho, M.J. Saraiva, H. Mohwald, G. Brezesinski, Controlling amyloid-beta peptide(1–42) oligomerization and toxicity by fluorinated nanoparticles, ChemBioChem 11 (2010) 1905–1913.
[40] M.D. Kirkitadze, M.M. Condron, D.B. Teplow, Identification and characterization of key kinetic intermediates in amyloid beta-protein fibrillogenesis, J. Mol. Biol. 312 (2001) 1103–1119.
[41] Y. Fezoui, D.B. Teplow, Kinetic studies of amyloid beta-protein fibril assembly – differential effects of alpha-helix stabilization, J. Biol. Chem. 277 (2002) 36948–36954.

Biochemical and Biophysical Research Communications 420 (2012) 141–147

Contents lists available at SciVerse ScienceDirect

Biochemical and Biophysical Research Communications

journal homepage: www.elsevier.com/locate/ybbrc

Suppression of *Arabidopsis* RING-DUF1117 E3 ubiquitin ligases, *AtRDUF1* and *AtRDUF2*, reduces tolerance to ABA-mediated drought stress

Soo Jin Kim, Moon Young Ryu, Woo Taek Kim *

Department of Systems Biology, College of Life Science and Biotechnology, Yonsei University, Seoul 120-749, Republic of Korea

ARTICLE INFO

Article history:
Received 21 February 2012
Available online 3 March 2012

Keywords:
Abscisic acid
Arabidopsis thaliana
DUF1117 motif
Drought stress response
Positive regulation
RING E3 ubiquitin ligases

ABSTRACT

Among approximately 480 RING domain-containing E3 Ub ligases in *Arabidopsis*, three, At3g46620, At5g59550, and At2g39720, have a domain-of-unknown-function (DUF) 1117 motif in their C-terminal regions. At3g46620 and At5g59550 were identified as homologous ABA- and drought-induced *RING-DUF1117* genes and were designated *AtRDUF1* and *AtRDUF2*, respectively. Single and double knock-out mutations of *AtRDUFs* resulted in hyposensitive phenotypes toward ABA in terms of germination rate and stomatal closure and markedly reduced tolerance to drought stress relative to wild-type plants. These results are discussed in the context that AtRDUF1 and AtRDUF2 play combinatorial, but still distinguishable, roles in ABA-mediated dehydration stress responses.

1. Introduction

Ubiquitin (Ub) is a conserved 76-amino-acid-long small polypeptide. Ub is attached to diverse cellular proteins by consecutive catalytic reactions of E1 Ub activating enzyme, E2 Ub conjugating enzyme, and E3 Ub ligase, resulting in post-translational protein modification [1–3]. The ubiquitination system plays a critical role in plant growth and development as approximately 6% of the *Arabidopsis* proteome is associated with the Ub-26S proteasome pathway and more than 1400 different E3 Ub ligase genes exist in the *Arabidopsis* genome [4,5]. The Ub-26S proteasome pathway functions in diverse physiological processes in higher plants, including cell cycles and circadian rhythms, environmental stress responses, and hormone perception and signaling [3–8].

Arabidopsis contains approximately 480 really-interesting-new-gene (RING) domain-containing E3 Ub ligases [3,9,10]. Among various cellular functions of RING E3 Ub ligase members is the positive or negative regulation of osmotic and drought stress responses [11–17]. RING E3s are also involved in the modulation of water stress responses in monocot rice [18–21]. Thus, functions of RING E3 Ub ligases in osmotic and dehydration stress responses are likely widely conserved in higher plants.

The plant stress-hormone abscisic acid (ABA) is a key mediator in drought stress responses. ABA reduces transpirational water loss by triggering stomata closure and induces abiotic stress-associated genes [22,23]. Here, we identified two homologous RING E3 Ub ligases that were highly activated by ABA and dehydration. These genes were designated *AtRDUF1* and *AtRDUF2* as both contain a RING domain and a domain-of-unknown-function (DUF) 1117 motif. Single as well as double knock-out mutations of the *AtRDUFs* resulted in hyposensitive phenotypes to ABA and reduced tolerance to drought stress relative to wild-type plants. These results suggest that AtRDUF1 and AtRDUF2 participate in the positive regulation of ABA-dependent drought stress responses in *Arabidopsis*.

2. Materials and methods

2.1. Plant materials and stress treatments

Arabidopsis thaliana ecotype Columbia (Col-0) seeds were briefly rinsed with 30% sodium hypochlorite solution (bleach) and grown on MS medium supplemented with 1% sucrose, 12 μg/ml vitamin B5, and 0.8% agar (pH 5.7) in a 25 °C growth chamber. Light-grown 10-day-old seedlings and mature plants were subjected to drought, high-salinity, and ABA treatments as previously described [15]. The *atrduf1* (SALK_129323) and *atrduf2* (GABI_750A10) T-DNA insertion mutant alleles were obtained from the Arabidopsis Biological Resource Center (http://www.arabidopsis.org). Homozygous T_5 lines were selected through self-crossing. A double knock-out mutant was subsequently obtained by crossing *atrduf1* and *atrduf2*.

Abbreviations: DUF, domain of unknown function; MBP, maltose binding protein; RING, really interesting new gene; sGFP, soluble green fluorescence protein; Ub, Ubiquitin.

* Corresponding author. Fax: + 82 2 312 5657.
E-mail address: wtkim@yonsei.ac.kr (W.T. Kim).

0006-291X/$ - see front matter © 2012 Elsevier Inc. All rights reserved.
doi:10.1016/j.bbrc.2012.02.131

2.2. Reverse transcription polymerase chain reaction (RT-PCR) and quantitative RT-PCR (qRT-PCR) analyses

Isolation of total RNA from drought- and ABA-treated samples was performed using an RNA extraction kit (Intron Biotechnology, Kyungkido, Korea). cDNA synthesis, RT-PCR, and real-time qRT-PCR analyses were conducted as described previously [16] using an IQ5 light cycler (Bio-Rad, Hercules, CA) with SYBR Premix Ex Taq II (Takara, Kyoto, Japan). All primers used in this study are listed in Supplementary Table S1.

2.3. Promoter-GUS assays

The *AtRDUF1*$_{promoter}$*-GUS* and *AtRDUF2*$_{promoter}$*-GUS* constructs were generated and transformed into wild-type *Arabidopsis* by the method described previously [16]. Promoters of both genes contained 0.9 kb upstream region from the initiation codon. T_3 homozygous transgenic plants were obtained. Transgenic plant tissues were subjected to GUS staining as described by Cho et al. [16].

2.4. In vitro self-ubiquitination assay

The MBP-AtRDUF1 and MBP-AtRDUF2 fusion proteins (300 ng) were expressed in *Escherichia coli* strain BL21, purified using amylose resin (New England BioLabs), and subjected to *in vitro* self-ubiquitination assays as described previously [14]. Protein gel-blot analyses were conducted using anti-MBP antibody (New England BioLabs) or anti-Ub antibody (Santa Cruz Biotechnology, Santa Cruz, CA) as described by Son et al. [24].

2.5. Seed germination assay and stomatal aperture measurement

Seeds from wild-type, *atrduf1*, *atrduf2*, and *atrduf1atrduf2* plants were grown on 1× MS media containing ABA (0, 0.2, or 0.4 μM) (Sigma–Aldrich, St. Louis, MO) at 22 °C with a 16-h light/8-h dark photoperiod. The percentages of normal green cotyledon development were recorded after 5 and 9 d. Mature rosette leaves were treated with ABA (0, 0.1, 1.0, or 10 μM) and stomatal movement profiles were examined using Multigauge version 3.1 software (Fujifilm, Tokyo, Japan).

2.6. Survival rate determination after drought stress

Wild-type and mutant plants grown for 18 d under normal growth conditions were further grown for 8 d without water supply. Plants were irrigated and growth patterns were monitored after 3 d. Survival was determined as the ability to grow after re-watering [14]. Mature detached rosette leaves were incubated at room temperature for 5 h. The leaf weights were measured and expressed as the percent of initial fresh weight.

3. Results

3.1. AtRDUF1 and AtRDUF2 are ABA- and drought-induced RING-DUF1117 E3 Ub ligases

From the *in silico* database (http://www.genevestigator.com), two homologous putative RING E3 Ub ligase genes induced by ABA and drought were identified: At3g46620 (GenBank accession number NM_114529) and At5g59550 (NM_125347). The predicted At3g46620 and At5g59550 proteins are composed of 395 amino acids (43.2 kDa) and 407 amino acids (44.4 kDa), respectively, with a single RING domain and a single DUF1117 motif in their C-terminal regions (Fig. 1A). Therefore, they were designated AtRDUF1 and AtRDUF2. AtRDUF1 and AtRDUF2 share 67% identity and are 34–36% conserved compared with *Arabidopsis* At2g39720 RING-DUF1117. Additionally, they are 34–43% identical to poplar (*Populus trichocarpa*), grape (*Vitis vinifera*), and clover (*Medicago truncatula*) putative RING proteins (Supplementary Fig. S1A and B). The Cys-X_2-Cys-X_{14}-Cys-X_1-His-X_2-His-X_2-Cys-X_{10}-Cys-X_2-Cys motif is well conserved in their RING domains, indicating that AtRDUF1 and AtRDUF2 belong to the C3H2C3-type RING subfamily (Supplementary Fig. S1C). The C-terminal DUF1117 motifs were 85% conserved in the two *Arabidopsis* RING proteins (Supplementary Fig. S1D).

RT-PCR analysis showed that *AtRDUF1* and *AtRDUF2* were activated in light-grown 10-day-old plants by drought (0.5–2 h), high-salinity (300 mM NaCl for 1.5–3 h), and ABA (100 μM for 1–3 h) (Fig. 1B). Promoter-GUS assays showed that both *AtRDUF1* and *AtRDUF2* promoter (0.9 kb upstream region) activities were heightened in leaf tissues, including guard cells, in response to stress and ABA (Fig. 1C). In roots, *AtRDUF1* was induced in developing lateral root primordia and root tips, whereas *AtRDUF2* expression was found in vascular tissues of tap roots. Therefore, *AtRDUF1* and *AtRDUF2* are ABA- and drought-inducible genes with distinct induction profiles in roots.

3.2. AtRDUF1 and AtRDUF2 displayed in vitro E3 Ub ligase enzyme activities

MBP-AtRDUF1 and MBP-AtRDUF2 fusion proteins were expressed in *E. coli*, purified, and incubated in the presence or absence of ATP, Ub, E1 (*Arabidopsis* His-UBA1), and E2 (*Arabidopsis* His-UBC8). The reaction mixtures were subjected to protein gel-blot analysis with anti-MBP or anti-Ub antibody. MBP-AtRDUFs possessed *in vitro* E3 Ub ligase activities (Fig. 2) as evidenced by the formation of high-molecular-mass smear ladders [24,25]. These ubiquitinated bands were not produced in reactions lacking ATP, Ub, E1, or E2. In addition, MBP-AtRDUF1^{C255S} and MBP-AtRDUF2^{C239S} derivatives, in which conserved Cys residues were replaced by Ser in their RING domains, were unable to produce high-molecular-mass self-ubiquitinating ladders. Thus, AtRDUF1 and AtRDUF2 are ABA- and drought-inducible RING-DUF1117 E3 Ub ligases.

3.3. Loss-of-function mutations of AtRDUFs resulted in hyposensitive phenotypes toward ABA

To investigate *in vivo* functions of AtRDUFs, loss-of-function mutants of *AtRDUF1* and *AtRDUF2* were analyzed. The *atrduf1* mutant contained a T-DNA insertion after nucleotide 886 on chromosome 3 (line SALK_129323), whereas the *atrduf2* mutant contained double T-DNA insertions after nucleotides 685 and 713 in an antisense direction on chromosome 5 (line GABI_750A10) (Supplementary Fig. S2). A homozygous double knock-out mutant was subsequently obtained by crossing *atrduf1* and *atrduf2* (Supplementary Fig. S2). RT-PCR showed that, although low levels of truncated mRNAs were produced in the mutant plants, full-length *AtRDUF1* and *AtRDUF2* transcripts were undetectable in single and double knock-out mutants after high-salt treatment, indicating that *AtRDUF1* and *AtRDUF2* were silenced in the mutant plants (Supplementary Fig. S2).

Because *AtRDUF1* and *AtRDUF2* are ABA-inducible genes (Fig. 1), phenotypes of wild-type and loss-of-function *atrduf* mutants were compared in terms of ABA responses. Wild type and T_5 homozygous *atrduf1*, *atrduf2*, and *atrduf1atrduf2* mutant seeds were germinated in the presence of different concentrations of ABA (0, 0.2, and, 0.4 μM) and germination percentages were recorded with regard to cotyledon greening. *atrduf1* and *atrduf2* single mutant seedlings displayed hyposensitive phenotypes toward ABA as compared to wild-type seedlings. With 0.4 μM ABA, germination

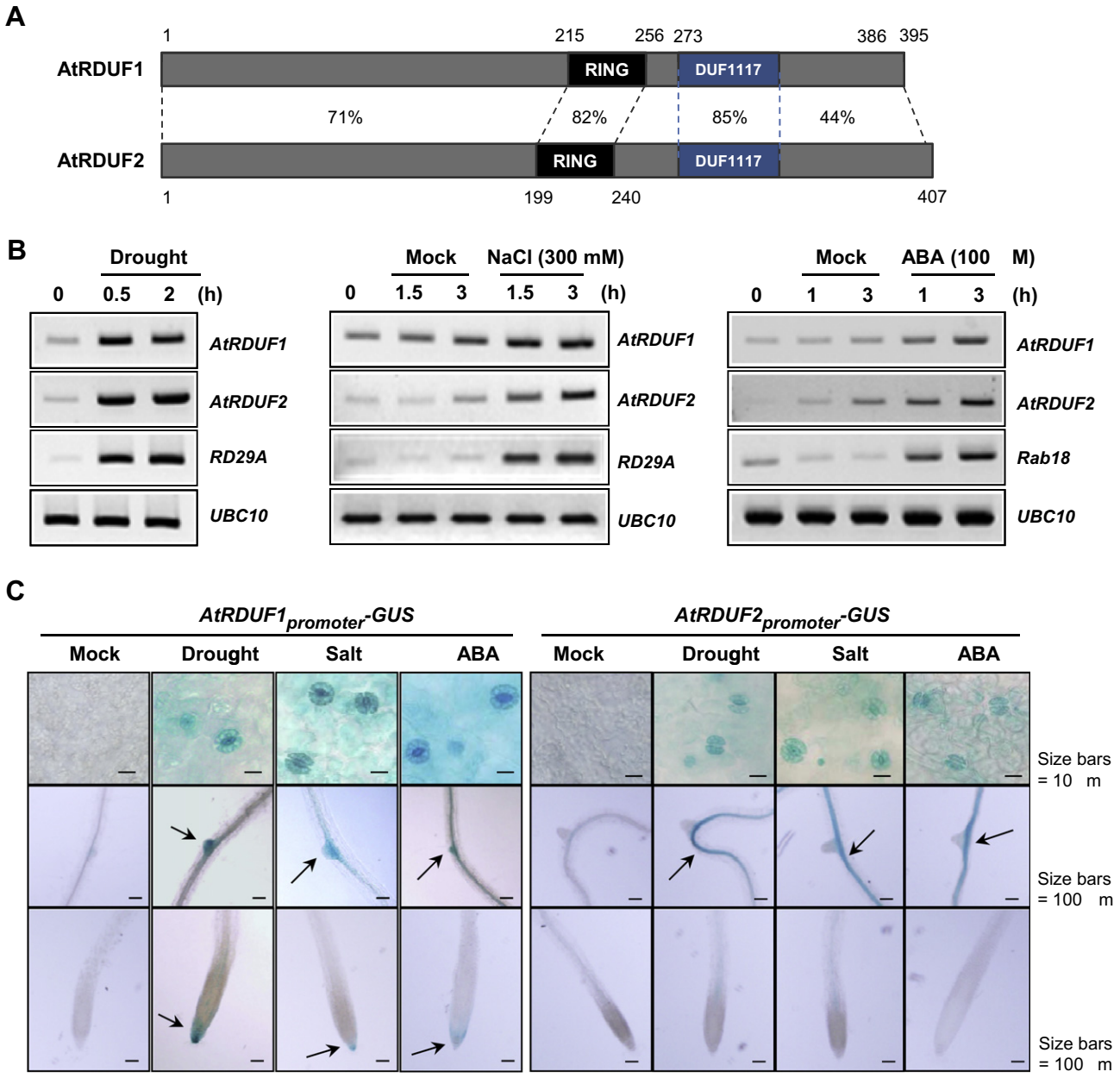

Fig. 1. Structure and expression of *AtRDUF1* and *AtRDUF2*. (A) Schematic representation of AtRDUF1 and AtRDUF2. Sequence identities between each domain of AtRDUF1 and AtRDUF2 are indicated. (B) RT-PCR analysis of *AtRDUF1* and *AtRDUF2* in response to drought, ABA, and high-salinity stresses. *RD29A* and *Rab18* are marker genes for osmotic stress and ABA, respectively. *Ubiquitn10* (*UBC10*) was a loading control. (C) $AtRDUF_{promoter}$*-GUS* assays. Histochemical localization of GUS activities in guard cells, developing lateral root primordia, root tips, and vascular tissues of tap roots are shown. GUS-specific signals are indicated by arrows. Scale bars lengths are indicated to the right panel of the figures.

percentages of wild-type and mutants were 22.2% and 44.4–47.2%, respectively, 5 days after stratification (Fig. 3A). The sensitivity of *atrduf1atrduf2* double knock-out seedlings to ABA was slightly increased relative to those of single mutants. Germination percentage of double mutants was 57.4% 5 d after germination with 0.4 μM ABA (Fig. 3A). Thus, germination rates of *atrduf1*, *atrduf2*, and *atrduf1atrduf2* mutants were markedly higher than those of wild-type plants in response to ABA.

Subsequently, ABA-mediated stomatal movement profiles were analyzed. Mature rosette leaves of wild-type and mutant plants were treated with ABA (0, 0.1, 1.0, and 10 μM) for 2 h and stomatal apertures were measured. With 1.0 μM ABA, average stomatal apertures (ratio of width to length) of wild-type, *atrduf1*, *atrduf2*, and *atrduf1atrduf2* plants were 0.10 ± 0.011, 0.18 ± 0.027, 0.18 ± 0.029, and 0.19 ± 0.028, respectively (Fig. 3B). After treatment with 10 μM ABA, stomatal apertures of wild-type plants were further reduced to 0.06 ± 0.012, whereas those of mutant plants were only slightly reduced (0.16 ± 0.025–0.18 ± 0.029). These results clearly suggest that ABA-dependent stomatal movement in *atrduf* single and double mutant leaves was markedly hindered relative to wild-type plants.

Consistently, real-time qRT-PCR analysis showed that ABA-induced marker genes, including *RD29A*, *RD29B*, *RD20*, and *RD22*, were significantly down-regulated in *atrduf* mutant leaves (Fig. 3C). Collectively, suppression of *AtRDUF1* and *AtRDUF2* resulted in hyposensitive phenotypes to ABA in terms of germination percentage (Fig. 3A) and stomatal closure (Fig. 3B and C). Because developmental and morphological patterns of wild-type and mu-

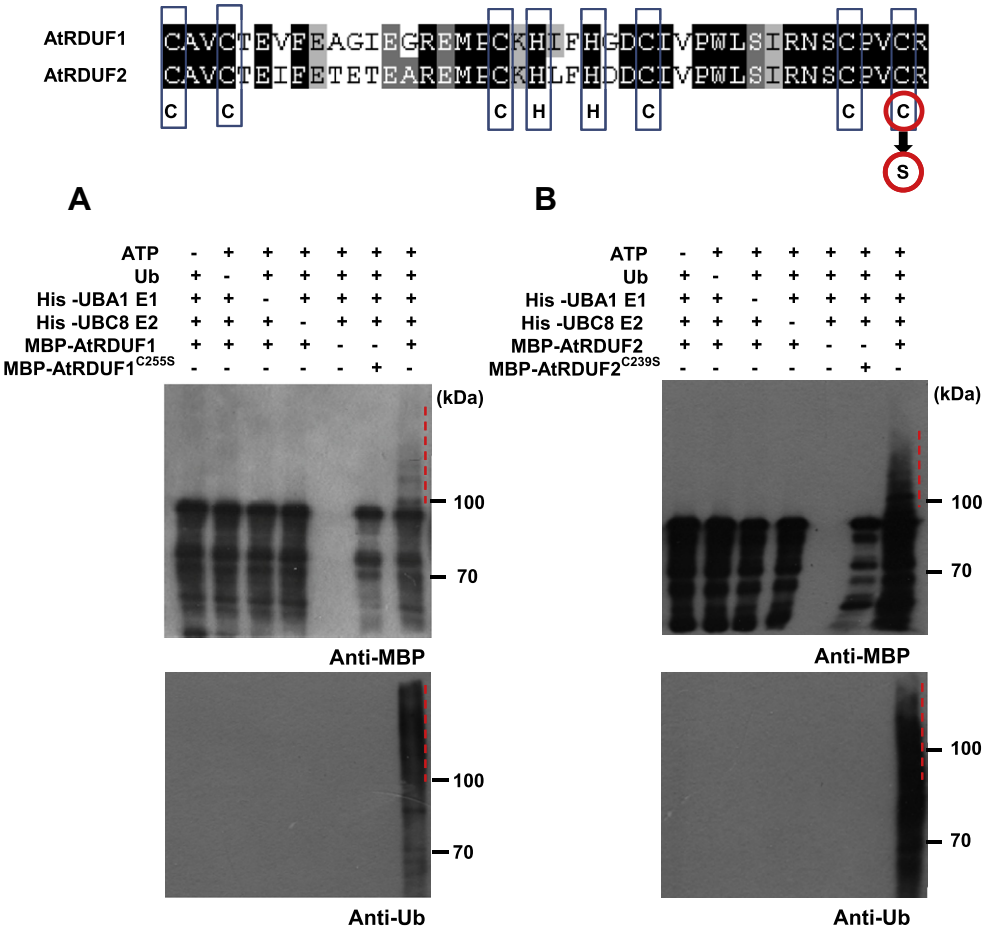

Fig. 2. *In vitro* AtRDUF self-ubiquitination assays. MBP-AtRDUF1 and MBP-AtRDUF1^{C255S} (A) and MBP-AtRDUF2 and MBP-AtRDUF2^{C239S} (B) fusion proteins (300 ng) were expressed in *E. coli*, purified, and incubated at 30 °C for 1 h in the presence or absence of ATP, Ub, E1 (*Arabidopsis* His-UBA1), and E2 (*Arabidopsis* His-UBC8). Reactions were subjected to protein gel-blot analyses with anti-MBP antibody (upper panels) or anti-Ub antibody (lower panels). High-molecular-mass self-ubiquitinating ladders are indicated by vertical dashed lines.

tant plants were indistinguishable without ABA treatment, AtRDUF1 and AtRDUF2 likely positively participate in ABA responses.

To further characterize the function of AtRDUFs, we attempted to construct *AtRDUF*-over-expressing transgenic plants under the control of the 35S CaMV promoter. Although *AtRDUF1-sGFP* and *AtRDUF2-sGFP* transcripts were constitutively expressed in numerous independent over-expressing transgenic lines, corresponding AtRDUF-sGFP proteins were undetectable in *35S:AtRDUF-sGFP* plants using anti-GFP antibody (Supplementary Fig. S3). In contrast, high levels of control sGFP were clearly detected in *35S:sGFP* transgenic plants. It was previously reported that *Arabidopsis* RING E3 Ub ligase Rma homologs (Rma1, Rma2, and Rma 3) were rapidly degraded in *35S:HA-Rma1* over-expressing transgenic plants via an Ub-26S proteasome pathway [14]. Thus, it is possible that AtRDUF-sGFP may be ubiquitinated and degraded in over-expressing transgenic lines.

3.4. Suppression of AtRDUFs reduced drought stress tolerance

Because AtRDUFs are positive regulators of ABA responses (Fig. 3) and are induced by drought (Fig. 1), drought tolerance phenotypes of wild-type and mutant plants were compared. Healthy 18-day-old wild-type and mutant plants were further grown for 8 d without water supply followed by 3 d of re-watering. Under these water-stressed conditions, survival percentages of wild-type, *atrduf1*, *atrduf2*, and *atrduf1atrduf2* plants were 80%, 50%, 27%, and 23% (n = 60 for each group), respectively (Fig. 4A). Water stress-induced marker genes were down-regulated in dehydrated *atrduf2* mutant leaves compared to wild-type leaves (Fig. 4B). Furthermore, leaf water content of *atrduf* mutants reduced more rapidly than that of wild-type plants during the dehydration process. After a 5-h incubation at room temperature, wild-type and mutant detached rosette leaves retained 55.6% and 45.4–47.4% of their fresh weights, respectively, suggesting that mutant leaves were more susceptible to water stress than wild-type leaves (Fig. 4C).

4. Discussion

AtRDUF1 and *AtRDUF2* were initially identified as ABA- and drought-induced RING-DUF1117 E3 Ub ligase genes based on *in silico* data. RT-PCR and promoter-GUS analyses confirmed that they were activated by ABA and osmotic stress (Fig. 1). Loss-of-function mutations of *AtRDUF1* and *AtRDUF2* resulted in hyposensitive phenotypes toward ABA during germination and post-germination growth (Fig. 3). Furthermore, *atrduf* mutants were highly susceptible to dehydration stress (Fig. 4). Thus, AtRDUF1 and AtRDUF2 are likely involved in the positive regulation of ABA-mediated drought responses.

During the characterization of *AtRDUF1* and *AtRDUF2*, two unexpected results were obtained. First, the AtRDUF-sGFP proteins were not expressed in *35S:AtRDUF-sGFP* transgenic over-expressing lines. This result was not due to the sGFP fusion protein because

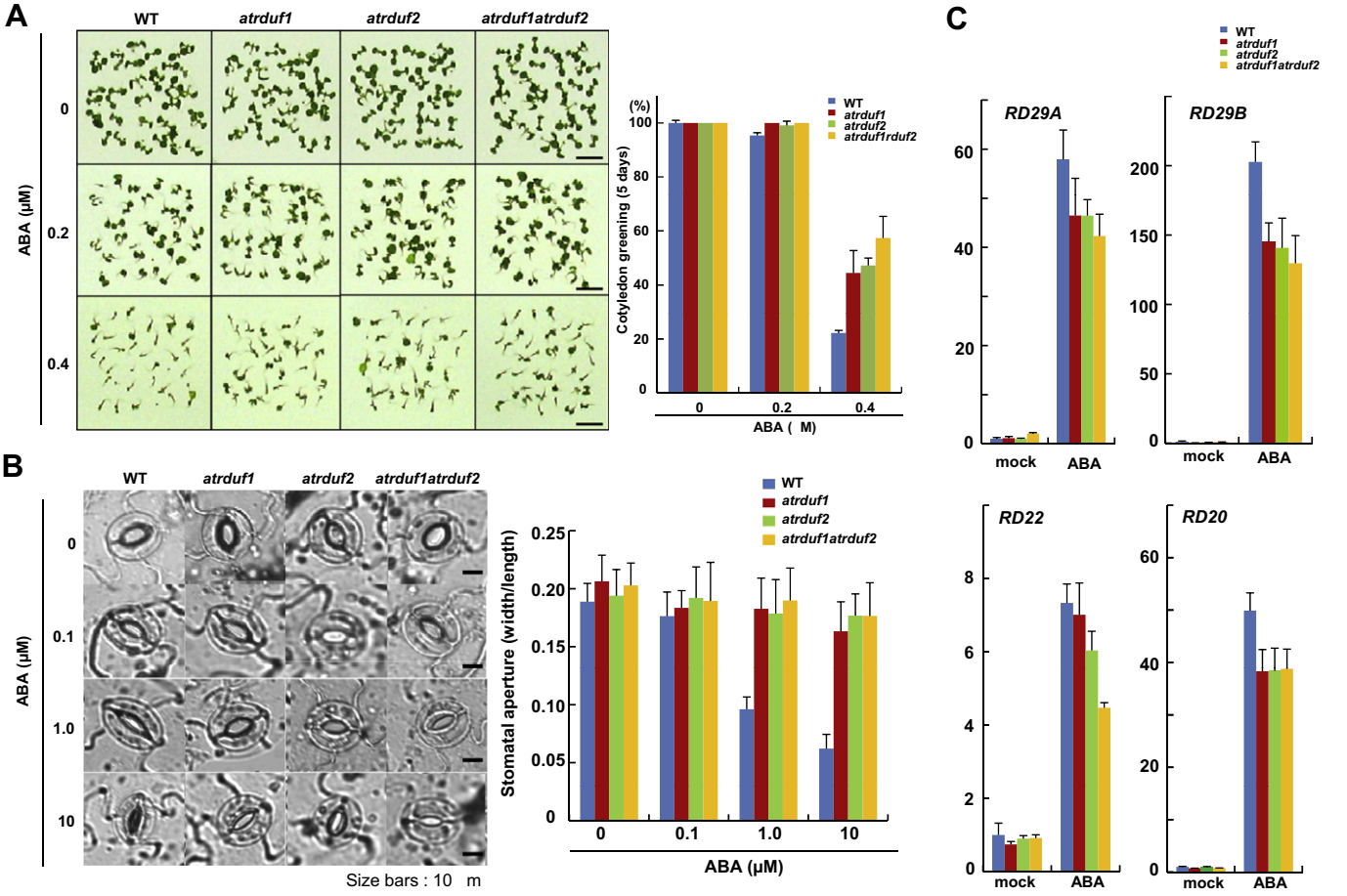

Fig. 3. Phenotypic analysis of *atrduf* mutants in response to ABA. (A) Germination percentage of wild-type, *atrduf1*, *atrduf2*, and *atrduf1atrduf2* plants. Wild-type and mutant seeds were germinated in the absence or presence of ABA (0.2 and 0.4 μM). Germination percentages were determined with regard to development of normal cotyledons 5 d after stratification. Data represent means ± SD ($n > 35$) from three independent experiments. Bars = 0.5 cm. (B) Stomatal movement profiles of wild-type and mutant plants. Rosette leaves were incubated with ABA (0, 0.1, 1.0, and 10 μM) for 2 h and stomatal apertures were measured using 50 guard cells from each sample. Data represent means ± SD ($n = 50$). Bars = 10 μm. (C) Real time qRT-PCR analysis of ABA-induced marker genes in wild-type and mutant plants. Total RNA was isolated from 1.0 μM ABA-treated wild-type and mutant leaves. Induction profiles of ABA-inducible genes (*RD29A*, *RD29B*, *RD22*, and *RD20*) were determined by real-time qRT-PCR. Data represent means ± SD from three independent experiments. Mean values were normalized to the transcript level of an internal control, glyceraldehyde-3-phosphate dehydrogenase C subunit (*GAPDHC*).

high levels of sGFP were detected in *35S:sGFP* transgenic lines (Supplementary Fig. S3). Bacterially expressed AtRDUFs possessed self-ubiquitinating activities (Fig. 2). Thus, it was postulated that cellular levels of AtRDUFs were tightly regulated and they were ubiquitinated by themselves or other E3s resulting in rapid degradation in the over-expressing lines through the Ub-26S proteasome pathway. This view was partially supported by the results that, while the AtRDUF2-sGFP was not expressed in tobacco transient expression system, the AtRDUF2^{C239S}-sGFP and AtRDUF2^{H222A}-sGFP mutant proteins, which lost their E3 Ub ligase activity, were highly accumulated in tobacco cells (Supplementary Fig. S4). These results were in agreement with previous results that, although *Arabidopsis* RING E3 *HA-Rma* mRNA levels were high in over-expressing transgenic plants, the corresponding proteins were rapidly degraded [14].

The second unexpected result was that the phenotypes of the *atrduf1atrduf2* double mutants were not more severe than those of single mutants, but rather comparable to the single mutants in both ABA responses and drought susceptibility (Figs. 3 and 4). The reason for these results is currently unknown. The defensive mechanisms of higher plants to environmental stress are often interconnected in a combinatorial web [26,27]. *Arabidopsis* contains approximately 480 RING E3s and, thus, subsets are possibly functionally coordinated to effectively cope with drought stress. We speculated that double-mutations of *AtRDUFs* may activate other RING E3s by as-yet an unidentified mechanism to mitigate cellular damages caused by drought stress. This complementation may result in comparable phenotypes between *atdruf* single- and double-mutants. Alternatively, as both AtRDUF1 and AtRDUF2 are working together, loss of one affects the other and, therefore, a double mutation would not compound the mutant phenotypes. Additional experiments, such as microarray analyses, are required to further understand this finding.

A pair of RING E3s often functions redundantly against dehydration stress. For instance, DRIP1 and DRIP2, AtRma1 and AtRma2/3, AtAIRP1 and AtAIRP2, and RHA2a and RHA2b, play combinatorial roles in ABA signaling and/or drought responses [13–17]. This coordination could be helpful for effective defensive processes. As AtRDUF1 and AtRDUF2 share a high degree of sequence identity (Fig. 1) and knock-out mutations of each gene resulted in similar phenotypes to ABA-mediated drought stress responses (Figs. 3 and 4), it is likely that cellular functions of AtRDUF1 and AtRDUF2 are redundant. However, promoter-GUS assays indicated that the ABA- and drought-induction of *AtRDUF1* and *AtRDUF2* were distinct

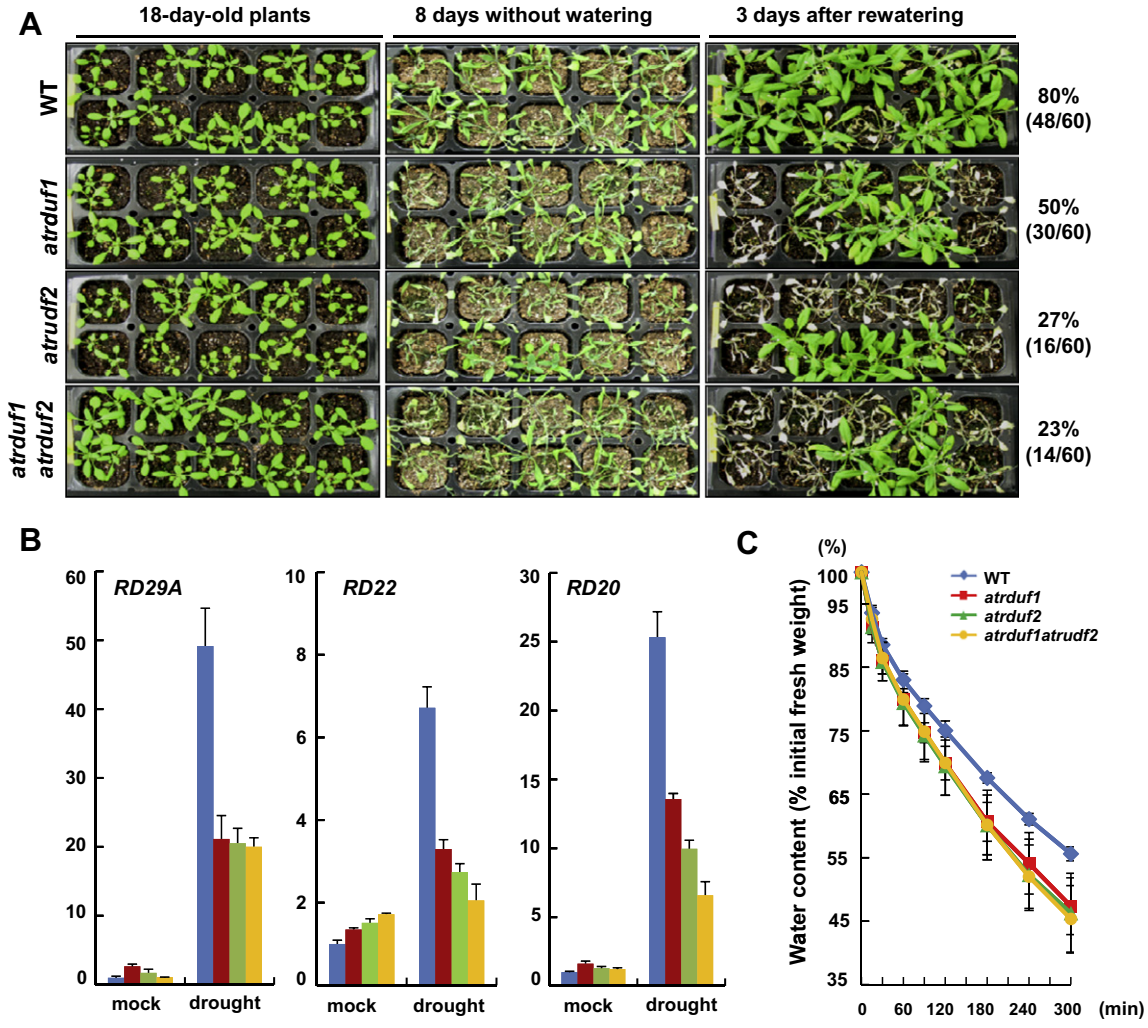

Fig. 4. *AtRDUF* mutations reduced tolerance to drought stress. (A) Survival rates of wild-type and *atrduf* mutant plants after drought stress. Healthy 18-day-old wild-type, *atrduf1*, *atrduf2*, and *atrduf1atrduf2* plants were grown for 8 d without water supply. Dehydrated plants were irrigated and their survival rates were recorded after 3 d. (B) Real time qRT-PCR analysis of drought-induced marker genes in wild-type and mutant plants. Total RNA was isolated form drought-treated wild-type and mutant leaves. Induction profiles of drought-inducible genes (*RD29A*, *RD22*, and *RD20*) were determined by real-time qRT-PCR as described in Fig. 3C. (C) Detached leaf water loss rates. Detached rosette leaves from wild-type and mutant plants were incubated for 5 h at room temperature. Reduction of leaf fresh weights was recorded and expressed as the percentage of initial fresh weight of the leaves. The experiments were repeated three times independently. Data represent means ± SD ($n = 7$).

in roots (Fig. 1). AtRDUF1 and AtRDUF2 may play combinatorial, but still distinguishable, roles in ABA-mediated drought responses.

There are three *Arabidopsis* RING-DUF1117 E3s [9,10], AtRDUF1, AtRDUF2, and At2g39720. At2g39720 is distantly related to AtRDUF1 and AtRDUF2 (Supplementary Fig. S1) and may have different roles. In conclusion, our data indicate that AtRDUF1 and AtRDUF2 are *Arabidopsis* RING-DUF1117 E3s and positively participate in ABA-mediated drought stress responses.

Acknowledgments

This work was supported by Grants from the National Research Foundation (2010-0000782) and the National Center for GM Crops (PJ008152) of the Next Generation BioGreen 21 Program funded by the Rural Development Administration, Republic of Korea, to W.T.K.

Appendix A. Supplementary data

Supplementary data associated with this article can be found, in the online version, at doi:10.1016/j.bbrc.2012.02.131.

References

[1] B.T. Dye, B.A. Schulman, Structural mechanisms underlying posttranslational modification by ubiquitin-like proteins, Annu. Rev. Biophys. Biomol. Struct. 36 (2007) 131–150.

[2] T. Hunter, The age of crosstalk: phosphorylation, ubiquitination, and beyond, Mol. Cell 28 (2007) 730–738.

[3] R.D. Vierstra, The ubiquitin-26S proteasome system at the nexus of plant biology, Nat. Rev. Mol. Cell. Biol. 110 (2009) 385–397.

[4] J. Smalle, R.D. Vierstra, The ubiquitin 26S proteasome proteolytic pathway, Annu. Rev. Plant Biol. 55 (2004) 555–590.

[5] J. Moon, G. Parry, M. Estelle, The ubiquitin-proteasome pathway and plant development, Plant Cell 16 (2004) 3181–3195.

[6] K. Dreher, J. Callis, Ubiquitin, hormones and biotic stress in plants, Ann. Bot. (Lond) 99 (2007) 787–822.

[7] J.H. Lee, W.T. Kim, Regulation of abiotic stress signal transduction by E3 ubiquitin ligases in *Arabidopsis*, Mol. Cells 31 (2011) 201–208.

[8] W.J. Lyzenga, S.L. Stone, Abiotic stress tolerance mediated by protein ubiquitination, J. Exp. Bot. 63 (2012) 599–616.

[9] E. Kraft, S.L. Stone, L. Ma, N. Su, Y. Gao, O.S. Lau, X.W. Deng, J. Callis, Genome analysis and functional characterization of the E2 and RING-type E3 ligase ubiquitination enzymes of Arabidopsis, Plant Physiol. 139 (2005) 1597–1611.

[10] S.L. Stone, H. Hauksdóttir, A. Troy, J. Herschleb, E. Kraft, J. Callis, Functional analysis of the RING-type ubiquitin ligase family of Arabidopsis, Plant Physiol. 137 (2005) 13–30.

[11] J.H. Ko, S.H. Yang, K.H. Han, Upregulation of an Arabidopsis RING-H2 gene, XERICO, confers drought tolerance through increased abscisic acid biosynthesis, Plant J. 47 (2006) 343–355.

[12] Y. Zhang, C. Yang, Y. Li, N. Zheng, H. Chen, Q. Zhao, T. Gao, H. Guo, Q. Xie, SDIR1 is a RING finger E3 ligase that positively regulates stress-responsive abscisic acid signaling in Arabidopsis, Plant Cell 19 (2007) 1912–1929.

[13] F. Qin, Y. Sakuma, L.S. Tran, K. Maruyama, S. Kidokoro, Y. Fujita, M. Fujita, T. Umezawa, Y. Sawano, K. Miyazono, M. Tanokura, K. Shinozaki, K. Yamaguchi-Shinozaki, Arabidopsis DREB2A-interacting proteins function as RING E3 ligases and negatively regulate plant drought stress-responsive gene expression, Plant Cell 20 (2008) 1693–1707.

[14] H.K. Lee, S.K. Cho, O. Son, Z. Xu, I.H. Hwang, W.T. Kim, Drought stress-induced Rma1H1, a RING membrane-anchor E3 ubiquitin ligase homolog, regulates aquaporin levels via ubiquitination in transgenic Arabidopsis plants, Plant Cell 21 (2009) 622–641.

[15] M.Y. Ryu, S.K. Cho, W.T. Kim, The Arabidopsis C3H2C3-type RING E3 ubiquitin ligase AtAIRP1 is a positive regulator of an ABA-dependent response to drought stress, Plant Physiol. 154 (2010) 1983–1997.

[16] S.K. Cho, M.Y. Ryu, D.H. Seo, B.G. Kang, W.T. Kim, The Arabidopsis RING E3 ubiquitin ligase AtAIRP2 plays combinatory roles with AtAIRP1 in ABA-mediated drought stress responses, Plant Physiol. 157 (2011) 2240–2257.

[17] H. Li, H. Jiang, Q. Bu, Q. Zhao, J. Sun, Q. Xie, C. Li, The Arabidopsis RING finger E3 ligase RHA2b acts additively with RHA2a in regulating abscisic acid signaling and drought response, Plant Physiol. 156 (2011) 550–563.

[18] H. Liu, H. Zhang, Y. Yang, G. Li, Y. Yang, X. Wang, B.M. Basnayake, D. Li, F. Song, Functional analysis reveals pleiotropic effects of rice RING-H2 finger protein gene *OsBIRF1* on regulation of growth and defense responses against abiotic and biotic stresses, Plant Mol. Biol. 68 (2008) 17–30.

[19] G.G. Park, J.J. Park, J. Yoon, S.N. Yu, G. An, A RING finger E3 ligase gene, *Oryza sativa* Delayed Seed Germination 1 (OsDSG1), controls seed germination and stress responses in rice, Plant Mol. Biol. 74 (2010) 467–478.

[20] H. Bae, S.K. Kim, S.K. Cho, B.G. Kang, W.T. Kim, Overexpression of OsRDCP1, a rice RING domain-containing E3 ubiquitin ligase, increased tolerance to drought stress in rice (*Oryza sativa* L.), Plant Sci. 180 (2011) 775–782.

[21] Y. Ning, C. Jantasuriyarat, Q. Zhao, H. Zhang, S. Chen, J. Liu, L. Liu, S. Tang, C.H. Park, X. Wang, X. Liu, L. Dai, Q. Xie, G.L. Wang, The SINA E3 ligase OsDIS1 negatively regulates drought response in rice, Plant Physiol. 157 (2011) 242–255.

[22] T.-H. Kim, M. Böhmer, H. Hu, N. Nishimura, J.I. Schroeder, Guard cell signal transduction network: Advances in understanding abscisic acid, CO_2, and Ca^{2+} signaling, Annu. Rev. Plant Biol. 61 (2010) 561–591.

[23] A.S. Raghavendra, V.K. Gonugunta, A. Christmann, E. Grill, ABA perception and signalling, Trends Plant Sci. 15 (2010) 395–401.

[24] O. Son, S.K. Cho, S.J. Kim, W.T. Kim, *In vitro* and *in vivo* interaction of AtRma2 E3 ubiquitin ligase and auxin binding protein 1, Biochem. Biophys. Res. Commun. 393 (2010) 492–497.

[25] L. Liu, Y. Zhang, S. Tang, Q. Zhao, Z. Zhang, H. Zhang, L. Dong, H. Guo, Q. Xie, An efficient system to detect protein ubiquitination by agroinfiltration in *Nicotiana benthamiana*, Plant J. 61 (2010) 893–903.

[26] I. Ahuja, R.C.H. de Vos, A.M. Bones, R.D. Hall, Plant molecular stress responses face climate change, Trends Plant Sci. 15 (2010) 664–674.

[27] F. Tardieu, C. Granier, B. Muller, Water deficit and growth. Co-ordinating processes without an orchestrator?, Curr Opin. Plant Biol. 14 (2011) 283–289.

Biochemical and Biophysical Research Communications 420 (2012) 148–155

Contents lists available at SciVerse ScienceDirect

Biochemical and Biophysical Research Communications

journal homepage: www.elsevier.com/locate/ybbrc

Effect of angiotensin II on proliferation and differentiation of mouse induced pluripotent stem cells into mesodermal progenitor cells

Toshiaki Ishizuka *, Hazuki Goshima, Ayako Ozawa, Yasuhiro Watanabe

Department of Pharmacology, National Defense Medical College, Tokorozawa, Saitama 359-8513, Japan

ARTICLE INFO

Article history:
Received 21 February 2012
Available online 3 March 2012

Keywords:
Angiotensin II
Superoxide
p38 MAPK
Induced pluripotent stem cells

ABSTRACT

Previous studies suggest that angiotensin receptor stimulation may enhance not only proliferation but also differentiation of undifferentiated stem/progenitor cells. Therefore, in the present study, we determined the involvement of the angiotensin receptor in the proliferation and differentiation of mouse induced pluripotent stem (iPS) cells. Stimulation with angiotensin II (Ang II) significantly increased DNA synthesis in mouse iPS cells cultured in a medium with leukemia inhibitory factor (LIF). Pretreatment of the cells with either candesartan (a selective Ang II type 1 receptor [AT_1R] antagonist) or Tempol (a cell-permeable superoxide scavenger) significantly inhibited Ang II-induced DNA synthesis. Treatment with Ang II significantly increased JAK/STAT3 phosphorylation. Pretreatment with candesartan significantly inhibited Ang II- induced JAK/STAT3 phosphorylation. In contrast, induction of mouse iPS cell differentiation into Flk-1-positive mesodermal progenitor cells was performed in type IV collagen (Col IV)-coated dishes in a differentiation medium without LIF. When Col IV-exposed iPS cells were treated with Ang II for 5 days, the expression of Flk-1 was significantly increased compared with that in the cells treated with the vehicle alone. Pretreatment of the cells with both candesartan and SB203580 (a p38 MAPK inhibitor) significantly inhibited the Ang II- induced increase in Flk-1 expression. Treatment with Ang II enhanced the phosphorylation of p38 MAPK in Col IV- exposed iPS cells. These results suggest that the stimulation of mouse iPS cells with AT_1R may enhance LIF-induced DNA synthesis, by augmenting the generation of superoxide and activating JAK/STAT3, and that AT_1R stimulation may enhance Col IV-induced differentiation into mesodermal progenitor cells via p38 MAPK activation.

1. Introduction

Stimulation of the angiotensin receptor by angiotensin II (Ang II) regulates many physiological responses in a variety of cell types. It has been suggested that activation of the Ang II type 1 receptor (AT_1R) enhances the proliferation of somatic cells, such as vascular smooth muscle cells, lung fibroblasts, and kidney mesangial cells [1–3]. In addition, it has been demonstrated that Ang II induces proliferation of hematopoietic progenitor cells isolated from murine bone marrow or human cord blood [4]. Han et al. also showed that Ang II may enhance DNA synthesis in mouse embryonic stem (ES) cells, predominantly through the AT_1R [5]. On the other hand, several studies have suggested the involvement of Ang II in the differentiation of stem/progenitor cells [6,7]. Zambidis et al. also showed that the differentiation of human hemangioblasts into either hematopoietic or endothelial progenitor cells may be modulated by angiotensin receptors [6]. In addition, Kim et al. showed that Ang II may induce the differentiation of human adipose tissue-derived mesenchymal stem cells into contractile smooth muscle-like cells [7]. Thus, these findings suggest that angiotensin receptor stimulation may enhance not only the proliferation but also the differentiation of undifferentiated pluripotent stem cells into mesodermal progenitor cells.

Takahashi and Yamanaka generated induced pluripotent stem (iPS) cells from mouse or human fibroblasts by introducing 4 transcription factors (Oct3/4, Sox2, Klf4, and c-Myc) [8]. These iPS cells may generate customized, patient-specific pluripotent cells. The clinical use of iPS cells may be a way to overcome the current obstacles in stem cell-based therapy, including the immunological intolerance of allogeneic cells and the ethical concerns of using ES cells. Thus, the molecular mechanisms that regulate the proliferation or differentiation of iPS cells are of great interest. Colonies of iPS cells are morphologically indistinguishable from those of ES cells. Moreover, ES cells and iPS cells have been shown to share many similarities, including self-renewal and multi-lineage differentiation [9]. However, it is not fully understood whether the growth and differentiation of both cell types rely on similar molecular mechanisms. In addition, to date, no studies have shown that mouse iPS cells express angiotensin receptors. Therefore, in the

* Corresponding author. Address: Department of Pharmacology, National Defense Medical College, 3-2, Namiki, Tokorozawa, Saitama 359-8513, Japan. Fax: +81 4 2996 5191.
E-mail address: tishizu@ndmc.ac.jp (T. Ishizuka).

0006-291X/$ - see front matter © 2012 Elsevier Inc. All rights reserved.
doi:10.1016/j.bbrc.2012.02.132

present study, we studied the expression of angiotensin receptors in mouse iPS cells and determined the involvement of angiotensin receptors in the proliferation and differentiation of mouse iPS cells.

2. Materials and methods

2.1. Murine iPS cell cultures

Germline-competent mouse iPS cell lines (20D17) were obtained from RIKEN BioResource Center (Tsukuba, Japan), in agreement with Kyoto University. Mouse iPS cells were expanded on mitomycin-C-treated mouse embryonic fibroblasts (MEFs) in 60 mm culture dishes (Nunc, Rochester, NY) coated with 0.1% gelatin at 37 °C in a 5% CO_2 environment. The culture medium was composed of Dulbecco's modified Eagle's medium (DMEM) containing 15% fetal bovine serum (FBS; Invitrogen, Carlsbad, CA), 0.1 mM nonessential amino acids (Invitrogen), 0.1 mM 2-mercaptethanol (Wako, Osaka, Japan), 100 U/ml of penicillin and 100 μg/ml of streptomycin (Invitrogen), and 1000 U/ml recombinant human leukemia inhibitory factor (LIF; Wako).

To eliminate contaminating MEFs, the iPS cell colonies were passaged up to 4 times without feeder cells on gelatin-coated 100 mm culture dishes. When cultures became confluent, the cell colonies were detached and dissociated into single cells, using 0.25% trypsin/ethylenediaminetetraacetic acid (EDTA; Invitrogen), and then re-plated at a density of 1×10^6 cells/dish. After 24 h incubation, the culture medium was replaced by serum-free DMEM with or without LIF for 24 h before the experiments. To assess the viability of the iPS cells, the total number of surviving cells was counted after staining with a 0.4% trypan blue solution (Sigma, St. Louis, MO) and the cell survival rate was calculated as the percentage of the total number of re-plated cells.

2.2. Immunofluorescence staining

Twenty-four hours following re-plating onto gelatin- coated 4-well chamber slides (Nunc), the cells were grown in serum-free DMEM with LIF for 24 h. The cells were fixed with 4% paraformaldehyde at 4 °C for 30 min. The sections were then incubated in blocking solution (10% FBS in phosphate-buffered saline [PBS]) for 1 h at room temperature and incubated with monoclonal rabbit anti-AT_1R antibody or anti-AT_2R antibody (1:100; Santa Cruz Biotechnology, Santa Cruz, CA) in PBS containing 2.5% FBS at 4 °C overnight. The sections were then incubated with goat anti-rabbit IgG conjugated with Alexa Fluor 594 (1:200; Invitrogen) in PBS for 1 h at room temperature. Between the steps, the sections were washed 5 times for 5 min in PBS. The fluorescence images were visualized using fluorescence microscopy (IX 71; Olympus, Tokyo, Japan).

2.3. BrdU incorporation

Incorporation of 5-bromo-2′-deoxyuridine (BrdU) was used to monitor cellular DNA synthesis. The enzyme-linked immunosorbent assay (ELISA) for the detection of BrdU incorporation into cellular DNA using a BrdU Labeling and Detection Kit III (Roche, Mannheim, Germany) was performed according to the manufacturer's instructions. Twenty-four hours following re-plating onto gelatin-coated 96-well plates, the cells were grown in serum-free DMEM with or without LIF for 24 h and treated with or without Ang II (Sigma), candesartan (a selective AT_1R antagonist; Takeda Pharmaceutical Co., Osaka, Japan), and PD123319 (a selective AT_2R antagonist; Sigma). After the 24 h treatment, BrdU (10 μM) was added and incorporated into freshly synthesized DNA for 2 h. Following cell fixation, a peroxidase-labeled antibody to BrdU was added. In the final step, the peroxidase substrate was added. In this reaction, the peroxidase enzyme catalyzed the cleavage of the substrate, yielding a colored product. Absorbance of the sample was determined using the Bio-Rad Model 3550 microplate reader (Bio-Rad) at a wavelength of 405 nm with the reference wavelength set at 490 nm.

2.4. Differentiation of mouse iPS cells into mesodermal progenitor cells

Induction of mouse iPS cell differentiation into mesodermal progenitor cells was performed on type IV collagen (Col IV)-coated dishes in differentiation medium as described previously [10,11]. The mouse iPS cells were dissociated and resuspended in α-minimum essential medium (Invitrogen) supplemented with 10% FBS, 50 μM β-mercaptoethanol, and 0.1 mM nonessential amino acids, without LIF. They were then transferred to Col IV-coated 35 mm dishes or 4-well chamber slides (1.25×10^5 cells per cm^2; Becton Dickinson, Rutherford, NJ), and cultured with or without Ang II for 5 days. The differentiated cells, on 35 mm dishes, were

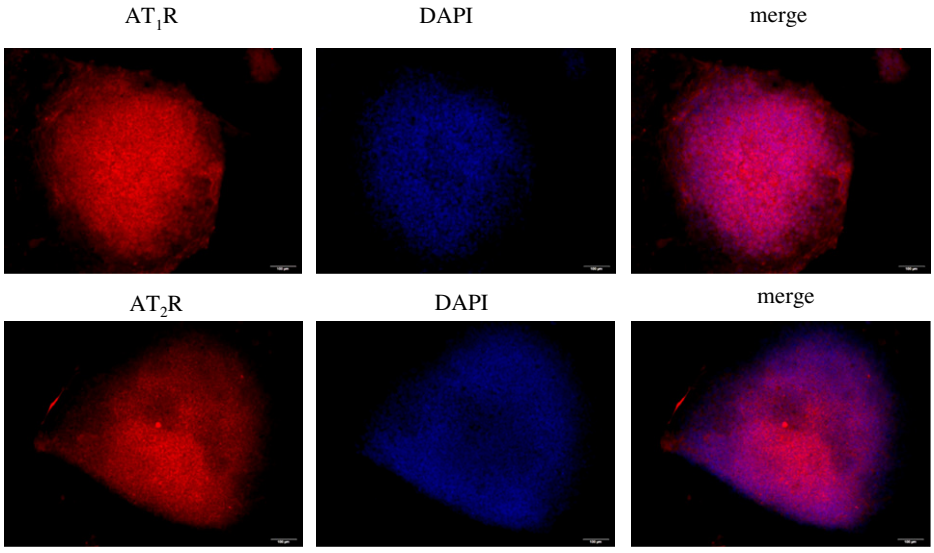

Fig. 1. The Ang II type 1 receptor (AT_1R) or type 2 receptor (AT_2R) is expressed in cultured mouse iPS cells. Representative immunofluorescence images of mouse iPS cells cultured with LIF depicting immunolabeling for the AT_1R, AT_2R, or DAPI. The scale bars show 100 μm.

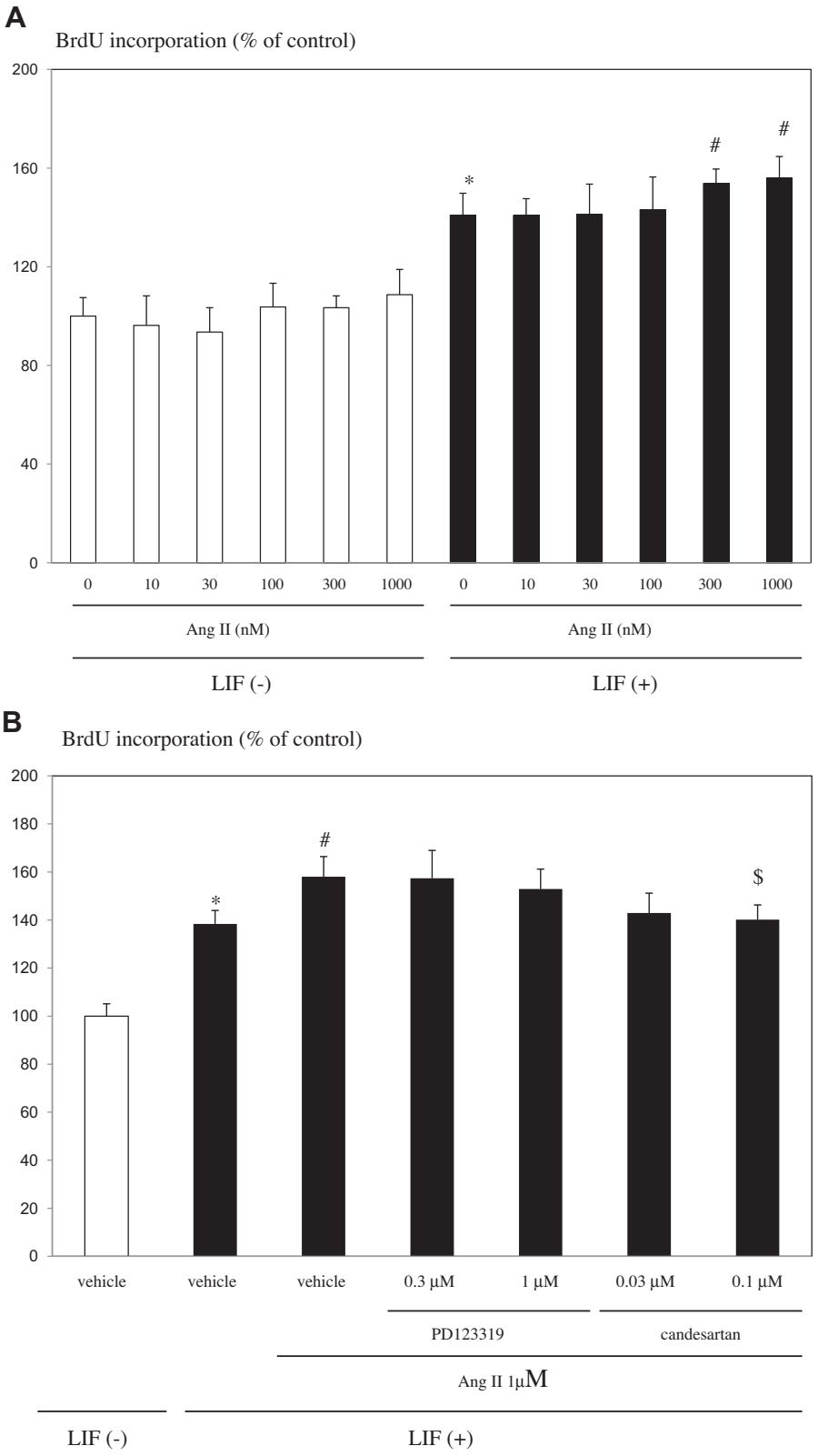

Fig. 2. The effects of Ang II or angiotensin receptor antagonists on the DNA synthesis of mouse iPS cells cultured with or without LIF. (A) Mouse iPS cells were stimulated with Ang II (10, 30, 100, 300, or 1000 nM) for 24 h in a serum-free medium with or without LIF. (B) Mouse iPS cells were pretreated with PD123319 (0.3 or 1 μM) or candesartan (0.03 or 0.1 μM) for 30 min and then incubated with Ang II (1 μM) for 24 h in a serum-free medium with LIF and pulsed with 10 μM BrdU for 2 h. (C) Mouse iPS cells were pretreated with Tempol (30 or 100 μM) for 30 min and then incubated with Ang II (1 μM) for 24 h in a serum-free medium with LIF. The controls consisted of cultures grown in the absence of Ang II under LIF-free conditions. After the cells were pulsed with 10 μM BrdU for 2 h, incorporation of BrdU into the DNA was measured as described in the Section 2. Values represent the mean ± SE of 4 independent experiments performed with triplicate dishes. $^{*}P < 0.05$ versus vehicle without LIF; $^{\#}P < 0.05$ versus vehicle with LIF; $^{\$}P < 0.05$ versus Ang II 1 μM with LIF.

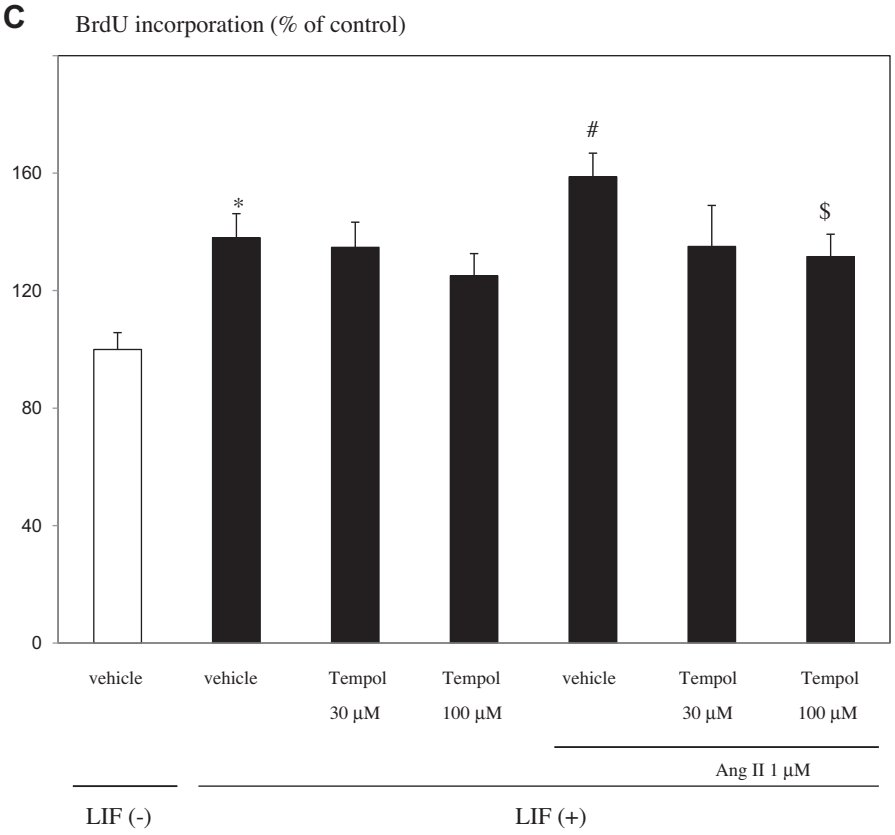

Fig. 2 (*continued*)

harvested for western blot and flow cytometry analyses to quantitatively evaluate Flk-1 expression.

2.5. Western blot analysis

Cells were lysed in a cold buffer containing 50 mM Tris (pH 7.4), 150 mM NaCl, 2 mM EDTA, 1% Triton X-100, 10 mM $Na_4P_2O_7$, 20 mM NaF, 1 mM Na_3VO_4, and 10 mg/ml of aprotinin; the lysates were then centrifuged at 15,000 rpm for 15 min. The protein extracts (15 μg each) were subjected to electrophoresis on a 7.5–15% sodium dodecyl sulfate–polyacrylamide (SDS) gel and blotted onto a polyvinylidene difluoride membrane with a semi-dry blotting apparatus. After blocking the blots, primary antibodies were applied at the following dilutions in PBS containing 2% bovine serum albumin (BSA): rabbit anti-mouse phospho-p38 MAPK (Cell Signaling Technology, Beverly, MA), rabbit anti-mouse p38 MAPK (Cell Signaling Technology), rabbit anti-mouse phospho-JAK (Santa Cruz Biotechnology), rabbit anti-mouse JAK (Santa Cruz Biotechnology), rabbit anti-mouse phospho-Stat3 (Cell Signaling Technology), rabbit anti-mouse Stat3 (Cell Signaling Technology), rabbit anti-mouse Flk-1 (Santa Cruz Biotechnology), and rabbit anti-mouse β-actin (Acris Antibodies GmbH, Hiddenhausen, Germany) at 2000:1. The respective secondary peroxidase-conjugated antibody was added and the immunoreactive proteins were visualized using an ECL Western Blotting Detection Kit (Amersham Biosciences, Piscataway, NJ). The immunoreactive bands were densitometrically analyzed using a luminescent image analyzer (LAS 3000; Fuji Film, Tokyo, Japan) and software for image analysis (Multi Gauge ver. 3.1; Fuji Film). The density of the bands was normalized using β-actin as an internal standard.

2.6. Flow cytometry analysis

After induction of the Flk-1-positive cells, the cells were harvested and stained with phycoerythrin (PE)-conjugated monoclonal rat anti-mouse Flk-1 antibody (1:200; BD Pharmingen, San Diego, CA) at 4 °C for 60 min. PE-conjugated rat IgG (BD Pharmingen) served as a control. Flow cytometry analysis was performed on 20,000 gated events using a FACS Calibur (Becton Dickinson). The data were analyzed using the Cell Quest program (Becton Dickinson).

2.7. Statistical analysis

All results were expressed as the means ± the standard error of the mean. Comparisons between the means of multiple groups were performed by one-way analysis of variance and Scheffe's multiple comparison test. In all tests, differences were considered statistically significant at $P < 0.05$.

3. Results

3.1. Mouse iPS cells express the angiotensin receptor

We performed immunofluorescence staining to determine whether mouse iPS cells could potentially express AT_1R or AT_2R. The immunofluorescence images showed that both AT_1R and AT_2R had a honeycomb-like staining pattern, and that the staining for AT_1R or AT_2R did not merge with nuclear staining with 4′,6-diamidino-2-phenylindole (DAPI). Thus, both the AT_1R and the AT_2R may be expressed on the surface of mouse iPS cells (Fig. 1).

3.2. Effects of Ang II or angiotensin receptor antagonists on mouse iPS cell proliferation

We initially examined the effect of Ang II on the proliferation of mouse iPS cells cultured with or without LIF. Although Ang II

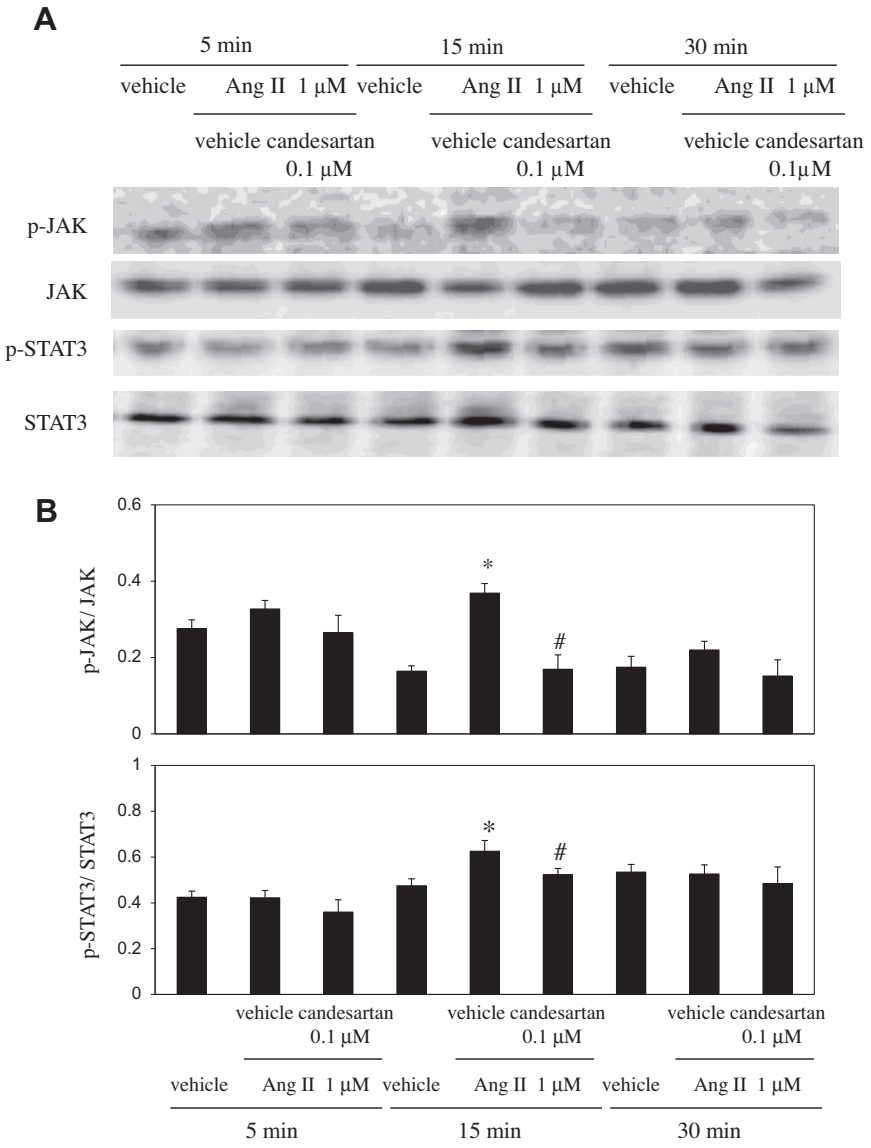

Fig. 3. The effects of Ang II or candesartan on JAK/STAT3 phosphorylation in mouse iPS cells cultured with LIF. (A) The mouse iPS cells were stimulated with Ang II (1 μM) for the indicated time periods (5, 15, or 30 min). The cell extracts were fractionated by SDS–PAGE, and western blot analysis was performed using antibodies against phosphorylated and total JAK or STAT3, as described in the Section 2. The blots shown are representative of 4 independent experiments. (B) Bar graphs indicate quantitative analysis of the bands by using densitometric analysis. Values were normalized by the optical density values of the total JAK or STAT3 bands. $^{*}P < 0.01$ versus 15 min with the vehicle. $^{\#}P < 0.05$ versus 15 min with Ang II (1 μM).

treatment did not affect BrdU incorporation under LIF-free conditions, Ang II treatment significantly increased the incorporation of BrdU into mouse iPS cells cultured with LIF (Fig. 2A).

To confirm the involvement of angiotensin receptors in the increased proliferation of the mouse iPS cells cultured with LIF, we pretreated the cells with a selective AT_1R antagonist, candesartan, or a selective AT_2R antagonist, PD123319. It was observed that pretreatment with 0.1 μM candesartan significantly inhibited the Ang II-induced increase in BrdU incorporation (Fig. 2B). However, 1 μM of PD123319 did not affect the Ang II-induced increases in BrdU incorporation.

3.3. Effect of a superoxide scavenger on the Ang II-induced DNA synthesis of mouse iPS cells

It was reported that Ang II activates the generation of superoxide anions in rat vascular smooth muscle cells [12]. Chan et al. suggested that reactive oxygen species may be involved in the intracellular signaling process that induces the proliferation of a wide range of mammalian cell types [13].

Thus, we determined the effect of Tempol (a cell-permeable superoxide scavenger) on the proliferation of mouse iPS cells. The DNA synthesis of vehicle-treated cells cultured with LIF was not inhibited by the pretreatment with Tempol (Fig. 2C). In contrast, the DNA synthesis of Ang II-treated cells cultured with LIF was significantly inhibited by pretreatment with 100 μM Tempol (Fig. 2C).

3.4. Effect of Ang II on the activation of JAK/STAT in mouse iPS cells cultured with LIF

Stimulation of mouse ES cells with LIF activated the Janus kinase (JAK)/signal transducers and activators of the transcription 3 (STAT3) pathway through the LIF receptor/gp130 complex [14]. This pathway has been shown to play a crucial role in LIF-induced mouse ES cell renewal [14]. We examined the involvement of the JAK/STAT3 pathway in Ang II-induced DNA synthesis. We found

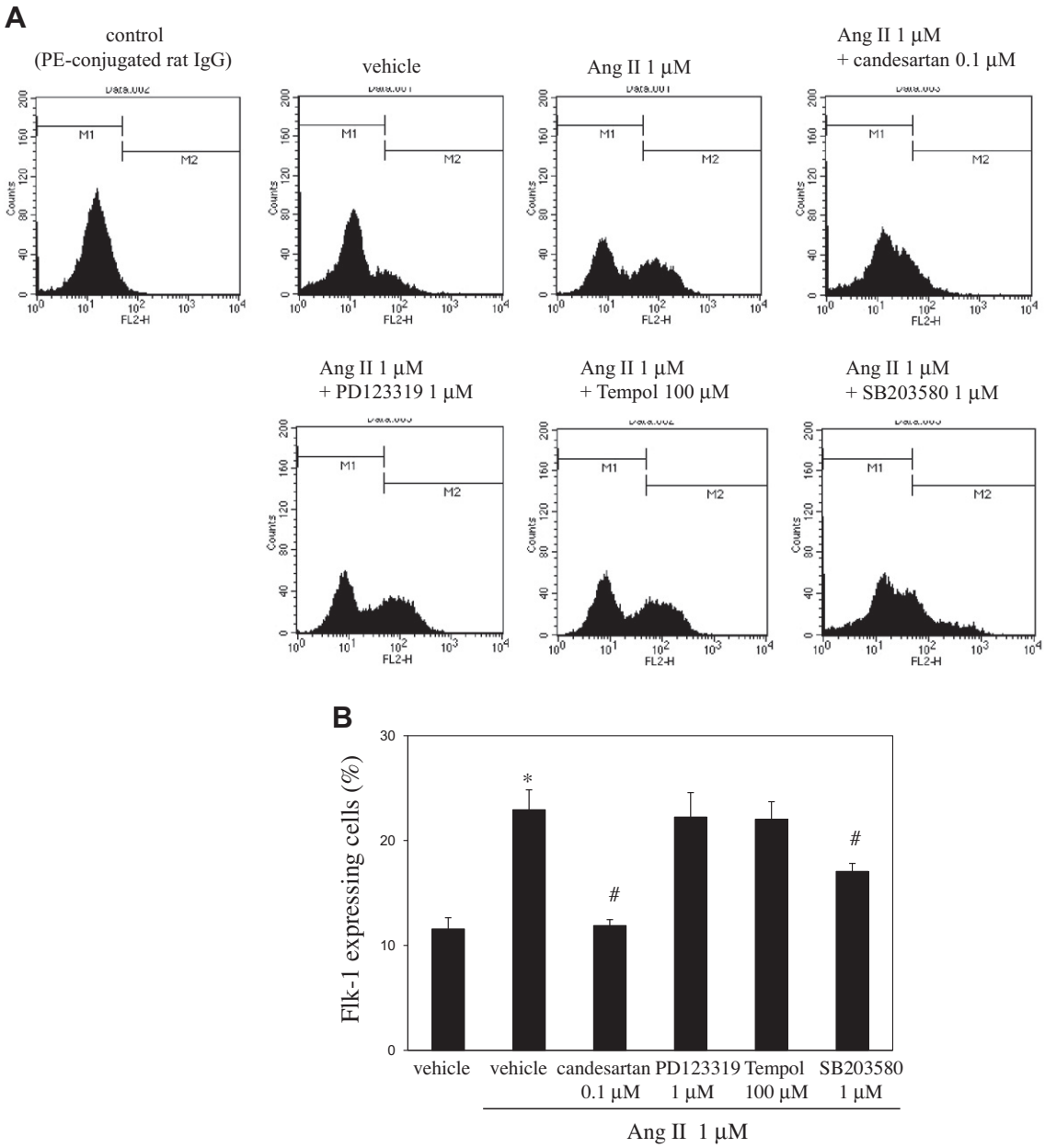

Fig. 4. The effects of Ang II, candesartan, PD123319, Tempol, or SB203580 on Flk-1 expression or p38 MAPK phosphorylation in mouse iPS cells exposed to Col IV. (A) The Col IV-exposed iPS cells were pretreated with candesartan (0.1 μM), PD123319 (1 μM), or Tempol (100 μM), or SB203580 (1 μM) for 30 min and then incubated with Ang II (1 μM) for 5 days. Representative histograms show the expression of Flk-1 in differentiated iPS cells evaluated by single-color flow cytometry as described in the Section 2. (B) Bar graphs indicate the percentage of cells expressing Flk-1 as determined by flow cytometry analysis. (C) The cell extracts were fractionated by SDS–PAGE, and western blot analysis was performed using antibodies against Flk-1 or β-actin as described in the Section 2. The blots shown are representative of 4 independent experiments. The bar graphs indicate quantitative analysis of the bands by using densitometric analysis. The values were normalized to the optical density values of the Flk-1 or β-actin bands. (D) The Col IV-exposed iPS cells were pretreated with candesartan (0.1 μM) for 30 min and then stimulated with Ang II (1 μM) for 5, 15, or 30 min. The blots shown are representative of 4 independent experiments. The bar graphs indicate quantitative analysis of the bands by using densitometric analysis. $^{*}P < 0.05$ versus 5 min with the vehicle; $^{\#}P < 0.01$ versus 5 min with Ang II.

that treatment with Ang II significantly enhanced the JAK/STAT3 phosphorylation of mouse iPS cells cultured with LIF (Fig. 3A and B). In contrast, the JAK/STAT3 phosphorylation of Ang II-treated cells cultured with LIF was significantly inhibited by pretreatment with 0.1 μM candesartan (Fig. 3A and B).

3.5. Effects of Ang II or angiotensin receptor antagonists on the differentiation of mouse iPS cells into mesodermal progenitor cells

Similar to the results observed in previous studies [11], flow cytometry analysis revealed the presence of Flk-1-positive progenitor cells in Col IV-exposed iPS cells (Fig. 4A and B). Western blot analysis confirmed that the differentiated cells expressed Flk-1 (Fig. 4C). When Col IV-exposed iPS cells were treated with Ang II for 5 days, the expression of Flk-1 was significantly increased compared with that in the cells treated with the vehicle alone (Fig. 4A–C). It was also observed that pretreatment with 0.1 μM candesartan significantly inhibited the Ang II-induced increase in Flk-1 expression. However, PD123319 did not affect the Ang II-induced increases in Flk-1 expression. In contrast, pretreatment with SB203580, a p38 MAPK inhibitor, significantly suppressed the Ang II-induced increases in Flk-1 expression. The treatment with

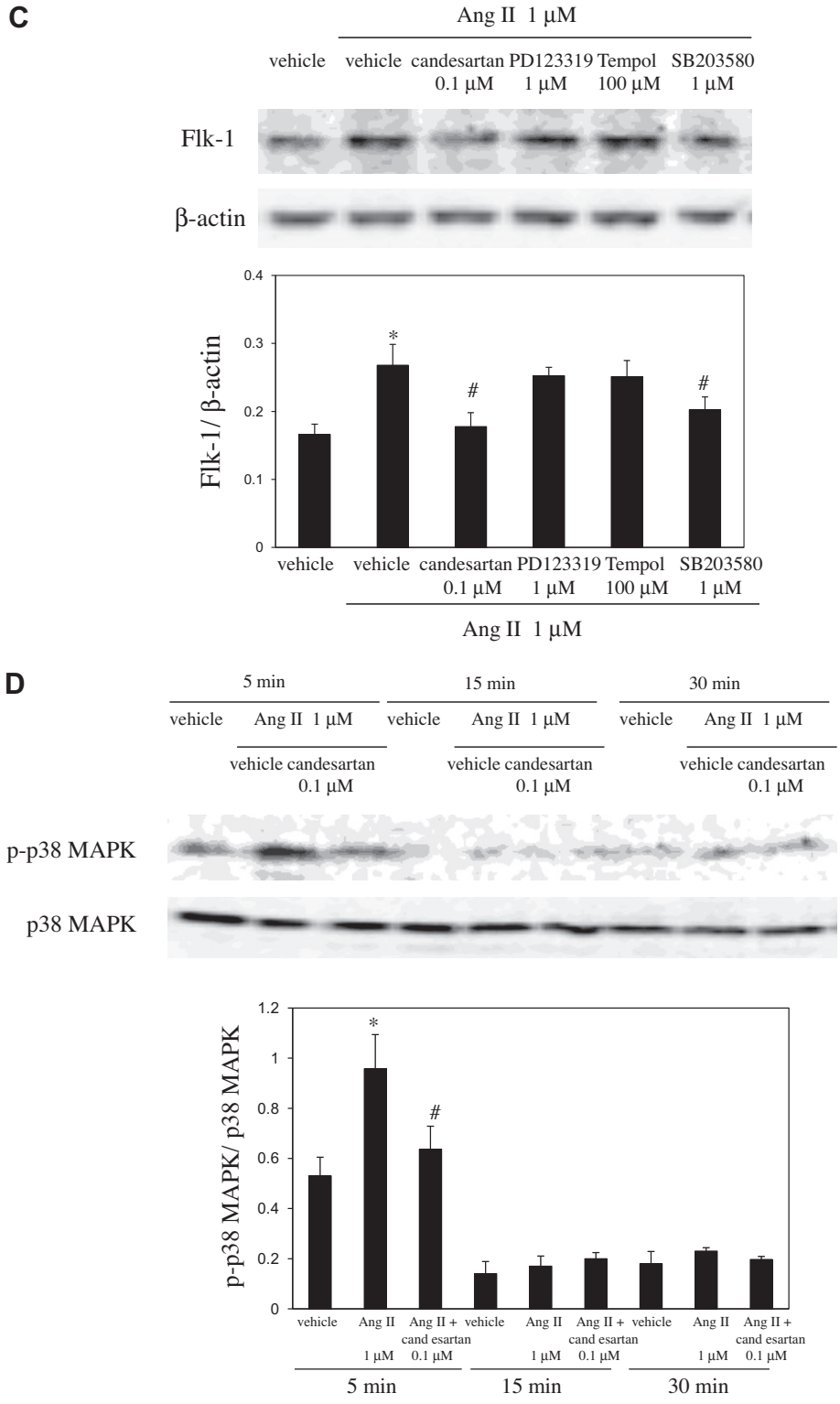

Fig. 4 (*continued*)

Ang II significantly enhanced the phosphorylation of p38 MAPK in Col IV-exposed iPS cells (Fig. 4D).

4. Discussion

In the present study, we demonstrated that undifferentiated mouse iPS cells express both AT_1R and AT_2R (Fig. 1). We also showed that treatment with Ang II significantly enhanced LIF-induced DNA synthesis in mouse iPS cells (Fig. 2A). The enhancement of LIF-induced DNA synthesis by Ang II was blocked by candesartan (a selective AT_1R antagonist) but not by PD123319 (a selective AT_2R antagonist) (Fig. 2B). Moreover, pretreatment with Tempol, a superoxide scavenger, significantly inhibited Ang II-enhanced DNA synthesis (Fig. 2C). We also found that stimulation with Ang II significantly enhanced the JAK/STAT3 phosphorylation of mouse iPS cells cultured with LIF (Fig. 3A and B). Previous

studies have suggested that the JAK/STAT signaling pathway may be an important link between the activation of the AT_1R and the proliferation of vascular smooth muscle cells [15,16]. Simon et al. reported that the JAK/STAT pathway was activated in mouse fibroblasts in response to reactive oxygen species [17]. In addition, Schieffer et al. showed that stimulation of the JAK/STAT pathway by Ang II may require superoxide anions, generated by NADPH oxidase, based on work with rat aorta smooth muscle cells [18]. These findings suggest that stimulation with AT_1R in the presence of LIF may augment LIF-induced JAK/STAT activation and enhance DNA synthesis in mouse iPS cells.

Previous studies have suggested that Flk-1-expressing cells may be multipotent mesodermal progenitor cells that are capable of differentiating into both cardiovascular and hematopoietic lineages [10,11]. Barreut et al. demonstrated that ES cells derived from p38 MAPK knockout mouse do not differentiate into mesodermal lineages and that the re-expression of p38 MAPK in these cells rescues their mesodermal differentiation defects [19]. In addition, Wu et al. showed that p38 MAPK may be crucial during the early stages of mouse ES cell differentiation into mesodermal lineages [20]. The present study showed that treatment with Ang II significantly enhanced Flk-1 expression in Col IV-exposed differentiated iPS cells (Fig. 4A–C). The enhancement of Flk-1 expression by Ang II was blocked by candesartan (a selective AT_1R antagonist) but not by PD123319 (a selective AT_2R antagonist). Moreover, pretreatment with SB203580, a selective p38 MAPK inhibitor, significantly inhibited the Ang II-enhanced Flk-1 expression. We also found that stimulation with Ang II significantly enhanced p38 MAPK phosphorylation in Col IV-exposed differentiated iPS cells (Fig. 4D). These findings suggest that p38 MAPK activation may be mainly involved in the Ang II-enhanced differentiation of mouse iPS cells into mesodermal progenitor cells. Schenke-Layland et al. showed that Col IV-differentiated iPS cell-derived Flk-1 positive cells had the capacity to differentiate into cardiomyocytes, vascular endothelial cells, or vascular smooth muscle cells [11]. We also confirmed that the Flk-1-positive cells derived from mouse iPS cells can differentiate into vascular endothelial cells or vascular smooth muscle cells (data not shown). Studies to determine whether Ang II treatment enhances the differentiation of mouse iPS cells into cardiovascular cells are under investigation.

Although the present study showed that undifferentiated mouse iPS cells express AT_2R, the effect of AT_2R remains unclear. Grady et al. showed that AT_2R was expressed highly and transiently in fetal brain tissues [21]. It was reported that the differentiation of doparminergic neurons from mesencephalic precursors is increased by AT_2R stimulation [22]. However, further studies to determine the involvement of AT_2R in the differentiation of mouse iPS cells into neural lineages are required.

The results of this study validate that AT_1R stimulation may lead to a significant increase in the proliferation and differentiation of mouse iPS cells into mesodermal progenitor cells. It is very important to establish a methodology in which both iPS cells and iPS cell-derived progenitor cells can be propagated to a greater degree, because these cells may be used as a future source of regenerative therapy. Thus, understanding the physiological role of AT_1R in mouse iPS cells may be useful in the development of better culture conditions.

Acknowledgments

This work was supported in part by a grant from the Smoking Research Foundation (No. 33) and the Scientific Research Program from the Japan Society for the Promotion of Sciences (No. 23059321) to Y.W., and by a Grant-in-aid for the Special Research Program from the National Defense Medical College (No. 23) and the Scientific Research Program from the Japan Society for the Promotion of Sciences (No. 22500687) to T.I.

References

[1] Z. Wang, P.J. Rao, S.D. Shillcutt, W.H. Newman, Angiotensin II induces proliferation of human cerebral artery smooth muscle cells through a basic fibroblast growth factor dependent mechanism, Neuroscience Letters 373 (2005) 38–41.
[2] R.P. Marshall, R.J. McAnulty, G.J. Laurent, Angiotensin II is mitogenic for human lung fibroblasts via activation of the type 1 receptor, American Journal of Respiratory and Critical Care Medicine 161 (2000) 1999–2004.
[3] A. Zhang, G. Ding, S. Huang, Y. Wu, X. Pan, X. Guan, R. Chen, T. Yang, C-Jun NH2-terminal kinase mediation of angiotensin II-induced proliferation of human mesangial cells, American Journal of Physiology Renal Physiology 288 (2005) F1118–F1124.
[4] K.E. Rodgers, S. Xiong, R. Steer, G.S. diZerega, Effect of angiotensin II on hematopoietic progenitor cell proliferation, Stem Cells 18 (2000) 287–294.
[5] H.J. Han, J.Y. Han, J.S. Hao, S.H. Lee, M.Y. Lee, Y.H. Kim, Ang II-stimulated DNA synthesis is mediated by Ang II receptor-dependent Ca^{2+}/PKC as well as EGF receptor- dependent PI3K/Akt/mTOR/p70S6K1 signal pathways in mouse embryonic stem cells, Journal of Cellular Physiology 211 (2007) 618–629.
[6] E.T. Zambidis, T.S. Park, W. Yu, A. Tam, M. Levine, X. Yuan, M. Pryzhkova, B. Peault, Expression of angiotensin- converting enzyme (CD143) identifies and regulates primitive hemangioblasts derived from human pluripotent stem cells, Blood 112 (2008) 3601–3614.
[7] Y.M. Kim, E.S. Jeon, W.R. Kim, S.K. Jho, S.W. Ryu, J.H. Kim, Angiotensin II-induced differentiation of adipose tissue-derived mesenchymal stem cells to smooth muscle-like cells, International Journal of Biochemistry and Cell Biology 40 (2008) 2482–2491.
[8] K. Takahashi, S. Yamanaka, Induction of pluripotent stem cells from mouse embryonic and adult fibroblast cultures by defined factors, Cell 126 (2006) 663–676.
[9] K. Okita, T. Ichisaka, S. Yamanaka, Generation of germline-competent induced pluripotent stem cells, Nature 448 (2007) 313–317.
[10] G. Narazaki, H. Uosaki, M. Teranishi, K. Okita, B. Kim, S. Matsuoka, S. Yamanaka, J.K. Yamashita, Directed and systematic differentiation of cardiovascular cells from mouse induced pluripotent stem cells, Circulation 118 (2008) 498–506.
[11] K. Schenke-Layland, K.E. Rhodes, E. Angelis, Y. Butylkova, S. Heydarkhan-Hagvall, C. Gekas, R. Zhang, J.I. Goldhaber, H.K. Mikkola, K. Plath, W.R. MacLellan, Reprogramming mouse fibroblasts differentiate into cells of the cardio vascular and hematopoietic lineages, Stem Cells 26 (2008) 1537–1546.
[12] K.K. Griendling, C.A. Mimeri, J.D. Ollerenshaw, R.W. Alexander, Angiotensin II stimulates NADH and NADPH oxidase activity in cultured vascular smooth muscle cells, Circulation Research 74 (1994) 1141–1148.
[13] E.C. Chan, F. Jiang, H.M. Peshavariya, G.J. Dusting, Regulation of cell proliferation by NADPH oxidase-mediated signaling potential roles in tissue repair, regenerative medicine and tissue engineering, Pharmacology and Therapy 122 (2009) 97–108.
[14] D.M. Kristensen, M. Kalisz, J.H. Nielsen, Cytokine signaling in embryonic stem cells, Acta Pathologica Microbiologica et Immunologica Scandinavica 113 (2005) 756–772.
[15] M.B. Marreno, B. Schieffer, W.G. Paxton, L. Heerdt, B.C. Berk, P. Delafontaine, K.H. Hernstein, The angiotensin II type 1 receptor associates with and stimulates JAK2 in rat aortic smooth muscle cells, Nature 375 (1995) 247–250.
[16] M.B. Marreno, B. Schieffer, J.B. Harp, B. Ling, Role of Janus kinases/signal transducer and activator of transcription and mitogen-activated protein kinase cascades in angiotensin II- and platelet-derived growth factor-induced vascular smooth muscle proliferation, Journal of Biological Chemistry 272 (1997) 24684–24690.
[17] A.R. Simon, U. Rai, B.L. Fanburg, B.H. Cochran, Activation of the JAK-STAT pathway by reactive oxygen species, American Journal of Physiology 275 (1998) C1640–C1652.
[18] B. Schieffer, M. Luchtefeld, S. Braun, A. Hilfiker, D. Hilfiker-Kleiner, H. Drexler, Role of NADPH oxidase in angiotensin II-induced JAK/STAT signaling and cytokine induction, Circulation Research 87 (2000) 1195–1201.
[19] E. Barruet, Q. Hadadeh, F. Peireti, V.W. Renault, Y. Hadial, D. Bernot, R. Toumaire, D. Negre, I. Juhan-Vague, M.C. Alessi, B. Binetruy, P38 mitogen activated protein kinase controls two-successive-steps during the early mesodermal commitment of embryonic stem cells, Stem Cells and Development 20 (2011) 1233–1246.
[20] J. Wu, J. Kubota, J. Hirayama, Y. Nagai, S. Nishina, T. Yokoi, Y. Asaoka, J. Seo, N. Shimizu, H. Kaiho, T. Watanabe, N. Azuma, T. Katada, H. Nishina, P38 mitogen-activated protein kinase controls a switch between cardiomyocyte and neuronal commitment of murine embryonic stem cells by activating myocyte enhancer factor 2C-dependent bone morphogenetic protein 2 transcription, Stem Cells and Development 19 (2010) 1723–1734.
[21] E.F. Grady, I.A. Seci, C.A. Griffin, M. Schambelam, J.E. Karynyak, Expression of AT2 receptors in the developing rat fetus, Journal of Clinical Investigation 88 (1991) 921–933.
[22] J. Rodriguez-Pallares, C.R. Quiroz, J.A. Parga, M.J. Guerra, J.L. Labandeira-Garcia, Angiotensin II increases differentiation of dopaminergic neurons from mesencephalic precursors via angiotensin type 2 receptors, European Journal of Neuroscience 20 (2004) 1489–1498.

Biochemical and Biophysical Research Communications 420 (2012) 156–160

Contents lists available at SciVerse ScienceDirect

Biochemical and Biophysical Research Communications

journal homepage: www.elsevier.com/locate/ybbrc

Hyperpolarization-activated cation current I_h of dentate gyrus granule cells is upregulated in human and rat temporal lobe epilepsy

Rainer Surges [a,b,*], Maria Kukley [c], Amy Brewster [d], Christiane Rüschenschmidt [a,b], Johannes Schramm [c], Tallie Z. Baram [d], Heinz Beck [a,b,e], Dirk Dietrich [c]

[a] Department of Epileptology, University of Bonn Medical Center, Sigmund-Freud-Str. 25, 53105 Bonn, Germany
[b] Laboratory of Experimental Epileptology and Cognition Research, University of Bonn Medical Center, Sigmund-Freud-Str. 25, 53105 Bonn, Germany
[c] Department of Neurosurgery, University of Bonn Medical Center, Sigmund-Freud-Str. 25, 53105 Bonn, Germany
[d] Departments of Anatomy/Neurobiology and Pediatrics, University of California at Irvine, Irvine, CA 92697-4475, USA
[e] Deutsches Zentrum für Neurodegenerative Erkrankungen e.V., Ludwig Erhard Allee 2, 53175 Bonn, Germany

ARTICLE INFO

Article history:
Received 23 February 2012
Available online 3 March 2012

Keywords:
Hippocampus
Rat pilocarpine model
Patch-clamp
h-Current
Human
Temporal lobe epilepsy

ABSTRACT

The hyperpolarization-activated cation current I_h is an important regulator of neuronal excitability and may contribute to the properties of the dentate gyrus granule (DGG) cells, which constitute the input site of the canonical hippocampal circuit. Here, we investigated changes in I_h in DGG cells in human temporal lobe epilepsy (TLE) and the rat pilocarpine model of TLE using the patch-clamp technique. Messenger-RNA (mRNA) expression of I_h-conducting HCN1, 2 and 4 isoforms was determined using semi-quantitative *in-situ* hybridization. I_h density was ~1.8-fold greater in DGG cells of TLE patients with Ammon's horn sclerosis (AHS) as compared to patients without AHS. The magnitude of somatodendritic I_h was enhanced also in DGG cells in epileptic rats, most robustly during the latent phase after status epilepticus and prior to the occurrence of spontaneous epileptic seizures. During the chronic phase, I_h was increased ~1.7-fold. This increase of I_h was paralleled by an increase in HCN1 and HCN4 mRNA expression, whereas HCN2 expression was unchanged. Our data demonstrate an epilepsy-associated upregulation of I_h likely due to increased HCN1 and HCN4 expression, which indicate plasticity of I_h during epileptogenesis and which may contribute to a compensatory decrease in neuronal excitability of DGG cells.

1. Introduction

The hyperpolarization-activated current I_h is a slowly activating, non-inactivating depolarizing cationic current which is activated by hyperpolarization beyond −50 to −70 mV. These unique biophysical properties provide the basis for the diverse roles ascribed to this current, i.e. control of resting membrane potential, passive membrane properties, pacemaker activity, rebound burst firing in heart and brain, reduction of dendritic summation and the presence of certain types of resonance behavior in neurons [1–8].

The specific function of h-channels in each neuronal population depends strongly on the voltage- and time-dependent properties of I_h. An important molecular mechanism for generating functionally diverse I_h is the differential expression of the four underlying HCN1-4 subunits. Homomeric channels formed by these HCN subunits display very different kinetics, steady-state voltage dependence and sensitivity to modulation by cAMP in heterologous expression systems [2]. Thus, regulation of the relative abundance of HCN subunit protein is likely to represent a key mechanism for plasticity of I_h. Importantly, the functional properties of I_h and the expression of the corresponding subunits are differentially modulated during postnatal development as well as in both acquired and genetic forms of epilepsy in a region- and time-dependent manner in different *in vitro* and *in vivo* models [6,9–18]. An emerging "leitmotiv", at least in CA1 hippocampal or neocortical neurons, seems to be the downregulation of the HCN1-subunit along with a decrease in somatodendritic I_h, followed, via an enhanced input resistance, by neuronal hyperexcitability in the chronic state.

Thus, a significant body of work has implicated alteration of HCN channels expression and altered magnitude and properties of I_h in epilepsy [reviewed in 8,19]. In temporal lobe epilepsy (TLE), the large majority of existing studies has focused on animal models and on the hippocampal pyramidal cell layer [20]. Remarkably, an early study suggested that changes in HCN expression might arise also in the dentate gyrus [21]. Therefore, here, we focus on the DGG cells, and examine somatodendritic I_h currents and the HCN expression levels in DGG cells of people with TLE and underlying Ammon's horn sclerosis (AHS) and in the rat pilocarpine-model of TLE.

* Corresponding author at: Department of Epileptology, University of Bonn Medical Center, Sigmund-Freud-Str. 25, 53105 Bonn, Germany. Fax: +49 228/28719351.
E-mail address: rainer.surges@googlemail.com (R. Surges).

0006-291X/$ - see front matter © 2012 Elsevier Inc. All rights reserved.
doi:10.1016/j.bbrc.2012.02.133

2. Material and methods

2.1. Pre- and postsurgical assessment of epilepsy patients

All patients had conventional scalp EEG recordings or intracranial recordings and brain MRI prior to neurosurgery. The histological grading of human hippocampus was performed according to Wyler and colleagues [22]. Investigation of human cerebral tissue was approved by the local ethics committee and written informed consent was obtained from each patient.

2.2. Pilocarpine-induced status epilepticus (SE)

Procedures on animals were performed in accordance with local guidelines and experiments were approved by the local animal care and use committee. Pilocarpine treatment of rats was carried out and animals were monitored as described in Supplementary material.

2.3. Semi-quantitative in situ hybridization (ISH) in rat hippocampus

ISH was carried out as described previously [10,21,23,24] on specimens obtained 30-60 days after SE. For details see Supplementary material.

2.4. Electrophysiology

Electrophysiological recordings of DGG cells were performed in both human and rat hippocampal slices using conventional patch clamp technique and established experimental procedures. See Supplementary material for details.

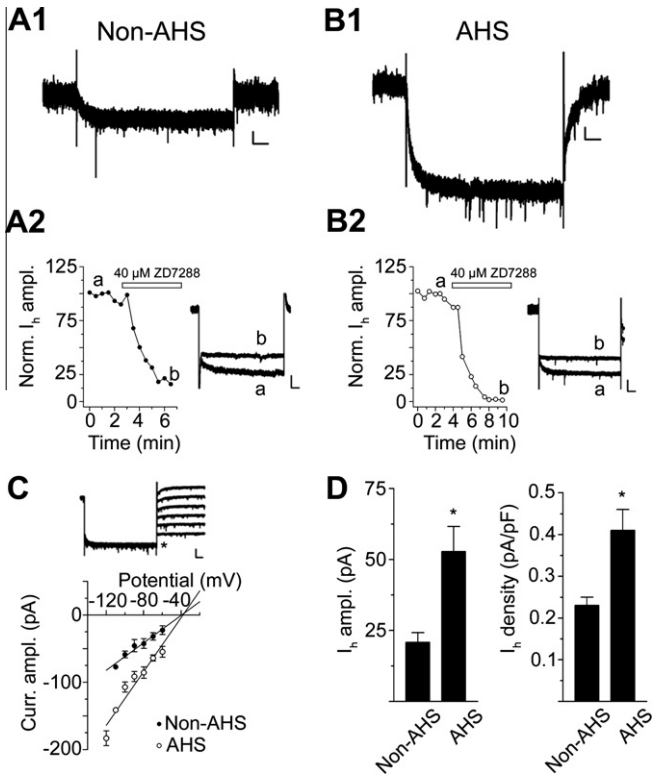

Fig. 1. I_h density is greater in DGG neurons of people with TLE due to AHS. I_h is elicited by voltage steps from −50 to −90 mV in both DGG neurons from the non-AHS (A1) and AHS-group (B1). Scaling 10 pA/0.5 s. The inward current is blocked by ZD7288 in both groups (A2, B2). Scaling 50 pA/0.1 s. (C) Reversal potential was around −39 mV in both conditions (upper panel, tail currents indicated with an asterisk, Scaling 100 pA/0.5 s; bottom panel; filled symbols: non-AHS group; open symbols: AHS-group). (D) I_h amplitudes (left panel) and current densities at −90 mV (right panel) were significantly greater in people with AHS.

2.5. Data analysis

I_h amplitudes in response to voltage steps were determined as the difference of the end of the instantaneous current component and the current amplitude in the steady-state. The reversal potential V_{rev}, was determined by analysis of tail currents and subsequent linear regression analysis (see Fig. 1C and Supplementary material). The conductance–voltage curves were fitted with a Boltzmann function of the form.

$$f(V) = 1/\left(1 + e^{-(V-V_{50})/\text{slope}}\right) \quad (1)$$

with V_{50} being the voltage of half-maximal activation.

The activation time course of I_h was fit with exponential functions of the form

$$f(t) = \sum A_i^* e^{-t/\tau i} + c.\ i = 1 \text{ or } 2. \quad (2)$$

Unpaired student's *t*-test was used for statistical analyses. *P* values <0.05 were considered as significant. All data are given as means ± SEM.

3. Results

3.1. I_h recordings in human TLE

Properties of I_h recorded in DGG cells from seven TLE patients with AHS (AHS-group) were compared to those from three patients without AHS (non-AHS). The clinical data of the patients are summarized in Supplementary Table 1. The intrinsic membrane properties of DGG cells were not significantly different between both groups (Supplementary Table 2). Gross morphology was not different between groups, as described previously [25]. However, upon a hyperpolarizing voltage step from −50 to −90 mV for 5 s, we observed a slowly developing inward current which was more pronounced in the AHS-group (Fig. 1A1 and B1). These currents were blocked by the I_h-channel blocker ZD7288 (40 µM, $n = 8$) in neurons from both tissues (Fig. 1A2 and B2) and had similar reversal potentials (AHS: −38.1 mV, $n = 7$; non-AHS group: −39.4 mV, $n = 6$; Fig. 1C), consistent with reported reversal potentials of I_h [5,13]. Application of 2 mM Cs^+ in two recordings also blocked this current component (data not shown). Taken together, these findings indicate that the recorded time-dependent inward currents were a result of activation of I_h channels.

The mean I_h amplitudes measured with hyperpolarizing voltage steps from −50 to −90 mV ($p = 0.0056$, $n = 8$ non-AHS; $n = 7$ AHS; Fig. 1D) and I_h current densities normalized to the cell capacitance were significantly higher in the AHS-group ($p = 0.0077$, $n = 8$ non-AHS; $n = 7$ AHS; Fig. 1D). The voltage-dependence of activation was significantly shifted to more depolarized potentials in the AHS-group (non-AHS group: $V_{50} = -85.9 \pm 2.3$ mV; AHS-group: $V_{50} = -78.2 \pm 2.7$ mV; $p = 0.0001$, Fig. 2A and D). The kinetics of I_h activation contained a fast and a slow component, and was examined by fitting with a bi-exponential function. The time constants of activation did not differ between groups (Fig. 2B). Likewise, the relative contribution of the fast current component to the total current amplitude varied between 66% and 73% in a voltage range between −90 and −120 mV in both groups and was not significantly different (Fig. 2C).

3.2. I_h recordings in rat pilocarpine model of TLE

Similar to the human, a slowly activating, non-inactivating inward conductance was seen upon voltage steps to −103 mV which

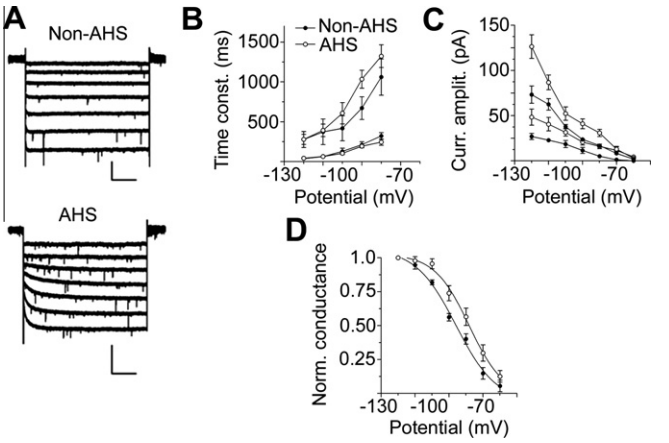

Fig. 2. Activation properties of I_h in human DGG neurons. (A) A family of current traces was elicited by stepping the voltage from −50 mV to more hyperpolarized potentials in 10 mV-steps (from −60 to −120 mV) in the non-AHS (upper panel) and AHS-group (lower panel). Scaling 100 pA/1 s. (B) Fast and slow time constants were not different in both conditions at different command potentials (filled symbols: non-AHS group; open symbols: AHS-group). (C) The amplitudes from the fast (the upper data points under each condition) and the slow time component (the lower data points under each condition) were derived from the bi-exponential fitting paradigms. There was no significant difference in the relative contributions of the fast and slow current component between both conditions. Symbols as in (B). (D) The voltage-dependence of activation was significantly shifted to more depolarized potentials in the AHS-group. Symbols as in (B).

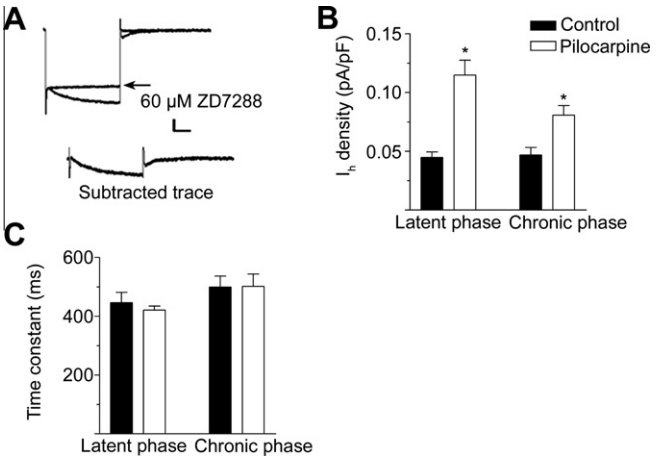

Fig. 3. I_h density is upregulated in DGG cells of rat hippocampal slices in the latent and chronic phase following pilocarpine-injection. (A) Inward currents elicited upon a voltage step from −63 to −103 mV in the absence and presence of ZD7288 (upper panel, indicated by an arrow). Lower trace obtained after subtraction of traces in the absence and presence of ZD7288. Recordings from a control animal. Scaling 10 pA/0.5 s. (B) I_h current densities during the latent and chronic phase (sham-control animals: black bars, SE-experienced animals: white bars). (C) Time constants at a potential of −103 mV were not different in controls and pilocarpine rats during latent ($p = 0.49$, $n = 9$ and 10 cells) and chronic phase ($p = 0.96$, $n = 13$ and 12 cells). Symbols as in (B).

was completely blocked by ZD7288 (60 µM) both in control ($n = 22$) and epileptic rats ($n = 22$, Fig. 3A, upper traces). Subtraction of the two traces allowed isolating I_h (Fig. 3A, lower trace).

We examined the magnitude of I_h in control and pilocarpine-treated rats at two different time points: 7–9 days following SE (latent phase, no spontaneous generalized seizures) and in the chronic epileptic phase 35–63 days following SE (all spontaneous generalized seizures). I_h density was enhanced in both groups, but most pronouncedly in the latent period (Fig. 3B, $p < 0.0001$ and $p = 0.0041$ for the latent and chronic group, respectively). This increase could not be explained by a change in driving force, as the reversal potential of I_h did not differ between groups (controls: −35.9 ± 2.3 mV, $n = 8$; pilocarpine-treated rats: −36.8 ± 2.3 mV, $n = 8$). The time course of activation was best fit with a mono-exponential equation with no significant differences between controls and pilocarpine-treated animals neither at early nor at late stages following SE (Fig. 3C).

To understand the neurobiological basis of the persistent increase in I_h in DGG cells of epileptic rats, we investigated the expression of the genes coding for the h-channels. We compared mRNA expression of HCN1, 2 and 4 channel isoforms in chronically epileptic, pilocarpine-treated rats versus the control group. Whereas HCN2 expression was not different in both groups (not shown), expression of HCN1 mRNA was significantly increased by 22% in the pilocarpine-treated (67.9 ± 4.0 nCi/gm) compared to control rats (55.4 ± 3.2 nCi/gm; $p < 0.05$, Fig. 4A). This effect was more pronounced for the HCN4 channel isoform. HCN4 mRNA level was enhanced by 52% in the granule cell layer of epileptic (70.75 ± 6.4 nCi/gm) relative to controls rats (46.75 ± 1.0 nCi/gm; $p < 0.05$; Fig. 4B).

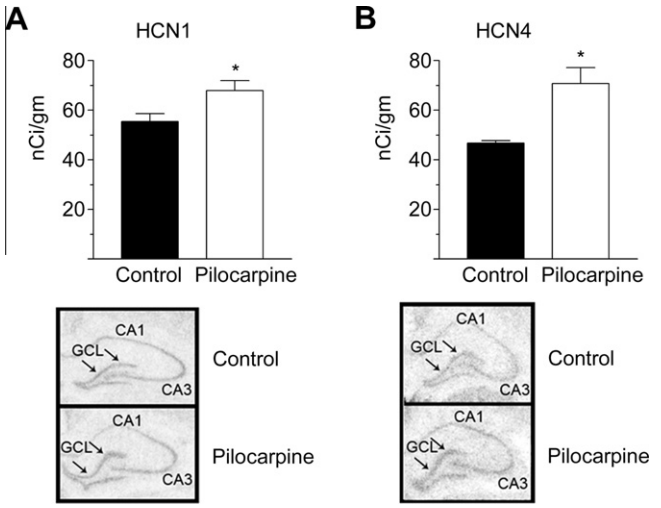

Fig. 4. Expression of both HCN1 and HCN 4 subunits is increased in epileptic animals following pilocarpine-induced SE. As depicted in the photomicrographs (A and B lower panels), HCN1 and HCN4 subunit mRNA signals were significantly increased in the granule cell layer (GCL) of the pilocarpine-group (A and B upper panels), with relatively little change in expression over the pyramidal cell layer of CA3. Brains from 4–9 animals were used per group. Asterisk indicates $p < 0.05$.

4. Discussion

The principal findings of the current studies are that (1) I_h density is greater in granule cell of the dentate gyrus in TLE patients with AHS as compared to those without AHS. (2) Similar findings are observed in the rat pilocarpine-model of TLE, where I_h changes precede the onset of chronic epilepsy. (3) Voltage-dependence but not kinetics of I_h is altered in the epileptic state, which might result from augmented contribution of HCN1 and HCN4 to the total HCN channels pool that conducts I_h.

4.1. Molecular mechanism of I_h upregulation

The observed upregulation of I_h in both human and rat DGG cells is most likely due to an enhanced expression of HCN1 and, at least in rat hippocampus, HCN4 subunit, as shown in Fig. 4 and as found previously [21]. This is in line with the observed shift of voltage-dependence of I_h to more depolarized potentials in

tissue from people with TLE due to AHS. In general, h-channels composed of HCN1 subunits display faster I_h activation than those composed of HCN2 and HCN4 subunits [13,26]. Strikingly, current kinetics was not faster in the AHS-group or in epileptic rats as compared to controls. This might be a result of the concomitant increase of HCN4 subunits. Furthermore, the properties of I_h in native hippocampus only partially overlap those of currents recorded in heterologous systems: in human and rat hippocampus, in addition to the intrinsic biophysical properties of each HCN isoform, a number of interacting molecules influence channel properties [18,27, reviewed in 28].

What are the molecular mechanisms and pathways involved in the upregulation of I_h and HCN channels in DGG cells? Although this question has not been directly addressed in the present work, a number of recent studies provide insights into regulation of HCN-expression in association with seizures and epilepsy. In the kainic acid-induced SE model of TLE, *downregulation* of HCN1 expression in CA1 pyramidal region was caused by an upregulation of a repressing transcription factor, neuron-restrictive silencer factor (NRSF) which suppresses transcription of a number of genes, amongst them the *HCN1* gene [20]. In addition, a reduction of HCN1 expression has been shown to involve transient Ca^{2+}-permeable AMPA receptor activation with subsequent activation of Ca^{2+}/calmodulin-dependent protein kinase II during *in-vitro* experiments in hippocampal slices [29]. Little is known, however, about mechanisms of *upregulation* of HCN expression. Reduction of NRSF levels might take place, or the enhanced expression might result from a myriad of cellular mechanisms that influence ion channel expression [30].

4.2. Significance for the pathophysiology of TLE and potential clinical implications

In previous studies, I_h expression appears to be differentially modulated in acquired and genetically caused epilepsies in a region- and time-dependent manner. For instance, in rat models of genetically caused absence epilepsies, impaired I_h with a concomitant decrease of HCN1 expression was found in cortical neurons [12], whereas thalamocortical neurons showed an decrease in cAMP responsiveness, explained by an increase of HCN1 expression [31,32]. Both phenomena favor onset of absence seizures. In models of acquired TLE, I_h currents and expression of underlying HCN1 and HCN2 subunits were temporarily reduced in dendrites of the entorhinal cortex following kainate-induced SE [11]. A further study found sustained reduction in HCN1 and 2 expression following kainate-induced SE in the CA1 region [16]. Likewise, in the rat pilocarpine model of TLE, dendritic I_h of CA1 pyramidal cells was progressively reduced during epileptogenesis, because of permanent reduction of HCN1-subunit expression and a persistent alteration of I_h-modulating phosphorylation pathways [6,15,18]. The significance of HCN1 downregulation is further strengthened by the observation that a primary loss of the HCN1 subunit facilitates onset of seizures and of epilepsy [33,34]. In a model of seizure-inducing hypoxia, somatic I_h in rat CA1 pyramidal was decreased [14], and a complex region-specific regulation of HCN1 and 2 in an *in vitro* model of epilepsy has been described, with commensurate alteration of burst activity [17].

Taken together, downregulation of I_h seems to be a leitmotiv in the early phases of epileptogenesis and epilepsy. However, relatively few studies in animal models have explored potentially compensatory alterations in HCN isoform expression and I_h in the chronic and even 'end stage' of TLE. Even fewer yet are studies in human tissue. In human neocortical neurons of patients with TLE, Wierschke and co-workers reported on reduced I_h density in patients with higher seizure frequencies; these observations support the notion that I_h contributes importantly to the regulation of neuronal excitability [35].

Focusing on the dentate gyrus, a major gateway into the hippocampal formation, we report here a robust, epilepsy-associated upregulation of I_h in DGG of human and rat hippocampus. Our findings are in line with a recent study reporting enhanced I_h in DGG of people with TLE with severe AHS as compared to those with mild or moderate AHS [36]. Whereas the mechanisms leading to this increase of HCN1 expression and I_h density are not fully understood, the teleological purpose is intriguing: augmented I_h in the epileptic dentate gyrus might serve as an attempt to compensate for abnormal hyperexcitability in the circuit for example, by dampening dendritic summation [1]. Alternatively, in response to augmented inhibition (hyperpolarizing), the increase in I_h might promote rebound depolarization and contribute to hyperexcitability of epileptic tissue [5,9]. Whereas other ion channels are also altered in epileptic DGG cells [37,38], the changes in I_h reported here should contribute to neuronal firing behavior, and might provide a drug target to both existing and future medications (see below).

4.3. Temporal profile of I_h upregulation

In human tissue, it is not possible to time the onset of HCN expression and I_h changes, because tissue is only available from chronic epileptic tissue. Therefore, the current studies employed also tissue from animal models. In the rat pilocarpine model employed here, an I_h upregulation was already present in the latent stage preceding the onset of spontaneous seizures, and may thus contribute to their onset. This increased I_h was associated with, and hence is likely a result of, an upregulation of both HCN1 and HCN4 mRNA in neurons of the dentate gyrus. Given the importance of I_h in attenuating postsynaptic potentials at dendrites and limiting their spread in pyramidal neurons of CA1 region and layer five of the somatosensory cortex [39,40], our data suggest that upregulation of I_h might be a protective mechanism resulting in maintained dentate gyrus gating. Dendrites of DGG neurons in rats without epilepsy have no or little I_h [41]. In view of the considerable increase of I_h, it is tempting to speculate that somatodendritic I_h in DGG neurons plays a role in signal integration only under pathophysiological circumstances such as epileptogenesis and chronic epilepsy, but not under physiological conditions.

4.4. Implications for epilepsy therapy

I_h is a target for the anticonvulsants acetazolamide, gabapentin and lamotrigine, all of which increase I_h [42–44]. It is therefore also possible that the observed upregulation of I_h renders its modulation by these antiepileptic drugs more effective, thereby dampening excitability. Such a mechanism operating in DGG cells may be particularly relevant in chronic epilepsy, when granule cells are one of the major preserved cell populations after the profound loss of neurons in the CA1, CA3 and CA4 subfields. Therefore, defining and understanding the changes in I_h and in its 'building blocks', the HCN channels, both in humans and animal models is important. The knowledge is a prerequisite for using this important channel as target for epilepsy therapy and prevention in the future.

Acknowledgements

This work was supported by the German–Israel collaborative research program of the Bundesministerium für Bildung und Forschung (BMBF), the Ministry of Science (MOS), the Deutsche Forschungsgemeinschaft (DFG) Projects SFB-TR3 (H.B., D.D.), DI 853/3 and DI 853/4 (D.D.), the BONFOR Program of the University of

Bonn, and NIH Grant NS35439. The sponsors had no role in study design, in the collection, analysis and interpretation of data or in the writing of the report. The authors declare no conflict of interest.

Author contributions: R.S. has contributed to the design of the experiments, data analysis and has written the manuscript. M.K. has performed the recordings in human hippocampus and contributed to data analysis. A.B. has done the in-situ immunhistochemistry, T.B.Z. has contributed to the design of the experiments, data analysis and writing of the manuscript. C.R. has performed the recordings in the rat pilocarpine model, respective data analysis and written a prior version of the manuscript. J.S. has provided neurosurgical specimen including informed consent. H.B. and D.D. have contributed to the design of the experiments, data analysis and writing of the manuscript.

Appendix A. Supplementary data

Supplementary data associated with this article can be found, in the online version, at doi:10.1016/j.bbrc.2012.02.133.

References

[1] J.C. Magee, Dendritic hyperpolarization-activated currents modify the integrative properties of hippocampal CA1 pyramidal neurons, J. Neurosci. 18 (1998) 7613–7624.
[2] R.B. Robinson, S.A. Siegelbaum, Hyperpolarization-activated cation currents: from molecules to physiological function, Annu. Rev. Physiol. 65 (2003) 453–480.
[3] B. Santoro, T.Z. Baram, The multiple personalities of h-channels, Trends Neurosci. 26 (2003) 550–554.
[4] R. Surges, T.M. Freiman, T.J. Feuerstein, Input resistance is voltage dependent due to activation of I_h channels in rat CA1 pyramidal cells, J. Neurosci. Res. 76 (2004) 475–480.
[5] R. Surges, M. Sarvari, M. Steffens, T. Els, Characterization of rebound depolarization in hippocampal neurons, Biochem. Biophys. Res. Commun. 348 (2006) 1343–1349.
[6] B. Marcelin, L. Chauvière, A. Becker, et al., H channel-dependent deficit of theta oscillation resonance and phase shift in temporal lobe epilepsy, Neurobiol. Dis. 33 (2009) 436–447.
[7] L.M. Giocomo, S.A. Hussaini, F. Zheng, et al., Grid cells use HCN1 channels for spatial scaling, Cell 147 (2011) 1159–1170.
[8] Y. Noam, C. Bernard, T.Z. Baram, Towards an integrated view of HCN channel role in epilepsy, Curr. Opin. Neurobiol. 21 (2011) 873–879.
[9] K. Chen, I. Aradi, N. Thon, et al., Persistently modified h-channels after complex febrile seizures convert the seizure-induced enhancement of inhibition to hyperexcitability, Nat. Med. 7 (2001) 331–337.
[10] A. Brewster, R.A. Bender, Y. Chen, et al., Developmental febrile seizures modulate hippocampal gene expression of hyperpolarization-activated channels in an isoform- and cell-specific manner, J. Neurosci. 22 (2002) 4591–4599.
[11] M.M. Shah, A.E. Anderson, V. Leung, et al., Seizure-induced plasticity of h channels in entorhinal cortical layer III pyramidal neurons, Neuron 44 (2004) 495–508.
[12] U. Strauss, M.H. Kole, A.U. Bräuer, et al., An impaired neocortical I_h is associated with enhanced excitability and absence epilepsy, Eur. J. Neurosci. 19 (2004) 3048–3058.
[13] R. Surges, A.L. Brewster, R.A. Bender, et al., Regulated expression of HCN channels and cAMP levels shape the properties of the h current in developing rat hippocampus, Eur. J. Neurosci. 24 (2006) 94–104.
[14] K. Zhang, B.W. Peng, R.M. Sanchez, Decreased IH in hippocampal area CA1 pyramidal neurons after perinatal seizure-inducing hypoxia, Epilepsia 47 (2006) 1023–1028.
[15] S. Jung, T.D. Jones, J.N. Lugo Jr, et al., Progressive dendritic HCN channelopathy during epileptogenesis in the rat pilocarpine model of epilepsy, J. Neurosci. 27 (2007) 13012–13021.
[16] K.L. Powell, C. Ng, T.J. O'Brien, et al., Decreases in HCN mRNA expression in the hippocampus after kindling and status epilepticus in adult rats, Epilepsia 49 (2008) 1686–1695.
[17] B.E. Adams, C.A. Reid, D. Myers, et al., Excitotoxic-mediated transcriptional decreases in HCN2 channel function increase network excitability in CA1, Exp. Neurol. 219 (2009) 249–257.
[18] S. Jung, J.B. Bullis, I.H. Lau, et al., Downregulation of dendritic HCN channel gating in epilepsy is mediated by altered phosphorylation signaling, J. Neurosci. 30 (2010) 6678–6688.
[19] A.S. Lewis, D.M. Chetkovich, HCN channels in behavior and neurological disease: too hyper or not active enough?, Mol Cell. Neurosci. 46 (2011) 357–367.
[20] S. McClelland, C. Flynn, C. Dubé, et al., Neuron-restrictive silencer factor-mediated hyperpolarization-activated cyclic nucleotide gated channelopathy in experimental temporal lobe epilepsy, Ann. Neurol. 70 (2011) 454–464.
[21] R.A. Bender, S.V. Soleymani, A.L. Brewster, et al., Enhanced expression of a specific hyperpolarization-activated cyclic nucleotide-gated cation channel (HCN) in surviving dentate gyrus granule cells of human and experimental epileptic hippocampus, J. Neurosci. 23 (2003) 6826–6836.
[22] A.R. Wyler, F.C. Dohan, J.B. Schweitzer, A.D. Berry, A grading system for hippocampal sclerosis, J. Epilepsy 5 (1992) 220–225.
[23] R.A. Bender, A. Brewster, B. Santoro, et al., Differential and age-dependent expression of hyperpolarization-activated, cyclic nucleotide-gated cation channel isoforms 1–4 suggests evolving roles in the developing rat hippocampus, Neuroscience 106 (2001) 689–698.
[24] A.L. Brewster, Y. Chen, R.A. Bender, et al., Quantitative analysis and subcellular distribution of mRNA and protein expression of the hyperpolarization-activated cyclic nucleotide-gated channels throughout development in rat hippocampus, Cereb. Cortex. 17 (2007) 702–712.
[25] D. Dietrich, H. Clusmann, T. Kral, et al., Two electrophysiologically distinct types of granule cells in epileptic human hippocampus, Neuroscience 90 (1999) 1197–1206.
[26] S. Chen, J. Wang, S.A. Siegelbaum, Properties of hyperpolarization-activated pacemaker current defined by coassembly of HCN1 and HCN2 subunits and basal modulation by cyclic nucleotide, J. Gen. Physiol. 117 (2001) 491–504.
[27] B. Gravante, A. Barbuti, R. Milanesi, et al., Interaction of the pacemaker channel HCN1 with filamin A, J. Biol. Chem. 279 (2004) 43847–43853.
[28] A.S. Lewis, C.M. Estep, D.M. Chetkovich, The fast and slow ups and downs of HCN channel regulation, Channels (Austin) 4 (2010) 215–231.
[29] C. Richichi, A.L. Brewster, R.A. Bender, et al., Mechanisms of seizure-induced 'transcriptional channelopathy' of hyperpolarization-activated cyclic nucleotide gated (HCN) channels, Neurobiol. Dis. 29 (2008) 297–305.
[30] D.J. Schulz, J.M. Goaillard, E. Marder, Variable channel expression in identified single and electrically coupled neurons in different animals, Nat. Neurosci. 9 (2006) 356–362.
[31] T. Budde, L. Caputi, T. Kanyshkova, et al., Impaired regulation of thalamic pacemaker channels through an imbalance of subunit expression in absence epilepsy, J. Neurosci. 25 (2005) 9871–9882.
[32] M. Kuisle, N. Wanaverbecq, A.L. Brewster, et al., Functional stabilization of weakened thalamic pacemaker channel regulation in rat absence epilepsy, J. Physiol. 575 (2006) 83–100.
[33] B. Santoro, J.Y. Lee, D.J. Englot, et al., Increased seizure severity and seizure-related death in mice lacking HCN1 channels, Epilepsia 51 (2010) 1624–1627.
[34] Z. Huang, M.C. Walker, M.M. Shah, Loss of dendritic HCN1 subunits enhances cortical excitability and epileptogenesis, J. Neurosci. 29 (2009) 10979–10988.
[35] S. Wierschke, T.N. Lehmann, C. Dehnicke, et al., Hyperpolarization-activated cation currents in human epileptogenic neocortex, Epilepsia 51 (2010) 404–414.
[36] M. Stegen, F. Kirchheim, A. Hanuschkin et al., Adaptive Intrinsic Plasticity in Human Dentate Gyrus Granule Cells during Temporal Lobe Epilepsy, Cereb. Cortex. 2011. [Epub ahead of print].
[37] M. Stegen, C.C. Young, C.A. Haas, et al., Increased leak conductance in dentate gyrus granule cells of temporal lobe epilepsy patients with Ammon's horn sclerosis, Epilepsia 50 (2009) 646–653.
[38] C.C. Young, M. Stegen, R. Bernard, et al., Upregulation of inward rectifier K^+ (Kir2) channels in dentate gyrus granule cells in temporal lobe epilepsy, J. Physiol. 587 (2009) 4213–4233.
[39] G. Stuart, N. Spruston, Determinants of voltage attenuation in neocortical pyramidal neuron dendrites, J. Neurosci. 18 (1998) 3501–3510.
[40] N.L. Golding, T.J. Mickus, Y. Katz, et al., Factors mediating powerful voltage attenuation along CA1 pyramidal neuron dendrites, J. Physiol. 568 (2005) 69–82.
[41] R. Krueppel, S. Remy, H. Beck, Dendritic integration in hippocampal dentate granule cells, Neuron 71 (2011) 512–528.
[42] T. Munsch, H.C. Pape, Upregulation of the hyperpolarization-activated cation current in rat thalamic relay neurones by acetazolamide, J. Physiol. 519 (1999) 505–514.
[43] N.P. Poolos, M. Migliore, D. Johnston, Pharmacological upregulation of h-channels reduces the excitability of pyramidal neuron dendrites, Nat. Neurosci. 5 (2002) 767–774.
[44] R. Surges, T.M. Freiman, T.J. Feuerstein, Gabapentin increases the hyperpolarization-activated cation current I_h in rat CA1 pyramidal cells, Epilepsia 44 (2003) 150–156.

Biochemical and Biophysical Research Communications 420 (2012) 161–165

Contents lists available at SciVerse ScienceDirect

Biochemical and Biophysical Research Communications

journal homepage: www.elsevier.com/locate/ybbrc

Desipramine selectively potentiates norepinephrine-elicited ERK1/2 activation through the α_{2A} adrenergic receptor

Christopher Cottingham, Adrian Jones, Qin Wang *

Department of Physiology & Biophysics, University of Alabama at Birmingham, Birmingham, AL 35294, USA

ARTICLE INFO

Article history:
Received 20 February 2012
Available online 3 March 2012

Keywords:
α_2 Adrenergic receptor
Antidepressant
Akt
ERK1/2
Norepinephrine

ABSTRACT

The precise physiological effects of antidepressant drugs, and in particular their actions at non-monoamine transporter targets, are largely unknown. We have recently identified the tricyclic antidepressant drug desipramine (DMI) as a direct ligand at the α_{2A} adrenergic receptor (AR) without itself driving heterotrimeric G protein/downstream effector activation [5]. In this study, we report our novel finding that DMI modulates α_{2A}AR signaling in response to the endogenous agonist norepinephrine (NE). DMI acted as a signaling potentiator, selectively enhancing NE-induced α_{2A}AR-mediated ERK1/2 MAPK signaling. This potentiation of ERK1/2 activation was observed as an increase in NE response sensitivity and a prolongation of the activation kinetics. DMI in a physiologically relevant ratio with NE effectively turned on ERK1/2 signaling that is lacking in response to physiological NE alone. Further, the DMI-induced ERK1/2 potentiation relied on heterotrimeric $G_{i/o}$ proteins and was arrestin-independent. This modulatory effect of DMI on NE signaling provides novel insight into the effects of this antidepressant drug on the noradrenergic system which it regulates, insight which enhances our understanding of the therapeutic mechanism for DMI.

1. Introduction

A complete picture regarding the mechanism of action of antidepressant medications remains elusive. Indeed, although more than half a century has passed since the introduction of the tricyclic antidepressant drug class [1], a mechanistic physiological model for how these drugs function is nonexistent. These drugs are, speaking generally, understood to be antidepressants by virtue of their ability to inhibit the reuptake of the monoamine neurotransmitters norepinephrine (NE) and serotonin via blockade of the NE and serotonin transporters [1]. However, reuptake inhibition alone is not sufficient to explain the antidepressant effects of these medications.

Our previous work has characterized the interaction of the tricyclic antidepressant drug desipramine (DMI), a class member with the strongest specificity for the noradrenergic over the serotonergic system [1], with the α_{2A} adrenergic receptor (AR). The α_{2A}AR, a prototypical GPCR, is a well-established key player in noradrenergic transmission as a regulator of NE synthesis and release from noradrenergic neuronal terminals [2] and of neuronal activity within the locus coeruleus [3,4], the primary brain region from which central noradrenergic neurons originate. Our work has established that DMI, as a direct α_{2A}AR ligand, selectively drives recruitment of the important interacting regulator protein arrestin to the receptor leading to receptor trafficking responses, while not driving coupling/activation of heterotrimeric G proteins to the receptor and classical signaling responses [5].

The present work is aimed at investigating the potential impact of DMI, acting as a direct α_{2A}AR ligand, on receptor-mediated signaling by the endogenous agonist NE. Given that DMI was shown to bind as an orthosteric ligand at the α_{2A}AR, we hypothesized that DMI would act as a competitive antagonist and block signaling induced by the endogenous α_{2A}AR agonist NE. Further, any antagonism will be dependent on the relative concentrations of DMI and NE when given together (e.g. the [DMI]/[NE] ratio), given that the α_{2A}AR has essentially identical intrinsic affinities for the two ligands (K_i values of 4.62 and 3.63 μM for DMI and NE, respectively) [5], contrasting with typical antagonist affinities that are 100- to 1000-fold higher. The α_{2A}AR classically couples to heterotrimeric G proteins of the $G_{i/o}$ family, leading to inhibition of adenylyl cyclase and voltage-gated Ca^{2+} channels, and activation of downstream effectors including inwardly-rectifying K^+ channels, MAPKs, and Akt [5–10]. Here, we have utilized activation of the ERK1/2 MAPK and Akt pathways as straightforward and reliable readouts for α_{2A}AR signaling. As well, these signaling pathways have both been more generally implicated in physiological antidepressant

Abbreviations: AR, adrenergic receptor; DMI, desipramine; ERK, extracellular signal-regulated kinase; FBS, fetal bovine serum; GPCR, G protein-coupled receptor; MAPK, mitogen-activated protein kinase; MEF, mouse embryonic fibroblast; NE, norepinephrine; PTx, pertussis toxin.

* Corresponding author. Address: 986 MCLM, 1918 University Blvd., Birmingham, AL 35294, USA. Fax: +1 205 975 9028.
E-mail address: qinwang@uab.edu (Q. Wang).

0006-291X/$ - see front matter © 2012 Elsevier Inc. All rights reserved.
doi:10.1016/j.bbrc.2012.02.135

responses [11,12]. By utilizing an *in vitro* heterologous cell model, we have been able to isolate and specifically study α_{2A}AR-mediated signal transduction in the absence complex confounding effects from the full complement of endogenous DMI molecular targets.

Through a combination of kinetic and response sensitivity analyses, we report here that DMI is in fact a potentiator that specifically facilitates NE-induced α_{2A}AR-mediated ERK1/2 signaling. We further show that this DMI-potentiated signaling remains dependent on heterotrimeric $G_{i/o}$ proteins and does not simply represent a switch to arrestin-mediated signal transduction. By comparison, we observed a general inhibitory effect of DMI on cellular Akt signaling. These data provide a novel example of a complex ligand/receptor relationship between DMI and the α_{2A}AR which cannot be explained by classical agonist/antagonist regulation of receptor function. As well, in the context of antidepressant pharmacotherapy, our findings add valuable and novel information to the understanding of the physiological mechanism of the antidepressant drug DMI.

2. Materials and methods

2.1. Cell culture

Mouse embryonic fibroblast (MEF) cells were cultured in Dulbecco's Modified Eagle Medium (DMEM, Invitrogen) supplemented with 10% fetal bovine serum (FBS, Atlanta Biologicals) and 1% penicillin/streptomycin (Invitrogen), and maintained in a humidified 5% CO_2 incubator. MEFs isolated from wild-type and arrestin2,3-null ($Arr2,3^{-/-}$) [13] animals and stably expressing N-terminal hemagglutinin (HA) epitope-tagged murine α_{2A}ARs were used for this study. Generation of HA-α_{2A}AR MEF lines expressing the receptor at an average density of 400 fmol/mg has been described [5].

2.2. Drugs and treatments

All drugs were obtained from Sigma unless otherwise noted. NE and DMI stocks of 10 mM were prepared freshly in distilled water prior to each experiment. For antagonist experiments, cells were pretreated with the selective α_{2A}AR antagonist BRL44408 (1 μM) for 5 min prior to stimulation with an NE/BRL combination. For pertussis toxin (PTx) experiments, cells were pretreated with PTx (List Biological Laboratories, Inc.) at a final concentration of 200 ng/ml or vehicle (in serum-free DMEM) for 24 h, and PTx was maintained during drug stimulation. All signaling experiments were done in the presence of 1 μM propranolol (βAR antagonist) and prazosin (α_1 and $\alpha_{2B/C}$AR antagonist) to pharmacologically isolate the α_{2A}AR.

2.3. SDS–PAGE and Western blot

SDS–PAGE (10% acrylamide gel) and Western blot were performed as previously described [5]. MEF cells were serum-starved overnight prior to all signaling assays. At least three independent samples were analyzed for each experimental group.

The following primary antibodies and dilutions were used: phospho-ERK1/2, p44/42 MAPK (T202/Y204) mouse monoclonal antibody (Cell Signaling), 1:16000; phospho-Akt (T308) rabbit polyclonal antibody (Cell Signaling), 1:4000; β-tubulin mouse antibody (University of Iowa Hybridoma Bank), 1:50000; total ERK, p44/42 MAPK rabbit polyclonal antibody (Cell Signaling). HRP-conjugated secondary antibodies and Immobilon Western detection system were obtained from Millipore. β-tubulin was selected as total protein/loading control for most experiments as both phospho-ERK1/2 and phospho-Akt were being analyzed simultaneously. Total ERK blots were performed after membrane stripping as previously described [5].

2.4. Data analysis

Densitometric analysis of dose response Western blot results was done using Scion Image software. Kinase activation for both ERK1/2 and Akt was determined as the ratio of optical density values obtained for phosphorylated kinase to those for total protein. All statistical analyses were carried out using GraphPad Prism software (GraphPad, San Diego, California), using Student's *t*-tests with $p < 0.05$ considered statistically significant.

3. Results and discussion

3.1. DMI alone does not initiate signaling but potentiates NE-induced α_{2A}AR-mediated ERK1/2 activation

We have previously established that NE, in the absence of input from β, α_1, and $\alpha_{2B/C}$ ARs, drives activation of ERK1/2 MAPK in an α_{2A}AR-dependent and G_i-dependent fashion [9,10]. α_{2A}AR-mediated ERK1/2 activation proceeds through the $G_{\beta\gamma}$ subunits and Ras [14,15]. For this study, we began confirming the absence of signal activation by DMI alone, as we have previously reported [5]. As shown in Fig. 1A, DMI alone does not initiate ERK1/2 signaling. We next assayed the kinetics of NE-induced signaling, alone or in combination with DMI, through time course analysis. 10 μM NE alone induces a robust activation of ERK1/2, peaking at 5 min and fully desensitized to baseline by 15 min (Fig. 1B). The kinetics of ERK1/2 activation observed here are consistent with our previous findings on NE-induced α_{2A}AR signaling [9,10]. When DMI was added (NE and DMI together at 10 μM), signaling was not blocked, but rather the time course was prolonged, with ERK1/2 activation

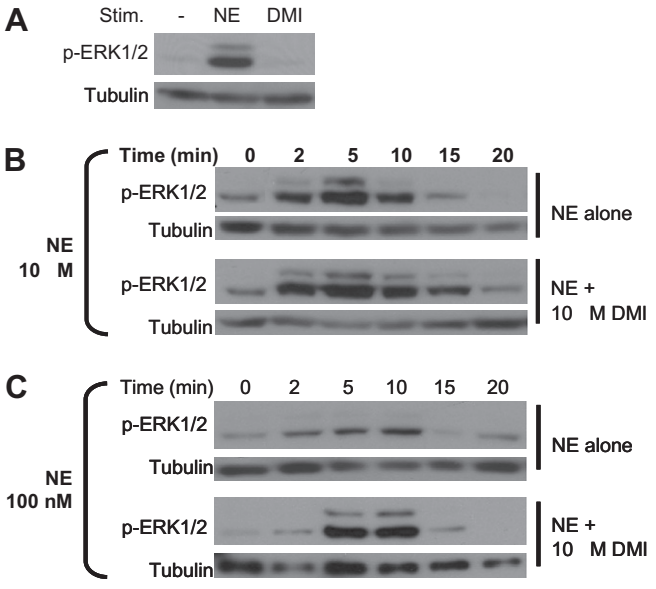

Fig. 1. DMI impacts the kinetics of NE-induced α_{2A}AR-mediated ERK1/2 signaling. All NE stimulations were done in the presence of propranolol (βAR antagonist) and prazosin (α_1 and $\alpha_{2B/C}$AR antagonist). (A) DMI does not itself drive ERK1/2 signaling. MEF cells were stimulated for 5 min with NE alone (as a positive control) or DMI alone. Whole cell homogenates were then analyzed by SDS–PAGE/Western blot, probing for phospho-ERK1/2 and tubulin (loading control). (B) and (C) MEF cells were stimulated for the indicated times with either 100 nM or 10 μM NE, alone or in combination with 10 μM DMI, and analyzed for ERK1/2 activation as in panel A. Blots shown are representative of three independent experiments.

elevated above baseline through 15 min (Fig. 1B). These data seem to contradict our initial hypothesis that DMI acts as a competitive antagonist.

The ability of competitive antagonists to block agonist actions is typically observed either when receptor/antagonist affinity greatly exceeds receptor/agonist affinity or at elevated [antagonist]/[agonist] ratios. Given the essentially identical affinity values for NE and DMI at the α_{2A}AR [5], we therefore chose to assay a much lower level of NE (100 nM), which alone induced a weak and transient activation of ERK1/2 having similar kinetics to those observed at 10 μM (Fig. 1C). Surprisingly, the addition of DMI (now at a 100-fold higher level than NE, 10 μM against 100 nM) did not block NE-induced signaling but rather resulted in a markedly enhanced level of ERK1/2 activation (Fig. 1C). Clearly, these data indicate that the interaction of DMI with the α_{2A}AR is not that of a classical antagonist. Although DMI itself binds to the orthosteric site without driving heterotrimeric G protein/downstream effector activation, it lacks the ability to block agonist-induced signaling at the receptor. In fact, it appears to function as a signaling potentiator, and so our hypothesis has already been refuted.

We further investigated this modulation of NE-induced signaling by dose response analysis, performed at the 5 min (peak activation) time point. This analysis was intended to determine if DMI alters the response sensitivity of NE-induced ERK1/2 activation by the α_{2A}AR. NE dose-dependently induced ERK1/2 activation, with modest activation beginning at 100 nM and more robust activation observed at 1, 10, and 100 μM, while the addition of DMI caused a clear leftward shift in the dose response (Fig. 2A).

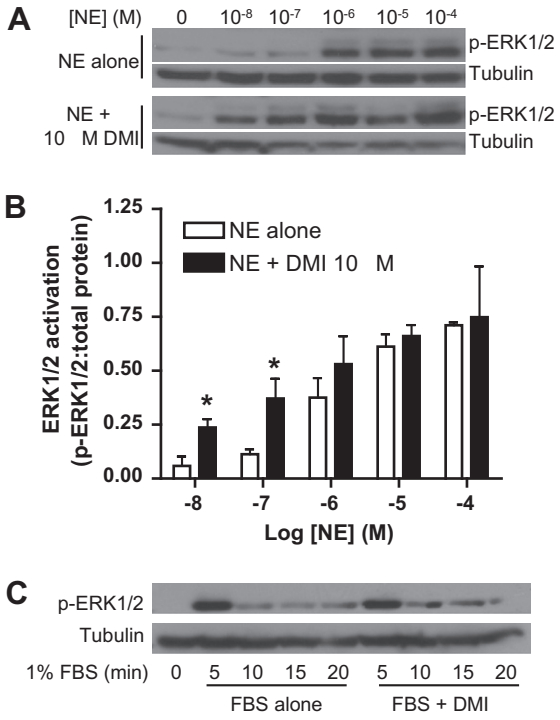

Fig. 2. DMI enhances α_{2A}AR-mediated ERK1/2 response sensitivity to NE. (A) MEF cells were stimulated for 5 min with NE at varying concentrations, ranging from 10 nM (10^{-8} M) to 100 μM (10^{-4} M), alone or in combination with 10 μM DMI, as indicated. Whole cell homogenates were then analyzed by SDS–PAGE/Western blot, probing for phospho-ERK1/2 and tubulin (loading control). Blots shown are representative of three independent experiments. (B) Densitometric quantitation for panel A, with signaling activation calculated as a ratio of phospho-kinase:total protein. Data are mean ± SEM obtained over three independent experiments. $^{*}p < 0.05$ vs. NE alone. (C) MEF cells were subjected to stimulation with 1% FBS for the indicated times, alone or in combination with 10 μM DMI, and analyzed as in panel A. Blots are representative of three independent experiments.

Densitometric analysis confirmed significantly greater ERK1/2 activation at by NE at 10 and 100 nM in the presence of DMI (Fig. 2B). The maximum efficacy of NE-induced ERK1/2 activation was unaffected by the addition of DMI (Fig. 2A and B). These findings correspond nicely with the data presented in Fig. 1, wherein the 5-min ERK1/2 response was clearly potentiated by DMI at 100 nM NE but not at 10 μM NE. Overall, our dose response analysis indicates that DMI enhances the ERK1/2 activation response sensitivity of the α_{2A}AR to NE stimulation and provides further evidence that the interaction of DMI with the α_{2A}AR has a potentiating rather than antagonizing effect on agonist-induced signaling.

Our observations at 10 nM NE have particular physiological relevance, given that this is the same concentration reached in the brain following reuptake inhibition by antidepressants like DMI [3,16]. The addition of DMI to 10 nM NE initiates ERK1/2 activation which is lacking with 10 nM NE alone. As well, the NE/DMI ratios at the 10 and 100 nM data points (100- to 1000-fold higher DMI) are representative of the physiological situation, given that therapeutic levels of DMI reach the micromolar range [5]. These data, then, are strongly supportive of a physiological and pharmacological role for the DMI-mediated potentiation of ERK1/2 signaling.

The possibility exists that DMI is modulating ERK1/2 signal transduction via a non-selective mechanism at some level other than the receptor. As well, ERK1/2 activation is not coupled exclusively to the α_{2A}AR, and can be activated and modulated by a number of upstream mediators. To address this issue of selectivity, we tested the ability of DMI to modulate the growth factor receptor-mediated signaling activity associated with acute FBS exposure. FBS stimulation alone induced a robust and transient ERK1/2 activation, signaling which was unaffected by the addition of DMI (Fig. 2C). Although these data do not definitively rule out an α_{2A}AR-independent mechanism for the potentiation of NE-induced ERK1/2 activation by DMI, they do lend support to the contention that DMI is selectively modulating α_{2A}AR-mediated ERK1/2 signaling.

3.2. Modulation of Akt signaling by DMI lacks selectivity

We next expanded our investigation to include a separate downstream effector activated by α_{2A}AR signal transduction, the Akt kinase. We confirmed that the observed Akt response to NE is both α_{2A}AR-mediated (blocked by the α_{2A}AR antagonist BRL44408) and G_i-dependent (PTx-sensitive) (Fig. 3A). Although G protein-mediated Akt signaling by the α_{2A}AR has not been specifically reported, based on previous studies at other $G_{i/o}$-coupled receptors [17], it seems likely that the receptor couples to Akt via $G_{\beta\gamma}$ subunit-mediated activation of PI3K. Additionally, we again confirmed our previous finding [5] that DMI alone does not drive activation of this downstream effector (Fig. 3B).

Analyzing the samples from our dose response analyses above for Akt activation revealed yet another surprise. While NE alone dose-dependently induced α_{2A}AR-mediated Akt activation, the addition of DMI attenuated this signaling (Fig. 3C), contrasting with its effects on ERK1/2 (Fig. 2). Densitometric analysis confirmed significantly reduced Akt activation at the highest NE levels of 10 and 100 μM (Fig. 3D). These data initially suggested that DMI selectively modulates NE-induced signaling through the α_{2A}AR, altering the signaling profile of the receptor to favor activation of ERK1/2 over Akt. However, in our FBS assay for selectivity, we found that the Akt activation driven by FBS was blocked by the addition of DMI (Fig. 3E). Therefore, DMI appears to inhibit cellular Akt activation through a general mechanism that lacks selectivity for the agonist-induced α_{2A}AR-mediated signaling.

Nevertheless, a more general physiological role for the observed Akt inhibitory effect should not be ruled out. Although a mechanistic explanation of course remains to be seen, that DMI exerts a

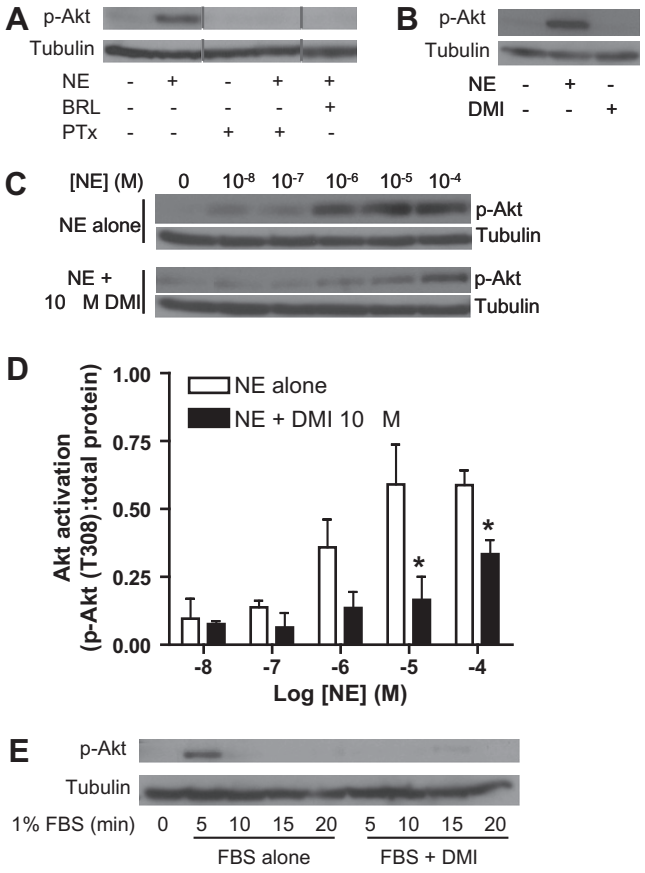

Fig. 3. Modulation of Akt signaling by DMI lacks selectivity. (A) MEF cells were subjected to 5 min stimulation with 10 μM NE alone, NE in combination with the α_{2A}AR antagonist BRL44408, or NE following treatment with pertussis toxin (PTx) as described in the Section 2. Whole cell lysates were analyzed by SDS–PAGE/Western blot for phospho-Akt and tubulin. Note that the lanes shown are from a single experiment but not all adjacent lanes. (B) MEF cells were stimulated for 5 min with 10 μM NE alone (positive control) or 10 μM DMI alone and analyzed as in panel A. (C) MEF cells were stimulated for 5 min with NE at varying concentrations, ranging from 10 nM (10^{-8} M) to 100 μM (10^{-4} M), alone or in combination with 10 μM DMI, as indicated, and analyzed as in panel A. (D) Densitometric quantitation for panel A, with signaling activation calculated as a ratio of phospho-kinase:total protein. Data are mean ± SEM obtained over three independent experiments. $^{*}p < 0.05$ vs. NE alone. (E). MEF cells were subjected to stimulation with 1% FBS for the indicated times, alone or in combination with 10 μM DMI, and analyzed as in panel A. All blots are representative of three independent experiments.

general inhibitory effect on cellular Akt activation is itself a novel finding with potential importance to antidepressant pharmacology. Activated Akt targets and phosphorylates (inactivates) a downstream kinase, GSK3, and this Akt/GSK3 pathway has been extensively implicated in antidepressant mechanisms of action [12]. Therefore, further study of the DMI/Akt phenomenon reported here seems to be warranted.

3.3. Desipramine-modulated α_{2A}AR-mediated ERK1/2 signaling is G_i-dependent and arrestin-independent

We have previously identified DMI as an arrestin-biased ligand at the α_{2A}AR, selectively driving arrestin recruitment to the receptor without inducing G protein coupling [5], and demonstrated critical involvement of the α_{2A}AR/arrestin complex for the *in vivo* antidepressant behavioral effects of DMI [18]. Therefore, a straightforward mechanistic explanation for the data presented thus far could be a switch from classical G protein-mediated to arrestin-mediated signal transduction by the α_{2A}AR in the presence of DMI. Although the α_{2A}AR-mediated ERK1/2 signaling reported thus far in the present and previous studies has been exclusively G protein-dependent, it is now a well-established general fact that GPCRs can signal via G protein-independent mechanisms utilizing arrestin for signal transduction [19,20].

Therefore, we postulated that a DMI-dependent switch from classical G protein-mediated signaling to novel arrestin-mediated signaling might provide a mechanistic explanation for the observed potentiation of NE-induced ERK1/2 signaling by DMI. Such a mechanism could also provide an attractive potential biochemical basis for our recent *in vivo* findings mentioned above [18]. However, our data unfortunately do not support this postulated mechanism, as the DMI-potentiated ERK1/2 signaling remains PTx-sensitive and therefore dependent on $G_{i/o}$ proteins (Fig. 4A). This finding also rules out the possibility of a change in the identity of the heterotrimeric G proteins coupling to the receptor, as PTx is inhibitory toward $G_{i/o}$ subfamily G proteins only. Additionally, repeating the dose response experiment in MEF cells lacking both ubiquitously-expressed arrestins (arrestin2 and 3, also known as β-arrestin 1 and 2) revealed that both NE-stimulated ERK1/2 activation and the potentiation of ERK1/2 signaling by DMI are preserved in the absence of arrestins. The mechanistic details of this G protein-dependent and arrestin-independent potentiation of NE-induced ERK1/2 by DMI remain to be determined.

3.4. Conclusions and implications

The data presented here provide the first evidence that the antidepressant drug DMI can selectively potentiate ERK1/2 signaling through the α_{2A}AR induced by its endogenous agonist NE. The potentiation effect is observed as enhanced activation by an NE/DMI combination when [DMI] exceeds [NE] (Figs. 1C, 2A and B), and a prolongation of the activation time course when [DMI] equals [NE] (Fig. 1B). The potentiation presents mainly as an enhancement of response sensitivity, as DMI does not have any significant effect the maximal NE-induced ERK1/2 activation (Fig. 2A and B), and is G protein-dependent (Fig. 4A) and arrestin-independent (Fig. 4B).

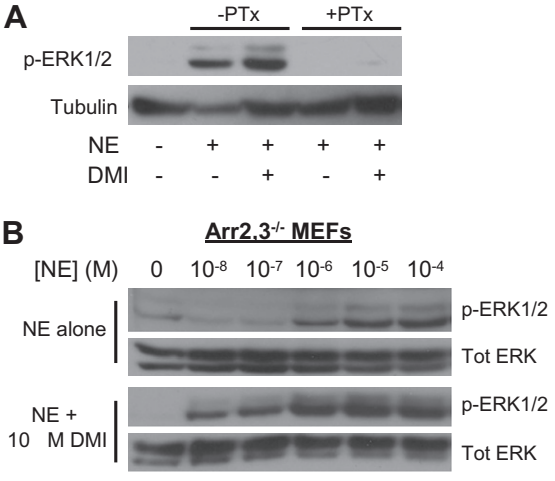

Fig. 4. DMI-modulated ERK1/2 signaling through the α_{2A}AR remains G_i-dependent and arrestin-independent. (A) MEF cells were subjected to pertussis toxin (+PTx) or vehicle (−PTx) treatment as described in methods, then stimulated with 10 μM NE alone or in combination with 10 μM DMI for 5 min. Whole cell homogenates were analyzed by SDS–PAGE/Western blot, probing for phospho-ERK1/2 and tubulin. (B) Arrestin2,3 double knockout (Arr2,3$^{-/-}$) MEFs were stimulated for 5 min with NE at varying concentrations, ranging from 10 nM (10^{-8} M) to 100 μM (10^{-4} M), alone or in combination with 10 μM DMI, as indicated. Homogenates were analyzed as in panel A, with the addition of stripping/probing for total ERK. Blots are representative of three independent experiments.

Selectivity is supported by the findings that while α_{2A}AR-mediated ERK1/2 activation is enhanced, an opposite and more general effect of DMI on Akt is observed (Fig. 3).

Our original hypothesis that DMI would serve as a functional antagonist of endogenous agonist-mediated signaling at the α_{2A}AR is soundly refuted by our data. In fact, it seems that the interaction of DMI with the α_{2A}AR is much more complex than any associated with classical ligands. Given that a switch in the signaling from G protein-mediated to arrestin-mediated transduction does not occur (Fig. 4), a mechanistic model of this complex interaction remains to be elucidated. The functional signaling data in this study could be interpreted as representing a positive allosteric modulation of the receptor by DMI. Although our past analysis indicates that DMI binds to the α_{2A}AR orthosterically [5], it is possible that DMI may interact with both the orthosteric site and an allosteric site, a phenomenon which has been reported for ligands at the M_2 muscarinic receptor [21]. DMI may bind to an allosteric site which is available only within the active conformation of the receptor, given that our previous analysis was carried out with an antagonist as the competing radioligand. These possibilities raised by our present data suggest a more rigorous analysis of the DMI/α_{2A}AR interaction is warranted, utilizing such approaches as the kinetic receptor binding techniques described by Limbird and more specifically designed to detect allosterism [22].

Alternatively, DMI may in fact be binding to the orthosteric site on the α_{2A}AR and modulating signaling in some other way, for example through a dimerization of DMI-bound receptor with NE-bound receptor which alters the receptor signaling profile. α_{2A}ARs are among the many GPCRs which have been shown to homodimerize [23], and dimerization has the potential to alter the signaling profiles of GPCRs as a kind of allosterism [24].

Regardless of the underlying mechanism, our findings have potential implications for antidepressant pharmacology. Our previous study [5] postulated a model whereby DMI exerts its therapeutic antidepressant effects through a downregulation of central nervous system α_{2A}AR expression, correcting the pathobiological increases in α_{2A}AR density and activity associated with clinical depression (reviewed in [25]). The present data demonstrate that DMI in a physiologically relevant ratio with NE can effectively turn on MAPK signaling at that is lacking in response to the physiological level (e.g. 10 nM, see Fig. 2A and B). This α_{2A}AR-activating effect could serve to counterbalance the beneficial α_{2A}AR-decreasing effect until a certain level of α_{2A}AR downregulation is attained. Such a model may represent an important component of the mechanistic basis underlying the significant delay of 3–6 weeks between the start of clinical antidepressant therapy and onset of symptom relief.

Role of the funding sources

The funding sources had no involvement in the study design, collection, analysis, and interpretation of data, writing of the report, or decision to submit the article for publication.

Acknowledgments

We thank Dr. Robert J. Lefkowitz (Duke University) for providing the Arr2,3$^{-/-}$ MEF line. This work has been supported by a National Institute of Mental Health grant (MH081917, QW), the UAB Training Program in Neurobiology of Cognition and Cognitive Disorders (National Institutes of Heath T32 Grant NS061788-03, CC), and the McNair Scholars Program (AJ).

References

[1] R.J. Baldessarini, Drug therapy of depression and anxiety disorders, in: L.L. Brunton, J.S. Lazo, K.L. Parker (Eds.), Goodman & Gilman's The Pharmacological Basis of Therapeutics, McGraw-Hill, Inc., New York, 2006, pp. 429–460.
[2] A.E. Knaus, V. Muthig, S. Schickinger, E. Moura, N. Beetz, R. Gilsbach, L. Hein, Alpha2-adrenoceptor subtypes-unexpected functions for receptors and ligands derived from gene-targeted mouse models, Neurochem. Int. 51 (5) (2007) 277–281.
[3] Y. Mateo, J. Pineda, J.J. Meana, Somatodendritic alpha2-adrenoceptors in the locus coeruleus are involved in the in vivo modulation of cortical noradrenaline release by the antidepressant desipramine, J. Neurochem. 71 (2) (1998) 790–798.
[4] L. Linner, L. Arborelius, G.G. Nomikos, L. Bertilsson, T.H. Svensson, Locus coeruleus neuronal activity and noradrenaline availability in the frontal cortex of rats chronically treated with imipramine: effect of alpha 2-adrenoceptor blockade, Biol. Psychiatry 46 (6) (1999) 766–774.
[5] C. Cottingham, Y. Chen, K. Jiao, Q. Wang, The antidepressant desipramine is an arrestin-biased ligand at the alpha2A adrenergic receptor driving receptor downregulation in vitro and in vivo, J. Biol. Chem. 286 (2011) 36063–36075.
[6] L.E. Limbird, Receptors linked to inhibition of adenylate cyclase: additional signaling mechanisms, The FASEB J: Official Publication Fed. Am. Societies Exp. Biol. 2 (11) (1988) 2686–2695.
[7] B. Kobilka, Adrenergic receptors as models for G protein-coupled receptors, Annu. Rev. Neurosci. 15 (1992) 87–114.
[8] J.G. Richman, J.W. Regan, Alpha 2-adrenergic receptors increase cell migration and decrease F-actin labeling in rat aortic smooth muscle cells, Am. J. Physiol. 274 (3 Pt 1) (1998) C654–662.
[9] Q. Wang, J. Zhao, A.E. Brady, J. Feng, P.B. Allen, R.J. Lefkowitz, P. Greengard, L.E. Limbird, Spinophilin blocks arrestin actions in vitro and in vivo at G protein-coupled receptors, Science 304 (5679) (2004) 1940–1944.
[10] Q. Wang, R. Lu, J. Zhao, L.E. Limbird, Arrestin serves as a molecular switch, linking endogenous alpha2-adrenergic receptor to SRC-dependent, but not SRC-independent, ERK activation. J. Biol. Chem. 281 (36) (2006) 25948–25955.
[11] C.H. Duman, L. Schlesinger, M. Kodama, D.S. Russell, R.S. Duman, A role for MAP kinase signaling in behavioral models of depression and antidepressant treatment, Biol. Psychiatry 61 (5) (2007) 661–670.
[12] X. Li, R.S. Jope, Is glycogen synthase kinase-3 a central modulator in mood regulation?, Neuropsychopharmacology 35 (11) (2010) 2143–2154.
[13] T.A. Kohout, F.S. Lin, S.J. Perry, D.A. Conner, R.J. Lefkowitz, Beta-Arrestin 1 and 2 differentially regulate heptahelical receptor signaling and trafficking, Proc. Natl. Acad. Sci. U.S.A. 98 (4) (2001) 1601–1606.
[14] J. Alblas, E.J. van Corven, P.L. Hordijk, G. Milligan, W.H. Moolenaar, Gi-mediated activation of the p21ras-mitogen-activated protein kinase pathway by alpha 2-adrenergic receptors expressed in fibroblasts, J. Biol. Chem. 268 (30) (1993) 22235–22238.
[15] W.J. Koch, B.E. Hawes, L.F. Allen, R.J. Lefkowitz, Direct evidence that Gi-coupled receptor stimulation of mitogen-activated protein kinase is mediated by G beta gamma activation of p21ras, Proc. Natl. Acad. Sci. U.S.A. 91 (26) (1994) 12706–12710.
[16] Y. Mateo, B. Fernandez-Pastor, J.J. Meana, Acute and chronic effects of desipramine and clorgyline on alpha(2)-adrenoceptors regulating noradrenergic transmission in the rat brain: a dual-probe microdialysis study, Br. J. Pharmacol. 133 (8) (2001) 1362–1370.
[17] C. Murga, L. Laguinge, R. Wetzker, A. Cuadrado, J.S. Gutkind, Activation of Akt/protein kinase B by G protein-coupled receptors. A role for alpha and beta gamma subunits of heterotrimeric G proteins acting through phosphatidylinositol-3-OH kinasegamma, J. Biol. Chem. 273 (30) (1998) 19080–19085.
[18] C. Cottingham, X. Li, Q. Wang, Noradrenergic antidepressant responses to desipramine in vivo are reciprocally regulated by arrestin3 and spinophilin, Neuropharmacology (2012), doi:10.1016/j.neuropharm.2012.02.011.
[19] J.D. Violin, R.J. Lefkowitz, Beta-arrestin-biased ligands at seven-transmembrane receptors, Trends Pharmacol. Sci. 28 (8) (2007) 416–422.
[20] S. Rajagopal, K. Rajagopal, R.J. Lefkowitz, Teaching old receptors new tricks: biasing seven-transmembrane receptors, Nat. Rev. Drug Discov. 9 (5) (2010) 373–386.
[21] D.S. Redka, L.F. Pisterzi, J.W. Wells, Binding of orthosteric ligands to the allosteric site of the M(2) muscarinic cholinergic receptor, Mol. Pharmacol. 74 (3) (2008) 834–843.
[22] L.E. Limbird, Cell Surface Receptors: A Short Course on Theory and Methods, Springer Science + Business Media, Inc., New York, 2005.
[23] K.M. Small, M.R. Schwarb, C. Glinka, C.T. Theiss, K.M. Brown, C.A. Seman, S.B. Liggett, Alpha2A- and alpha2C-adrenergic receptors form homo- and heterodimers: the heterodimeric state impairs agonist-promoted GRK phosphorylation and beta-arrestin recruitment, Biochemistry 45 (15) (2006) 4760–4767.
[24] N.J. Smith, G. Milligan, Allostery at G protein-coupled receptor homo- and heteromers: uncharted pharmacological landscapes, Pharmacol. Rev. 62 (4) (2010) 701–725.
[25] C. Cottingham, H. Chen, Y. Chen, Y. Peng, Q. Wang, Genetic variations of alpha2-adrenergic receptors illuminate the diversity of receptor functions. In: Wang, Q., (Ed.), Current Topics in Membranes, Vol. 67, Elsevier Inc., Amsterdam, 2011.

Biochemical and Biophysical Research Communications 420 (2012) 166–171

Contents lists available at SciVerse ScienceDirect

Biochemical and Biophysical Research Communications

journal homepage: www.elsevier.com/locate/ybbrc

Effect of shear stress, statins and TNF-α on hemostatic genes in human endothelial cells

N. Bergh *, P. Larsson, E. Ulfhammer, S. Jern

The Wallenberg Laboratory for Cardiovascular Research, Institute of Medicin, The Sahlgrenska Academy, University of Gothenburg, Gothenburg, Sweden

ARTICLE INFO

Article history:
Received 21 February 2012
Available online 3 March 2012

Keywords:
Shear stress
Simvastatin
Rosuvastatin
TNF-α
HUVEC
Hemostatic genes

ABSTRACT

Atherosclerotic plaque formation and progression are dependent on local shear stress patterns and inflammatory cytokines. Statins effectively reduce the progression of atherosclerosis and the incidence of cardiovascular events. However, the benefit of statins cannot be explained by cholesterol reduction alone. This study, investigated the non-lipid lowering effects of simvastatin and rosuvastatin on endothelial anti- and prothrombotic genes under different biomechanical and inflammatory stress conditions. Endothelial cells responded in a similar way to simvastatin and rosuvastatin. However, they were more sensitive to simvastatin. The statins had anti-inflammatory properties counteracting the TNF-α effect on the hemostatic genes studied. There was no observed synergistic effect between shear stress and simvastatin. Simvastatin had a counteracting effect on t-PA and PAI-1 compared to TNF-α and shear stress. Simvastatin blocked the TNF-α suppressive effect on thrombomodulin and eNOS, irrespective of shear stress. The strong inductive effect of TNF-α on VCAM-1 was counteracted by simvastatin and shear stress in an additive dose–response dependent way.

1. Introduction

Atherosclerosis, a chronic inflammatory disorder, is the underlying cause of the majority of acute coronary syndromes, sudden cardiac deaths and ischemic strokes. Although, there are numerous known systemic risk factors such as diet, smoking habits and genetics that play an important role in the development of atherosclerotic plaques, the disease has a non-random distribution throughout the arterial tree, *i.e.* primarily localized in the aortic arch and bifurcation of arteries. It is the pattern of shear stress that determines the distinct localization of atherosclerotic plaque [1,2]. An unfavorable flow profile causes a dysfunctional endothelial cell layer that renders the vascular wall vulnerable to atherogenesis [1,2]. Inflammatory stress, such as that caused by tumor necrosis factor-α (TNF-α), stimulates the expression of endothelial cell genes that promotes the atherosclerotic process [3,4]. A dysfunctional endothelial cell layer is more vulnerable to inflammatory stress.

3-Hydroxy-3-methylglutaryl coenzyme A (HMG-CoA) reductase inhibitors, or statins, are a class of cholesterol lowering drugs that is widely prescribed to treat hypercholesterolemia. Statins effectively reduce the progression of atherosclerosis and the incidence of cardiovascular events [5,6]. However, the benefit of statins in the clinic cannot be explained by cholesterol reduction alone. Statins have been shown in numerous studies to modulate endothelial cell gene expression independently of their cholesterol lowering effect [7,8].

To date, investigations of the effect of statins on gene expression in endothelial cells has primarily been limited to static cell culture and just a few studies have incorporated the concomitant effect of biomechanical stress [9,10]. To study the combination is essential since endothelial cells *in vivo* are continuously exposed to biomechanical stress and it is well established that shear stress has important regulatory effects on endothelial function and phenotype [11,12]. There are numerous reports on the combination of inflammatory stress and shear stress, mainly focusing on adhesion molecules (ICAM-1, VCAM-1, E-selectin) [3,4,13,14]. However, to our knowledge, there is only one previous report on the effects of the combination of shear stress, statins and inflammatory stress [15]. Greater understanding of the complex interactions between statins and inflammatory and biomechanical stress will provide better knowledge of and maybe new therapeutic indications for statin therapy.

In this study, we evaluated the pleiotropic effects of simvastatin and rosuvastatin on central hemostatic genes (t-PA, PAI-1, eNOS, thrombomodulin and VCAM-1). Further, the combination of statin, and various levels of biomechanical and inflammatory stress were investigated.

* Corresponding author. Address: Wallenberglaboratoriet, Brunastråket 16, Sahlgrenska University Hospital, SE 413 45 Göteborg, Sweden. Fax: +46 31 191416.
E-mail address: Niklas.Bergh@gu.se (N. Bergh).

0006-291X/$ - see front matter © 2012 Elsevier Inc. All rights reserved.
http://dx.doi.org/10.1016/j.bbrc.2012.02.136

2. Material and methods

2.1. Materials

Simvastatin sodium salt was purchased from Calbiochem and dissolved in DMSO to a concentration of 50 mM. Rosuvastatin was a kind gift from AstraZeneca. TNF-α was purchased from Sigma–Aldrich. Mevalonic acid lactone and geranylgeranyl diphosphate were obtained from Sigma–Aldrich, dissolved in DMSO to a concentration of 1 M. The final concentrations were obtained by dilution in endothelial cell growth medium (EGM-2).

2.2. Cell culture

Fresh umbilical cords were obtained from the maternity ward of the hospital and human umbilical vein endothelial cells (HUVECs) were prepared by collagenase (Sigma–Aldrich, St. Louis, MO, USA) digestion, [16]. Human coronary artery endothelial cells (HCAEC) were purchased from Clonetics. Cells were maintained in EGM-2 complete culture medium, consisting of EBM-2 basal medium (Clonetics/Cambrex, Walkersville, MD, USA) supplemented with 2% fetal bovine serum and growth factors (SingleQuots® kit, Clonetics) and incubated at 37 °C in a humidified 5% CO_2 incubator. The medium was replaced every 2–3 days and sub-cultures were obtained by trypsin/EDTA (Sigma–Aldrich) treatment of confluent monolayers. Cells at passage 1 were used in all experiments.

2.3. Static experiments

HUVECs and HCAECs were seeded in plastic culture plates (Nunc, Roskilde, Denmark) and grown to confluence. On the day of the experiment the cells were added fresh EGM-2 culture medium with or without statins and/or TNF-α. All cell cultures were performed in duplicate and the cells and the cultivating medium were harvested after 6, 24 and 48 h, respectively.

2.4. Flow experiments

The basal *ex vivo* perfusion system has previously been described [17]. Three vessels were connected in parallel to the two perfusion circuits in the *ex vivo* perfusion system. In each circuit, vessel one was exposed to laminar shear stress of less than 1 dyn/cm^2, vessel two had a laminar shear stress of 12.5 dyn/cm^2 and vessel three 25 dyn/cm^2. All vessels were shear stress stimulated for 24 h. As perfusion medium, endothelial cell growth medium was used, composed of 50% EGM-2 complete culture medium and 50% M199 medium (Cambridge, UK) supplemented with 2% heat-inactivated fetal bovine serum (FBS).

In the simvastatin shear stress study ($n = 4$), simvastatin was added to the perfusate medium in one of the two perfusion circuits. In the simvastatin-TNF-α shear stress study ($n = 3$), TNF-α was added to both perfusion circuits and simvastatin was only added to one of the two circuits.

2.5. Shear stress studies

Endothelial cells were grown to confluence within microslides, rectangular glass capillaries. Microslides with the following dimension was used: internal length (L), width (W) and depth (D) = 10 × 0.4 × 0.04 cm (Microslides, Camlab, Cambridge, UK) [18]. Wall shear stress in the microslides was calculated by the following formula $\tau = 6\eta Q/(W^2 D)$, where Q is the volume flow (ml/min) and η is the viscosity of the medium.

2.6. Real-time-PCR

Levels of tPA, PAI-1, thrombomodulin, VCAM-1 and eNOS were analyzed by real-time RT-PCR, performed on a ABI Prism 7700 Sequence Detection System (Applied Biosystem) as described in more detail previously [19]. Glyceraldehyde-3-phosphate dehydrogenase (GPDH) was used as an endogenous internal control.

2.7. Elisa

Total t-PA protein in cell culture medium from static cell cultures was determined by ELISA (TintElize, t-PA, Biopool) according to the manufacturer's protocol.

2.8. Statistics

The statistical evaluation was performed using one-way ANOVA and a paired Student's t-test. Data were presented as mean and standard error. All comparisons were done on samples from the same experiment to check for statistical significance. A p-value less than 0.05 was considered significant.

3. Results

3.1. Dose–response effect of statins on t-PA

The effect of simvastatin and rosuvastatin on t-PA mRNA levels in HUVECs under static culture is shown in Fig. 1. Simvastatin and rosuvastatin enhanced t-PA gene expression in a concentration dependent way, after 24 h stimulation ($p < 0.01$, one-way ANOVA). The endothelial cells were more sensitive to simvastatin than rosuvastatin. The induction of t-PA by simvastatin and rosuvastatin was completely eliminated by mevalonate (p = ns) and the induction was largely reduced by geranylgeranyl diphosphate (GGpp) (data not shown). The same stimulation patterns were also seen after 6 and 48 h (data not shown). The TNF-α suppressing effect on t-PA was counteracted by 3 μM simvastatin but not by 0.3 μM simvastatin Fig. 2.

The effect of simvastatin and rosuvastatin on t-PA protein levels was evaluated by ELISA. Similar as to the mRNA results, t-PA increased in a dose-dependent manner with the highest levels observed with 3 μM simvastatin after 48 h (data not shown).

To verify that the t-PA inductive effect was not confined to HUVECs, studies were repeated in HCAECs. At 24 h a similar dose response pattern was seen at the mRNA level. Even in HCAEC the most pronounced effect was observed with simvastatin 3 μM, (data not shown).

3.2. Interacting effects of simvastatin and TNF-α on hemostatic genes

Simvastatin and rosuvastatin suppressed PAI-1 gene expression in a concentration dependent way ($p < 0.01$, one-way ANOVA). The most pronounced effect was with simvastatin 3 μM which resulted in a 3-fold suppression of PAI-1 after 24 h ($p < 0.001$). This effect was confirmed at the protein level as well as in HCAEC (data not shown). TNF-α up-regulated PAI-1 2-fold ($p = 0.01$). TNF-α alone was a stronger stimulus than simvastatin and TNF-α combined (TNF-α compared to TNF-α + simvastatin: p = ns), Fig. 2.

Simvastatin up-regulated eNOS mRNA levels 4-fold as expected ($p < 0.001$). TNF-α down regulated eNOS 50%. However, the combination of the two stimuli interacted with each other so that the mRNA levels of eNOS were unaffected (control compared to TNF-α + simvastatin: p = ns), Fig. 2.

Simvastatin had a strong inducing effect on thrombomodulin (10-fold, $p < 0.001$) while TNF-α had a 50% suppressive effect

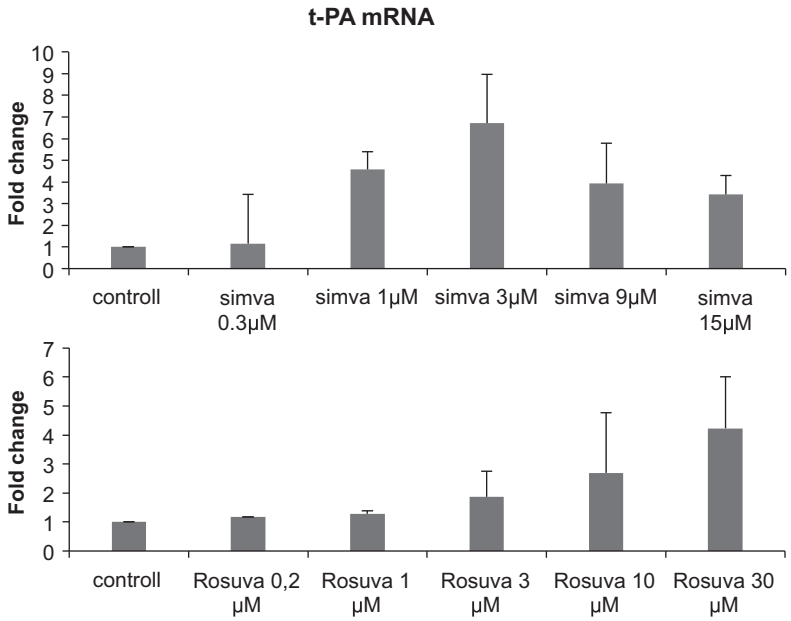

Fig. 1. Simvastatin and rosuvastatininduce t-PA mRNA expression in a dose response dependent way after 24 h. $n = 8$.

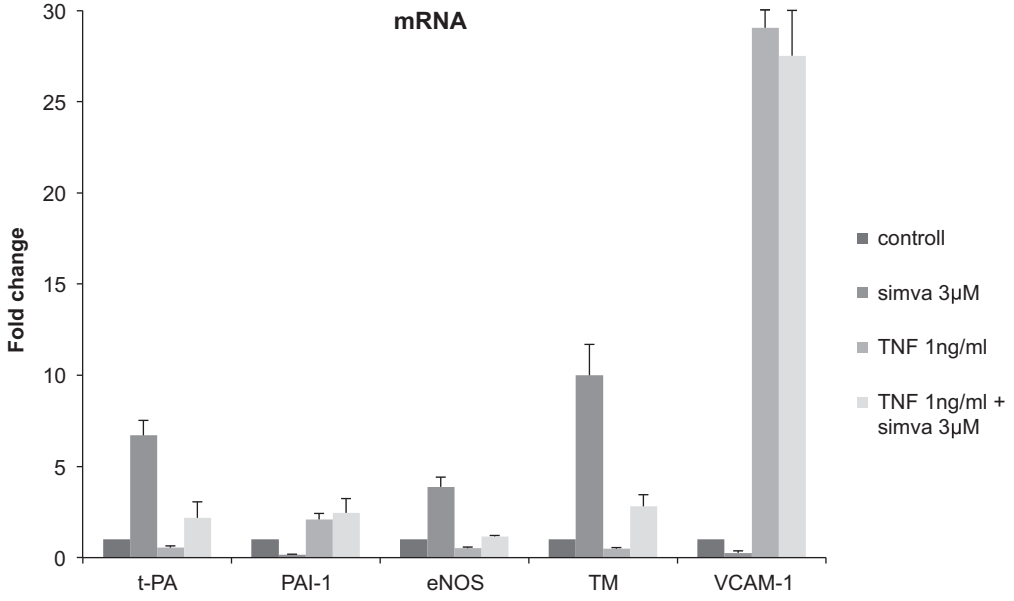

Fig. 2. Regulatory effect of simvastatin and/or TNF-α on HUVECs in static cell conditions on t-PA, PAI-1, thrombomodulin, VCAM-1 and eNOS for 24 h. $n = 5$.

($p < 0.01$). Simvastatin and TNF-α had opposing effects on thrombomodulin mRNA expression and the combination resulted in a 3-fold up-regulation, Fig. 2.

VCAM-1 was suppressed by simvastatin but strongly induced by TNF-α (0.25 and 29-fold, respectively). Simvastatin was not able to reverse the TNF-α effect (TNF-α compared to TNF-α + simvastatin: p = ns), Fig. 2.

3.3. Effect of shear stress and simvastatin

HUVECs were stimulated with three different shear stress levels (<1, 12.5 and 25 dyn/cm^2) in two identical perfusion circuits, A and B.

t-PA gene expression was down regulated by shear stress in a shear–stress dependent way, as previously reported ($p < 0.01$, one-way ANOVA) [19,20]. The combination of simvastatin and low shear stress up regulated t-PA mRNA levels almost 4-fold compared to low shear stressalone ($p < 0.01$). Moderate and high shear stress in combination with simvastatin counteracted each other. There was a tendency for a preserved small up regulation by simvastatin and moderate shear stress ($p = 0.06$, compared to low shear stress) which was erased by high shear stress (p = ns, compared to low shear stress), Fig. 3.

High and moderate shear stress up regulated PAI-1 as expected compared to low shear stress ($p < 0.01$). Simvastatin and low shear stress suppressed PAI-1 expression 2-fold ($p < 0.01$). The suppression of PAI-1 seen by simvastatin was erased by moderate and high

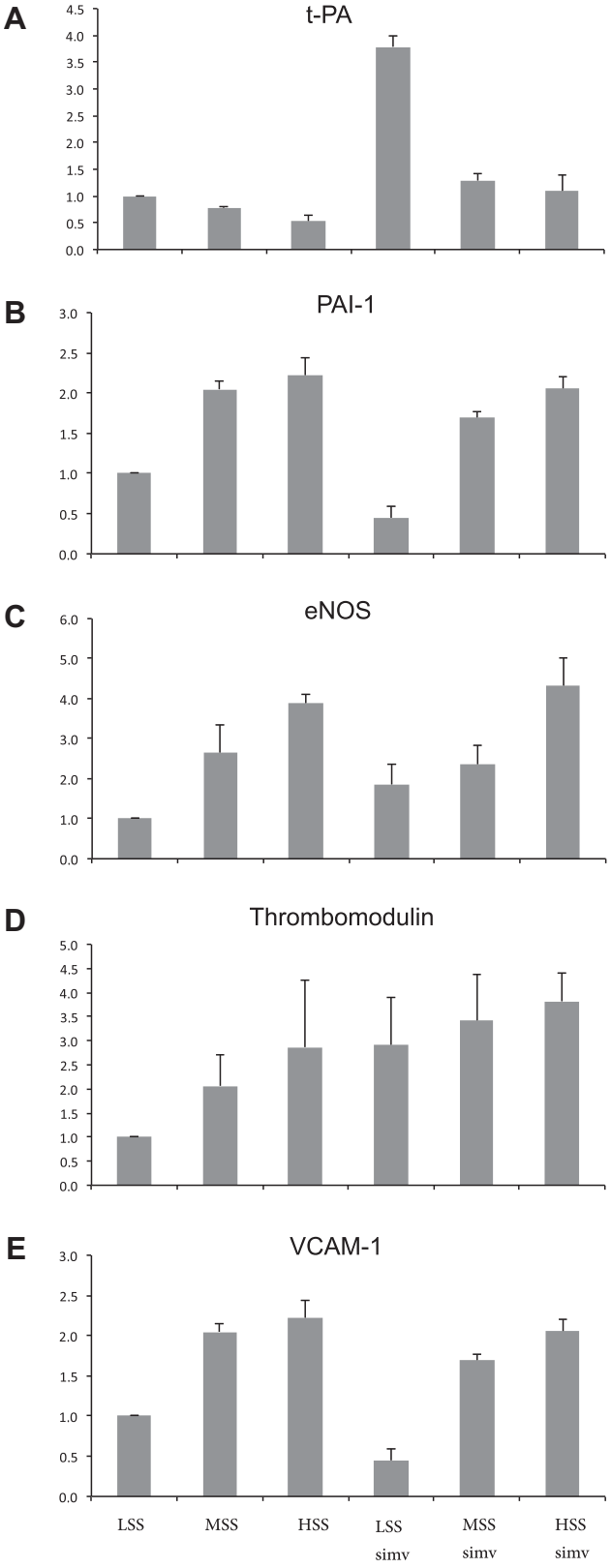

Fig. 3. Relative mRNA expression of t-PA, PAI-1, eNOS, thrombomodulin and VCAM-1 in HUVECs exposed to different levels of shear stress with or without simvastatin 3 μM for 24 h, $n = 4$. Statistical comparisons are made relative to low SS without simvastatin.

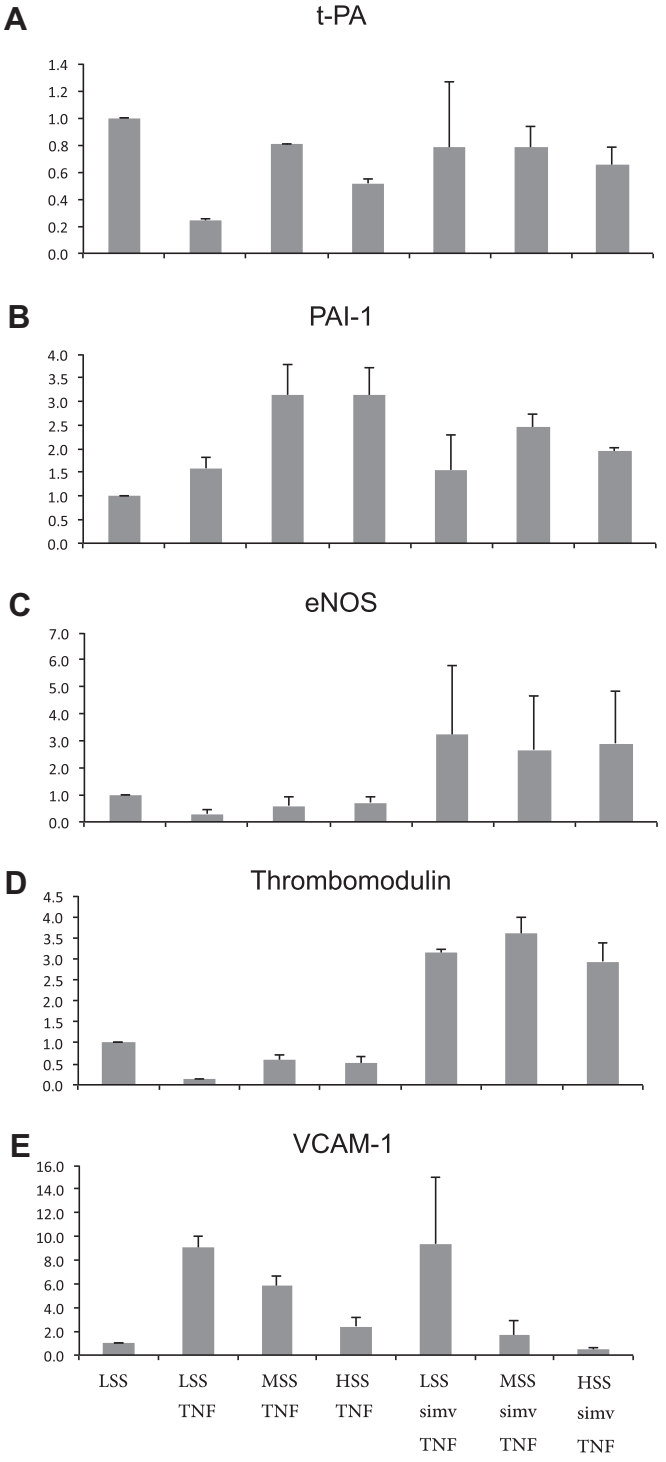

Fig. 4. Relative mRNA expression of t-PA, PAI-1, eNOS, thrombomodulin, and VCAM-1 in HUVECs exposed to different levels of shear stress and TNF-α with or without simvastatin 3 μM for 24 h, $n = 3$. Statistical comparisons are made relative to low SS without simvastatin and TNF-α.

shear stress. There was no difference between moderate and high shear stress with or without simvastatin (p = ns), Fig. 3.

Shear stress induced a distinct increase of eNOS as previously reported [19]. Simvastatin alone also induced an increase in eNOS. The two stimuli together did not have any synergistic effects on eNOS gene expression, Fig. 3.

Shear stress up-regulated thrombomodulin gene expression in a shear stress dependent way. Simvastatin increased the basal level of thrombomodulin ($p < 0.05$). Simvastatin in combination with

shear stress had an additive effect on thrombomodulin gene expression, Fig. 3.

Shear stress down regulated VCAM-1 in a shear–stress-response dependent way ($p < 0.01$). Simvastatin in combination with low shear stress, down regulated VCAM-1 (2-fold decrease, $p < 0.01$), although not as much as high shear stress alone (low shear stress + simvastatin compared to high shear stress, $p < 0.05$). Moderate or high shear stress and simvastatin down regulated VCAM-1 but the two stimuli did not seem to have any additive effects, Fig. 3.

3.4. Effect of shear stress, TNF-α and simvastatin

In these experimental series HUVECs were exposed to prolonged unidirectional shear stress and TNF-α (1nM) in perfusion circuit A and B. In perfusion circuit B simvastatin was added at a concentration of 3 μM. There was an external low shear stress control vessel (less than 1 dyn/cm^2) not exposed to TNF-α or simvastatin.

t-PA gene expression was down regulated 2-fold by low shear stress and TNF-α, ($p = 0.01$). However, moderate and high shear stress seems to be able to inhibit the t-PA down regulatory effect of TNF-α. A similar response has previously been shown by us [19]. In cells exposed to low shear stress, TNF-α and simvastatin, t-PA gene expression was maintained compared to low shear stress (p = ns). In cells exposed to middle or high shear stress, TNF-α and simvastatin, t-PA gene expression was suppressed in a similar way to cells exposed only to shear stress and TNF-α, Fig. 4.

PAI-1 mRNA expression was induced in an additive way by shear stress and TNF-α in accordance with previously published data [19]. The addition of simvastatin counteracted the inducing effect of TNF-α and low shear stress (p = ns compared to low SS). However, simvastatin was not able to fully reverse the inducing effect of moderate/high shear stress in combination with TNF-α, Fig. 4.

eNOS gene expression was suppressed by low shear stress and TNF-α ($p = 0.01$). High and moderate shear stress reversed the TNF-α inhibitory effect (p = ns compared to low shear stress). Interestingly, this TNF-α inhibitory effect was totally reversed by simvastatin in a shear stress independent way ($p < 0.05$ one-way ANOVA), Fig. 4.

Thrombomodulin gene expression was heavily suppressed by low shear stress and TNF-α (3-fold, $p < 0.01$). Moderate/high shear stress and TNF-α had a 2-fold suppression of thrombomodulin ($p < 0.05$). Interestingly, the TNF-α suppressive effect on thrombomodulin was totally blocked and there was a 3-fold up regulation by simvastatin and shear stress, Fig. 4.

VCAM-1 gene expression was heavily induced by TNF-α ($p < 0.01$ compared with low shear stress). Shear stress had a dose dependent suppressive effect on the TNF-α induction of VCAM-1 gene expression ($p < 0.01$, one-way ANOVA). Simvastatin in combination with TNF-α and low shear stress was not able to suppress VCAM-1 gene expression (p = ns compared to low shear stress + TNF-α). However, simvastatin in combination with TNF-α and moderate or high shear stress suppressed VCAM-1 in a shear stress-response dependent way, Fig. 4.

4. Discussion

Few previous studies have investigated the interactions between shear stress and statins on endothelial gene expression [9,10] and no other studies have focused on the effects of statins on t-PA and PAI-1. Only one previous report exists where the combined effects of shear stress, statins and inflammatory stress have been studied. However, they focused on the regulation of the adhesion molecules E-selectin and VCAM-1 [15]. Since the local biomechanical stress profile and systemic inflammation are tightly coupled to the development of atherosclerotic plaques, we think it is necessary to study these interactions. Increased knowledge of these pleiotropic effects may lead to reconsideration of the therapeutic window of statins.

In this study, we first evaluated the effect of simvastatin and rosuvastatin in static cell culture at the mRNA and protein level. Simvastatin has a lipophilic chemical structure while rosuvastatin has a hydrophilic structure. This may be important when studying the pleiotropic effects of statins since lipophilic molecules readily diffuse across cell membranes while hydrophilic ones does not. Consequently, simvastatin may be a potent inhibitor of the mevalonate pathway in a broad range of cells and tissues. Rosuvastatin with its hydrophilic structure is taken up into non-hepatic cells and tissues to a lesser extent than lipophilic compounds. Rosuvastatin has a marked selectivity, confirmed in animal models, for uptake into hepatocytes compared with non-hepatic cells [21,22].

Simvastatin had an inducing effect on t-PA gene expression in human umbilical endothelial cells. As expected, rosuvastatin, with its hydrophilic structure, had the same response pattern but at much higher concentrations and with lower amplitudes in t-PA responses. This effect was also verified in human coronary artery endothelial cells.

Simvastatin had an inhibitory effect on PAI-1 but could not counteract the inducing effect of TNF-α. However, thrombomodulin and eNOS, which have important anti-thrombotic and anti-inflammatory properties, were induced by simvastatin and the inhibitory effect of TNF-α was reversed by simvastatin.

Wall shear stress has been shown in numerous previous studies to have a regulatory effect on endothelial cell morphology and the expression of genes related to inflammation, blood coagulation, thrombosis and vascular constriction [11,23]. We have previously shown that shear stress have important gene regulatory effects [13,19,20] and interacted in a complex way with inflammatory stress [13] while tensile stress does not [19]. Physiological laminar shear stress had atheroprotective effects through counteracting the TNF-α effect on thrombomodulin, eNOS and VCAM-1. However, the effect on the intravascular fibrinolytic system was more complex to interpret. Laminar shear stress was not able to fully reverse the negative stimulus of TNF-α. Therefore we hypothesized that the addition of statins would have positive synergistic effects in combination with shear stress in counteracting the negative stress of cytokines.

In the present study, our findings show that simvastatin induces t-PA more than 3-fold and that the shear stress suppressive effect on t-PA gene expression is counteracted by simvastatin. PAI-1 is down regulated by simvastatin but shear stress seems to be the stronger stimulus and inhibits the statin effect. Shear stress and simvastatin had an additive effect on thrombomodulin. VCAM-1 was down regulated and eNOS was up regulated by shear stress and simvastatin. There seemed not to be any synergistic effects of the two stimuli.

As expected, t-PA gene expression was down regulated by TNF-α, which could to some degree be counteracted by moderate and high shear stress. Interestingly, in the low shear stress situation simvastatin could reverse the suppression of t-PA on TNF-α stimulated endothelial cells. This inhibitory effect of simvastatin could not be observed during high and moderate shear stress. The same pattern was observed even for PAI-1, where simvastatin was able to inhibit the TNF-α inducing effect on PAI-1 gene expression in the low shear stress situation, but not during moderate and high shear stress. The inhibitory effect of TNF-α on thrombomodulin and eNOS gene expression was surprisingly inhibited by simvastatin regardless of shear stress level.

Simvastatin seemed to have the most pronounced effect in the low shear stress situation, *i.e.* mainly the biomechanical stress

profile of the veins. Maybe this stimulation of the endogenous fibrinolysis, anti-thrombotic and anti-inflammatory effects observed in this study of simvastatin mainly in the low shear stress situation may account for the association of statins with a reduced risk of venous thrombosis [8,24]. The reduced risk of venous thrombosis seems to be confined to women using simvastatin as opposed to pravastatin, irrespective of dose prescribed [24] and non-statin lipid-lowering agents have not been shown to be associated with lower risk of venous thrombosis. This reinforces the idea that it is statin's pleiotropic effects that are of interest and not the lowering of cholesterol per se that is of importance. This is in accordance with our data on rosuvastatin since pravastatin has a hydrophilic structure and resembles the structure of rosuvastatin. This emphasizes that we can't look upon statins as one neutral pharmaceutical group but instead there seems to be heterogeneity between the individual statins that needs further examination. Further, the acute venous thrombosis, also called the classical "red thrombus" requires diminished or static blood flow and an underlying hypercoagulable state. Interestingly, in accordance with our data simvastatin has anticoagulation effects which are most pronounced in the low shear stress situation. However, the epidemiologic studies on statins and the risk for deep venous thrombosis are sparse and there are no randomized clinical trials to confirm these observations.

The effects of statins on VCAM-1 gene expression reported in the literature are contradictory. Several groups have reported that statins potentiated the effect of TNF-α resulting in enhanced VCAM-1 mRNA and protein levels [25], whereas other studies have demonstrated that statins decreased the induction of VCAM-1 mRNA and protein by TNF-α [26,27]. We found that simvastatin at a concentration of 3 μM had no effect on the TNF-α-induced increase in VCAM-1 gene expression. Few studies have evaluated the interactions between laminar shear stress and statins. Simvastatin had no further regulatory effect than laminar shear stress on VCAM-1 gene expression. This result is in line with what Rossi et al. [15] found, while Cicha et al. [26] showed that simvastatin and laminar shear stress potentiated each other. To the best of our knowledge, it is only Rossi et al. [15] who have reported data on the combination of laminar shear stress, statins and TNF-α. They studied adhesion molecules and found that laminar shear stress could reduce the potentiating effect of simvastatin on VCAM-1 gene expression in TNF-α activated endothelial cells. Our results showed that shear stress had an inhibiting effect on the TNF-α induced VCAM-1 gene expression. Simvastatin in combination with low shear stress did not have any further effect on VCAM-1 in TNF-α activated endothelial cells. However, simvastatin in combination with increasing levels of shear stress seemed to have an additive effect resulting in a powerful suppression of TNF-α stimulated VCAM-1 induction.

There are numerous reports on the pleiotropic effects of statins, biomechanical stress and inflammatory stress on endothelial gene expression, but there are far fewer examining the effect of two or more stimuli simultaneously. Combining the stimuli is more representative of *in vivo* conditions than static culture. To the best of our knowledge, our study is the first to evaluate the effect of statins on important marker genes representing different hemostatic functions of the endothelial cells exposed to different magnitudes of laminar shear stress with or without TNF-α stimulation.

References

[1] G. Dai, M.R. Kaazempur-Mofrad, S. Natarajan, Y. Zhang, S. Vaughn, B.R. Blackman, R.D. Kamm, G. Garcia-Cardena, M.A. Gimbrone Jr., Distinct endothelial phenotypes evoked by arterial waveforms derived from atherosclerosis-susceptible and -resistant regions of human vasculature, Proc. Natl. Acad. Sci. USA 101 (2004) 14871–14876.

[2] P.A. VanderLaan, C.A. Reardon, G.S. Getz, Site specificity of atherosclerosis: site-selective responses to atherosclerotic modulators, Arterioscler. Thromb. Vasc. Biol. 24 (2004) 12–22.

[3] J. Partridge, H. Carlsen, K. Enesa, H. Chaudhury, M. Zakkar, L. Luong, A. Kinderlerer, M. Johns, R. Blomhoff, J.C. Mason, D.O. Haskard, P.C. Evans, Laminar shear stress acts as a switch to regulate divergent functions of NF-kappa B in endothelial cells, Faseb J. 21 (2007) 3553–3561.

[4] H. Yamawaki, S. Lehoux, B.C. Berk, Chronic physiological shear stress inhibits tumor necrosis factor-induced proinflammatory responses in rabbit aorta perfused ex vivo, Circulation 108 (2003) 1619–1625.

[5] S.E. Nissen, S.J. Nicholls, I. Sipahi, P. Libby, J.S. Raichlen, C.M. Ballantyne, J. Davignon, R. Erbel, J.C. Fruchart, J.C. Tardif, P. Schoenhagen, T. Crowe, V. Cain, K. Wolski, M. Goormastic, E.M. Tuzcu, Effect of very high-intensity statin therapy on regression of coronary atherosclerosis: the ASTEROID trial, JAMA 295 (2006) 1556–1565.

[6] J. Shepherd, S.M. Cobbe, I. Ford, C.G. Isles, A.R. Lorimer, P.W. MacFarlane, J.H. McKillop, C.J. Packard, Prevention of coronary heart disease with pravastatin in men with hypercholesterolemia. West of Scotland Coronary Prevention Study Group, N. Engl. J. Med. 333 (1995) 1301–1307.

[7] S. Sen-Banerjee, S. Mir, Z. Lin, A. Hamik, G.B. Atkins, H. Das, P. Banerjee, A. Kumar, M.K. Jain, Kruppel-like factor 2 as a novel mediator of statin effects in endothelial cells, Circulation 112 (2005) 720–726.

[8] J.G. Ray, Dyslipidemia, statins, and venous thromboembolism: a potential risk factor and a potential treatment, Curr. Opin. Pulm. Med. 9 (2003) 378–384.

[9] J. Rossi, P. Jonak, L. Rouleau, L. Danielczak, J.C. Tardif, R.L. Leask, Differential response of endothelial cells to simvastatin when conditioned with steady, non-reversing pulsatile or oscillating shear stress, Ann. Biomed. Eng. 39 (2010) 402–413.

[10] J. Rossi, L. Rouleau, J.C. Tardif, R.L. Leask, Effect of simvastatin on Kruppel-like factor 2, endothelial nitric oxide synthase and thrombomodulin expression in endothelial cells under shear stress, Life Sci. 87 (2010) 92–99.

[11] R.J. Dekker, S. van Soest, R.D. Fontijn, S. Salamanca, P.G. de Groot, E. VanBavel, H. Pannekoek, A.J. Horrevoets, Prolonged fluid shear stress induces a distinct set of endothelial cell genes, most specifically lung Kruppel-like factor (KLF2), Blood 100 (2002) 1689–1698.

[12] N. Resnick, M.A. Gimbrone Jr., Hemodynamic forces are complex regulators of endothelial gene expression, FASEB J. 9 (1995) 874–882.

[13] N. Bergh, E. Ulfhammer, K. Glise, S. Jern, L. Karlsson, Influence of TNF-alpha and biomechanical stress on endothelial anti- and prothrombotic genes, Biochem. Biophys. Res. Commun. 385 (2009) 314–318.

[14] J.K. Tsou, R.M. Gower, H.J. Ting, U.Y. Schaff, M.F. Insana, A.G. Passerini, S.I. Simon, Spatial regulation of inflammation by human aortic endothelial cells in a linear gradient of shear stress, Microcirculation 15 (2008) 311–323.

[15] J. Rossi, L. Rouleau, A. Emmott, J.C. Tardif, R.L. Leask, Laminar shear stress prevents simvastatin-induced adhesion molecule expression in cytokine activated endothelial cells, Eur. J. Pharmacol. 649 (2010) 268–276.

[16] E.A. Jaffe, R.L. Nachman, C.G. Becker, C.R. Minick, Culture of human endothelial cells derived from umbilical veins. Identification by morphologic and immunologic criteria, J. Clin. Invest. 52 (1973) 2745–2756.

[17] N. Bergh, M. Ekman, E. Ulfhammer, M. Andersson, L. Karlsson, S. Jern, A new biomechanical perfusion system for ex vivo study of small biological intact vessels, Ann. Biomed. Eng. 33 (2005) 1808–1818.

[18] B.M. Cooke, S. Usami, I. Perry, G.B. Nash, A simplified method for culture of endothelial cells and analysis of adhesion of blood cells under conditions of flow, Microvasc. Res. 45 (1993) 33–45.

[19] N. Bergh, E. Ulfhammer, L. Karlsson, S. Jern, Effects of two complex hemodynamic stimulation profiles on hemostatic genes in a vessel-like environment, Endothelium 15 (2008) 231–238.

[20] E. Ulfhammer, M. Carlstrom, N. Bergh, P. Larsson, L. Karlsson, S. Jern, Suppression of endothelial t-PA expression by prolonged high laminar shear stress, Biochem. Biophys. Res. Commun. 379 (2009) 532–536.

[21] F. McTaggart, L. Buckett, R. Davidson, G. Holdgate, A. McCormick, D. Schneck, G. Smith, M. Warwick, Preclinical and clinical pharmacology of rosuvastatin, a new 3-hydroxy-3-methylglutaryl coenzyme A reductase inhibitor, Am. J. Cardiol. 87 (2001) 28b–32b.

[22] C.M. White, A review of the pharmacologic and pharmacokinetic aspects of rosuvastatin, J. Clin. Pharmacol. 42 (2002) 963–970.

[23] A.R. Brooks, P.I. Lelkes, G.M. Rubanyi, Gene expression profiling of vascular endothelial cells exposed to fluid mechanical forces: relevance for focal susceptibility to atherosclerosis, Endothelium 11 (2004) 45–57.

[24] C.J. Doggen, R.N. Lemaitre, N.L. Smith, S.R. Heckbert, B.M. Psaty, HMG CoA reductase inhibitors and the risk of venous thrombosis among postmenopausal women, J. Thromb. Haemost. 2 (2004) 700–701.

[25] S. Dunoyer-Geindre, Y. Dimitrova, R.J. Fish, N. Satta, G. Reber, E.K. Kruithof, P. de Moerloose, Fluvastatin increases the expression of adhesion molecules, monocyte chemoattractant protein-1 and tissue factor in HUVEC stimulated by patient IgG fractions containing antiphospholipid antibodies, Thromb. Haemost. 93 (2005) 339–345.

[26] I. Cicha, K. Beronov, E.L. Ramirez, K. Osterode, M. Goppelt-Struebe, D. Raaz, A. Yilmaz, W.G. Daniel, C.D. Garlichs, Shear stress preconditioning modulates endothelial susceptibility to circulating TNF-alpha and monocytic cell recruitment in a simplified model of arterial bifurcations, Atherosclerosis 207 (2009) 93–102.

[27] Y.S. Kim, Y. Ahn, M.H. Hong, K.H. Kim, H.W. Park, Y.J. Hong, J.H. Kim, W. Kim, M.H. Jeong, J.G. Cho, J.C. Park, J.C. Kang, Rosuvastatin suppresses the inflammatory responses through inhibition of c-Jun N-terminal kinase and nuclear factor-kappaB in endothelial cells, J. Cardiovasc. Pharmacol. 49 (2007) 376–383.

Biochemical and Biophysical Research Communications 420 (2012) 172–177

Contents lists available at SciVerse ScienceDirect

Biochemical and Biophysical Research Communications

journal homepage: www.elsevier.com/locate/ybbrc

Up-regulation of the betaine/GABA transporter BGT1 by JAK2

Zohreh Hosseinzadeh [a,1], Manzar Shojaiefard [a,b,1], Shefalee K. Bhavsar [a], Florian Lang [a,*]

[a] Department of Physiology, University of Tübingen, Gmelinstr. 5, D-72076 Tübingen, Germany
[b] Physiology Department of Fasa University of Medical Science, Iran

ARTICLE INFO

Article history:
Received 17 February 2012
Available online 3 March 2012

Keywords:
GABA transport
Osmolyte
Cell volume
Erythropoietin

ABSTRACT

Janus-activated kinase-2 JAK2 is activated by hyperosmotic shock and modifies the activity of several Na^+ coupled transporters. Carriers up-regulated by osmotic shock include the Na^+ coupled osmolyte transporter BGT1 (betaine/GABA transporter 1), which accomplishes the concentrative cellular uptake of γ-amino-butyric acid (GABA). The present study thus explored whether JAK2 participates in the regulation of BGT1 activity. To this end, cRNA encoding BGT1 was injected into *Xenopus* oocytes with or without cRNA encoding wild type JAK2, constitutively active ^{V617F}JAK2 or inactive ^{K882E}JAK2, and electrogenic GABA transport determined by dual electrode voltage clamp. In oocytes injected with cRNA encoding BGT1 but not in oocytes injected with water or with cRNA encoding JAK2 alone, the addition of 1 mM GABA to the extracellular fluid generated an inward current (I_{BGT}). In BGT1 expressing oocytes I_{BGT} was significantly increased by coexpression of JAK2 or ^{V617F}JAK2, but not by coexpression of ^{K882E}JAK2. According to kinetic analysis coexpression of JAK2 increased the maximal I_{BGT} without significantly modifying the concentration required for halfmaximal I_{BGT} (K_M). In oocytes expressing BGT1 and ^{V617F}JAK2 I_{BGT} was gradually decreased by JAK2 inhibitor AG490 (40 μM). The decline of I_{BGT} following disruption of carrier insertion with brefeldin A (5 μM) was similar in the absence and presence of the JAK2 inhibitor AG490 (40 μM). In conclusion, JAK2 is a novel regulator of the GABA transporter BGT1. The kinase up-regulates the carrier presumably by enhancing the insertion of carrier protein into the cell membrane.

1. Introduction

The Janus-activated kinase-2 JAK2 contributes to the signaling of several hormones and cytokines [1–3] including leptin [4], growth hormone [5,6], erythropoietin [2], thrombopoietin [2] and granulocyte colony-stimulating factor [2]. Excessive JAK2 activity may lead to the development of malignancy and JAK2 inhibitors may be effective in the treatment of myeloproliferative disorders [7–12]. The gain of function mutation ^{V617F}JAK2 has been detected in and presumably contributes to development of myeloproliferative disease [13–16].

JAK2 is activated by oxidative stress and ischemia [17] and by hypertonicity [18,19]. The sensitivity to osmotic cell shrinkage renders the kinase a candidate signaling molecule participating in the regulation of cell volume. Mechanisms up-regulated during osmotic cell shrinkage include the activity of Na^+ coupled osmolyte transporters, such as the betaine/GABA transporter BGT1 (SLC6A12) [20,21]. BGT1 belongs to superfamily of Na^+, Cl^- coupled transporters for neurotransmitters (e.g. dopamine, GABA, serotonin and norepinephrine), amino acids (e.g. glycine) [22], creatine [22], and the organic osmolytes betaine [23] and taurine [24]. BGT1 is expressed in liver [25–27], kidney [27], airways [28], and brain [27,29].

Osmotic cell shrinkage up-regulates BGT1 expression [30–32]. Beyond that, the carrier is regulated by ATP [33], Ca^{2+} [34], protein kinase C [35], prostaglandin E_2 [36,37] and the cytoskeleton [38,39].

Cellular accumulation of osmolytes protects against apoptosis and thus participates in the regulation of cell survival [40].

The present study explored whether the activity of BGT1 is influenced by regulated by JAK2. To this end, BGT1 was expressed in *Xenopus* oocytes with or without wild type JAK2, constitutively active ^{V617F}JAK2 or inactive ^{K882E}JAK2 and the electrogenic GABA transport determined utilizing dual electrode voltage clamp.

2. Materials and methods

2.1. Constructs

Constructs were used encoding wild type BGT1 [41], and wild-type human JAK2 (Imagenes, Berlin, Germany). Further, an inactive ^{K882E}JAK2 mutant [42] and the ^{V617F}JAK2 mutant [16] were generated by site-directed mutagenesis (QuikChange II XL Site-Directed Mutagenesis Kit; Stratagene, Heidelberg, Germany) according to

* Corresponding author. Fax: +49 7071/295618.
E-mail address: florian.lang@uni-tuebingen.de (F. Lang).
[1] These authors contributed equally this work.

0006-291X/$ - see front matter © 2012 Elsevier Inc. All rights reserved.
http://dx.doi.org/10.1016/j.bbrc.2012.02.137

the manufacturer's instructions [43]. The following primers were used:

- ^{V617F}JAK2: 5′-AGCATTTGGTTTTAAATTATGGAGTATGTTTCTGTGG AGACGAGA-3′;
- ^{V617F}JAK2: 5′-TCTCGTCTCCACAGAAACATACTCCATAATTTAAAA CCAAATGCT-3′;
- ^{K882E}JAK2: 5′-GGGAGGTGGTCGCTGTAGAAAAGCTTCAGCATAG T-3′; and
- ^{K882E}JAK2: 5′-ACTATGCTGAAGCTTTTCTACAGCGACCACCTCCC-3′.

Underlined bases indicate mutation sites. The mutants were sequenced to verify the presence of the desired mutation. The mutants were used for generation of cRNA as described previously [44].

2.2. Voltage clamp in Xenopus oocytes

Xenopus oocytes were prepared as previously described [45]. Where not indicated otherwise, 15 ng BGT1 cRNA on the first day and 10 ng of wild type JAK2 cRNA were injected on the second day or same day after preparation of the oocytes [46]. The oocytes were maintained at 17 °C in ND96 solution containing (in mM): 96 NaCl, 4 KCl, 1.8 $MgC1_2$, 0.1 $CaC1_2$, 5 HEPES, pH 7.4, gentamycin (100 mg/L), tetracycline (100 mg/L), ciprofloxacin (1.6 mg/L), theophylline (90 mg/L) where indicated, the JAK2 inhibitor AG490 (40 μM), actinomycin D (10 μM) or brefeldin A (5 μM) were added to the respective solutions. The voltage clamp experiments were performed at room temperature 4 days after injection [47]. Two-electrode voltage-clamp recordings were performed at a holding potential of −60 mV. The data were filtered at 10 Hz and

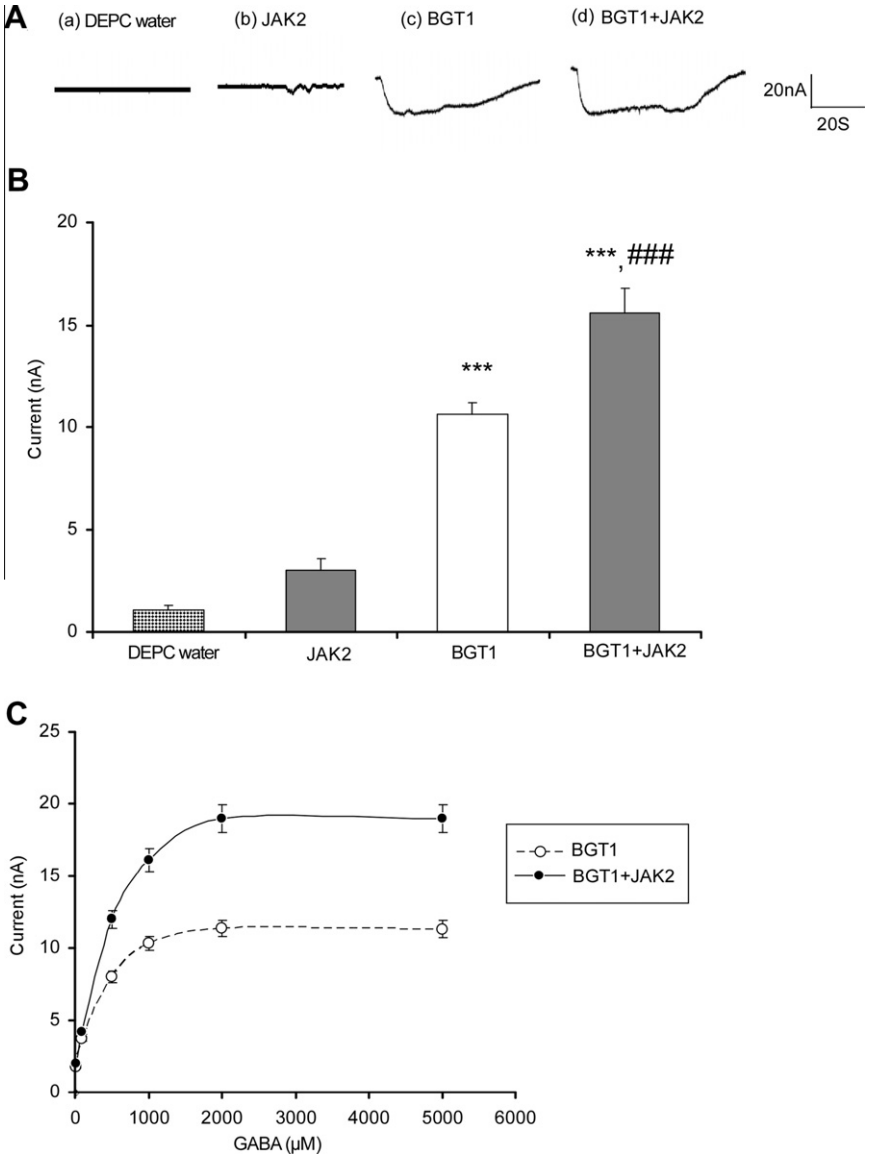

Fig. 1. Coexpression of JAK2 increases electrogenic GABA transport in BGT1-expressing *Xenopus* oocytes. (A) Representative original tracings showing GABA (1 mM)-induced current (I_{BGT}) in *Xenopus* oocytes injected with water (a), expressing wild type JAK2 alone (b), or expressing BGT1 without (c) or with (d) additional coexpression of wild type JAK2. (B) Arithmetic means ± SEM (n = 7) of GABA (1 mM)-induced current (I_{BGT}) in *Xenopus* oocytes injected with water (H_2O, dotted bar), expressing JAK2 alone (JAK2, dark gray bar), or expressing BGT1 without (BGT1, white bar) or with (BGT1 + JAK2, dark gray bar) additional coexpression of wild type JAK2. *** Indicates statistically significant ($p < 0.001$) difference from the absence of BGT1. ### Indicates statistically significant ($p < 0.001$) difference from the absence of JAK2. (C) Arithmetic means ± SEM (n = 3) of GABA-induced current (I_{BGT}) as a function of GABA concentration in *Xenopus* oocytes expressing BGT1 without (open circles, dashed line), or with (closed circles, solid line) additional coexpression of wild type JAK2.

recorded with a Digidata A/D–D/A converter and Clampex V.9 software for data acquisition and analysis (Axon Instruments) [48]. The control superfusate (ND96) contained 96 mM NaCl, 2 mM KCl, 1.8 mM $CaCl_2$, 1 mM $MgCl_2$ and 5 mM HEPES, pH 7.4. γ-Amino-butyric acid (GABA) was added to the solutions at a concentration of 1 mM, unless otherwise stated. The flow rate of the superfusion was approx. 20 ml/min, and a complete exchange of the bath solution was reached within about 10 s.

2.3. Statistical analysis

Data are provided as means ± SEM, *n* represents the number of oocytes investigated. All experiments were repeated with at least 2–3 batches of oocytes; in all repetitions qualitatively similar data were obtained. Data were tested for significance using ANOVA or *t*-test, as appropriate. Results with $p < 0.05$ were considered statistically significant.

3. Results

In order to test whether Janus kinase-2 (JAK2) modifies the function of the betaine/GABA transporter (SLC6A12), cRNA encoding the carrier was injected with or without additional injection of cRNA encoding JAK2 and electrogenic transport of GABA estimated from the GABA (1 mM) induced inward current (I_{BGT}). In neither non-injected nor water-injected *Xenopus* oocytes addition of 1 mM GABA to the bath solution induced an appreciable I_{BGT}. Accordingly *Xenopus* oocytes do not express appreciable endogenous electrogenic GABA transport (Fig. 1A). Moreover, no appreciable I_{BGT} was detected in *Xenopus* oocytes expressing wild type JAK2 alone (Fig. 1B). A robust I_{BGT} was, however, observed in *Xenopus* oocytes injected with cRNA encoding BGT1. The additional injection of cRNA encoding wild type JAK2 was followed by a significant increase of I_{BGT} in BGT1 expressing *Xenopus* oocytes (Fig. 1B).

A further series of experiments was performed to determine, whether JAK2 increased BGT1 activity by enhancing the maximal transport rate or by increasing the affinity of the carrier. Kinetic analysis of the GABA-induced currents in BGT1-expressing *Xenopus* oocytes (Fig. 1C) yielded a maximal current of 12 ± 1 nA ($n = 3$) in *Xenopus* oocytes expressing BGT1 alone, and 21 ± 1 nA ($n = 3$) in *Xenopus* oocytes expressing BGT1 together with JAK2. Accordingly, the maximal transport rate was significantly higher in *Xenopus* oocytes expressing BGT1 together with JAK2 than in *Xenopus* oocytes expressing BGT1 alone. The GABA concentration required for half-maximal current (K_M) approached 200 ± 57 μM ($n = 3$) in *Xenopus* oocytes expressing BGT1 alone, and 360 ± 75 μM ($n = 3$) in *Xenopus* oocytes expressing BGT1 together JAK2. The K_M was not significantly different between *Xenopus* oocytes expressing BGT1 together with JAK2 and *Xenopus* oocytes expressing BGT1 alone.

Increasing the amount of cRNA encoding JAK2 injected from 10 to 14 ng significantly ($p < 0.01$) increased I_{BGT} from 20 ± 1 nA ($n = 5$) to 25 ± 1 nA ($n = 5$). Increasing the ambient pH from 7.4 to 7.8 increased I_{BGT} from 18 ± 1 nA ($n = 5$) to 23 ± 1 nA ($n = 5$) in BGT1 + JAK2 expressing oocytes and from 16 ± 1 nA ($n = 5$) to 21 ± 1 nA ($n = 5$) in oocytes expressing BGT1 alone. Thus, JAK2 increased I_{BGT} to a similar extent at pH 7.4 and pH 7.8 and thus did not appreciably modify pH sensitivity of the carrier.

The effect of wild type JAK2 was mimicked by the gain of function mutant ^{V617F}JAK2 but not by the inactive mutant ^{K882E}JAK2 (Fig. 2A and B). The effect of ^{V617F}JAK2 tended to be higher than

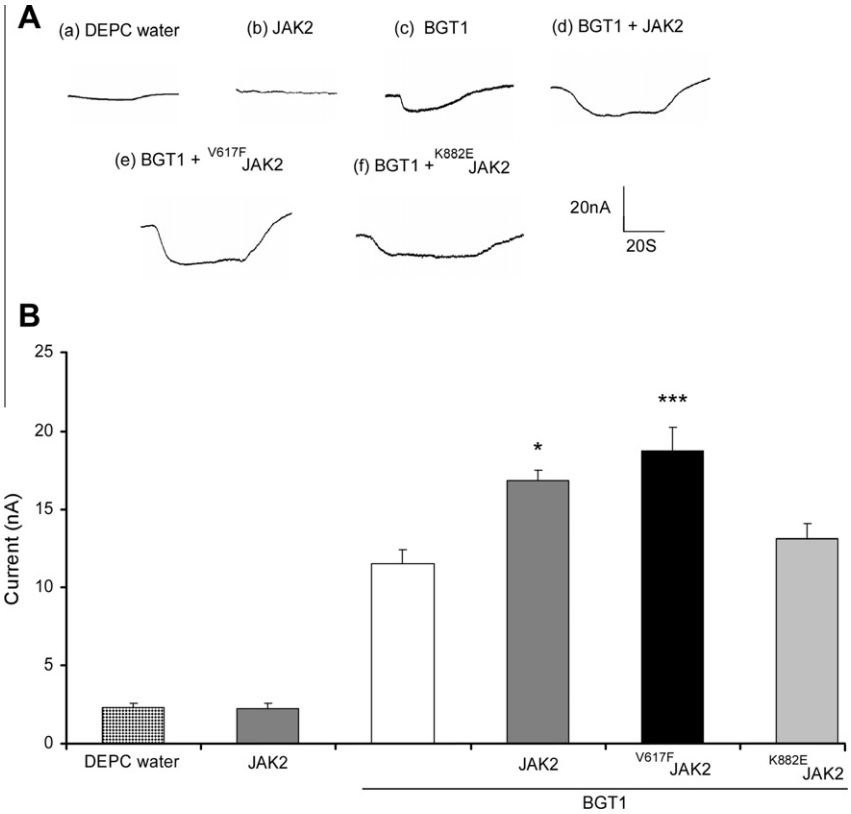

Fig. 2. The effect of JAK2 is mimicked by ^{V617F}JAK2 but not by the inactive mutant ^{K882E}JAK2. (A) Representative original tracings showing GABA (1 mM)-induced current (I_{BGT}) in *Xenopus* oocytes injected with water (a), or expressing JAK2 alone (b) BGT1 alone (c), BGT1 with JAK2 (d), with constitutively active ^{V617F}JAK2 (e), or with the inactive mutant ^{K882E}JAK2 (f). (B) Arithmetic means ± SEM ($n = 15$) of GABA (1 mM)-induced current (I_{BGT}) in *Xenopus* oocytes injected with water (H_2O, dotted bar), expressing JAK2 alone (JAK2, dark gray bar), expressing BGT1 without (BGT1, white bar) or with wild type JAK2 (BGT + JAK2, dark gray bar), with constitutively active ^{V617F}JAK2 (BGT1 + ^{V617F}JAK2, black bar) or with the inactive mutant ^{K882E}JAK2 (BGT1 + ^{K882E}JAK2, light gray bar) *,*** indicates statistically significant ($p < 0.5$, $p < 0.001$) difference to expression of BGT1 alone.

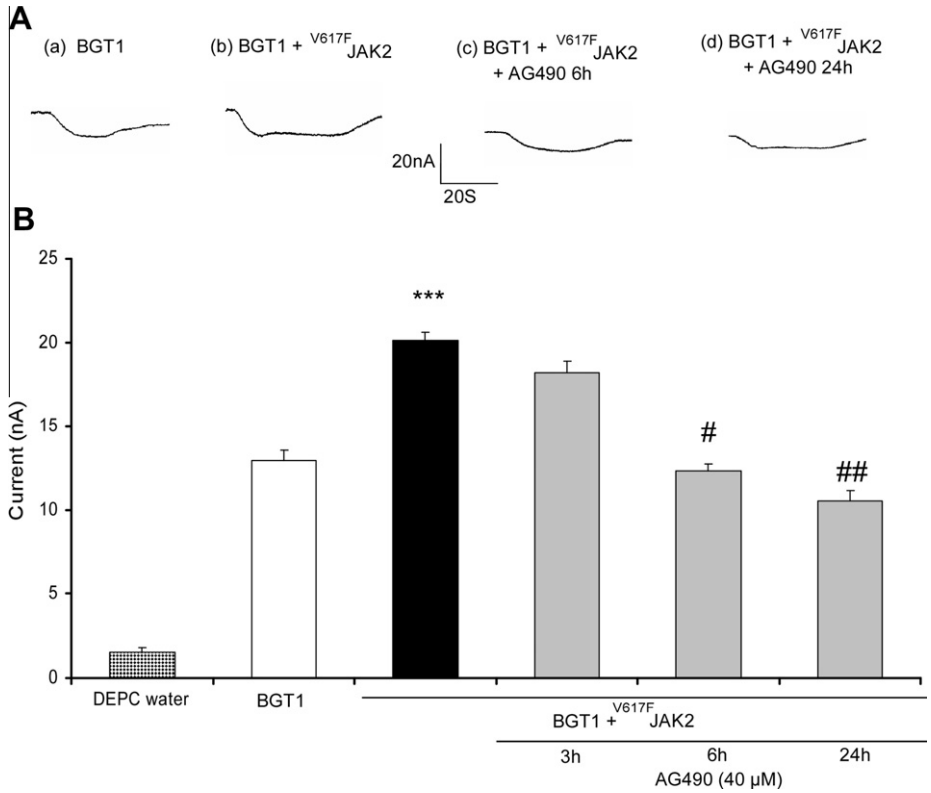

Fig. 3. The effect of ^{V617F}JAK2 is reversed by the JAK2 inhibitor AG490. (A) Representative original tracings showing GABA (1 mM)-induced current (I_{BGT}) in *Xenopus* oocytes injected with BGT1 (a) or BGT1 + ^{V617F}JAK2 without (b) or with a 6 h (c) or 24 h (d) pretreatment with JAK2 inhibitor AG490 (40 μM). (B) Arithmetic means ± SEM (n = 15) of GABA (1 mM)-induced current (I_{BGT}) in *Xenopus* oocytes injected with water (H_2O, dotted bar), or expressing BGT1 with constitutive active ^{V617F}JAK2 (black and gray bars) in the absence of inhibitor (black bar, 0H) or following pretreatment with the JAK2 inhibitor AG490 (40 μM, light gray bars) for the indicated time periods. $^{\#,\#\#}$ indicates statistically significant ($p < 0.05$, $p < 0.01$) difference from the absence of JAK2 inhibitor AG490. *** Indicates statistically significant ($p < 0.001$) difference from BGT1 alone (absence of JAK2).

that of wild type JAK2, an effect, however, not reaching statistical significance. To the extent that ^{V617F}JAK2 is more effective than JAK2, wild type JAK2 may not be fully activated in *Xenopus* oocytes.

Treatment of *Xenopus* oocytes expressing both BGT1 and ^{V617F}JAK2 with the JAK2 inhibitor AG490 (40 μM) resulted in a decrease of I_{BGT} (Fig. 3). The effect of the inhibitor on I_{BGT} reached statistical significance within 6 and 24 h of preincubation with AG490.

In theory, the increase of I_{BGT} in BGT1 expressing *Xenopus* oocytes by coexpression of ^{V617F}JAK2 could have resulted from accelerated clearance of carrier protein from the cell membrane. To explore the stability of I_{BGT}, the BGT1-expressing *Xenopus* oocytes were treated with 5 μM brefeldin A, a substance blocking the insertion of new carrier protein into the cell membrane. As shown in Fig. 4A, in the presence of brefeldin A I_{BGT} declined similarly fast in *Xenopus* oocytes expressing BGT1 together with ^{V617F}JAK2 and in *Xenopus* oocytes expressing BGT1 alone. The observation suggests that ^{V617F}JAK2 enhances I_{BGT} by a mechanism other than accelerating carrier clearance from the cell membrane.

Inhibition of transcription by incubation (1–2 days) with actinomycin D (10 μM) did not significantly modify I_{BGT}, which remained significantly higher in *Xenopus* oocytes expressing BGT1 together with ^{V617F}JAK2 than in *Xenopus* oocytes expressing BGT1 alone (Fig. 4B). Thus, the effect of JAK2 does not require transcription.

4. Discussion

The present study reveals a novel regulator of the betaine/GABA transporter BGT1 (SLC6A12). In BGT1 expressing *Xenopus* oocytes coexpression of the Janus Kinase 2 (JAK2) significantly increased the electrogenic transport of GABA. The effect of wild type JAK2 was mimicked by the gain of function mutant ^{V617F}JAK2 but not by the inactive ^{K882E}JAK2. Thus, kinase activity was required for this effect. Coexpression of the kinase did not significantly affect the substrate affinity but significantly enhanced the maximal transport rate. The ability of JAK2 to modify transport has already been demonstrated earlier [49,50]. More recent studies revealed the ability of JAK2 to up-regulate the Na^+ coupled glucose transporter SGLT1 (SLC5A1) [51], the Na^+ coupled neutral amino acid transporter B(0)AT (SLC6A19) [52] and the glutamate transporters EAAT1–4 [48].

The decline of BGT1 activity following inhibition of carrier insertion into the cell membrane by brefeldin A was similar in the presence and absence of the JAK2 inhibitor AG490, an observation suggesting that JAK2 did modify the clearance of carrier protein from the cell membrane. The observation may point to the ability of JAK2 to enhance carrier insertion into the cell membrane. In view of the impact of brefeldin A on the trafficking of a wide variety of molecules, the evidence is, however, rather circumstantial.

Exposure of JAK2 and BGT1 expressing oocytes to the JAK2 inhibitor AG490 does not appreciably affect BGT1 activity within the first 3 h, an observation pointing to indirect effects of JAK2 on carrier function. JAK2 may regulate carrier activity by influencing protein abundance rather than direct inactivation of the carrier. Alternatively, the inhibitor may gain access to the carrier only with delay.

The effect of JAK2 on BGT1 is observed in the presence of actinomycin, which disrupts gene transcription. Thus, the observed effects of JAK2 are not explained by effects on gene transcription.

As JAK2 activity is activated by hypertonicity [18,19], the kinase presumably contributes to the up-regulation of BGT1 activity during osmotic cell shrinkage. Osmotic cell shrinkage is well known to up-regulate the activity of osmolyte transporters [53–55]. It must

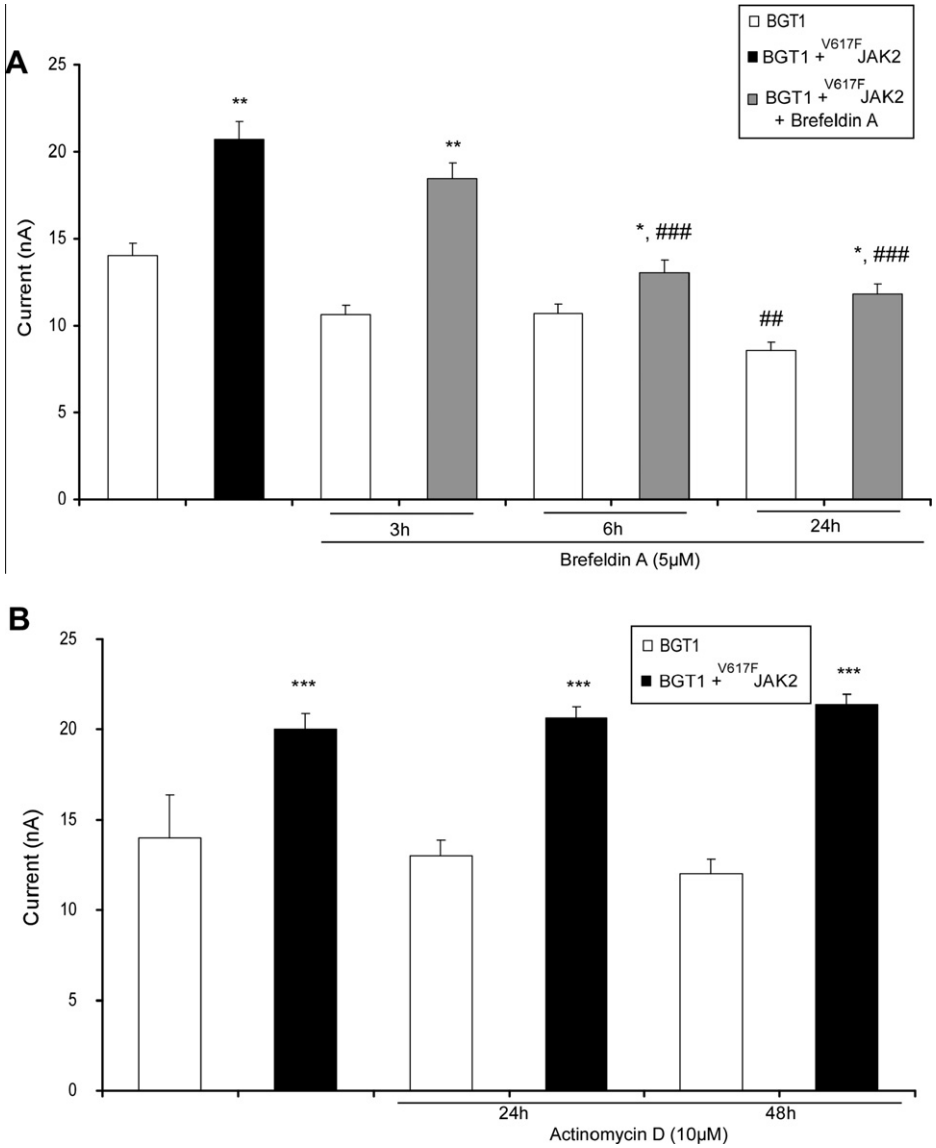

Fig. 4. Effects of brefeldin A and actinomycin D on BGT1 and BGT1 + ^{V617F}JAK2 expressing *Xenopus* oocytes. (A) Arithmetic means ± SEM (n = 15) of GABA (1 mM)-induced current (I_{BGT}) in *Xenopus* oocytes injected with cRNA encoding BGT1 with ^{V617F}JAK2 and exposed to 5 μM brefeldin A for the indicated time periods in the absence (black bars) and presence (light gray bars) of Brefeldin A (5). *,** Indicates statistically significant ($p < 0.05$, $p < 0.01$) from the absence of JAK2; $^{\#\#}$, $^{\#\#\#}$ indicates statistically significant difference ($p < 0.01$, $p < 0.001$) from the absence of brefeldin A. (B) Arithmetic means ± SEM (n = 7) of GABA (1 mM)-induced current (I_{BGT}) in *Xenopus* oocytes injected with cRNA encoding BGT1 without (white bars) and with JAK2 (black bars) in the presence and absence of 10 μM actinomycin D 1–2 days prior to the measurement. *** Indicates statistically significant different ($p < 0.001$) from the absence of ^{V617F}JAK2.

be kept in mind that the osmolyte carriers are up-regulated by stimulation of gene expression [53], which apparently does not play a major role in the present observations. JAK2 has previously been shown to enhance the activity of cell volume regulatory Na^+/H^+ exchanger (NHE) [56], which similarly serves to increase cell volume following osmotic cell shrinkage [57].

In conclusion, the present paper presents evidence, for the first time, that JAK2 up-regulates the GABA transporter BGT1 (SLC6A12). The observed JAK2 sensitive regulation of BGT1 could well contribute to cellular osmoregulation.

Acknowledgments

The authors acknowledge the meticulous preparation of the manuscript by Lejla Subasic and Sari Rübe and technical support by Elfriede Faber. This study was supported by the Deutsche Forschungsgemeinschaft.

References

[1] E.N. Noon-Song, C.M. Ahmed, R. Dabelic, J. Canton, H.M. Johnson, Controlling nuclear JAKs and STATs for specific gene activation by IFNgamma, Biochem. Biophys. Res. Commun. 410 (2011) 648–653.
[2] J.L. Spivak, Narrative review: thrombocytosis, polycythemia vera, and JAK2 mutations: the phenotypic mimicry of chronic myeloproliferation, Ann. Intern. Med. 152 (2010) 300–306.
[3] A.F. Lopez, T.R. Hercus, P. Ekert, D.R. Littler, M. Guthridge, D. Thomas, H.S. Ramshaw, F. Stomski, M. Perugini, R. D'Andrea, M. Grimbaldeston, M.W. Parker, Molecular basis of cytokine receptor activation, IUBMB Life 62 (2010) 509–518.
[4] D.L. Morris, L. Rui, Recent advances in understanding leptin signaling and leptin resistance, Am. J. Physiol. Endocrinol. Metab. 297 (2009) E1247–E1259.
[5] N. Yang, J. Jiang, L. Deng, M.J. Waters, X. Wang, S.J. Frank, Growth hormone receptor targeting to lipid rafts requires extracellular subdomain 2, Biochem. Biophys. Res. Commun. 391 (2010) 414–418.
[6] A.J. Brooks, M.J. Waters, The growth hormone receptor: mechanism of activation and clinical implications, Nat. Rev. Endocrinol. 6 (2010) 515–525.
[7] F.P. Santos, S. Verstovsek, JAK2 inhibitors: what's the true therapeutic potential?, Blood Rev 25 (2011) 53–63.

[8] A. Pardanani, A.M. Vannucchi, F. Passamonti, F. Cervantes, T. Barbui, A. Tefferi, JAK inhibitor therapy for myelofibrosis: critical assessment of value and limitations, Leukemia 25 (2011) 218–225.
[9] R. Baskin, A. Majumder, P.P. Sayeski, The recent medicinal chemistry development of Jak2 tyrosine kinase small molecule inhibitors, Curr. Med. Chem. 17 (2010) 4551–4558.
[10] K. Ho, F. Valdez, R. Garcia, C.A. Tirado, JAK2 translocations in hematological malignancies: review of the literature, J. Assoc. Genet. Technol. 36 (2010) 107–109.
[11] S.T. Oh, J. Gotlib, JAK2 V617F and beyond: role of genetics and aberrant signaling in the pathogenesis of myeloproliferative neoplasms, Expert. Rev. Hematol. 3 (2010) 323–337.
[12] A. Tefferi, Novel mutations and their functional and clinical relevance in myeloproliferative neoplasms: JAK2, MPL, TET2, ASXL1, CBL, IDH and IKZF1, Leukemia 24 (2010) 1128–1138.
[13] X.L. Shen, W. Wei, H.L. Xu, M.X. Zhang, X.Q. Qin, W.Z. Shi, Z.P. Jiang, Y.J. Chen, F.P. Chen, JAK2V617F/STAT5 signaling pathway promotes cell proliferation through activation of pituitary tumor transforming gene 1 expression, Biochem. Biophys. Res. Commun. 398 (2010) 707–712.
[14] S. Venkitachalam, F.Y. Chueh, C.L. Yu, Nuclear localization of lymphocyte-specific protein tyrosine kinase (Lck) and its role in regulating LIM domain only 2 (Lmo2) gene, Biochem. Biophys. Res. Commun. 417 (2012) 1058–1062.
[15] X. Yao, P. Balamurugan, A. Arvey, C. Leslie, L. Zhang, Heme controls the regulation of protein tyrosine kinases Jak2 and Src, Biochem. Biophys. Res. Commun. 403 (2010) 30–35.
[16] R.A. Mahfouz, R. Hoteit, Z. Salem, A. Bazarbachi, A. Mugharbel, F. Farhat, A. Ziyadeh, A. Ibrahim, A. Taher, JAK2 V617F gene mutation in the laboratory work-up of myeloproliferative disorders: experience of a major referral center in Lebanon, Genet. Test. Mol. Biomarkers 15 (2011) 263–265.
[17] M. Kurdi, G.W. Booz, JAK redux: a second look at the regulation and role of JAKs in the heart, Am. J. Physiol. Heart Circ. Physiol. 297 (2009) H1545–H1556.
[18] M.N. Garnovskaya, Y.V. Mukhin, T.M. Vlasova, J.R. Raymond, Hypertonicity activates Na^+/H^+ exchange through Janus kinase 2 and calmodulin, J. Biol. Chem. 278 (2003) 16908–16915.
[19] P. Gatsios, L. Terstegen, F. Schliess, D. Haussinger, I.M. Kerr, P.C. Heinrich, L. Graeve, Activation of the Janus kinase/signal transducer and activator of transcription pathway by osmotic shock, J. Biol. Chem. 273 (1998) 22962–22968.
[20] J.S. Handler, H.M. Kwon, Regulation of renal cell organic osmolyte transport by tonicity, Am. J. Physiol. 265 (1993) C1449–C1455.
[21] S.A. Kempson, M.H. Montrose, Osmotic regulation of renal betaine transport: transcription and beyond, Pflugers Arch. 449 (2004) 227–234.
[22] D.L. Christie, Functional insights into the creatine transporter, Subcell. Biochem. 46 (2007) 99–118.
[23] M. Takenaka, S.M. Bagnasco, A.S. Preston, S. Uchida, A. Yamauchi, H.M. Kwon, J.S. Handler, The canine betaine gamma-amino-n-butyric acid transporter gene: diverse mRNA isoforms are regulated by hypertonicity and are expressed in a tissue-specific manner, Proc. Natl. Acad. Sci. USA 92 (1995) 1072–1076.
[24] S. Uchida, H.M. Kwon, A. Yamauchi, A.S. Preston, F. Marumo, J.S. Handler, Molecular cloning of the cDNA for an MDCK cell Na(+)- and Cl(−)-dependent taurine transporter that is regulated by hypertonicity, Proc. Natl. Acad. Sci. USA 89 (1992) 8230–8234.
[25] T. Peters-Regehr, J.G. Bode, R. Kubitz, D. Haussinger, Organic osmolyte transport in quiescent and activated rat hepatic stellate cells (Ito cells), Hepatology 29 (1999) 173–180.
[26] C. Weik, U. Warskulat, J. Bode, T. Peters-Regehr, D. Haussinger, Compatible organic osmolytes in rat liver sinusoidal endothelial cells, Hepatology 27 (1998) 569–575.
[27] Y. Zhou, S. Holmseth, R. Hua, A.C. Lehre, A.M. Olofsson, I. Poblete-Naredo, S.A. Kempson, N.C. Danbolt, The betaine-GABA transporter (BGT1, slc6a12) is predominantly expressed in the liver and at lower levels in the kidneys and at the brain surface, Am. J. Physiol. Renal Physiol. 302 (2012) F316–F328.
[28] S. Zaidi, G. Gallos, P.D. Yim, D. Xu, J.R. Sonett, R.A. Panettieri Jr., W. Gerthoffer, C.W. Emala, Functional expression of gamma-amino butyric acid transporter 2 in human and guinea pig airway epithelium and smooth muscle, Am. J. Respir. Cell Mol. Biol. 45 (2011) 332–339.
[29] K.K. Madsen, H.S. White, A. Schousboe, Neuronal and non-neuronal GABA transporters as targets for antiepileptic drugs, Pharmacol. Ther. 125 (2010) 394–401.
[30] S.A. Kempson, Differential activation of system A and betaine/GABA transport in MDCK cell membranes by hypertonic stress, Biochim. Biophys. Acta 1372 (1998) 117–123.
[31] H. Miyakawa, J.S. Rim, J.S. Handler, H.M. Kwon, Identification of the second tonicity-responsive enhancer for the betaine transporter (BGT1) gene, Biochim. Biophys. Acta 1446 (1999) 359–364.
[32] V. Nadkarni, K.H. Gabbay, K.M. Bohren, D. Sheikh-Hamad, Osmotic response element enhancer activity. Regulation through p38 kinase and mitogen-activated extracellular signal-regulated kinase kinase, J. Biol. Chem. 274 (1999) 20185–20190.
[33] S.A. Kempson, J.M. Edwards, A. Osborn, M. Sturek, Acute inhibition of the betaine transporter by ATP and adenosine in renal MDCK cells, Am. J. Physiol. Renal Physiol. 295 (2008) F108–F117.
[34] S.A. Kempson, J.M. Edwards, M. Sturek, Inhibition of the renal betaine transporter by calcium ions, Am. J. Physiol. Renal Physiol. 291 (2006) F305–F313.
[35] S. Massari, C. Vanoni, R. Longhi, P. Rosa, G. Pietrini, Protein kinase C-mediated phosphorylation of the BGT1 epithelial gamma-aminobutyric acid transporter regulates its association with LIN7 PDZ proteins: a post-translational mechanism regulating transporter surface density, J. Biol. Chem. 280 (2005) 7388–7397.
[36] G.W. Moeckel, L. Zhang, A.B. Fogo, C.M. Hao, A. Pozzi, M.D. Breyer, COX2 activity promotes organic osmolyte accumulation and adaptation of renal medullary interstitial cells to hypertonic stress, J. Biol. Chem. 278 (2003) 19352–19357.
[37] W. Neuhofer, D. Steinert, M.L. Fraek, F.X. Beck, Prostaglandin E2 stimulates expression of osmoprotective genes in MDCK cells and promotes survival under hypertonic conditions, J. Physiol. 583 (2007) 287–297.
[38] J.C. Basham, A. Chabrerie, S.A. Kempson, Hypertonic activation of the renal betaine/GABA transporter is microtubule dependent, Kidney Int. 59 (2001) 2182–2191.
[39] J.L. Bricker, S. Chu, S.A. Kempson, Disruption of F-actin stimulates hypertonic activation of the BGT1 transporter in MDCK cells, Am. J. Physiol. Renal Physiol. 284 (2003) F930–F937.
[40] R.R. Alfieri, A. Cavazzoni, P.G. Petronini, M.A. Bonelli, A.E. Caccamo, A.F. Borghetti, K.P. Wheeler, Compatible osmolytes modulate the response of porcine endothelial cells to hypertonicity and protect them from apoptosis, J. Physiol. 540 (2002) 499–508.
[41] I. Matskevitch, C.A. Wagner, C. Stegen, S. Broer, B. Noll, T. Risler, H.M. Kwon, J.S. Handler, S. Waldegger, A.E. Busch, F. Lang, Functional characterization of the Betaine/gamma-aminobutyric acid transporter BGT-1 expressed in *Xenopus* oocytes, J. Biol. Chem. 274 (1999) 16709–16716.
[42] J. Feng, B.A. Witthuhn, T. Matsuda, F. Kohlhuber, I.M. Kerr, J.N. Ihle, Activation of Jak2 catalytic activity requires phosphorylation of Y1007 in the kinase activation loop, Mol. Cell Biol. 17 (1997) 2497–2501.
[43] M.R. Mohamed, I. Alesutan, M. Foller, M. Sopjani, A. Bress, M. Baur, R.H. Salama, M.S. Bakr, M.A. Mohamed, N. Blin, F. Lang, M. Pfister, Functional analysis of a novel I71N mutation in the GJB2 gene among Southern Egyptians causing autosomal recessive hearing loss, Cell Physiol. Biochem. 26 (2010) 959–966.
[44] K. Eckey, N. Strutz-Seebohm, G. Katz, G. Fuhrmann, U. Henrion, L. Pott, W.A. Linke, M. Arad, F. Lang, G. Seebohm, Modulation of human ether a gogo related channels by CASQ2 contributes to etiology of catecholaminergic polymorphic ventricular tachycardia (CPVT0, Cell Physiol. Biochem. 26 (2010) 503–512.
[45] C. Bohmer, M. Sopjani, F. Klaus, R. Lindner, J. Laufer, S. Jeyaraj, F. Lang, M. Palmada, The serum and glucocorticoid inducible kinases SGK1-3 stimulate the neutral amino acid transporter SLC6A19, Cell Physiol. Biochem. 25 (2010) 723–732.
[46] R. Rexhepaj, M. Dermaku-Sopjani, E.M. Gehring, M. Sopjani, D.S. Kempe, M. Foller, F. Lang, Stimulation of electrogenic glucose transport by glycogen synthase kinase 3, Cell Physiol. Biochem. 26 (2010) 641–646.
[47] M. Dermaku-Sopjani, M. Sopjani, A. Saxena, M. Shojaiefard, E. Bogatikov, I. Alesutan, M. Eichenmuller, F. Lang, Downregulation of NaPi-IIa and NaPi-IIb Na-coupled phosphate transporters by coexpression of Klotho, Cell Physiol. Biochem. 28 (2011) 251–258.
[48] Z. Hosseinzadeh, S.K. Bhavsar, M. Sopjani, I. Alesutan, A. Saxena, M. Dermaku-Sopjani, F. Lang, Regulation of the glutamate transporters by JAK2, Cell Physiol. Biochem. 28 (2011) 693–702.
[49] T.W. Gong, D.J. Meyer, J. Liao, C.L. Hodge, G.S. Campbell, X. Wang, N. Billestrup, C. Carter-Su, J. Schwartz, Regulation of glucose transport and c-fos and egr-1 expression in cells with mutated or endogenous growth hormone receptors, Endocrinology 139 (1998) 1863–1871.
[50] I. Yokota, H. Hayashi, J. Matsuda, T. Saijo, E. Naito, M. Ito, Y. Ebina, Y. Kuroda, Effect of growth hormone on the translocation of GLUT4 and its relation to insulin-like and anti-insulin action, Biochim. Biophys. Acta 1404 (1998) 451–456.
[51] Z. Hosseinzadeh, S.K. Bhavsar, M. Shojaiefard, A. Saxena, K. Merches, M. Sopjani, I. Alesustan, F. Lang, Stimulation of the glucose carrier SGLT1 by JAK2, Biochem. Biophys. Res. Commun. 408 (2011) 208–213.
[52] S.K. Bhavsar, Z. Hosseinzadeh, K. Merches, S. Gu, S. Broer, F. Lang, Stimulation of the amino acid transporter SLC6A19 by JAK2, Biochem. Biophys. Res. Commun. 414 (2011) 456–461.
[53] J.S. Handler, H.M. Kwon, Regulation of the myo-inositol and betaine cotransporters by tonicity, Kidney Int. 49 (1996) 1682–1683.
[54] E.K. Hoffmann, S.F. Pedersen, Sensors and signal transduction pathways in vertebrate cell volume regulation, Contrib. Nephrol. 152 (2006) 54–104.
[55] H. Pasantes-Morales, S. Cruz-Rangel, Brain volume regulation: osmolytes and aquaporin perspectives, Neuroscience 168 (2010) 871–884.
[56] S.D. Coaxum, M.N. Garnovskaya, M. Gooz, A. Baldys, J.R. Raymond, Epidermal growth factor activates Na(+/)H(+) exchanger in podocytes through a mechanism that involves Janus kinase and calmodulin, Biochim. Biophys. Acta 1793 (2009) 1174–1181.
[57] F. Lang, G.L. Busch, M. Ritter, H. Volkl, S. Waldegger, E. Gulbins, D. Haussinger, Functional significance of cell volume regulatory mechanisms, Physiol. Rev. 78 (1998) 247–306.

Biochemical and Biophysical Research Communications 420 (2012) 178–182

Contents lists available at SciVerse ScienceDirect

Biochemical and Biophysical Research Communications

journal homepage: www.elsevier.com/locate/ybbrc

Involvement of tristetraprolin in transcriptional activation of hepatic 3-hydroxy-3-methylglutaryl coenzyme A reductase by insulin

Gene C. Ness *, Jeffrey L. Edelman, Patricia A. Brooks

Department of Molecular Medicine, College of Medicine, University of South Florida, Tampa, FL 33612, USA

ARTICLE INFO

Article history:
Received 14 February 2012
Available online 3 March 2012

Keywords:
AU-rich RNA binding proteins
HMG-CoA reductase transcription
siRNA
Insulin
In vivo electroporation

ABSTRACT

Several AU-rich RNA binding element (ARE) proteins were investigated for their possible effects on transcription of hepatic 3-hydroxy-3-methyglutaryl coenzyme A reductase (HMGR) in normal rats. Using *in vivo* electroporation, four different siRNAs to each ARE protein were introduced together with HMGR promoter (−325 to +20) luciferase construct and compared to saline controls. All four siRNAs to tristetraprolin (TTP) completely eliminated transcription from the HMGR promoter construct. Since insulin acts to rapidly increase hepatic HMGR transcription, the effect of TTP siRNA on induction by insulin was tested. The 3-fold stimulation by insulin was eliminated by this treatment. In comparison, siRNA to AU RNA binding protein/enoyl coenzyme A hydratase (AUH) had no effect. These findings indicate a role for TTP in the insulin-mediated activation of hepatic HMGR transcription.

1. Introduction

3-Hydroxy-3-methylglutaryl coenzyme A reductase (HMGR), the enzyme that catalyzes the rate-limiting step in cholesterol biosynthesis, responds rapidly to various stimuli. In rats subjected to controlled light and dark periods, hepatic HMGR activity and immunoreactive protein levels increase rapidly upon entering the dark period when the animals start eating [1]. Administration of insulin to diabetic rats increases hepatic HMGR activity, immunoreactive protein, mRNA levels and the rate of transcription within 1 h [2–4]. Also HMGR activity is increased 3-fold within 1 h after sub-culturing L1210 tumor cells[1], reaching a maximum of nearly 20-fold after 10 h. The half-life of hepatic HMGR protein is 2.5 h [5] while the half-life of hepatic mRNA is about 3 h in normal rats [6]. Thus, HMGR can be regarded as a rapid response gene.

Rapid response genes typically have AU-rich sequences in the 3′-untranslated regions (3′UTR) of their mRNAs. These mofits consist of AUUUA pentamers and UUAUUUAUU nomers [7]. The 3′UTR of HMGR has several AUUUA sequences and a UUAUUUAUU sequence located at 3122–3130 of the rat sequence [8]. These AU-rich sequences are generally thought to function as targets for the binding of AU-rich binding proteins (ARE-BPs) that promote degradation of these short-lived mRNAs by removal of the poly-A tail [9]. However, some ARE-BPs such as HUR act to stabilize mRNAs [10]. T-cell inhibitor of apoptosis-1 (TIA-1) and TIA-1 related protein (TIAR) act as translational repressors [11]. Although tristetraprolin (TTP) has been widely shown to be involved in mRNA degradation [7], recent reports have demonstrated that this CCCH zinc finger-containing protein acts to inhibit NF-kappaB-dependent transcription [12,13].

Since hepatic HMGR is a rapid response gene, we sought to determine whether any of these ARE-BPs play a role in modulating its expression. We carried out *in vivo* electroporation studies with siRNAs to several ARE-BPs to determine whether any of these proteins affect transcriptional activation of hepatic HMGR. Surprisingly, all four siRNAs to TTP abolished transcription of hepatic HMGR.

2. Materials and methods

2.1. Experimental animals

Male Sprague–Dawley rats weighing 125–150 g were purchased from Harlan (Madison, WI). The rats were housed in a reversed lighting cycle room (12 h dark/12 h light) and fed Harland Teklad 22/5 rodent chow. The animals were killed at the third hr of the dark period when hepatic HMGR expression is at its maximum.

Abbreviations: ARE, AU-rich RNA binding element; ARE-BP, AU-rich RNA binding element binding protein; TTP, tristetraprolin; HMGR, 3-hydroxy-3-methylglutaryl coenzyme A reductase; AUH, AU RNA binding protein/enoyl coenzyme A hydratase; HUR, human antigen R; TIA-1, T-cell inhibitor of apoptosis-1; TIAR, tein; AUF1, A + U-rich element-binding factor 1; KSRP, KH-type splicing regulatory protein; TNF-α, tumor necrosis factor α.

* Corresponding author. Address: University of South Florida, College of Medicine, Department of Molecular Medicine, 12901 Bruce B. Downs Blvd. Box 07, Tampa, FL 33612, USA. Fax: +1 813 974 5798.
E-mail address: gness@hsc.usf.edu (G.C. Ness).

[1] G.C. Ness and M. Watkins, unpublished observations.

0006-291X/$ - see front matter © 2012 Elsevier Inc. All rights reserved.
doi:10.1016/j.bbrc.2012.02.138

Diabetes was induced in rats by a single subcutaneous injection of streptozotocin (Sigma), 65 mg/kg in 0.1 M sodium citrate, pH 5.5. Diabetes was confirmed by the presence of urinary glucose detected with Clinistix (Bayer). Some of the diabetic rats were injected subcutaneously with 3.0 units/100 g of recombinant human insulin, Novolin 70/30 (Novo Nordisk) 2 h before killing the animals. All procedures were carried out according to protocol 3571 approved by the University of South Florida Institutional Animal Care and Use Committee.

2.2. Materials

Four different (A–D) siRNAs each to TTP (cat# LQ-098940-01-0010), HuR (cat# LQ-080370-00-0010), AUF1 (cat# LQ-099225-01-0010), AUH (cat# LQ-090133-01-0010), TIA1 (cat# LQ-095224-01-0010), KSRP (cat# LQ-093278-01-0010) were purchased from Dharmacon. Polyclonal antibodies to TTP (#ab33058), and AUF1 (#ab61193) were purchased from Abcam. A polyclonal antibody to AUH (#sc-82518) was purchased from Santa Cruz Biotechnology. A mouse monoclonal antibody to HuR (sc-5261) was purchased from Santa Cruz Biotechnology. SuperSignal West Pico Chemiluniscent Substrate was purchased from Pierce.

2.3. In vivo electroporation

Ten micro grams of −325/+70 HMGR promoter in pGL3-Basic [4] with and without 5 μg of siRNAs to several ARE-BPs was introduced in duplicate in the left, right and medial liver lobes of the rats. pHRL-CMV Renilla vector was co-electroporated at a 1–2000 dilution to control for electroporation efficiency. The electroporation procedure and parameters used were as previously described [14,15].

2.4. Luciferase assays

Twenty-four hour after *in vivo* electroporation, the electroporated sites in the liver lobes were removed using a 5 mm cork-borer. The liver piece, approximately 0.1 g, was homogenized in passive lysis buffer (Promega) and processed for luciferase activity using the dual luciferase assay kit from Promega [15]. Luciferase activity was calculated as the ratio of firefly (reporter) to *Renilla* (transfection control).

2.5. Western blotting analysis

Liver nuclear extracts were prepared as previously described [16]. Protein concentrations were determined using the Bradford assay. Twenty micro grams of protein in 20 μl of 0.25 M sucrose were mixed with 20 μl of Laemmli sample buffer containing 2% SDS and 5% 2-mercaptoethanol and denatured at 94 °C. The denatured samples were subjected to electrophoresis on pre-cast 4–20% SDS PAGE gels. Dual color precision plus protein standard markers were applied to one lane. After electrophoresis for 1 h the proteins were transferred to nitrocellulose membranes. Detection of TTP and AUF1 was done with 1–1000 dilutions of the primary rabbit antibodies and 1–10,000 dilutions of goat secondary antibodies. Detection of HuR was preformed using a 1–100 dilution of the primary mouse monoclonal antibody and a 1–10,000 dilution of the goat secondary antibody. Immunoreactive proteins were visualized using SuperSignal West Pico Chemiluniscent substrate and exposure times ranging from 2 s to 5 min. Quantitation was performed with a Bio-Rad Quantity One 4.6.6 densiometer equipped with a ChemiDoc XRS scanner.

3. Results

3.1. Effects of ARE-BP siRNAS on hepatic HMGR promoter activity

Since it has been established that insulin acts to rapidly increase expression of hepatic HMGR by increasing the rate of transcription, we embarked on a series of experiments using siRNAs to several ARE-BPs to see if they would act to decrease HMGR promoter activity. To test this in a physiological setting, HMGR promoter constructs with and without the siRNAs were introduced into liver lobes of normal rats by *in vivo* electroporation.

All four of the siRNAs to TTP completely abolished HMGR promoter activity (Fig. 1). Two of the four siRNAS to HuR and TIA1 significantly reduced HMGR promoter activity; but the other two had no effect. siRNA B to KH-type splicing regulatory protein(KSRP) significantly reduced promoter activity but the other three siRNAs did not. siRNAs to AUH had no effect while two siRNAs to AUF1 appeared to stimulate promoter activity.

3.2. Effects of diabetes and insulin treatment on hepatic ARE-BP protein levels

Since hepatic HMGR is rapidly induced by insulin [4] and ARE-BP proteins are known to participate in modulating the expression of "immediate-early response" genes [17,18], we sought to determine whether the levels of any of these proteins are quickly changed in response to insulin. Western blotting analysis of liver nuclear extracts was performed. Administration of insulin markedly increased TTP levels (Fig. 2). This is in agreement with a previous report showing that insulin treatment dramatically increased TTP mRNA levels within 10 min [19]. AUF1 protein levels were increased slightly but not significantly by insulin while HUR levels were not affected (Fig. 2). AUH could not be detected.

3.3. Effect of TTP siRNA on the rapid activation of hepatic HMGR promoter activity

Since siRNAs to TTP abolished HMGR promoter activity in livers of normal rats, we wished to determine their effect on the rapid, near 3-fold increase in HMGR transcription caused by insulin treatment of diabetic rats [4]. The HMGR promoter luciferase construct was introduced by *in vivo* electroporation in duplicate into the left, right and medial lobes of diabetic rats. TTP siRNA was co-electroporated into the left lobe while AUH siRNA was co-electroporated into the right lobe. The medial lobe had only the HMGR construct. Twenty-two hours later, the rats were given 3 units per 100 g of insulin. Two hours later, the rats were killed and the electroporated areas were punched out and analysized for luciferase activity. Introduction of TTP siRNA decreased HMGR promoter activity to about 38% (Fig. 3A), which agrees with the magnitude of the increase in transcription caused by insulin in these animals (Fig. 3B). In contrast, siRNA to AUH had no effect (Fig. 3A). In parallel experiments, siRNA to AUF1 also had no effect while HUR D siRNA caused a 50% reduction, which was not statistically significant, and HUR A siRNA had no effect (Fig. 3A). However, insulin did not alter levels of HUR in liver nuclear extracts (Fig. 2).

4. Discussion

The *in vivo* experiments presented in this report show that siRNAs to TTP dramatically reduce hepatic HMGR transcription as well as the insulin promoted increase in HMGR transcription. In the original report describing TTP, it was noted that other proteins with proline-rich regions are involved in transcriptional activation [19]. The finding that insulin induces TTP mRNA within 10 min led

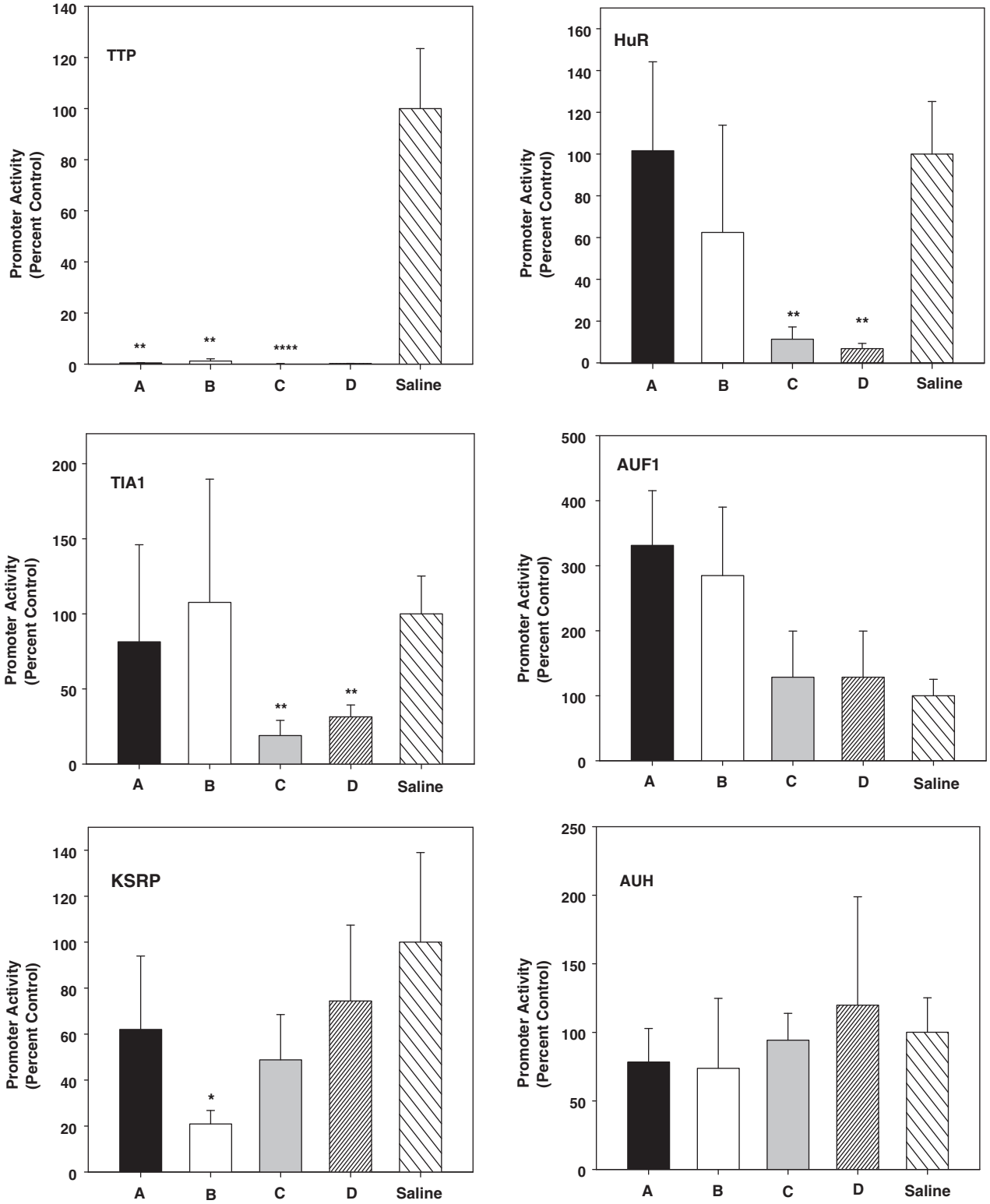

Fig. 1. Effects of siRNAs to several AU-rich RNA binding proteins on transcription of HMGR. Normal rats were transfected with HMGR promoter luciferase with siRNAs to ARE-BPs or saline. Four siRNAs were used for each ARE-BP. Typically, two siRNAs in duplicate HMGR promoter were introduced by *in vivo* electroporation into the left and right liver lobes while HMGR promoter with saline was introduced into the medial lobe. The data are expressed as means ± SD for at least four duplicates of siRNAs, A–D for each ARE-BP. Significant differences are $^{**}p < 0.01$, $^{*}p < 0.05$.

to speculation that TTP might be involved in stimulating transcription of genes by insulin.

Subsequent to this report [19], numerous studies have appeared showing that TTP is an RNA-binding protein that recognizes AU-rich elements found in mRNAs with short half-lives. [20–23,7,24]. The binding of TTP to these mRNAs causes rapid degradation. TTP−/− mice develop an inflammatory syndrome [20]. The macrophages from these mice overexpress TNFα due to prolonged mRNA half-live. TTP was shown to specifically bind to the ARE of TNFα and cause its rapid degradation [21]. A recent genome-wide analysis

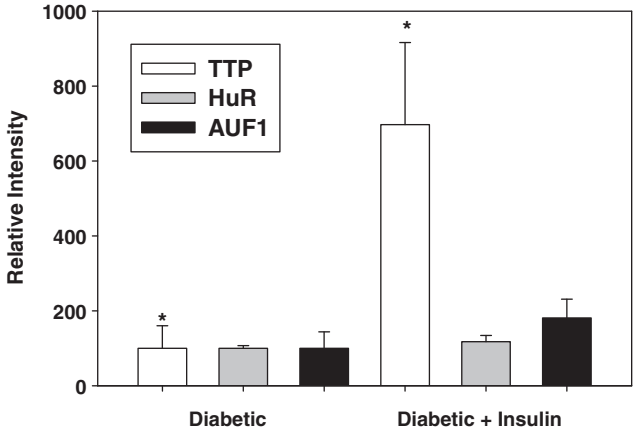

Fig. 2. Effect of insulin treatment on protein levels of AU-rich RNA binding proteins in liver nuclear extracts. Nuclear extracts were subjected to Western blotting analysis followed by densitometric analysis. The data are expressed as means ± SD for five animals in each group. Significant difference is denoted as $p < 0.05$.

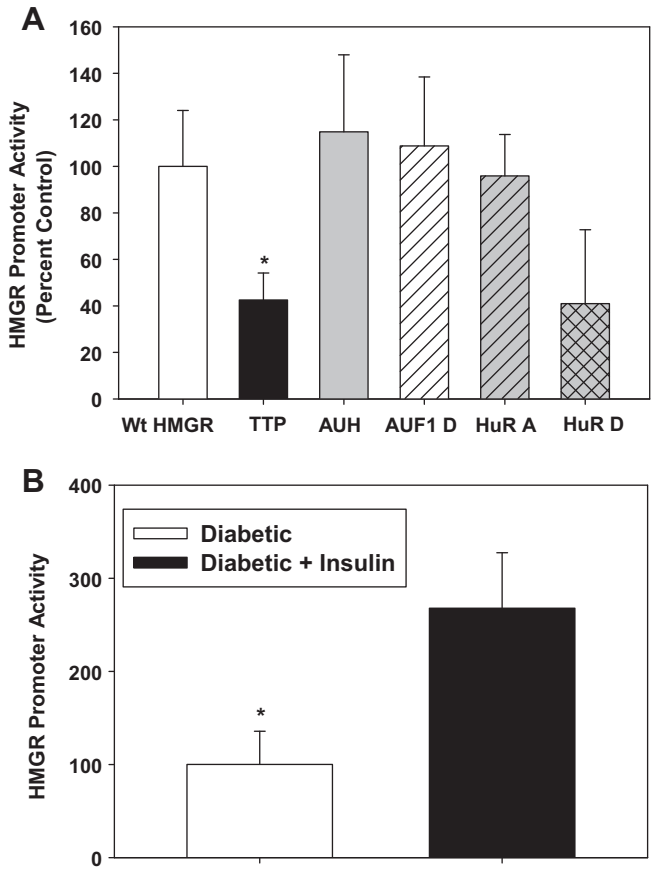

Fig. 3. Effects of siRNAs to AU-rich RNA binding proteins on the insulin-promoted increase in hepatic HMGR transcription. In A, experiments were performed as described in Fig. 1 except that the diabetic rats were injected with insulin at the time of surgery. The animals were killed two hrs later. The promoter activity is expressed relative to the luciferase activity observed in punches of HMGR promoter with saline (Wt HMGR). A pool of siRNAs A–D were used for TTP and AUH. HuR A and HuR D siRNAs were also evaluated. The data are expressed as means ± SD for at least four duplicates in each group. In B, the effect of insulin treatment of HMGR promoter (luciferase activity) activity is presented for at least five duplicate punches as means ± SD. Significant differences are denoted as $p < 0.05$.

found 250 mRNAs to be stabilized in TT−/− mouse embryonic fibroblasts [23].

Nevertheless the data reported in this communication indicate a role for TTP in transcriptional activation of hepatic HMGR by insulin. There are several possible ways by which TTP could be involved. It could directly bind the HMGR promoter. CTF/NF-1, a CCAAT box binding protein has a C-terminal region that is a transcriptional activation domain containing approximately 25% proline residues [25]. TTP has three repeats of Pro-Pro-Pro-Pro. TTP could also bind to a DNA binding protein to stimulate transcription of HMGR; perhaps in response to phosphorylation of TTP via insulin signaling. Another possibility might relate to the mRNA degrading activity of TTP. TTP could target an HMGR transcriptional repressor; leading to derepression.

Acknowledgments

This work was supported by a grant from The National Institutes of Diabetes and Digestive and kidney Diseases (R01DK075414) and does not necessarily represent the official views of the NIDDK or the National Institutes of Health.

References

[1] G.C. Ness, C.M. Chambers, The diurnal variation of hepatic HMG-CoA reductase activity is due to changes in the level of immunoreactive protein, Arch. Biochem. Biophys. 327 (1996) 41–44.
[2] G.C. Ness, L. Wiggins, Z. Zhao, Insulin increases hepatic 3-hydroxy-3-methylglutaryl coenzyme A reductase mRNA and immunoreactive protein levels in diabetic rats, Arch. Biochem. Biophys. 309 (1994) 193–194.
[3] G.C. Ness, Z. Zhao, L. Wiggins, Insulin and glucagon modulate hepatic 3-hydroxy-3-methylglutaryl-coenzyme A reductase activity by affecting immunoreactive protein levels, J. Biol. Chem. 269 (1994) 29168–29172.
[4] W.R. Lagor, E.D. de Groh, G.C. Ness, Diabetes alters the occupancy of the hepatic 3-hydroxy-3-methylglutaryl-CoA reductase promoter, J. Biol. Chem. 280 (2005) 36601–36608.
[5] R.K. Keller, Z. Zhao, C.M. Chambers, G.C. Ness, Farnesol is not the nonsterol regulator mediating degradation of HMG-CoA reductase in rat liver, Arch. Biochem. Biophys. 328 (1996) 324–330.
[6] W.S. Simonet, G.C. Ness, Transcriptional and posttranscriptional regulation of rat hepatic 3-hydroxy-3-methylglutaryl-coenzyme A reductase by thyroid hormones, J. Biol. Chem. 263 (1988) 12448–12453.
[7] G. Stoecklin, S.A. Tenenbaum, T. Mayo, S.V. Chittur, A.D. George, T.E. Baroni, P.J. Blackshear, P. Anderson, Genome-wide analysis identifies interleukin-10 mRNA as target of tristetraprolin, J. Biol. Chem. 283 (2008) 11689–11699.
[8] G.A. Reynolds, S.K. Basu, T.F. Osborne, D.J. Chin, G. Gil, M.S. Brown, J.L. Goldstein, HMG-CoA reductase: a negatively regulated gene with unusal promoter and 5′ untranslated regions, Cell 38 (1984) 275–285.
[9] E. Carballo, W.S. Lai, P.J. Blackshear, Feedback inhibition of macrophage tumor necrosis factor-alpha production by tristetraprolin, Science 281 (1998) 1001–1005.
[10] C-Y. A. Chen, N. Xu, A-B. Shyu, Highly selective actions of HuR in antagonizing AU-rich element-mediated mRNA destabilization, Mol. Cell. Biol. 22 (2002) 7268–7278.
[11] K. Masuda, B. Marasa, J.L. Martindale, M.K. Halushka, M. Gorospe, Tissue- and age-dependent expression of RNA-binding proteins that influence mRNA turnover and translation, Aging 1 (2009) 681–698.
[12] J. Liang, T. Lei, Y. Song, N. Yanes, Y. Qi, M. Fu, RNA-destabilizing factor tristetraprolin negatively regulates NF-kB signaling, J. Biol. Chem. 284 (2009) 29383–29390.
[13] Y.M. Schichl, U. Resch, R. Hofer-Warbinek, R. de Martin, Tristetraprolin impairs NF-kB/p65 nuclear translocation, J. Biol. Chem. 284 (2009) 29571–29581.
[14] W.R. Lagor, R. Heller, E.D. de Groh, G.C. Ness, Functional analysis of the hepatic HMG-CoA reductase promoter by *in vivo* electroporation, Exp. Biol. Med. 232 (2007) 353–361.
[15] L.R. Boone, M.I. Niesen, M. Jaroszeski, G.C. Ness, *In vivo* identification of promoter elements and transcription factors mediating activation of hepatic HMG-CoA reductase by T_3, Biochem. Biophys. Res. Commun. 385 (2009) 466–471.
[16] D. Lopez, J.F. Abisambra Socarras, M. Bedi, G.C. Ness, Activation of the hepatic LDL receptor promoter by thyroid hormone, Biochim. Biophys. Acta 1771 (2007) 1216–1225.
[17] S. Sanduja, F.F. Blanco, D.A. Dixon, The roles of TTP and BRF proteins in regulated mRNA decay, Wiley Interdiscip. Rev. RNA 2 (2010) 42–57.
[18] C.Y. Chen, A.B. Shyu, Selective degradation of early-response-gene mRNAs: functional analyses of sequence features of the AU-rich elements, Mol. Cell. Biol. 14 (1994) 8471–8482.
[19] W.S. Lai, D.J. Stumpo, P.J. Blackshear, Rapid insulin-stimulated accumulation of an mRNA encoding a proline-rich protein, J. Biol. Chem. 265 (1990) 16556–16563.
[20] G.A. Taylor, E. Carballo, D.M. Lee, W.S. Lai, M.J. Thompson, D.D. Patel, D.I. Schenkman, G.S. Gilkeson, H.E. Broxmeyer, B.F. Hayes, P.J. Blackshear, Immunity 4 (1996) 445–454.

[21] E. Carballo, W.S. Lai, P.J. Blackshear, Science 281 (1998) 1001–1005.
[22] W.S. Lai, E. Carballo, J.R. Strum, E.A. Kennington, R.S. Phillips, P.J. Blackshear, Evidence that tristetraprolin binds to AU-rich elements and promotes the deadenylation and destabilization of tumor necrosis factor alpha mRNA, Mol. Cell Biol. 19 (1999) 4311–4323.
[23] W.S. Lai, J.S. Parker, S.F. Grisson, D.J. Stumpo, P.J. Blackshear, Novel mRNA targets for tristetraprolin (TTP) identified by global analysis of stabilized transcripts in TTP-deficients fibroblasts, Mol. Cell Biol. 26 (2006) 9196–9208.
[24] R.L. Ogilvie, J.R. Sternjohn, B. Rattenbacher, I.A. Vlasova, D.A. Williams, H.H. Hau, P.J. Blackshear, P.R. Bohjanen, Tristetraprolin mediates interferon-gamma mRNA decay, J. Biol. Chem. 284 (2009) 11216–11223.
[25] N. Mermod, E.A. O'Neill, T.J. Kelly, R. Tjian, The proline-rich transcriptional activator of CTF/NF-1 is distinct from the replication and DNA binding domain, Cell 58 (1989) 741–753.

Biochemical and Biophysical Research Communications 420 (2012) 183–187

Contents lists available at SciVerse ScienceDirect

Biochemical and Biophysical Research Communications

journal homepage: www.elsevier.com/locate/ybbrc

Increases thermal stability and cellulose-binding capacity of *Cryptococcus* sp. S-2 lipase by fusion of cellulose binding domain derived from *Trichoderma reesei*

Jantaporn Thongekkaew [a,*], Hiroko Ikeda [b], Haruyuki Iefuji [b]

[a] Department of Biological Science, Faculty of Science, Ubon-Ratchathani University, Warinchumrab, Ubon-Ratchathani 34190, Thailand
[b] Application Research Division, National Research Institute of Brewing, 3-7-1 Kagamiyama, Higashi-Hiroshima 739-0046, Japan

ARTICLE INFO

Article history:
Received 14 February 2012
Available online 3 March 2012

Keywords:
Lipase
Cryptococcus sp. S-2
Cellulose binding domain
Thermal stability
Cellulose-binding capacity
Immobilization

ABSTRACT

To improve the thermal stability and cellulose-binding capacity of *Cryptococcus* sp. S-2 lipase (CSLP), the cellulose-binding domain originates from *Trichoderma reesei* cellobiohydrolase I was engineered into C-terminal region of the CSLP (CSLP-CBD). The CSLP and CSLP-CBD were successfully expressed in the *Pichia pastoris* using the strong methanol inducible alcohol oxidase 1 (AOX1) promoter and the secretion signal sequence from *Saccharomyces cerevisiae* (α factor). The recombinant CSLP and CSLP-CBD were secreted into culture medium and estimated by SDS–PAGE to be 22 and 27 kDa, respectively. The fusion enzyme was stable at 80 °C and retained more than 80% of its activity after 120-min incubation at this temperature. Our results also found that the fusion of fungal exoglucanase cellulose-binding domain to CSLP is responsible for cellulose-binding capacity. This attribute should make it an attractive applicant for enzyme immobilization.

1. Introduction

Lipases or triacylglycerol hydrolase (E.C. 3.1.1.3) catalyse the hydrolysis and synthesis of relatively long-chain acylglycerols with acyl chain lengths of >10 carbon atoms. In addition, they act on substrates at the lipid–water interface. This phenomenon is known as interfacial activation. By contrast, esterases hydrolyse only soluble esters of fatty acids with acyl chain lengths of ⩽10 carbon atoms [1]. Lipases are ubiquitous enzymes found in mammals, plants and microorganisms [2–4]. Microbial lipases are interesting because they are generally secreted following or concomitant with synthesis in the cytosol. The most prominent microbial function of extracellular lipases is lipid digestion for nutrient acquisition. These enzymes might help a microorganism to grow in carbohydrate-restricted environments or environments where lipids are the sole carbon source [5].

Microbial lipases have attracted particular attention owing to their high production potential, diverse properties, availability and relative ease of preparation. Important applications in biotechnology include chemistry of fats and oils (e.g. hydrolysis of fats and oils and synthesis of esters with surfactant properties), medical and therapeutic fields (e.g. reagents for plasmatic triglyceride analysis, supplements for patients with pancreatic insufficiencies, reagents for stereospecific synthesis of pharmacologically active products), in food technology (e.g. modification of flavor, acceleration of fermentation, improvement in preservation, formulation of oils) and in cleaning (e.g. washing powders) [6].

Cryptococcus sp. S-2 lipase (CSLP) is a low-molecular-mass (22 kDa) which exhibited maximum lipolytic activity at pH 7.0 and at 37 °C [7]. This enzyme could efficiently be used for the industrial production of biodiesel from vegetable oil and methanol [8] and it was also revealed to have an excellent bioplastic-digesting ability [9]. Unfortunately this enzyme rapidly loses its activity when incubated at temperatures over 50 °C [7]. In addition, the cost of free enzymes using can be an obstacle to the widespread use of enzymatic processing. This could be reduced by allowing the enzyme to react more efficiently; one way could be to anchor the enzyme to its substrate. For these reason, the fusion of cellulose binding domain (CBD) to lipase for allowing the enzyme to enhance thermal stability and to anchor the enzyme to its substrate by immobilization onto cellulose were investigated.

Cellulose binding domains (CBDs) are found in other plant cell wall hydrolases such as β-mannanase [10], acetyl xylan esterase [11] and arabino furanosidases [12] as well as xylanases [13] and cellulases [14]. The exact biological function of these domains *in vivo* is unknown; however in the previously reported, they have been shown to enhance either the catalytic activity of the enzyme by increasing the enzyme concentration around the substrate [15] or increasing the thermal stability of enzymes [16,17].

In this work, we have engineered the CBD from *Trichoderma reesei* cellobiohydrolase I into the C-terminal region of CSLP. Both recombinant native CSLP and fusion genes (CSLP-CBD) were expressed in *Pichia pastoris*. Thus, to improve the performance of the CSLP to resist inactivation at high temperatures and to reduce

* Corresponding author. Fax: +66 45 288 380.
E-mail address: jantaporn_25@yahoo.com (J. Thongekkaew).

0006-291X/$ - see front matter © 2012 Elsevier Inc. All rights reserved.
doi:10.1016/j.bbrc.2012.02.139

the enzyme addition by investigation of cellulose-binding capacity for the fusion enzyme has been the goal of this work.

2. Materials and methods

2.1. Strains and plasmids

The plasmid pPIC9 which contains CSLP was obtained from the National Research Institute of Brewing; Japan was used as the lipase cDNA source. pPICZαA vector served as the yeast expression vector. *Escherichia coli* strain DH5α (TAKARA BIO INC, Japan) was employed as the host of plasmid pPICZαA vector. *Pichia pastoris* strain X-33 (Invitrogen®, USA) served as the host strain for the transformation.

2.2. Construction and transformation of the recombinant plasmid

The *E. coli/P. pastoris* shuttle vector, pPICZαA, was used to achieve secreted expression of lipases. The plasmid pPIC9 which contains CSLP was used as a template for polymerase chain reaction (PCR) amplification using the primers fCSLPXhoI (5′TCTCTCGAG**AAGAGAGCCACGTCCAGCGCTTGTCCGCAG**TAC) and CSLPXhoR (5′AACTCGAGTTAGGCCGACCCGCCAAGCTTGTT**G**). This gene was introduced an *Xho*I sites at the 5′-end and the 3′-end of the CSLP gene; letters in bold indicate the CSLP coding sequence and *Xho*I sites are underlined. The PCR product was digested with *Xho*I and ligated to the pPICZαA which digested with the same restriction enzymes. This resulted in the expression vector pPICZαA/CSLP (Fig. S1A).

For the pPICZαA/CSLP-CBD vector construction (Fig. S1B) the CBD was taken from *Trichoderma reesei* cellobiohydrolase I by polymerase chain reaction (PCR) amplification using the primers fCSLPHinCBD (5′AAGCTT**GGCGGGTCGGCCAGCGGCGGCAACCCTCCCGGCGGAAA**) and CBDXhoR (5′AACTCGAG**TTACAGGCACTGAGAGTAG**). This gene was introduced a *Hind*III site at the 5′-end and an *Xho*I -site at the 3′-end of the CBD gene; restriction sites are underlined and the letters in bold indicate the cellulose binding domain coding sequence. The PCR product was digested with *Hind*III and *Xho*I and ligated to pPICZα/CSLP which digested with the same restriction enzymes. The constructed plasmids, pPICZαA/CSLP and pPICZαA/CSLP-CBD, were transformed into *E. coli* DH5α and transformants were selected on Luria–Bertani agar containing 25 mg mL^{-1} zeocin. The selection was checked by restriction analysis and sequencing. For *P. pastoris* integration, about 10 mg of recombinant plasmid was linearized with *Sac*I, and transformed in *P. pastoris* by electroporation with a Bio-Rad Gene Pulser (Bio-Rad®, USA) following the instruction of the manufacturer. The transformants were selected at 30 °C on the YPD containing 100 $mgmL^{-1}$ zeocin agar plates. The integration of the CSLP and CSLP-CBD gene into the genome of *P. pastoris* was confirmed by PCR. Positive clones yielded an approximately 660 and 860-bp DNA product which was the predicted size of *CSLP* and *CSLP-CBD*, respectively.

2.3. Expression of recombinant lipase in P. pastoris

A single colony of recombinant *P. pastoris* X-33 carrying pPICZαA/CSLP or pPICZαA/CSLP-CBD from YPD containing 100 mg mL^{-1} zeocin agar plates were precultured in 50 mL of fresh buffered minimal glycerol medium, BMG [13.4 g yeast nitrogen base, 0.4 mg biotin, 10 mL glycerol, and 100 mL 1 M K_2HPO_4/KH_2PO_4, pH 6.0 per liter] at 30 °C for 24 h in a shaking incubator (OD_{600} ~5–6). Cells were harvested, pellets resuspended in 100 mL BMM medium (100 mM potassium phosphate, pH 6.0, 13.4 g L^{-1} YNB without amino acids, 4×10^{-4} g L^{-1} biotin and 5 g L^{-1} methanol) and grown at 30 °C [18]. Absolute methanol was added at intervals of 24 h to a final concentration of 0.5% to maintain gene expression. After 4 days, the supernatant was collected and assayed for lipase activity.

2.4. Protein analysis

Sodium dodecyl sulfate–polyacrylamide gel electrophoresis (SDS–PAGE) on 15% polyacrylamide was performed by the method of Laemmli [19]. The protein fractions were boiled for 5 min and applied to the gel. Proteins were visualized by Coomassie brilliant blue R 250 staining. The protein concentration was determined by the Bradford assay using bovine serum albumin as a standard [20].

2.5. Lipase activity assay

Lipase activity was assayed spectrophotometrically using *p*-nitrophenyl butyrate (*p*-NPB) as substrate. Enzyme solution (50 μl) was added to 450 μl substrate solution consisting of 2.5 mM *p*-NPB in 2% Triton X-100 and 100 mM sodium acetate, pH 5.5, which was freshly prepared before use. The reaction mixture was incubated at 37 °C for 15 min and stopped by adding 2 ml of acetone. The release of *p*-nitrophenol was measured at 410 nm against a blank containing only buffer and carried out under the conditions described above. One unit of enzyme activity was defined as the amount of enzyme that released 1 μmol of *p*-nitrophenol min^{-1}. Under the conditions used, the extinction coefficient at 410 nm of *p*-nitrophenol was 0.62 mM^{-1} cm^{-1}.

2.6. Effect of temperature on enzyme activity and stability

Temperature optima of the fusion and native enzymes were determined using the standard assay in 100 mM sodium acetate, pH 5.5, at temperatures ranging from 30 to 70 °C. Thermal stability was determined by incubating the aliquot enzymes in 50 mM sodium acetate buffer (pH 5.5) an interval 30 min at various temperatures (50–90 °C). After cooling the samples on ice for 10 min, residual activity was determined using the standard assay.

2.7. Cellulose-binding capacity of CSLP-CBD

Binding experiments were performed by mixing 50 mg mL^{-1} of insoluble cellulose (SIGMACELL® (Sigma, USA) or Avicel (Merck

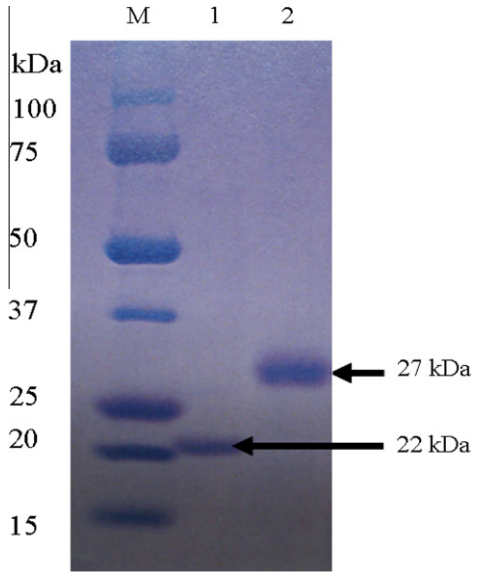

Fig. 1. SDS–PAGE of recombinant CSLP and CSLP-CBD. Lane M: standard protein marker; lane 1: recombinant CSLP; lane 2: recombinant CSLP-CBD.

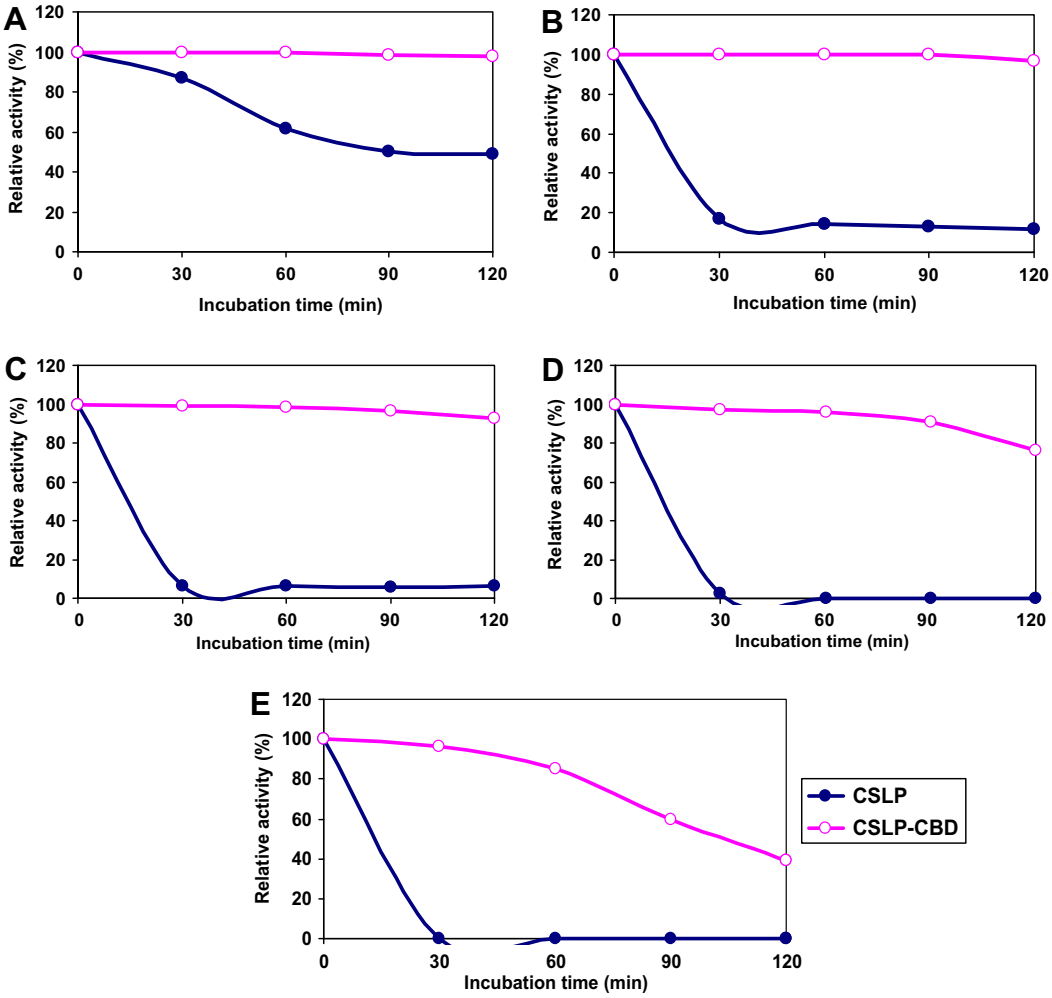

Fig. 2. Thermal stability of recombinant CSLP and CSLP-CBD at 50 °C (A); 60 °C (B); 70 °C (C); 80 °C (D) and 90 °C (E). Thermal stability was carried out by incubating the enzyme in 50 mM sodium acetate buffer (pH 5.5) at different temperatures (50–90 °C) for 30, 60, 90 and 120 min before the remaining activity was assayed (at 37 °C in 50 mM sodium acetate buffer (pH 5.5) for 15 min).

and Fluka, USA). The mixture was incubated at room temperature with continuous stirring for 1 h and the cellulose were sediment by centrifuging at 12,000 rpm for 5 min. The supernatant was collected and assayed its lipase activity. Unbound enzyme was determined by measuring residual activity in the supernatant. Assay was carried out in duplicate.

3. Results

3.1. Expression of the recombinant lipases in P. pastoris

Yeast expression vectors containing the genes for CSLP or CSLP-CBD were constructed and transformed into *P. pastoris* X-33 strain by electroporation methods. The transformants were selected on YPDS plate containing zeocin and the integration of target genes into AOX1 location in the genome was further confirmed by PCR. The most desired integrant was chosen for small-scale induction. The sizes of recombinant CSLP and CSLP-CBD, determined by SDS–PAGE were 22 kDa and 27 kDa, respectively (Fig. 1). The size of recombinant CSLP is similar to that of the native lipase secreted by *Cryptococcus* sp. S-2. However, the fusion of CBD domain resulted in 66 extra amino acids existing in C-terminal region of the fusion protein. Both CSLP and fusion enzyme was the major protein (over 95% of total protein as detected on SDS–PAGE) secreted by *P. pastoris* into culture medium. Thus, the procedure for protein purification was not necessary.

3.2. Effect of temperature on lipase activity

The optimal reaction temperatures for recombinant CSLP and CSLP-CBD were both at about 30–40 °C (Fig. S2).

3.3. Thermal stability of recombinant CSLP and fusion enzyme

The recombinant CSLP is not stable at 50 °C. However, the fusion enzyme was more stable at this temperature which retained the activity 100% after 120 min of incubation (Fig. 2A). Even incubating at 60–80 °C, the fusion enzyme still remained more than 80% of its total activity (Fig. 2B–D). These results indicated that fusion of the CBD improved the thermal stability of this lipase. Moreover, the ability to bind to cellulose with thermal stability showed that the fusion enzyme did not alter the thermal stability since fusion enzyme was virtually the same as those of the native enzyme (Fig. 3).

3.4. Cellulose-binding analysis

Binding experiments showed that the fusion enzyme was able to bind to SIGMACELL® as well as Avicel, whereas the native enzyme, which is lack of CBDs, did not show any significant adsorption to either of these polysaccharides (Fig. 4). This result indicates that the affinity of the fusion enzyme towards insoluble cellulose is

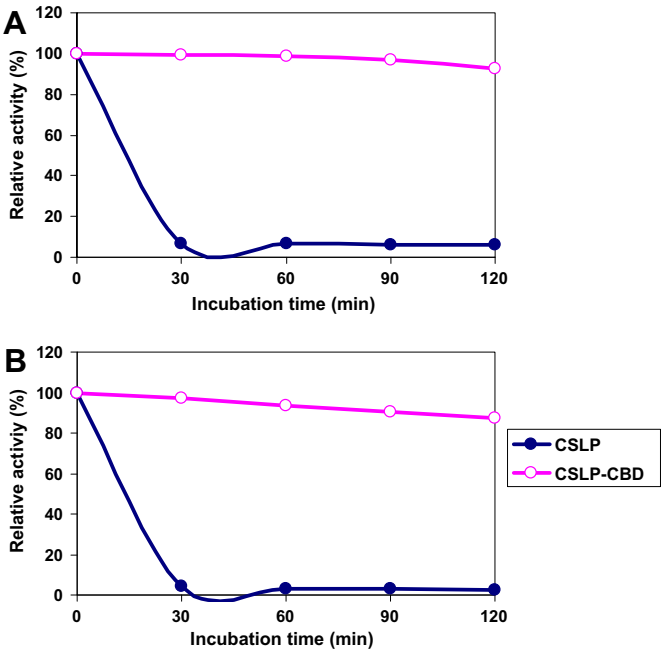

Fig. 3. Effect of cellulose binding on thermal stability of the recombinant CSLP and CSLP-CBD. (A) Free enzyme; (B) Immobilized enzyme.

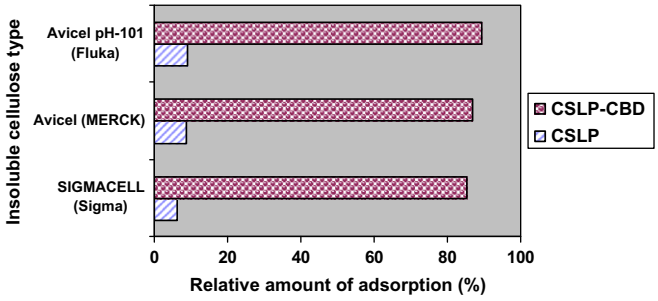

Fig. 4. Adsorption of recombinant CSLP and CSLP-CBD to insoluble cellulose.

due to the presence of the CBDs and not the catalytic domain of *Cryptococcus* sp. S-2 lipase which has an immobilizing function.

4. Discussion

In this study, the fusion CSLP gene with fungal cellulose binding domain was designed and expressed in *P. pastoris* in order to produce enzyme preparations with enhanced thermal stability and cellulose-binding capacity compared to the preparations with the native CSLP gene. Both of the native CSLP and fusion genes were successfully expressed in *P. pastoris*. CSLP and CSLP-CBD are the predominant protein (over 95% of purity) in extracellular medium. The molecular mass of recombinant CSLP-CBD is 27 kDa as estimated by SDS–PAGE. There is thus a 5-kDa difference in the molecular mass of the CSLP. This is caused by the C-terminal fusion of fungal cellulose binding domain. The recombinant CSLP and CSLP-CBD obtained from *P. pastoris* showed their temperature optima at 30–40 °C, which is almost the same as the native CSLP obtained from *Cryptococcus* sp. S-2 [7]. For the thermal stability, the fusion enzyme demonstrated increases in its thermal stability since more than 85% of its total activity retained after either 120 min incubation at 60–80 °C or 60 min incubation at 90 °C. However, the thermal stability of the recombinant CSLP decreased more quickly than the fusion enzyme when incubating at a temperature over 60 °C, the CSLP only retained 10% of its total activity (99% for fusion enzyme). As a result, fungal cellulose binding domain was significantly improved the thermostability of CSLP. These results showed that we have successfully proved the thermostabilizing function of fungal cellulose binding domain which correlates well with the previous report of this domain property [17].

To confirm whether this domain has the cellulose-binding capacity, we found that the fusion enzyme was adsorbed to insoluble cellulose (SIGMACELL® or Avicel) more than 80% while the lack of CBD enzyme (CSLP) was adsorbed less than 10%. This result indicates that the cellulose-binding domain was function. It is well documented that cellulases/enzymes with CBD show Avicel absorbable activity. This result correlates with the previous reported [21,22]. These features suggested that the fusion enzyme could reduce the quantity of enzyme supplement during industrial processing and therefore save the cost. Due to the enhanced thermal stability and cellulose-binding capacity, our fusion enzyme might be useful in various industrial applications.

Acknowledgments

We would like to thank Dr. Kazuo Masaki, National Research Institute of Brewing, Japan, for his helpful discussions. We are gratefully acknowledged the Scientific Cooperative Research under Japan Society for the promotion of Science (JSPS) and National Research Council of Thailand (NCRT) Asian Core Program for a financial support.

Appendix A. Supplementary data

Supplementary data associated with this article can be found, in the online version, at doi:10.1016/j.bbrc.2012.02.139.

References

[1] R. Verge, Interfacial activation of lipases: facts and artifacts, Trends Biotechnol. 15 (1997) 32–38.
[2] M. Iwai, Y. Tsujisaka, Lipases, in: B. Borgstrom, H.L. Brockman (Eds.), Elsevier, Amsterdam, Netherlands, 1984, pp. 443–469.
[3] A.H.C. Huang, Lipid Metabolism Plants, in: T.S. Moore (Ed.), CRC Press, Boca Raton, FL, 1993, pp. 473–502.
[4] K.D. Mukherjee, M.J. Hill, Lipases: Their Structure, Biochemistry, and Application, in: P. Woolley, S.B. Petersen (Eds.), Cambridge University Press, Cambridge, UK, 1994, pp. 49–75.
[5] F. Stehr, M. Kretschmar, C. Kroger, B. Hube, W. Schafer, Microbial lipases as virulence factor, J. Mol. Catal. B: Enzym. 22 (2003) 347–355.
[6] K.E. Jaeger, T. Eggert, Lipases for biotechnology, Curr. Opin. Biotechnol. 13 (2002) 390–397.
[7] N.R. Kamini, T. Fujii, T. Kurosu, H. Iefuji, Production, purification and characterization of an extracellular lipase from the yeast, *Cryptococcus* sp. S-2, Process Biochem. 36 (2000) 317–324.
[8] N.R. Kamini, H. Iefuji, Lipase catalyzed methanolysis of vegetable oils in aqueous medium by *Cryptococcus* sp. S-2, Process Biochem. 37 (2001) 405–410.
[9] K. Masaki, N.R. Kamini, H. Ikeda, H. Iefuji, Cutinase-like enzyme from the yeast *Cryptococcus* sp. strain S-2 hydrolyzes polylactic acid and other biodegradable plastics, Appl. Environ. Microbiol. 71 (2005) 7548–7550.
[10] H. Stalbrand, A. Saloheimo, J. Vehmaanpera, B. Henrissat, M. Penttila, Cloning and expression in *Saccharomyces cerevisiae* of a *Trichoderma reesei* beta-mannanase gene containing a cellulose binding domain, Appl. Environ. Microbiol. 61 (1995) 1090–1097.
[11] L.M.A. Ferreira, T.M. Wood, G. Williamson, C. Faulds, G.P. Hazlewood, G.W. Black, H.J. Gilbert, A modular esterase from *Pseudomonas fluorescens* subsp. *cellulosa* contains a noncatalytic cellulose-binding domain, Biochem. J. 294 (1993) 349–355.
[12] G.W. Black, J.E. Rixon, J.H. Clarke, G.P. Hazlewood, M.K. Theodorou, P. Morris, H.J. Gilbert, Evidence that linker sequences and cellulose-binding domains enhance the activity of hemicellulases against complex substrates, Biochem. J. 319 (1996) 515–520.
[13] A. Blanco, P. Diaz, J. Zueco, P. Parascandola, F.I.J. Pastor, A multidomain xylanase from a *Bacillus* sp. with a region homologous to thermostabilizing domains of thermophilic enzymes, Microbiology 145 (1999) 2163–2170.
[14] P. Béguin, J.P. Aubert, The biological degradation of cellulose, FEMS Microbiol. Rev. 13 (1994) 25–58.

[15] N. Din, N.R. Gilkes, B. Tekant, R.C. Miller Jr., R.A.J. Warren, D.G. Kilburn, Non-hydrolytic disruption of cellulose fibers by the binding domain of a bacterial cellulase, Bio Technol. 9 (1991) 1096–1099.
[16] H. Iefuji, M. Chino, M. Kato, Y. Iimura, Raw-starch-digesting and thermostable α-amylase from the yeast *Cryptococcus* sp. S-2: purification, characterization, cloning and sequencing, J. Biochem. 318 (1996) 989–996.
[17] J. He, B. Yu, K.Y. Zhang, X.M. Ding, D.W. Chen, Thermostable carbohydrate binding module increases the thermostability and substrate-binding capacity of *Trichoderma reesei* xylanase 2, New Biotechnol. 26 (2009) 53–59.
[18] J.M. Cregg, J.L. Cereghino, J. Shi, D.R. Higgins, Recombinant protein expression in *Pichia pastoris*, Mol. Biotechnol. 16 (2000) 23–52.
[19] U.K. Laemmli, Cleavage of structural proteins during the assembly of the head of bacteriophage T4, Nature (London) 227 (1970) 680–685.
[20] M.M. Brandford, A rapid sensitive method for the quantitation of microgram quantities of protein utilizing the principle of protein-dye binding, Anal. Biochem. 72 (1976) 248–254.
[21] E. Ong, N.R. Gilkes, R.C. Miller, R.A.J. Warren, D.G. Kilburn, Enzyme immobilization using a cellulose-binding domain: properties of a β-glucosidase fusion protein, Enzyme Microb. Technol. 13 (1991) 59–65.
[22] E. Shpigel, A. Goldlust, G. Efroni, A. Avraham, A. Eshel, M. Dekel, O. Shoseyov, Immobilization of recombinant heparinase I fused to cellulose-binding domain, Biotechnol. Bioeng. 65 (1999) 17–23.

Biochemical and Biophysical Research Communications 420 (2012) 188–192

Contents lists available at SciVerse ScienceDirect

Biochemical and Biophysical Research Communications

journal homepage: www.elsevier.com/locate/ybbrc

Crystal structure of the Rasputin NTF2-like domain from *Drosophila melanogaster*

Tina Vognsen, Ole Kristensen *

Biostructural Research, Department of Drug Design and Pharmacology, Faculty of Health Sciences, University of Copenhagen, Universitetsparken 2, DK-2100 Copenhagen, Denmark

ARTICLE INFO

Article history:
Received 21 February 2012
Available online 3 March 2012

Keywords:
Rin
Rasputin
G3BP
RasGAP
NTF2
Crystal structure
Ras signaling

ABSTRACT

The crystal structure of the NTF2-like domain of the *Drosophila* homolog of Ras GTPase SH3 Binding Protein (G3BP), Rasputin, was determined at 2.7 Å resolution. The overall structure is highly similar to nuclear transport factor 2: It is a homodimer comprised of a β-sheet and three α-helices forming a cone-like shape. However, known binding sites for RanGDP and FxFG containing peptides show electrostatic and steric differences compared to nuclear transport factor 2. A HEPES molecule bound in the structure suggests a new, and possibly physiologically relevant, ligand binding site.

1. Introduction

The Ras signaling pathway is a complex network of cell signaling events important for cell proliferation and differentiation. Ras proteins cycle between an active GTP-binding form and an inactive GDP-binding form. This is done with help from guanine nucleotide exchange factors (GEFs) and Ras GTPase Activating Protein (RasGAP). In response to signals from tyrosine kinase receptors, GEFs like Son of Sevenless (SOS) activate Ras by exchanging GDP with GTP, while RasGAP is a negative regulator that promotes GTP hydrolysis. In its active state, Ras stimulates a cascade of downstream effectors such as RAF and MAPK leading to cell proliferation (reviewed in [1]).

One of many proteins suggested being involved in regulation of Ras activity is the Ras GTPase Activating Protein SH3 Domain Binding Protein (G3BP). As the name implies, G3BP binds to the SH3 domain of RasGAP and can hereby impinge on Ras signaling [2]. In humans, G3BP exists in three isoforms: G3BP1, G3BP2a and G3BP2b. The main difference between these three variants is the number of PxxP motifs found in the central region of the protein [3]. These motifs were initially considered to be the binding site of RasGAP [4]. However, later studies have shown that binding takes place through the N-terminal NTF2-like domain residue 11–133 in human G3BP1 [3]. Recently, RasGAP has been questioned as a genuine binding partner for G3BP [5] and the current understanding of G3BP as a regulator of Ras signaling might, thus, be subject for revision. Regardless of its binding to RasGAP, the G3BP NTF2-like domain is highly conserved between species. It is suggested to play a role in nuclear transport, possibly in a manner similar to nuclear transport factor 2 (NTF2) [2], which is a small 14 kDa protein involved in nuclear-cytoplasmic transport. The NTF2-like domain is furthermore involved in dimer formation of the G3BP protein [6]. In addition to the NTF2-like domain and the PxxP repeats, G3BP also contains a RNA-binding domain and glutamate- and glycine-rich regions. These domains contribute to the multifunctionality of G3BP, that besides regulation of Ras and stress granule assembly also has been implicated in RNA metabolism [7,8] and NFκB signaling [9]. Moreover, human G3BP1 and G3BP2 is overexpressed in cancer tumors [10,11], but the detailed mechanisms and involvement of the various G3BP functions related to this disease scenario remains unclear.

Due to the importance of Ras in *Drosophila* eye development, *Drosophila melanogaster* has in several studies served as a model organism in studies of Ras signaling [12–14]. The *Drosophila* homolog of G3BP, encoded by the *Rin* gene, was identified in the year 2000 and named Rasputin [13]. It shares significant sequence identity over its full length to human G3BPs and is, based on defects in ommatidial polarization in *Rin*−/− mutant flies, suggested to be an effector of Ras and Rho signaling [13]. Furthermore, it is reported that Rasputin, similar to G3BP, is recruited to stress granules [6]. Here we report the crystal structure of the NTF2-like domain of Rasputin, which shares 54.2% and 55.6% sequence identity with the NTF2-like domains of human G3BP1 and G3BP2a, respectively.

* Corresponding author. Fax: +45 3533 6001.
E-mail addresses: tv@farma.ku.dk (T. Vognsen), ok@farma.ku.dk (O. Kristensen).

0006-291X/$ - see front matter © 2012 Elsevier Inc. All rights reserved.
doi:10.1016/j.bbrc.2012.02.140

2. Materials and methods

2.1. Protein production

Artificial gene synthesis (ShineGene Molecular Biotech Inc., Shanghai) was used to generate an optimized template for *Escherichia* coli expression of the Rasputin (UniProt ID Q9NH72, residues 15–130) NTF2-like domain.

Polymerase chain reaction (PCR) amplification of the DNA was achieved using the following primers: (a) 5′-CATGCTAGCCATATGTCTGTTGGGAGAGAGTTTGTC-3′ and (b) 5′-GCTGTTCGAAGGCGGCCGCTTACTGGTAACGAAAAATATCAT-3′.

The PCR product was digested with NotI and NdeI and cloned into the pET28a(+) expression vector (Novagen). The construct contained a thrombin-cleavable His6-tag leaving four additional vector-derived N-terminal residues (GSHM) after proteolysis. Verification of the recombinant vectors containing the target gene was done by DNA sequencing (Eurofins MWG Operon).

The plasmid was transformed into *E. coli* BL21(DE3) and expressed in ZYM-5052 autoinduction media [15]. The harvested cells were suspended in PBS buffer containing 20 μg/mL RNAse A, 20 μg/mL DNAse I and protease inhibitor (Roche, inhibitor cocktail tablets) before lysis in a cell disruptor (Constant Systems Ltd.). Cell debris was removed by centrifugation (30,000*g*, 30 min) and the supernatant applied to a HisTrap HP column (GE Healthcare) equilibrated with buffer A (20 mM Na_2HPO_4, 30 mM imidazole, 300 mM NaCl, pH 8) and eluted using a linear gradient of buffer B (20 mM Na_2HPO_4, 1 M imidazole, 300 mM NaCl, pH 8). The His6-tag was removed by addition of 2 U thrombin (bovine, Calbiochem) per milligram protein and overnight incubation at room temperature. Size exclusion chromatography (Superdex 75 HR, GE Healthcare) was used as a final purification step (buffer: 10 mM Tris–HCl, 300 mM NaCl, pH 8). The protein concentration was estimated using a Bradford protein assay (Bio-Rad) and the purity checked with SDS–PAGE (Invitrogen).

2.2. Crystallization and data collection

Initial crystallization conditions were based on previously reported results for the NTF2-like domain of human G3BP1 [16]. Rasputin crystals were obtained using hanging drop vapor-diffusion at room temperature and grew with a rectangular prismatic shape to a maximum dimension of 100 μm along the longest edge within 2 weeks. The crystallization drop contained 2 μL of reservoir solution (2.2 M diammonium phosphate and 0.1 M HEPES, pH 7) and 2 μL of protein (2 mg/mL). The crystals were transferred briefly to a cryo solution containing 2 M diammonium phosphate, 0.1 M HEPES, pH 7 and 20% glycerol prior to flash cooling in liquid nitrogen. Diffraction data were collected at the European Synchrotron Radiation Facility (ESRF), Grenoble, beamline ID14.1 and processed using the XDS [17] pipeline in the xia2 software [18].

2.3. Structure determination and refinement

The structure was initially solved in spacegroup $C222_1$ by molecular replacement using Phaser [19] as implemented in the CCP4 suite [20]. A 1.7 Å structure of the human G3BP1 NTF2-like domain (PDB ID 3Q90, chain B) was used as search model. The obtained model was rebuilt and refined using PHENIX [21]. Post-mortem twinning analysis was performed using PHENIX after data processing in spacegroup P1 [22]. Parallel structure determination and refinement was performed in the subgroups C2 and $P2_1$. Four TLS-groups (chain A: residue 14–63, 64–139 and chain B: residue 14–64, 65–130) were derived from the TLSMD web server [23] and used in refinement. Manual correction of the model was carried out using Coot [24] and the structure was validated with MolProbity [25]. All figures were prepared in PyMol (The PyMOL Molecular Graphics System, Version 1.3, Schrödinger, LLC).

2.4. Accession number

Crystallographic coordinates and structure factors have been deposited at the Protein Data Bank with accession code 3ujm.

3. Results and discussion

3.1. Crystal structure of the Rasputin NTF2-like domain

The crystal structure of the Rasputin NTF2-like domain was solved by molecular replacement and refined at a resolution of 2.7 Å with *R* and *R*-free values of 19.9% and 24.2%. Initially, the structure was solved in space group $C222_1$, but stagnation in *R* values during refinement led us to explore potential crystal twinning problems and further refinement in the subgroups C2 and $P2_1$. Our analysis and parallel refinements concluded that the data did not suffer from twinning effects and the final structure was satisfactorily refined in space group $P2_1$ with two molecules per asymmetric unit.

Both polypeptide chains could be traced from residue 14 to 130 including a vector-derived methionine at the N-terminal. In addition, the model contains 34 water molecules and two HEPES molecules. Structure validation showed good overall stereochemistry (Table 1), but notably two residues from each chain, Ser116 and Pro117, were found in the disallowed regions. These residues are located in a tight loop, which might distort the geometry, and despite that somewhat unfavorable conformations persists after

Table 1
Data reduction and refinement statistics. Values in parenthesis refer to the highest resolution bin.

Data collection	
X-ray source, wavelength (Å)	ID14.1/ESRF, 0.93
Space group	$P2_1$
Cell dimensions (Å)	a = 39.20, b = 80.38, c = 39.20 and γ = 92.60
Monomer per asymmetric unit	2
Resolution range (Å)	39–2.74 (2.81–2.74)
Reflections	6272 (477)
Average multiplicity	4.2 (4.3)
Completeness (%)	97.5 (96.6)
$\langle I/\sigma I\rangle$	19.8 (3.1)
R_{merge}[a] (%)	5.3 (43.5)
Refinement	
R_{work}/R_{free}[b] (%)	19.87/24.24
Number of atoms	
Protein	1927
Water	34
HEPES	30
Average B-factor (Å²)	
Protein	63.37
Water	49.22
HEPES	87.62
Rms deviation	
Bond lengths (Å)	0.002
Angles (°)	0.642
Ramachandran plots[c]	
Most favored regions (%)	91.7

[a] $R_{merge} = \Sigma_{hkl}(\Sigma_i(I_{hkl,i} - \langle I_{hkl}\rangle))/\Sigma_{hkl,i}\langle I_{hkl}\rangle$, where $I_{hkl,i}$ is the intensity of an individual measurement of the reflection with Miller indices *h*, *k*, and *l*, and $\langle I_{hkl}\rangle$ is the mean intensity of that reflection.

[b] $R_{work} = \Sigma_{hkl}(F_{obs,hkl} - F_{calc,hkl})/F_{obs,hkl}$, where $F_{obs,hkl}$ and $F_{calc,hkl}$ are the observed and calculated structure factor amplitudes. R_{free} is equivalent to the R_{work}, but calculated with 5% of the reflections omitted from the refinement process.

[c] Values from MolProbity [25].

extensive model-building and refinement efforts, the model provides a reasonable fit to the electron density. Data collection and refinement statistics are summarized in Table 1. The crystal structure of the Rasputin NTF2-like domain reveals a homodimer with each chain comprised of a beta-sheet (βI–βV) and three alpha helices (αI–αIII) forming a cone-like shape highly similar to other published NTF2 domains (Fig. 1).

3.2. Comparison to other NTF2 domains

A Dali search shows significant structural similarity to human G3BP1 NTF2-like domain, nuclear transport factor 2 from various organisms, UBP3-associated protein BRE5, P15 and nuclear RNA export factor 2, with the human G3BP1 NTF2-like domain (PDB ID 3q90) being the closest related structure (*Z*-score 21.6, rmsd 0.8) followed by nuclear transport factor 2 from *Cryptosporidium parvum* (PDB ID 1zo2, *Z*-score 20.5, rmsd 1.1). Overall, the Rasputin NTF2-like domain shares the same fold as the G3BP1 NTF2-like domain and nuclear transport factor 2. The main structural differences between the NTF2-like domains from Rasputin and human G3BP1 are found in the loop regions. Compared to the Rasputin NTF2-like domain, G3BP1 has seven and two partly disordered residues, respectively, inserted between residues 48 and 49 and 116 and 117 in loop VI and loop VII. The corresponding loops in nuclear transport factor 2 are comparable in length to those of Rasputin. Thus, in these two loop regions, the Rasputin NTF2-like domain exhibits higher similarity to nuclear transport factor 2 than to human G3BP1.

Nuclear transport factor 2 stimulates protein translocation by binding RanGDP in the cell nucleus and exporting it to the cytoplasm [26]. RanGDP binding occurs by insertion of a conserved phenylalanine residue into a hydrophobic pocket of nuclear transport factor 2 in addition to polar interactions at the rim of the cavity [27]. A somewhat similar but more narrow and less hydrophobic pocket can be found in the Rasputin structure (Fig. 3A). The reduced size of the pocket is caused by the two residues Tyr129 and Arg104, which also contributes to the decrease in hydrophobicity compared to Nuclear Transport factor 2 (Fig. 3B). These two residues are conserved throughout the G3BP family and could be suspected to hinder RanGDP binding. However, RanGDP and RanGTP have previously been reported to bind weakly to human G3BP1 [28]. It is, thus, possible that weak binding also occurs between the drosophila homolog of the NTF2-like domain and RanGDP and/or RanGTP.

Through binding to FxFG repeat containing nucleoporins, nuclear transport factor 2 translocates through the nuclear pore complex (NPC) [29]. A comparable role for Rasputin in nuclear transportation could be indicated by a corresponding binding site for the FxFG repeat. In nuclear transport factor 2, the FxFG repeat is accommodated in a hydrophobic depression at the dimer interface [30]. A similar unambiguous depression is not present at the corresponding location in Rasputin. This suggests that the FxFG repeat either does not bind or that binding takes place at a different site. Other NTF2-like domain containing proteins, including TAP15/p15 and Importin β have been shown to bind FG and GLFG repeats at other locations [31,32]. However, their binding sites are not conserved in the Rasputin structure.

3.3. Dimer interface

Analysis from the PISA server [33] shows an indisputable high significance score for dimerization of Rasputin, with a total buried surface of 1210 Å^2 upon complex formation. This result is in agreement with the elution-profile from size-exclusion chromatography (data not shown). The dimer interface of the Rasputin NTF2-like domain (Fig. 2) is somewhat less hydrophobic than the interfaces of G3BP1 and nuclear transport factor 2. It involves 30 residues from each chain and is stabilized by 28 hydrogen bonds and eight salt bridges in addition to hydrophobic contacts formed at two patches involving I46, L52 and I126 on one patch and A82, L84,

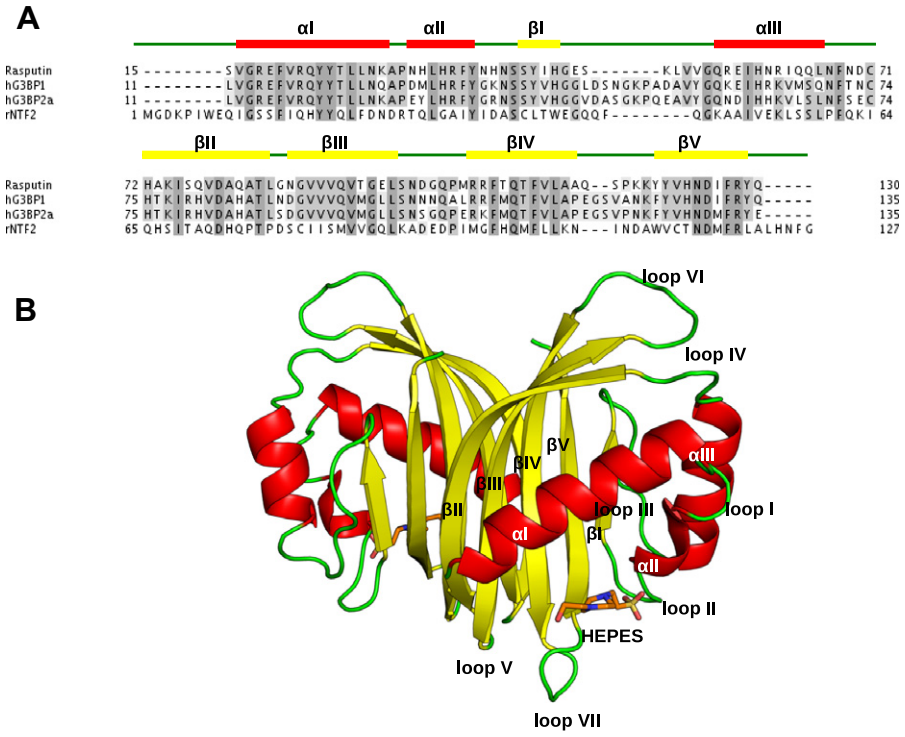

Fig. 1. (A) Sequence alignment of the NTF2-like domains from Rasputin, human G3BP1 and G3BP2a and rat nuclear transport factor 2. (B) Cartoon representation of the dimeric Rasputin NTF2-like domain.

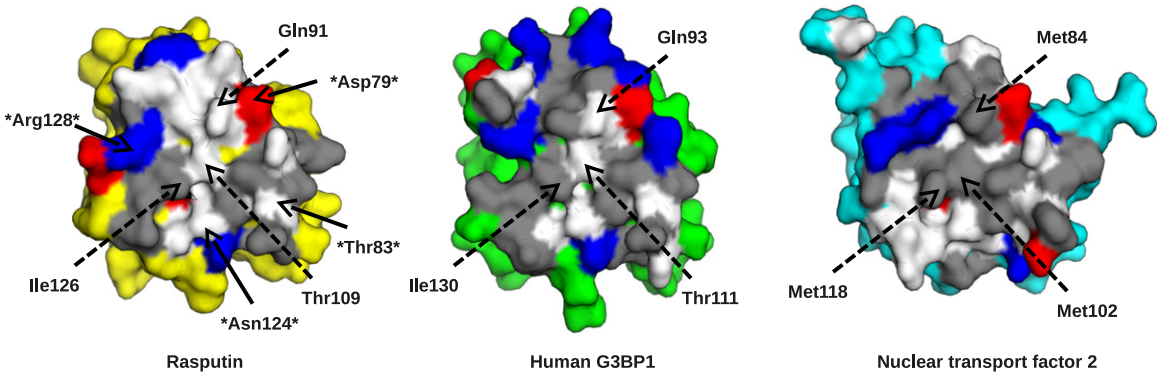

Fig. 2. Surface representation of the dimer interfaces of NTF2-like domains from Rasputin (yellow), human G3BP1 (green, PDB ID 3q90) and nuclear transport factor 2 (cyan, PDB ID 1oun). Interface residues are colored by residue type (gray: hydrophobic, red: acidic, blue: basic, white: polar). * indicates residues conserved between the three structures. Dashed arrows indicate positions equivalent to Met84, Met102 and Met118 in nuclear transport factor 2. (For interpretation of the references to color in this figure legend, the reader is referred to the web version of this article.)

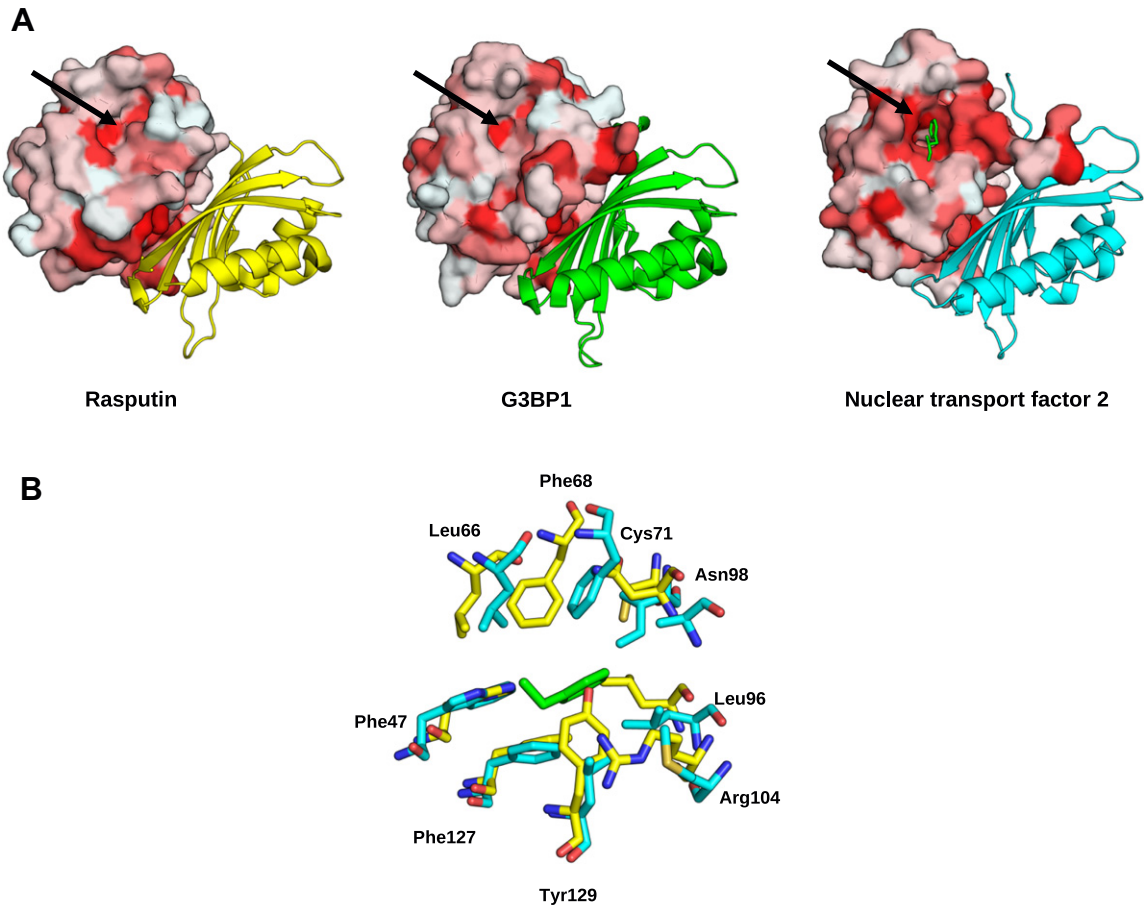

Fig. 3. Comparison of RanGDP binding sites from nuclear transport factor 2 (PDB ID 1a2k), Rasputin and human G3BP1 (PDB ID 3q90). (A) Surface representation colored according to Eisenberg's hydrophobicity scale [37]. Phe72 of RanGDP is shown as sticks (green). (B) Close-up of the RanGDP binding site. Ran Phe72 is shown in green, nuclear transport factor 2 in cyan and Rasputin in yellow. Residue labels refer to Rasputin. (For interpretation of the references to color in this figure legend, the reader is referred to the web version of this article.)

G85, G87, V89, V90, V11 and A113 on another patch. A salt bridge formed by Asp79 and Arg128 in addition to a hydrogen bond between Thr83 and Asn124 is conserved between *Drosophila* Rasputin, human G3BPs and nuclear transport factor 2. Thus, these polar interactions might play a crucial role in dimerization. Another residue, Met118 in rat nuclear transport factor, have in mutational studies been shown to be important in dimer formation [34]. In Rasputin and human G3BPs this residue is not conserved but has been replaced by the somewhat smaller isoleucine retaining the hydrophobic character at this position. Two other methionines located at position 84 and 102 in nuclear transport factor 2 have also been implicated in dimer formation [34]. However, these residues are not conserved in Rasputin and human G3BPs where they have been replaced by glutamine and threonine, respectively.

Nuclear transport factor 2 is primarily dimeric both under *in vivo* and *in vitro* conditions, but a significant proportion of cellular NTF2 is likely to be monomeric [34] and the ability of the NTF2 dimer to dissociate is implicated as an important feature to facilitate release of RanGDP after entry to the nucleus through the NPC [35]. The common features of Rasputin and nuclear transport factor 2 could, despite differences in hydrophobicity, suggest a similar monomer/dimer equilibrium for the *Drosophila* Rasputin.

3.4. HEPES binding in a new possible ligand binding site

Each of the two chains in the homodimer harbors a HEPES molecule located in a depression between the helices αI, αII and loop VII as shown in Fig. 1. The HEPES molecule was modeled with the sulfonic acid group at the bottom of the binding site, placing this electron-dense part of the molecule also in the most significant volume of electron density, which was visible even at the early stages of refinement. In this orientation, the ligand is held in place by van der Waals interactions, a possible hydrogen bond to the Lys118 carbonyl oxygen and electrostatic stabilization of the sulfonic acid moiety by the Lys30 sidechain from a symmetry related molecule. Despite the complex nature of HEPES protonation states [36], hydrogen bonding seems unlikely between the sulfonic acid group of the ligand and the proximate carbonyl groups of Tyr120 and Arg37. Alternatively, the HEPES molecule could also be modeled in an inverted orientation corresponding to a 180° rotation, placing the sulfonic acid group towards the solvent with a possibility to hydrogen bond the NE2 atom of Gln23. Regardless of this ambiguity in the orientation of the HEPES molecule, the position of the ligand may indicate a potentially important binding site of the Rasputin NTF2-like domain. This area has, based on molecular modeling, previously been suggested to be the binding site for the RasGAP SH3 domain and a similar depression can be found in the crystal structure of the G3BP1 NTF2-like domain. Thus, the binding of a HEPES molecule might support this depression as a binding site for the SH3 domain of G3BP or other ligands.

Acknowledgments

We appreciate the support in data collection from the staff at ESRF, Grenoble (beamline ID14-1). This work was supported by the Alfred Benzon Foundation, the Brdr. Hartmann Foundation, the Danish Natural Science Council through DANSCATT and by a University of Copenhagen PhD fellowship (TV).

References

[1] S.L. Campbell, R. Khosravi-Far, K.L. Rossman, G.J. Clark, C.J. Der, Increasing complexity of Ras signaling, Oncogene 17 (1998) 1395–1413.
[2] K. Irvine, R. Stirling, D. Hume, D. Kennedy, Rasputin, more promiscuous than ever: a review of G3BP, Int. J. Dev. Biol. 48 (2004) 1065–1077.
[3] D. Kennedy, J. French, E. Guitard, K. Ru, B. Tocque, J. Mattick, et al., Characterization of G3BPs tissue specific expression chromosomal localisation and rasGAP 120 binding studies, J. Cell. Biochem. 187 (2002).
[4] F. Parker, F. Maurier, I. Delumeau, M. Duchesne, D. Faucher, L. Debussche, et al., A Ras-GTPase-activating protein SH3-domain-binding protein, Mol. Cell. Biol. 16 (1996) 2561–2569.
[5] A. Annibaldi, A. Dousse, S. Martin, J. Tazi, C. Widmann, Revisiting G3BP1 as a RasGAP binding protein: sensitization of tumor cells to chemotherapy by the RasGAP 317–326 sequence does not involve G3BP1, PLoS One 6 (2011) e29024.
[6] H. Tourrière, K. Chebli, L. Zekri, B. Courselaud, J.M. Blanchard, E. Bertrand, J. Tazi, The RasGAP-associated endoribonuclease G3BP assembles stress granules, J. Cell. Biol. 160 (2003) 823–831.
[7] R. Atlas, L. Behar, E. Elliott, I. Ginzburg, The insulin-like growth factor mRNA binding-protein IMP-1 and the Ras-regulatory protein G3BP associate with tau mRNA and HuD protein in differentiated P19 neuronal cells, J. Neurochem. 89 (2004) 613–626.
[8] H. Tourriere, I. Gallouzi, K. Chebli, J.P. Capony, J. Mouaikel, P. Van Der Geer, J. Tazi, RasGAP-associated endoribonuclease G3BP: selective RNA degradation and phosphorylation-dependent localization, Mol. Cell. Biol. 21 (2001) 7747.
[9] M. Prigent, I. Barlat, H. Langen, C. Dargemont, IkappaBalpha and IkappaBalpha/NF-kappa B complexes are retained in the cytoplasm through interaction with a novel partner, RasGAP SH3-binding protein 2, J. Biol. Chem. 275 (2000) 36441–36449.
[10] E. Guitard, F. Parker, R. Millon, J. Abecassis, B. Tocqué, G3BP is overexpressed in human tumors and promotes S phase entry, Cancer Lett. 162 (2001) 213–221.
[11] J. French, R. Stirling, M. Walsh, H.D. Kennedy, The expression of Ras-GTPase activating protein SH3 domain-binding proteins, G3BPs, in human breast cancers, Histochem. J. 34 (2002) 223–231.
[12] D.A. Wassarman, M. Therrien, G.M. Rubin, The Ras signaling pathway in Drosophila, Curr. Opin. Genet. Dev. 5 (1995) 44–50.
[13] C. Pazman, C.A. Mayes, M. Fanto, S.R. Haynes, M. Mlodzik, Rasputin, the Drosophila homologue of the RasGAP SH3 binding protein, functions in ras- and Rho-mediated signaling, Development (Cambridge, UK) 127 (2000) 1715–1725.
[14] P.J. Sung, A.B. Rodrigues, A. Kleinberger, S. Quatela, E.A. Bach, M.R. Philips, Cytosolic Ras supports eye development in Drosophila, Mol. Cell. Biol. 30 (2010) 5649–5657.
[15] F.W. Studier, Protein production by auto-induction in high-density shaking cultures, Protein Expression Purif. 41 (2005) 207–234.
[16] T. Vognsen, I.R. Möller, O. Kristensen, Purification, crystallization and preliminary X-ray diffraction of the G3BP1 NTF2-like domain, Acta Crystallogr., Sect. F: Struct. Biol. Cryst. Commun. 67 (2011) 48–50.
[17] W. Kabsch, Xds, Acta Crystallogr., Sect. D: Biol. Crystallogr. 66 (2010) 125–132.
[18] G. Winter, Xia2 : an expert system for macromolecular crystallography data reduction, J. Appl. Crystallogr. 43 (2009) 186–190.
[19] A.J. McCoy, R.W. Grosse-Kunstleve, P.D. Adams, M.D. Winn, L.C. Storoni, R.J. Read, Phaser crystallographic software, J. Appl. Crystallogr. 40 (2007) 658–674.
[20] M.D. Winn, C.C. Ballard, K.D. Cowtan, E.J. Dodson, P. Emsley, P.R. Evans, et al., Overview of the CCP4 suite and current developments, Acta Crystallogr., Sect. D: Biol. Crystallogr. 67 (2011) 235–242.
[21] P.D. Adams, P.V. Afonine, G. Bunkóczi, V.B. Chen, I.W. Davis, N. Echols, et al., PHENIX: a comprehensive Python-based system for macromolecular structure solution, Acta Crystallogr., Sect. D: Biol. Crystallogr. 66 (2010) 213–221.
[22] P.H. Zwart, R.W. Grosse-Kunstleve, A.A. Lebedev, G.N. Murshudov, P.D. Adams, Surprises and pitfalls arising from pseudosymmetry, Acta Crystallogr., Sect. D: Biol. Crystallogr. 64 (2008) 99–107.
[23] J. Painter, E.a. Merritt, TLSMD web server for the generation of multi-group TLS models, J. Appl. Crystallogr. 39 (2006) 109–111.
[24] P. Emsley, B. Lohkamp, W.G. Scott, K. Cowtan, Features and development of Coot, Acta Crystallogr., Sect. D: Biol. Crystallogr. 66 (2010) 486–501.
[25] V.B. Chen, W.B. Arendall, J.J. Headd, D.A. Keedy, R.M. Immormino, G.J. Kapral, et al., MolProbity all atom structure validation for macromolecular crystallography, Acta Crystallogr., Sect. D: Biol. Crystallogr. 66 (2010) 12–21.
[26] M.S. Moore, G. Blobel, Purification of a Ran-interacting protein that is required for protein import into the nucleus, Proc. Natl. Acad. Sci. USA 91 (1994) 10212–10216.
[27] M. Stewart, H.M. Kent, A.J. McCoy, Structural basis for molecular recognition between nuclear transport factor 2 (NTF2) and the GDP-bound form of the Ras-family GTPase Ran, J. Mol. Biol. 277 (1998) 635–646.
[28] I.G. Macara, Transport into and out of the nucleus, Microbiol. Mol. Biol. Rev. 65 (2001) 570–594.
[29] M. Stewart, R.P. Baker, R. Bayliss, L. Clayton, R.P. Grant, T. Littlewood, Y. Matsura, Molecular mechanism of translocation through nuclear pore complexes during nuclear protein import, FEBS Lett. 498 (2001) 145–149.
[30] R. Bayliss, S.W. Leung, R.P. Baker, B.B. Quimby, A.H. Corbett, M. Stewart, Structural basis for the interaction between NTF2 and nucleoporin FxFG repeats, EMBO J. 21 (2002) 2843–2853.
[31] R. Bayliss, T. Littlewood, L.A. Strawn, S.R. Wente, M. Stewart, GLFG and FxFG nucleoporins bind to overlapping sites on importin-beta, J. Biol. Chem. 277 (2002) 50597–50606.
[32] S. Fribourg, I.C. Braun, E. Izaurralde, E. Conti, Structural basis for the recognition of a nucleoporin FG repeat by the NTF2-like domain of the TAP/p15 mRNA nuclear export factor, Mol. Cell 8 (2001) 645–656.
[33] E. Krissinel, K. Henrick, Inference of macromolecular assemblies from crystalline state, J. Mol. Biol. 372 (2007) 774–797.
[34] C. Chaillan-Huntington, P.J. Butler, J.a. Huntington, D. Akin, C. Feldherr, M. Stewart, NTF2 monomer–dimer equilibrium, J. Mol. Biol. 314 (2001) 465–477.
[35] C. Chaillan-huntington, C. Villa, M. Stewart, Dissecting the Interactions between NTF2 RanGDP, and the Nucleoporin XFXFG Repeats, Biochemistry 275 (2000) 5874–5879.
[36] P. Sledź, R. Kamiński, M. Chruszcz, M.D. Zimmerman, W. Minor, K. Woźniak, An experimental charge density of HEPES, Acta Crystallogr., Sect. B: Struct. Sci. 66 (2010) 482–492.
[37] D. Eisenberg, E. Schwarz, M. Komaromy, R. Wall, Analysis of membrane and surface protein sequences with the hydrophobic moment plot, J. Mol. Biol. 179 (1984) 125–142.

Biochemical and Biophysical Research Communications 420 (2012) 193–198

Contents lists available at SciVerse ScienceDirect

Biochemical and Biophysical Research Communications

journal homepage: www.elsevier.com/locate/ybbrc

Gangliosides and chondroitin sulfate desensitize and internalize B2 bradykinin receptors ☆

Ayaka Shimazaki, Tetsuto Nakagawa, Junya Mitoma, Hideyoshi Higashi *

Division of Glyco-Signal Research, Institute of Molecular Biomembrane and Glycobiology, Tohoku Pharmaceutical University, 4-4-1 Komatsushima, Aoba-ku, Sendai, Miyagi 981-8558, Japan

ARTICLE INFO

Article history:
Received 20 February 2012
Available online 3 March 2012

Keywords:
Bradykinin
B2 receptor
Ganglioside
Chondroitin sulfate
GRK
Calcium mobilization

ABSTRACT

Prolonged or repeated agonist activation of G-protein-coupled receptors (GPCRs) initiates their desensitization and internalization, rendering them unresponsive to agonist activation. We analyzed how gangliosides and chondroitin sulfate affect B2 bradykinin (BK) receptors (B2Rs). Gangliosides and chondroitin sulfate did not stimulate intracellular Ca^{2+} release from B2R-expressing CHO-K1 cells, but repeated exposure desensitized B2Rs to BK stimulation. Microscopic observation of DsRed-fused B2Rs revealed that several gangliosides and chondroitin sulfate C (CSC) effectively internalized B2Rs. Ganglioside-CSC treatment of B2R mutant-expressing cells failed to desensitize and internalize the mutant receptors. As this mutant lacks the first extracellular domain and cannot activate GPCR kinase (GRK), gangliosides and CSC likely initiate B2R desensitization and endocytosis through GRK-mediated B2R phosphorylation.

1. Introduction

Bradykinin (BK) is a key regulator of vascular tone that has been implicated in pathological disorders such as inflammation, pain, and cancer (for review see [1]). BK stimulation of bradykinin B2 receptors (B2Rs) leads to activation of the Gαq/11 family of heterotrimeric G proteins in many cell types, which in turn stimulates the activity of phosphatidylinositol-specific phospholipase C (PLC) to yield PI hydrolysis and increase intracellular Ca^{2+}. Glycans of glycolipids, glycoproteins, and proteoglycans all are exposed to cell surfaces and contribute to intercellular recognition.

Gangliosides are acidic glycolipids that are major components of glycoconjugates in the brain. Exposure of neuronal cells to nanomolar concentrations of b-series gangliosides, such as GT1b, stimulate the transient increase of intracellular Ca^{2+} concentrations, activation of cdc42, and formation of filopodia [2], suggesting that gangliosides stimulate a cell surface glycan receptor. Since neuronal cells ubiquitously express B2Rs [3], and because BK is one of the known ligands for a G-protein-coupled receptor (GPCR) that activates cdc42 [4], we analyzed the interaction between gangliosides and B2Rs. For this purpose, we introduced B2R to CHO-K1 cells, which express undetectable levels of endogenous B2R and the response to the ganglioside was examined. We also analyzed chondroitin sulfate, another major acidic glycan in whole body since glycoconjugates other than gangliosides should contribute to early morphological brain development whereas morphological development of the brain is apparently normal in ganglioside deficient mice [5]. We found that chondroitin sulfate C (CSC) stimulated neuronal cells to release Ca^{2+} from intracellular store in the similar way as GT1b and that CSC activated B2R expressing in yeast cells. However, in CHO-K1 cells expressing transfected B2R, gangliosides and chondroitin sulfate did not induce Ca^{2+} release, instead they did stimulate desensitization to BK and endocytosis of B2Rs.

2. Materials and methods

2.1. Plasmids and constructs

Plasmids encoding human long variant (hB2R) and rat short variant B2R, starting at the second initiating ATG coding Met31 (rsB2R), were prepared by insertion of B2R cDNA between EcoRI and BamHI sites of pIRES2-EGFP (Clontech). Plasmids encoding B2R-DsRed fusion proteins were prepared by insertion of B2R cDNA (without stop codon) between EcoRI and AgeI sites of pDsRed-Monomer-N1 vector (Clontech). The cDNAs encoding the rat

Abbreviations: BK, bradykinin; B2R, B2 bradykinin receptor; CSC, chondroitin sulfate C; CSE, chondroitin sulfate E; GRK, G-protein-coupled receptor kinase; GM1, Galβ3GalNAcβ4(Neu5Acα3)Galβ4GlcCer; GD1a, Neu5Acα3Galβ3GalNAcβ4(Neu5Acα3)Galβ4GlcCer; GD1b, Galβ3GalNAcβ4(Neu5Acα8Neu5Acα3)Galβ4GlcCer; GT1b, Neu5Acα3Galβ3GalNAcβ4(Neu5Acα8Neu5Acα3)Galβ4GlcCer; GPCR, G-protein-coupled receptor; BSS, balanced salt solution.

☆ This study was supported by the "Academic Frontier" Project for Private Universities, Japan.

* Corresponding author. Fax: +81 22 727 0077.
E-mail address: hhigashi@tohoku-pharm.ac.jp (H. Higashi).

0006-291X/$ - see front matter © 2012 Elsevier Inc. All rights reserved.
http://dx.doi.org/10.1016/j.bbrc.2012.02.142

B2R variants, starting at amino acid Gln65 (B2R-ΔE1) [6], were constructed by polymerase chain reaction (PCR) and subcloned into pDsRed-Monomer-N1. For B2R-ΔE1, an initiating ATG was introduced to start translation at Gln65. The identity of the constructs was confirmed by DNA sequencing.

2.2. Cell culture

NG108-15 neuroblastoma-glioma hybridoma cells were cultured as described previously [2].

CHO-K1 cells were grown in alpha minimum essential medium (α-MEM) supplemented with 10% (v/v) fetal calf serum and kept in a humidified 5% CO_2/95% air atmosphere at 37 °C. CHO-K1 cells were transiently transfected with plasmids using GeneJuice (Merck) per the manufacturer's instructions. Transfection efficiency was 15–25%.

HEK293 cells were grown in Dulbecco's modified Eagle's medium with 5.5 mM glucose supplemented with 10% (v/v) fetal calf serum and kept in a humidified 5% CO_2/95% air atmosphere at 37 °C. HEK293 cells were transiently transfected with plasmids using Lipofectamine 2000 (Invitrogen) per the manufacturer's instructions. Transfection efficiency was 90% or more.

2.3. Yeast strain, manipulations and Gα expression and Ste2p deletion construct

Saccharomyces cerevisiae strain YKG005 (MATa ura3-52 lys2-801 ade2-101 his3-200 leu2-3 sst2Δ1 far1Δ1 ste2Δ1 gpa1Δ3::GPA1-Gαq-c5 pep4Δ2 trp1-901 fus1::FUS1-HIS3 can1Δ::FUS1-CAN1 FUS2::FUS2-lacZ) was derived from YPH499 (MATa ura3-52 lys2-801 ade2-101 trp1-Δ63 his1-Δ200 leu2-Δ1) by a series of one-step gene replacements [7]. The FUS1-HIS3 reporter gene was integrated at the FUS1 locus. The FUS2-lacZ reporter gene was integrated for the β-galactosidase reporter assay. A yeast/mammalian G protein αq-subunit chimera, GPA1-Gq-c5, was constructed by replacing the C-terminal five amino acids of Gpa1p with those of a mammalian Gαq protein [8].

2.4. Plasmid for yeast transformation

Plasmid pYSF1 was derived from pYES2 (Invitrogen) by replacing the GAL1 promoter and the T7 promoter/primer sites with a STE2 promoter (0.42 kb), α factor leader (0.26 kb), FLAG tag, and a polylinker (EcoRI, XhoI, SmaI, BglII, BanIII, BamHI, ApaI, SalI, and SacII) at the position between the SpeI and NotI sites of pYES2. To express the human B2R, plasmid pYSF-B2R was created by inserting the B2R open reading frame into the EcoRI site of pYSF1. To express the murine B2R, plasmid pYSF-B2R was created by inserting the B2R open reading frame between the EcoRI and BamHI sites of pYSF1. To express the human AT1a angiotensin II receptor, plasmid pYSF-AT1a was created by inserting the AT1a open reading frame between the EcoRI and SalI sites of pYSF1. Preparation of the yeast competent cells and transformation was performed using a Fast-Yeast Transformation Kit (Geno Tech, Mo) according to the manufacturer's manual. Yeast expressing the two GPCRs was prepared by a co-transformation of the plasmids.

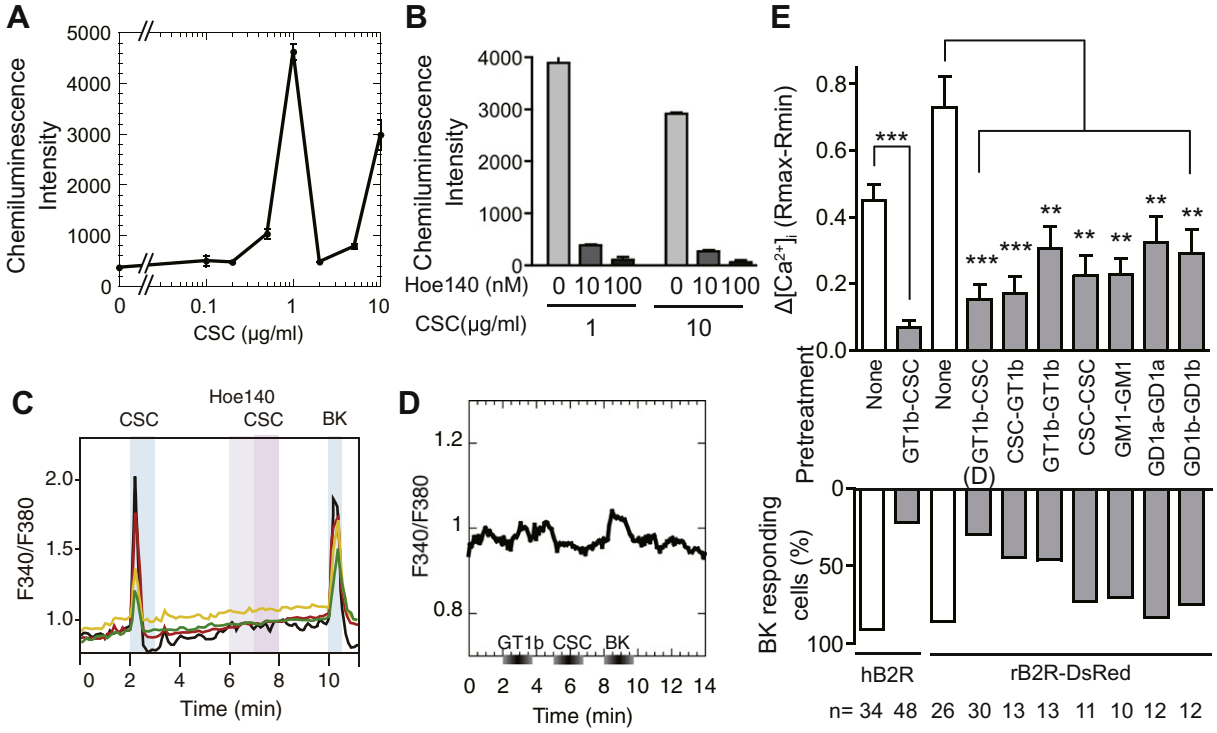

Fig. 1. B2R desensitization in non-neuronal cells after repeated treatment with gangliosides and CSC which stimulate B2R in neuronal cells and yeast cells. A, Activation of B2R signal by exogenously applied CSC in yeast reporter assay. Intensities of chemiluminescence produced by reporter β-galactosidase are shown as the reactivity. Error bar, standard error of three samples. B, Reactivity of 1 or 10 μg/ml of CSC to yeast expressing B2R was determined with or without Hoe140 at indicated concentrations. Blank value (without CSC) = 734 was subtracted from each value. Hoe140 significantly ($P < 0.05$) inhibited CSC induced B2R activities. C, NG108-15 neuroblastoma-glioma hybridoma cells were exposed to 1 μg/ml of CSC and 1 nM of B2 antagonist Hoe140 followed by CSC and 1 μM BK as indicated. Intracellular Ca^{2+} concentrations were monitored by fluorescence microscopy with Fura-2 as an indicator. Relative Ca^{2+} levels are expressed as a ratio of fluorescence at excitation wavelengths of 340–380 nm. D, CHO-K1 cells expressing DsRed-fused rat B2R (rB2R-DsRed) were exposed to 10 ng/ml GT1b, 1 μg/ml CSC, and 10 nM BK as indicated and intracellular Ca^{2+} concentrations were monitored as C. The average ratios of 30 individual cells are plotted. E, top, Peak increases in $[Ca^{2+}]_i$ of human B2R (hB2R) or rB2R-DsRed expressing CHO-K1 cells induced by 10 nM BK after indicated treatment as shown in D for example and without glycan treatment (None). Bottom, Percentage of BK-responding cells in among cells expressing EGFP or DsRed. *n*, numbers of cells analyzed. $^{***}P < 0.001$; $^{**}P < 0.01$.

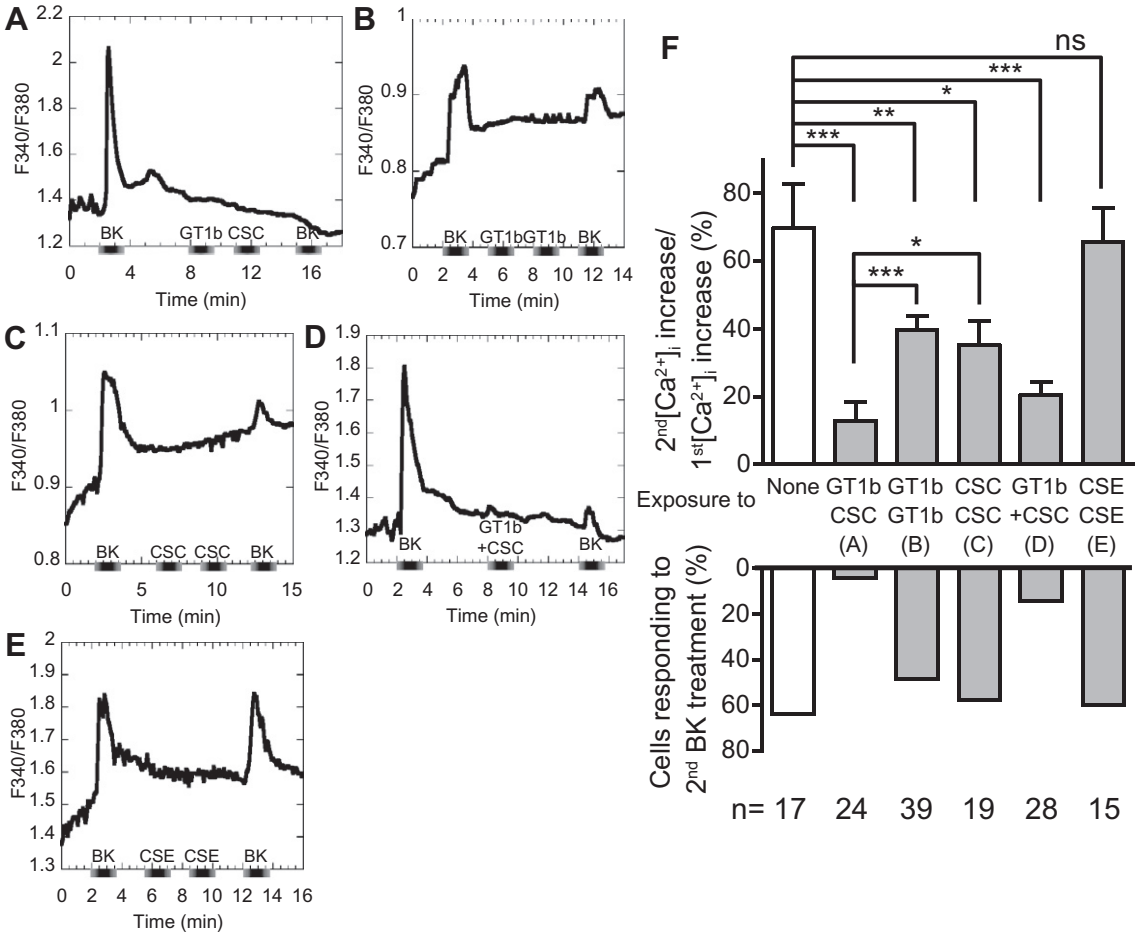

Fig. 2. B2R desensitization caused by repeated exposure to gangliosides and CSC. rB2R-DsRed was expressed in CHO-K1 (A, C, D, and E) and HEK293 (B) cells. The cells were exposed to 10 nM BK, 10 ng/ml GT1b, 1 μg/ml CSC, and 1 μg/ml CSE as indicated. The average ratios of individual cells that responded to the first BK treatment are plotted. Numbers of cells analyzed (*n*) are indicated in F. F, top, Percentage of peak increases in $[Ca^{2+}]_i$ induced by the second BK treatment. The percentage was calculated by dividing the peak increases in $[Ca^{2+}]_i$ induced by the second BK treatment by the peak increases in $[Ca^{2+}]_i$ induced by the first BK treatment (see A–E) and without glycan treatment (None). Bottom, Percentage of second BK-responding cells in among the first BK-responding cells. $^{***}P < 0.001$; $^{**}P < 0.01$; $^{*}P < 0.05$.

2.5. Yeast reporter assay for mammalian GPCR and ligand binding

The yeast cells (1×10^5) were suspended with ligands in a 40 μl SD-ura medium, pH 7.0, in 96-well flat-bottom white microplates. After incubation, (5 h at 30 °C), 40 μl of chemiluminescent substrate solution for the reporter β-galactosidase, and a Gal-Screen System for the yeast cell culture (Applied Biosystems) was added to the reaction mixture and incubated an additional 1 h. The chemiluminescence was determined using an Applied Biosystems TR717 Microplate Luminometer.

2.6. Ca^{2+} imaging

The Ca^{2+} indicator Fura-2 was loaded into cells as its acetoxymethyl ester (AM) derivative. A stock solution of 1 mM Fura-2-AM (Dojindo Labs., Kumamoto, Japan) in DMSO was diluted 400-fold into culture media and added to cells cultured on glass-bottom dishes (Asahi Glass Co., Tokyo, Japan). Cells were then incubated at 37 °C for 1–2 h to load and sensitize the Ca^{2+} probe through the cleaving of its AM group with cytosolic esterase. Images were acquired at emission wavelengths between 490 and 530 nm while exciting sequentially at 340 and 380 nm (exposure time: 0.1–2 s). The images were then analyzed as described previously [9,10] using an image processor (Aqua Q, Hamamatsu Photonics, Hamamatsu, Japan) connected to a cooled CCD camera (Orca, Hamamatsu Photonics).

Cells were exposed to stimulants by using the bath application method. Fura-2-loaded cells were conditioned with a flow of balanced salt solution (BSS), pH 7.3, consisting of 130 mM NaCl, 5.4 mM KCl, 20 mM HEPES, 5.5 mM glucose, 0.8 mM $MgSO_4$, and 1.8 mM $CaCl_2$ (1.75 ml/min) at 34 °C. The extracellular media in the assay dish was maintained at 1 ml. Thereafter, the cells were exposed to the stimulating reagent by changing the BSS flow to the reagent-containing BSS flow. After 1 min of exposure, the media was exchanged with BSS by changing the flow to BSS without the reagent. Thus, through this bath application method, the concentration of applied reagents reached maximum levels about 40 s after starting the application of the reagent and almost completely washed out about 40 s after the end of the application.

2.7. Other materials

Gangliosides were kindly provided by Dr. Yoshio Hirabayashi (Laboratory for Molecular Membrane Neuroscience, RIKEN Brain Science Institute, Wako, Saitama, Japan). Chondroitin sulfates were purchased from Seikagaku Co., Tokyo, Japan. BK and Hoe140, a B2-selective antagonist, were purchased from Peptide Institute Co., Osaka, Japan.

2.8. Statistical analysis

Results are presented as means ± SEM. The statistical significance between groups was assessed by 2-tailed unpaired Student's *t*-tests.

3. Results

3.1. Effects of chondroitin sulfates on B2R signaling in yeast and neuronal cells

We previously found that nanomolar levels of b-series gangliosides such as GT1b and GD1b induce Ca^{2+} release in neuronal cells [2] and we recently have found that around 10 nM of these gangliosides stimulate B2R signals in neuronal cells as well as in yeast cells expressing mammalian B2R [11]. As chondroitin sulfate is another acidic glycan widely distributed in mammalian body and plays neuro-regulatory roles like gangliosides, we first screened if chondroitin sulfate activate B2R in yeast reporter assay in which a yeast pheromone receptor, Ste2, was replaced with mammalian GPCR and the mammalian GPCR signal was linked via a chimeric yeast/mammalian Gα protein to the yeast pheromone receptor signaling pathway constructed to express reporter β-galactosidase. We tested commercially obtained chondroitin sulfate samples and found that chondroitin sulfate C and E activate B2R signals in all the B2R expressing yeast clones being CSC most potent (Fig. S1). Yeast coexpressing B2R and AT1a angiotensin II receptor, which form heterodimers with B2R [12], reacted better than yeast expressing solely B2R. Using one of the coexpressing clones, GqAB14, we examined dose–response of CSC and found that CSC showed at least two peaks of effective concentrations, around 1 μg/ml and over 10 μg/ml (Fig. 1A). CSC induced activation was inhibited by B2 antagonist Hoe140. Hoe140 at 10 and 100 nM reduced 1 and 10 μg/ml of CSC activities in similar degrees (Fig. 1B) suggesting that CSC is unlikely to compete with Hoe140 for B2R binding. Thus, we decided to use 1 μg/ml of CSC for the further experiments to avoid unexpected physicochemical effects by the strong acidity of the sulfate groups possibly brought by higher concentrations of CSC. We then examined the effect of CSC on a neuronal cell line, NG108-15 neuroblastoma-glioma hybridoma cells, which respond to GT1b by releasing Ca^{2+} [2]. CSC induced transient increase of intracellular Ca^{2+} levels as seen in ganglioside exposure and the reaction was inhibited when the cells were pretreated with Hoe140 (Fig. 1C). Thus, the effects of CSC on NG108-15 cells were similar to GT1b.

3.2. Reduced response of B2R to BK after repeated treatment with gangliosides and CSC

As shown previously [2] and above, neuronal cells respond to gangliosides and CSC in a similar way, we examined effects of those glycans on B2R exogenously introduced to CHO-K1 cells, which express undetectable levels of endogenous B2R, or to HEK293 cells, around 10% of which express endogenous B2R. As effective concentration ranges observed with neuronal cells and yeast reporter assay is around 10 ng/ml for GT1b and GD1b [2,11], and 1 μg/ml for CSC, we tested the effects of the glycans at these concentrations.

Treating B2R-overexpressing CHO-K1 and HEK293 cells with 10 nM BK transiently increased intracellular Ca^{2+} levels. Repeated treatment with BK caused the cells to become desensitized to BK. Human B2R, rat B2R, and DsRed-fused rat B2R were activated and desensitized. When the cells were pretreated sequentially with 10 ng/ml GT1b and 1 μg/ml CSC, 70–78% of the cells stopped responding to 10 nM BK (Fig. 1D, E). However, when the cells were exposed once to either of these two glycans, the cells still responded to BK and displayed increased Ca^{2+} levels (data not shown). The reversed sequential treatment—exposing the cells first to CSC and then to GT1b—also caused the cells to become desensitized to BK (Fig. 1E). The same occurred with repeated treatments with either GT1b or CSC (Fig. 1E). These results indicated that

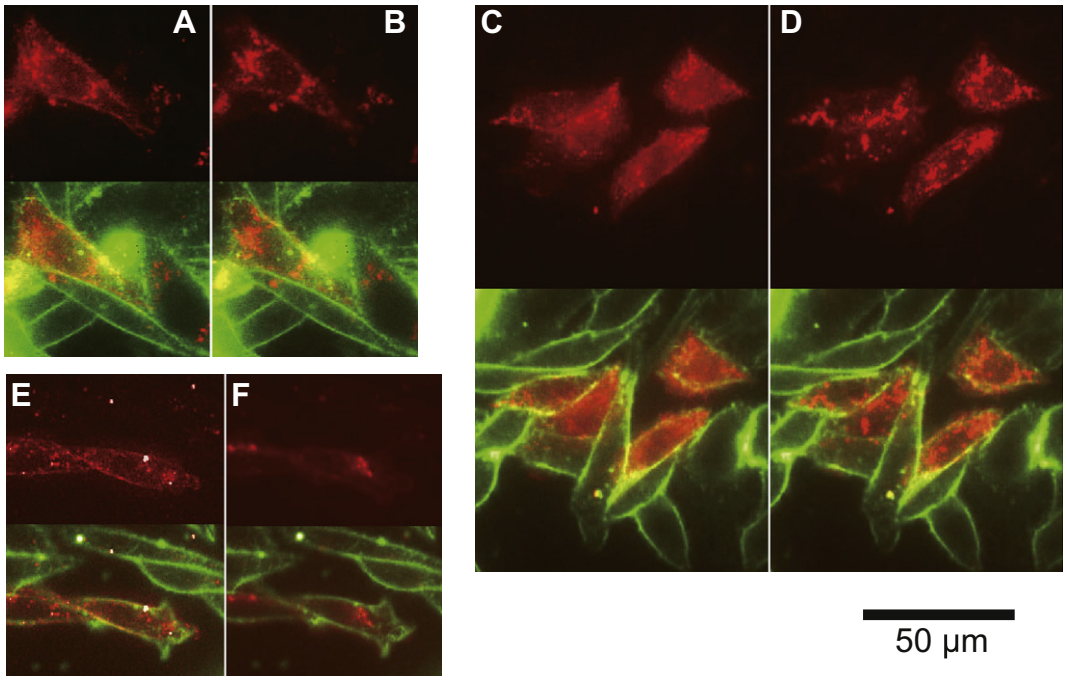

Fig. 3. Expression pattern of rat B2R-DsRed in CHO-K1 cells before and after B2R desensitization. Cells before (A, C, and E) and after sequential exposure to 10 nM BK, 10 ng/ml GT1b, and 1 μg/ml CSC (B, D, and F) of DsRed images. Plasma membrane was stained with a lipophilic styryl dye MF43-1FX (Molecular Probes) after the treatment per the manufacturer's instructions. Fluorescence images were obtained at an excitation wavelength of 560 nm for the DsRed and of 485 nm for MF43-1FX. Top and bottom of each figures are DsRed image (red) and DsRed image merged with MF43-1FX image (green), respectively. Scale bar, 50 μm.

repeated treatment with glycans induced B2R desensitization. We also examined the effects of other related glycans and found that GM1, GD1a, and GD1b affected the cells similarly to GT1b (Fig. 1E).

To verify that the B2R-expressing cells are capable of responding to BK before glycan treatment, we exposed the cells first to 10 nM BK, treated them sequentially with glycans (GT1b and CSC), and then exposed them a second time to BK (Fig. 2). More than 95% of the cells failed to respond to BK after the sequential GT1b–CSC treatment (Fig. 2A, F). Exposing the cells to the GT1b–CSC mixture similarly reduced BK reactivity (Fig. 2D, F). Exposing the cells twice to either GT1b or CSC also reduced BK reactivity, but the effects were weaker than those observed when cells were exposed sequentially to each glycan (Fig. 2B, C, F). In contrast to CSC, chondroitin sulfate E (CSE) was not effective in reducing BK reactivity (Fig. 2E, F), indicating that glycan structure, not acidity, determines whether a glycan desensitizes B2Rs to BK.

3.3. Internalization of B2R by ganglioside or CSC treatment

Fluorescent microscopic images of cells expressing rat B2R-DsRed revealed that some B2R-DsRed were distributed across cell surfaces (Fig. 3A, C, E). After desensitization with gangliosides and CSC, cell-surface fluorescence disappeared; however, the fluorescence intensity of small vesicle-like structures in the cytosol increased (Fig. 3B, D, F). These results suggested that the repeated glycan treatment caused B2R-DsRed to be internalized.

3.4. Glycan-induced internalization probably depends on GPCR receptor kinase (GRK)

Truncated rat B2R mutant (B2RΔE1), which lacks the first extracellular domain, cannot be desensitized and internalized, as it cannot be phosphorylated by GRK [6]. All the cells expressing B2RΔE1-DsRed responded to BK stimulation and released Ca^{2+}, even after repeated GT1b and CSC treatment, without significant reduction of the response (Fig. 4). Thus, gangliosides and CSC desensitized B2R most likely by stimulating GRK-mediated B2R phosphorylation.

4. Discussion

We here demonstrated that ganglioside and CSC application to non-neuronal cells that express the BK B2 receptor desensitizes and internalizes B2Rs without inducing Gαq/11 protein-mediated Ca^{2+} release.

GPCRs constitute the largest family of proteins that convert external stimuli into intracellular activity [13]. Signal transduction of GPCRs is tightly controlled: Prolonged or repeated agonist stimulation desensitizes and internalizes these receptors such that ligands cannot access the receptors [14,15]. This modulatory process seems to involve agonist-induced receptor phosphorylation [16–18]. In the present study, although gangliosides and CSC stimulated the desensitization and internalization of B2R, they

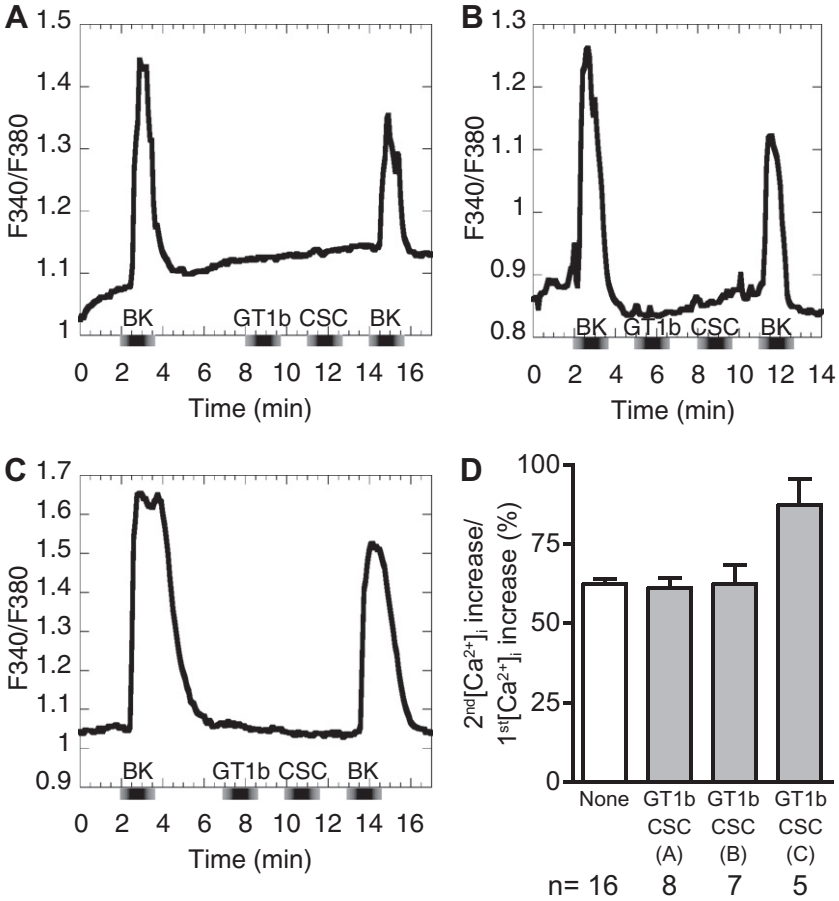

Fig. 4. Sequential glycan treatment failed to desensitize a B2R mutant lacking the first extracellular domain. A DsRed-fused rat B2R mutant lacking the first extracellular domain (B2RΔE1-DsRed) was expressed in CHO-K1 (A, B) and HEK293 (C) cells. The cells were exposed to 10 nM BK, 10 ng/ml GT1b, and 1 μg/ml CSC as indicated. The average ratios of individual cells are plotted. Numbers of cells analyzed (*n*) are indicated in D. All the cells that responded to the first BK stimulation also responded to the second BK stimulation. D, Percentage of peak increases in $[Ca^{2+}]_i$ induced by the second BK treatment over those induced by the first BK treatment of A–C (GT1b/CSC) and without glycan treatment (None).

failed to activate G-protein-coupled phospholipase and subsequent Ca^{2+} release (Figs. 1 and 2). Because a B2R mutant unable to activate GRK was not desensitized and internalized by gangliosides and CSC (Fig. 4), the glycan-stimulated desensitization and internalization of B2R seems to involve B2R phosphorylation followed by β-arrestin recruitment, as in the case of agonist-induced receptor desensitization and internalization.

Among the glycans we tested, the GT1b and CSC combination seemed to be the most potent and effective in desensitizing and internalizing B2Rs. However, even though we examined the individual effects of several glycans, we tested only a few glycan combinations.

The B2 antagonist Hoe140 (at 100 nM) showed little, if any, effects on glycan-stimulated desensitization and internalization (data not shown), also suggesting that the glycan-induced B2R desensitization was not accompanied by B2R activation.

B2R participates in the regulation of blood pressure, inflammation, and pain. B2Rs are distributed ubiquitously in cells throughout the body, including neuronal tissues. Gangliosides and chondroitin sulfates also are distributed not only in neuronal tissues but also throughout the body. These glycans probably regulate B2R function. Recently, we determined that b-series gangliosides such as GT1b and GD1b generate and enhance pain [19]. Unlike b-series gangliosides, a-series gangliosides such as GM1 and GD1a do not generate and enhance pain [19]. As GM1 and GD1a stimulated B2R desensitization in the present study, these gangliosides and CSC may play a role in pain relief through B2R desensitization.

We previously found that b-series gangliosides induce Ca^{2+} release in neuronal cells [2] and we recently have found that ganglioside GT1b stimulate B2R signals in neuronal cells as well as in yeast cells expressing mammalian B2R [11]. The present study using B2R-expressing non-neuronal cells did not produce such results. Thus, it remains unclear whether B2Rs directly participate in ganglioside-mediated neuronal cell excitation. This issue will be addressed in a future study. In neuronal cells, another factor may mediate ganglioside-associated regulation of G-protein-coupled signaling.

Acknowledgments

We thank Dr. Yoshio Hirabayashi (Laboratory for Molecular Membrane Neuroscience, RIKEN Brain Science Institute, Wako, Saitama, Japan) for the generous gift of various gangliosides.

Appendix A. Supplementary data

Supplementary data associated with this article can be found, in the online version, at doi:10.1016/j.bbrc.2012.02.142.

References

[1] L.M. Leeb-Lundberg, F. Marceau, W. Muller-Esterl, D.J. Pettibone, B.L. Zuraw, International union of pharmacology. XLV. Classification of the kinin receptor family: from molecular mechanisms to pathophysiological consequences, Pharmacol. Rev. 57 (2005) 27–77.
[2] N. Chen, S. Furuya, H. Doi, Y. Hashimoto, Y. Kudo, H. Higashi, Ganglioside/calmodulin kinase II signal inducing cdc42-mediated neuronal actin reorganization, Neuroscience 120 (2003) 163–176.
[3] E.Y. Chen, D.F. Emerich, R.T. Bartus, J.H. Kordower, B2 bradykinin receptor immunoreactivity in rat brain, J. Comp. Neurol. 427 (2000) 1–18.
[4] R. Kozma, S. Ahmed, A. Best, L. Lim, The Ras-related protein Cdc42Hs and bradykinin promote formation of peripheral actin microspikes and filopodia in Swiss 3T3 fibroblasts, Mol. Cell. Biol. 15 (1995) 1942–1952.
[5] T. Yamashita, Y.P. Wu, R. Sandhoff, N. Werth, H. Mizukami, J.M. Ellis, J.L. Dupree, R. Geyer, K. Sandhoff, R.L. Proia, Interruption of ganglioside synthesis produces central nervous system degeneration and altered axon-glial interactions, Proc. Natl. Acad. Sci. USA 102 (2005) 2725–2730.
[6] S. AbdAlla, E. Zaki, H. Lother, U. Quitterer, Involvement of the amino terminus of the B(2) receptor in agonist-induced receptor dimerization, J. Biol. Chem. 274 (1999) 26079–26084.
[7] R. Rothstein, Targeting, disruption, replacement, and allele rescue: integrative DNA transformation in yeast, Methods Enzymol. 194 (1991) 281–301.
[8] A.J. Brown, S.L. Dyos, M.S. Whiteway, J.H. White, M.A. Watson, M. Marzioch, J.J. Clare, D.J. Cousens, C. Paddon, C. Plumpton, M.A. Romanos, S.J. Dowell, Functional coupling of mammalian receptors to the yeast mating pathway using novel yeast/mammalian G protein alpha-subunit chimeras, Yeast 16 (2000) 11–22.
[9] Y. Kudo, A. Ogura, Glutamate-induced increase in intracellular Ca^{2+} concentration in isolated hippocampal neurons, Br. J. Pharmacol. 89 (1986) 191–198.
[10] N. Chadborn, B. Eickholt, P. Doherty, S. Bolsover, Direct measurement of local raised subplasmalemmal calcium concentrations in growth cones advancing on an N-cadherin substrate, Eur. J. Neurosci. 15 (2002) 1891–1898.
[11] Y. Kanatsu, N.H. Chen, J. Mitoma, T. Nakagawa, Y. Hirabayashi, H. Higashi, Gangliosides stimulate bradykinin B2 receptors to promote calmodulin kinase II-mediated neuronal differentiation, J. Biochem. in press.
[12] S. AbdAlla, H. Lother, U. Quitterer, AT1-receptor heterodimers show enhanced G-protein activation and altered receptor sequestration, Nature 407 (2000) 94–98.
[13] E.J. Neer, Heterotrimeric G proteins: organizers of transmembrane signals, Cell 80 (1995) 249–257.
[14] S.S. Ferguson, Evolving concepts in G protein-coupled receptor endocytosis: the role in receptor desensitization and signaling, Pharmacol. Rev. 53 (2001) 1–24.
[15] R.J. Lefkowitz, G protein-coupled receptors. III. New roles for receptor kinases and beta-arrestins in receptor signaling and desensitization, J. Biol. Chem. 273 (1998) 18677–18680.
[16] S.K. Bohm, E.F. Grady, N.W. Bunnett, Regulatory mechanisms that modulate signalling by G-protein-coupled receptors, Biochem. J. 322 (Pt 1) (1997) 1–18.
[17] N.J. Freedman, R.J. Lefkowitz, Desensitization of G protein-coupled receptors, Recent Prog. Horm. Res. 51 (1996) 319–353.
[18] J.G. Krupnick, J.L. Benovic, The role of receptor kinases and arrestins in G protein-coupled receptor regulation, Annu. Rev. Pharmacol. Toxicol. 38 (1998) 289–319.
[19] S. Watanabe, K. Tan-No, T. Tadano, H. Higashi, Intraplantar injection of gangliosides produces nociceptive behavior and hyperalgesia via a glutamate signaling mechanism, Pain 152 (2011) 327–334.

Biochemical and Biophysical Research Communications 420 (2012) 199–204

Contents lists available at SciVerse ScienceDirect

Biochemical and Biophysical Research Communications

journal homepage: www.elsevier.com/locate/ybbrc

Rapamycin suppresses the recurrent excitatory circuits of dentate gyrus in a mouse model of temporal lobe epilepsy

Haiyun Tang [a], Hongyu Long [a], Chang Zeng [a], Yi Li [a], Fangfang Bi [a], Jinhui Wang [b], Hao Qian [b], Bo Xiao [a,*]

[a] Department of Neurology, Xiangya Hospital, Central South University, Changsha, Hunan 410008, China
[b] State Key Lab for Brain and Cognitive Sciences, Institute of Biophysics, Chinese Academy of Sciences, Beijing, China

ARTICLE INFO

Article history:
Received 22 February 2012
Available online 3 March 2012

Keywords:
Dentate gyrus
Epilepsy
Mouse
Rapamycin
Whole cell patch clamp

ABSTRACT

Recurrent excitatory circuits and abnormal recurrent excitatory inputs are essential in epileptogenesis. Studies in temporal lobe epilepsy have shown that mossy fiber sprouting, which represents synaptic reorganization, renders the formation of abnormal recurrent excitatory circuits and inputs. The mammalian target of rapamycin (mTOR) pathway has recently been proved important in mossy fiber sprouting. In the present study, rapamycin, a mTOR inhibiter, was injected into the mouse of temporal lobe epilepsy. Electrophysiological and histological properties of the hippocampus were investigated by whole cell patch clamp, extracellular recording and Timm staining. Following the development of epilepsy, frequency of spontaneous excitatory postsynaptic currents (EPSCs) and amplitude of antidromically evoked EPSCs in granule cells were remarkably increased, as well as the epileptiform activity and mossy fiber sprouting were detected, which indicated the formation of abnormal recurrent excitatory circuits. By the use of rapamycin, frequency of spontaneous EPSCs, amplitude of antidromically evoked EPSCs, the epileptiform activity and mossy fiber sprouting were all remarkably suppressed. Our findings suggested an anti-epileptogenic role of rapamycin by suppressing the recurrent excitatory circuits of dentate gyrus.

1. Introduction

Epilepsy, one of the most common neurological diseases that lead to significant morbidity and mortality, affects around 1% of the world's population (WHO, 2005). The traditional antiepileptic drugs (AEDs), such as phenytoin, valproate and carbamazepine, have been aimed mainly to suppress seizure activity, but not to correct the underlying brain abnormalities that cause epilepsy [1]. Hence new strategies that are not just "anti-seizure" but truly "anti-epileptogenic" are anticipated to prevent or further reverse epileptogenesis [2].

Mammalian target of rapamycin (mTOR), a serine–threonine protein kinase, regulates intracellular responses to different extracellular stimuli or intracellular signals [3,4]. In the brain, mTOR regulates neuronal differentiation, axon growth, dendritic arborization, synaptic plasticity, as well as neuronal survival [5–8]. Accumulative studies have shown the possible involvement of mTOR pathway in epileptogenesis of various kinds of epilepsy including both genetic and acquired ones [9–15]. In the tuberous sclerosis complex (TSC) and cortical dysplasia models, mTOR is over-activated, and rapamycin, the mTOR inhibitor, can reverse the underlying brain abnormalities associated with epileptogenesis [9,10,14,15]. Rapamycin treatment in kainite or pilocarpine induced status epilepticus model prevents the inappropriate mTOR activation and decreases hippocampal neuronal death, neurogenesis, and axonal sprouting, in addition to the decreased seizure activity including seizure frequency and duration [11–13]. These studies suggest that rapamycin has anti-epileptogenic actions; however, it remains controversial. There is a recent study which demonstrates that rapamycin suppresses mossy fiber sprouting without reducing seizure frequency in a mouse model of temporal lobe epilepsy [16]. Obviously, further studies are required to clarify the role of mTOR pathway in epileptogenesis.

In the present study, we investigated the epileptogenic role of mTOR pathway in temporal lobe epilepsy by electrophysiological technology for the first time. It is widely considered that mossy fiber sprouting is related to the development of recurrent excitatory circuits in dentate gyrus, which may alter the normal gating function of the dentate gyrus and trigger seizures [17–20]. We tested the hypothesis that rapamycin would prevent mossy fiber sprouting and further suppress the electrophysiological events

Abbreviations: EPSC, excitatory postsynaptic current; IML, inner molecular layer; MFS, mossy fiber sprouting; mTOR, mammalian target of rapamycin; PILO, pilocarpine; Rap, rapamycin; SE, status epilepticus; TLE, temporal lobe epilepsy; Veh, vehicle.

* Corresponding author.
E-mail address: xiaobo62_xy@yahoo.com.cn (B. Xiao).

0006-291X/$ - see front matter © 2012 Elsevier Inc. All rights reserved.
doi:10.1016/j.bbrc.2012.02.143

suggestive of recurrent excitatory circuits in the hippocampal granule cell layer (e.g., [19,20]).

2. Materials and methods

2.1. Animals and drug treatment

Young adult male mice (C57BL/6, 6–8 weeks of age, weighing 20–25 g) were purchased from Experimental Animal Center (Central South University, Changsha, Hunan, China). The animals were randomly allocated to four group: sham-control group (treated with saline, A), positive-control group (treated with PILO, B), vehicle group (treated with PILO + Veh, C), and rapamycin group (treated with PILO + Rap, D). Following the typical protocol used previously by our group [21], scopolamine methyl nitrate (Sigma, St. Louis, MO) was given initially (1 mg/kg, i.p.), and pilocarpine (PILO) (Sigma, St. Louis, MO) was administrated 30 min later (300–320 mg/kg, i.p.) in group B, C, and D. After the PILO injection, animals were monitored for a minimum of 5 h to assess the severity and duration of the behavioral seizures. Diazepam (10 mg/kg, i.p.) was administered 2 h after the onset of stage 3 or greater seizures, according to Racine's standard classification [22]. Group A were also given the same drugs as above, except saline was used instead of PILO.

Rapamycin (LC Labs) was initially dissolved in 100% ethanol, stored at −20 °C, and diluted in a vehicle solution containing 5% Tween 80, 5% PEG 400, and 4% ethanol immediately before injection. Rapamycin (6 mg/kg d, i.p.) for rapamycin group and vehicle (of same volume) for vehicle group were injected 24 h after the onset of PILO induced status epilepticus for 6 consecutive days, then the injection was given every other day until the end of the study [11]. The procedures were approved by The Animal Ethics Committee of Central South University in China.

3. Electrophysiology

3.1. Preparation and incubation of hippocampal slices

In our previous study [21], by 8 weeks after PILO induced status epilepticus, the majority of the animals had developed spontaneous seizures, and the recurrent excitatory circuits had been constructed for electrophysiological study. Eight mice for each group were deeply anesthetized by chloral hydrate (300 mg/kg) and quickly decapitated. The brains were placed in the oxygenated (95% O_2 and 5% CO_2) ice-cold artificial CSF (ACSF) containing the following reagents (in mM): choline chloride 110, KCl 2.5, NaH_2PO_4 1.3, $NaHCO_3$ 25.0, $CaCl_2$ 0.5, $MgCl_2$ 7, glucose 20, Na-ascorbate 1.3, and Na-pyruvate 0.6. Coronal slices (300 μm thick) were cut using a Leica VT1000S vibratome, and were incubated in the oxygenated (95% O_2 and 5% CO_2) ACSF composed of the following reagents (in mM): NaCl 125, KCl 2.5, NaH_2PO_4 1.3, $NaHCO_3$ 25, $CaCl_2$ 2, $MgCl_2$ 1.3, Na-ascorbate 1.3, Na-pyruvate 0.6, and glucose 10. After recovery at room temperature for at least 1 h, the slices were transferred to the recording chamber.

3.2. Recording methods

Recordings were performed using MultiClamp-700B and inputted into pClamp9 with 50 kHz sampling rate (Axon Instrument Inc., Foster CA, USA). Transient capacitance was compensated, and output bandwidth filter was 3 kHz. The pipettes (6–8 MΩ) for whole cell recordings were filled with the standard solution that contained (mM) 150 K-gluconate, 5 NaCl, 0.4 EGTA, 4 Mg-ATP, 4 Na-phosphocreatine, 0.5 Tris–GTP and 10 HEPES (pH 7.4 adjusted by 2 M KOH). Fresh pipette solution was filtered with centrifuge filters (0.1 μm pores) before use and the osmolarity was 295–305 mOsm. The pipettes (2–6 MΩ) for extracellular recordings were filled with 1 M NaCl.

Whole cell recordings were performed from dentate granule cells for the spontaneous excitatory postsynaptic currents (EPSCs). The sEPSCs were recorded at resting membrane potential under gap-free mode for 5 min, and only cells with V_m that was more negative than −60 mV on break-in were accepted [20]. Series resistance ranged between 10 and 20 MΩ, and the results were deleted if the access resistance changed >20%. Every detected event was examined, and only sEPSCs, characterized by a typical fast raising phase and slow decay phase, were included in the analysis [20]. Recording and analysis of the electrophysiological data were done by an investigator without knowledge of the treatment.The antidromically evoked EPSCs were recorded in the dentate gyrus with an electrode antidromically stimulating the mossy fibers. The bipolar stimulating electrode (WPIA360) was placed in stratum lucidum of area CA3b > 100 μm from the opening of the dentate hilus. Then, an extracellular recording electrode was used to probe for the location in the granule cell body layer where the antidromic population spike was of maximal amplitude. With the extracellular recording electrode positioned at this location, the stimulating electrode was moved perpendicularly to the pyramidal cell body layer until the stimulation evoked an antidromic population spike of the greatest possible amplitude. The final optimization of the antidromic population spike amplitude was achieved by adjusting the depth of both the stimulating and recording electrodes [23]. The stimulus current was set to 50% maximal value (5 mA), and rectangular pulses of 100 μs duration were applied every 30 s. Following this, whole cell patch-clamp recordings were made from dentate granule cells located close to the extracellular recording electrode. The antidromically evoked EPSCs were studied at a holding potential of −70 mV in the presence of 30 μM bicuculline methiodide (Sigma, St. Louis, MO) to block inhibitory postsynaptic currents. Every cell was recorded for ten responses, and the amplitude was the average of 10 responses.To observe epileptiform activity, extracellular recordings were performed with the recording pipette placed into the granule cell layer. The bipolar stimulating electrode was placed in the CA3b to evoke population spikes. The stimulus current was set to maximal value (10 mA). Recordings were initially obtained in normal ACSF. Slices that did not represent epileptiform activity would bath in 30 μM bicuculline and 6 mM potassium.

3.3. Timm staining

The slices used for electrophysiological recordings from each group were used for observing mossy fiber sprouting (MFS) in inner molecular layer (IML) with Timm staining. The slices were incubated in 0.4% Na_2S in a 0.1 M phosphate buffer for 15 min, and fixed with 4% paraformaldehyde in 0.1 M phosphate buffer over night. Then, the slices were resectioned at 30 μm on a cryostat, mounted on slides, and stained in 60 ml of 50% gum arabic, 10 ml of 2 M citrate buffer, 30 ml of 0.5 M hydroquinone, and 0.8–1.2 ml of 17% silver nitrate. After washing, sections were dehydrated in alcohol, cleared in xylene, and mounted on slides with permount. Images were acquired using Nikon eclipse TE 2000-E (400×). Mossy fiber sprouting was assessed according to previously published criteria [24]. The Timm scores of the brain sections were evaluated by an investigator blinded to the experimental conditions.

3.4. Statistical analysis

Statistical analysis was performed with SPSS version 13.0 (SPSS Inc, Chicago, IL, USA). Data were expressed as mean ± SD.

Differences between multiple groups were assessed by one-way ANOVA. Cumulative frequency distributions of spontaneous EPSCs were compared using the Kolmogorov–Smirnov (KS) two-sample test. $P < 0.05$ was considered statistically significant.

4. Results

4.1. Rapamycin attenuates the increase of frequency of spontaneous EPSCs in granule cells

Previous studies have proposed that the frequency of spontaneous EPSCs (sEPSCs) in granule cells increased with time after kainite treatment, suggesting an increase in excitatory synaptic input to granule cells [20]. To know whether inhibition of mTOR pathway could block the increase of frequency of sEPSCs, whole cell recordings were performed in granule cells at their resting membrane potential from saline treated mice ($n = 16$ granule cells, 8 mice), PILO treated mice ($n = 18$ granule cells, 8 mice), PILO + Veh treated mice ($n = 16$ granule cells, 8 mice) and PILO + Rap treated mice ($n = 18$ granule cells, 8 mice). The frequency of sEPSCs was demonstrated by inter-event intervals indirectly, and a shorter inter-event interval is associated with higher frequency. Cumulative distributions of inter-event intervals were constructed for each group and compared using the Kolmogorov–Smirnov (KS) two-sample test (Fig. 1E). The average frequency of each group was also calculated directly and compared using one-way ANOVA (Fig. 1F). The results showed that the PILO treated mice had a much higher frequency of sEPSCs compared with the saline treated ones ($P < 0.001$, Fig. 1A&A1, B&B1, E, F). PILO + Rap treated mice had a much lower frequency of sEPSCs compared with the PILO + Veh treated ones ($P < 0.001$, Fig. 1C&C1, D&D1, E, F). Saline treated mice and PILO + Rap treated mice were not statistically different. These results suggested that rapamycin attenuates the increase of frequency of spontaneous EPSCs in granule cells.

4.2. Rapamycin decreases the amplitude of antidromically evoked EPSCs in granule cells

We recorded 26 cells from PILO treated mice, with 19 cells responding to antidromically evoked mossy fibers, and 29 cells from saline treated mice with 13 cells responding. Thus, antidromically evoked EPSCs were more frequently observed in PILO treated mice (73.1%) than saline treated ones (44.8%). The average amplitude of antidromically evoked EPSCs from PILO treated mice was 141.7 pA, about three times as large as saline treated mice, which was 38.9 pA ($P < 0.001$, Fig. 2E). Antidromic stimulation of the mossy fibers evoked EPSCs in 19 of 27 granule cells from PILO + -Veh treated mice, in contrast to the 24 of 26 granule cells from PILO + Rap treated mice. The response rate was 70.4% and 92.3% for PILO + Veh and PILO + Rap treated mice respectively. Therefore, rapamycin did not decrease the frequency of antidromically evoked EPSCs. On the other hand, the average amplitude of antidromically evoked EPSCs from PILO + Veh treated mice was 164.1 pA, compared with 55.4 pA from PILO + Rap treated mice (the difference was high significant, $P < 0.001$, Fig. 2E). In summary, rapamycin decreases the amplitude of antidromically evoked EPSCs after status epilepticus.

4.3. Rapamycin suppresses the epileptiform activity under the conditions of reduced inhibition and increased extracellular potassium

Mossy fiber sprouting is often considered to form new recurrent excitatory circuits to facilitate epilepsy. We detected epileptiform activity, which was defined as repetitive firing of population spikes, in the dentate gyrus by antidromic stimulation of mossy fiber in CA3b area. In normal ACSF, neither the slices from saline treated mice nor the ones from PILO treated mice exhibited epileptiform activity. However, in perfusion with 30 μM bicuculline and 6 mM potassium, 3 of 8 mice from the PILO treated group showed

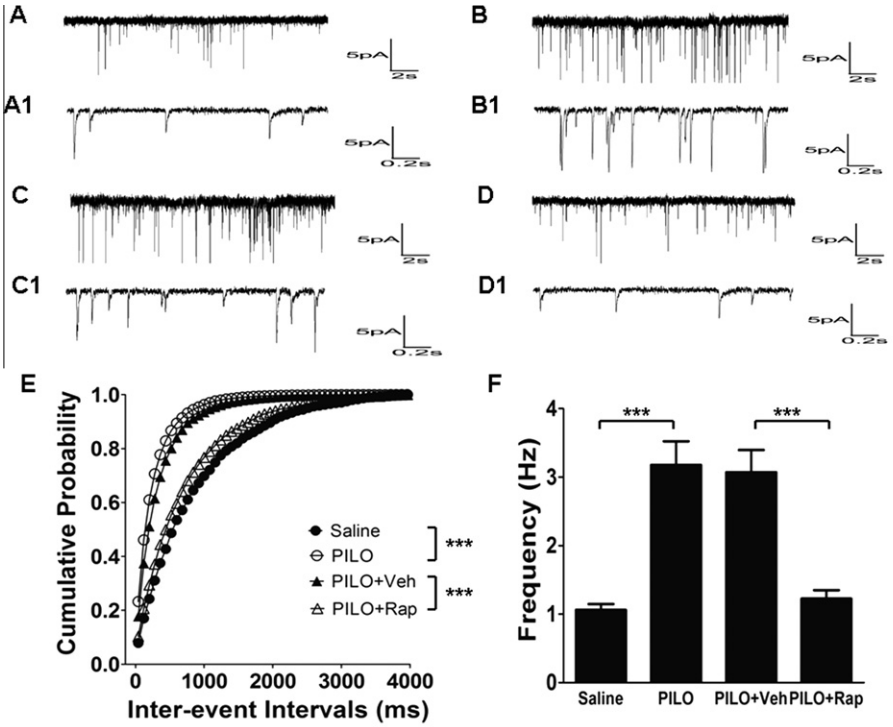

Fig. 1. Representative recordings of spontaneous EPSCs in granule cells. (A&A1) Saline treated mice. (B&B1) PILO treated mice. (C&C1) PILO + Veh treated mice. (D&D1) PILO + Rap treated mice. (E) Cumulative probability plot of inter-event intervals and (F) the average frequency of sEPSCs revealed an increased frequency of sEPSCs from PILO treated mice compared with saline treated ones. Rapamycin attenuated the increase of frequency in granule cells (Kolmogorov–Smirnov (KS) two-sample test for E, one-way ANOVA for F, $^{*}P < 0.05$, $^{**}P < 0.01$, $^{***}P < 0.001$).

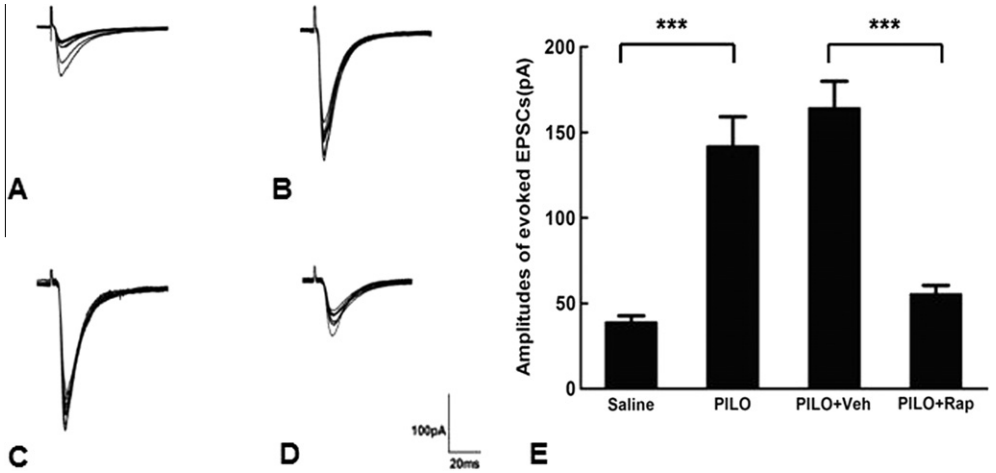

Fig. 2. Examples of antidromically evoked EPSCs. Ten responses were recorded for each cell. (A) Saline treated mice. (B) PILO treated mice. (C) PILO + Veh treated mice. (D) PILO + Rap treated mice. (E) The average amplitude of antidromically evoked EPSCs for each group. Rapamycin significantly decreased the amplitude of antidromically evoked EPSCs in granule cells (***$P < 0.001$ by one-way ANOVA).

epileptiform activities consisting of four to five population spikes, while none of the saline treated mice exhibited epileptiform activities (Fig. 3A, B). In vehicle and rapamycin group, none manifested epileptiform activity in normal ACSF. But in perfusion with 30 μM bicuculline and 6 mM potassium, 2 of 8 mice from PILO + Veh treated group expressed epileptiform activities, compared with 4 of 8 mice from PILO + Rap treated group expressed two population spikes with a much smaller second one (Fig. 3C, D). Statistical analysis of the number of population spikes indicated that rapamycin suppresses the epileptiform activity in perfusion with reduced inhibition and increased extracellular potassium (Fig. 3E).

4.4. Inhibition of mTOR pathway reduces mossy fiber sprouting in IML

Mossy fiber sprouting (MFS) develops gradually in a period of weeks to months after status epilepticus. Timm staining was conducted to test whether rapamycin could reduce MFS 8 weeks after status epilepticus. We observed an extensive sprouting of mossy fibers in the dentate gyrus in PILO treated mice (Fig. 4A&A1, B&B1), especially in the slices showing epileptiform activity. Rapamycin treatment significantly attenuated the MFS, while vehicle treatment did not alter the intense MFS (Fig. 4C&C1, D&D1). Quantitative analysis by assessing the score of MFS also confirmed that the severity of MFS was significantly reduced in the rapamycin treated group (Fig. 4E).

5. Discussion

mTOR pathway was chronically activated after PILO induced status epilepticus, and rapamycin inhibited the activation of mTOR pathway in the present study (Supplementary, Fig. 1), which is consistent with previous study [9–15]. The role of mTOR pathway in epileptogenesis has been demonstrated on histology and behavior [9–15]. Zeng et al. observed that rapamycin treatment could inhibit several major aspects of epileptic histopathology, including neuronal degeneration, mossy fiber sprouting, and neurogenesis. Rapamycin treatment before status epilepticus could block epilepsy [11]. Huang et al. also demonstrated the potential role

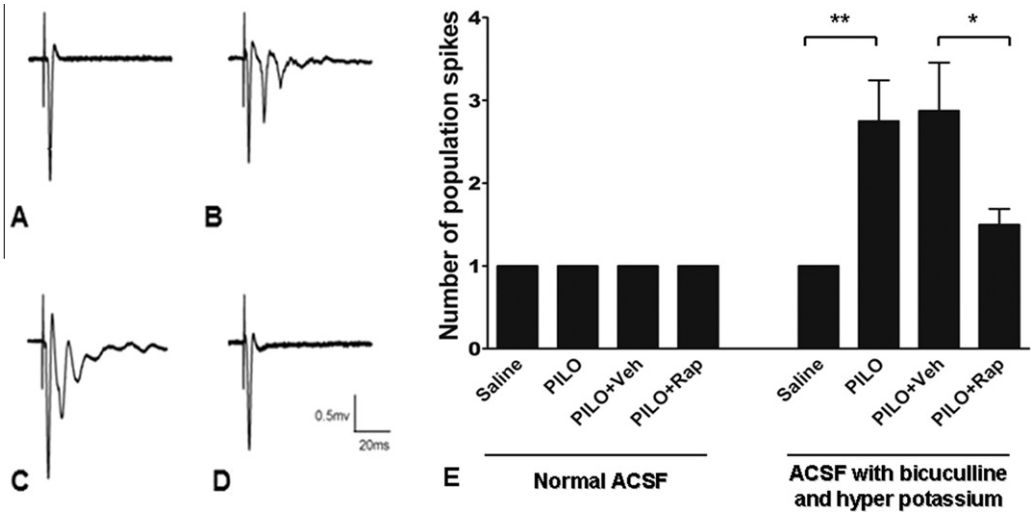

Fig. 3. Examples of extracellular recordings in the granule cell layer by antidromical stimulation to the mossy fibers in perfusion with 30 μM bicuculline and 6 mM potassium. (A) Saline treated mice showed an isolated population spike. (B) PILO and (C) PILO + Veh treated mice showed epileptiform activity (more than three population spikes). (D) PILO + Rap treated mice showed two population spikes with a second, much smaller one. (E) Statistical analysis of the number of population spikes indicated that rapamycin suppresses the epileptiform activity in reduced inhibition and increased extracellular potassium.

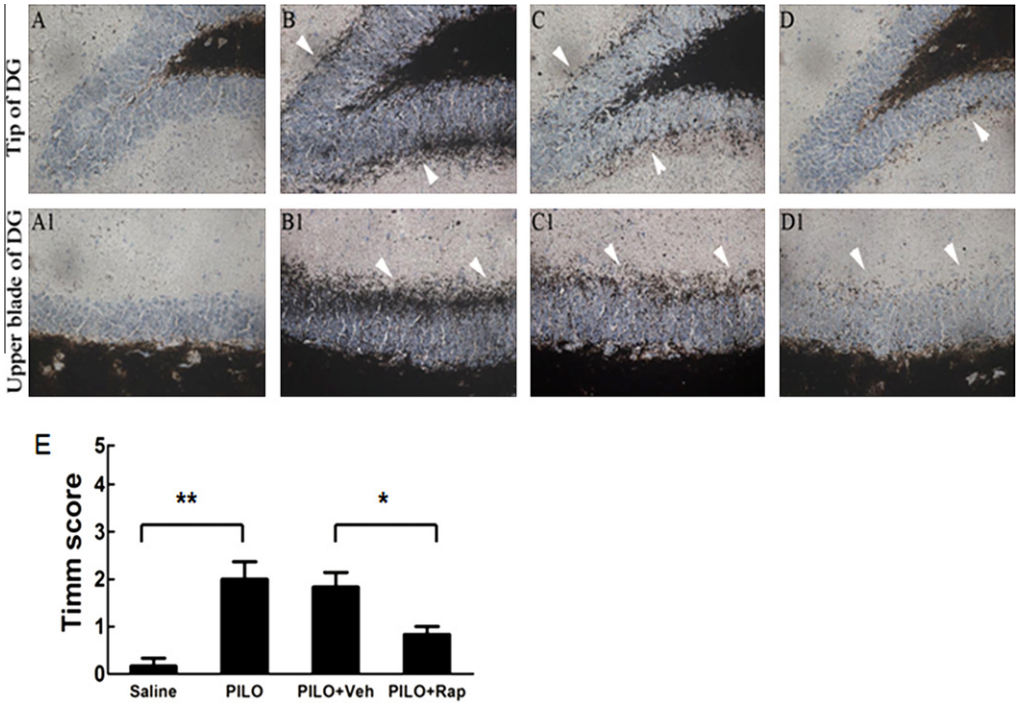

Fig. 4. Representative images of Timm's staining (white arrow heads) showed the mossy fibers in the tip and upper blade of dentate gyrus (DG). (A&A1) Saline treated mice showed no mossy fiber staining. (B&B1) PILO treated mice showed obvious mossy fiber staining. (C&C1) PILO + Veh treated mice showed obvious mossy fiber staining as well. (D&D1) PILO + Rap treated mice showed only traces of the stains. E, Quantitative analysis by assessing Timm score demonstrated that the rapamycin treatment significantly attenuated the MFS. $^{*}P < 0.05$, $^{**}P < 0.01$ by one-way ANOVA ($n = 8$ for each group).

of mTOR pathway in epileptogenesis by suppressing mossy fiber sprouting and seizure activity with rapamycin even when given after the development of spontaneous recurrent seizures [13]. However, Buckmaster et al. argued that rapamycin suppressed mossy fiber sprouting, but did not affect seizure frequency [16]. Our study explored the electrophysiological effect of rapamycin on temporal lobe epilepsy for the first time and, in turn, further substantiated the notion of mTOR pathway's involvement in epileptogenesis.

An increase in frequency of spontaneous EPSCs in granule cells was observed 8 weeks after SE, and it was suppressed by rapamycin. The increased frequency implies increased presynaptic release probability [20]. The presynaptic release of dentate gyrus comes from perforant path, CA3, hilus, as well as novel recurrent excitatory circuits in epileptic mice. Previous studies have demonstrated that inputs from perforant path remain unchanged and inputs from CA3, hilus are destroyed greatly by status epilepticus [20,23,25]. The novel recurrent excitatory circuits which are mediated by sprouted mossy fiber sprouting have been considered responsible for the increase of frequency of spontaneous EPSCs after PILO induced status epilepticus [20,26,27]. Rapamycin reduced the mossy fiber sprouting in this study, which is in line with others reports [11–13], and may consequently decrease new excitatory synapses between mossy fiber-granule cells and granule-granule cells, thus attenuating the increase of frequency of spontaneous EPSCs in granule cells.

The amplitudes of antidromically evoked EPSCs in granule cells were significantly increased after PILO treatment, and rapamycin decreased the amplitudes to relatively normal level. Membrane properties including resting membrane potential, input resistance, threshold potential, and action potential amplitude were similar from all groups (Table 1). These findings suggest that changes in synaptic transmission, rather than changes in intrinsic firing properties, underlie the change of granule cells excitability [27].

Table 1
Membrane properties were not significantly different among four groups.

	Resting potential (mV)	Input resistance (MΩ)	Threshold potential (mV)	Action potential amplitude (mV)	*N*
Saline	−72 ± 1.4	100.5 ± 7.9	30.9 ± 7.6	90.2 ± 4.9	133
PILO	−71 ± 2.1	105 ± 10.8	25.5 ± 6.9	89.5 ± 7.8	19
PILO + Veh	−72.6 ± 2.5	109 ± 9.3	29.9 ± 10.2	91.4 ± 6.3	19
PILO + Rap	−70.8 ± 1.9	104 ± 10.2	35.1 ± 9.3	92.5 ± 5.2	24

Resting potential was defined as the V_m at break-in. Input resistance was defined by the steepest slope of the *I–V* curve based on steady-state responses to a family of current pulses. The threshold potential was measured from resting potential to the start point of the rising phase of spikes. Action potential amplitude was measured from resting potential to peak.

Evidences suggest that larger mossy fiber terminals and recurrent excitatory circuits resulted from mossy fiber sprouting contribute to hyperexcitability of granule cells in PILO treated mice [23,27]. Rapamycin suppresses mossy fiber sprouting, and then decreases the amplitude of antidromically evoked EPSCs in granule cells. Other elements such as glutamate receptors, glutamate release, and ion channels may influence synaptic transmission also. But two previous studies have found that rapamycin did not alter neurotransmitter release, activity of ion channels (including voltage-gated sodium and potassium currents) in vitro, as well as neuronal excitability [29,30].

The poly-spiking epileptiform activity was believed to have resulted from the establishment of recurrent excitatory circuits [19,28]. Rapamycin demonstrated the ability to suppress epileptiform activity as there was none such poly-spiking epileptiform activity detected in slices from PILO + Rap treated mice in perfusion with 30 μM bicuculline and 6 mM potassium. Timm staining revealed that the growth of mossy fibers in dentate gyrus was

suppressed by rapamycin. This may serve as an explanation for the lesser epileptiform activity seen after rapamycin treatment. Less mossy fiber sprouting would lead to fewer establishments of the recurrent excitatory circuits.

In summary, rapamycin suppressed recurrent excitatory circuits in the dentate gyrus, reduced epileptiform activity, and inhibited both spontaneous and evoked EPSCs, possibly through inhibiting mTOR pathway and repressing mossy fiber sprouting after SE in the current study. This serves as yet another piece of supporting evidence for the role of mTOR system in the epileptogenesis of temporal lobe epilepsy and for the antiepileptogenic potential of rapamycin.

Acknowledgments

This study was supported by grants from National Natural Science Foundation of China (81071048, 81100967).

Appendix A. Supplementary data

Supplementary data associated with this article can be found, in the online version, at doi:10.1016/j.bbrc.2012.02.143.

References

[1] N.R. Temkin, Antiepileptogenesis and seizure prevention trials with antiepileptic drugs: meta-analysis of controlled trials, Epilepsia 42 (2001) 515–524.
[2] W. Loscher, Animal models of epilepsy for the development of antiepileptogenic and disease-modifying drugs. A comparison of the pharmacology of kindling and post-status epilepticus models of temporal lobe epilepsy, Epilepsy Res. 50 (2002) 105–123.
[3] D.R. Bolster, S.J. Crozier, S.R. Kimball, L.S. Jefferson, AMP-activated protein kinase suppresses protein synthesis in rat skeletal muscle through down-regulated mammalian target of rapamycin (mTOR) signaling, J. Biol. Chem. 277 (2002) 23977–23980.
[4] K. Inoki, Y. Li, T. Zhu, J. Wu, K.L. Guan, TSC2 is phosphorylated and inhibited by Akt and suppresses mTOR signalling, Nat. Cell. Biol. 4 (2002) 648–657.
[5] S. Wullschleger, R. Loewith, M.N. Hall, TOR signaling in growth and metabolism, Cell 124 (2006) 471–484.
[6] N. Abe, S.H. Borson, M.J. Gambello, F. Wang, V. Cavalli, Mammalian target of rapamycin (mTOR) activation increases axonal growth capacity of injured peripheral nerves, J. Biol. Chem. 285 (2010) 28034–28043.
[7] J. Jaworski, S. Spangler, D.P. Seeburg, C.C. Hoogenraad, M. Sheng, Control of dendritic arborization by the phosphoinositide-3′-kinase-Akt-mammalian target of rapamycin pathway, J. Neurosci. 25 (2005) 11300–11312.
[8] S.J. Tang, G. Reis, H. Kang, A.C. Gingras, N. Sonenberg, E.M. Schuman, A rapamycin-sensitive signaling pathway contributes to long-term synaptic plasticity in the hippocampus, Proc. Natl. Acad. Sci. USA 99 (2002) 467–472.
[9] L.H. Zeng, L. Xu, D.H. Gutmann, M. Wong, Rapamycin prevents epilepsy in a mouse model of tuberous sclerosis complex, Ann. Neurol. 63 (2008) 444–453.
[10] C.H. Kwon, X. Zhu, J. Zhang, S.J. Baker, MTor is required for hypertrophy of Pten-deficient neuronal soma in vivo, Proc. Natl. Acad. Sci. USA 100 (2003) 12923–12928.
[11] L.H. Zeng, N.R. Rensing, M. Wong, The mammalian target of rapamycin signaling pathway mediates epileptogenesis in a model of temporal lobe epilepsy, J. Neurosci. 29 (2009) 6964–6972.
[12] P.S. Buckmaster, E.A. Ingram, X. Wen, Inhibition of the mammalian target of rapamycin signaling pathway suppresses dentate granule cell axon sprouting in a rodent model of temporal lobe epilepsy, J. Neurosci. 29 (2009) 8259–8269.
[13] X. Huang, H. Zhang, J. Yang, J. Wu, J. McMahon, Y. Lin, Z. Cao, M. Gruenthal, Y. Huang, Pharmacological inhibition of the mammalian target of rapamycin pathway suppresses acquired epilepsy, Neurobiol. Dis. 40 (2010) 193–199.
[14] J. Zhou, J. Blundell, S. Ogawa, C.H. Kwon, W. Zhang, C. Sinton, C.M. Powell, L.F. Parada, Pharmacological inhibition of mTORC1 suppresses anatomical, cellular, and behavioral abnormalities in neural-specific Pten knock-out mice, J. Neurosci. 29 (2009) 1773–1783.
[15] M.C. Ljungberg, C.N. Sunnen, J.N. Lugo, A.E. Anderson, G. D'Arcangelo, Rapamycin suppresses seizures and neuronal hypertrophy in a mouse model of cortical dysplasia, Dis. Model. Mech. 2 (2009) 389–398.
[16] P.S. Buckmaster, F.H. Lew, Rapamycin suppresses mossy fiber sprouting but not seizure frequency in a mouse model of temporal lobe epilepsy, J. Neurosci. 31 (2011) 2337–2347.
[17] M. Lynch, T. Sutula, Recurrent excitatory connectivity in the dentate gyrus of kindled and kainic acid-treated rats, J. Neurophysiol. 83 (2000) 693–704.
[18] P. Molnar, J.V. Nadler, Mossy fiber-granule cell synapses in the normal and epileptic rat dentate gyrus studied with minimal laser photostimulation, J. Neurophysiol. 82 (1999) 1883–1894.
[19] J.P. Wuarin, F.E. Dudek, Electrographic seizures and new recurrent excitatory circuits in the dentate gyrus of hippocampal slices from kainate-treated epileptic rats, J. Neurosci. 16 (1996) 4438–4448.
[20] J.P. Wuarin, F.E. Dudek, Excitatory synaptic input to granule cells increases with time after kainate treatment, J. Neurophysiol. 85 (2001) 1067–1077.
[21] Y. Li, Z. Peng, B. Xiao, C.R. Houser, Activation of ERK by spontaneous seizures in neural progenitors of the dentate gyrus in a mouse model of epilepsy, Exp. Neurol. 224 (2010) 133–145.
[22] R.J. Racine, Modification of seizure activity by electrical stimulation. II. Motor seizure, Electroencephalogr. Clin. Neurophysiol. 32 (1972) 281–294.
[23] M.M. Okazaki, P. Molnar, J.V. Nadler, Recurrent mossy fiber pathway in rat dentate gyrus: synaptic currents evoked in presence and absence of seizure-induced growth, J. Neurophysiol. 81 (1999) 1645–1660.
[24] J.E. Cavazos, G. Golarai, T.P. Sutula, Mossy fiber synaptic reorganization induced by kindling: time course of development, progression, and permanence, J. Neurosci. 11 (1991) 2795–2803.
[25] R.S. Sloviter, C.A. Zappone, B.D. Harvey, A.V. Bumanglag, R.A. Bender, M. Frotscher, "Dormant basket cell" hypothesis revisited: relative vulnerabilities of dentate gyrus mossy cells and inhibitory interneurons after hippocampal status epilepticus in the rat, J. Comp. Neurol. 459 (2003) 44–76.
[26] P.S. Buckmaster, G.F. Zhang, R. Yamawaki, Axon sprouting in a model of temporal lobe epilepsy creates a predominantly excitatory feedback circuit, J. Neurosci. 22 (2002) 6650–6658.
[27] H.E. Scharfman, A.L. Sollas, R.E. Berger, J.H. Goodman, Electrophysiological evidence of monosynaptic excitatory transmission between granule cells after seizure-induced mossy fiber sprouting, J. Neurophysiol. 90 (2003) 2536–2547.
[28] P.R. Patrylo, F.E. Dudek, Physiological unmasking of new glutamatergic pathways in the dentate gyrus of hippocampal slices from kainate-induced epileptic rats, J. Neurophysiol. 79 (1998) 418–429.
[29] D. Daoud, H.H. Scheld, E.J. Speckmann, A. Gorji, Rapamycin: brain excitability studied in vitro, Epilepsia 48 (2007) 834–836.
[30] S. Ruegg, M. Baybis, H. Juul, M. Dichter, P.B. Crino, Effects of rapamycin on gene expression, morphology, and electrophysiological properties of rat hippocampal neurons, Epilepsy Res. 77 (2007) 85–92.

Biochemical and Biophysical Research Communications 420 (2012) 205–209

Contents lists available at SciVerse ScienceDirect

Biochemical and Biophysical Research Communications

journal homepage: www.elsevier.com/locate/ybbrc

Measurement of hemoglobin in whole blood using a partial least squares regression model with selected second derivative near infrared transmission spectral signals

Yan Zhou [a], Chunli Zheng [a], Hui Cao [b,*], Xingzhi Li [a], Jibin Sha [c]

[a] School of Energy and Power Engineering, Xi'an Jiaotong University, Xi'an 710049, PR China
[b] School of Electrical Engineering, Xi'an Jiaotong University, Xi'an 710049, PR China
[c] School of Life Science and Technology, Xi'an Jiaotong University, Xi'an, Shaanxi 710049, PR China

ARTICLE INFO

Article history:
Received 23 February 2012
Available online 3 March 2012

Keywords:
Hemoglobin
Whole blood
Near-infrared spectra
Signal selection
Partial least squares

ABSTRACT

In this work, we propose a signal selection procedure for determination of hemoglobin (Hb) concentration in whole blood using near infrared (NIR) transmission spectral signals. A dataset of 190 whole blood NIR transmission spectra with reference Hb concentrations was used to evaluate the method. Spectral signals were selected based on the squared correlation coefficient (R^2) between the signal and the Hb concentration. An improved uninformative variable elimination (UVE) procedure was performed to remove redundant signals from the primary selected signal set. A partial least squares (PLS) regression model was built with the final selected signals and the corresponding Hb concentrations. The results indicate that the proposed method is effective at increasing the predictive power of the NIR–PLS spectral model for determining Hb concentration in whole blood samples.

1. Introduction

Hemoglobin (Hb), a metalloprotein in whole blood, is one of the most common analytes used in biochemical and biomedical research [1,2]. The traditional procedure for determining Hb concentration in blood can provide precise results but requires reagent and blood lysis [3,4]. Thus, much research on whole blood spectra has been performed, and several novel approaches for Hb determination using whole blood spectra have been proposed [5–11]. The spectral signals of different Hb species are similar in the near infrared (NIR) region [5,6], so the total level of Hb in blood may be obtained using spectroscopy without having to separate the mixture of different Hb species. For the whole blood NIR spectra in the region from 1000 nm to 2500 nm, the original absorbance signals correlate poorly with Hb concentration [5], but a small number of the second derivative absorbance signals within this region correlate well with Hb concentration [6].

From a chemometric perspective, the quality of a calibration model depends in part on the quality of the variables and the modeling method. The whole blood NIR spectral signals within the mentioned region provide a limited number of high Hb correlation signals, and existing Hb spectral models are based on these high Hb correlation signals [7–10]. This method may lose spectral information in the low Hb correlation signals. Moreover, existing methods mainly use the least-squares regression method for modeling. Such a method is not applicable to cases where the number of signals exceeds the number of samples [7–10], as is typically the case for practical blood spectral signal datasets. Thus, many signals in such datasets cannot be used.

To overcome these limitations, a partial least squares (PLS) regression model for Hb determination using Visible-NIR spectral signals from 500 nm to 800 nm was developed [11]. PLS regression is the most popular method for building a relationship between spectral signals and the associated analyte concentrations [11–15]. In particular, it can handle the above situations in a signal dataset without large covariance information loss. NIR spectral signals combined with PLS regression have already been applied to predict different component levels in blood [16,17]. For whole blood Hb prediction using Visible-NIR spectral signals within the region from 500 nm to 800 nm, a PLS model that uses all available signals performs much better than a PLS model that uses only the high Hb correlation signals [11]. This result suggests that the signals from low Hb correlations also contain useful information for quantitating Hb. It should also be noted that not all of the low object analyte correlation signals are informative for analyte determination. In other words, some signals contain noise [18]. Thus, to improve predictive power, it is important to implement an effective signal selection procedure that can prevent informative signal loss while removing uninformative signals. As stated above, however, no specific signal selection procedures for whole blood spectral signals have yet been used.

* Corresponding author.
E-mail address: speclab@mail.xjtu.edu.cn (H. Cao).

0006-291X/$ - see front matter © 2012 Elsevier Inc. All rights reserved.
doi:10.1016/j.bbrc.2012.02.144

When signals are properly selected, the corresponding reduced PLS model (based on the selected signals) is more effective for analyte prediction than the full PLS model (based on all available signals) [18–23]. The most direct signal selection procedure is one based on the correlation coefficients (R^2) between signals and the analyte concentration [11,18]. Specifically, the signals with large values of R^2 are selected first, and the number of selected signals is predefined [11,18]. During this procedure, many uninformative signals with high analyte correlations may be selected, while lots of informative signals with low analyte correlations are not. This method therefore leads to superfluous selection and information loss [11]. The most efficient method for the removal of unnecessary signal is the uninformative variable elimination (UVE) procedure, in which signals with less importance than the artificial signals added in the signal matrix are removed [19]. The UVE procedure offers an effective way of removing the most redundant signals, but it is still prone to superfluous selection if the artificial variables are not suitably generated.

The goal of this study was to augment the predictive power of the NIR–PLS (1100–2500 nm) model for whole blood Hb concentration determination. Signals were first selected based on the reference R^2s, and then an improved uninformative elimination (UVE) procedure was carried out to remove the remaining uninformative signals. Finally, the selected signals and the corresponding Hb concentrations were used to build a PLS prediction model, and analysis of variance (ANOVA) tests were performed between the new model and existing models.

2. Materials and methods

2.1. Dataset

The dataset used in this study was previously presented in Ref. [8]. Transmission spectra of 190 whole blood samples were obtained using a NIRSystems 6500 spectrometer. Each spectrum has 700 signals from 1100 nm to 2498 nm with a 2 nm interval. The system light path was adjusted to a vertical mode using a platform. A 2 cm diameter stainless steel cylinder with a quartz window was used as the sample cell, and 200 μL of whole blood was transferred from a pipette into the sample cell, providing a sample thickness of 0.6 mm. The empty cell was used as a reference for transmission measurements. The total Hb concentrations from 10.3 to 17.3 g/dL were evaluated with the standard method.

2.2. Data preprocessing

The $-\log(T)$ values of the original transmission spectral signals at all wavelengths were calculated as the absorbance signals. The dataset was divided into a calibration set of 143 samples and a validation set of 47 samples. The two sets have a similar distribution and range of Hb concentrations. Table 1 presents the statistic properties of the two sets.

The calibration set was used to build prediction models, and the validation set was used to compare the models. A signal smoothing procedure was also studied, in which each signal in a spectrum was replaced by the mean value of the signals within a certain window.

Table 1
Statistic properties of calibration set and validation set.

Statistic property	Calibration set	Validation set
Number of samples	143	47
Minimum (g/dL)	10.60	10.30
Maximum (g/dL)	17.30	17.30
Mean (g/dL)	13.68	13.94
Standard deviation (g/dL)	1.64	1.65

The optimum width of the smoothing window was determined using the R^{2*} curve (detailed in Section 3). Then, the first derivative and the second derivative absorbance signals were calculated using the smoothed spectral signals. Both the spectral signals and the reference Hb concentrations for the two sets were centered around the mean values of the calibration set.

2.3. Data analysis

The leave-one-out root-mean-squared error of cross validation (RMSECV), the root-mean-squared error of prediction (RMSEP) [24] and the squared correlation coefficient (R^2) were used to compare the predictive power of various models. The significance of the differences in predictive performance was evaluated using ANOVA [25]. The test was performed on the absolute values of the prediction errors. This test is a well-accepted method for testing the difference between prediction models.

2.4. Signal selection procedure

Signals were selected in descending order of the corresponding R^2 values. The number of signals selected was determined by the RMSECV value curve. To reduce information loss, some signals with low R^2 values were also added. An iterative signal selection procedure was proposed, in which signals are reselected using an iteration loop of the original UVE procedure [19]. The iteration loop commences when the original UVE procedure [19] terminates, and the selected signal (variable) matrix is used as a new signal dataset for another UVE procedure. The whole procedure ceases when both the RMSECV value and the number of selected signals no longer decrease.

2.5. PLS regression model

A PLS model was built with the selected signals and the corresponding concentrations, and the latent variables were determined using the predicted residuals error sums of squares (PRESS) statistic with leave-one-out cross validation [26].

3. Results and discussion

3.1. Hb correlations of spectral signals

Fig. 1A, B, C shows the original, the first derivative and the second derivative signals of the absorbance spectra, respectively. Fig. 1D, E, F shows the R^2 curves (between the Hb concentration and the present signal) for the three spectral signals.

A large baseline distortion of the absorbance spectra can be clearly observed in Fig. 1A but not in Fig. 1B or Fig. 1C, which correspond to the first derivative and the second derivative spectra, respectively. Because each first derivative spectral signal was calculated by subtracting between the associated adjacent signals of the original spectrum, similar distortions in the adjacent signals can be offset automatically. As a result, the baseline distortion can be reduced during the derivative procedure. In Fig. 1A, peaks are present at 1450 nm, 1950 nm and 2495 nm. All of the signals within the peak regions correlate very weakly with the Hb concentration (according to the R^2 values in Fig. 1D). In Fig. 1B, three peaks are evident in similar regions. The first derivative absorbance signals within the regions also correlate very weakly with the Hb concentration (according to the R^2 values in Fig. 1E). These observations indicate that the main variance in the signal is introduced by unknown blood components rather than by Hb. In Fig. 1E, two obvious peaks can be found in the R^2 curve for the first derivative absorbance signals, and the largest R^2 value is approximately 0.8 at

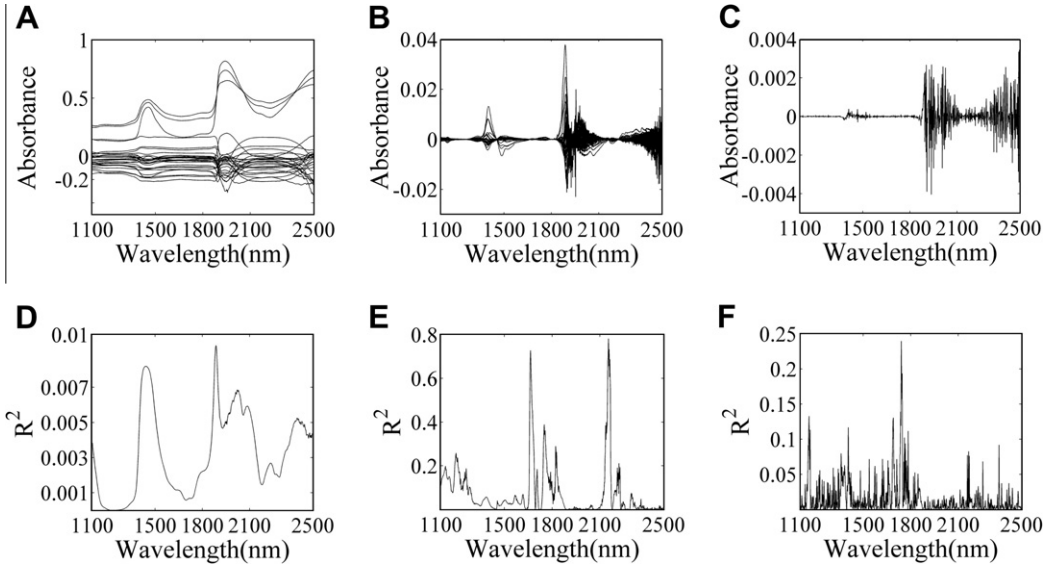

Fig. 1. Three types of whole blood spectral signals and the corresponding R^2 curves. (A) The absorbance signals. (B) The first derivative of the absorbance signals. (C) The second derivative of the absorbance signals. (D) R^2 curve for the absorbance signals. (E) R^2 curve for the first derivative absorbance signals. (F) R^2 curve for the second derivative absorbance signals.

a wavelength of 2150 nm. It can be observed that only a small number of signals correspond to large R^2 values (>0.6). The R^2 values of the second derivative absorbance signals are generally smaller than those of the first derivative absorbance signals. The total number of high Hb correlation signals is small, and the intensities of these signals are weak. Spectral signal variance introduced by unknown components may contribute unneeded variance to the signal dataset, perhaps distorting the PLS model structure and leading to a poor prediction of Hb concentration.

3.2. Width of smoothing window

Fig. 2 presents the R^{2*} vs. the width of the smoothing window. In this paper, R^{2*} represents the largest R^2 value in the R^2 curve.

As shown in Fig. 2, the width of the smoothing window dramatically impacts the R^{2*} value for the first derivative and the second derivative absorbance signals. The R^{2*} value for the first derivative absorbance signals increases rapidly as the width of the smoothing window increases and decreases slowly after reaching the maximum of 0.88. The R^{2*} value for the second derivative absorbance signals increases faster than that for the first derivative absorbance signals, reaching a maximum value of approximately 9 when the width of the smoothing window is at 15. It is quite clear that the R^{2*} value of the second derivative absorbance signals is more stable than that for the first derivative absorbance signals when the smoothing window width increases further. In Fig. 2, the R^{2*} value corresponding to the absorbance signals does not change much as the width of the smoothing window increases. These results indicate that the correlation with Hb concentration for the first derivative and second derivative absorbance signals can be enhanced with a suitably wide smoothing window; the optimum window width can be determined based on the largest R^{2*} in Fig. 2. The R^* augmentation for the second derivative absorbance signals is more obvious than that for the first derivative absorbance signals. This result can be explained by the fact that the noise is evenly distributed for all signals and can therefore be offset during the smoothing procedure. The second derivative absorbance signals are obtained using the first derivative absorbance signals, and therefore they are more sensitive to noise. Consequently, when the power of the noise decreases, the Hb correlations for the second derivative absorbance signals increase much faster than those for the first derivative absorbance signals. With smoothing, not only does the power of the noise decrease but also the power of the informative signals. Therefore, the proper width of the smoothing window must be optimized.

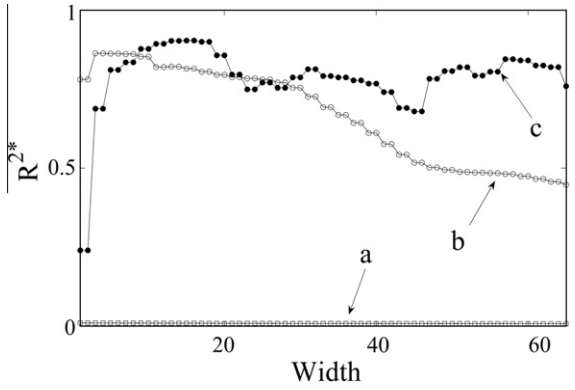

Fig. 2. R^{2*} vs. the width of the smoothing window. Here, a, b and c represent the R^{2*} value curves for the absorbance signals, the first derivative absorbance signals and the second derivative absorbance signals, respectively.

3.3. Hb correlations of smoothed spectral signals

Fig. 3 shows the R^2 curves of the three types of spectral signals. The original absorbance signals have been smoothed with a window of 15 points. Compared to the R^2 values shown in Fig. 1, the R^2 values for the original absorbance signals and the first derivative absorbance signals did not change much, and the number of first derivative absorbance signals with large R^2 values (>0.6) is still small. In contrast, the R^2 values of the second derivative absorbance signals increased significantly. Two obvious peaks (at 1698 nm and 1746 nm) are present in the R^2 curve for the second derivative absorbance signals. The R^2 values within the vicinities of the two peaks range from 0.8 to 0.9. It should also be noted that the total number of signals with a large R^2 is still small. Only approximately 3.57% of the signals correspond to R^2 values larger than 0.6. These results indicate that the Hb correlations for the second derivative absorbance signals can be augmented by adjusting the width of the smoothing window.

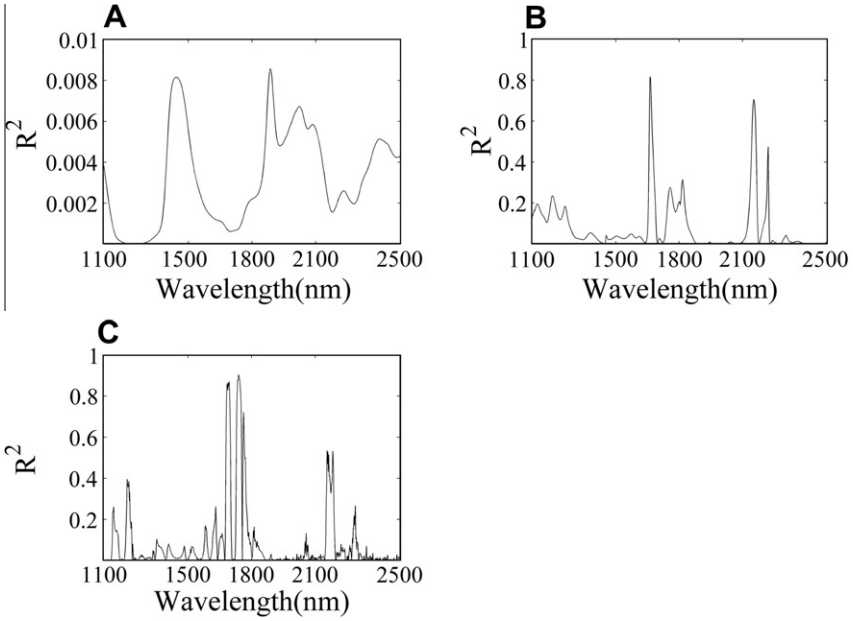

Fig. 3. R^2 curves for the three types of smoothed whole blood spectral signals. (A) R^2 for the smoothed absorbance signals. (B) R^2 for the smoothed first derivative absorbance signals. (C) R^2 for the smoothed second derivative absorbance signals.

3.4. Signal selection

Fig. 4 depicts the RMSECV values (for calibration data set) vs. the number of selected signals. Each signal was selected on the basis of the reference R^2 in descending order. It is clear that the RMSECV value decreases rapidly as the number of selected signals increases. A clear RMSECV value minimum was achieved at approximately 40, which indicates a suitable number of signals. After 40 signals have been selected, the RMSECV value increases slowly. The ratio of the object signal variance to the total signal variance may increase as more signals with high object correlations are selected; thus, the predictive power of the PLS model that is based on them increases, and the RMSECV value drops quickly when more signals are selected at the beginning of the procedure. The high object correlation signals are limited in number, however. Consequently, with more signals being selected, more noise is also introduced, which may abate the predictive power of the PLS model. During this procedure, some low Hb correlation signals, which may be used to compensate the errors introduced by noise, cannot be discriminated from the others. Additionally, many uninformative signals are also selected for the modeling. As shown in Fig. 4, in the region from 40 to 110, the RMSECV value does not increase very much. Hence, in this study, the signals in this region were also selected to compensate for the signal loss from those with high Hb correlations. The proposed UVE iteration procedure was performed to remove uninformative signals.

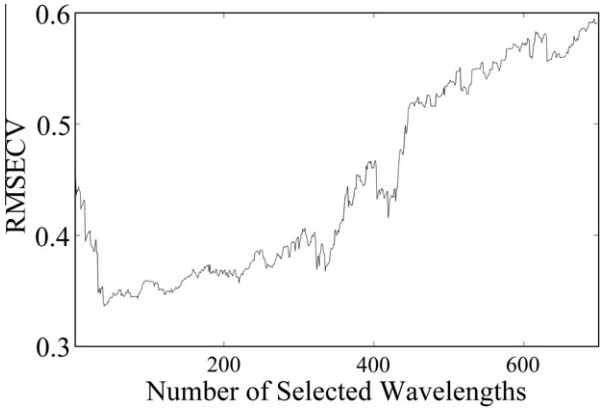

Fig. 4. RMSECV values vs. the number of selected signals.

3.5. Prediction power comparison

Table 2 presents a comparison of the predictive power of different methods. RMSEP, R^2 based on the validation set for each model are all presented, as well as the p values for the one-way ANOVA performed between the previous model and the present model. RMSECV for the calibration set was also given. Various blood Hb prediction models were built using Hb concentrations with different amounts of the reference smoothed second derivative blood transmission NIR signals: (1) the signal at the wavelength with the max R^2 value (univariate regression model); (2) the signals at all wavelengths (full PLS model); (3) the signals at the wavelengths selected using UVE (reduced PLS model); (4) the signals at the wavelengths selected using the R^2 and RMSECV curves shown in Fig. 4 (reduced PLS model); and (5) the signals at the wavelengths selected using the proposed procedure (reduced PLS model). The first two methods lack any signal selection procedures, while the last three use different signal selection procedures.

Table 2
Predictive power comparison.

Method	Validation set			Calibration set
	R^2	RMSEP	p value	RMSECV
UR	0.9462	0.4435	–	0.5124
PLS	0.9223	0.4634	0.8465	0.5902
PLS-UVE	0.9574	0.3382	0.0383	0.3953
PLS-R^2	0.9588	0.3411	0.8470	0.3364
Proposed method	0.9676	0.3003	0.5050	0.3179

The models are sorted according to increasing prediction power, and the p values for the significance testing by a one-way ANOVA of the improvement compared to the previous model are given.
UR, univariate regression.
PLS, partial least squares.
PLS-UVE, partial least squares with elimination of uninformative variables.
PLS-R^2, partial least squares with squared correlation coefficient.
RMSECV, root mean-squared error of cross-validation.
RMSEP, root-mean-squared error of prediction.

The most accurate prediction was clearly achieved by our new procedure, and the most inaccurate prediction was produced by the full PLS model. The best result was achieved with a RMSEP value of 0.3003, which can be confirmed by the corresponding RMSECV value of 0.3179 and R^2 value of 0.9676. The full PLS model, using all of the signals between 1100 nm and 2500 nm, produced the largest RMSEP value of 0.4634. The full PLS model was not significantly different ($p < 0.8465$) from the univariate regression model. A comparison between the full PLS model and the univariate regression model also indicates that apart from the signal with the max R^2, all of the remaining spectral signals introduce more noise rather than contribute information to the model. This result is quite different from that presented in Ref. [11] but can be explained by the fact that not all spectral signals with low Hb correlations are useful for compensating the errors and only signals with high interferon correlations can be exploited for compensation. Although the signals between 650 nm and 800 nm show low Hb correlations [11], they most likely correlate well with unknown components or other interfering factors in the blood. The second derivative transmission spectral signals in the range from 1100 nm to 2500 nm most likely contain very few signals that correlate well with the interferon factors. A significant difference was not observed between the methods with different signal selection procedures. In contrast, a significant difference can be found between the full PLS model and the PLS model with UVE procedure ($p < 0.0383$). This result confirms that an effective signal selection procedure can enhance the predictive power of the model. As shown in Figs. 1 and 4, most of the signals correlate poorly with Hb concentration but do not corrupt the full PLS model, which indicates that the signal variance introduced by other components can be reduced during the PLS regression procedure.

In this study, the number of signals selected by the UVE was 207, which was much smaller than the total 700; the RMSEP value (0.3382) for the reference-reduced PLS model was also quite smaller than that for the full PLS model (0.4634). This result suggests that incorporating UVE with PLS can improve the original model, even if the number of high Hb correlation signals is very small. It should be noted that the selected signals are with both high and low Hb correlations.

The PLS-R^2 method, which used only the signals with the first 40 largest R^2s, produced an RMSEP value of 0.3411. The number of selected signals was determined by the minimum in the RMSECV curve shown in Fig. 4, which is much smaller than that for the PLS–UVE. This method performs slightly but not significantly ($p < 0.8470$) better than the PLS–UVE. The most uninformative signals probably correlate poorly with Hb and cannot be removed completely during the UVE procedure; thus, they decrease the predictive power of the PLS model. Moreover, this result suggests that some of the signals with high Hb correlations (within the 40 signals) are useless for improving the model, as their absence (in the UVE procedure) does not decrease the prediction significantly. The model based on the proposed method provides the lowest RMSEP 0.3003 with only 47 signals but is not significantly different from the previous model ($p < 0.5050$). This result indicates that the proposed UVE procedure combined with a pre-R^2-wave selection is more efficient than the original procedure. The signals that can be exploited to compensate for the signal loss are those with the first 110 largest R^2 values. The selected signals include both signals with R^2s larger than 0.8 and signals with R^2s smaller than 0.1. Some signals with large R^2 values must be redundant for the modeling.

Acknowledgments

We are grateful for the dataset provided by Karl Norris.

References

[1] G. Edgren, V. Bagnardi, R. Bellocco1, H. Hjalgrim, K. Rostgaard, M. Melbye, M. Reilly, H.O. Adami, P. Hall, O. Nyrén, Pattern of declining hemoglobin concentration before cancer diagnosis, J. Cancer 127 (2010) 1429–1436.
[2] C.S. Broberg, A.R. Jayaweera, G.P. Diller, S.K. Prasad, S.L. Thein, B.E. Bax, J. Burman, M.A. Gatzoulis, Seeking optimal correlation between oxygen saturation and hemoglobin concentration in adults with cyanosis from congenital heart disease, Am. J. Cardiol. 107 (2011) 595–599.
[3] E.J. van Kampen, W.G. Zijlstra, Standardization of hemoglobinometry. II. The hemoglobincyanide method, Clin. Chim. Acta 6 (1961) 538–544.
[4] E. Mieczkowska, R. Koncki, Ł. Tymecki, Hemoglobin determination with paired emitter detector diode, Anal. Bioanal. Chem. 399 (2011) 3293–3297.
[5] J.T. Kuenstner, K.H. Norris, V.F. Kalasinsky, Spectrophotometry of human hemoglobin in the midinfrared region, Biospectroscopy 3 (1997) 225–232.
[6] J.T. Kuenstner, K.H. Norris, Spectrophotometry of human hemoglobin in the near infrared region from 1000 to 2500 nm, J. Near Infrared Spectrosc. 2 (1994) 59–65.
[7] J.T. Kuenstner, K.H. Norris, W.F. McCarthy, Measurement of hemoglobin in unlysed blood by near-infrared spectroscopy, Appl. Spectrosc. 48 (1994) 484–488.
[8] J.T. Kuenstner, K.H. Norris, Near infrared hemoglobinometry, J. Near Infrared Spectrosc. 3 (1995) 11–18.
[9] I. Valyi-Nagy, K.J. Kaffka, J.M. Jako, E. Gonczol, G. Domjan, Application of near infrared spectroscopy to the determination of haemoglobin, Clin. Chim. Acta 264 (1997) 117–125.
[10] M. Rendell, E. Anderson, W. Schlueter, J. Mailliard, D. Honigs, R. Rosenthal, Determination of hemoglobin levels in the finger using near infrared spectroscopy, Clin. Lab. Haem. 25 (2003) 93–97.
[11] Y.J. Kim, S. Kim, J.W. Kim, G. Yoon, Data preprocessing and partial least squares regression analysis for reagent less determination of hemoglobin concentrations using conventional and total transmission spectroscopy, J. Biomed. Opt. 6 (2001) 177–182.
[12] D.M. Haaland, E.V. Thomas, Partial least-squares methods for spectral analyses. 1. Relation to other quantitative calibration methods and the extraction of qualitative information, Anal. Chem. 60 (1988) 1193–1202.
[13] P. Geladi, B.R. Kowalski, Partial least-squares regression: a tutorial, Anal. Chim. Acta 185 (1986) 1–17.
[14] S. de Jong, SIMPLS:an alternative approach to partial least squares regression, Chemom. Intell. Lab. Syst. 18 (1993) 251–263.
[15] C.M. Wehlburg, D.M. Haaland, D.K. Melgaard, New hybrid algorithm for transferring multivariate quantitative calibrations of intra-vendor near-infrared spectrometers, Appl. Spectrosc. 56 (2002) 877–886.
[16] H. Arimoto, M. Tarumi, Y. Yamada, Temperature-insensitive measurement of glucose concentration based on near infrared spectroscopy and partial least squares, Opt. Rev. 10 (2003) 74–76.
[17] S.B. Zhang, B.R. Soller, S. Kaur, K. Perras, T.J. Vander Salm, Investigation of noninvasive in vivo blood hematocrit measurement using NIR reflectance spectroscopy and partial least-squares regression, Appl. Spectrosc. 54 (2000) 294–299.
[18] W. Wu, B. Walczak, D.L. Massart, K.A. Prebble, I.R. Last, Spectral transformation and wavelength selection in near-infrared spectra classification, Anal. Chim. Acta 315 (1995) 243–255.
[19] V. Centner, D.L. Massart, O.E. de Noord, S. de Jong, B.M. Vandeginste, C. Sterna, Elimination of uninformative variables for multivariate calibration, Anal. Chem. 68 (1996) 3851–3858.
[20] R. Put, M. Daszykowski, T. Baczek, Y. Vander Heyden, Retention prediction of peptides based on uninformative variable elimination by partial least squares, J. Proteome Res. 5 (2006) 1618–1625.
[21] J. Koshoubu, T. Iwata, S. Minami, Elimination of the uninformative calibration sample subset in the modified UVE (uninformative variable elimination)–PLS (partial least squares) method, Anal. Sci. 17 (2001) 319–322.
[22] M. Daszykowski, I. Stanimirova, B. Walczak, F. Daeyaert, M.R. De Jonge, J. Heeres, L.M.H. Koymansc, P.J. Lewi, H.M. Vinkers, P.A. Janssen, D.L. Massart, Improving qsar models for the biological activity of hiv reverse transcriptase inhibitors: aspects of outlier detection and uninformative variable elimination, Talanta 68 (2005) 54–60.
[23] J. Moros, J. Kuligowski, G. Quintás, S. Garrigues, M. de la Guardia, New cut-off criterion for uninformative variable elimination in multivariate calibration of near-infrared spectra for the determination of heroin in illicit street drugs, Anal. Chim. Acta 630 (2008) 150–160.
[24] W. Saeys, K. Beullens, J. Lammertyn, H. Ramon, T. Naes, Increasing robustness against changes in the interferent structure by incorporating prior information in the augmented classical least-squares framework, Anal. Chem. 80 (2008) 4951–4959.
[25] H.R. Cederkvist, A.H. Aastveit, T. Næs, A comparison of methods for testing differences in predictive ability, J. Chemom. 19 (2005) 500–509.
[26] M. Stone, Cross-validatory choice and assessment of statistical predictions, J. R. Stat. Soc. Ser. B – Stat. Methodol. 36 (1974) 111–147.

Biochemical and Biophysical Research Communications 420 (2012) 210–215

Contents lists available at SciVerse ScienceDirect

Biochemical and Biophysical Research Communications

journal homepage: www.elsevier.com/locate/ybbrc

Toxicoproteomic analysis of a mouse model of nonsteroidal anti-inflammatory drug-induced gastric ulcers

Kaname Ohyama [a,b,*], Akina Shiokawa [a], Kosei Ito [b,c], Ritsuko Masuyama [c], Tomoko Ichibangase [d], Naoya Kishikawa [a], Kazuhiro Imai [d], Naotaka Kuroda [a]

[a] Department of Environmental and Pharmaceutical Sciences, Graduate School of Biomedical Sciences, Nagasaki University, Nagasaki, Japan
[b] Nagasaki University Research Centre for Genomic Instability and Carcinogenesis (NRGIC), Nagasaki, Japan
[c] Department of Cell Biology, Graduate School of Biomedical Sciences, Nagasaki University, Nagasaki, Japan
[d] Research Institute of Pharmaceutical Sciences, Musashino University, Nishitokyo-shi, Tokyo, Japan

ARTICLE INFO

Article history:
Received 1 March 2012
Available online 9 March 2012

Keywords:
Nonsteroidal anti-inflammatory drugs
Gastric ulceration
Fluorogenic derivatization-liquid chromatography tandem mass spectrometry
Toxicoproteomics

ABSTRACT

Nonsteroidal anti-inflammatory drugs (NSAIDs) are valuable agents; however, their use has been limited by their association with mucosal damage in the upper gastrointestinal tract. NSAIDs inhibit cyclooxygenase and consequently block the synthesis of prostaglandins, which have cytoprotective effects in gastric mucosa; these effects on prostaglandins have been thought to be major cause of NSAID-induced ulceration. However, studies indicate that additional NSAID-related mechanisms are involved in formation of gastric lesions. Here, we used a toxicoproteomic approach to understand cellular processes that are affected by NSAIDs in mouse stomach tissue during ulcer formation. We used fluorogenic derivatization-liquid chromatography-tandem mass spectrometry (FD-LC-MS/MS)—which consists of fluorogenic derivatization, separation and fluorescence detection by LC, and identification by LC-tandem mass spectrometry—in this proteomic analysis of pyrolic stomach from control and diclofenac (Dic)-treated mice. FD-LC-MS/MS results were highly sensitive; 10 differentially expressed proteins were identified, and all 10 were more highly expressed in Dic-treated mice than in control mice. Specifically, expression levels of 78 kDa glucose-regulated protein (GRP78), heat shock protein beta-1 (HSP27), and gastrin were more than 3-fold higher in Dic-treated mice than in control mice. This study represents a first step to ascertain the precise actors of early NSAID-induced ulceration.

1. Introduction

Nonsteroidal anti-inflammatory drugs (NSAIDs) are some of the most prescribed drugs worldwide; however, their use has been limited by their association with mucosal injury to the upper gastrointestinal tract. As many as 25% of chronic NSAIDs users may develop ulcer disease, and 2–4% of the ulcers may bleed or perforate [1,2]. In the United States, these gastrointestinal events result in more than 100,000 hospital admissions annually and between 7000 and 10,000 deaths [3]. NSAIDs inhibit cyclooxygenase (COX) and consequently block the synthesis of prostaglandins, which have cytoprotective effects in gastric mucosa; this has been thought to be the major mechanism of the NSAID-induced ulceration [4]. However, there is some evidence that COX inhibition is not the sole mechanism by which NSAIDs cause gastrotoxic effects, suggesting that formation of gastric lesions result from other NSAID-mediated processes [5].

Proteomics is the large-scale study of gene expression at the protein level, and it provides information on dynamic cellular activity. As an integration of proteomics, toxicology, and bioinformatics, toxicoproteomics mainly focuses on changes in protein expression in cells or tissues following or during exposure to toxins, including pharmaceuticals [6,7]. Therefore, toxicoproteomic analysis of stomach tissue is a good approach to understand the cellular processes that result in NSAID-induced gastric ulcer; however, such analysis has been not yet performed.

In proteomic studies, comparative expression profiling of proteins has been usually performed using two-dimensional electrophoresis (2-DE). However, the 2-DE method has some drawbacks with regard to the reproducibility of the data. Imai and colleagues developed an easily reproducible and highly sensitive proteomic approach, fluorogenic derivatization-liquid

Abbreviations: Dic, diclofenac; ER, endoplasmic reticulum; FD-LC-MS/MS, fluorogenic derivatization-liquid chromatography-tandem mass spectrometry; GRP78, 78 kDa glucose-regulated protein; HSP27, heat shock protein beta-1; MAPK, mitogen-activated protein kinase; NSAIDs, nonsteroidal anti-inflammatory drugs.

* Corresponding author at: Department of Environmental and Pharmaceutical Sciences, Graduate School of Biomedical Sciences, Nagasaki University, 1-14 Bunkyo-machi, Nagasaki 852-8521, Japan. Fax: +81 95 819 2446.
E-mail address: k-ohyama@nagasaki-u.ac.jp (K. Ohyama).

0006-291X/$ - see front matter © 2012 Elsevier Inc. All rights reserved.
http://dx.doi.org/10.1016/j.bbrc.2012.03.009

chromatography-tandem mass spectrometry (FD-LC-MS/MS) [8–10]. This method involves fluorogenic derivatization of proteins, followed by high-performance liquid chromatography (LC) of the derivatized proteins, isolation of those proteins that are differentially expressed in treatment groups, enzymatic digestion of the isolated proteins, and identification of the isolated proteins via LC-tandem MS using a database-searching algorithm. This method enables highly sensitive detection of proteins due to the fluorogenic derivatization which utilizes a non-fluorescent reagent to yield highly fluorescent products.

The aim of this study was to use FD-LC-MS/MS to understand the cellular processes in gastric tissues that are affected by administration of diclofenac (Dic) which is one of NSAIDs most frequently used in clinical setting. To our knowledge, this report describes the first comprehensive analysis of differential protein expression in stomach tissue using a mouse model of NSAID-induced gastric lesions.

2. Materials and methods

2.1. Animal treatment and tissue processing

Male C57BL/6J mice (9 weeks old) were purchased from Japan SLC (Nagasaki, Japan) and acclimatized for 1 week before experiment. Animal care and experimental procedures were performed in accordance with the Guide for the Care and Use of Laboratory Animals (National Institute of Health) with approval from the Institutional Animal Care and Use Committee of the Graduate School of Biomedical Sciences, Nagasaki University. Mice received a single intraperitoneal injection of Dic (0.1 g/kg dissolved in saline, Tokyo Chemical Industry, Tokyo, Japan) or of saline alone, as a negative control. The animals were deprived of food but had free access to tap water for 24 h prior Dic or saline injection. Pyloric stomach samples for FD-LC-MS/MS analysis were isolated from each mouse 6 h after saline or Dic was administered. Each sample was immediately rinsed with phosphate buffer saline and frozen at −196 °C. Samples were homogenized using the Frozen Cell Crasher (Microtec Co. Ltd., Chiba, Japan). Four mice were used in each experimental group.

2.2. Histologic staining of NSAID-induced gastric lesions

The stomachs were fixed with 10% neutral buffered formalin, embedded in paraffin, and then cut into sections (4 μm thick) at 1 mm horizontal intervals from the fundus to the pylorus; these sections were stained with hematoxylin–eosin (H&E). We examined the stomach tissues collected at 6 h and 24 h after treatment.

2.3. Extraction of proteins and determination of total protein concentration

Each sample of homogenized pyloric stomach tissue (50 mg) was suspended in 250 μl of 10 mM 3-[(3-cholamidopropyl)-dimethylammonio] propanesulfonate (CHAPS) solution (Dojindo Laboratories, Kumamoto, Japan), and the homogenates were centrifuged at 5000*g* for 15 min at 4 °C. The supernatant of each sample was then collected and stored as the soluble fraction at −80 °C until use. The total protein content of each supernatant sample was determined using the Quick Start Bradford Protein assay kit (Bio-Rad Laboratory, Hercules, CA, USA) and bovine serum albumin as a protein standard according to the manufacturer's instructions. After determination of total protein content in the soluble fractions, the supernatant was diluted with CHAPS solution to a concentration of 4.0 mg total protein/ml and used as a starting protein sample.

2.4. FD-LC-MS/MS method

A 10 μl volume of sample was combined with 85 μl of a mixture of 0.83 mM tris(2-carboxyethyl)phosphine hydrochloride (Tokyo Chemical Industry), 3.33 mM ethylenediamine-*N*,*N*,*N*′,*N*′-tetraacetic acid (Dojindo Laboratories), and 16.6 mM CHAPS in 6 M guanidine hydrochloride buffer solution (pH 8.7, Tokyo Chemical Industry). Then, this sample was subsequently mixed with 5 μl of 140 mM 7-chloro-*N*-[2-(dimethylamine)ethyl]-2,1,3-benzoxadiazole-4-sulfonamide (DAABD-Cl, Tokyo Chemical Industry), which is the fluorogenic derivatization reagent, in acetonitrile (Merck KGaA, Darmstadt, Germany). After each reaction mixture was incubated in a 50 °C water bath for 5 min, 3 μl of 20% trifluoroacetic acid (TFA, Nacalai Tesque, Kyoto, Japan) was added to each sample to stop the derivatization reaction. A portion (20 μl) of each reaction mixture (8 μg protein) was injected into the HPLC-fluorescence detection system consisting of a Shimadzu Prominence series HPLC system (Kyoto, Japan), a fluorescence detector (Shimadzu RF-10 A_xL; λex. 395 nm; λem. 505 nm), and a Sunniest C8-WP column (ChromaNik Technologies, Tokyo, Japan) at a flow rate of 0.55 ml/min and a column temperature of 60 °C. The mobile phase consisted of 0.1% TFA in (A) water and (B) acetonitrile. The gradient elution was established with the following condition: 10% B held for 10 min; to 18% B in 30 min; to 32% B in 130 min; to 37% B in 215 min; to 42% B in 411 min; to 46% B in 486 min; to 52% B in 569 min; to 65% B in 600 min; to 70% B in 610 min. Corresponding peak heights were compared to identify differential protein profiles. Each subject protein in eluant recovered from the above HPLC system was concentrated into a 5 μl volume under reduced pressure, and these concentrates were used in subsequent identification procedures. The residue was diluted with 240 μl of 50 mM ammonium bicarbonate solution (pH 7.8) (Nacalai Tesque), 5 μl of 10 mM calcium chloride (Nacalai Tesque), and 5 μl of 20 ng/μl trypsin (Promega, Wisconsin, WI, USA), and the resultant mixtures were incubated for 6 h at 37 °C. Each mixture was then concentrated to 20 μl under reduced pressure. Each peptide mixture was subjected to an LC-electrospray ionization-tandem mass spectrometer (LTQ XL, Thermo Fisher Scientific, Waltham, MA, USA) equipped with the custom nanoLC system consisting of an LC pump (LC-20AD, Shimadzu) with LC flow splitter (Accurate, Dionex, Sunnyvale, CA, USA) and an HCT PAL autosampler (CTC Analytics, Zwingen, Switzerland). The sample was loaded onto a precolumn (300 μm i.d. × 5.0 mm, L-C-18, Chemicals and Evaluation and Research Institute, Tokyo, Japan) in the injection loop and washed using 0.1% TFA in 2% acetonitrile. Peptides were separated and ion-sprayed into MS by a nano HPLC column (75 μm i.d. × 15 cm, Acclaim PepMap100C18, 3 μm, Dionex) with a spray voltage from 1.5 to 2.5 kV. Separation was performed, employing a gradient from 5% to 50% mobile phase B (0.1% formic acid in 90% acetonitrile) over a period of 30 min (mobile phase A: 0.1% formic acid); 50% to 100% mobile phase B in 30.1 min; 100% mobile phase B held for 10 min. The mass spectrometer was configured to optimize the duty cycle length with the quality of data acquired by progressing from a full scan of the sample to three tandem MS scans of the three most intense precursor masses (as determined by Xcaliber® software [Thermo Fisher Scientific] in real time). The collision energy was normalized to 35%. All the spectra were measured with an overall mass/charge ratio range of 400–1500. The transfer capillary temperature was set at 200 °C. MS/MS data were extracted using Proteome Discoverer 1.2 (Thermo Fisher Scientific). Spectra were searched against a murine subdatabase from the public non-redundant protein database, International Protein Index version 3.82, maintained by The European Bioinformatics Institute with the following search parameters: mass type, monoisotopic precursor and fragments; enzyme, trypsin (KR); enzyme limits, full enzymatic cleavage allowing up

to two missed cleavages; peptide tolerance, 1.2 Da; fragment ion tolerance, 0.8 Da; ion and ion series calculated, B and Y ions; static modification, C (fluorogenic derivatization); differential modifications, M (oxidation), N and Q (deamidation). Initial searching results were filtered with the following parameter: single, double, and triple charge peptides with a correlation factor (XCorr) greater than 1.6, 2.0, and 2.4, respectively. Ubiquitous keratins and trypsin were excluded as potential matches.

2.5. Statistical analysis

Differences in peak heights between control and Dic-treated mice were determined by unpaired two-tailed Student's *t*-test. $P < 0.05$ was considered to be significant.

3. Results and discussion

3.1. Development of a mouse model of NSAID-induced gastric injury

Our first aim was to develop a mouse model of NSAID-induced gastric ulcer. A single dose of Dic induced multiple ulcers and erosions in mouse stomach mucosa within less than 24 h (Fig. 1). Following Dic injection, the damage observed after 24 h was more severe and wider than that observed after 6 h. The lesions were most abundant in the pyloric region; only a few lesions were evident in the body or fundic regions of stomachs, and the duodenum was free of any apparent ulceration. NSAID-induced ulcerations in clinical settings are most frequently found in the pyloric stomach [11,12], and our finding was consistent with this observation. Therefore, the mouse model used here was adequate for our subsequent toxicoproteomic study, and this study focused on profiling differential protein expression in the pyloric stomach. The number of ulcers in mouse intestine was reported not to be significantly changed at longer than 6 h post-treatment [13]. Also, understanding the pathogenesis during early ulcer formation is effective for the prevention; therefore, we decided to collect tissue samples at 6 h after administration of Dic or saline for the proteomic analysis.

3.2. Differential profiling and protein identification

Typical chromatograms from FD-LC of control and Dic-dosing samples are depicted in Fig. 2. The height of each peak indicates the expression level of an individual protein. Expression of 10 proteins differed significantly between Dic-treated and saline-treated mice ($P < 0.05$; Table 1); the peaks representing these proteins are numbered in Fig. 2. Each differentially expressed protein was more highly expressed in the Dic group than in the control group. The expression of 78 kDa glucose-regulated protein (GRP78, Peak No. 7), heat shock protein beta-1 (HSP27, Peak No. 6), and gastrin (Peak No. 1) was more 3-fold higher in the Dic-dosing group than in the control group.

Endoplasmic reticulum (ER) is an organelle that participates in protein synthesis, folding and modification of membrane and secretory proteins, and maintenance of cellular calcium homeostasis. The conditions or stresses that interfere with ER function are called ER stress [14]. Chemical toxins and oxidative stress can all disrupt ER function and result in ER stress [15–17]. Cells experiencing ER stress initiate the ER stress response, which facilitates protein refolding and prevents aggregation of irreversible misfolding proteins. GRP78 (Peak No. 7) is a resident ER protein and a member of the HSP70 family of charperones; GRP78 binds to hydrophobic patches of nascent polypeptides in ER to prevent protein disaggregation. GRP78 also plays a key role in ER stress-induced apoptosis signaling. Cells initially adapt to ER stress by inducing ER-resident stress proteins such as GRP78 and GRP94 [14,18,19]; however, if this adaption is not sufficient, ER-initiated apoptosis signaling and proteins such as CCAAT/enhancer-binding protein homologous protein (CHOP), c-Jun-N-terminal kinase (JNK), and caspase-12 are activated [20–22]. GRP78 acts as an apoptotic regulator. Evidence shows that the overexpression of GRP78 might prevent ER stress-induced cell death by reducing levels of CHOP and inducing forma-

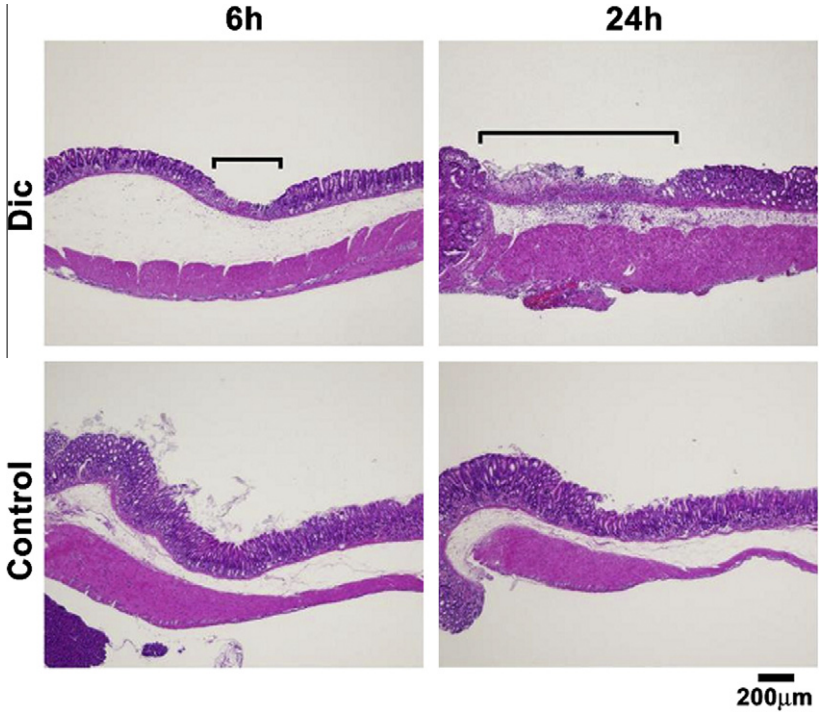

Fig. 1. Representative Dic-induced gastric ulcers in the pyloric region at 6 h and 24 h after treatment in C57BL/6J. H&E staining was performed as described in Material and methods section.

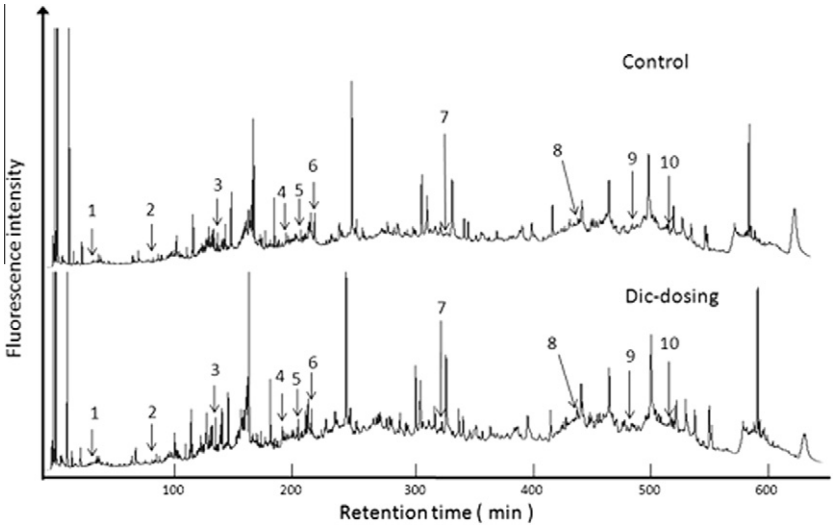

Fig. 2. Representative chromatograms of proteins derivatized with DAABD-Cl in mouse pyloric stomach. The upper and lower chromatograms were obtained with samples from saline-treated and Dic-treated mice, respectively. The peaks of differentially expressed proteins are numbered in each chromatogram.

Table 1
List of proteins identified by FD-LC-MS/MS method.

Peak number[a]	Protein name	Dic-dosing/ control ratio[b]	Molecular mass (kDa)	SEQUEST score	Peptide hit	Coverage by mass	Accession[c]
1	Gastrin	3.7**	11.6	6.85	2	22.77	IPI00319752.1
2	Actin	2.2*	41.7	15.86	3	25.60	IPI00110850.1
3	40S ribosomal protein S20-like	1.7*	12.9	33.55	5	37.39	IPI00987717.1
4	Calponin-1	2.2*	29.1	15.63	4	16.34	IPI00228258.1
5	Aminoacyl tRNA synthase complex-interacting multifunctional protein 1	2.7*	35.1	2.24	1	33.00	IPI00006252.3
6	Heat shock protein beta-1 (HSP27)	4.2**	19.4	21.47	6	38.86	IPI00623819.1
7	78 kDa glucose-regulated protein (GRP78)	5.2**	72.4	55.53	15	23.21	IPI00319992.1
8	ADP/ATP translocase 2	2.0**	32.9	5.36	2	7.38	IPI00127841.3
9	Phosphoglycerate kinase 1	2.3**	44.5	54.58	8	21.58	IPI00555069.3
10	Glutathione *S*-transferase A4 (GST-α)	1.9**	25.5	38.49	4	26.13	IPI00323911.3

[a] Peak numbers correspond to those in Fig. 2.
[b] Dic-dosing/control ratio: the ratio of the amount of a protein in the Dic group relative to that in the control group.
[c] IPI number is simply a series of digits that are assigned consecutively to each sequence processed by the International Protein Index. Significant differences between the control and Dic groups are indicated by $^{*}(P \leqslant 0.05)$ or $^{**}(P \leqslant 0.01)$.

tion of a complex that includes GRP78, caspase-7, and caspase-12 [23–26]. Tsutsumi et al. reported that induction of apoptosis by NSAIDs via a CHOP pathway is involved in NSAID-induced gastric lesion formation [27,28]. They also found that GRP78 was overexpressed in cells exposed to NSAIDs, and they proposed that GRP78 could be developed as an antiulcer drug because it suppresses apoptosis [28].

The heat shock protein (HSP) family has been long associated with a generalized cellular stress response, particularly in terms of chaperoning misfolded proteins. In addition to this well-documented function, HSP27 (Peak No. 6) may mediate cell survival directly. Several studies indicate that HSP27 diminishes the activation of procaspase-9 by inhibiting the interaction between procaspase-9 and cytochrome *c*, thus preventing the proper formation of the apoptosome complex [29,30]. Furthermore, HSP27 can inhibit caspase-3 activity by interacting with the procaspase-3 molecule [29,31]. These observations are consistent with a scenario in which HSP27 inhibits apoptosis by targeting the pathways downstream of the mitochondrial release of cytochrome *c*. Therefore, the overexpression of HSP27 that we observed may indicate that HSP27 expression was elevated for counteracting or suppressing NSAID-induced apoptosis.

Gastrin (Peak No. 1) was originally identified as a potent stimulant of gastric acid secretion and the increased acid secretion may contribute to ulcer formation. Mitogen-activated protein kinase (MAPK) pathways are important signal transduction cascades that link extracellular stimuli to intracellular responses. Among the different MAPK pathways described in the literature (e.g., extracellular signal-regulated kinase pathway, JNK pathway, and p38-MAPK pathway), JNK and p38-MAPK are associated with cellular apoptosis, and p38-MAPK signaling is reportedly necessary for CHOP induction and apoptosis [32]. Gastrin activates the p38-MAPK pathway [33,34]; therefore, gastrin may activate CHOP or enhance activated CHOP and thereby, cause in NSAID-induced ulceration. On the other hand, HSP27 is reportedly phosphorylated by several kinases downstream of p38-MAPK [35,36], and this phosphorylation is induced by ER stress [37]. Recently, Ock et al. reported that indomethacin-induced cytotoxicity was accompanied by HSP27 phosphorylation in cell culture experiments and that HSP27 dephosphorylation protected stomach tissue from indomethacin-induced damage in an animal experiment [38]. Furthermore, the activation of p38-MAPK by gastrin can enhance the cytotoxic effects of phosphorylated HSP27. In these contexts, inhibiting expression or activity of gastrin may help prevent NSAID-induced gastric damage.

Calponin-1 (Peak No. 4) is known to activate protein kinase C (PKC) autophosphorylation [39], and PKC is able to phosphorylate Raf, an upstream activator of MAPK/ERK. Calponin-1 may

up-regulate MAPK by promoting the formation of a signaling complex comprising PKC, Raf, MAPK, and ERK.

We found that glutathione *S*-transferase (GST)-α (Peak No. 10) expression was 1.9-fold higher in the Dic group than in the control group. GST-α may have been overexpressed because it functions in a detoxification system against chemical toxins. Similarly, van Lieshout reported that NSAIDs increased GST-α expression in the upper digestive tract in rats [40].

In this study, COX enzymes were not found to be altered by administration of Dic. This may be because NSAIDs action is not directed towards the transcription or translation of the COX genes but only to the enzymatic activity of the proteins [41,42].

In summary, in order to understand the cellular processes that are altered in a mouse model of NSAID-induced gastric ulceration, FD-LC-MS/MS was applied to differential proteomic analysis of pyloric stomach tissues from saline- and Dic-treated mice. Using this toxicoproteomic method, we identified significantly altered and elevated expression of 10 proteins. Of these proteins, three (GRP78, HSP27, and gastrin) are involved in cellular apoptosis, which is supposed to partially cause for gastric lesions; moreover, expression of these three was more highly elevated than that of the other 7 differentially expressed proteins. Our hypothetical model of NSAID-induced gastric lesion formation is summarized in Fig. 3. This study represents a first step to ascertain the precise actors of early NSAID-induced ulceration. Further analyses of GRP78, HSP27, and gastrin are necessary to determine if they are a potential target for protective intervention against the ulceration.

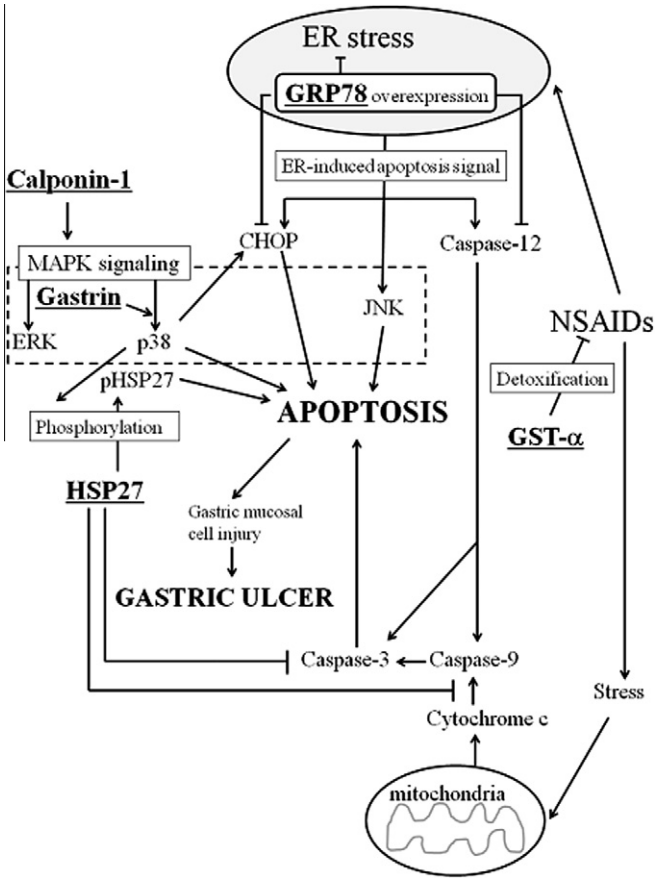

Fig. 3. Hypothetical model of NSAID-induced gastric injury. NSAIDs induce ER stress. Excess ER stress, which cannot be fully ameliorated by chaperones, activates an ER-induced apoptosis signal that leads to activation of p38-MAPK, JNK, and CHOP. GRP78 and HSP27 inhibit CHOP and caspases-3, -9, and -12. Activation of p38-MAPK by gastrin results in acceleration of apoptosis signaling and phosphorylation of HSP27. GST-α detoxifies NSAIDs.

Acknowledgments

This work was supported by the Special Coordination Funds for Promoting Science and Technology of the Ministry of Education, Culture, Sports, Science and Technology (MEXT). This work was supported by The Shimabara Science Promotion Foundation. The authors thank ChromaNik Technologies for kindly supplying Sunniest C8-WP column.

References

[1] F.E. Silverstein, G. Faich, J.L. Goldstein, et al., Gastrointestinal toxicity with celecoxib vs. nonsteroidal anti-inflammatory drugs for osteoarthritis and rheumatoid arthritis: the CLASS study: a randomized controlled trial. Celecoxib Long-term Arthritis Safety Study, JAMA 284 (2000) 1247–1255.
[2] F.L. Lanza, F.K.L. Chan, E.M.M. Quigley, Guidelines for prevention of NSAID-related ulcer complications, Am. J. Gastroenterol. 104 (2009) 728–738.
[3] G. Singh, Recent consideration in nonsteroidal anti-inflammatory drug gastropathy, Am. J. Med. 105 (1998) 31S–38S.
[4] R. Langenbach, S.G. Morham, H.F. Tiano, et al., Prostaglandin synthase 1 gene disruption in mice reduces arachidonic acid-induced inflammation and indomethacin-induced gastric ulceration, Cell 83 (1995) 483–492.
[5] C. Musumba, D.M. Pritchard, M. Pirmohamed, Cellular and molecular mechanisms of NSAID-induced peptic ulcer, Aliment. Pharmacol. Ther. 30 (2009) 517–531.
[6] Y. Ge, R.J. Preston, R.D. Owen, Toxicoproteomics and its application to human health risk assessment, Proteomics Clin. Appl. 1 (2007) 1613–1624.
[7] L.R. Bandara, S. Kennedy, Toxicoproteomics-a new preclinical tool, Drug Discov. Today 7 (2002) 411–418.
[8] M. Masuda, C. Toriumi, T. Santa, et al., Fluorogenic derivatization reagents suitable for isolation and identification of cystein-containing proteins utilizing high-performance liquid chromatography-tandem mass spectrometry, Anal. Chem. 76 (2004) 728–735.
[9] T. Ichibangase, K. Moriya, K. Koike, et al., A proteomic method revealing disease-related proteins in livers of hepatitis-infected mouse model, J. Proteome Res. 6 (2007) 2841–2849.
[10] K. Ohyama, M. Tomonari, T. Ichibangase, et al., A toxicoproteomic study on cardioprotective effects of pre-administration of docetaxel in a mouse model of adriamycin-induced cardiotoxicity, Biochem. Pharmacol. 80 (2010) 540–547.
[11] F.L. Lanza, Endoscopic studies of gastric and duodenal injury after the use of ibuprofen, aspirin, and other nonsteroidal anti-inflammatory agents, Am. J. Med. 13 (1984) 19–24.
[12] J.F. Fries, S.R. Miller, P.W. Spitz, et al., Toward an epidemiology of gastropathy associated with nonsteroidal anti-inflammatory drug use, Gastroenterology 96 (1989) 647–655.
[13] V. Ramirez-Alcantara, A. LoGuidice, U.A. Boelsterli, Protection from diclofenac-induced small intestinal injury by the JNK inhibitor SP600125 in a mouse model of NSAID-associated enteropathy, Am. J. Physiol. Gastrointest. Liver Physiol. 297 (2009) G990–G998.
[14] R.J. Kaufman, Stress signaling from the lumen of endoplasmic reticulum: coordination of gene transcriptional and translational controls, Genes Dev. 13 (1999) 1211–1233.
[15] Y. Kozutsumi, M. Segal, K. Normington, et al., The presence of malfolded proteins in the endoplasmic reticulum signals the induction of glucose-regulated proteins, Nature 322 (1988) 462–464.
[16] K. Mori, Tripartile management of unfolded proteins in the endoplasmic reticulum, Cell 101 (2000) 451–454.
[17] R.V. Rao, H.M. Ellerby, D.E. Bredesen, Coupling endoplasmic reticulum stress to the cell death program, Cell Death Differ. 11 (2004) 372–380.
[18] S.K. Wooden, L.J. Li, D. Navarro, et al., Transactivation of the grp78 promoter by malfolded proteins, glycosylation block, and calcium ionophore is mediated through a proximal region containing a CCAT motif which interacts with CTF/NF-I, Mol. Cell. Biol. 11 (1991) 5612–5623.
[19] H. Liu, R.C. Bowes III, B. van de Water, et al., Endoplasmic reticulum chaperones GRP78 and calreticulin prevent oxidative stress, Ca^{2+} disturbances, and cell death in renal epithelial cells, J. Biol. Chem. 272 (1997) 21751–21759.
[20] S. Oyadomari, M. Mori, Roles of CHOP/GADD153 in endoplasmic reticulum stress, Cell Death Differ. 11 (2004) 381–389.
[21] F. Urano, X. Wang, A. Bertolotti, et al., Coupling of stress in the ER to activation of JNK protein kinases by transmembrane protein kinase IRE1, Science 287 (2000) 664–666.
[22] N. Morishima, K. Nakanishi, H. Takenouchi, et al., An endoplasmic reticulum stress-specific caspase cascade in apoptosis. Cytochrome *c*-independent activation of caspase-9 by caspase-12, J. Biol. Chem. 277 (2002) 34287–34294.
[23] J.A. Morris, A.J. Dorner, C.A. Edwards, et al., Immunoglobulin binding protein (Bip) function is required to protect cells from endoplasmic reticulum stress

but is not required for the secretion of selective proteins, J. Biol. Chem. 272 (1997) 4327–4334.
[24] T. Nakagawa, H. Zhu, N. Morishima, et al., Caspase-12 mediates endoplasmic reticulum-specific apoptosis and cytotoxicity by amyloid-beta, Nature 403 (2000) 98–103.
[25] H.Y. Fu, T. Minamino, O. Tsukamoto, et al., Overexpression of endoplasmic reticulum-resident chaperone attenuates cardiomyocyte death induced by proteasome inhibition, Cardiovasc. Res. 79 (2008) 600–610.
[26] M.S. Gorbatyuk, T. Knox, M.M. LaVail, et al., Restoration of visual function in P23H rhodopsin transgenic rats by gene delivery of Bip/Grp78, Proc. Natl. Acad. Sci. USA 107 (2010) 5961–5966.
[27] W. Tomisato, S. Tsutsumi, T. Hoshino, et al., Role of direct cytotoxic effects of NSAIDs in the induction of gastric lesions, Biochem. Pharmacol. 67 (2004) 575–585.
[28] S. Tsutsumi, T. Gotoh, W. Tomisato, et al., Endoplasmic reticulum stress response is involved in nonsteroidal anti-inflammatory drug-induced apoptosis, Cell Death Differ. 11 (2004) 1009–1016.
[29] C.G. Concannon, S. Orrenius, A. Samali, Hsp27 inhibits cytochrome *c*-mediated caspase activation by sequestering both pro-caspase-3 and cytochrome *c*, Gene Expr. 9 (2001) 195–201.
[30] C. Garrido, J.M. Bruey, A. Fromentin, et al., HSP27 inhibits cytochrome *c*-dependent activation of procaspase-9, FASEB J. 13 (1999) 2061–2070.
[31] P. Pandey, R. Farber, A. Nakazawa, et al., Hsp27 functions as a negative regulator of cytochrome *c*-dependent activation of procaspase-3, Oncogene 19 (2000) 1975–1981.
[32] T. DeVries-Seimon, Y. Li, P.M. Yao, et al., Cholesterol-induced macrophage apoptosis requires ER stress pathways and engagement of the type A scavenger receptor, J. Cell Biol. 171 (2005) 61–73.
[33] S. Dehez, L. Daulhac, A. Kowalski-Chauvel, et al., Gastrin-induced DNA synthesis requires p38-MAPK activation via PKC/Ca^{2+} and Src-dependent mechanisms, FEBS Lett. 496 (2001) 25–30.
[34] D. Subramaniam, S. Ramalingam, R. May, et al., Gastrin-mediated interleukin-8 and cyclooxygenase-2 gene expression: differential transcriptional and posttranscriptional mechanism, Gastroenterology 134 (2008) 1070–1082.
[35] D. Stokoe, D.G. Campbell, S. Nakielny, et al., MAPKAP kinase-2; a novel protein kinase activated by mitogen-activated protein kinase, EMBO J. 278 (1992) 3985–3994.
[36] L. New, Y. Jiang, M. Zhao, et al., PRAK, a novel protein kinase regulated by the p38 MAP kinase, EMBO J. 17 (1998) 3372–3384.
[37] H. Ito, I. Iwamoto, Y. Inaguma, et al., Endoplasmic reticulum stress induces the phosphorylation of small heat shock protein, Hsp27, J. Cell Biochem. 95 (2005) 932–941.
[38] C.Y. Ock, Y.J. Lim, Y.J. Kim, et al., Acid pump antagonist-provoked HSP27 dephosphorylation and accentuation rescues stomach from indomethacin-induced damages, J. Dig. Dis. 12 (2011) 71–81.
[39] B. Leinwever, A.M. Parissenti, C. Gallant, et al., Regulation of protein kinase C by the cytoskeletal protein calponin, J. Biol. Chem. 275 (2000) 40329–40336.
[40] E.M.M. van Lieshout, D.M. Tiemessen, W.H.M. Peters, et al., Effects of nonsteroidal anti-inflammatory drugs on glutathione *S*-transferases of the rat digestive tract, Carcinogenesis 18 (1997) 485–490.
[41] M. Barrios-Rodiles, K. Keller, A. Belley, et al., Nonsteroidal antiinflammatory drugs inhibit cyclooxygenase-2 enzyme activity but not mRNA expression in human macrophages, Biochem. Biophys. Res. Commun. 225 (1996) 896–900.
[42] S.E. Elliott, W. McKnight, G. Cirino, et al., A nitric oxide-releasing nonsteroidal anti-inflammatory drug accelerates gastric ulcer healing in rats, Gastroenterology 109 (1995) 524–530.

Biochemical and Biophysical Research Communications

Correspondence regarding production may be sent to:

Biochemical and Biophysical Research Communications, Elsevier Inc.

525 B Street, Suite 1800, San Diego, California 92101-4495, USA
Telephone +1 (619) 699-6857, Fax +1 (619) 699-6859, E-mail bbrc@elsevier.com

0006-291X(20120330)420:1;1-V

Cover photo. The cover photo graphic is taken from figure 1A of the paper 'Susceptibility of Antiviral Drugs Against 2009 Influenza A (H1N1) Virus' published in the journal (BBRC Volume 385, pages 390–394). It is reproduced by kind permission of the authors – Supot Hannongbua, et al.